Eur. Phys. J. Spec. Top. (2024) 233:1–208
https://doi.org/10.1140/epjs/s11734-023-01076-0

THE EUROPEAN PHYSICAL JOURNAL SPECIAL TOPICS

Review

The CompactLight Design Study

G. D'Auria[1,a], E. Adli[34], M. Aicheler[12], A. Aksoy[20], D. Alesini[11], R. Apsimon[4,8], J. Arnsberg[9], R. Auchettl[6], A. Bainbridge[3,4], K. Balazs[2], D. Bantekas[18], J. Bedolla[4,8], M. Behtouei[11], M. Bellaveglia[11], M. vd Berg[5], A. Bernhard[9], A. Bignami[18,33], M. Breitenbach[27], M. Breukers[5], G. Burt[4,8], J. Cai[4,8], M. Calvi[23], F. Cardelli[11], M. Carpanese[7], H. M. Castaneda Cortes[3,4], A. Castilla[4,8], A. Cianchi[26], J. Clarke[3,4], L. Cowie[3,4], M. Croia[11], A. Cross[25], M. Danailov[1], G. Dattoli[7], S. Deleval[2], S. Di Mitri[1], M. Diomede[11], R. Dowd[6], D. Dunning[3,4], J. Easton[25], W. Fang[17], S. Fatehi[9], A. Faus-Golfe[22], M. Ferianis[1], M. Ferrario[11], L. Ficcadenti[11], A. Gallo[11], E. Gazis[18,30], N. Gazis[18,33], R. Geometrante[21], J. Gethmann[9], R. Gioppo[1], A. Giribono[11], D. González-Iglesias[16], V. Goryashko[13], S. Grohmann[9], Q. Gu[17], Y. Han[22], A. Hinton[3,4], A. Hobi[27], R. Hoekstra[31,32], X. Huang[17], M. Jacewicz[13], J. Jones[3,4], F. Kaertner[35], A. Karagiannaki[29], M. Kokole[28], R. Kotitsa[30], D. Kotsopoulos[29], B. Krasch[9], A. Latina[2], P. Lepercq[22], X. Liu[2], T. G. Lucas[10,24,32], O. J. Luiten[10], M. Maheshwari[3,4], J. Mahnic[28], A. Mak[13], J. Marcos[15], E. Marin[15], K. Marinov[3,4], B. G. Martínez[16], B. Mercier[22], M. Migliorati[11,14], T. Milharcic[28], A. Mostacci[11,14], R. Mu noz[15], V. Musat[2], P. H. A. Mutsaers[10], Z. Nergiz[20], F. Nguyen[7], L. Nix[25], L. Palumbo[11,14], M. Parodi[2], R. Pavlica[21], L. Pellegrino[11], D. E. Pereira[16], F. Perez[15], A. Petralia[7], L. Piersanti[11], J. Pockar[28], K. Pramatari[29], H. Priem[5], U. Primozic[28], R. Rassool[19], S. Reiche[23], P. Revilak[27], S. C. Richter[2,9], R. Rochow[1], C. Rossi[2], P. Salén[13], T. Schmidt[23], D. Schoerling[2], D. Schulte[2], J. Scifo[11], S. Sheehy[19], B. Shepherd[3,4], B. Spataro[11], S. Stapnes[2], X. F. D. Stragier[10], I. Syratchev[2], C. Tabacco[1], J. Tan[17], E. Tanke[18,33], G. Taylor[19], I. Telahi[30], N. Thompson[3,4], E. Trachanas[18,33], K. S. Tzanetou[30], C. Vaccarezza[11], J. Vainola[12], A. Vannozzi[11], M. Volpi[19], C. Wang[17], P. Williams[3,4], X. Wu[2], W. Wuensch[2], J. Yap[19], M. Zangrando[1], K. Zhang[23], L. Zhang[25], Y. Zhao[2], Z. Zhao[17], and D. Zhu[6]

[1] Elettra-Sincrotrone Trieste S.C.p.A., AREA Science Park, Basovizza, 34149 Trieste, Italy
[2] CERN, 1211 Geneva 23, Switzerland
[3] ASTeC, STFC Daresbury Laboratory, Keckwick Lane, Warrington WA4 4AD, UK
[4] Cockcroft Institute, SciTech Daresbury, Warrington WA4 4AD, UK
[5] VDL ETG Precision, 5652 Eindhoven, North Brabant, The Netherlands
[6] ANSTO–Australian Synchrotron, Clayton, Australia
[7] ENEA C. R. Frascati-Fusion and Nuclear Safety Department, Via E. Fermi 45, 00044 Frascati (Roma), Italy
[8] Engineering Department, Lancaster University, Lancaster LA1 4YR, UK
[9] Karlsruhe Institute of Technology (KIT), Karlsruhe, Germany
[10] Eindhoven University of Technology (TU/e), Eindhoven, The Netherlands
[11] INFN–Laboratori Nazionali di Frascati, Via E Fermi 54, 00044 Frascati (Roma), Italy
[12] University of Helsinki-Helsinki Institute of Physics, Helsinki, Finland
[13] FREIA Laboratory, Department of Physics and Astronomy, Uppsala University, Uppsala, Sweden
[14] Sapienza, University of Rome, Rome, Italy
[15] ALBA Synchrotron-CELLS, Barcelona, Spain
[16] Instituto de Física Corpuscular (IFIC), University of Valencia-CSIC, Valencia, Spain
[17] Shanghai Institute of Applied Physics, Shanghai, China
[18] Department of Physics, Institute of Accelerating Systems and Applications (IASA), Panepistimioupoli Zografou, Athens, Greece
[19] ARC Centre of Excellence for Particle Physics, The University of Melbourne, Melbourne, Australia
[20] Institute of Accelerator Technology, Ankara University, Ankara, Turkey
[21] Kyma S. p. A., AREA Science Park, 34149 Trieste, Italy
[22] CNRS, Centre National de la Recherche Scientifique, Laboratoire de Physique des 2 infinis Irène Joliot-Curie–IJCLab, 91405 Orsay Cedex, France
[23] Paul Scherrer Institute, Forschungsstrasse 111, 5232 Villigen PSI, Switzerland
[24] Free University Amsterdam, De Boelelaan 1105, 1081 HV Amsterdam, The Netherlands
[25] The University of Strathclyde, 16 Richmond St, Glasgow, Scotland G1 1XQ, UK
[26] Tor Vergata University of Rome, Via Cracovia 50, 00133 Rome, Italy
[27] Bilfinger Noell GmbH, Rotterdam, The Netherlands
[28] Kyma Tehnologija d.o.o., Kraška ulica 2, 6210 Sežana, Slovenia
[29] Athens University of Economics and Business, 76 Patission Street, 10434 Athens, Greece
[30] National Technical University of Athens, Patission Complex 42, Patission Street, 10682 Athens, Greece

[31] University of Groningen, 9747 AG Groningen, The Netherlands
[32] Advanced Research Center for Nanolithography ARCNL, Science Park 106, 1098 XG Amsterdam, The Netherlands
[33] European Spallation Source ERIC, ESS Campus, Partikelgatan 2, 224 84 Lund, Sweden
[34] University of Oslo, P. O. Box 1072, Blindern, 0316 Oslo, Norway
[35] Center for Free-Electron Laser Science, Notkestraße 85, 22607 Hamburg, Germany

Received 14 April 2023 / Accepted 7 December 2023 / Published online 22 March 2024

Abstract CompactLight is a Design Study funded by the European Union under the Horizon 2020 research and innovation funding programme, with Grant Agreement No. 777431. CompactLight was conducted by an International Collaboration of 23 international laboratories and academic institutions, three private companies, and five third parties. The project, which started in January 2018 with a duration of 48 months, aimed to design an innovative, compact, and cost-effective hard X-ray FEL facility complemented by a soft X-ray source to pave the road for future compact accelerator-based facilities. The result is an accelerator that can be operated at up to 1 kHz pulse repetition rate, beyond today's state of the art, using the latest concepts for high brightness electron photoinjectors, very high gradient accelerating structures in X-band, and novel short-period undulators. In this report, we summarize the main deliverable of the project: the CompactLight Conceptual Design Report, which overviews the current status of the design and addresses the main technological challenges.

1 Executive summary

Synchrotron radiation (SR) is a fundamental and indispensable research tool in various scientific and technological fields and their applications, including materials science, condensed-matter physics, atomic and molecular physics, life science and medicine, chemistry, and environmental sciences. For this reason, the use of synchrotron radiation has increased tremendously in the last decades, as testified by the number of synchrotron light sources built to serve the users' communities across many scientific and engineering disciplines.

The latest generation of SR sources is based on free electron lasers (FELs) driven by linacs. These facilities, with sub-picosecond pulse lengths and wavelengths down to the hard X-ray range, feature unprecedented performance in peak brightness, exceeding by many orders of magnitude that of third-generation synchrotrons and enabling important complementary research opportunities. Despite the great scientific and technological benefits that X-ray FELs can provide, a few such facilities are currently operating worldwide due to the high costs and complexity preventing their wide diffusion. Only major accelerator laboratories have the resources and expertise to construct and operate them.

With the launch of this H2020 design study, funded by the European Commission under GA No. 777431, the CompactLight Collaboration aims to facilitate the widespread development of X-ray FEL facilities across Europe and beyond by making them more affordable to construct and operate through an optimum combination of emerging and innovative accelerator technologies. A partnership of 23 international laboratories and academic institutions, three private companies and 5 third parties has been created, which brings together the world's leading experts in this field.

The FEL specifications, based on this design study, have been driven by the demands of its potential users, considering the photon characteristics required by their current and desired future experiments. To reach these objectives, the CompactLight Conceptual Design Report (CDR) has been based on the latest concepts for bright electron photoinjectors, high-gradient X-band structures at 12 GHz, and innovative short-period undulators.

Compared to existing facilities for the same operating wavelengths, the technical solutions adopted ensure that the CompactLight facility can operate with a lower electron beam energy and will have a significantly more compact footprint—the total length of the facility is just over 480 m, which is, for example, more than 250 m less than the total length of SwissFEL. These enhancements make the proposed facility more attractive and more affordable to build and operate. As suggested by the users' wish list, the key elements considered for the design study have been the following:

- High FEL stability in pulse energy and pulse duration.
- FEL synchronization better than 10 fs.
- Photon pulse duration less than 50 fs.
- A repetition rate from 1 Hz up to 1 kHz.
- FEL pump-probe capabilities with a large photon energy difference.

[a] e-mail: gerardo.dauria@elettra.eu (corresponding author)

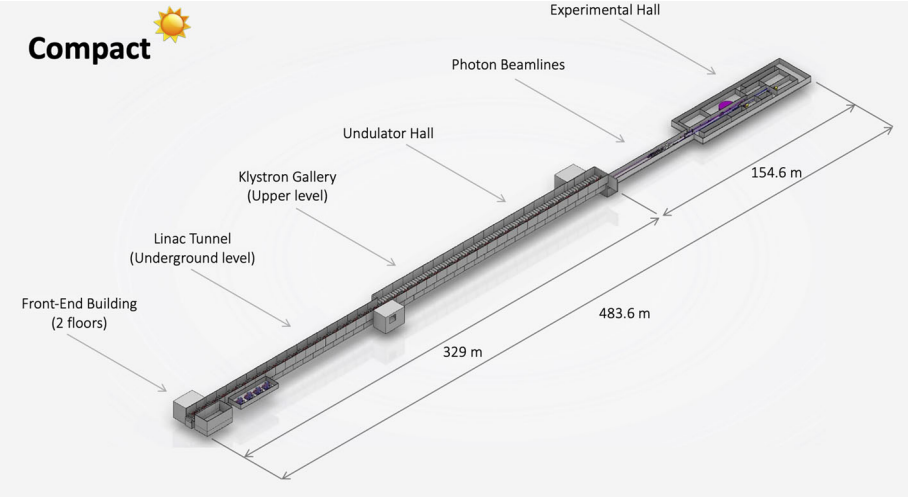

Fig. 1 View of the XLS facility. The total length is 483.6 m

- Small focused spot size.
- Variable polarization, linear and elliptical.
- Tunability up to higher photon energies.
- Two-bunch operation.
- Two-color pulse generation.

Based on these requirements, CompactLight has been designed as a hard X-ray facility, covering the wavelength range from 0.8 Å up to 5 nm (16–0.25 keV) with two separate FEL beamlines:

(i) a soft X-ray (SXR) FEL able to deliver photons from 5.0 nm to 0.6 nm (0.25–2 keV) operating up to 1 kHz repetition rate (high rep rate);
(ii) a hard X-ray FEL source (HXR) ranging from 6.0 Å to 0.8 Å (2–16 keV) with maximum 100 Hz repetition rate (low rep rate).

Key elements proposed in the design are the dual-bunch photoinjector and the two-beam deflectors adopted for the linac. Both give huge flexibility for the facility operation, with different combinations of SXR and HXR operating modes at high and low repetition rates, as requested by the users.

The design presented in the CDR includes a facility baseline layout and two main upgrades, with the most advanced option allowing the simultaneous operation of both FEL beamlines in SXR/HXR pump-probe configuration at 100 Hz repetition rate. It also includes a preliminary evaluation of the experimental hall, the photon beamlines and the X-ray optics for controlling the focus, intensity, and spectral bandwidth of produced photons. An indicative layout for the buildings presented as a 3-D CAD model is shown in Fig. 1. For more details on CompactLight integration, services, and cost analyses, see [1].

The CDR also includes preliminary evaluations of a soft X-ray FEL and an extremely compact and relatively inexpensive photon source based on inverse compton scattering (ICS) using CompactLight technology. Compared with the full CompactLight facility, this soft X-ray FEL can be considered a quite affordable solution in terms of cost and complexity in case of limited funding capabilities. In addition, the ICS source, with its wide range of applications, is very attractive and can be easily installed and operated on university campuses, small laboratories, and hospitals.

Various innovations and advanced systems have been designed specifically for the CompactLight facility. In particular:

- **Electron source**. For the electron source, we have designed an innovative C-band photoinjector with an operating gradient up to 180 MV/m, that can deliver two 75 pC e-bunches per RF pulse, with less than 0.2 mmmrad normalized emittance. The remaining part of the booster linac, up to the first bunch compression, at 300 MeV, consists of a full C-band linac.
- **Beam linearizer** The development of very high-frequency linearizers is of broad importance for accelerators that require short bunches, including high-frequency RF and plasma accelerators. We have designed a Ka-band system operating at 36 GHz for the XLS longitudinal phase space linearization. The Ka-band system is based on a 300 mm traveling-wave structure, powered with 3 MW RF and operating with an integrated gradient of

12.7 MV. We have identified two possible options for the RF source: a high-order mode multi-beam klystron (HOM MBK) and a gyroklystron.

- **Sub-harmonic deflecting system** An S-band (3 GHz) sub-harmonic deflecting structure, operated in the TM110 mode, has been designed to separate the two bunches before the injection into a septum magnet, which separates them into the two FEL lines. The transverse separation between the two beams at the septum is 2.5 mm. The spacing between the two bunches, 6 or 10 X-band RF cycles, is 1.5 or 2.5 RF cycles at the S-band. Thus, the two bunches can be placed at the crest and trough of the RF cycle of the sub-harmonic deflector, so that the kicks applied to the two bunches are in opposite directions and the separation is maximized for a given kick voltage.
- **Undulator chain** In the CompactLight design, the same undulator line is used in both the SXR and the HXR FEL lines. Particular care has been taken to ensure that the undulator parameters are chosen appropriately to balance the output performance equally between the SXR and the HXR. This feature allows the facility to be more compact and cost-effective. The undulator chain foresees an innovative helical superconducting undulator, with 13 mm period and 4.2 mm gap followed by an APPLE X afterburner with 19 mm period and 5 mm gap. The length of each module is 1.75 m.

Each of these innovative systems can also be used "standalone" in a variety of accelerator applications (i.e., future high-energy particle colliders, compact accelerators for medicine, plasma drivers, etc.) where conventional systems cannot meet the challenging performance requested. These systems can be considered as "building blocks" both for large and small photon facilities, based on low- or high-energy electron linacs, with different complexities and costs, that can be installed and operated from large Scientific Infrastructures or at the level of University laboratories, with limited space and funding capabilities, i.e., inverse compton sources (ICS), nowadays strongly growing [2, 3].

In conclusion, this CDR presents the design of an extremely bright and compact hard X-ray FEL beyond today's state of the art. It describes the technical concepts and the parameters used for the facility design, with the objective of providing a reference document for future FEL designers. It also represents an effective solution that makes X-ray FELs more affordable to construct and operate, even for small laboratories or academia with limited space and funding capabilities.

2 Introduction

In the last decades, the X-ray research community has witnessed significant increases in the performances of synchrotron light sources, with a rapid succession of first, second, and third generations of X-ray light source facilities constructed worldwide. From the early 1950s to the 1970s, the cycling electron synchrotrons, developed for physics research, were considered the first-generation light sources. At that time, Synchrotron Radiation (SR) was mostly considered a parasitic effect responsible for unwanted energy loss and its properties were studied to validate theoretical models. The power of using SR for spectroscopy and diffraction was first realized in the 1960s and 1970s. In the mid-1970s, the demand for SR in Europe, Japan, and the US led to the construction of second-generation light sources—rings fully dedicated to SR research. The bending electromagnets in the accelerator were the primary sources of the SR. In the late 1980s, other specialized devices, periodic magnetic structures called wigglers and undulators, were specifically developed to generate high-intensity radiation. Third-generation SR sources were based upon these devices, with dedicated straight sections in the storage rings for their insertion. The first third-generation sources began operation in the early 1990s.

The main figure of merit for SR is the brightness, which defines the intensity of radiation within a given bandwidth around the desired wavelength, focused onto a sample of a given area within a particular solid angle. Although spectacular, the brightness of third-generation sources is far from the fundamental limit in the X-ray region. Single-pass free-electron lasers (FELs), light sources based on linear accelerators and long undulators, can overcome the limitations of ring-based X-ray sources. FELs can produce extremely high brightness radiation by inducing a density modulation in the electron bunch at X-ray wavelengths. This is achieved by interacting the bunch with an optical field in the spatially periodic magnetic field of the undulator. When electrons are bunched at a given wavelength, the power radiated varies as the number of electrons to the power of four-thirds rather than linearly as for an unbunched beam. The characteristics of linac-based X-ray FELs (XFELs) are extraordinary, particularly their short pulse duration, peak brightness, and coherence. The peak brightness of the XFELs at SLAC and DESY is $\sim 10^{10}$ times higher than that of third-generation storage ring sources, with ~ 100 times shorter pulses. Linac-based short-wavelength FELs constitute the fourth-generation light sources. Since the successful operation of FELs in Germany (FLASH [4, 5]), Japan (SACLA [6]), Italy (FERMI [7, 8]), and the USA (LCLS [9, 10]), new X-ray FELs have been built and commissioned in Germany (European XFEL [11, 12]), Switzerland (SwissFEL [13, 14]), and South Korea (PAL-XFEL [15]), while others are now being constructed in China (SHINE [16]) and USA (LCLS-II [17, 18]). Several other countries have considered or are actively considering FEL facilities. European examples include the UK, Turkey, Sweden, The Netherlands, and France. Also, the Canadian Scientific and Engineering

community recognizes the need to establish a free-electron laser (FEL)-based program of research focused on applications in chemistry, biology, physics, materials science, nanotechnology, earth and environmental science, and medicine [19]. The strong scientific case for FEL beams is apparent from the present facilities' inability to meet the scientific community's demands. At FERMI, little more than 30% of the proposed experiments are currently awarded facility beam time, and a similar situation exists at FLASH.

A major factor in the cost of XFELs is the choice of accelerator technology adopted. Most existing facilities use S-band linear accelerators, given the maturity of the technology. Although consolidated through many decades of use, this technology is not optimal. At comparable accelerating fields, a higher frequency accelerating structure can achieve higher gradients and lower power requirements than those of lower frequency structures. The successful construction and operation of SACLA at the C band is testimony to the effectiveness of a higher accelerating frequency. In this case, an 8 GeV electron beam, with the characteristics required to drive an XFEL, can be generated in the space of 400 m, compared to 600 m at S-Band (including injector and bunch compressors). Subsequently, SwissFEL also adopted C-band technology. X-band technology further improves the situation and is expected to be more than half the required length of the accelerator and associated infrastructure compared to these machines. For large-scale accelerator projects such as SR light sources and FELs the cost, the breakdown is typically 70% for the civil engineering, accelerator, and the first beamlines, and 30% for personnel and management. Simple scaling of the accelerator length can result in 20–25% savings. In recent years, research and development of X-band accelerator technologies have seen tremendous progress in the context of the next generation of electron-positron linear colliders, where very high gradients are necessary to achieve the multi-TeV beam energy target for particle physics. The CLIC [20] study at CERN is the most remarkable example—here, accelerating gradients three-to-five times larger than those in operational linacs have been demonstrated in prototype accelerating structures. Thanks to linear collider research and development, X-band technology has reached a maturity level that encourages envisioning other possible applications beyond particle physics.

The CompactLight Design Study [1] enables the use of this world-leading accelerator technology, developed for the most advanced particle accelerators of the future, to benefit today's society. High-frequency X-band structures can also run at low gradients and high repetition rates (kHz regime), enabling a new set of operational scenarios for higher repetition rate X-ray FELs, currently in great demand for scientific and technological applications. In parallel to X-band developments, undulators have made significant improvements in capability in recent years, with the promise of more to come. Two new undulator technologies have been proven on light source facilities—cryogenic permanent magnet undulators (CPMUs) and superconducting undulators (SCUs). Both of these continue to improve in performance as confidence and experience develop, but neither has been applied to an XFEL design—until now. Reducing the required electron beam energy through the use of more advanced undulators results in additional cost savings roughly proportional to the energy reduction. The application of higher frequency acceleration and advanced undulators also facilitates upgrading existing facilities to higher energy, with the possibility of minimal or no increase in civil construction. This Design Study, based on validated high-gradient X-band and novel undulator technologies, now enables upgrades of existing FELs (e.g., FERMI) to higher energies within physical space limitations that would otherwise be impossible. It will also allow the existing facilities to expand their user communities and scientific programs, taking advantage of the higher photon energies that it will be possible to generate.

The Horizon2020-INFRADEV 01-2017 call funded this Design Study. This call aims "to support the conceptual and technical design and preparatory actions for new research infrastructures of a clear European dimension and interest. Major upgrades of existing infrastructures may also be considered if the result is intended to be equivalent to, or capable of replacing, an existing infrastructure". The Design Study started on 1st January 2018 and ended on 31st December 2021.

The CompactLight design presented in this report now opens the way to constructing a class of affordable regional and national FELs with world-leading X-ray performance. It has helped prime the capability of the industry to supply components for accelerators competitively. This Design Report discusses the major design choices that have been made, framed in terms of their scientific, strategic, and technological relevance and ambition. It enables the development of new research infrastructures and upgrades existing ones.

2.1 Motivation for CompactLight

SR has become a fundamental and indispensable tool for studying the matter, as shown by many synchrotron light source facilities in operation worldwide (close to 80), serving tens of thousands of users yearly. The SR user community spreads across a multitude of scientific and engineering disciplines, including materials science, condensed-matter physics, atomic and molecular physics, life science and medicine, chemistry, and environmental sciences. The impact of SR across these disciplines is evidenced by the five Nobel prizes awarded in the past 20 years to scientists whose research has been made possible by SR.

The latest generation of SR sources is based on FELs driven by linacs and features unprecedented pulse duration, brightness, and coherence performance. The use of XFELs, in the short time that they have been available, has

already led to significant insights in a number of scientific fields, such as atomic physics, plasma physics, solid-state physics, and macromolecular crystallography. As researchers develop new exploitation techniques, increasingly based on enhanced output from FELs such as two color pulses, femtosecond and sub-femtosecond photon pulse lengths, and increasingly coherent pulses, the scientific reach of FELs will continue to expand. The CompactLight aim is to facilitate the widespread development of XFEL facilities across Europe and beyond by making them more affordable to construct and operate through an optimum combination of emerging and innovative accelerator technologies. The collaboration has designed a hard X-ray (HXR) FEL facility using the latest concepts for bright electron photoinjectors, high gradient accelerating structures, and novel short-period undulators. The resulting facility benefits from a lower electron beam energy than current facilities due to the enhanced undulator performance, is significantly more compact due to the lower beam energy and the high-gradient acceleration, and has a much lower electrical power consumption. These ambitious yet realistic design features result in much lower construction and running costs, thus making X-ray FELs affordable, even by national institutions or academia. This Design Study is anticipated to enable FEL facilities to proliferate across Europe and beyond even more rapidly than third-generation light sources have managed to do over the past decades.

In recent years, intense electron-accelerator developments have been driven by the XFEL, linear collider communities, and other applications such as Compton scattering sources. Relevant advances include:

- Lower emittance and higher repetition-rate photoinjectors.
- High-gradient linacs—gradients in excess of 100 MV/m are now routinely achieved.
- High-efficiency klystrons—techniques to bring efficiencies above 60% at high frequency have been demonstrated.
- Advanced concept undulators—cryogenic permanent magnet undulators and superconducting undulators—have been demonstrated and used operationally on the third-generation light sources in recent years.
- Improved diagnostics—including X-band deflectors for longitudinal bunch dynamics.
- Better beam dynamics and optimization tools—including those developed for linear colliders.

It is believed that by taking these developments, making other new advances, and optimizing them together in this comprehensive study, a facility has been designed with significantly lower cost and size than existing facilities.

2.2 The objectives of CompactLight

The key objective of the CompactLight Design Study has been to demonstrate, through this conceptual design, the feasibility of an innovative, compact and cost-effective FEL facility suited for user demands identified with leading academics during the design study. To achieve this, the high-level objectives were:

- to determine the user demands and design parameters for a compact and cost-effective hard X-ray FEL facility;
- to advance innovative designs for X-band and undulator technology as new standards for accelerator-based compact photon sources;
- to present a flexible design that can be adapted to local implementation demands with photon source options for soft and hard X-rays and inverse compton scattering (ICS) generated light.

These high-level objectives have been achieved and are articulated in this Conceptual Design Report.

The main cost driver for every FEL is the beam energy. The project has significantly lowered the electron beam energy requirement by taking advantage of the latest technological undulator innovations. SwissFEL is currently the most ambitious operating XFEL in terms of undulator technology. By implementing a room-temperature in-vacuum device, they are able to achieve 12 keV photon output at 5.8 GeV. By implementing advanced superconducting undulator technology, the CompactLight FEL can achieve a higher photon energy of 16 keV at the lower electron beam energy of 5.5 GeV. For comparison, note that the CompactLight undulator could generate 12 keV photons at only 4.8 GeV, much lower than the SwissFEL example.

A substantial fraction of the FEL's cost, space requirements, and power consumption are due to the linac that accelerates the electron beam. Normal conducting X-band technology can provide efficient, high-gradient acceleration at a limited cost. Research and development in high-energy physics laboratories has developed this technology and demonstrated high-performance prototypes. The CompactLight goal has been to optimize and make this technology available for FELs by adapting the design to FEL specifications. The project developed a unique concept where the linac repetition rate is traded off against an accelerating gradient, so that the facility can operate at 1 kHz in the soft X-ray region and at 100 Hz in the hard X-ray region. The 1 kHz option is a key performance parameter that meets the requirements of FEL users for a higher repetition rate at longer wavelengths.

2.3 Organization of the design study

From the launch of the design study, the collaboration subdivided the project into seven interlinking Work Packages (WPs). WP1 provided the overall management and coordination of the project. WP2 carried out the overall design process. WPs 3–6 carried out the designs of specific technical systems (electron injector, linac, undulators, and beam dynamics) and provided the input into WP2 necessary for the overall design, optimisation, and integration. WP7 addressed the strategic and user liaison issues related to the objectives of CompactLight. Approximately halfway through the design study, it was appreciated that the project would benefit from an additional technical WP on diagnostics, so WP8 was created.

The CompactLight collaboration consists of 25 partners and five third parties. Three partners are from outside Europe, two based in Australia and one in Shanghai. Three of the partners are industrial companies that are active in the supply of components for particle accelerators. A detailed list of CompactLight partners is provided:

1. Elettra, Sincrotrone Trieste S.C.p.A, Italy.
2. CERN, European Organization for Nuclear Research, Switzerland.
3. STFC, Science and Technology Facilities Council–Daresbury Laboratory, United Kingdom.
4. SINAP, Shanghai Institute of Applied Physics, Chinese Academy of Sciences, China.
5. IASA, Institute of Accelerating Systems and Applications, Greece.
6. UU, Uppsala Universitet, Sweden.
7. UoM, The University of Melbourne, Australia.
8. ANSTO, Australian Nuclear Science and Technology Organisation, Australia.
9. UA-IAT, Ankara University Institute of Accelerator Technologies, Turkey.
10. ULANC, Lancaster University, United Kingdom.
11. VDL ETG, VDL Enabling Technology Group Eindhoven BV, The Netherlands.
12. TU/e, Technische Universiteit Eindhoven, The Netherlands.
13. INFN, Istituto Nazionale di Fisica Nucleare, Italy.
14. Kyma, Kyma S.r.l., Slovenia.
15. SAPIENZA, University of Rome “La Sapienza”, Italy.
16. ENEA, Agenzia Nazionale per le Nuove Tecnologie, l’Energia e lo Sviluppo Economico Sostenibile ENEA, Italy.
17. ALBA, Consorcio para la Construccion Equipamiento y Explotacion del Laboratorio de Luz Sincrotron, Spain.
18. CNRS, Centre National de la Recherche Scientifique CNRS, France.
19. KIT, Karlsruher Institut für Technologie, Germany.
20. PSI, Paul Scherrer Institut PSI, Switzerland.
21. CSIC, Agencia Estatal Consejo Superior de Investigaciones Científicias, Spain.
22. UH/HIP, University of Helsinki-Helsinki Institute of Physics, Finland.
23. VU, VU University Amsterdam, The Netherlands.
24. USTR, University of Strathclyde, United Kingdom.
25. UniToV, University of Rome “Tor Vergata”, Italy.
26. BNG, Bilfinger Noell GmbH, Germany.

Excellent communication within WPs and between WPs has been key to the successful delivery of this design study. All WPs have held regular telephone and video meetings, and many cross-WP video meetings have been held. In addition, two face-to-face meetings of the full collaboration were held per year, each typically 3 days in duration, until the coronavirus pandemic prevented this. At that point, these continued as video conferences. Different collaboration members hosted the face-to-face meetings on each occasion. There have also been a number of smaller face-to-face meetings per year, either between WPs to address specific issues or for all WP leaders to address management and organizational issues. A specific meeting between members of the collaboration and leading European academic users of XFELs was held at CERN during the first year of the study to discuss the detailed user requirements for CompactLight.

A key feature of the design study has been the close involvement of industry. Three partners are industrial companies with experience supplying high-tech components to accelerator projects. In addition, specific companies that supply leading RF equipment were invited to face-to-face meetings of the full collaboration to inform their ongoing developments and to hear their views on technical limitations. The involvement of all of these companies has been extremely fruitful. It has ensured that the conceptual design of CompactLight takes advantage of the latest products, benefits from the industry’s wealth of experience, and pushes the technological boundaries. CompactLight has strongly influenced the future direction of product development within these companies and given them a deeper understanding of the long-term requirements for the next generation of FEL projects.

2.4 The impact of CompactLight

The ESFRI Roadmap 2016 "Strategy Report on Research Infrastructures" asserts, *SR facilities are powerful attractors and contribute to European scientific and industrial competitiveness*. It further states, *Free Electron Laser sources provide a novel way to probe matter and have very high, largely unexplored, potential for science and innovation*. The CompactLight facility aims to have the same scientific potential as the facilities considered for the ESFRI roadmap. Still, it also aims to be a pathfinder for facilities with a significantly smaller footprint and cost. The project aims at making X-ray FELs small and inexpensive enough to be within national and even university scale, yet with uncompromised scientific potential.

The currently operating facilities are significantly oversubscribed, which is expected to continue. Although new XFEL facilities have come online recently, the available facilities still do not meet the increasing demand for FEL light (from a large variety of sciences as the user base develops). CompactLight aims to promote the spread of national and international research infrastructures for photon science to help satisfy this large demand. This design study has addressed the key points that will make FELs more affordable for smaller countries or universities. The design of CompactLight, discussed in this report in detail, will have a direct impact in a number of critical areas that will aid in the further dissemination of XFEL facilities across Europe and beyond:

- **Cost**: The total facility construction and operating costs have been reduced compared with other XFELs using the most advanced injector, linac, and undulator technologies without compromising performance.
- **Power consumption**: The power consumption has been reduced with respect to other XFELs using the more efficient X-band RF technology.
- **Footprint**: The physical scale of CompactLight has been significantly reduced compared to other XFELs, which further impacts the cost and the ability of universities to host such a facility on their campuses.

3 Science goals and photon output requirements

3.1 Summary of science case

3.1.1 Introduction

Research at modern accelerator-driven light sources continues to deepen our knowledge of the natural world, from the subtle workings of life to matter under extreme conditions and has a profound impact on our industrial, economic, and societal evolution. A new generation of light sources based on coherent SR produced by Free-Electron Lasers enables, for example, characterization of the structure of biomolecules with sub-Å resolution, paving the way to controlling how they function. Currently, the FEL is the brightest man-made source of light, enabling a new era of science and innovation. This section gives a few examples of groundbreaking research enabled by XFELs and points out new perspectives for X-ray science that would be opened by the highly flexible structure of double X-ray pulses from the CompactLight FEL.

3.1.2 Taste of groundbreaking science with XFELs

3.1.2.1 Scattering

While X-ray scattering techniques have been extensively used for decades at synchrotron light sources, the high photon flux of coherent FEL pulses opened a new regime in X-ray science—the high-resolution determination of the structure of molecules, microcrystals, and matter under extreme conditions. Below, some examples of such high-resolution applications are discussed in more detail.

Bio-imaging

The structure of biomolecules, such as proteins, viruses, or cells, is fundamental to their function. Hence, the high-resolution structure determination enabled by coherent X-ray radiation is critical in biology and life sciences and allows, for example, rational drug design and the understanding of human biochemistry. A key method in this context is 'diffraction-before-destruction' in which the ultrashort duration of the X-ray pulse is exploited for outrunning the sample radiation damage. It offers the opportunity to image important bio-objects that can only be formed in smaller crystals, such as membrane proteins or even single particles, with varying resolution. In particular, hard X-rays with wavelengths in the Å range provide extremely high resolution [21], while soft X-rays offer useful information about larger structures, for example, living cells, with high throughput. The ultrashort,

intense X-ray pulses provided by FELs additionally allow measurement of the dynamics of biologically relevant molecules on their natural femtosecond timescale.

Structure determination of micrometer-sized, or smaller, crystals at FELs is often done using serial femtosecond crystallography. Typically, a liquid jet provides a stream of crystals that crosses the X-ray beam, and the high intensity of the FEL beam enables the collection of diffraction images of thousands of randomly oriented crystals. These can be reconstructed into a 3D image with resolution at the atomic scale [22, 23]. Major progress with respect to sample delivery has been made recently by increasing the speed of the liquid jet, which enables a fresh sample with every X-ray pulse at MHz repetition rate [24, 25]. Simultaneous detector frame-rate development has also been carried out [26]. Another viable sample delivery method uses fixed targets. It has important advantages, such as an order of magnitude increase in the probability of hitting the sample with the X-ray pulse. This sample delivery method currently requires low kHz repetition rates.

A major scientific driver of XFELs is the potential for single-particle imaging (SPI) of biological molecules at atomic resolution [27]. Although this goal is far from being reached, several measurements of biological objects have been at lower resolution. SPI has tremendous potential for observing the dynamics of biological, chemical, and physical systems [28].

Matter under extreme conditions Intense laser pulses applied to solid materials can produce nanosecond or sub-nanosecond dynamic compression into extreme pressure regimes. The material response to the unexplored pressure and temperature conditions created by such compression can be uniquely explored in diffraction experiments with 100 fs temporal resolution that resolves the atomic motion. Moreover, the brightness and small focus of the XFEL pulse relaxes the pulse energy requirement of the optical pump laser, which can then also be focused on a small spot.

Studies of shock waves probed by 8 keV X-rays at FELs have measured the ultimate compressive strength, associated with a purely elastic response, of copper and the plastic flow occurring at higher strain orders [29]. Diffraction studies have also been applied to investigations of phase transitions and melting. For example, melting of Bi was observed after a few nanoseconds upon the release of dynamically 8–14 GPa induced compression [30]. At LCLS, shock pressures exceeding 120 GPa were used to demonstrate the conversion of graphite to diamond and lonsdaleite phases [31], and complicated structures, including linear guest structures arranged as chains in channels of the host structure, have been observed.

High energy-density plasmas are characterized by temperatures above 1 eV (about 11,600 K) and densities higher than that of a typical solid, such as found in planet cores, stellar interiors, intense laser–matter interactions, and fusion experiments. High-brightness (hard-)X-ray FELs are well adapted for such studies as they satisfy the requirements for generating and detecting the hot and dense plasmas deep into the sample. The XFEL also provides the necessary spatial resolution and temporal resolution, ranging from attosecond electron dynamics to compression processes on the nanosecond timescale.

3.1.2.2 Spectroscopy

X-ray spectroscopy provides complementary information to imaging and diffraction measurements of a system's chemical and electronic properties, and the techniques can be performed simultaneously [32]. X-ray absorption spectroscopy (XAS) and X-ray emission spectroscopy (XES) enable element-specific measurements of the unoccupied and occupied electronic states. In contrast, X-ray photoelectron spectroscopy (XPS) is highly sensitive to the chemical surroundings and offers surface sensitivity. The high peak-brightness FEL pulses allow new approaches to spectroscopic experiments, such as nonlinear excitations, single-shot detection, and femtosecond time-resolved measurements.

The potential for multiphoton excitation of atoms and molecules by FELs has been exploited for the formation of two-site double core-hole (tsDCH) states that could be detected using XPS [33, 34]. These states are created by the ejection of one core electron on separate atoms and require high peak intensities to ionize the second atom before Auger decay occurs in the first atom. These states have received attention due to the significantly enhanced chemical sensitivity compared with single core-hole states.

XES and XAS studies carried out at XFELs have been helpful in understanding important chemical processes. Electron transfer is essential in biological systems and for artificial light harvesting. XES and XAS measurements on an electron-harvesting chromophore performed at SACLA demonstrated the potential of these methods for monitoring fundamental chemical processes [35]. Moreover, resonant inelastic X-ray scattering has proven a capable tool for investigating excited state dynamics in solution via detection of orbital interaction [36]. The potential of using XAS and XES at FELs for understanding catalytic reactions has also been demonstrated at LCLS, where these techniques have enabled the observation of CO oxidation on a Ru surface [37, 38].

3.1.2.3 Time-resolved experiments

Ultrafast magnetism X-ray magnetic circular dichroism (XMCD) spectra, obtained as the difference between XAS data with opposite circular polarization, offer a way to probe the magnetic properties of materials. Recently,

the high peak brightness of the soft-X-ray FEL was exploited in a demonstration of time-resolved (tr) XMCD, which was applied to investigate the element-specific all-optical switching dynamics in GdFeCo with femtosecond temporal resolution [39]. Moreover, sub-picosecond demagnetization dynamics were studied by tr-XMCD using hard X-rays resonant with the Pt L3 edge (11.6 keV) [40].

XFEL pulses offer an efficient tool for probing ultrafast magnetization dynamics on a femtosecond timescale with nanometer resolution. For example, soft X-ray holography using circular polarization has demonstrated 15 nm resolution [41]. Time-resolved soft X-ray resonant diffraction studies at LCLS detected Gd spin reversal within the first picosecond in ferromagnetic GdFeCo. It was explained by a nanoscale flow of angular momentum from Fe-rich to Gd-rich regions induced by the optical pump [42]. Controlling magnetic properties via spins opens the door to faster data storage and processing devices.

Strongly correlated electron systems In strongly correlated electron systems, the interaction between electrons is non-negligible and may strongly influence the character of the material. Light-induced insulator–metal transitions (IMT), dominantly driven by electron correlation effects, as opposed to large structural changes (so-called Mott transitions), are a promising route toward faster electronics. Time-resolved X-ray diffraction experiments at FELs following the structural dynamics of the THz-induced IMT in VO_2 have shown that the electronic metallization dynamics and structural phase transitions can occur on different timescales [43]. This opens the door to efficient conductivity switching in correlated-electron systems.

XFEL pulses are also useful for studying the lattice changes associated with light-induced superconductive phases. For example, THz pulses have been shown to create superconducting properties in cuprate materials, and using femtosecond X-ray diffraction, the behavior of the lattice structure was investigated for this exotic state. These studies revealed that the nonlinear excitation of the crystal lattice structure creates a displaced lattice geometry, which causes drastic changes in the electronic structure and may cause destabilization of the charge-density-wave order—both may favor superconductivity [44].

Water dynamics

Water is a surprisingly complex liquid that is still far from understood. Its complexity and anomalous properties are due to its ability to form highly disordered hydrogen-bonded networks. X-ray FELs permit resolving water structural dynamics on a sub-100 fs timescale and atomic length scale. In a recent experiment at LCLS [45] using 8.2 keV photons, water structural motion was observed from the decay of speckle contrast when tuning the pulse duration from 10 to 120 fs. The work showed that cage effects due to hydrogen bonding play an important role in the slower dynamics of water upon cooling.

3.1.3 New possibilities offered by the simultaneous use of two FELs

The CompactLight facility can combine X-ray pulses from two parallel FELs, independently tunable in photon energy and temporal separation, at a single sample in a ‘dual’ endstation. This enables measurements with a large photon-energy separation between two X-ray pulses and pump-probe experiments using long and flexible time delays. The photon beamline design presented in Sect. 6.2 includes three dual stations combining two soft X-rays, two hard X-rays, or one soft and one tender X-ray. The simultaneous access to a wide range of absorption edges with a large photon-energy separation offers the possibility to, for example, pump and probe different sites of a molecule associated with different atomic species [46] at the dual SXR station. Two hard X-ray pulses with highly tunable photon energies may be exploited at the dual HXR station for two-color diffraction, in which two datasets are recorded simultaneously for more efficient crystal structure measurements [47]. The dual soft/tender station permits concurrent spectroscopic (soft X-rays) and scattering (tender X-rays) measurements that provide simultaneous insight into chemical and structural dynamics and can be useful in, for example, heterogeneous catalysis [48]. Moreover, the capability of using a soft X-ray pump that excites a specific resonance, followed by a tender X-ray pulse that probes the structural dynamics in an X-ray pump-probe scheme, will be highly beneficial.

3.1.4 User engagement

From day 1, the specifications and design of the CompactLight facility were driven by the demands of potential users and the associated Science Case. Several communication channels with users were established, and several interactions were undertaken. This started with two informal meetings with potential academic and industry users in the UK immediately after the project commenced. A specially developed questionnaire was then sent to over 50 FEL experts within Europe. The CompactLight consortium sent representatives to the Science@FELs Conference in Stockholm, Sweden, in June 2018 and the Attosecond and FEL Science Conference in London, UK, in July 2018, to hear about the latest scientific achievements using FEL facilities and to informally interact with leading researchers to gather their views on the parameters and performance of future FELs. The interaction with FEL

users culminated in a dedicated CompactLight User Meeting that was held from the 27th to the 28th of November 2018 at the European Organisation for Nuclear Research (CERN) in Geneva, Switzerland.[1] The primary objective of the meeting was to consult potential users on the photon characteristics required by their current and future experiments. The findings on the science requirements for the CompactLight FEL are summarized in the deliverable D2.1.

3.1.5 Science requirements of a next-generation FEL

Science opportunities with FEL light sources are far-reaching, and there is an increased interest in using FELs to explore:

1. materials far from equilibrium, such as in light-induced superconductivity;
2. nonlinear X-ray optics;
3. multi-dimensional attosecond spectroscopy;
4. charge migration and ultrafast X-ray damage in biomolecules;
5. surface chemistry and pathways for catalysis;
6. matter under extreme conditions.

Furthermore, the trends toward shorter pulse durations and higher photon pulse energies are clear. During the discussions with users, there were also strong requests for improving the coherence and stability properties of FEL radiation pulses and much better synchronization to external laser sources. The CompactLight design addresses these challenges.

In conjunction with the CompactLight User Meeting held at CERN, a preliminary survey was conducted through the use of an online questionnaire. The purpose was to gather quantitative information about the user requirements for the photon characteristics. According to the survey, the respondents expressed interest in experiments such as (i) pump-probe diffraction, (ii) serial crystallography, (iii) time-resolved spectroscopy, and (iv) time-resolved scattering.

With regard to the tunability, there was a clear demand for photon energies as low as 0.2 keV and as high as 20 keV. The mean photon energy of the desired tunable range is about 4 keV. In the design, a compromise on the highest photon energy of 16 keV was made, covering most user experiments. The preferable pulse energy range was 3–100 μJ, and the demand on the *stability* was stringent with the RMS fluctuation in pulse energy requested to stay below 10%.

Most respondents preferred a pulse duration of 10–100 fs, a repetition rate higher than 100 Hz, a degree of transverse coherence higher than 70%, a coherence time of 1–100 fs, a bandwidth of 0.1–1%, and a microfocus of 0.1–100 μm. For pump-probe experiments, most respondents wanted the synchronization between the FEL and the external laser to be in the order of 10 fs. Two-color pulse operation with a wide tunability in the relative photon energy and the time delay between the pulses was strongly requested.

3.2 FEL requirements

3.2.1 Introduction

This section summarizes all of the discussions and interactions that the CompactLight collaboration held with potential facility users during the project's first year. The exploitation of FELs by numerous groups covering diverse research topics highlights why FELs are fundamental engines of discovery. The diversity also means that it is impossible to meet all users' current and future needs with a single facility. Indeed, there is a risk that the facility's performance would be compromised by trying to satisfy all requirements, and no users would be entirely satisfied. The CompactLight collaboration understood this issue and distilled all user input into a coherent specification fully aligned with the prime strategic objective of generating a compact and affordable FEL facility design.

3.2.2 CompactLight output specification

The required specification of the CompactLight FEL is summarized in Table 1. The following bullet points expand on this specification and explain the priorities that were used to inform the technical design work, and which were balanced against the top level objectives of compactness and low cost.

- Seeding of the FEL enhances the output quality significantly in terms of improved temporal coherence and wavelength stability and should be implemented at all wavelengths where feasible.

[1] https://indico.cern.ch/event/750792.

Table 1 Main parameters of the CompactLight FEL

Parameter	Unit	Soft-X-ray FEL	Hard-X-ray FEL
Photon energy	keV	0.25-2.0	2.0–16.0
Wavelength	nm	5.0–0.6	0.6–0.08
Repetition rate	Hz	250–1000	100
Pulse duration	fs	0.1–50	1–50
Polarization		Variable, selectable	Variable, selectable
Two-pulse delay	fs	$\pm$ 100	$\pm$ 100
Two-color separation	%	20	10
Synchronization	fs	< 10	< 10

- Peak brightness is key to many experiments and should be maximized.
- Extreme synchronization between different photon sources for time-resolved pump-probe experiments is vital and the design should enable synchronization of the FEL with a conventional laser to better than 10 fs.
- Two pulses and two wavelengths are essential for many experiments. The design should provide these capabilities.
- The repetition rate for the soft X-ray FEL should be 1kHz.
- The photon pulse bandwidth should be minimized to maximize the peak brightness.
- The facility output should cover the range between 250 eV and 16.0 keV with all photon energies within this range being accessible from at least one of the FEL beamlines.
- The 2 keV 'boundary' between the soft-X-ray FEL and the hard-X-ray FEL is not rigid and should be determined when considering all the technical options, including electron beam energies, undulator performance, and X-ray optics capabilities.
- Tuning across photon energies should primarily be achieved by undulator scanning rather than energy scanning to maximize the efficient operation of the facility.
- The FEL output pulses should be evenly spaced in time and not provided in a burst mode.
- To maximize the efficient use of the facility, simultaneous operation of both the soft- and hard-X-ray FELs would be beneficial.
- Output pulse energies should be competitive with the other facilities.
- Variable, selectable polarization is required at the sample for all photon energies.
- Generating pulses as short as 100 attoseconds is desirable but may take significant extra space and cost.
- Stability in all its aspects is important to many experiments and should be considered in all technical designs of systems and subsystems. The RMS fluctuation in FEL pulse energy should stay below 10%.

The target performance of CompactLight in terms of peak brightness is shown graphically in Fig. 2. The peak brightness is expected to be comparable to the state-of-the-art X-ray FEL facilities which are currently in operation.

3.3 FEL physics

Madey [50] first proposed the free-electron laser (FEL) in 1971 and published the seminal theory of a small gain process in a relativistic electron beam and undulator system. The first experimental demonstrations of amplification [51] and lasing [52] were achieved at Stanford a few years later. The historical development of the FEL and the theory of FEL physics are reviewed extensively in several excellent articles, for example [53–56]. This section provides a relatively concise general summary to convey the basic principles and give the background to the parameter choices made in the CompactLight design. Section 3.3.1 describes the FEL process, Sect. 3.3.2 details the basic output properties of the SASE FEL, Sect. 3.3.3 motivates the requirement for a high-brightness electron beam to drive the FEL, and Sect. 3.3.4 describes how the performance of the FEL can be quantified as a function of the electron beam properties.

3.3.1 Description of FEL process

In the FEL, a highly relativistic electron bunch with Lorentz factor $\gamma = E/mc^2$ takes a sinusoidal path through an undulator's periodically alternating transverse magnetic field. It emits synchrotron radiation due to its transverse acceleration. The resonant wavelength λ_r of the FEL is given by the same expression used for on-axis spontaneous

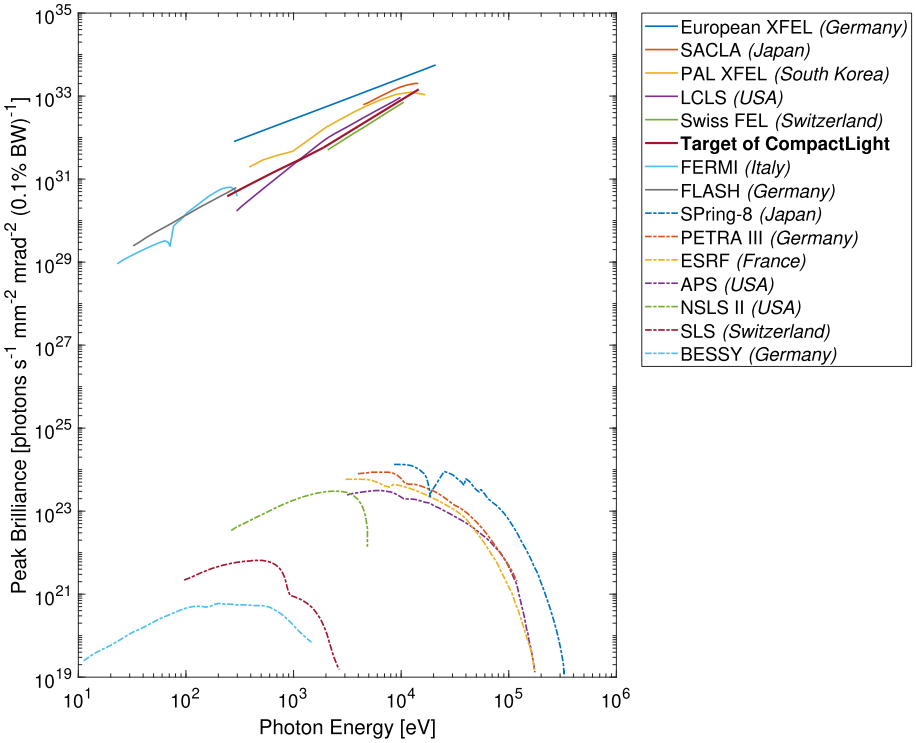

Fig. 2 Peak brightness as a function of photon energy for a selected set of X-ray sources. Free-electron laser facilities are shown in solid lines, and synchrotron facilities are shown in dashed lines. This figure is adapted from Fig. 1 in [49]

undulator radiation

$$\lambda_r = \frac{\lambda_w}{2\gamma^2}\left(1 + a_w^2\right). \tag{1}$$

Here, λ_w is the period of the undulator magnetic field and a_w is called the undulator deflection parameter, defined as

$$a_w = \frac{eB\lambda_w}{2\pi mc}, \tag{2}$$

with e the electron charge, m the electron mass, and c the speed of light in a vacuum. For a helical undulator $B = B_0$ with B_0 the peak field, whereas for a planar undulator, $B = B_0/\sqrt{2}$. Using these definitions, Eq. 1 is true for helical and planar undulators.

For typical undulator parameters of a period in the tens of millimeters and deflection parameter approximately unity, it is found from Eq. 1 that the beam energy must be in the multi-GeV range to reach sub-nanometre wavelengths. The resonance condition also shows why the FEL wavelength can be smoothly and continuously tuned over a fairly wide range—it is only necessary to change the on-axis magnetic field to change the wavelength. Such field tuning can typically give a factor of around four in wavelength tuning while maintaining a sufficient on-axis magnetic field for lasing. A much wider wavelength range is accessible by changing the electron beam energy, although this requires adjusting multiple accelerator parameters, so it is less convenient (but still common). The resonance condition also shows that to minimize the electron beam energy required for a given wavelength. The undulator period should be as short as possible. Minimizing the electron beam energy and undulator period contributes to compacting the facility. This fact has been exploited in the CompactLight design. However, the on-axis field reduces as the undulator period is reduced relative to the undulator gap. Once the period is reduced to about the same as the gap, the magnetic flux starts to flow from one magnetic pole to the adjacent one of opposite polarity on the *same* side of the array, rather than across the gap where the electron bunch will see it. Therefore, to maintain an axis field and an efficient FEL interaction, the gap must also be reduced as the period is decreased. Unfortunately, this increases the strength of resistive wall wakefields within the undulator vessel, which can degrade the FEL performance. Therefore, choosing the minimum undulator period is a balance between

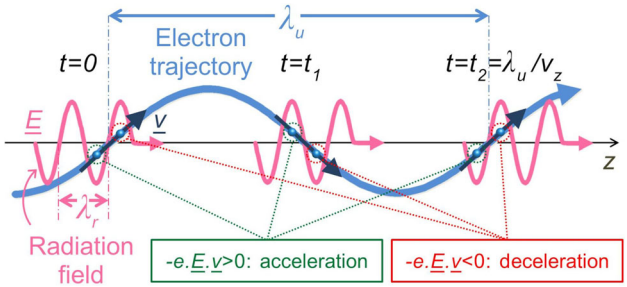

Fig. 3 Schematic of the undulator resonance condition. As the electrons traverse one undulator period, the radiation propagates forward relative to the electrons by one radiation wavelength, allowing sustained energy transfer. Depending upon their longitudinal alignment, electrons either gain or lose energy, which leads to a modulation in the electron beam energy. Figure constructed following the approach of [57]

achieving a compact design and one in which the wakefields are acceptably small. This balance has been achieved in the CompactLight design.

The resonance condition can be derived in the case of spontaneous emission by considering how the broadband synchrotron radiation emitted by the electrons from N periods of their sinusoidal trajectory interferes constructively and destructively to create a radiation pulse with a bandwidth of approximately $1/N$. In the case of the FEL mechanism, it is more instructive to start from the fact that the average longitudinal velocity of the electrons v_z is very slightly less than c, partly due to the wiggles in their trajectory and partly because $v = \beta c$ and $\beta < 1$ by a tiny amount. As the electrons travel through the undulator, they propagate in the presence of their spontaneous emission. The transverse component of the electron velocity can then couple to the transverse component of the spontaneous emission electric field, allowing an energy transfer to occur. The resonant wavelength of the FEL is the distance the electrons slip back with respect to the light over each undulator period—this is because light at this wavelength has an electric field which *maintains a constant relative phase* with respect to the oscillating electron transverse velocity, and so, this coupling between electrons and light is maintained allowing a *continuous* energy transfer. Depending on their phase, some electrons gain energy, while others lose energy. This sets up a sinusoidal energy modulation along the electron bunch with period λ_r. The process is illustrated schematically in Fig. 3.

All this time, the electrons are still emitting, but because they are distributed randomly in phase, their emission is incoherent with power P proportional to the number of emitting electrons N_e. However, the energy modulation in the bunch starts to convert into a density modulation due to longitudinal dispersion in the undulator—the electrons that have gained energy are now deflected less in the magnetic field and thus take a shorter path, moving ahead of the electrons that have lost energy and are deflected more to follow a longer path. This way, the electrons start to 'microbunch' themselves at the resonant wavelength, see Fig. 4. This then increases the coherence of their emission, increasing the power and amplifying the co-propagating field. Because the field is growing, the energy modulation increases, increasing bunching through the longitudinal dispersion, and so on, in a positive-feedback loop in which the radiation power grows exponentially.

Eventually, the growth of the radiation power saturates. The strongest emission occurs when the electrons moving in one direction due to their positive energy offset meet up with those moving in the other direction due to their negative energy offset, and the microbunching is maximized. This radiation emission power P is proportional to $N_e^{4/3}$. In a 75 pC electron bunch $N_e \approx 5 \times 10^8$ the small nonlinearity in the power scaling gives a huge increase in radiation power compared to the spontaneous emission case where $P \propto N$. After this point, the dispersion continues as before, but now the positive and negative energy offset electrons move past each other and the bunching decreases, which dampens the radiation emission.

3.3.2 Output properties of the SASE FEL

This section summarizes the main properties of high-gain FELs in the standard Self-Amplified Spontaneous Emission (SASE) [58] operating mode. This is the mode of operation for the CompactLight baseline configuration.

3.3.2.1 Temporal structure

As described above, the electron bunch emits spontaneous emission at the start of the undulator, amplified exponentially by the FEL mechanism. The temporal profile of the initial spontaneous emission is noisy, because the electrons entering the undulator are randomly distributed, so each electron emits radiation at a different phase. The further evolution of the radiation pulse temporal profile is then dependent on the relative slippage between

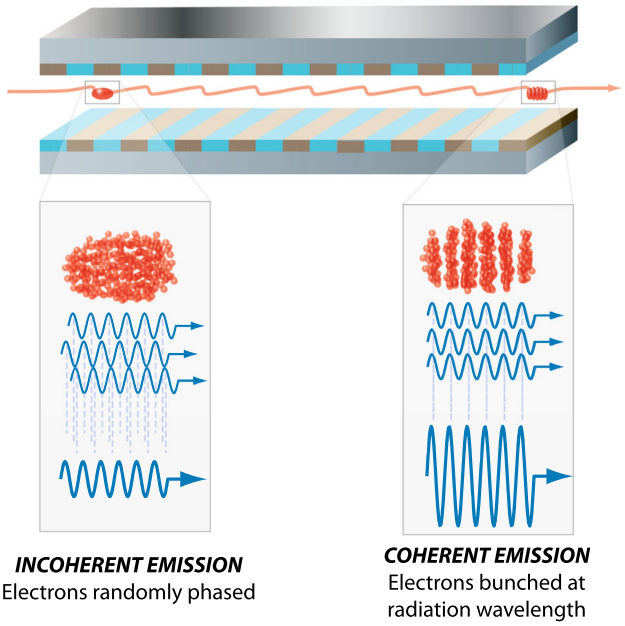

Fig. 4 Simple schematic of the FEL mechanism, showing the incoherent emission from the randomly phased electrons as they enter the undulator, which develops into coherent emission from the microbunched electrons at the end of the undulator

radiation and electrons. At saturation, the radiation pulse comprises a random superposition of many spikes with uncorrelated phases [59]. The maximum peak-to-peak distance between spikes is $2\pi l_c$ where the co-operation length is defined by

$$l_c = \frac{\lambda_r}{4\pi\rho}. \tag{3}$$

Here, ρ is the fundamental dimensionless FEL parameter [58], or Pierce parameter. This parameter expresses the strength of the coupling between the electrons and the radiation in the FEL mechanism. It is very useful for predicting the output performance and the required tolerances for many system parameters. It typically takes values $\approx 10^{-4} - 10^{-3}$ for SXR-HXR FELs. The FEL parameter is defined using a collection of system parameters and fundamental constants and can be expressed as

$$\rho = \frac{1}{\gamma_r}\left(\frac{\bar{a}_w \omega_p}{4ck_w}\right)^{\frac{2}{3}}, \tag{4}$$

where

$$\omega_p = \left(\frac{e^2 n_p}{\epsilon_0 m}\right)^{\frac{1}{2}}, \tag{5}$$

is the plasma frequency for peak electron number density of the electron bunch n_p.

The physical interpretation of the cooperation length l_c is that it is the slippage between electrons and radiation over the so-called "nominal" gain length

$$l_g = \frac{\lambda_w}{4\pi\rho}, \tag{6}$$

where l_g is related to the e-folding power gain length L_g as $l_g = \sqrt{3}L_g$. The co-operation length, therefore, defines the scale at which collective effects evolve throughout the electron beam. Different regions along the beam develop autonomously from the localised noise source for a sufficiently long electron beam and are, therefore, uncorrelated in phase. In this sense, the SASE process can be considered as a 'localised' collective process. Typically, in the

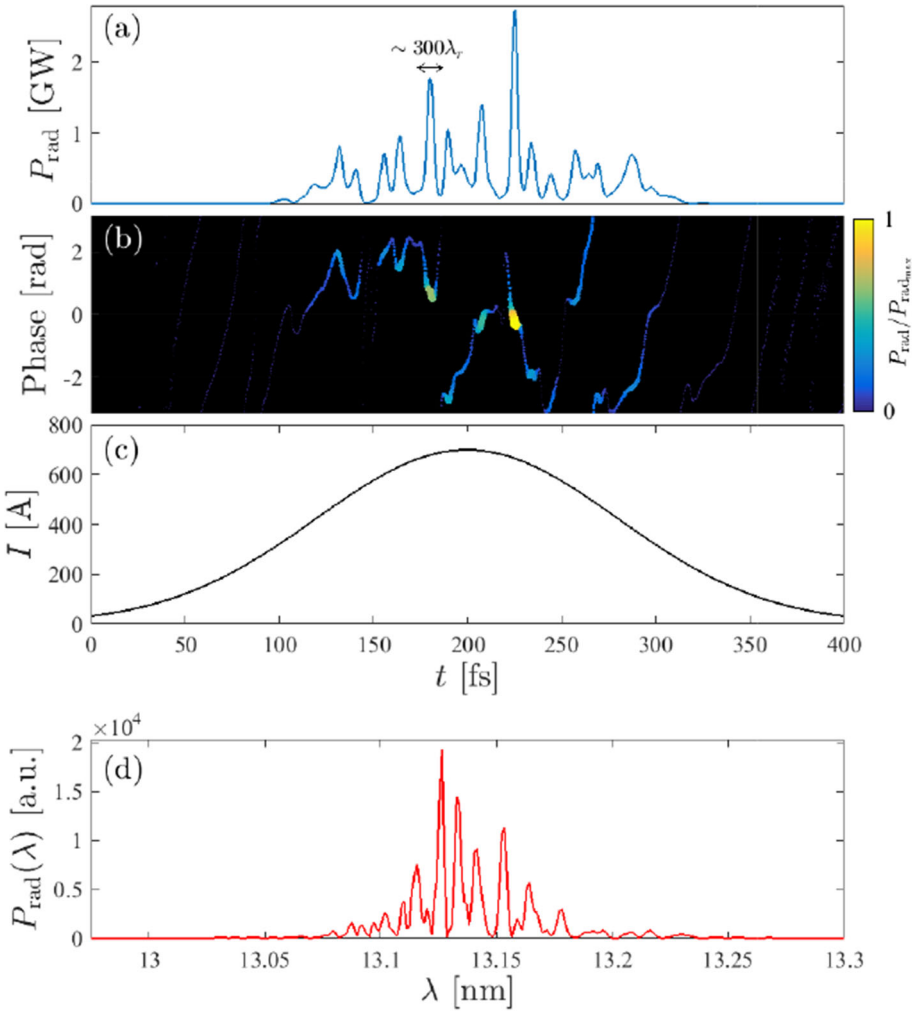

Fig. 5 Example of SASE properties. The plots show simulation results for a high-gain SASE FEL with parameters similar to FLASH [4]; results are shown at saturation: **a** radiation temporal profile consisting of multiple spikes, **b** radiation phase showing phase correlation within but not between spikes, **c** the idealised Gaussian current profile used in the simulation, and **d** the radiation spectrum, also consisting of multiple spikes

X-ray region, the electron bunch length $l_b \gg 2\pi l_c$, so there are many random spikes in the radiation pulse which has a total length similar to that of the electron bunch.

The co-operation length also parameterises the SASE radiation coherence. The coherence time is [60]

$$\tau_{\rm coh} \simeq \frac{1}{\rho\omega}\sqrt{\frac{\pi \ln N_c}{18}}, \tag{7}$$

where $N_c = I/(e\rho\omega)$ with I the electron bunch current. This can be simplified using (3), and by noting that for typical X-ray FELs, the square root term evaluates to $\simeq 1.6$ to show that the coherence length is typically about 3 co-operation lengths, $l_{coh} \simeq 3l_c$, or half the peak-to-peak spacing of the SASE spikes.

The features of a typical SASE pulse are illustrated in Fig. 5, which shows simulation results for a high-gain SASE FEL with parameters similar to FLASH [4]. Figure 5a shows the intensity profile comprising multiple random spikes. Figure 5b shows the radiation phase, color-coded to indicate the associated radiation intensity. The phase is seen to vary randomly from spike to spike but is almost constant within each spike, showing that individual spikes have good temporal coherence. Figure 5c shows the electron bunch current profile. In the simulation, the current is averaged over slices one wavelength long. This shows that even if the electron bunch is perfectly smooth over this scale, the output pulse will be noisy due to the shot noise at sub-wavelength scales. Finally, Fig. 5d shows the output pulse spectrum, which also comprises multiple random spikes.

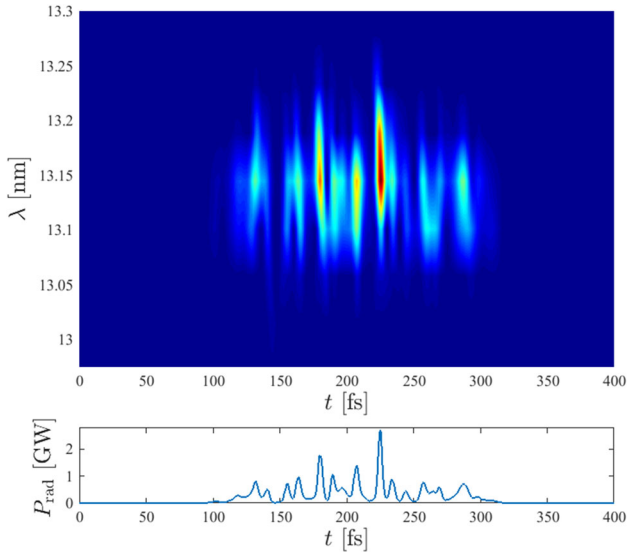

Fig. 6 Time-wavelength plot of the simulated SASE FEL pulse shown in Fig. 5a. The top panel shows a windowed Fourier transform of the output pulse, and the bottom panel shows the intensity profile. Each temporal spike is seen to have the full gain bandwidth

3.3.2.2 Bandwidth

The pulse shown in Fig. 5 is just one example of a typical SASE output pulse. In practice, each pulse has a different arrangement of spikes, temporally and spectrally, due to the start-up from noisy spontaneous emission. It is important to note that although the number of temporal spikes is approximately the same as the number of spectral spikes, there is no one-to-one correspondence between them. Each temporal spike does not have a distinct wavelength but has the full bandwidth of the envelope, which is the gain bandwidth of the FEL system. This can be seen clearly in Fig. 6, which shows a windowed Fourier transform of the simulated FEL pulse in Fig. 5a.

The gain bandwidth can be derived analytically. The result is that the relative rms bandwidth narrows with distance z traveled through the undulator as $\sigma_\lambda \simeq 2\rho\sqrt{\pi l_g/z}$. The FEL approaches saturation at $z \gtrsim 10 l_g$, so the relative rms bandwidth of the saturated output is

$$\sigma_\lambda \simeq \rho. \tag{8}$$

3.3.2.3 Power, pulse energy, and flux

As the electron bunch travels through the undulator, its kinetic energy is converted into the energy of the radiation field. At saturation, the mean relative electron energy loss is $(|\langle\gamma\rangle - \gamma_r|)/\gamma_r \approx \rho$ thus ρ is a fundamental indicator of FEL performance—it represents the efficiency of the conversion of electron beam power to radiation power. The peak radiation power at saturation is therefore given by

$$P_{\rm rad} \approx \rho P_{\rm beam} = \rho I_{\rm peak}[{\rm A}]\ E[{\rm eV}], \tag{9}$$

where $P_{\rm beam}$, $I_{\rm peak}$ and E are the electron beam peak power, peak current, and energy, respectively. Typically, for short-wavelength high-gain FELs, with ρ in the range 10^{-4} to 10^{-3}, the electron beam energy is in the tens of GeV, and the peak current is a few kA, so FEL peak output power is in the tens of GW.

The pulse energy is the instantaneous power integrated over the pulse duration. With peak powers in the tens of GW and pulse durations 10–100 fs, the pulse energy is typically 100 μJ to a few mJ. The number of photons per pulse is the pulse energy divided by the photon energy, typically 5×10^{10} to 5×10^{11}. Higher harmonics are also present in the FEL output, with intensity less than a few percent of the fundamental [61]. FEL facilities also produce spontaneous undulator radiation, the power of which can be on the order of the FEL power for hard X-ray FELs [62]. Nevertheless, the FEL radiation is many orders of magnitude brighter than this because it has narrower angular and spectral distributions.

3.3.2.4 Transverse coherence

The radiation emission over the first few gain lengths of the FEL process has significantly higher order mode content. Still, since the growth of the field is driven most strongly on-axis, this favors coupling to the fundamental

Gaussian mode—higher order modes are wider or even have a minimum on-axis and are therefore driven less strongly [56]. By the time the FEL is close to saturation, the fundamental mode strongly dominates, and the output beam is close to diffraction limited [63–65]. Beyond saturation, the transverse coherence starts to degrade due to the growth in higher order transverse modes.

3.3.2.5 Brightness

As discussed, an FEL produces high peak power pulses, narrow bandwidth, and near-diffraction limited transverse coherence. This means that it is possible to focus an intense flux of near-monochromatic photons onto a small area, making the X-ray FEL an extremely useful scientific tool. The flux, bandwidth, and transverse coherence are collectively quantified by the spectral brightness, defined as

$$B = \frac{\Phi}{4\pi^2 \Sigma_x \Sigma_{\theta x} \Sigma_y \Sigma_{\theta y}}, \tag{10}$$

where Φ is the spectral flux, the number of photons per second divided by the relative bandwidth, and Σ represents a quadrature sum of the photon beam and electron beam rms beam sizes or divergences. Under the assumption that the FEL output is close to diffraction limited and that the FEL undulator is very long, this simplifies to

$$B = \frac{4\Phi}{\lambda^2}, \tag{11}$$

then using that the relative bandwidth $\sigma_\lambda \simeq \rho$ the expression for peak spectral brightness, in units of photons/s/mm^2/mrad^2/0.1% BW, becomes

$$B \simeq 8 \times 10^9 \frac{P}{\rho \lambda}. \tag{12}$$

For $P_{\text{rad}} \simeq 10$ GW, $\rho \simeq 10^{-3}$ and $\lambda = 0.1$ nm, this gives $B \simeq 8 \times 10^{32}$ photons/s/mm^2/mrad^2/0.1% BW, exceeding the peak brightness available from storage ring sources by at least eight orders of magnitude.

3.3.3 Requirement for a high-brightness electron beam

The FEL interaction requires a small initial energy spread in the electron beam. This is because, as described earlier, the undulator introduces longitudinal dispersion. This is required for the microbunching to develop from the energy modulation—without it, the FEL would not work. However, if the incoming beam has an initial uncorrelated energy spread, this translates via dispersion to longitudinal smearing of the microbunching, dampening the FEL interaction. A full analysis shows that the initial relative energy spread of the electron beam should be less than the FEL-induced modulation, which increases to ρ at saturation [62], leading to the criterion

$$\frac{\sigma_E}{E} < 0.5\rho. \tag{13}$$

As well as minimizing the energy spread, maximizing the FEL parameter ρ is useful. This helps in many other ways—from (9) and (6), making ρ as large as possible maximizes the output power and minimizes the gain length (thus minimizing the undulator length). It is also found that the allowed relative tolerances on many other system errors, such as undulator field errors, scale with ρ. It is clear, therefore, that the FEL parameter is fundamental and not just a convenient scaling parameter, and to obtain the best FEL performance and maintain that performance in the presence of spreads or errors in system parameters, the FEL parameter should be maximized. It is convenient to express ρ as

$$\rho \propto \frac{1}{\gamma} \left(\frac{I_{\text{peak}} a_w^2 \lambda_w^2}{\sigma_b^2} \right)^{\frac{1}{3}}, \tag{14}$$

where σ_b is the electron beam radius. Together, the parameters γ, a_w and λ_w define the FEL wavelength *via* the resonance condition (1) so for a specified FEL wavelength, these are not free. The FEL parameter is therefore maximized by *increasing the peak current* and *reducing the transverse beam size*. The beam size scales as the square root of the beam transverse emittance—this is a measure of the electron beam quality and is approximately

the product of the beam size and beam divergence

$$\varepsilon_x = \sqrt{\langle x^2 \rangle \langle x'^2 \rangle - \langle x x' \rangle^2}, \tag{15}$$

where x is the horizontal offset, and $x' = dx/dz$ is the angle of the particle trajectory relative to the axes (assuming $\langle x \rangle = \langle x' \rangle = 0$). The vertical emittance, ε_y, is defined equivalently. Therefore, a small emittance is required to obtain a small beam radius σ_b and maintain it over a reasonable distance. Minimizing the emittance also minimizes the spread in angular divergence of the electrons in the bunch, which minimizes the spread in path lengths of their trajectories, which degrades the microbunching (analogous to the way in which a spread in electron energies also degrades the microbunching through longitudinal dispersion).

It is also found that for the most efficient transverse overlap of the electrons and radiation, the transverse phase space of the electron beam must be less than that of the diffraction-limited photon beam, giving

$$\varepsilon < \frac{\lambda_r}{4\pi}. \tag{16}$$

The requirement on electron beam emittance becomes increasingly stringent at shorter wavelengths.

Taken together, the peak current, energy spread, and transverse emittance can be expressed as the electron beam brightness

$$B_e = \frac{I}{c\sigma_E \gamma^2 \varepsilon^2}, \tag{17}$$

so a high brightness beam is necessary to meet the requirements for high peak current, small energy spread, and small transverse emittance [66]. It should be noted, however, that although a high brightness electron bunch is necessary, it is not always sufficient—a bunch must be correctly configured, for example, meeting Eqs. (13) and (16), to be optimal.

To deliver high brightness beams to the FEL requires a high-brightness electron source and a system for accelerating and manipulating the electron bunches to maintain brightness in the presence of degrading effects such as coherent synchrotron radiation (CSR) emission from dipole magnets in the beam transport system, wakefields, and micro-bunching instability. The fact that beams can be delivered with sufficient brightness for X-ray FELs to operate testifies to the tremendous developments in numerous areas, including low-emittance photoinjectors and CSR compensation and prevention.

3.3.4 Quantification of beam quality effects

In the previous section, it is shown that the electron bunch driving the FEL must have high brightness and that to achieve this, the bunch must have high peak current, small energy spread and small emittance. The criteria given for energy spread and emittance are, however, *soft* limits. For example, if the emittance criterion given by Eq. 16 is not satisfied, the FEL might still lase, but its performance will be suboptimal—the output power might be reduced somewhat from the case of an ideal electron bunch, or the transverse mode quality might be degraded. It is, therefore, necessary to quantify exactly how the FEL performance depends on these beam quality factors.

In addition, the design of the undulator lattice must be optimized for the best performance. This involves determining the most suitable length for the individual modules that comprise the long FEL undulator; understanding the effect of diffraction and electron beam transport in the gaps between the modules; calculating the effect on the FEL performance of resistive wall wakefields; determining the allowed tolerances for undulator misalignments and electron beam trajectory straightness. Two main approaches have been adopted in the CompactLight design process for setting the initial target beam parameters and for assessing the predicted FEL performance using a simulated bunch that has been tracked through the whole accelerator.

3.3.4.1 The Ming Xie semi-analytical approximation

The Ming Xie semi-analytical approximation [67, 68] is based on the basic performance formulae given above, for example, those for power output and FEL gain length, but includes adjustment factors that quantify the effects of energy spread and emittance. These adjustment factors are derived from multidimensional fits to sets of FEL simulations. The approximation allows rapid estimates of FEL performance. An example is given in Fig. 7, which shows typical calculations of the CompactLight FEL saturation power for 16 keV photon output as a function of energy spread and normalized emittance. The nominal chosen working point (WP) is marked. As can be seen, the FEL performance at 16 keV is strongly dependent on the electron beam quality.

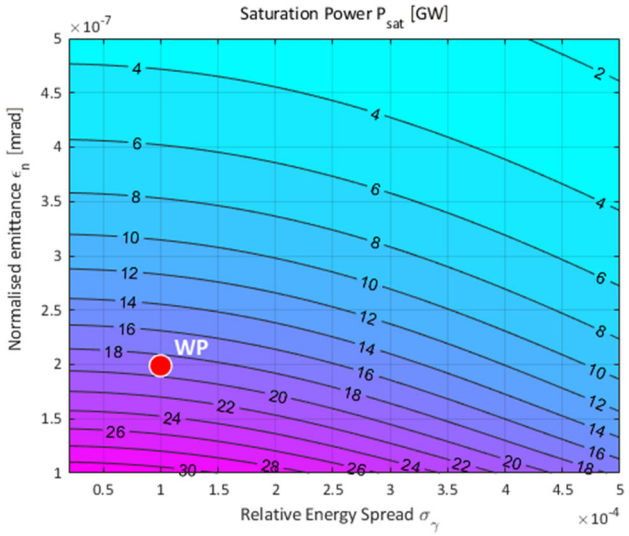

Fig. 7 Typical calculations, using the Ming Xie approximation, of the CompactLight FEL saturation power, for 16 keV photon output, as a function of energy spread and normalized emittance. The nominal CompactLight working point (WP) is marked

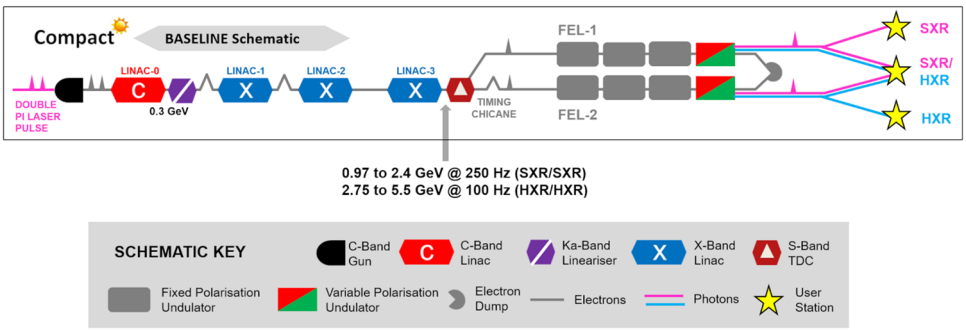

Fig. 8 CompactLight baseline schematic layout

3.3.4.2 FEL simulation codes

The Ming Xie approach assumes long, uniform, perfect undulators with electron bunches that have constant longitudinal parameters (for example, current, emittance, beam size, and energy spread). To include realistic bunch distributions and undulator lattices, it is necessary to use FEL simulation codes. CompactLight Deliverable 6.1 presented a summary and comparison of some available codes. The FEL code used most extensively in the CompactLight design process was Genesis1.3 [69, 70]. This code is well supported, has the most functionality and flexibility, and produces reliable results, which have been benchmarked against operating FELs on many occasions.

4 Systems design and performance

4.1 Facility overview

4.1.1 Key features

As discussed in Sect. 3.1.4, the user requirements for CompactLight were established by interacting with existing and potential FEL users in a variety of formats. The user input was distilled into a comprehensive photon output specification, as summarized in Table 1. The facility has been designed specifically to satisfy this specification. A Baseline configuration satisfies the majority of the user case, and two upgrades fully satisfy the user requirements.

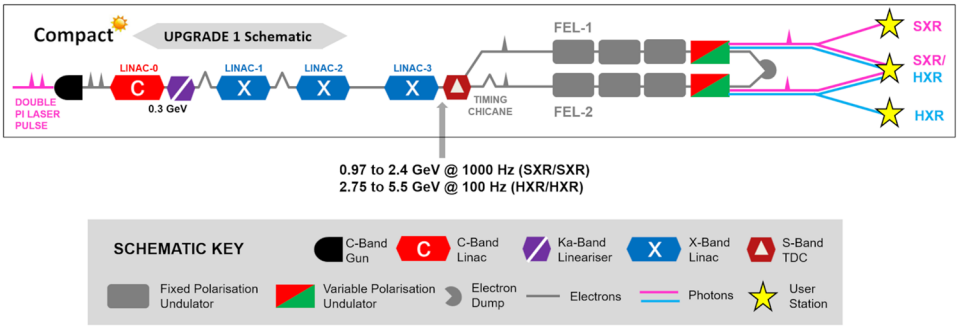

Fig. 9 CompactLight upgrade-1 layout

4.1.1.1 Baseline configuration

Figure 8 shows the baseline layout. The unique features and technical innovations of the Baseline are:

- **C-band RF gun and injector** with dual repetition rate and velocity bunching capabilities.
- **Compact X-band linacs** for high gradient acceleration and reduced footprint.
- **Low beam energy of 5.5** GeV compared to the existing facilities with comparable or **higher photon energy reach**.
- **Short-period in-vacuum superconducting undulators** with helical polarization for minimisation of FEL saturation length and electron beam energy, with associated **Cryomodule structure and cooling concepts**.
- **Dual-wavelength regimes using the same undulators**—soft X-rays over the range 0.25–2 keV from a low energy (0.95–2.4 GeV) electron beam, and hard X-rays over the range 2–16 keV from a high energy (2.75–5.5 GeV) electron beam.
- **Dual-mode linac** to drive the SXR FEL at 250–1000 Hz and the HXR FEL at 100 Hz.
- **K-band 36** GHz**linearisер cavity** for optimisation of electron bunch longitudinal phase space
- **K-band 36** GHz**power source designs** including *multi-beam klystron* and *gyroklystron*.
- **Double FEL concept** enabling the simultaneous operation of two SASE FEL lines which can drive either FEL-pump FEL-probe experiments at a single endstation, or independent experiments at two different end-stations.
- **Sub-harmonic bunch separator** for splitting twin bunches into the twin FELs.
- **Controllable spectral separation of the twin pulses** in soft and hard X-rays by independent tuning of the two identical undulator lines.
- **Controllable temporal separation of the twin FEL pulses** at the endstation, from perfect synchronization to ±100 fs.
- **Apple-X** afterburner undulators, including *solutions for magnetic force compensation*, for independently selectable polarization of the twin FEL pulses and fast helicity switching at a single endstation.
- **Full polarization control** from 0.25 to 12 keV and selectable L/R circular polarization from 12 to 16 keV.

4.1.1.2 Upgrade configurations

Further to the baseline design, two upgrade scenarios have been designed that add additional capability, in particular, higher repetition rates, improved FEL coherence and HXR/SXR or SXR/HXR FEL-pump FEL-probe capability. Taken together, the baseline and upgrades fully satisfy the user requirements. The schematic layouts of the two upgrades are shown in Figs. 9 and 10. The Unique features and innovations of Upgrade-1 are:

- **1 kHz repetition rate in SXR** by upgrading the linac to *dual-source*, which adds additional klystron power while keeping the average RF power in the structures constant, and triggering *industrial development*.

Upgrade-2 adds three additional features beyond Upgrade-1:

- **Soft X-ray self-seeding** using a grating monochromator to provide fully coherent soft X-ray FEL output.
- **Hard X-ray Self-seeding** using a diamond crystal wake monochromator to provide much-improved longitudinal coherence in the HXR, compared to SASE.
- **SXR/HXR FEL-pump FEL-probe capability with controllable delay of ±100** fs by the addition of a SXR bypass line containing an additional linac module to allow simultaneous soft and hard X-ray pulses at 100 Hz, with independent tuning of wavelength and polarization. These can be used in independent experiments at two separate end stations or combined in a single end station.

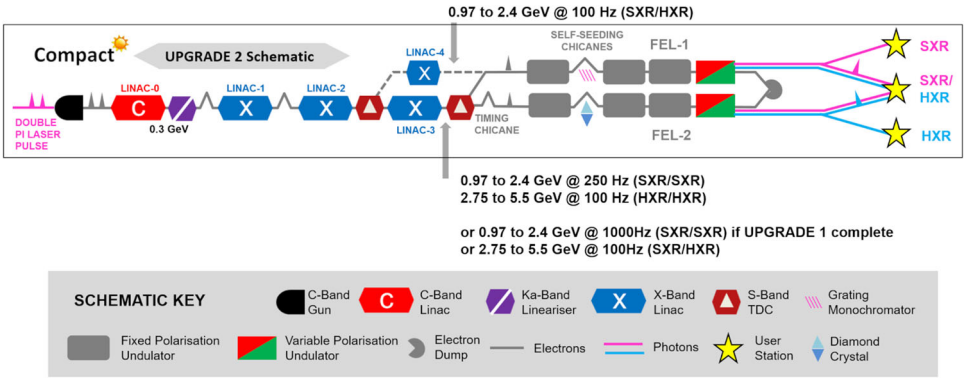

Fig. 10 CompactLight upgrade 2 layout

Table 2 Operating modes

Operating mode	FEL-1 Wavelength	FEL-2 wavelength	L0–L3 Rep. Rate (Hz)	L3 output Energy (GeV)	L4 Rep. Rate (Hz)	L4 output energy (GeV)
Baseline						
B-HH	HXR	HXR	100	2.75–5.5	–	–
B-SS	SXR	SXR	250	0.95–2.4	–	–
Upgrade-1						
U1-HH	HXR	HXR	100	2.75–5.5	–	–
U1-SS	SXR	SXR	1000	0.95–2.4	–	–
Upgrade-2						
U2-SH	SXR	HXR	100	2.75–5.5	100	0.95–2.4

Full details of Upgrade-1 are given in Sect. 5.2. Simulation studies of the SXR and HXR self-seeding modes of Upgrade-2 are presented in Sect. 4.2.4.

4.1.2 Operating modes

The operating modes for the baseline design and upgrade configurations are summarized in Table 2. All operating modes FEL-1 and FEL-2 can be sent to separate user stations **or** sent to the same user station with ±100 fs separation.

4.1.3 Layout description

The total length of the facility, including the building, is 483 m. By comparison, SwissFEL is 740 m. Figure 11 shows an ISO view. This section summarizes the layouts and main features of the different parts of the facility. Full details and parameters are given in Sect. 5.

4.1.3.1 Injector

CompactLight uses a normal conducting 2.5 cell C-Band photo-cathode RF gun with 160 MV/m field on the copper cathode. Space for a laser heater to minimize the impact of micro-bunching instability on the FEL performance is allocated. The following C-Band linac structures have a gradient 15 MV/m and accelerate the beam to 300 MeV with a short Ka-band lineariser cavity with a maximum peak accelerating voltage of 17 MV. After the lineariser is the first bunch compressor (BC1) and a small X-Band diagnostic deflector. For full details, see Sect. 5.1.

4.1.3.2 Main Linac

A two-stage magnetic compression scheme is adopted in the main linac, in addition to optional velocity bunching implemented in the injector. The main linac comprises X-band accelerating structures. The maximum beam energy is 5.5 GeV. This was chosen as it is lower than comparable facilities such as SwissFEL yet in combination with

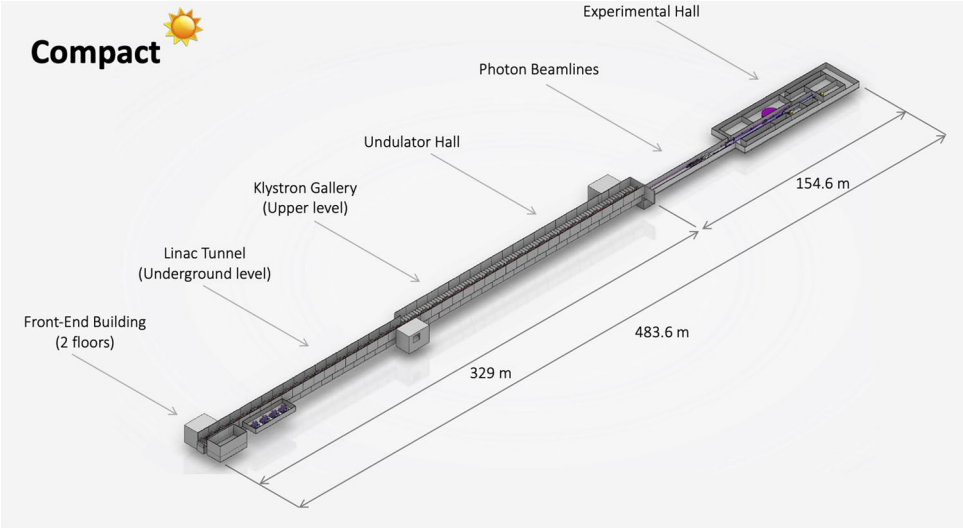

Fig. 11 ISO view of the XLS facility. The total length is 483.6 m

advanced short-period undulators allows a photon energy reach up to 16 keV which exceeds the highest photon energies available from SwissFEL.

The magnetic lattice of the main linac is based on an FODO cell interleaved by low-β_x insertions for the magnetic compressors. The linac fill factor is $> 70\%$ in all sections. The total linac length from the cathode to the exit of Linac-3 (HXR beam line) is less than 190 m, and includes 104 X-band accelerating structures.

The main linac is powered by standardized RF units based on CLIC technology, which can be used in all the main and sub-design variants. The RF unit will include klystron, RF compressor, and waveguide components. This choice greatly simplifies the industrialisation process, considerably reducing production costs. For full details of the linac design and configuration, see Sect. 5.2; for details of the beam dynamics, see Sect. 5.3.2.

4.1.3.3 Bunch compressors

The magnetic bunch compressors are symmetric four-dipole chicanes with beam diagnostics in the inner drift region. Small quadrupole magnets in the outer branches of the chicane are used for tweaking residual dispersion. The local compression factors are ≈ 9 at BC1 and ≈ 5 at BC2, for a maximum total compression factor of 100 when operating the injector in velocity bunching mode. For full details, see Sect. 5.3.2.2.

4.1.3.4 RF distribution system layout

The baseline configuration of the layout runs in *dual mode* where a single RF source supplies the linac in two operating modes, at 100 Hz and 250 Hz. This is the cheapest solution but is limited in repetition rate to 250 Hz. The peak accelerating gradient is 65 MV/m at 100 Hz and 32 MV/m at 250 Hz with magnet strengths scaled depending on the gradient to obtain the same optical functions along the linac. An X-band SLED is adopted at 100 Hz, and is bypassed at 250 Hz. Upgrade-1 and Upgrade-2 operate in *dual source mode*—here, an additional klystron is connected to the RF module, so two RF sources supply the linac at repetition rate 100 Hz and 1 kHz. The RF distribution connects two klystrons to four accelerating structures. These form one accelerating module of 3.6 m active length. For full details, see Sect. 5.2.1.2.

4.1.3.5 Twin bunch system

The photoinjector laser is split into two pulses separated by 3 or 5 RF cycles of the C-band gun, so the temporal spacing is either 500 ps or 833 ps. The two pulses generate identical electron bunches with the same RF accelerating phase. The time separation corresponds to 6 or 10 RF cycles in the X-band linac. The separation of 500 ps is the minimum at which beam break-up instability of the trailing bunch is kept well under control, with a projected emittance growth at the linac end below 10%. The twin bunches follow identical dynamics in the accelerator. In the Baseline and Upgrade-1 configuration, they will be separated in the horizontal plane after the linac by an S-band transverse deflecting cavity. The bunch separations correspond to a half-integer number of RF cycles of the deflecting cavity, so that kicks deflect the twin bunches with opposite signs horizontally. About 30 MV peak deflecting voltage at the maximum beam energy of 5.5 GeV will impose angular kicks of half a degree, allowing the two bunches to be separated by ≈ 5 mm after a 0.5 m-long drift section. Here, a DC out-of-vacuum thin septum magnet directs the leading bunch to FEL-1 and the trailing bunch to FEL-2. A schematic of this beam

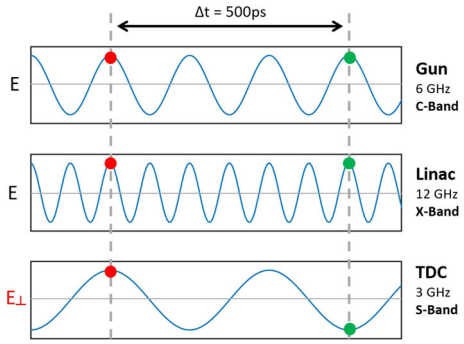

Fig. 12 Schematic showing how the twin bunches, separated here by 500 ps, are spaced by 3 RF cycles in the C-Band RF gun, six cycles in the X-Band linac, and 1.5 cycles in the S-band transverse deflecting cavity where they are deflected in opposite directions. A DC-thin septum magnet follows the deflector

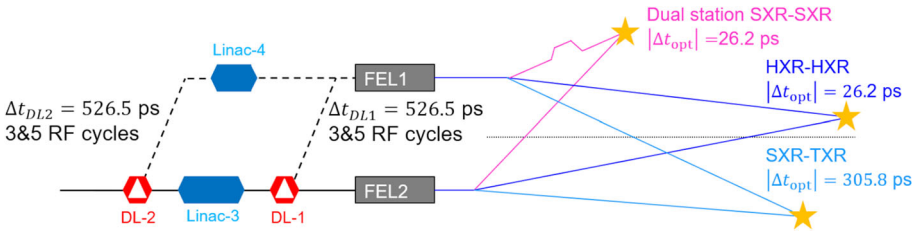

Fig. 13 Schematic layout of the accelerator with the full upgrade, two doglegs (DL-1) and (DL-2), two undulators, and three dual endstations. The relative optical delays are indicated

manipulation, showing how the twin bunches sit within the RF buckets at the three different RF frequencies for a bunch spacing of 500 ps, is shown in Fig. 12.

Pump-probe experiments typically require a continuous scan of the relative delay of the pump and the probe pulse by at least a few ps around synchronization. The leading bunch directed to FEL-1 has to be delayed with respect to the trailing bunch. The delay was required, so that the pulses from the twin FELs can be synchronized at the dual end-stations for pump-probe experiments, with allowance made for the optical path lengths of the photon beamlines, is 526 ps. This is accomplished by a dog-leg-like switchyard from the septum to FEL-1. The FEL undulator lines are laterally separated by ≈ 2.5 m. Fine-tuning of the pump-probe relative delay is done by a small 4-dipole chicane in front of the FEL-2 line and by a split-and-delay line on the photon beam path toward the end stations. Upgrade-2 allows the simultaneous generation of SXR and HXR FEL pulses at 100 Hz. In this case, the splitting system and dog leg are replicated at the end of Linac-2, so bringing the leading bunch to FEL-1 for SXR emission. Only the trailing bunch reaches the end of Linac3 for HXR production. The full twin bunch system is shown in Fig. 13, which shows the spacing between the twin bunches in the linacs, the required delay in the spreaders, and the path length variations in the optical beamlines. For full details of the twin bunch system, see Sect. 5.3.2.4.

4.1.3.6 Undulator lattice

The main undulators are 1.75 m-long in-vacuum helical superconducting undulators (SCUs) with a period of 13 mm. This undulator technology was chosen after a thorough comparative assessment of a broad range of options, reported in detail in deliverable D5.2 and summarized in Sect. 6.1.1. To cover the required wavelength range of the facility, the choice of undulator technology was made in combination to keep the electron beam energy lower than comparable facilities. The optimisation of the undulator period and module length is detailed in Sect. 6.1.2. The period was optimized to obtain balanced performance across the HXR and SXR wavelength ranges using the same undulator beamlines. The undulator modules are separated by gaps of 0.5 m containing a quadrupole, a phase shifter and a beam position monitor. There are two identical parallel undulator beamlines with an axis separation of 2.5 m. The SCUs for FEL-1 and FEL-2 have opposite helicity to allow for fast L-R polarization switching experiments when the pulses from the two FELs are combined at a dual endstation. After

the SCU undulators, there are, in each beamline, two variably polarizing APPLE-X afterburner undulators for the production of variably polarizing FEL output. For details of the undulator design and optimisation, see Sect. 6.1.

4.1.3.7 Photon beamlines and end stations

The photon transport system starts with a front end containing a bremsstrahlung collimator, a photon shutter and a set of photon diagnostics. The front end is followed by photon beamlines and an experimental area hosting user endstations. The SXR endstations are primarily concentrated on the FEL-1 side, whereas the HXR ones are mostly located on the FEL-2 side. The path lengths in the beamlines are set to synchronize pulses from the twin FELs at the dual endstations.

The experimental area comprises 5 X-ray hutches, 2 laser laboratories, 2 control rooms, and a technical gallery to access the hutches. The hutches host refocusing optics, photon diagnostics, endstations, local control electronics, and data acquisition systems. The optical laser beam can be transported from the laser room, located upstream of the hutches, to incoupling mirrors positioned close to the endstations. The hutches and laser laboratories are surrounded by a technical gallery for easy access. For full details of the photon beamlines, see Sect. 6.2.

4.1.3.8 Building design and infrastructure

The CompactLight building, shown in Fig. 11, comprises a number of different sub-buildings and sections. The design follows a hybrid approach with shielding blocks separating the underground Linac Tunnel from the Infrastructure Hall. The Linac Tunnel section is 4 m wide, and the Infrastructure hall is 7 m wide and accommodates 50 klystrons, 50 modulators, nearly 300 electronic rack units and the necessary space for routing waveguides and pipes and cable trays through direct penetrations to the tunnel. Downstream of Linac-2, the tunnel and Infrastructure Hall widths increase to accommodate the SXR bypass line required for Upgrade-2. The Experimental Hall contains the photon beamlines with front-end diagnostics, shielded end-stations, laboratories, and auxiliary spaces. Space for a laser laboratory, a magnet laboratory, a loading bay/assembly room, and user laboratories has been allocated. For full details, see [71].

4.2 FEL performance

The performance of CompactLight has been analyzed and optimized via detailed simulations of the accelerator and free-electron laser. This section of the report presents the results of this work. The emphasis is on performance in the Hard X-ray regime—here, the demands on the electron bunch quality are most stringent. For example, from Eq. 13, the electron bunch energy spread must be less than the FEL ρ-parameter which reduces as the photon energy increases, and similarly, from Eq. 16, the beam emittance requirement is more stringent for higher photon energies.

At the start of the project, a 'nominal' electron bunch was defined that would enable the FEL to satisfy the output requirements. The parameters of this bunch were determined through semi-analytical FEL performance calculations, initial FEL simulations, considerations of undulator technology options, estimates of emittance and energy spread at the electron source, and degradation due to collective effects during beam acceleration and transport to the FEL. This process was iterative, combining input from a range of work packages. The resulting parameters for the nominal electron bunch are shown in Table 3. Note that the energy, emittance, and energy spread are assumed to be constant along the bunch.

In Sect. 4.2.1, the performance of the FEL using this nominal bunch is presented via simulations using the code Genesis 1.3 at photon energies from 2 to 16 keV. These results indicate the relative FEL performance at different photon energies and confirm that the nominal bunch parameters are satisfactory. Later, in the project, once the accelerator design was complete, it was possible to simulate the FEL with a fully tracked electron bunch. Several iterations of accelerator optimisation were performed, with FEL simulations informing the quality of the FEL output. As will be seen, the performance with the final iteration of the tracked bunch exceeds the performance

Table 3 Parameters of the nominal electron bunch

Parameter	Unit	Value
Bunch profile		Gaussian
Energy	GeV	5.5
Peak current	kA	5.0
Normalized emittance	mm mrad	0.2
RMS energy spread	keV	550
Bunch charge	pC	75

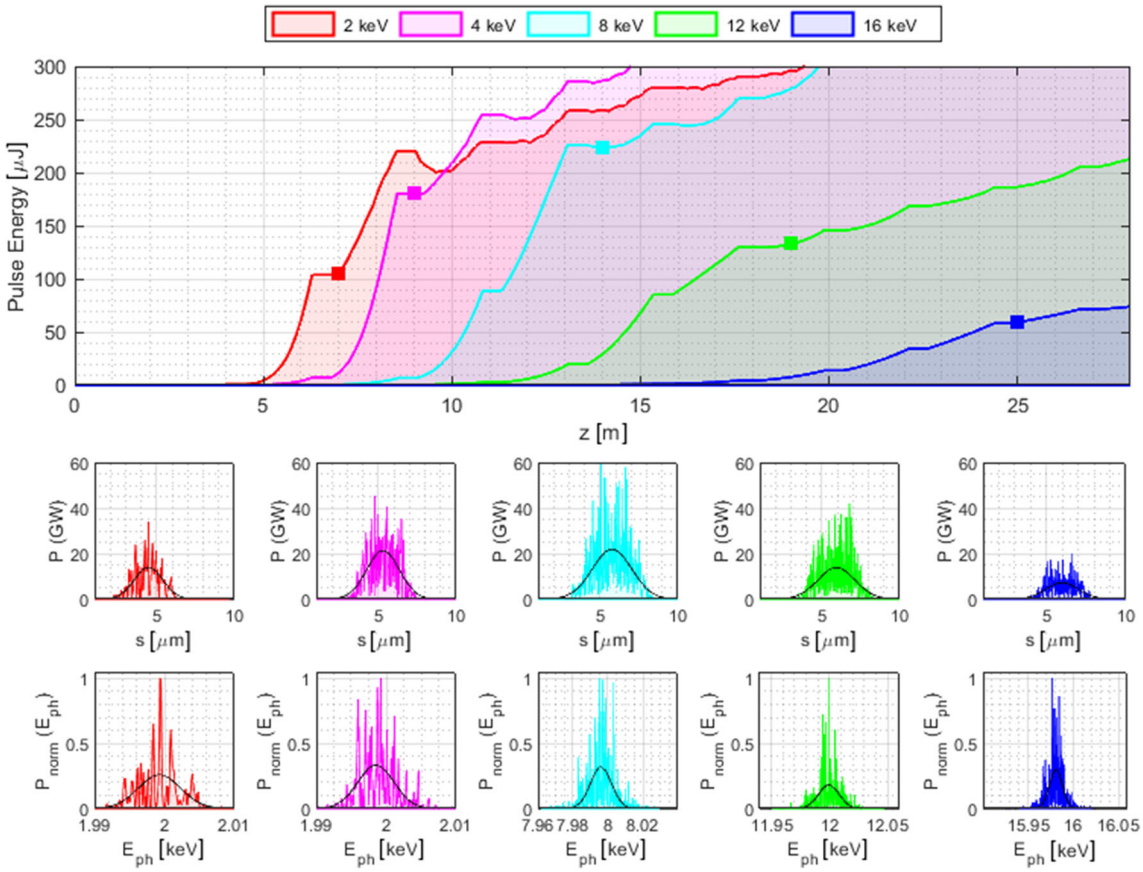

Fig. 14 Pulse energy growth, pulse profiles, and spectra for HXR FEL operation using the nominal bunch

with the nominal bunch. These results are presented in Sects. 4.2.2 and 4.2.3. In Sect. 4.2.2, the performance of the FEL with the tracked bunch is compared to that of a 'static error' bunch which is an equivalent tracked bunch but with degraded emittance. The purpose is to check for sufficient contingency in the design, so that the FEL can still satisfy the user specification. The FEL operation here is at 16 keV where the degraded emittance is expected to be most detrimental. In Sect. 4.2.3, dynamic errors are added to the bunch. The performance with the nominal tracked bunch is used as a control. Realistic errors are added to the accelerator parameters, for example, RF phase and gradient errors, to assess the expected performance and shot-to-shot stability of the FEL output in the presence of these dynamic errors.

In Sect. 4.2.4, studies are presented of the performance of the SXR and HXR self-seeded schemes introduced in Upgrade-2, using the nominal electron bunch, to demonstrate the change in performance compared to the SASE operation of the baseline configuration. Finally, in Sect. 4.2.5, a summary is given of the predicted FEL performance at different wavelengths and in different operating modes. To obtain the best possible predictions of FEL performance at different photon energies, the 16 keV results from the fully tracked bunch with dynamic errors are scaled according to the results obtained using the nominal bunch at different photon energies.

4.2.1 SASE FEL performance with nominal electron bunch

Figure 14 show the pulse energy growth, pulse profiles and spectra for HXR FEL operation using the nominal bunch. The pulse profiles and spectra are shown at the relevant saturation points, indicated by the colored squares on the pulse energy plot. Saturation is the point where the pulse energy growth starts to deviate from exponential. The black curves on the profiles and spectra are Gaussian fits, used to determine the averaged peak power and FWHM bandwidth data to calculate the peak brightness. Figure 15 summarizes the data over the range of pulse energies. The brightness is calculated using Eq. 11 and then normalized to the measured bandwidth.[2] The calculations show that the maximum pulse energy is 225 μJ at 8 keV, but that the minimum bandwidth and

[2]Calculations of the FEL transverse coherence at 16 keV, quantified via the M^2 parameter, have indicated that typically at saturation $M^2 \approx 1.5$, suggesting that the brightness is overestimated here by about this factor.

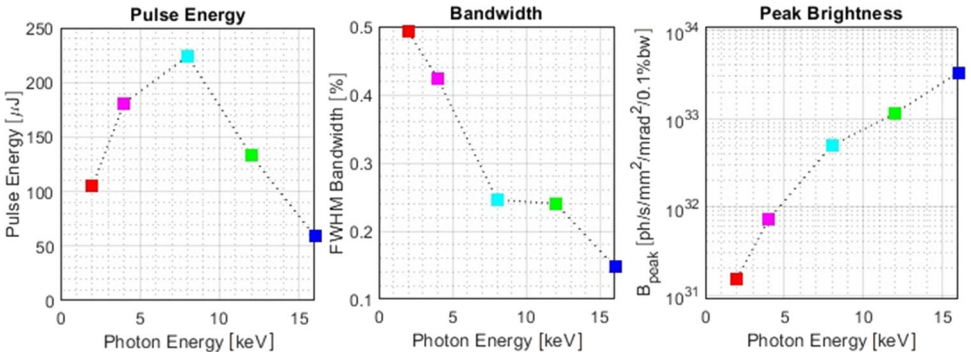

Fig. 15 Saturation pulse energy, FWHM bandwidth, and peak brightness for HXR FEL operation using the nominal bunch

maximum brightness occur at 16 keV where the FWHM bandwidth is 0.15% and the peak brightness is 3×10^{33} ph/s/mm^2/mrad^2/0.1% BW.

4.2.2 SASE FEL performance with tracked bunch and static error bunch

The properties of the tracked bunch are shown in Fig. 16. The normalized slice emittance in both transverse planes is less than 0.15 mm.mrad along the whole bunch—this is significantly smaller than the normalized emittance of 0.2 mm mrad for the nominal bunch. A small longitudinal energy chirp and a 20 μm transverse shear are in the horizontal plane. The slice energy spread is approximately 1000 keV, double the value of the nominal bunch. To create a static error bunch, the emittance was artificially increased at the laser heater to a value comparable with the average emittance obtained at the end of Linac-3 from 100 random seeds of static errors and realistic

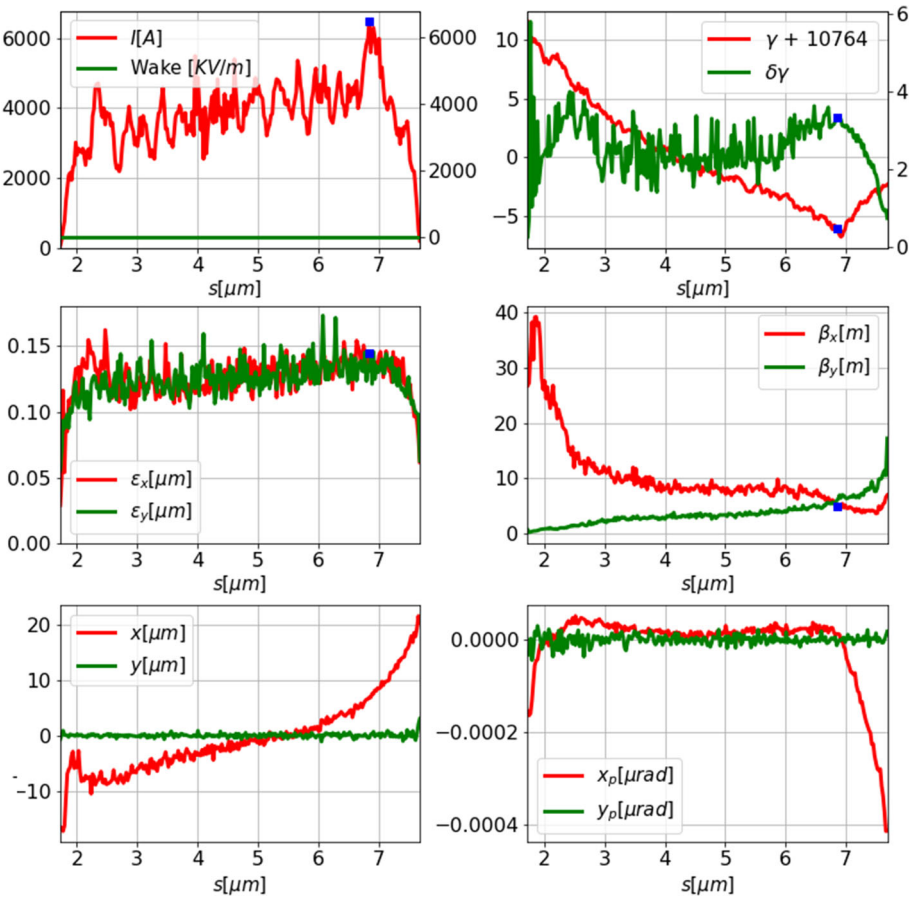

Fig. 16 Slice properties of the tracked bunch used for the S2E simulation

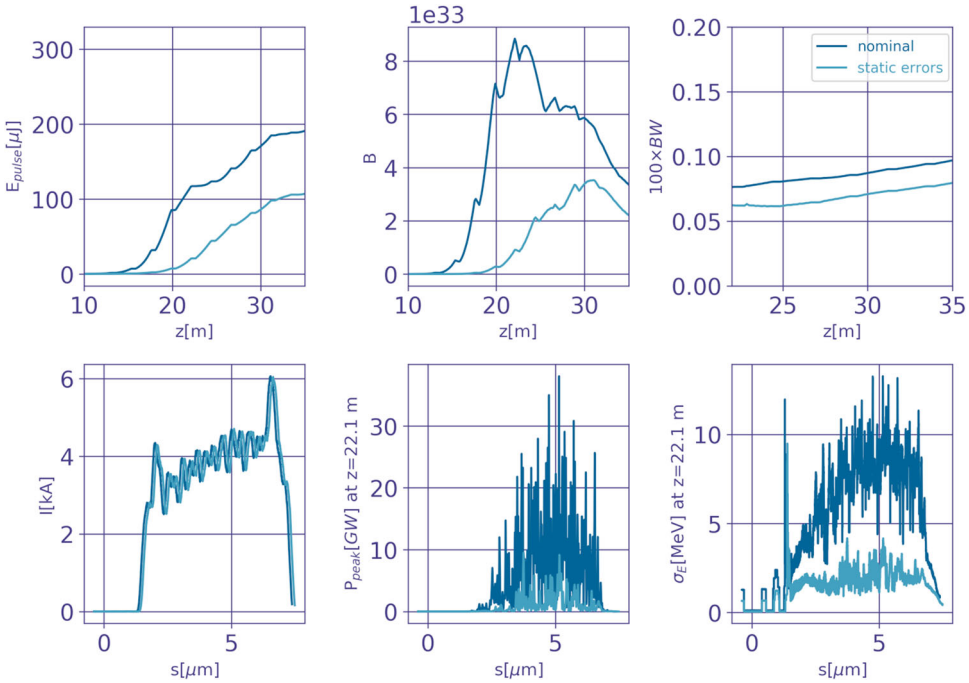

Fig. 17 Comparison of 16 keV FEL pulse energies (top left), FEL pulse peak brightness (top centre), pulse bandwidth (top right) as a function of distance along the undulator axis, and current profiles (bottom left), peak FEL power (bottom centre), and energy spread (bottom right) along the bunch for the tracked bunch (dark blue) and the static error bunch (light blue)

beam-based alignment. The static error bunch was propagated through the machine with a rematched lattice. At the FEL, the normalized emittance is less than 0.2 mm.mrad over all slices, an increase of approximately 0.05 mm.mrad over the tracked bunch. All other slice properties are unchanged.

Figure 17 shows a comparison of FEL performance between the tracked bunch and the static error bunch. The highest peak brightness obtained for the tracked bunch is 8.9×10^{33} ph/s/mm^2/mrad^2/0.1% bandwidth at 22 m along the undulator axis. Here, the brightness is calculated directly from Eq. 10 with the electron and photon beam sizes and divergences derived directly from the simulation results. At this distance, the FEL bandwidth is 0.076%. The pulse energy at the highest peak brightness is 116 μJ. The error bunch generates a pulse for which the brightness saturates later, at about 31 m, and has a narrower bandwidth and reduced pulse energy. The highest peak brightness for the pulse generated by the static error bunch is 3.52×10^{33} ph/s/mm^2/mrad^2/0.1% BW which is about 40% the value of the highest peak brightness for the tracked bunch. The performance of the static error bunch is not as good as that of the tracked bunch. However, it should be noted that:

- Although the saturation length is slightly longer than for the tracked bunch, it is still comfortably within the 36 m length of the undulator included in the design.
- The brightness comfortably exceeds the user minimum requirement of 10^{33} ph/s/mm^2/mrad^2/0.1% bandwidth.

This demonstrates that sufficient contingency has been built into the accelerator design to account for a degraded emittance.

To help understand the dependence of the FEL performance on a wider range of emittance values, a set of simulations was done in which the transverse phase space of the tracked bunch, as it enters the undulator, was artificially expanded by multiplying the x, y, x', and y' values for each electron by scaling factors. The results are shown in Fig. 18. The left-hand plot shows the peak brightness, and the right-hand plot shows the saturation length. The tracked bunch working point is at the bottom left corner of each plot. The dotted line in the saturation length plot is the 36 m contour shown because this is the length of the CompactLight undulator. The results confirm an acceptable level of contingency in the design to cope with a reasonable increase in emittance over the nominal values.

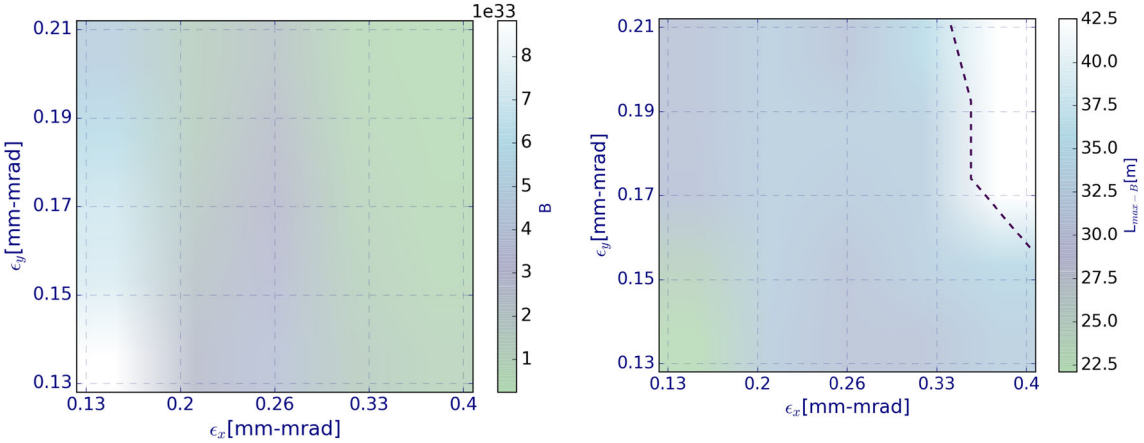

Fig. 18 Contour plots of FEL peak brightness (left-hand side) and saturation length (right-hand side) for the tracked bunch with artificially increased emittances. The dotted line on the right-hand side plot corresponds to a saturation length of 36 m, which is the undulator length specified in the design

4.2.3 SASE FEL performance with dynamic error bunches

Table 38 in Sect. 5.3.3.3 shows the distribution of errors applied to the accelerator parameters to generate the dynamic error bunches. Figures 19, 20, and 21 summarize the results of the FEL simulations. Figure 19 compares the relative RMS variation of the pulse energy and peak brightness along the undulator. Each tracked bunch simulation has a different shot noise seed, so that the stability of the output due to the intrinsic SASE noise can be seen. The dynamic error bunches also have different shot noise seeds. Hence, the stability depends both on the intrinsic SASE noise and the errors in the accelerator parameters—these results are, therefore, a good indication of the predicted FEL stability as experienced by the users.

The user requirement stated in Sect. 3.2 is that the RMS stability of the FEL pulse energy should be less than 10%. This value is achieved at $z = 23.5$ m, just over 1 m further than the distance at which the highest peak brightness is reached, but at this position, the peak brightness is still very close to the maximum, and the pulse energy is still increasing. This distance is therefore chosen as the 'point of comparison'. The distributions of pulse energies and peak brightness at the point of comparison for the tracked bunches and the dynamic error bunches are shown in Fig. 20.

Figure 21 shows the evolution of pulse energy and peak brightness along the undulator. The results for the tracked bunch are shown in blue—the average over 200 SASE shot noise realisations is shown in dark blue, with the individual simulations in light blue. The results for the dynamic error bunches are shown in green—the average over 200 bunches is shown in dark green and the individual simulations in light green.

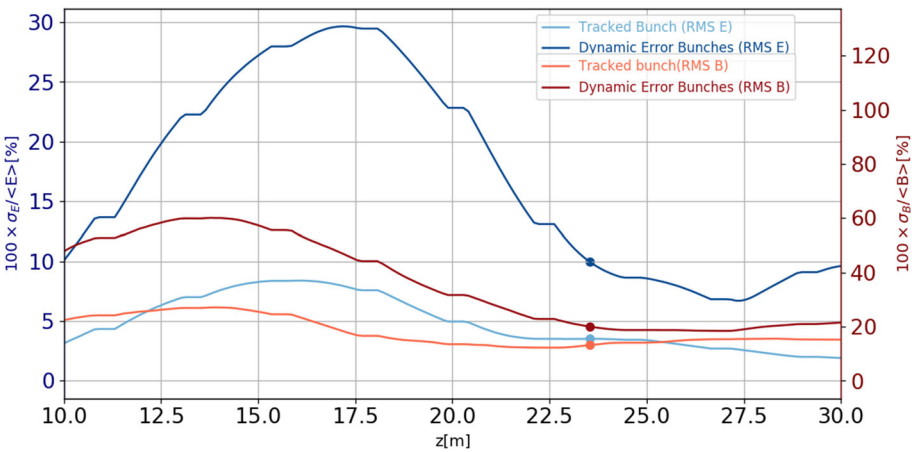

Fig. 19 Comparison of RMS of the pulse energies and peak brightness distributions obtained from the dynamic error bunches and tracked bunch along the undulator

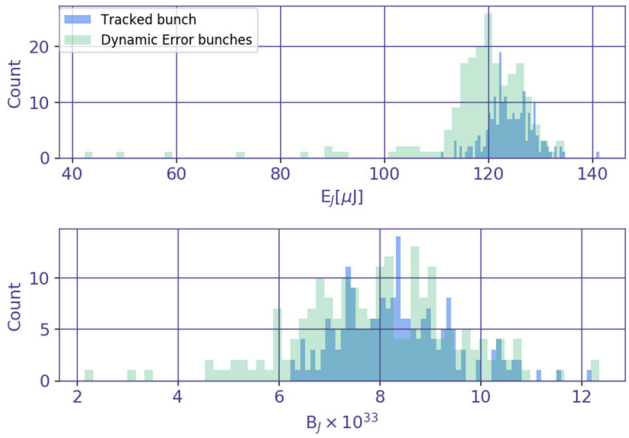

Fig. 20 Histograms of pulse energy (top) and peak brightness (bottom) for 200 tracked bunches with SASE shot noise and 200 dynamic error bunches

When averaged over noise realisations, the highest peak brightness for the tracked bunch is $9.23{\times}10^{33}$ ph/s/mm^2/mrad^2/0.1% BW. However, at the point of comparison, it has reduced slightly to $8.3{\times}10^{33}$ ph/s/mm^2/mrad^2/0.1% BW. The saturation length for the dynamic error bunches is slightly longer than for tracked bunches, but the distance at which the highest peak brightness is reached is unchanged. At the point of comparison, the average peak brightness is 7.9×10^{33} ph/s/mm^2/mrad^2/0.1% BW—around 5% lower than for the tracked bunches. The average pulse energy for the dynamic error bunches at the point of comparison is 118 μJ, 5% less than for the tracked bunch.

Therefore, the inclusion of dynamic errors in the bunch distributions causes a small decrease in averaged peak brightness and pulse energy and increases the fluctuations in the FEL output. However, the user requirements that RMS fluctuations in pulse energy should be less than 10% and that the peak brightness should exceed 10^{33} ph/s/mm^2/mrad^2/0.1% BW are both satisfied.

4.2.4 Upgrade-2: self-seeding performance

Upgrade-2 includes self-seeding [72] options for both the HXR and SXR beamlines. The generic method is that the FEL pulse is extracted at some point along the undulator line before saturation and filtered to reduce its spectral width, hence increasing its coherence length. The filtered pulse is then used as a seed and injected into the second section of the undulator line to be amplified to saturation. The method used to filter the pulse depends on the wavelength regime. The CompactLight design follows the methods used in the existing FEL facilities, both in the SXR [73] and the HXR [74]. In the SXR, a compact grating monochromator is used. This replaces an undulator module. In the HXR, a diamond crystal is used, with the crystal orientation adjusted, such that a notch is taken out of the spectrum at the appropriate photon energy. The output pulse from the crystal then contains a trailing monochromatic wake used as the seed pulse. In both cases, the electron beam must be diverted in a small chicane around the optical elements, with the path length of the electron bunch to overlap with the seed pulse in the second undulator section. The chicane has another useful function—the longitudinal dispersion, parameterised to first order by the chicane matrix element R_{56}, has the effect of smearing out the noisy FEL-induced microbunching induced in the first undulator section, which otherwise would re-imprint itself upon the seed pulse in the second undulator section, reducing the coherence length.

The next sections summarize the design and simulation studies that have been done to show the feasibility of the schemes in the SXR and HXR for the CompactLight parameters and illustrate the performance enhancement compared to the baseline SASE operation.

4.2.4.1 SXR self-seeding

The SXR self-seeding monochromator is based on the design described in [75] for the European XFEL, modified to accept a large photon-energy range (0.25–2 keV). Figure 22 shows a schematic of the layout. The monochromator consists of a plane grating that creates an angular dispersion of the X-ray beam in the plane perpendicular to the electron-bunch chicane. The beam is then focused by the cylindrical mirror M1 on the exit slit, which selects a narrow bandwidth. By keeping a constant beam deviation angle at the grating and thus a constant incidence angle on M1, a fixed focus position at the exit slit is provided for all photon energies. The beam is refocused to the undulator entrance, separately in the horizontal and vertical plane, by two cylindrical mirrors, M2 and M3. All optics are coated with platinum to provide sufficient damage threshold and reflectance across the photon-energy

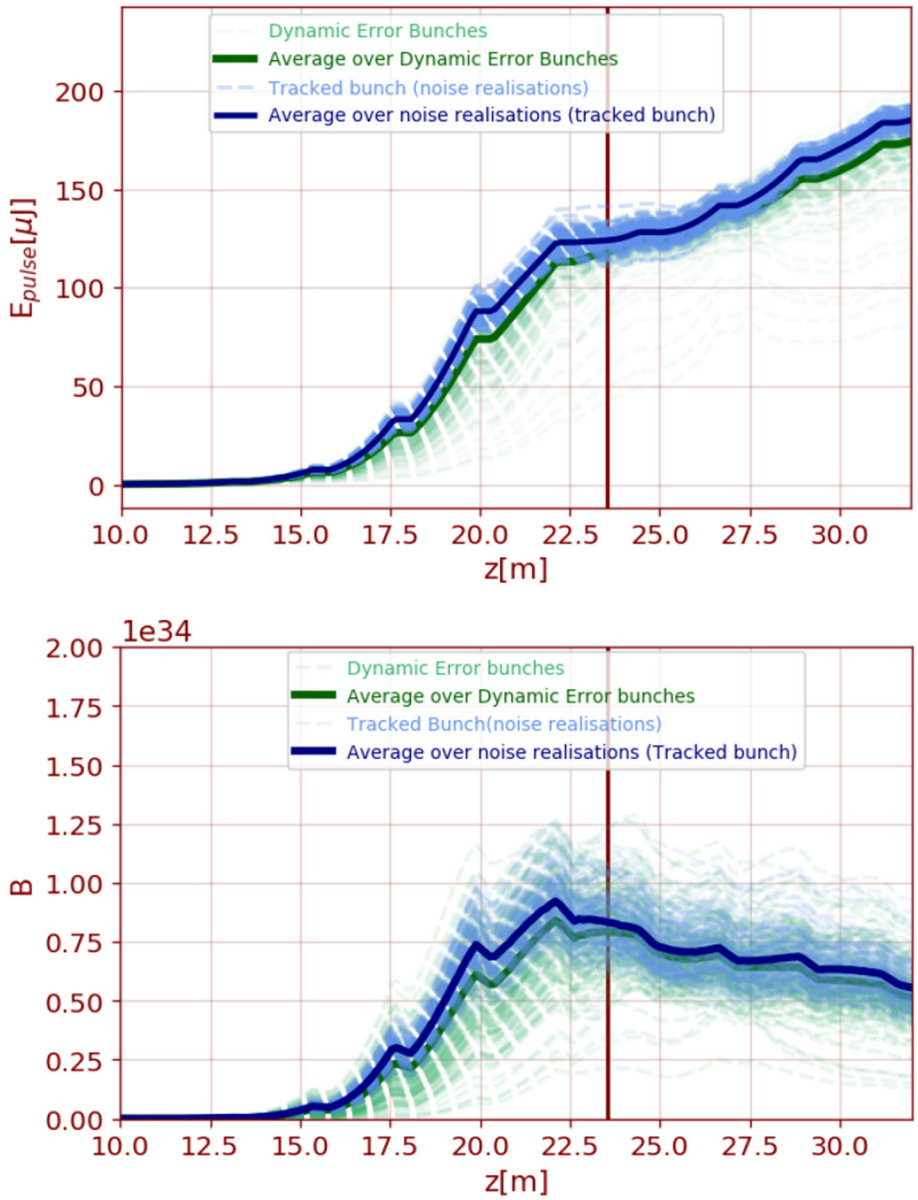

Fig. 21 Comparison of 16 keV FEL pulse energy (top) and peak brightness (bottom) for 200 tracked bunches with SASE shot noise and for 200 dynamic error bunches

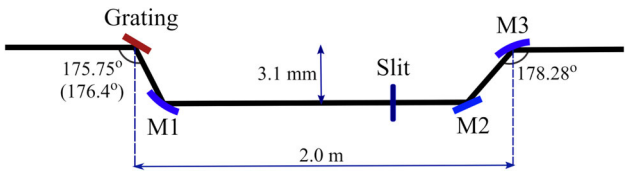

Fig. 22 Schematic of the SXR grating monochromator. The two beam deviation angles at the grating are associated with the 500 l/mm and 1000 l/mm (in parenthesis) gratings. The blaze angles of the gratings are 1.3° (500 l/mm) and 0.9° (1000 l/mm)

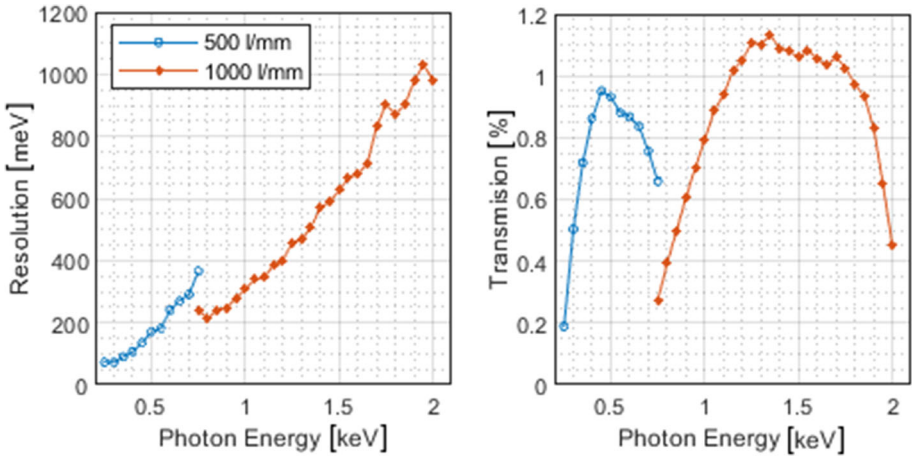

Fig. 23 Resolution and transmission of the SXR self-seeding monochromator

range. Two gratings with different line densities (500 l/mm and 1000 l/mm) enable high transmission over the whole photon-energy range. The resolution and transmission of the monochromator are shown in Fig. 23.

The parameters used for the FEL simulations were the nominal ones shown in Table 3 with the electron bunch energy reduced to $E = 2.36$ GeV. The undulator parameter was $a_w = 1.013$ giving FEL resonance at 2 keV ($\lambda = 0.62$ nm). The optimum location to position the monochromator was found to be after the second undulator module. At this point, the output pulse from the monochromator had sufficient intensity to dominate the electron beam shot noise power yet the energy spread growth in the electron bunch was not enough to prohibit exponential gain in the second undulator section. Placing the monochromator at other locations gave poorer results.

Figure 24 shows the simulated FEL pulse profile entering and exiting the monochromator. The centre plot shows the incident pulse spectrum and the extent of the hard-edged 1000 meV bandwidth centred at $\lambda = 0.618$ nm. The output pulse is seen to have a smooth profile with a peak power reduced from 1300 to 0.8 MW due to the filtering and the 0.45% transmission. Although the pulse power has been much reduced, it is still sufficient to dominate the SASE shot noise emission in the second undulator section, as shown.

For 2 keV operation, the increase in the photon path length when passing the monochromator is $\Delta s = 0.144$ mm. The electron is delayed by the same amount in a compact chicane. For any dipole chicane, the R_{56} term is twice the electron beam path length increase compared to on-axis propagation. This is applied as a simple linear transform to the electron bunch as it enters the second undulator section. The effect of the longitudinal dispersion on the microbunching induced by the FEL process in the first undulator section is shown in Fig. 25—it is seen to be completely suppressed.

Figure 26 shows the FEL performance in the second undulator section after the monochromator. The pulse energy grows to 70 μJ at a distance of $z = 6.5$ m and 140 μJ at $z = 8.5$ m. The pulse profiles at these two pulse energies are shown [(b) and (c)] in comparison to SASE pulses with the same pulse energies. The SASE simulations have identical undulator, electron beam, and simulation parameters. The 70 μJ self-seeded pulse has a somewhat

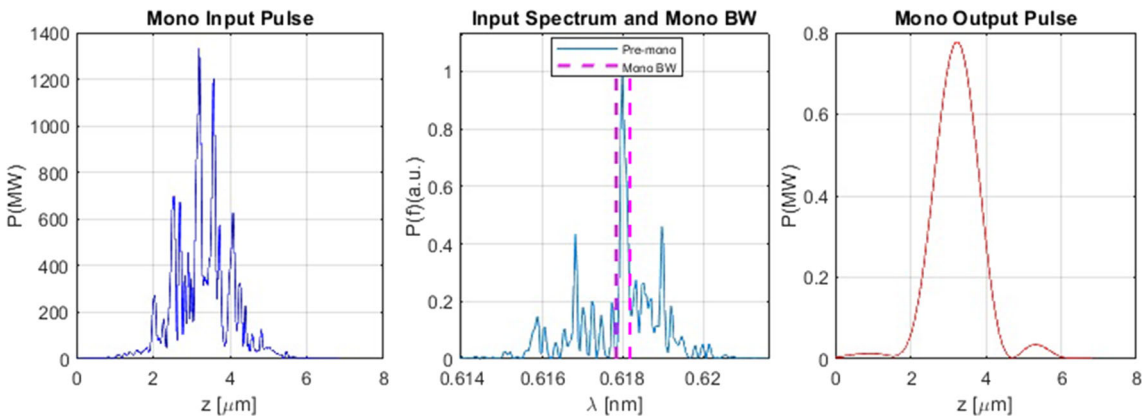

Fig. 24 Monochromator input pulse power profile (left), spectrum and monochromator bandwidth (centre), and output pulse (right)

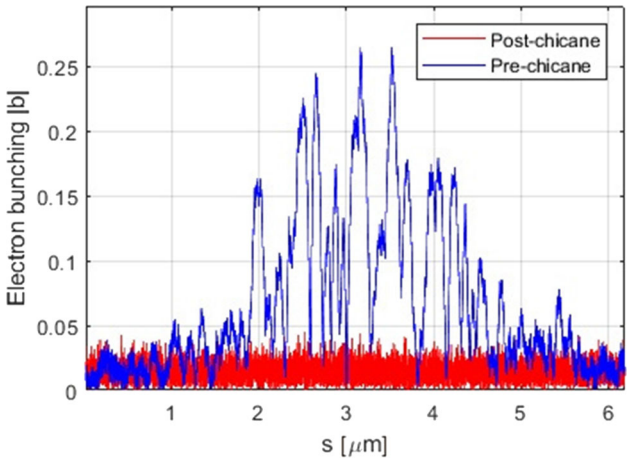

Fig. 25 Electron beam microbunching before and after the chicane

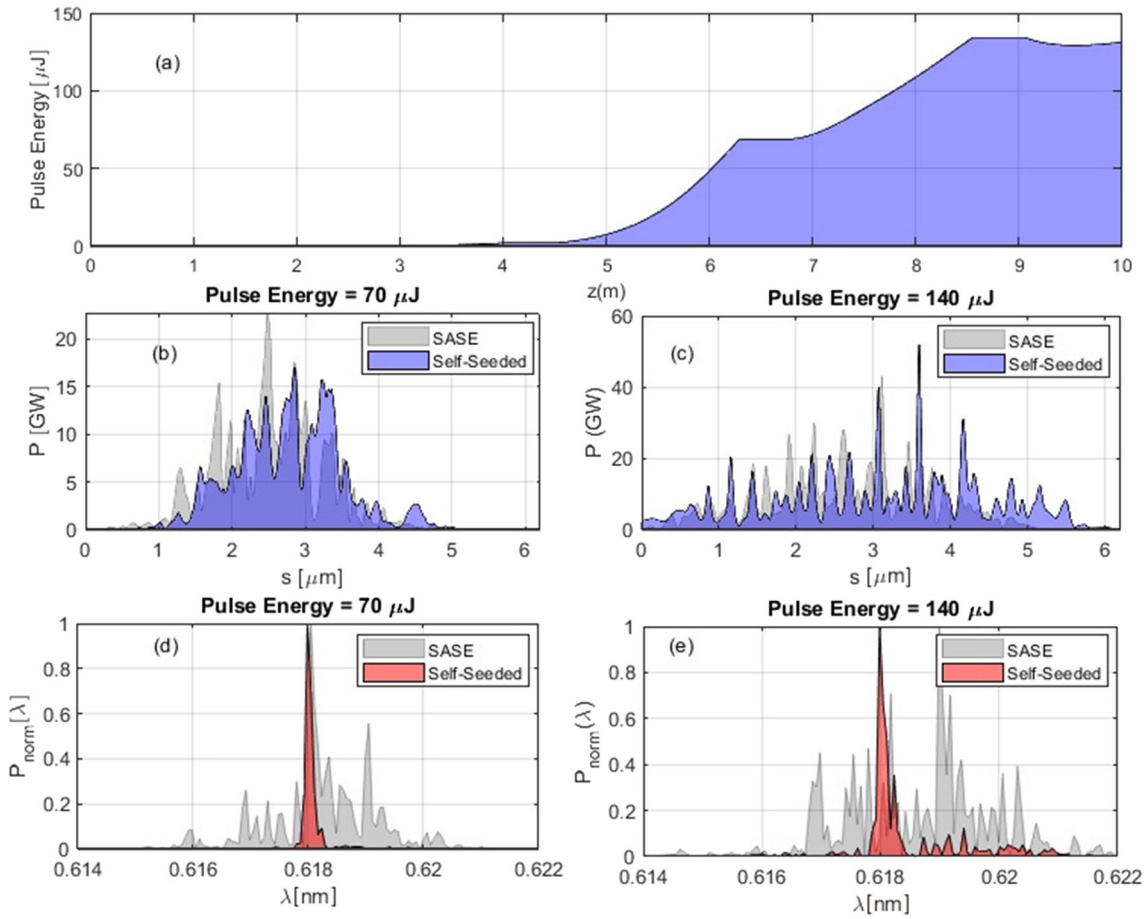

Fig. 26 SXR Self-Seeding simulation results for output at 2 keV: **a** Growth of pulse energy vs distance z through second undulator section. **b** Self-seeded pulse profile at $z = 6.5$ m with pulse energy 70 μJ (in blue) and equivalent SASE pulse of the same pulse energy (in grey). **c** Self-seeded pulse profile at $z = 8.5$ m with pulse energy 140 μJ (in blue) and equivalent SASE pulse of the same pulse energy. **d** Spectra of 70 μJ self-seeded pulse (red) and equivalent SASE pulse (grey). Both spectra were normalized to peak values. **e** Spectra of 140 μJ self-seeded pulse (red) and equivalent SASE pulse (grey)

smoother profile than the equivalent SASE pulse, but a much smaller FWHM bandwidth of $\Delta\lambda/\lambda_0 = 2 \times 10^{-4}$. At 140 μJ, the self-seeded pulse profile looks qualitatively similar to the equivalent SASE pulse, and again, the FWHM spectrum is far narrower, although not so clean. The FWHM length of the 70 μJ self-seeded pulse is $\Delta s = 1.3$ μm. The time-bandwidth product of the pulse, a measure of how close the pulse is to the transform limit, can be estimated as

$$\Delta\nu\Delta t = \frac{1}{\lambda}\frac{\Delta\lambda}{\lambda_0}\Delta s = 0.42, \tag{18}$$

which is very close to the value of a Gaussian pulse with constant phase. Note that the time-bandwidth product of the 140 μJ pulse has not been calculated, because the pulse profile is too irregular to reasonably determine the FWHM pulse duration.

An initial analysis of the stability of self-seeding vs. SASE was made, based on 20 self-seeded shot noise realisations and 20 SASE simulations. The results are shown in Fig. 27. At saturation, the relative rms fluctuation of the self-seeded pulse energy was 12% compared to 9% for SASE. The self-seeded spectra showed very good shot-to-shot reproducibility with stability of the central wavelength.

In summary, a realistic SXR self-seeding scheme has been designed and simulated. The results indicate that at 2 keV photon energy near-transform-limited pulses with an energy >70 μJ can be produced.

4.2.4.2 HXR self-seeding

The parameters used for the FEL simulations were the nominal ones, as shown in Table 3. The undulator parameter was $a_w = 0.6174$, giving FEL resonance at 16 keV ($\lambda = 0.0775$ nm).

As described above, the monochromator for HXR operation is a diamond crystal, with the crystal orientation adjusted for transmission at the appropriate photon energy. The output pulse from the crystal contains a trailing monochromatic wake which is used as the seed pulse [76]. The monochromator was modelled using an approach based on dynamic diffraction theory developed for SwissFEL [77, 78], which agrees well with the model by Geloni et al. [76].

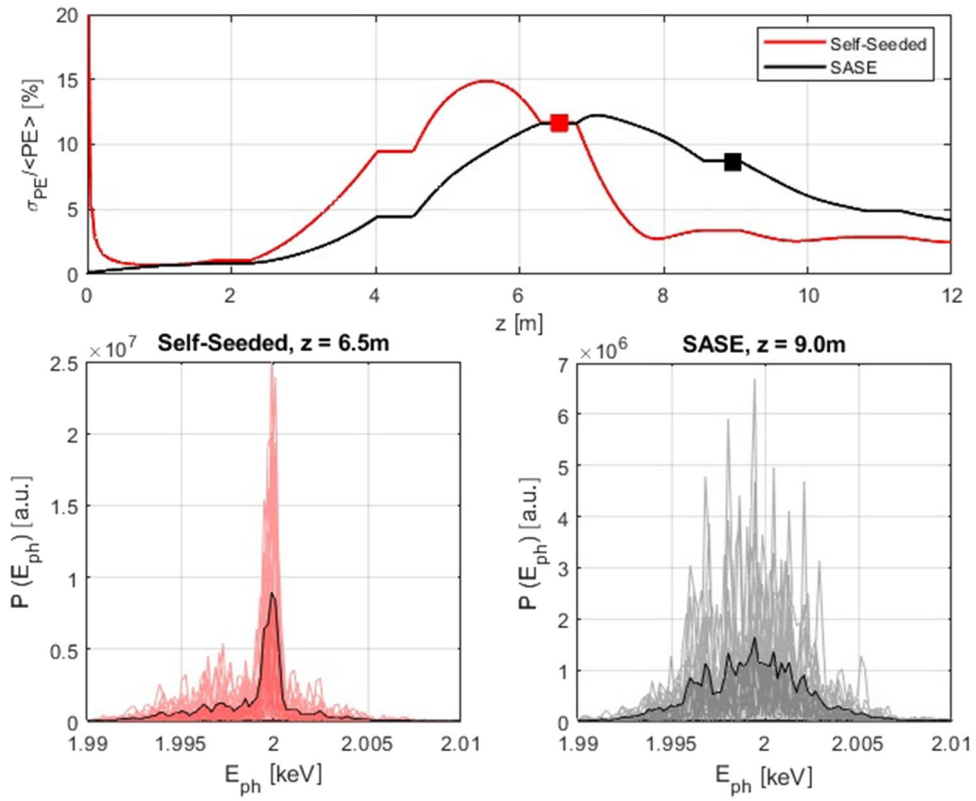

Fig. 27 Stability of SXR self-seeding vs SASE operation. The top plot shows the relative rms stability of the pulse energy vs distance through the undulator, for self-seeding and SASE. The colored squares indicate the saturation points. The bottom left plot shows the spectra of 20 shot-noise realisations (light pink) and the average overall shots (darker pink). The bottom right plot shows the equivalent data for SASE

Optimisation of the setup requires determining the monochromator's location and the crystal thickness. This was carried out fairly coarsely due to the computationally intensive demands of the simulations but with promising results. FEL simulations for varying lengths of the first undulator section (up to the monochromator) were carried out for five-shot noise realisations. The monochromatic wake was calculated for various crystal thicknesses. The wake is composed of a series of peaks, the peak power of which decreases with distance behind the main pulse, such that the first trailing pulse is most effective for self-seeding. Increasing the thickness of the crystal increases the peak power of the peaks in the wake while reducing their duration and separation. Taking each case into the second undulator, simulation stage requires the delay applied to the electron bunch to be appropriately set to overlap with the wake. Also, as described in the previous section, the corresponding R_{56} should be applied, which reduces micro-bunching from the first stage. For optimum performance, the second undulator stage should also be detuned to take into account energy lost from the electron beam up to that point.

It was found that a combination of eight undulator modules in the first stage, together with a crystal thickness of 0.2 mm, was suited to give good performance. Figure 28 shows the simulated FEL pulse profile entering and exiting the monochromator. The central plot and its inset show the filtering effect applied by the crystal at $\lambda = 0.077566$ nm and the pulse spectrum before and after this is applied. The plot of the output pulse on the right is scaled to show the trailing monochromatic wake, which has significantly lower power than the input pulse but is sufficient to dominate the shot noise emission in the second undulator section. In the right plot, the results for four other shot noise realisations are shown. The required electron beam delay to overlap with the wake is 7 μm in this case, with R_{56} =14 μm applied as a simple linear transformation to the electron bunch before the second undulator section.

Figure 29 shows the simulated performance of the self-seeding scheme compared to SASE. For the self-seeded case, the pulse energy reaches ∼50 μJ after six undulator modules of the second stage, and ∼100 μJ after eight undulator modules. The pulse temporal profiles and spectra at these two pulse energies are shown in comparison to equivalent SASE simulation results taken at the same pulse energies. Similar to the SXR results, the temporal profile for the lower pulse energy case (50 μJ here) is somewhat smoother than the equivalent SASE pulse, while the bandwidth is significantly reduced to $\Delta\lambda/\lambda_0 = 2 \times 10^{-5}$. The time–bandwidth product in this case has been estimated to be 0.57, which is close to a Gaussian with constant phase. The higher pulse energy case has a qualitatively degraded temporal profile while retaining a clean, narrow spectrum. Note that unlike Fig. 26, the top plot in Fig. 29 shows distance from the start of the first undulator section, to show a comparison with SASE, with the other four shot-noise realisations from Fig. 28 also shown for the self-seeded case.

4.2.4.3 Self-seeding summary

Realistic SXR and HXR self-seeding schemes have been designed and simulated. The results indicate that at 2 keV photon energy near-transform-limited pulses with an energy >70 μJ can be produced, and that at 16 keV photon energy single wavelength pulses with energy 100 μJ can be produced. The simulations shown here indicate that self-seeding schemes can, therefore, introduce a significant brightness enhancement over SASE of a factor of 15–20, as shown in Fig. 30.

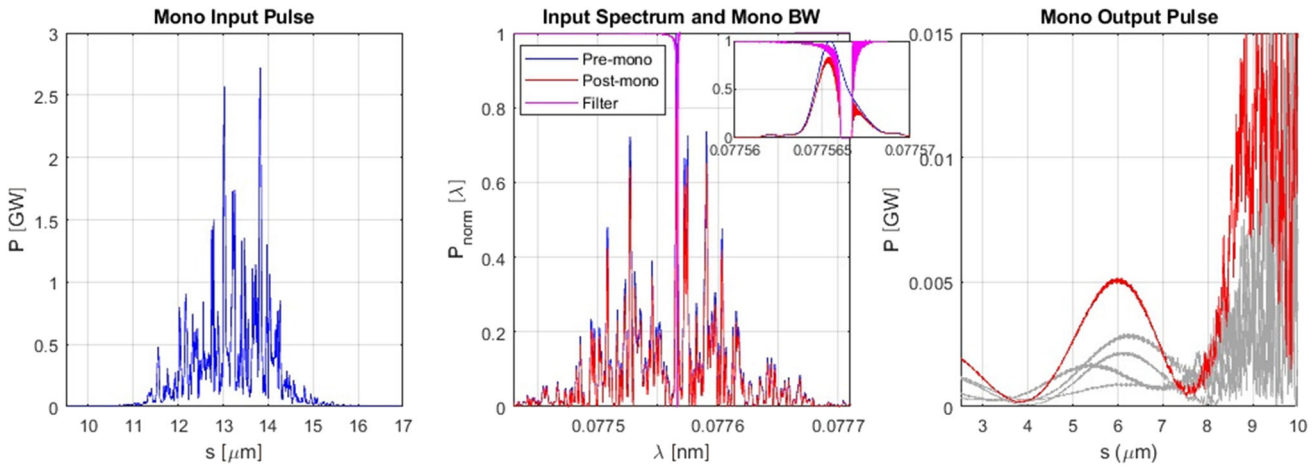

Fig. 28 Monochromator input pulse power profile (left), spectrum and monochromator bandwidth (centre, with zoomed horizontal axis in the inset), and output pulse (right). In the right plot only are shown results for four other shot noise realisations

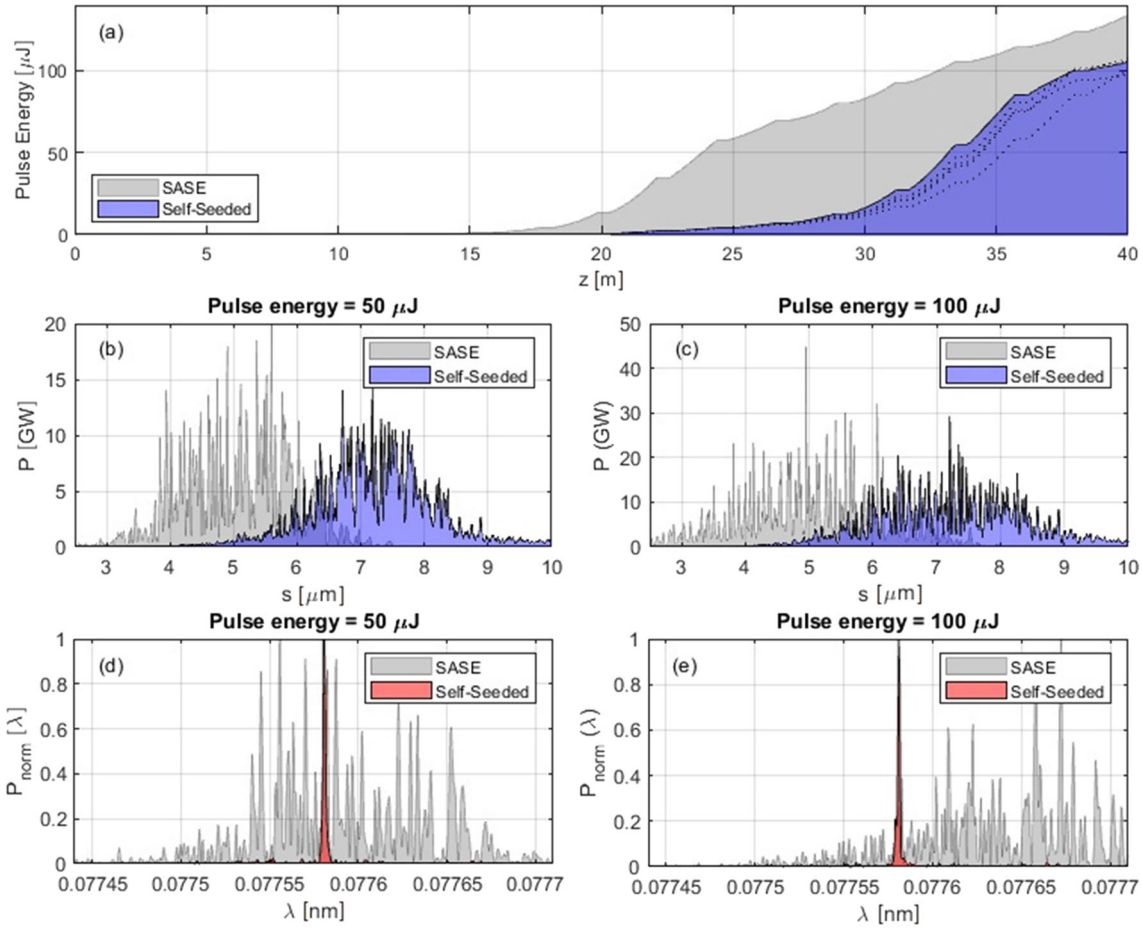

Fig. 29 HXR Self-Seeding simulation results for output at 16 keV: **a** Growth of pulse energy vs distance z from the start of the first undulator section (dashed lines are other shot-noise cases). **b** Self-seeded pulse profile at $z = 33.5$ m (6 modules/13.1 m in the second stage) with pulse energy 50 μJ (in blue) and equivalent SASE pulse of the same pulse energy (in grey). **c** Self-seeded pulse profile at $z = 38.0$ m (8 modules/17.6 m in the second stage) with pulse energy 100 μJ (in blue) and equivalent SASE pulse of the same pulse energy. **d** Spectra of 50 μJ self-seeded pulse (red) and equivalent SASE pulse (grey). Both spectra were normalized to peak values. **e** Spectra of 100 μJ self-seeded pulse (red) and equivalent SASE pulse (grey)

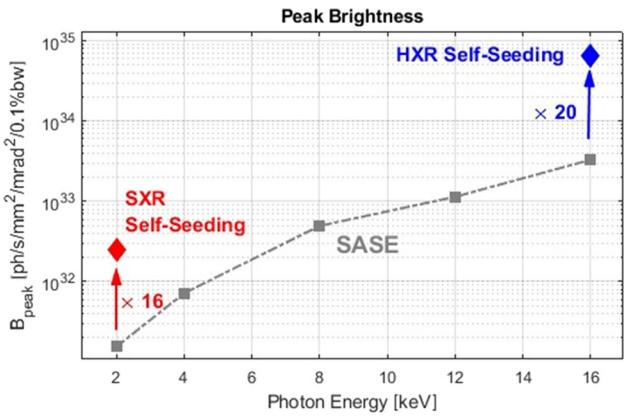

Fig. 30 Figure showing enhancement of peak brightness compared to SASE for the SXR and HXR self-seeding examples. The electron bunch is an ideal Gaussian current profile with constant nominal slice parameters

4.2.5 Summary of FEL performance

The predicted performance of the CompactLight FEL is summarized in Table 4. The SASE output figures at 16 keV are directly taken from the simulations using the tracked electron bunches with added dynamic errors, averaged over 200 bunches, and are the best available predictions of FEL performance. The SASE output figures at other photon energies are derived from the SASE results at 16 keV but scaled to the relevant photon energies according to the simulation results of the nominal bunch reported in Sect. 4.2.1. The self-seeded results are taken directly from the simulations, which used nominal electron bunches, so they are not directly comparable with the SASE results.

5 Accelerator

5.1 Injector

The XLS injector system extends from the electron source to the Bunch Compressor 1 (BC-1) exit, corresponding to an upper energy of 300 MeV. At about 300 MeV the electron beam experiences a transition from the "space-charge" dominated regime to the "emittance dominated" regime and the emittance compensation process, performed within the injector itself, can be considered accomplished. The target injector parameters are reported in Table 5.

To achieve these parameters, the injector design incorporates various components, as shown in Fig. 31, from the electron source (including the cathode material definition and laser system specifications), to the capture sections

Table 4 Summary of predicted FEL performance in SASE and self-seeded modes

	SASE					Self-seeded	
Photon energy (keV)	2	4	8	12	16	2	16
Pulse energy (μJ)	210	362	448	266	118	70	100
Bandwidth (% RMS)	0.19	0.17	0.13	0.10	0.07	0.01	0.001
Brightness[a]	0.04	0.17	1.2	2.7	7.9	0.17	47

[a](10^{33} ph/s/mm^2/mrad^2/0.1% BW)

Table 5 Target injector parameters

Parameter	Unit	After VB and/or BC-1
Charge Q	pC	75
Beam energy	MeV	300
RMS bunch duration σ_t	fs	350
Peak current	A	60
RMS energy spread	%	0.5
Projected RMS norm. emittance	μm	0.2
Repetition rate	Hz	100–1000

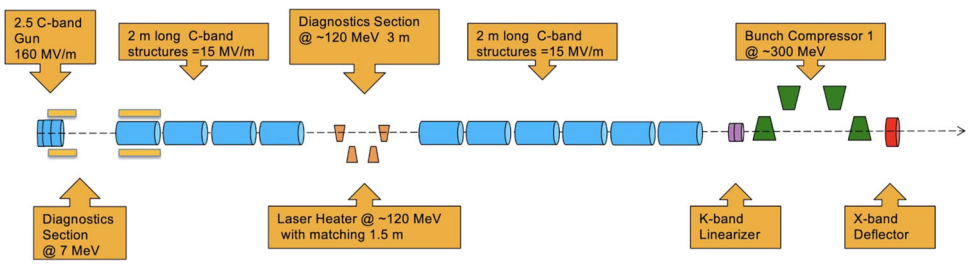

Fig. 31 Injector layout

needed to boost the beam energy up to 300 MeV (including the possibility of operating in Velocity Bunching configuration and/or with a magnetic compressor system). Additional components are required to provide the proper parameters optimization. These are the higher harmonics RF structure, see Sect. 5.2.8, for longitudinal phase space linearization, the X-band RF deflector system, see Sect. 5.4.1.4, to provide adequate longitudinal diagnostics, and the Laser Heater, to prevent possible micro-bunch instabilities in BC1. Various diagnostics tools have also been considered to monitor the beam quality along the injector itself and are described in Sect. 5.4.

The final injector design uses the same injector for both the operational modes, high (1 kHz) and low (100 Hz) repetition rate. This implies operating the whole injector at a moderate accelerating gradient while keeping the beam quality within the requirements. This choice is less expensive than a scheme with a dedicated injector for each operational mode. The final layout, see Fig. 31, includes a 2.6 cell C-Band RF Gun followed by a C-Band Booster up to 150 MeV, partially embedded in a long solenoid, a laser heater, a second C-band booster up to 300 MeV, a K-Band Linearizer, and a Magnetic Compressor BC1. To fulfil the FEL operating modes, the XLS injector will use a gun and a photoinjector laser able to operate with two e-pulses, for each RF pulse, spaced by 3 or 5 RF cycles of the C-band frequency A Copper Cathode driven by a 1 kHz Ti:Sa Laser is the choice for the electron source. This configuration meets the design goals of the XLS injector of Table 5, as shown in the beam dynamics Sect. 5.3. The following paragraphs describe the technical characteristics of the main components not described in other sections.

5.1.1 2.5 Cell C-band RF gun and solenoid design

5.1.1.1 RF gun design

The strategy for the design of the 2.5 cell RF gun has been that typically implemented in the high gradient structure design, based on the reduction of the surface electric field, surface modified Poynting vector [79] and pulsed heating [80]. To this purpose, the gun is fed with short RF pulses ($\tau < 300$ ns) and the coupling with the input waveguide is axial, through the last iris, with a mode launcher [81]. Standard couplers on the full cell, even if strongly rounded [82–84] cannot be used because of the high magnetic field and, as a consequence, high pulsed heating on the coupling holes. These two implementations (short RF pulses and mode launcher) reduce the pulsed heating (that scales with the square root of the RF pulse length), the breakdown rate (that scales with τ^5), the average dissipated power, and the surface magnetic field on the input coupler. The reduction of the average dissipated power is important, in the CompactLight case, for the high repetition rate operation (1 kHz). Also, the geometry of the standing-wave (SW) cells has been optimized introducing an elliptical shape of the irises to reduce the surface electric field. The electromagnetic design has been performed using ANSYS HFSS [85] and the simulated gun geometry is shown in Fig. 32. The four-port mode launcher has been designed following the criteria illustrated in [86] and the four ports allow complete cancellation of the dipole and quadrupole field components, typically induced by simple mode launchers. The main parameters of the structure are given in Table 6.

The structure is fed with 300 ns RF input pulses at 1 kHz repetition rate with a copper cathode peak field of 160 MV/m. The RF pulse length and cathode peak field have been chosen as a compromise between the required peak input power from the klystron, average dissipated power into the gun, and beam dynamics performance. For the same reason, instead of the original 1.5 cell gun [87, 88], the design adds one more accelerating cell to increase

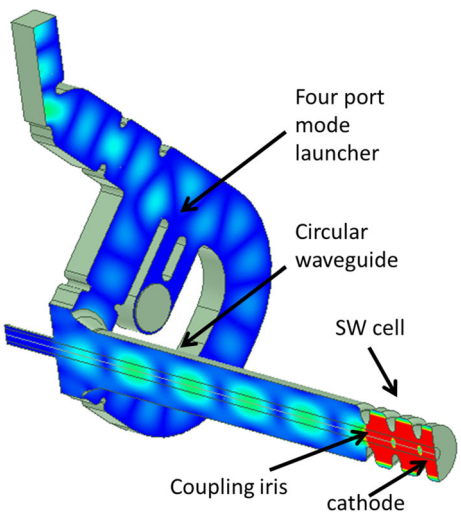

Fig. 32 Gun geometry simulated by ANSYS-HFSS

Table 6 Main parameters of the C-band gun

Parameter	Unit	Value
Working frequency	GHz	5.996
$E_{\mathrm{cath}}/P_{\mathrm{diss}}^{1/2}$	MV/(mMW$^{1/2}$)	52
RF input power	MW	18
Cathode peak field	MV/m	160
Cathode type		Copper
Rep. rate	Hz	1000
Quality factor		11,800
Filling time	ns	164
Coupling coefficient		3
RF pulse-length	ns	300
$E_{\mathrm{surf}}/E_{\mathrm{cath}}$		0.9
Modified Poynting vector	W/μ m^2	2.5
Pulsed heating	°C	<20
Average diss. power	W	2300

the beam energy at the gun exit that is now comparable with that of a 1.6 cell S-band gun operating at 120 MV/m cathode peak field [89]. The RF source is a 20 MW C-band klystron with an average power, at 1 kHz, similar to that of the klystron currently in use at SwissFEL [70]. This klystron is currently not commercially available, but from preliminary evaluations, we believe that it may be available in the next 3–5 years.

The gun is directly fed by the klystron through a circulator. Commercial circulators that operate at this level of power already exist [90] and can be adopted. The coupling coefficient has been designed to minimize the required input power for the 160 MV/m cathode peak field operation and the average dissipated power. Figure 33 shows the average dissipated power in the gun and the required input power as a function of the RF pulse length for three different coupling coefficients. The 300 ns operation with a coupling coefficient equal to 3 has been chosen as a good compromise between the required input power and the average dissipated power in the gun. The profiles of the input, reflected, dissipated power and cathode peak field are given in Fig. 34.

The magnitude and phase of the on-axis longitudinal accelerating field are reported in Fig. 35. The plot shows

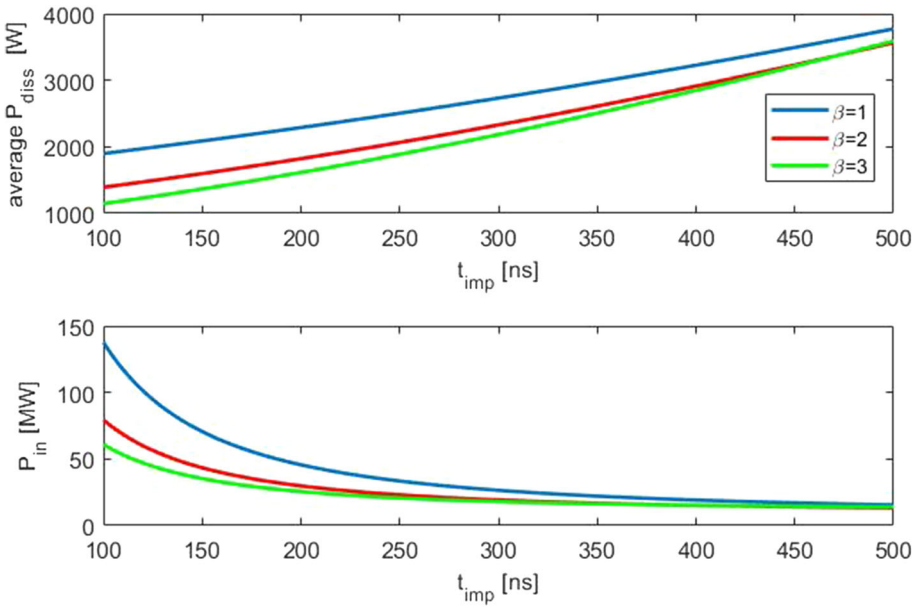

Fig. 33 Average dissipated power (upper plot) and required input power (bottom plot) as a function of the rf pulse-length, for three different coupling coefficients

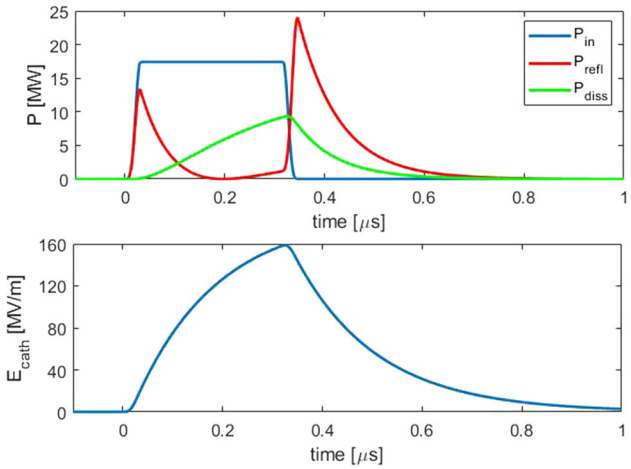

Fig. 34 Input, reflected, dissipated power (upper plot) and cathode peak field (bottom plot) as a function of time for a 300 ns pulse-length with 30 ns rise time

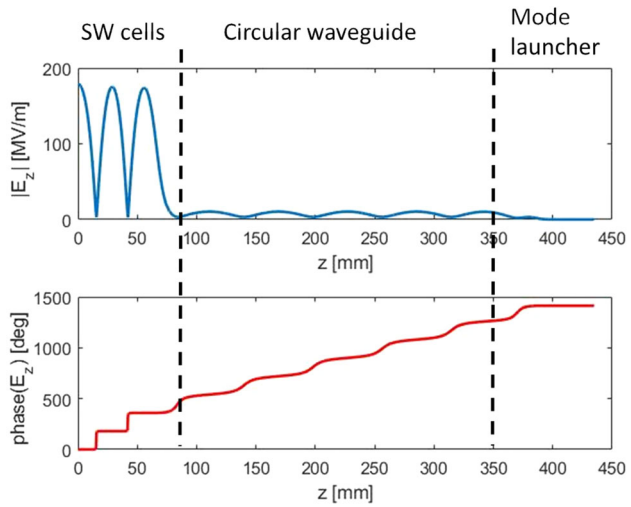

Fig. 35 Magnitude and phase of the longitudinal accelerating field on axis

the standing-wave accelerating field in the first 2.5 cells operating on the π-mode and the propagating field into the circular waveguide (phase plot). In the beam dynamics calculations, we have also taken into account the contribution of the field in the circular waveguide itself.

5.1.1.2 Thermo-mechanical analysis

The operation at 1 kHz with 300 ns RF pulses, results in an average dissipated power into the gun body of more than 2 kW. For this reason, a careful design of the cooling system has been performed. The gun cooling system integrates four cooling channels, as shown in Fig. 36: three for the cells and one for the cathode, with a total flow of about 20 liter/min for the channel. The 3D model of the gun, including cooling channels, has been implemented in the Ansys Workbench (WB) [85] environment. With this code, the fully coupled thermal, structural and electromagnetic analysis has been performed. The heat load obtained by the electromagnetic analysis has been imported in the thermal analysis module. The final temperature distribution is given in Fig. 37a and the corresponding deformation is depicted in Fig. 37b. The deformed structure has then been simulated and the detuning has been evaluated to be about 1 MHz, while the field distribution is basically unperturbed thanks to the uniform cooling system design. This detuning can be either compensated by changing the water temperature

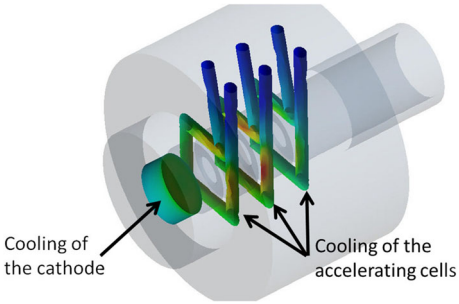

Fig. 36 Gun cooling system simulated in ANSYS

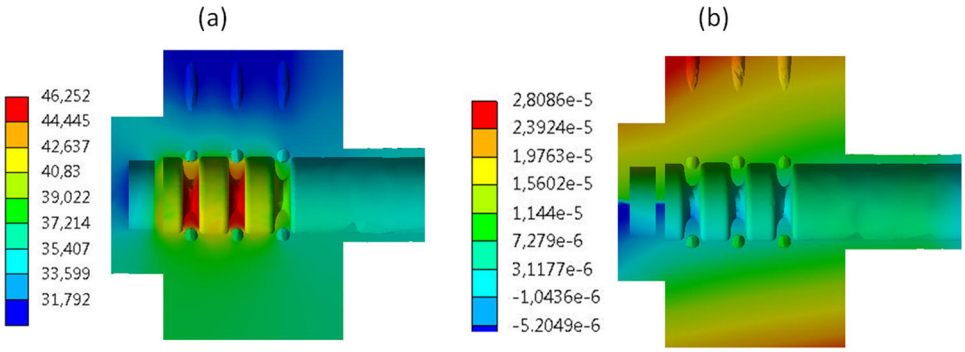

Fig. 37 **a** Gun temperature distribution and corresponding deformation (**b**)

during operation by about 15 deg, or by designing the structure with a resonant frequency higher than the nominal one.

5.1.1.3 Gun solenoid design

The sketch of the RF gun with mode launcher and solenoid is given in Fig. 38. The solenoid around the circular waveguide has been designed using Poisson Superfish [91]. The simulated structure and the magnetic field profiles on axis are given in Fig. 39. The main solenoid parameters are reported in Table 7. To cancel the magnetic field on the cathode and prevent an increase of the beam emittance [92], a bucking coil is foreseen to be located at the back of the RF gun. Figure 39b shows the effect of the backing coil on the magnetic field at the cathode position at 165 mm from the coordinate $z = 0$. Both the electromagnetic field in the RF gun and circular waveguide and the solenoid field have been inserted in the beam dynamics simulations.

5.1.1.4 Photocathode and laser systems

The photo-cathode is the key component of a photoinjector, since the overall quality of the electron beam and the reliability of the photoinjector depend on material type, robustness, roughness, and lifetime. The electron beam produced by the photo-cathode is emitted via the photoelectric effect using a laser source of appropriate

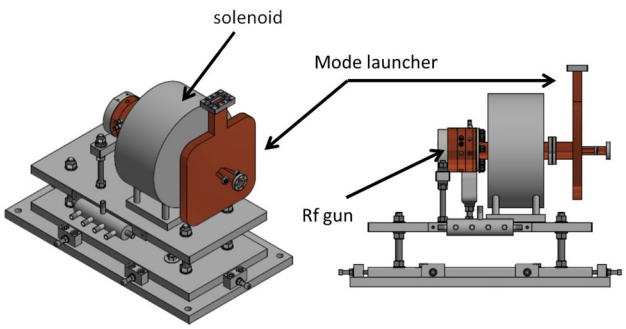

Fig. 38 Sketch of the RF gun with mode launcher and solenoid

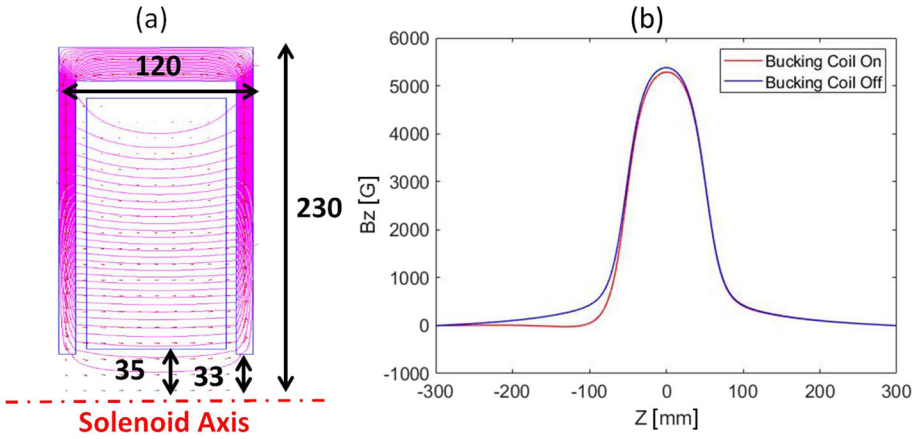

Fig. 39 **a** Solenoid simulated by the code Poisson and magnetic field profile on axis (**b**)

Table 7 Main gun solenoid parameters

Parameter	Unit	Value
$B_{\max}$	T	0.53
Bore radius	mm	33
Solenoid length	mm	120
Yoke material		Low carbon steel
Integrated field	T mm	59.4
Good field region radius	mm	10 mm
Integrated field variation		3×10^{-5}
Number of turns		336
Conductor dimension	mm	5.6 × 5.6/bore 3.6
Nominal current	A	164
Nominal voltage	V	40
Inductance	mH	3
Resistance	mΩ	242
Water flow rate	l/min	3.72
Temperature drop	°C	25
Pressure drop	bar	2.72
Bucking coil conductor diameter	mm	1.6
Bucking coil radius	mm	72
Bucking coil number of turns		700
Bucking coil nominal current	A	7.5

wavelength. The longitudinal and transverse electron beam profiles are determined by the laser time and spatial structure [93].

To satisfy the CompactLight requirements, the design adopts a metallic photo-cathode. This choice is based on the results obtained worldwide in different laboratories, and on the ASTRA [94] simulation studies, comparing the transverse emittance and the normalized transverse emittance between the cathode materials Cs_2Te vs Cu. The S-/C-band of the e-gun has been studied, with a solenoid after the photo-cathode, at the Ferrario working point. The proper laser parameters have been studied for the final selection of wavelength, pulse duration, pulse length, pulse energy, intrinsic emittance, and QE tuning, plus the repetition rate, the longitudinal-transverse and 3D pulse profile optimization. The GIOTTO [95] code was implemented and provided optimization results of the normalized transverse emittance [96]. Simulations have been done also to optimize transverse/longitudinal emittance, beam size, and bunch length, with 1.6, 2.5, and 5.6 cavity cells, with various cavity voltages and solenoid distances from

the photo-cathode [97]. The most suitable candidate metal was found to be copper (Cu) [97]. The photo-cathode is centred on the flange and closes the RF gun half-cell.

The main criteria for the selection of the cathode have been the high quantum efficiency, high robustness, and fast response time in addition to low intrinsic emittance, low surface roughness, and high lifetime. Moreover, the photo-cathode is also subject to surface modification and contamination due to laser radiation, RF field breakdown, and low vacuum pressure. A Cu photo-cathode, due to its fast response time (10^{-16} s $< \tau < 10^{-14}$ s), is useful for laser pulse shaping and for its robustness and lifetime. Cu photo-cathodes are minimally reactive with respect to other materials, they require about 10^{-9} Torr vacuum level, and they are compatible with the environment of the RF cavity, whose walls are also made of Cu [93]. For all these reasons, an oxygen-free polycrystalline Cu photo-cathode has been chosen for CompactLight.

The required electron beam distribution defines the characteristics of the laser system to be used for the photoemission. In general, metal photo-cathodes require UV light, generated from 3rd or 4th harmonic conversion from an IR fundamental wavelength. Photo-cathode drive lasers for high brightness electron beam applications must have very specific capabilities driven by two major considerations: (1) the low photoemission efficiency for robust photo-cathodes requires high UV pulse energy given the required charge; (2) the emittance compensation process is most successful with uniform temporal and spatial laser energy distribution. Additionally, low amplitude and time jitter from pulse-to-pulse, as well as stable pointing stability, are needed to ensure high performance. The laser pulses have to be synchronized with the master oscillator to extract electrons at the specified phase of the RF wave [98, 99].

The photo-cathode laser system will be based on a Ti:Sapphire laser at 800 nm with about 100 fs pulse duration. The photo-cathode pulses are up-converted via harmonic generation to the 3rd harmonic at 266 nm; the wavelength required for electron extraction out of the copper cathode. The laser system must deliver an excess of 50 μJ energy per pulse at a wavelength of 266 nm to the photo-cathode at a repetition rate of 1 kHz. This energy requirement comes from the typical quantum efficiency of copper photo-cathodes, which is of the order of 10^{-5} [100]. Considering the worst case QE of 10^{-6} the requested energy per pulse will be about 100 μJ, a typical value for a Ti:Sapphire laser system. Indeed, in both cases, a commercial Ti:Sapphire laser system as https://amplitude-laser.com/frequence/khz-en [101] can be used. Table 8 reports the technical specification of a such laser system.

The emittance compensation scheme requires that the laser pulse must have a uniform transverse and flat-top longitudinal profile at the cathode to compensate for the non-linear space-charge field with proper magnetic

Table 8 The technical specification of the Ti:Sapphire laser system (ARCO)

Specifications	ARCO C (100 Hz) & ARCO M (1 kHz)					
Repetition Rate [1]	100 Hz for Arco C	1 kHz for Arco M				
Energy Per Pulse [2,3]	6 mJ @ 100 Hz	5 mJ @ 1 kHz	12 mJ @ 100 Hz	10 mJ @ 1 kHz	25 mJ @ 100 Hz	20 mJ @ 1 kHz
Pulse Width (fwhm) [4]	< 100 fs or < 35 fs or < 20 fs					
Central Wavelength (nm) [5]	800 ± 10					
Average Power (W)	5		10		20	
Pump Lasers	Terra		Terra Duo		2 Terra Duo	
Pulse To Pulse Energy Stability (RMS)[6]	0,7 %		0,7 %		0,5 %	
Power Stability (RMS) [7]	1 %					
Nanosecond Contrast [8]	< 5.10^{-4}					
Picosecond Contrast [9]	< 5 10^{-7} @ 300 - 50 ps & < 10^{-6} @ 50 - 10 ps & < 10^{-5} @ 1 ps					
Beam Quality M^2	< 1.3					
Pointing Stability	< 10 μrad RMS					
Polarization	Linear horizontal					
Warm-up Time	< 1 hour					

[1] Please contact factory for specifications at other repetition rates
[2] 5 mJ / 9 mJ / 20 mJ @ 100 Hz or 4 mJ / 9 mJ / 16 mJ @ 1 kHz for pulse duration < 25 fs
[3] 790 nm +/- 10 nm for 100 fs pulse duration. Other central wavelengths, please contact factory
[4] Factory-set, must be specified when ordered and will be optimized prior to shipment
[5] Over 2000 pulses
[6] Over 8 hours under stable environmental conditions
[7] Pre-pulse, regenerative amplifier replicas
[8] Measured with third order cross-correlator (SEQUOIA)

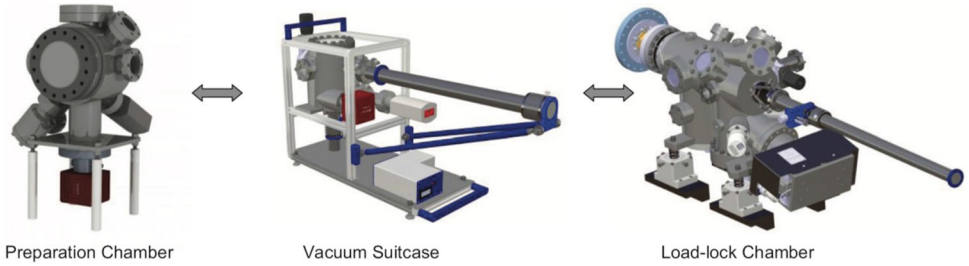

Fig. 40 First step is the photo-cathode plugs preparation inside the chamber (left), and the photo-cathode plugs are then transported by using the vacuum suitcase (centre) inside the load-lock system (right)

focusing. For the longitudinal flat-top profile, there is in fact a rise time of about 1 ps and an FWHM value of about 4 ps. Such a temporal and spatial laser energy distribution on the cathode has been demonstrated to reduce the emittance [102, 103]. A small portion of the laser pulse will be used for the laser heater—for details, see Sect. 5.1.3.

It is important to use a load-lock system for the RF gun to guarantee a fast and safe photo-cathode exchange under vacuum conditions. Without a load-lock system, the photo-cathode exchange takes 2–3 days and the photo-cathode surface gets contaminated in the atmosphere during installation, leading to undesired QE degradation [104]. A given system must be implemented in the photo-cathode area using a suitable design—Fig. 40 shows the SWISSFEL load lock system from the photo-cathode preparation to the RF gun insertion [104].

5.1.2 C-band booster

5.1.2.1 C-band RF modules

The C-band booster comprises four 2 m-long traveling-wave accelerating structures installed after the photoinjector, to boost the beam energy up to 120 MeV of the laser heater; see the RF feeding system in Fig. 41. In addition, six more structures are planned to be installed before the first bunch compressor to further increase the beam energy up to 300 MeV. The C-band structure parameters are listed in Table 9 and they have been determined using the algorithm in [105]. Each structure has a linear tapering of the irises. The average dimension of the iris, $\langle a \rangle$, and the tapering angle have been chosen in order to maximize the structure efficiency, as given in Fig. 42 where the effective shunt impedance has been plotted as a function of the average iris radius. In Fig. 43, the same parameter is plotted as a function of the tapering angle for the case $\langle a \rangle = 6.6$ mm. All calculations assumed the klystron parameters listed in Table 10, 2 m-long structures and the BOC pulse-compressor parameters similar to those already implemented for SwissFEL [106]. The klystron operating parameters reported in Table 10, 15 MW peak power, 2 μs RF pulse-length and 1 kHz repetition rate, are an evolution of those of the C-band klystron currently

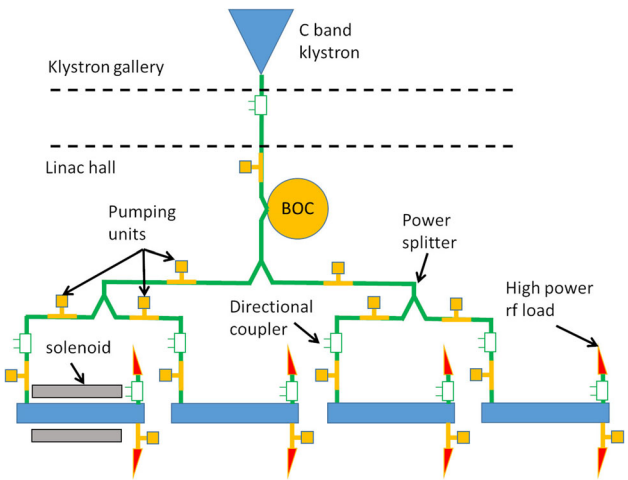

Fig. 41 Schematic layout of the C-band booster feeding system

Table 9 Main parameters of the C-band structures

Parameter	Unit	
Working frequency	GHz	5.996
Phase advance per cell	rad	$2\pi/3$
Average iris radius $\langle a \rangle$	mm	6.6
Iris radius **a**	mm	6.94–6.26
Number of cells per structure		120
Accelerating cell length	mm	16.67
Structure length $\mathbf{L_s}$	m	2
Shunt impedance **R**	MΩ/m	71–77
Effective shunt impedance $\mathbf{R_s}$	MΩ/m	190
Group velocity v_g/c	%	2.4–1.6
Filling time	ns	336
Average acceleration gradient	MV/m	15
Required input power per module	MW	9
Number of structure in the module		4

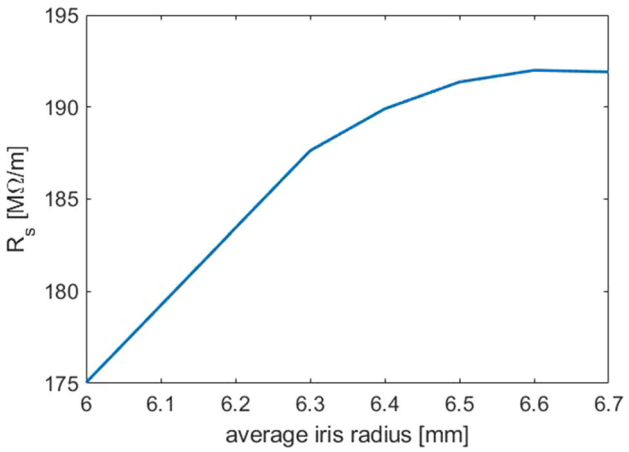

Fig. 42 Effective shunt impedance as a function of the average iris radius

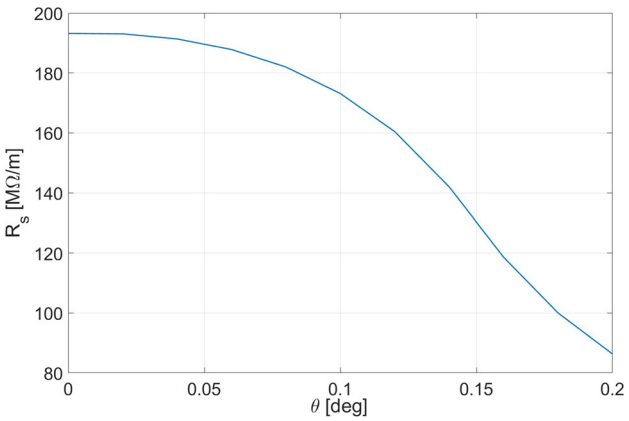

Fig. 43 Effective shunt impedance as a function of the tapering angle for the case $\langle a \rangle = 6.6$ mm

Table 10 Main parameters of the C-band llystron

Parameter	Unit	Value
Operating frequency	GHz	5.996
Klystron pulse-length	μs	2
Klystron peak power	MW	15
Repetition rate	Hz	1000
Q_0 of BOC		216,000
Q_E of BOC		19,100

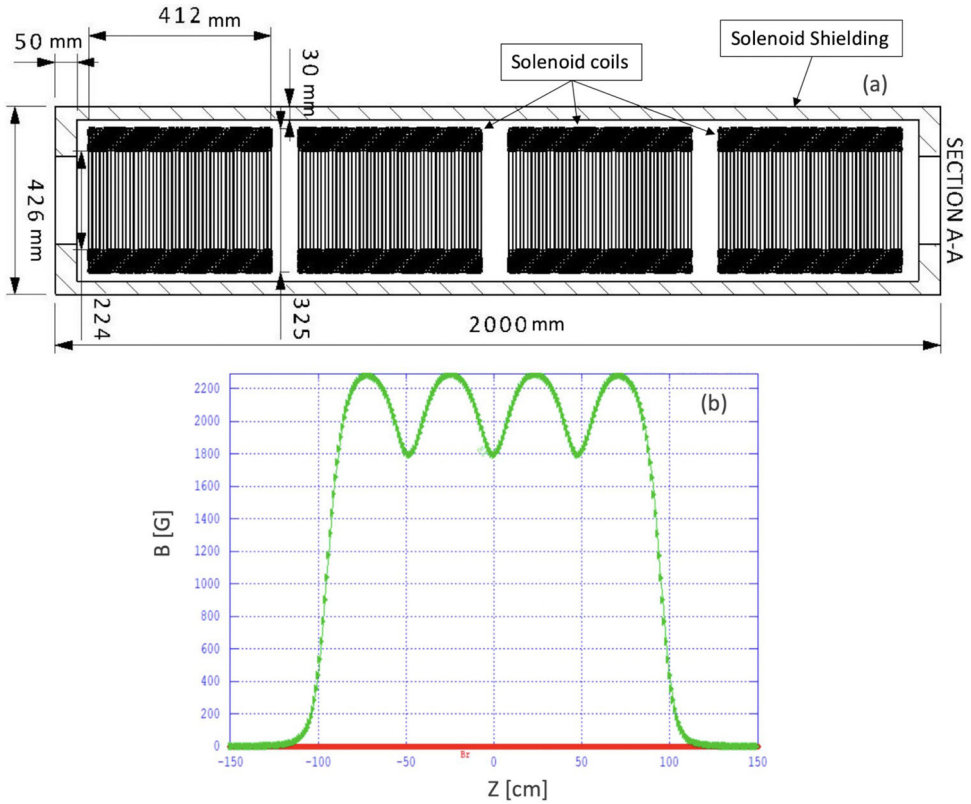

Fig. 44 **a** Geometry of the C-band solenoid simulated with Poisson-Superfish; **b** longitudinal magnetic field on axis

in operation at the SwissFEL linac [70]. Currently, this type of klystron is not available on the market, but, based on information received from the industry, it could be available in the next 3–5 years.

5.1.2.2 C-band structure solenoid

For the beam emittance compensation process, a long solenoid is placed around the first accelerating structure. The solenoid has been designed using the code Poisson Superfish [91]. It is a four-coil solenoid with iron shielding, as illustrated in Fig. 44a, where the simulated geometry is shown. Figure 44b shows the profile of the magnetic field on the axis. The main parameters of the solenoid are reported in Table 11.

5.1.3 Laser heater

The brightness of X-ray FELs is affected by the uniformity of the longitudinal density and energy distribution of the electron beam injected into the undulator. Such uniformity can be spoiled by several collective processes occurring during acceleration and time compression. Among them, the microbunching instability (MBI) is one of the most significant [107]. Driven by a combination of longitudinal space-charge force (LSC), coherent synchrotron radiation (CSR), and energy dispersion in magnetic compressors, the MBI induces a broadband modulation of the

Table 11 Main C-band structure solenoid parameters

Parameter	Unit	Value
B_{max}	T	0.22
Bore radius	mm	100
Total solenoid length	m	2
Single coil length	mm	418
Yoke material		Low carbon steel
Total integrated field	T mm	40
Good field region radius	mm	20 mm
Integrated field variation		10^{-4}
Number of turns per coil		288
Conductor dimension	mm	8×8/bore 6
Nominal current per coil	A	278
Nominal voltage per coil	V	153
Inductance per coil	mH	9.17
Resistance per coil	mΩ	553
Water flow rate per coil	l/min	2
Temperature drop per coil	°C	20
Pressure drop per coil	bar	2.43

electron beam energy and longitudinal charge distribution. This process originates with shot noise and cathode-induced non-uniformities in the particle distribution and is further stimulated and amplified by bunch length compression, in proportion to the bunch peak current. At the undulator entrance, the electron beam can have significant longitudinal energy and density modulations at micron to sub-micron scale lengths. Longer wavelength modulations can degrade the FEL spectrum, especially in externally seeded FEL schemes, while those at shorter wavelengths may appear as an increased slice energy spread and therefore translate into reduced FEL gain and intensity.

As a means to control the MBI, Saldin et al. [108] proposed the addition of a device commonly referred to as a "laser heater" (LH). This device adds a controlled amount of incoherent energy spread to the electron beam and suppresses further MBI growth via energy Landau damping. The ability of an LH to increase the final electron beam brightness was initially demonstrated at the LCLS hard X-ray FEL, where both a reduction of the FEL gain length and an increase of the photon flux were observed [109]. This section presents the specifications of the CompactLight LH system.

5.1.3.1 Footprint

The CompactLight LH consists of a short, planar undulator located in a magnetic chicane, where an external laser pulse is superimposed to the electron beam. The electron-laser interaction within the undulator produces an energy modulation on the longitudinal scale length of the laser wavelength. The dispersion in the second half of the chicane smears the energy modulation in time, leaving the beam with a larger incoherent energy spread. The LH chicane includes two screen stations for spatial alignment of laser and electron beam, two Beam Position Monitors for online electron beam trajectory control, and a screen and a BPM on each side of the undulator. A schematic is shown in Fig. 45. The electron beam size is 80 µm in both transverse planes at the location of the LH

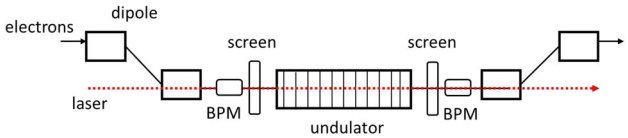

Fig. 45 Top view (not to scale) of the LH system. The overall length is approximately 1.5 m

undulator, as predicted by particle tracking runs.

5.1.3.2 Laser

The external laser pulse consists of a small portion of the 800 nm Ti:Sa photocathode drive laser pulse, extracted before the latter is harmonically up-converted to the UV. The LH laser pulse temporal duration should completely cover the electron beam duration. It is therefore specified to be at least 20 ps FWHM. The LH laser pulse energy, expected to be up to several 10's μJ level, can be attenuated by a polarimeter. A separate shutter can completely block the pulse.

5.1.3.3 Undulator

The undulator consists of eight 40 mm-long periods and a peak field of 0.4 T. The vertical gap can be remotely changed to resonantly match the external laser wavelength for electron beam energies in the range 100–140 MeV. The undulator parameter is around 1 for efficient laser–electron interaction. The relative energy bandwidth of the undulator is 12%.

5.1.3.4 Chicane

The symmetric 4-dipole chicane has a twofold scope. First, it allows the laser to be transversely aligned to the electron beam and perfectly overlapped with it. Second, it smears out the laser-induced energy modulation and transforms it into an uncorrelated energy spread. This happens by virtue of the linear transport matrix terms from the undulator to the chicane end.

Smearing becomes effective when the electrons' phase shift is larger than the laser wavelength. The design assumes that the phase shift is twice the modulation wavelength for a safe operation, that is

$$\sqrt{\langle \Delta z^2 \rangle} = 2\pi \sqrt{(R_{51}\sigma_{x,W})^2 + (R_{52}\sigma'_{x,W})^2 + (R_{56}\sigma_\delta)^2} \geq 2\lambda_L, \tag{19}$$

where, however, $R_{51} = 0$ due to the achromatic lattice. $\sigma'_{x,W} = \sqrt{\epsilon_{n,x}/(\gamma_0 \beta_W)} \approx 10\,\mu\text{rad}$ is the RMS beam divergence at the waist and $\sigma_\delta \approx 10^{-5}$ is the relative uncorrelated energy spread.

The coefficients R_{52} and R_{56} can be expressed as function of the chicane geometry

$$\begin{aligned} R_{52} &\approx \theta(l_d + l_b), \\ R_{56} &\approx \theta^2\left(l_d + \tfrac{2}{3} l_b\right), \end{aligned} \tag{20}$$

where the approximation is for small dipole bending angle $\theta \ll 1$, l_d is the length of the outer arms and l_b is the dipole arc length. It is apparent that the effect of energy smearing by R_{56} is θ-times smaller than the effect induced by the angular dispersion R_{52}, and the former can, therefore, be neglected. The minimum value of the latter can be calculated from Eq. 19 as ≈ 23 mm. This translates also into the value of the horizontal dispersion function η_x at the centre of the chicane, and to approximately the distance of the deflected trajectory from the straight one. Thus, the chicane vacuum chamber needs to be to be 33 mm wide horizontally. The non-deflected electron beam propagates 5 mm from the right-hand wall. When deflected, the beam translates 23 mm from the straight trajectory ($R_{52} \approx 23$ mm), so that 5 mm are left from the chamber's left side. The chamber is assumed to be round in the outer dipole magnets and tapered to an elliptical geometry internally to the chicane.

The dipole length is 0.1 m and Eq. 20 defines the length of the outer drifts for the specified R_{52} as a function of the dipole bending angle. The total chicane length is the sum of the 4 dipole lengths, outer drifts, undulator length, and an additional 0.3 m to insert diagnostics at the undulator ends (see Fig. 45). Such lengths are shown in Fig. 46. The total LH system is 1.4 m long for 5 deg (0.087 rad) bending angle. The dipole field is $B_{y,b} = \frac{E[\text{GeV}]}{0.2998} \frac{\theta_b}{l_b} = 0.34$ T. Fig 46 also shows the horizontal emittance growth induced, respectively, by the particles' energy change in the undulator dispersive region as a consequence of the interaction with the laser beam (slice emittance growth), and by CSR in the four dipole magnets (see Eq. 21). The former contribution is estimated in the pessimistic assumption of full chromatic filamentation of the transverse phase space and plotted for a fixed R_{52}. The latter is the sum in quadrature of the contribution from each dipole [110]. It is shown that 5° bending angle ensures negligible emittance growth from both effects is given by

$$\begin{aligned} \left(\frac{\Delta\epsilon_x}{\epsilon_x}\right)_{chrom} &\leq \frac{1}{2}\left(\frac{R_{52}\sigma_{E,LH}}{\sigma_{x,W}E}\right)^2, \\ \left(\frac{\Delta\epsilon_x}{\epsilon_x}\right)_{csr} &\approx 7.5 \cdot 10^{-3} \frac{\beta_x}{\gamma_0}\left(\frac{N_e r_e l_b^2}{R^{5/3}\sigma_z^{4/3}}\right)^2, \end{aligned} \tag{21}$$

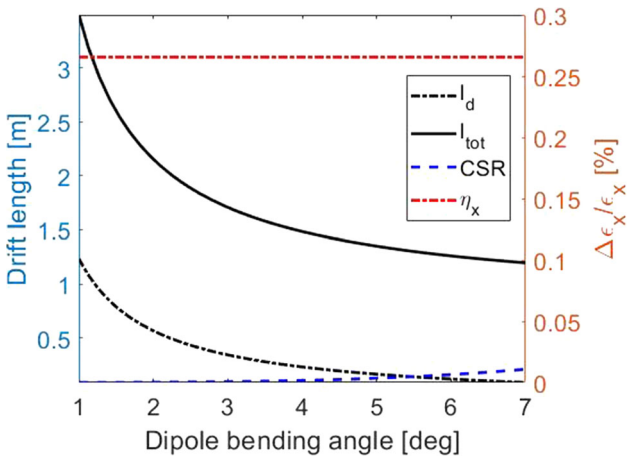

Fig. 46 Outer drift and total chicane length (left axis) and horizontal emittance growth induced by horizontal dispersion and CSR (right axis) vs. dipole bending angle, for fixed $R_{52} = 23$ mm

where N_e is the number of electrons in a bunch, r_e is the classical electron radius, R is the dipole's curvature radius, and σ_z is the RMS bunch length.

5.1.3.5 Summary table

Table 12 summarizes the laser heater system specifications. The nominal values refer to the RMS-induced energy spread of 12 keV at the beam energy of 120 MeV. The ranges are evaluated for up to 30 keV RMS-induced energy spread.

5.2 RF systems and structures

The CompactLight linac is composed of 24 X-band RF modules which provide a beam energy of up to 5.5 GeV at a repetition rate of 100 Hz and an energy of 2.4 GeV at a repetition rate of 1 kHz. This flexibility in operation is a major innovation of CompactLight and allows a wide range of experiments to be carried out. The linac has a large impact on facility performance and represents a major part of the overall cost; consequently, a significant effort was put into its design. The linac begins at the output of the injector and first bunch compressor. At this point, the beam is fully relativistic, with an energy of 300 MeV, and the linac ends when the beam has achieved its final energy of 2.5–5.5 GeV, depending on the operating mode. Two additional X-band RF modules are added to the low-energy beamline as part of Upgrade-2. The linac is composed of repeated modules of standardized layout and composition, with three types that incorporate four, two, and one quadrupole per module for low, medium, and high energy parts of the linac, respectively.

The most important design considerations for the RF module are optimizing beam dynamics in the linac, maximizing power efficiency, providing power source configurations with required operating modes, and minimizing overall cost. The main components of the RF module are the modulator, klystron, pulse compressor, waveguide network, and accelerating structure. The accelerating structure design is of crucial importance, since it interacts directly with the beam, determining issues, such as emittance growth and power efficiency of acceleration.

The RF part of the linac module is described in Sect. 5.2.1. The main subsystems—support and alignment, vacuum, and focusing magnets—are described in Sects. 5.2.2, 5.2.3, and 5.2.4, respectively. Layout summaries that describe integration are presented in Sect. 5.2.5. A summary of the discussion of the strategy of industrial supply is given in Sect. 5.2.6—for more details on this particular topic, see CompactLight deliverable D4.3.

In addition to the main X-band linac RF modules, CompactLight contains other high-power RF systems that carry out important functions: two sub-harmonic separator systems, a harmonic energy spread linear system, and four POLARIX deflecting diagnostic systems. These systems were added during the design process, and significant work on them was carried out. Descriptions of the former two systems have been added to this report. The POLARIX systems is described in the CompactLight diagnostics deliverable D8.1.

Two sub-harmonic separator systems are used in CompactLight to direct the two successive bunches in a train into the two respective beamlines. In one location, this is so that one bunch goes into the low energy beam line and in the other the two bunches go into their respective undulators for double pulse light production, enabling FEL pump-FEL probe experiments. The sub-harmonic separator system operates at 3 GHz and is described in Sect. 5.2.7. The sub-harmonic separator is also referred to as a transverse deflecting cavity (TDC)

Table 12 Laser heater specifications

	Units	Nominal value	Range
Electron beam			
Charge	pC	75	≥ 300
Duration, RMS	ps	3	1–3
Energy	MeV	120	100-140
Natural energy spread, RMS	%	0.001	≤ 0.2
Norm. emittance (x,y)	µm rad	0.2	0.15–0.3
Betatron function at Und. (x,y)	m	7.5, 7.5	≤ 25
Laser beam			
Wavelength	nm	780	760–800
Bandwidth, FWHM	%	1	<5%
Peak power	MW	0.1	≤ 5
Duration, FWHM	ps	20	10–30
Pulse energy	µJ	2	≤ 100
Repetition rate	kHz	0.1, 0.25,1	
Average power	mW	2	≤ 100
Size at waist, RMS (x,y)	mm	0.15	0.05–0.300
Undulator			
Period length	mm	40	
Vertical gap, full	mm	21	15–28
Undulator parameter		1.5	1.2–1.8
Peak field	T	0.4	0.1–1.1
Number of periods		8	
Total length	m	0.32	≤ 0.36
Chicane			
Number of dipoles		4	
Bending angle	mrad	87	0–100
Arclength	m	0.1	≤ 0.15
Peak field	T	0.4	≤ 0.8
Outer drift length	m	0.15	
Total length	m	1.4	1.3–1.8
Maximum horiz. dispersion	mm	23	≤ 30
Chromatic emittance growth	%	$< 0.5\%$	
CSR emittance growth	%	$< 0.1\%$	

CompactLight has implemented a harmonic linearizer system as in other XFELs. However, because the injector uses C-band accelerating structures, we have chosen a linearising frequency of 36 GHz, in the Ka-band. Such a high frequency is not found in the existing user facilities; however, it is close to the 30 GHz frequency once used by the CLIC study and thus exploits years of development. Commercial power sources are not available; thus, CompactLight has made comprehensive designs for two power source options, a gyroklystron amplifier and a multi-beam klystron Ka-band power source. The associated pulse-compressor system, low-loss waveguide transport, and lineariser structure have been designed, as well. The Ka-band (36 GHz) harmonic lineariser system is described in Sect. 5.2.8.

A layout of the facility is shown in Fig. 47 and the locations of the different systems described above are indicated.

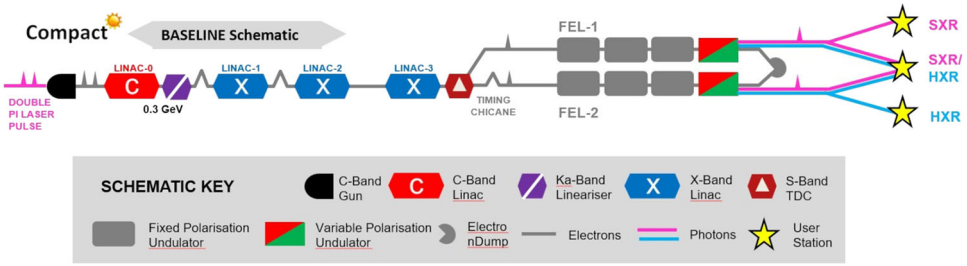

Fig. 47 Schematic layout of the CompactLight facility. The RF systems covered in this report are the X-band linac module, the Ka-band lineariser, and the S-band bunch separator (TDC)

5.2.1 RF system

The accelerating structures must be designed to enable special operating conditions that give CompactLight unique experimental capabilities; multiple gradient and repetition rate combinations and two-bunch operation. The extreme gradient and repetition rate combinations are a high-gradient 65 MV/m at 100 Hz mode and a high-repetition-rate 30 MV/m at 1 kHz mode. The structure parameters are optimized for both radio-frequency and beam dynamics performance and have higher order transverse mode suppression for stable two-bunch operation. The cooling circuit has been designed to accommodate the high average power of the high-repetition rate mode and optimized for the minimum difference between operating modes.

The CompactLight linac is composed of X-band modules, described in detail in the CompactLight deliverable D4.2, which each contain four Traveling Wave Accelerating Structures (TWASs) fed by a 50 MW klystron and pulse-compressor system. One klystron can feed several structures through a waveguide network using pulse compression. Thus, the X-band linac can be composed of a sequence of RF modules with four structures.

There are several important parameters to be determined during optimisation, for example, the structure length and the profile of the diameters of the irises along the structure length as well as their thicknesses. These parameters directly influence the total number of structures needed for each module and the linac as a whole, which determines the total required number of klystrons and pulse compressors. One important goal is to maximize the RF efficiency, to minimize the total number of klystrons. The average accelerating gradient and the average iris radius of the structure, which define the compactness and affect the stability of the machine, are provided as input specifications to the electromagnetic design. The study of the electromagnetic design is followed by investigating the thermo-mechanical properties, which are presented in Sects. 5.2.1.1 and 5.2.1. Finally, in Sect. 5.2.6, the route toward an industrialisation of the accelerator is described based on a breakdown of the various production processes.

5.2.1.1 Electromagnetic design and optimization of the accelerating structure

There are many steps in the design and optimization of a linac based on traveling-wave structures. The most important parameters are the ones that directly influence the total number of structures that are needed. As already said, one important goal is to maximize the RF efficiency, which has the consequence of minimizing the total number of klystrons. The most important steps used during optimisation are listed below [111]:

- Optimisation of the regular cell of the accelerating structure, with the electromagnetic simulations according to beam dynamics requirements. The design of the regular cell has been carried out using the simulation tool ANSYS HFSS [85]. A sketch of the cell geometry is shown in Fig. 48, where a is the cell iris radius, b the outer radius, t the iris thickness, r_0 the radius of the cell rounding, and r_1/r_2 is the aspect ratio of the elliptical profile of the iris. The cell length d is determined by specification of the operating frequency of 11.9942 GHz and a cell phase advance of $2\pi/3$, and is equal to 8.332 mm. The design process aimed at minimizing the modified Poynting vector normalized to the average accelerating gradient Sc_{max}/E_{acc}^2 while maximizing RF efficiency. The latter is quantified by the shunt impedance per unit length R parameter. An elliptical shape of the irises was implemented to minimize the peak modified Poynting vector on its surface. It has been found that $r_1/r_2 = 1.3$ is a good compromise between expected high-gradient performance and efficiency. An r_0 equal to 2.5 mm has been chosen. Once the iris shape was defined, the main cell parameters (shunt impedance per unit length R, quality factor Q, group velocity v_g, normalized modified Poynting vector Sc_{max}/E_{acc}^2) were calculated as a function of the iris radius a and the iris thickness t. The a value was varied in the 2–5 mm range, while t value in the 1.5–2.25 mm range. On the basis of these computed parameters, it was possible to complete the design of the accelerating structures.

- Analytical optimization of the structure length. With the average iris radius of the structure defined, the next step in the design of the structure was to find the optimal length of both constant-impedance (CI) and constant-gradient (CG) structures. This required also simulating the RF pulse-compressor, so formulae of the SLED pulse compression system [112] for constant impedance and constant gradient structures [113, 114] implemented in MATLAB code were used [105, 111, 115]. The effective shunt impedance as a function of the accelerating structure attenuation is reported in Fig. 49 for a CI and a CG structure, while the optimal structure length as a function of the structure average iris aperture is reported in Fig. 50. For the CI structure, the optimal length is 0.890 m, while for the CG structure, it is 0.818 m. These values have been used as the basis for a numerical optimization of the iris tapering as described in Sect. 5.2.1.
- Iris tapering Two-bunch operation in CompactLight is needed for FEL pump-FEL probe experiments. Two-bunch operation requires restraining the impact of the long-range transverse wakefield in the accelerating structures. This is because the long-range transverse wakefield excited by the front bunch affects the trajectory of the second bunch which causes an emittance growth. Long-range transverse wakefield suppression is required. This can be achieved by a variation of the iris diameter along the length of the structure, which results in a detuning of the synchronous frequency of the most important transverse modes. This causes decoherence in the transverse wake and thus suppression of its amplitude [116–120]. The bunches will be separated and transferred into two FEL lines after the linac acceleration. The separation is achieved by a sub-harmonic transverse deflecting structure which is working at S-band (2.998 GHz). Thus, the spacing for S-band between the two bunches should be $n + 0.5$ rf cycles (0.5, 1.5, 2.5, etc.), where n is an integer from 0. This results in a spacing of $4n + 2$ rf cycles at the X-band. The rf design of the transverse deflecting structure is presented in the CompactLight deliverable D4.2. A Gaussian-like aperture tapering combined with a linear iris thickness tapering was adopted to minimize the long-range transverse wakefield and a multi-parameter optimization of the tapering parameters was performed and compared to a more standard linear iris design. The long-range transverse wakefield of the Gaussian-like iris design is shown in Fig. 51. The blue line is the wakefield of the linear iris design, while the red line is the wakefield of the Gaussian-like iris design. The optimum compromise between fundamental-mode performance and a minimum bunch spacing distance gives a bunch spacing of 10th RF cycle. The wakefield of the new design at the second bunch is 3.65 V/pC/mm/m. The envelope of the wakefield is smaller than that of the linear iris design at the 10th RF cycle, ensuring a more robust operation.
- Input and output RF power couplers The input and output RF power couplers are of the magnetic coupling type with a z-type geometry to minimize pulsed surface heating. A dual feed and racetrack geometry avoids dipolar and strongly minimizes quadrupolar, components of the electromagnetic fields, respectively, which can adversely affect beam dynamics. Full details of the RF coupler design can be found in the CompactLight Deliverable D4.2. From a scan of coupler dimensions, the obtained reflection coefficient at the input port is − 44.9 dB for the input coupler and − 37 dB for the output one. For the input coupler, there is a pulsed heating of 24 °C. This value can be considered absolutely safe for high-field operation.
- Mechanical and thermal design of the accelerating structure One important aspect of the optimized design of the accelerating structure is the thermo-mechanical simulation work, that informs the design of a cooling system to handle the average thermal load during operation. The main input for the optimisation is the calculated average dissipated power per structure. The preliminary design of the cooling system was based on four cooling channels distributed around the cells. The dimensions and the distribution of the cooling channels were studied with a thermal analysis performed with a commercial code. In the simulation, different cooling scenarios were considered, e.g., by varying the temperature, the water flux and the lengths of the channels. The maximum difference in temperature of the accelerating part of the cell is the main parameter contributing to the cell detuning. Therefore, deformation due to this difference in temperature was used to gauge the results of the simulations. The design was done in two iterations with an intermediate correction of RF dimensions based on the first iteration of the thermal results. The worst-case heat load is expected at 1000 Hz repetition rate leading to 2.2 kW dissipated power in the structure. The deformation is mostly caused by the difference between the operating temperature and the temperature at which the disks were made and measured (20 °C). After the first verification, a second iteration of the simulations was done, again for 1000 Hz repetition rate. This iteration included variable thickness of the cavities and additional details such as thermocouple channels. The results from the study are presented in Table 13. The deformations due to the temperature difference within a disk are also included in the table. In the second iteration, the deformation increased slightly but can be corrected if the dimensions are adjusted for the operating temperature. The deformation due to the temperature difference in the disk itself has not changed, staying below 0.5 μm. An optimization for the 100 Hz repetition rate with the heat load of 1000 W was also studied. The full details of this modelling, as well as that for the 1000 Hz case, can be found in Deliverable D4.3.

The final, main parameters of the accelerating structure are reported in Table 14.

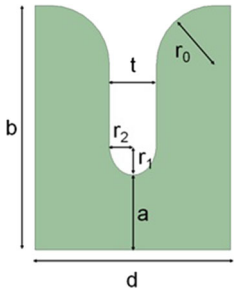

Fig. 48 Sketch of the single cell with main parametrized dimensions

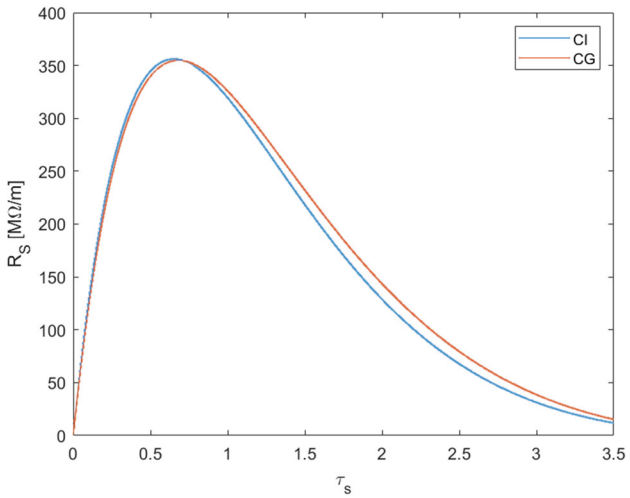

Fig. 49 Effective shunt impedance as a function of the section attenuation for CI and CG structures

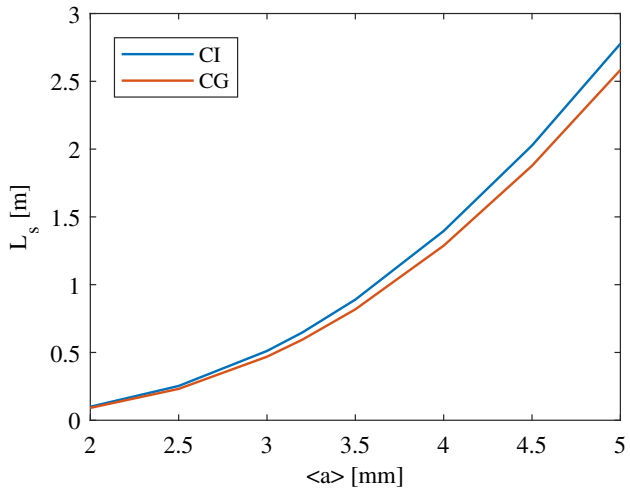

Fig. 50 Optimal structure length as function of the average iris radius for CI and CG structures

5.2.1.2 RF module layout

From the considerations in Sect. 5.2.1.1, it was found that a good compromise between RF performance and wakefield is represented by a 0.9 m structure (109 cells) with a Gaussian profile of the iris diameter. These structures are optimally powered and assembled in groups of four, fed by a single klystron and one SLED pulse compressor. A second klystron is added for high repetition rate operation, as will be described in more detail

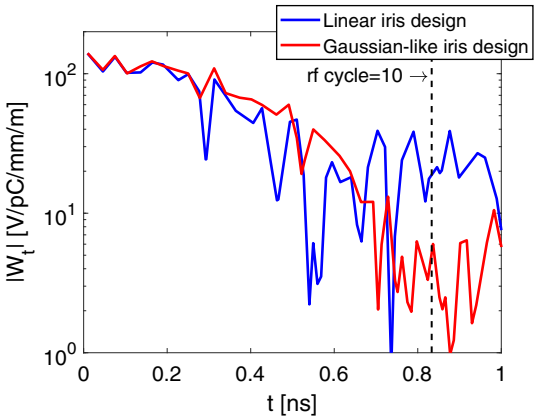

Fig. 51 Long-range transverse wakefields of the initial design and the Gaussian-like iris design

Table 13 Results after RF verification

	Temperature min–max (ΔT) [°C]	Deformation due to temperature difference with the disk (μm)	Total deformation (μm)
Disk 2	36.5–38.1 (1.6)	0.10–0.40	1.09–11.1
Disk 54	37.7–39.7 (2.0)	0.12–0.48	0.97–12.0
Disk 106	37.1–38.9 (1.8)	0.11–0.41	0.73–11.5

below. This arrangement forms the RF module, a basic unit repeated to achieve the desired beam energy. Full details of RF module design can be found in the CompactLight deliverable D4.2.

In Table 14, the main parameters of the structures and the module are reported, while, in Fig. 52, a sketch of the RF module is shown.

A symmetric binary tree layout has been adopted for the power distribution. The employment of a circular overmoded waveguide, connecting the modulator hall with the linac hall, minimizes the attenuation of power. Two mode converters are then necessary at the ends.

A 50 MW klystron is used for low repetition rate operation (100 Hz and 250 Hz), while a 10 MW one is employed for high repetition rate operation (up to 1 kHz). The first RF source is the CPI VKX-8311A klystron [121] that can provide 50 MW peak power, with a pulse-length of 1.5 μs and a repetition rate of 100 Hz. This source is under routine use by the CLIC group at CERN in the X-Boxes [122, 123] and will be installed at the upcoming test facility TEX at INFN-LNF in Frascati. The second source is a prototype designed by CPI or Canon that is currently in development. Another valid option is the Canon E37113 klystron that can provide 6 MW peak power, with a pulse-length of 5 μs and a repetition rate of 400 Hz [124]. This klystron is also used at CERN for the XBox-3 [125]. In this case, two klystrons of this kind are required for each RF module.

The external quality factor of the SLED compressor has been chosen to maximize the RF efficiency of the module (i.e., the effective shunt impedance) while keeping the modified Poynting vector in the accelerating structure well below the theoretical threshold of 4 Wμm^2 [79]. This value should not be exceeded to provide stable operation at the specified accelerating gradient at a pulse length of 200 ns. In the CompactLight case, the pulse length is 146 ns, which gives a theoretical limit of 4.4 Wμm^2.

The 250 Hz operating mode can be used with the baseline layout, in which only the 50 MW CPI klystrons are present. In this case, the klystron pulse is reduced to the structure filling time, and the SLED compressor is bypassed. This results in lower input power to the accelerating structures, so this operating mode has a maximum accelerating gradient of 30 MV/m. 30 MV/m is also produced in the 1 kHz repetition rate.

In the *Baseline configuration*, as seen in Fig. 47, the linac module consists of a single RF source that can run in dual mode: high-energy at repetition rates of 100 Hz and low-energy at 250 Hz. Two upgrade scenarios are foreseen for the RF system. In *Upgrade I*, the same klystron can be used with a higher repetition rate, 250 Hz, for providing up to 2 GeV for photon production. For *Upgrade II*, shown in Fig. 53, a second klystron, with 10 MW output power and a 1 kHz repetition rate, is added and connected to the waveguide system via a high-power switch, shown in Fig. 52. With such a configuration, the facility can be operated in a high-energy, moderate repetition rate mode and a low-energy, high repetition rate mode. The primary cost drivers of the RF module are the accelerating structures, klystrons and modulators. The latter two are commercial items, so costs and design are well understood, and they will be presented in the sections below. Complete commercially supplied X-band accelerating structures

Table 14 Main parameters of the RF structures and modules

Parameter	Units	Value		
Frequency	GHz	11.994		
Phase advance per cell	rad	$2\pi/3$		
Average iris radius a	mm	3.5		
Iris radius a	mm	4.3–2.7		
Iris thickness t	mm	2.0–2.24		
Number of cells per structure		109		
Accelerating cell length	mm	8.332		
Structure length L_s	m	0.9		
Group velocity v_g/c	%	4.7–0.9		
Filling time t_f	ns	146		
Peak klystron power (100–250 Hz)	MW	50		
Peak klystron power (1000 Hz)	MW	10		
RF pulse-length (250 Hz)	μs	1.5 (0.15)		
Waveguide power attenuation	%	≈ 10		
Unloaded SLED Q-factor Q_0		180,000		
External SLED Q-factor Q_E		23,300		
Shunt impedance R	MΩ/m	85–111		
Effective shunt impedance R_s	MΩ/m	349		
Peak modified Poynting vector	Wμm^2	3.4		
Repetition rate	Hz	100	250	1000
SLED		On	Off	On
Required klystron power	MW	44	44	9
Available klystron output power	MW	50	50	10
RF pulse-length	μs	1.5	0.15	1.5
Average accelerating gradient	MV/m	65	30	30
Energy gain per module	MeV	234	108	108

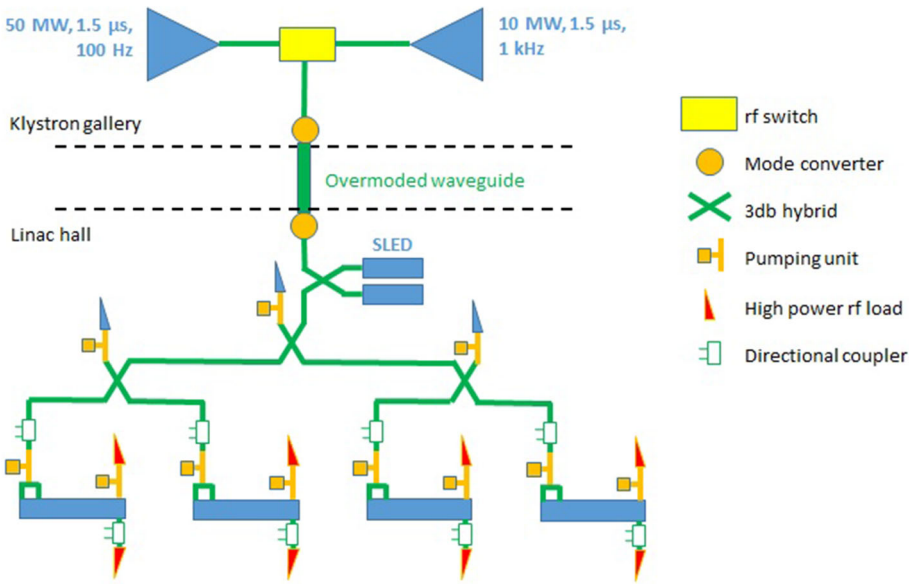

Fig. 52 Sketch of the RF module

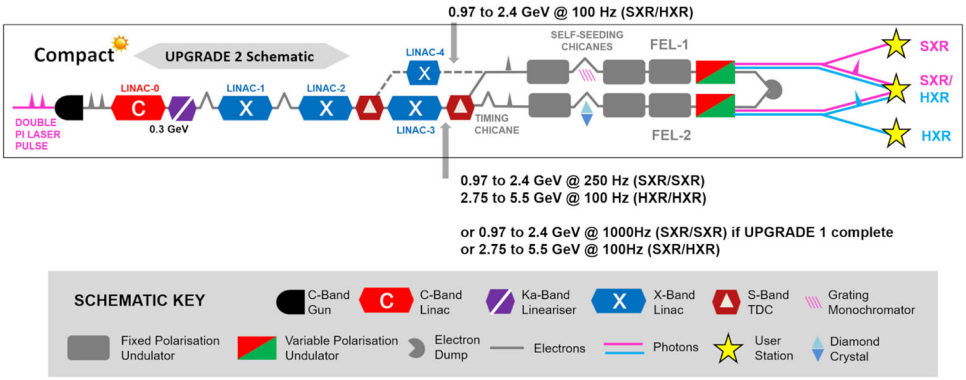

Fig. 53 Schematic layout of the CompactLight facility including Upgrade II

are not currently available, and until now, producing these structures has required combining fabrication steps at both accelerator laboratories and industrial suppliers.

5.2.1.3 RF power sources and components

The main RF source adopted for the RF module is the CPI VKX-8311A klystron [121]. It is a pulsed klystron operating at 11.994 GHz, 50 MW peak power, 5 kW average power. It is electromagnet-focused, liquid-cooled, and the waveguide output is WR-90. Two options for the high repetition rate operations are available: a new source from CPI and/or Canon, presently still in the R &D phase, or the Canon E37113 klystron already available [124]. In the case of adoption of the Canon E37113 model, 2 klystrons per module would be needed to guarantee the 30 MV/m gradient at 1 kHz. We remark that both the CPI VKX-8311A and the Canon E37113 klystrons have been successfully tested and are currently used in the CLIC test facilities, so they represent a reliable solution for the machine. Direct consequences of the activities of the CompactLight collaboration are the R &D activities necessary for the 1 kHz repetition rate 10 MW klystron, which are now underway at the companies.

The state-of-the-art modulator technology for pulsed linacs is based on solid-state HV modulators. A reliable solution for CompactLight is the Scandinova K series modulator [126]. Thanks to the modular design, the K series is able to support RF peak power up to 100 MW. A summary of the parameters of X-band power sources relevant for CompactLight under development at the time of writing of this report can be found in Deliverable 4.2.

The main high-power RF components of the module are 3 dB splitters, directional couplers, hybrids, phase shifters, loads, waveguides, and the SLED pulse compressor. These can be based on the high-power components developed at CERN by the CLIC collaboration, and the design and test of these components are described in [127]. The main components, with their key parameters, are detailed in Fig. 54.

Two options for the RF loads are stainless steel high-power loads [128] and 3D printed loads such as the compact and spiral loads, both designed and tested at CERN [129]. Stainless steel high-power loads have reached 31 MW at 50 Hz and 30 MW at 200 Hz, depending only on the power and attenuation from the upstream structure. 3D printing technology has also been successfully used to fabricate RF loads. This allows complex geometries to be produced from materials such as titanium. The power splitter is based on the one developed and high-power tested in the CLIC study [130, 131].

The adopted pulse-compressor, described in [132, 133], is the SLEDX developed at CERN by the CLIC group (Fig. 55). It is a compact device of 1 m length where the storage cavities operate in the H_{01} mode. The cavities are 45 cm long and have unloaded Q-factor of 1.8×10^5. With such a device, obtaining a flat pulse with a power gain of 4.3 is possible. For CompactLight, there is no need to have flat pulses, so larger (average) power gains might be achieved. The simulations and design used the SLED cavity concept indicated that implementing a Barrel Open Cavity (BOC) pulse-compressor type would improve performance [106].

5.2.2 Support and alignment system

All components influencing the electron beam need to be positioned with great care to not degrade the beam, particularly through the generation of short-range transverse wakefields. Beam dynamics simulations indicate that the centre of each component along the beamlines needs to be positioned within a horizontal and vertical tolerance of 100 µm. By first aligning the individual components, such as the accelerating structures, beam screens, and magnets relative to each other on the module girder, the entire girder can then be aligned with respect to successive girders and the beam. A 3D engineering design view of a typical XLS module can be seen in Fig. 56.

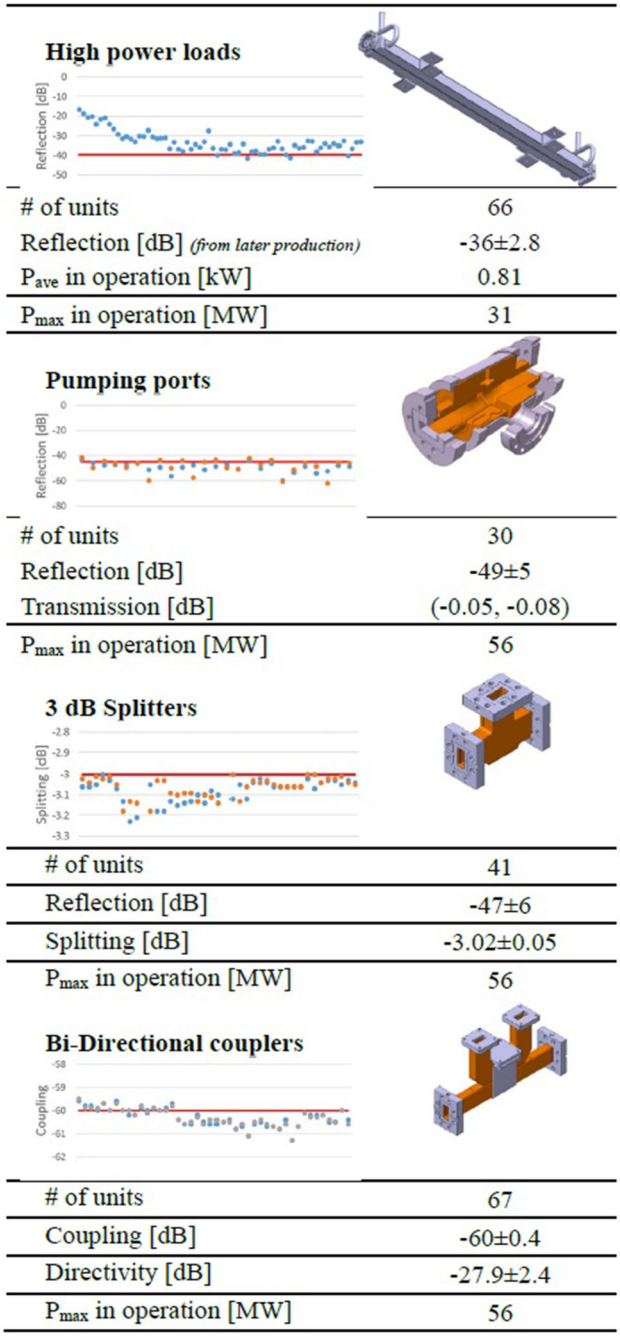

Fig. 54 Main parameters of RF components developed by the CLIC group at CERN

Four 103 cm-long accelerating structures are installed on top of one common girder into one CompactLight Module. An individual 6 DoF adjustment system aligns each of the structures to a precision within 10 μm rms with respect to the beam axis. The module also supports quadrupole magnets and their associated beam position monitors (BPMs). As described in Sect. 5.2.4, the magnets are equipped with integrated steering dipoles to avoid an expensive motorized platform on top of the common girder for moving the quadruple magnet during operation. The girder material considered is black steel, which is supported and aligned by means of jacks that have already been used for Linac4 installation at CERN.

The survey and alignment philosophy is very similar to the one proposed for eSPS at CERN documented in the CDR [134]. Each accelerating structure and quadrupole will be fiducialised independently, e.g., its mechanical axis will be determined w.r.t. external targets at a metrology lab or using a laser tracker. Once all the components are fiducialised, they will be pre-aligned on the common girder w.r.t. the geodetic network using laser tracker

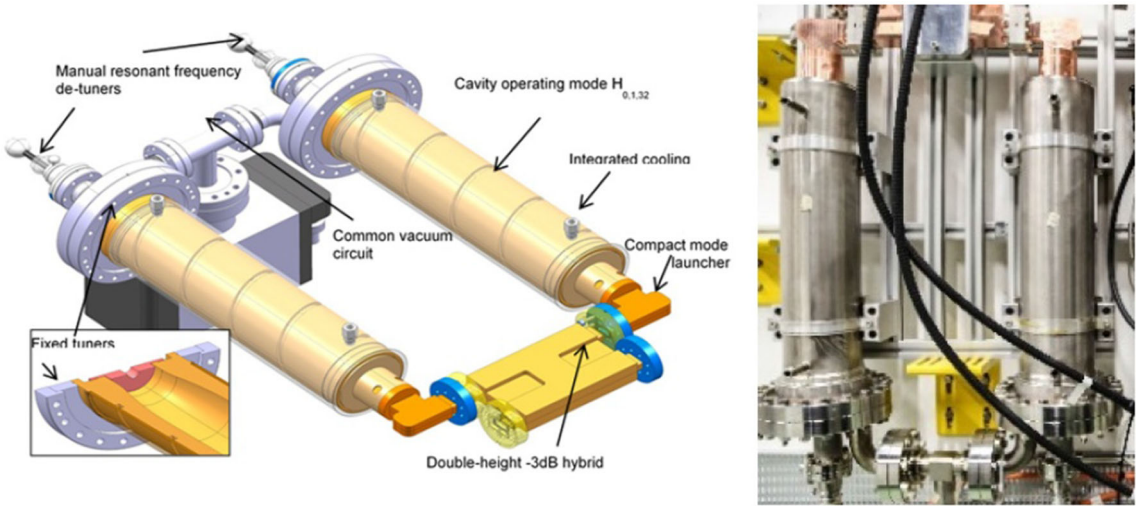

Fig. 55 SLED pulse-compressor 3D drawing (left) and as installed in the X-band facilities at CERN (right)

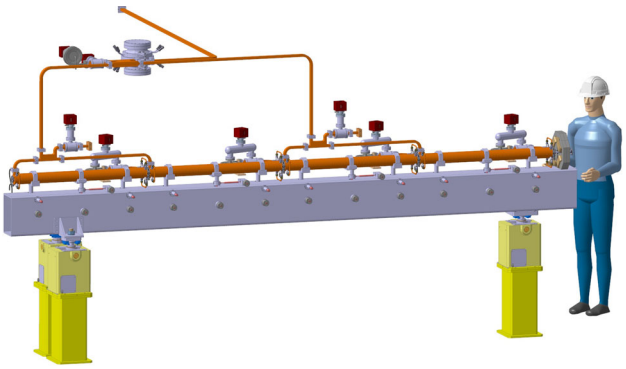

Fig. 56 Engineering design 3D view of a typical XLS module

measurements to better than ± 0.3 mm. Different options exist for the smoothing (final relative alignment) of the modules to better than ± 0.1 mm and can be chosen at a later stage. Full details are available in Deliverable D4.2.

5.2.3 Vacuum system

The vacuum requirements for CompactLight have not been studied in detail, but similar needs were assumed for SwissFEL. These requirements can certainly be met by designing the vacuum system for the various linacs based on local compact pumps fully integrated into the module design. The resulting system is very similar to the systems considered for CLIC [135] and eSPS [134]. It consists of NEG cartridge pumps installed directly on the accelerating structure vacuum manifold. Vacuum tests have been carried out on a similar system for CLIC and documented in the Project Implementation Plan [135]. These tests were performed on dedicated accelerating structures with an NEG pump with nominal pumping speed 100 l/s^{-1} combined with a sputter ion pump providing 5 l/s^{-1} pumping speed. After activation of the NEG cartridge, the pressure decreased with time (1/t) and reached 3×10^{-9} mbar along the beam axis after 100 h pumping.

In addition, a T-shape connector has to be installed on each vacuum line. Installed on the pumping port of the AS, it is equipped with a NEG pump on one side and a manual all-metal right angle valve on the other side allowing the rough pumping and an eventual leak detection procedure for each module.

Vacuum gauges, a set of Pirani and Penning gauges, are installed on each module. This allows pressure measurement from atmospheric pressure down to 10^{-10} mbar. This is needed during the operation and commissioning of the vacuum system. Vacuum gauges also provide signals for interlocks of vacuum sector valves and machine protection systems.

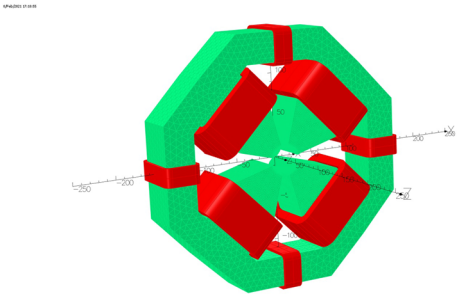

Fig. 57 Quadrupole design for the XLS linacs including vertical and horizontal corrector coils

Table 15 XLS quadrupole technical details

Parameter	Units	Value
Integrated max. strength	T	2.72
Aperture	mm	25
Max. gradient	T/m	40.5
Conductor cross-section	mm	10 x 48
Conductor current density	A/mm^2	5.4
Steel yoke length	mm	52
Magnetic length	mm	67
Total length including overhang	mm	82
Height and width	mm	302
Height and width including corrector coils	mm	310

For flexibility and safety reasons, it was decided to contain each accelerator module in its own longitudinal vacuum sector. Hence, a space reservation of 10 cm is foreseen at the beginning of each module for a vacuum sector valve. These are off-the-shelf items and can be commercially provided with ease and easily integrated.

5.2.4 Magnets

Quadrupole magnets are necessary for guiding the beam during transport along the various linacs (see for example Fig. 47). These are arranged in a FODO lattice configuration and are fully integrated in the various versions of the XLS modules (see Sect. 5.2.5). The magnetic design for a single standard quadrupole magnet used through the facility has been developed taking into account the requirements specific to the CompactLight beams, as shown in Fig. 57.

The magnet length has been minimized, so that the filling factor for RF structures in the various different linacs can be kept high (see Sect. 5.2.5), thus giving highest overall accelerating gradient and minimum facility length. The overall envelope of the magnet and other key numbers are summarized in Table 15.

The quadrupole magnets have been designed to be used at all positions, thus energies, along the linac. Hence, only one magnet design needs to be developed and manufactured reducing cost and increasing reliability. Each of the magnets needs individual powering to account for the different energies. Nevertheless, having one single quadrupole design for all the accelerators makes this a very economical choice.

As for the requirements of beam steering through the accelerator, given the moderate energies of the electron beam, the choice was made to include corrector coils directly on the magnet yoke instead of an adjustable mechanical support capable of moving the entire magnet. This means that the magnets will be pre-positioned with respect to the accelerating structures on their common girder and then will stay in place. The beam position monitors attached are integrated into the quadrupoles and are described in detail in the ComapctLight deliverable D8.1.

5.2.5 System integration

For the linacs (as can be seen for example in Fig. 47), a specific standardized "module" has been designed and is repeated as often as necessary for a given linac. This approach minimizes the number of variants and enables series production as much as possible. Powers for the different operation modes can be found in Sect. 5.2.1. The accelerating structure temperature stabilisation for the various different operation modes is achieved by

demineralised water circulation at the reference temperature of 28 °C. The water consumption is estimated in the order of 6 l/min per accelerating structure.

For the various linac sections, beam dynamics imposes different distributions of the optical elements resulting in three different spacings of the quadrupoles along the entire beamline: one accelerating structure per quadrupole, two per quadrupole, and four per quadrupole. Hence, the module layout has to accommodate this variation and is split up into three different module layouts detailed hereafter.

5.2.5. Low-energy module

The schematic module layout for the lowest energy sections of the beamline is shown in Fig. 58. The distinct characteristic of the low-energy module is that there is a single accelerating structure in between the quadrupoles. This also makes this version of the module the longest of the three with the lowest RF fill factor. The impact is limited, since only a few of these module types are needed. The powering scheme (100 Hz–1 kHz) can be switched between the two klystrons remotely, and no change in hardware is necessary. This makes the overall machine quite flexible and new operation scenarios could be applied multiple times per day.

5.2.5.2 Medium energy module

Figure 59 shows the schematic layout of the medium energy module with two accelerating structures per quadrupole which shortens the module considerably and increases the RF fill factor with respect to the low energy version.

5.2.5.3 High-energy module

The high-energy module layout can be seen in Fig. 60 with only one quadrupole per module. This results in a slightly shorter module with respect to the medium energy version and a slightly increased RF fill factor. This will be the most common module seen in the various linac sections.

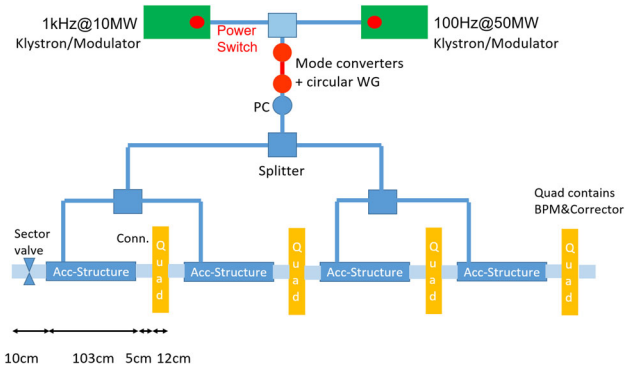

Fig. 58 XLS RF module layout for lowest energy section in the linac (up to 0.3 GeV). Module length: 5.10 m; RF-fill factor: 71%

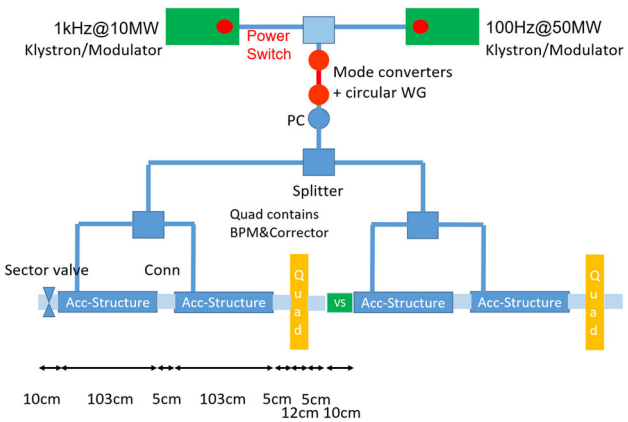

Fig. 59 XLS RF module layout for medium energy section in the linac (up to 2.0 GeV). VS = View Screen. Module length: 4.86 m; RF-fill factor: 74%

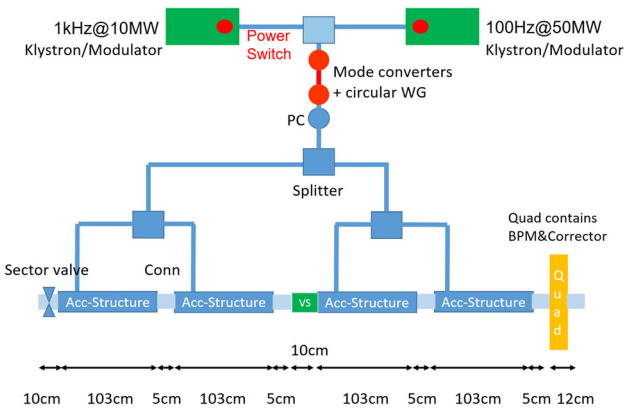

Fig. 60 XLS RF module layout for medium energy section in the linac (up to 5.5 GeV). VS = view screen. Module length: 4.69 m; RF-fill factor: 77%

5.2.6 Industrialization

To produce an entire accelerator section within tolerance for minimum cost with a short lead-time, the production process has to be of an industrialized level with, e.g., low rejection rate, a high degree of mechanisation/automation, and a high degree of reproducibility.

The challenges in the industrialization of accelerator structures are predominantly in the (sub) micrometer-machining of the copper parts and the consecutive assembly of the accelerator section due to the very strict mechanical tolerances. In state-of-the-art X-band designs, these tolerances are approaching the limits of machining techniques available to date.

The typical work-flow of high-precision mono parts is as follows:

- Production of bulk material.
- Pre-machining by high-precision technology machines with an accuracy of 10 μm.
- Thermal annealing at 240 °C to release the stress in the material.
- Final-machining with alternating single-point diamond machining and measurement steps.
- Metrology with a touch probe and interferometers to ensure that the final part is within specification.
- Cleaning by ultrasonic cleaning method, followed by a vapor degreasing
- Packaging to avoid oxidization, and damage during handling, transport, and storage.

As the final machining steps are the most time- and cost-consuming, it is important to minimize the amount of material allowance after pre-machining. By this, the final machining can be done in a limited number of passes. This optimisation has to be done throughout the entire production chain, i.e., from raw material to final product. Individual machined parts need to be joined into (sub)assemblies that form the accelerator structure. As the RF components need to be used in a vacuum environment, the assemblies have to be vacuum-tight. There are a few techniques that are used to achieve this: bolt-connection, welding, vacuum brazing, and diffusion bonding. After any joining technique, leak testing is performed as one of the last (mechanical) testing steps, often down to 10^{-10} mbar.

The production costs of the mono-parts can be divided into several categories (Table 16) following the manufacturing flow. The items listed under general are non-recurring engineering (NRE) cost that are related to programming the CNC-machines and hence only applicable for a new design, i.e., once a particular design has been manufactured, these costs are omitted in all following production runs.

The machining steps are divided into two categories, pre- and end-machining, where the pre-machining steps take place in a regular machine shop with precision-technology (PT) and high-precision-technology (HPT) capabilities. End-machining will take place in a dedicated manufacturing area in which the ultrahigh-precision-technology (UPT) machines are placed in a temperature controlled environment with a maximum temperature fluctuation of ± 0.1 °C. It is foreseen that the manufacturing strategy to date can be further optimized due to new developments in the HPT and UPT machining accuracy and combined milling/turning machine centers (Table 16 right two columns).

Table 16 Cost breakdown

Item	Operation	To date		Optimized	
		Costs	Total	Costs	Total
General	Work preparation	1.5%	12.3%	1.5%	12.3%
	Programming PT/HPT	3.1%		3.1%	
	Programming UPT	4.6%		4.6%	
	Programming 3D metrology	3.1%		3.1%	
Tooling	Mill	1.5%	4.6%	1.5%	4.6%
	Diamond tool	3.1%		3.1%	
Pre machining	Sawing	1.5%	22.1%	1.5%	18.0%
	Turning PT	13.0%		15.0%	
	Milling HPT	6.1%		–	
	Annealing	1.5%		1.5%	
End machining	Flycutting	5.0%	61.0%	–	54.2%
	Turning UPT Pre-machining	–		15%	
	Turning UPT End-machining	39.0%		22.5%	
	Cleaning	1.7%		1.7%	
	Metrology	15.3%		15.0%	
		100%		90%	

5.2.7 Sub-harmonic deflector system

Two-bunch operation for FEL pump and FEL probe experiments is part of the baseline specification. The spacing between the two bunches is 6 or 10 X-band RF cycles, the minimum spacing is determined by sufficient higher order transverse mode suppression in the accelerating structure. An S-band splitter is used to separate the two bunches and feed them into a septum magnet which separates them into the two FEL lines. The transverse separation between the two beams at the septum is 2.5 mm. A schematic is shown in Fig. 61. A sub-harmonic deflector deflecting structure, working at S-band, is used to split the two bunches [136–138]. In contrast to the accelerating structure which operates in the TM_{010} mode, the transverse deflecting structure operates in the TM_{110} mode. The transverse magnetic fields of TM_{010} mode and TM_{110} mode are shown in Fig 62.

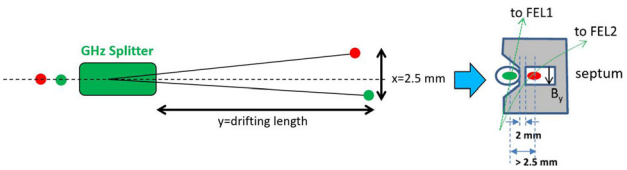

Fig. 61 Schematic figure of the S-band splitter system

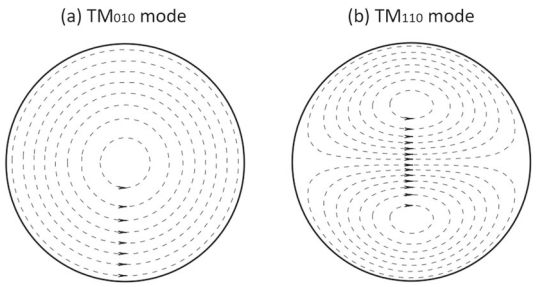

Fig. 62 The transverse magnetic fields of **a** TM_{010} mode and **b** TM_{110} mode

The magnetic field of the TM_{110} mode creates a transverse kick to the beam. The bunch will then follow an angled trajectory downstream of the deflector. The relation between transverse movement and longitudinal movement is given by

$$\frac{x}{y} = \frac{V_{\perp} e}{E}, \tag{22}$$

where x is the transverse displacement, y is the drift length, $V_{\perp}$ is the transverse deflecting voltage, e is the charge of the electron, and E is the electron energy. The S-band deflector operates at 2.998 GHz. The spacing between the two bunches, 6 or 10 X-band RF cycles, is 1.5 or 2.5 RF cycles at S-band. Thus, the two bunches can be placed at the crest and trough of the RF cycle of the sub-harmonic deflector, so that the kicks applied to the two bunches are in opposite directions and the separation is maximized for a given kick voltage. The bunch energy in the hard X-ray mode is 5.5 GeV. The required deflecting distance for one bunch from the beam axis after drifting is 1.25 mm. The deflecting voltage can be calculated from Eq. (22). Both traveling-wave and standing-wave deflecting structures have been designed for the sub-harmonic deflector system. The power capability for the deflector system is presented next in Sect. 5.2.7.1, followed by the details of the traveling-wave and standing-wave structure designs.

5.2.7.1 Power source capability

The klystron for the sub-harmonic deflector system is a CPI S-band klystron (VKS8262G1) [139]. It can reach a maximum power of 7.5 MW with maximum pulse width 5.0 μs. The maximum repetition rate is 400 Hz. This type of klystron has already been applied at IFIC S-band test-stand in Valencia. According to the manufacturer, this klystron has the potential to operate at 1 kHz. An S-band spherical pulse-compressor is used to increase the peak power to the deflecting cavity. An average power gain factor of 5.29 is achieved by compressing the 4.5 μs klystron pulse to a 300 ns pulse. The pulse shape is shown in Fig. 63. The intrinsic quality factor of the spherical cavity is 100,000. The coupling factor is set at 7. We assume that the available power for the structure in 1 kHz operation is 6 MW with consideration of the losses.

5.2.7.2 Traveling-wave transverse deflector design

The traveling-wave transverse deflecting structure works at $\frac{2\pi}{3}$ mode. The single cell electrical field is shown in Fig. 64. Constant impedance design is chosen for easy fabrication. The length of the whole traveling-wave structure can be easily modified by adding or reducing cells to achieve the required deflecting voltage at the same input power. To prevent the excitation of the modes with polarity rotated at 90°, two longitudinal rods (radius = 9.525 mm) crossing the cells off-axis have been inserted, as shown in Fig. 64. The resonance frequencies of such modes are shifted far enough from the operating mode frequency to be negligible. The calculated frequency shift for the rotated modes due to the rods is about +17.3 MHz, while the working mode is practically unperturbed. The main RF parameters are summarized in Table 17.

The deflecting voltage increases when increasing the cell number at the same input power. The required length of the traveling-wave deflecting structure to separate two 5.5 GeV bunches at different drift length is shown in Fig. 65. The schematic figure of the traveling-wave deflector system is shown in Fig. 66. The structure consists of 15 cells, with a total length of 0.5 m. The filling time is 62.5 ns. The pulse-compressor compresses 6 MW, 1.09 μs

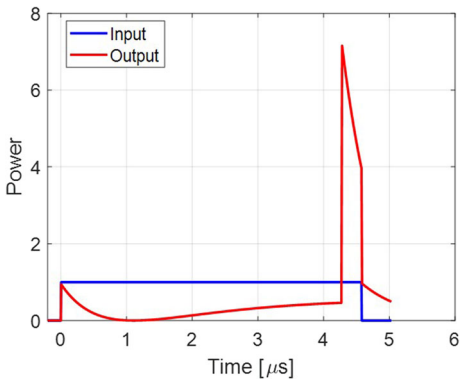

Fig. 63 The input and output pulse shape of the pulse-compressor

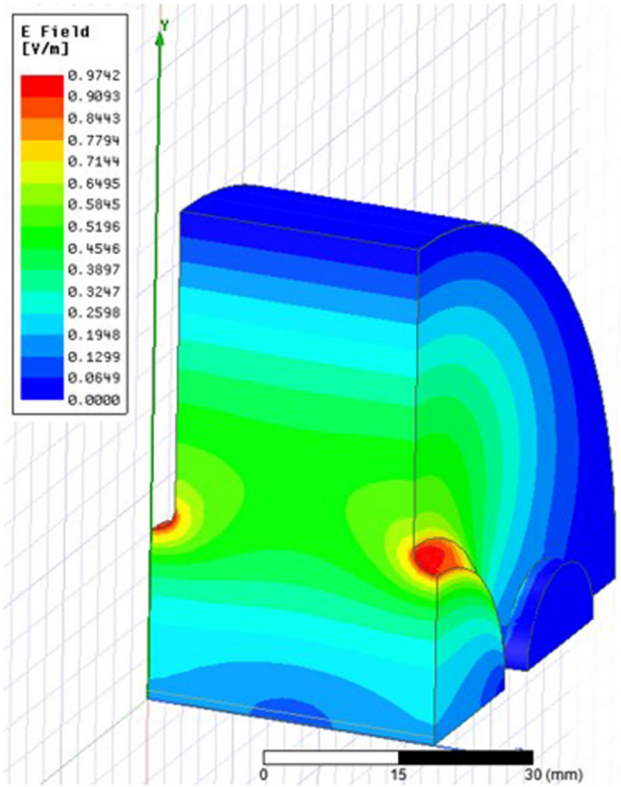

Fig. 64 The electrical field of single cell of traveling-wave transverse deflecting structure

Table 17 The RF parameters of the single cell of the traveling-wave transverse deflecting structure

Parameter	Units	Value
Cell length	mm	33.3
Operating frequency	GHz	2.998
Shunt impedance	MΩ/m	20.25
Quality factor		12369
Group velocity	v_g/c_0	0.027

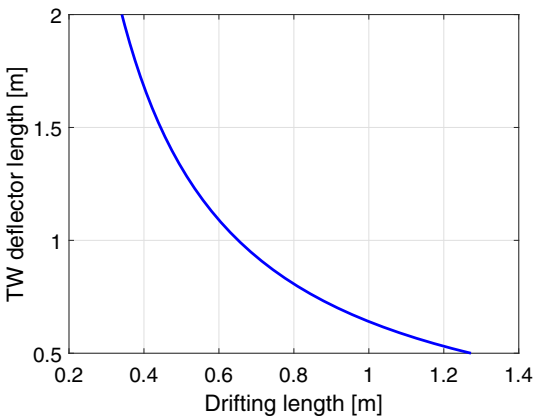

Fig. 65 Traveling-wave deflecting structure length versus drifting length. The input power is 31.74 MW

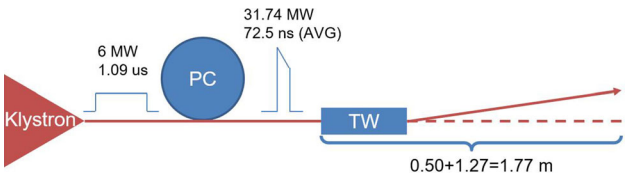

Fig. 66 Schematic figure of the traveling-wave deflector system. PC is the pulse-compressor and TW is the traveling-wave structure. The length of the structure is 0.5 m and the drift length is 1.27 m

klystron pulse to 31.74 MW, 72.5 ns output pulse which includes the rise time of the system and the fill time of the structure. The deflecting voltage of the structure, with 31.74 MW input power, is 5.4 MV.

5.2.7.3 Standing-wave transverse deflector design

The single-cell shape of the standing-wave transverse deflecting structure is similar to that of the traveling-wave structure, as shown in Fig. 67. Two longitudinal rods (radius = 8 mm) crossing the cells off-axis have been inserted to suppress the excitation of the polarizing modes. The resonant frequencies of such modes are shifted far enough from the operating mode frequency to be negligible. The calculated frequency shift for the rotated modes due to the rods is +9.1 MHz. The RF parameters are summarized in Table 18.

Two standing-wave deflecting structures consisting of 3 cells and 5 cells have been designed. The structures are designed for critical coupling. The filling time, defined as $2Q_L/\omega$, is 830 ns. The time to fill 99% of the maximum electrical field in the structure at a constant input power is 3776 ns. There is high reflection from the standing-wave structure during the filling period of the pulse, especially in the initial part, that represents a risk of damage to the klystron. One solution to deal with the reflected power is to use a circulator to isolate the power source and the reflection from the structure. The schematic figure of the standing-wave deflector system with circulator is shown in Fig. 68. The pulse width of the klystron is 3.78 μs. Figure 69 shows a schematic of the standing-wave deflector system with 3 dB hybrid coupler. Another scheme to eliminate the reflection is to use two identical standing-wave structures and a 3 dB hybrid coupler. When the two structures are filled with a relative 90° phase shift, the 3 dB hybrid coupler can separate the wave from the klystron from the wave that leaves the cavities. The input power of each structure is 3 MW. The comparison between the two schemes of 3-cell and 5-cell standing-wave structures is summarized in Table 19.

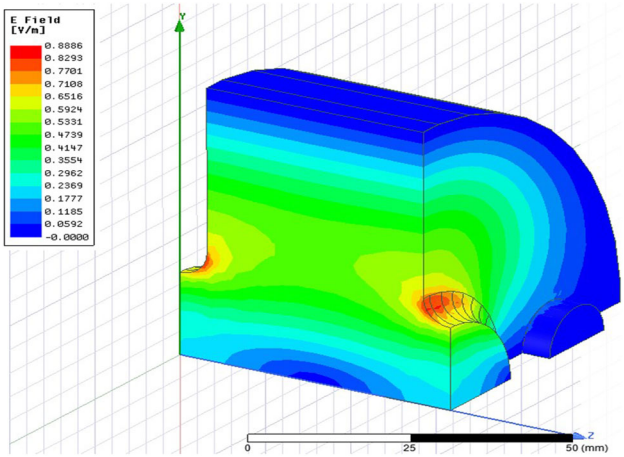

Fig. 67 The electrical field of single cell of standing-wave transverse deflecting structure

Table 18 The RF parameters of the single cell of the standing-wave transverse deflecting structure

Parameter	Units	Value
Cell length	mm	50
Operating frequency	GHz	2.998
Shunt impedance	MΩ/m	21.1
Quality factor		15642

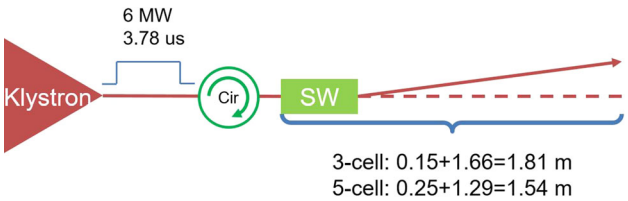

Fig. 68 Schematic figure of the standing-wave deflector system with circulator. The length of the 3-cell standing-wave structure is 0.15 m and the drifting length is 1.66 m. The length of the 5-cell standing-wave structure is 0.25 m and the drifting length is 1.29 m

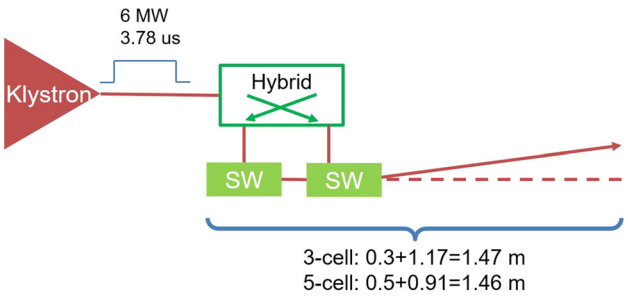

Fig. 69 Schematic figure of the standing-wave deflector system with 3 dB hybrid coupler. The length of the two 3-cell standing-wave structures is 0.3 m and the drifting length is 1.17 m. The length of the two 5-cell standing-wave structures is 0.5 m and the drifting length is 0.91 m

Table 19 Information of various standing-wave deflector systems

	Number of structures	Length of the structure [m]	Drifting length [m]	Deflecting voltage [MV]
3-cell SW structure with circulator	1	0.15	1.66	4.15
5-cell SW structure with circulator	1	0.25	1.29	5.33
3-cell SW structure with 3 dB hybrid	2	0.15	1.17	5.87
5-cell SW structure with 3 dB hybrid	2	0.25	0.91	7.53

5.2.8 Harmonic linearizer system

To compress the bunch length, an energy chirp in the longitudinal phase space of the bunch is combined with a magnetic chicane. The C-band RF system of the injector introduces an energy chirp in the bunch by operating off-crest. However, this chirp can be non-linear due to the curvature of the RF wave over the bunch length. This nonlinearity can cause temporal current spikes and longitudinal wakefields in the undulator section, which may hinder FEL performance. To linearize the energy chirp, a higher harmonic RF system is used. The higher the harmonic used, the lower the RF voltage required, with the required voltage scaling approximately with the square of the harmonic number. Most injectors use a 3rd or 4th harmonic, but this is mostly due to those harmonic numbers being standard RF frequencies for L and S band injectors. However, in the case of CompactLight, which has a C-band injector, this frequency would be a 18 GHz or 24 GHz RF system, neither of which is widely available and requires the development of bespoke RF amplifiers. While higher frequencies result in lower required voltages, there are potential issues associated with high frequencies. A higher frequency means a larger ratio of the aperture to the wavelength (as impedance limits fix the aperture) resulting in a lower shunt impedance and higher group velocity. A higher frequency in theory requires tighter tolerances (although the higher group velocity partially offsets that), and the available RF power drops sharply with frequency. A 12 GHz RF system would be a 2^{nd} harmonic requiring a high voltage. A detailed study of periodic cells at all sensible harmonics converged to 36 GHz (Ka-band) as being the optimum choice for Compactlight. This frequency choice also means that experience with

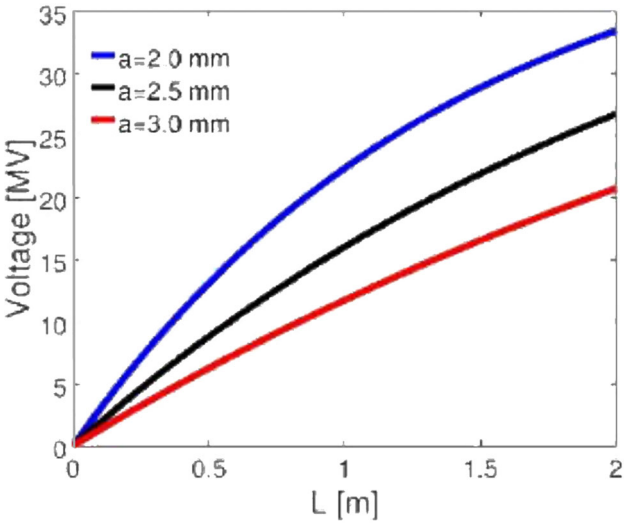

Fig. 70 Analytical estimate of the required voltage as a function of the Ka-band length, for different iris aperture radii

30 GHz RF technology early in the CLIC study can be applied to CompactLight [140]. The development of very high-frequency linearizers is of broad importance for accelerators which require short bunches, including high-frequency RF and plasma accelerators. Further information about the injector and its optimization can be found in the ComapctLight deliverable D3.4.

The requirements of the linearizer system

The requirements for the linerizer are fairly complex as the linearizing effect is perturbed by the short-range longitudinal wakefield. As such, the required voltage depends strongly on the structure length and aperture. The structure should provide a peak accelerating voltage of 12.75 MV (which includes a 20% overhead) at a frequency of 36 GHz for a 30 cm structure; however, as the wakes act in tandem with the structure, the required voltage depends on the cavity length and aperture. The required voltage for a 2 mm aperture radius as a function of cavity length is shown in Fig. 70.

Under the effect of transverse short-range wakefields, the bunch tail gets a transverse deflection due to the wakefield excited by the bunch head. Given the relatively long bunch at the Ka-band and the small iris aperture, this deflection can induce beam breakup. The action amplification factor, A, allows estimation of the deflection amplitude as a function of the distance from the head of the bunch, z

$$A(z) = \frac{J_f}{J_i} = \sqrt{1 + \left(\beta \frac{eQL_{\text{cav}} w_\perp(z)}{E_{\text{beam}}}\right)^2}. \tag{23}$$

In this formula, J_i and J_i indicate, respectively, the action before and after the Ka-band, β is the optical beta function at the Ka-band (assumed to be 5 m), e is the electron charge, Q is the total bunch charge, L_{cav} is the length of the Ka-band, E_{beam} is the beam energy, and $w_\perp(z)$ is the wake potential expressed in V/pC/m/mm following the approximation defined in [141]. Due to wakefields, the aperture size is limited by a minimum radius which is dependent on the cavity length, as given in Fig. 71. Acceptable amplification factors are defined here as below 1.1, i.e., $< 10\%$ amplification.

The phase stability of the RF system is limited by charge stability, with a 30 cm structure requiring a phase stability of 0.25 degrees. The amplitude stability is limited by variation in arrival time to 0.25%.The phase and amplitude jitter/stability will be dominated by the variation in the modulator voltage. We assume a 0.005% variation in voltage; hence, the RF source should not have its amplitude or phase vary by more than the specified amounts with a 0.005% voltage variation.

5.2.8.1 Ka band power sources

A rough estimate of the likely pulse compression factors and structure parameters led to a power requirement of around 3 MW from the RF amplifier for a 300 mm long structure, with pulse lengths of around 1000 μs and a repetition rate of 1 kHz. Traditional single-beam klystrons commonly used at RF frequencies to drive accelerators are unlikely to be able to produce this power at Ka-band; hence, bespoke amplifiers are required. Two approaches have been identified—a higher-order-mode multi-beam klystron (HOM MBK) and a Gyro-Klystron.

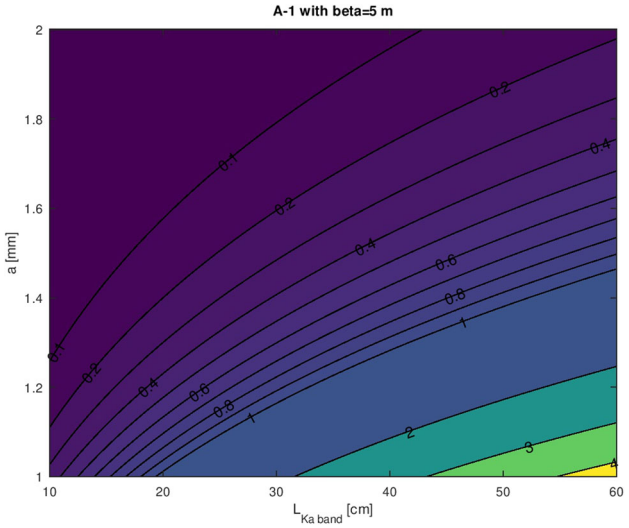

Fig. 71 The fraction of the action amplification factor exceeding one under the effects of short-range wakefields in the Ka-band lineariser, as a function of the Ka-band length and of the aperture radius

In both devices, higher-order-mode cavities are utilized allowing better power handling. In both cases, extensive numerical Particle-in-Cell code modelling has validated the novel designs. RF amplifier development is a long risky process, so a single technology has not been selected at this stage and both options require further commercial development and prototyping.

A third amplifier concept has been identified to generate very high powers which would allow far higher gradients and hence shorter linearizer structures. This is the use of a klystron up-converter. In this concept, a high-power X-band klystron is used, but the output cavity is replaced with a 36 GHz cavity to generate RF power using the third-beam harmonic current. As the cavity is a monopole, cavity peak fields and power density would be much higher in this design, and there seems no requirement for shorter linearizers; hence, this option was not selected as baseline. Further development of this concept is required.

Multi-beam klystron

As klystrons scale in frequency, the aperture sizes in the cavities decrease and as such the beam must have a smaller radius, increasing the current density in the beam, in turn decreasing the RF efficiency. A multi-beam klystron allows the beam current to be spread across many beams reducing the current density in each. However, it would be impossible to fit a large number of cathodes in an area consistent with a standard Ka-band cavity. In addition, the peak fields would be very high for a TM_{110} mode cavity and would be very high at Ka-band with a power of 3 MW. Hence, to create a high-power klystron in the frequency range of interest we need to move to a higher-order-mode (HOM) cavity which would be oversized compared to the wavelength. A coaxial HOM cavity was chosen to base the design upon; however, one problem to be considered is ensuring the beam excites the correct mode and not one of the many others at nearby frequencies.

To make the device compact and avoid the use of an oil tank, a beam voltage of 60 kV was chosen. Assuming the klystron would be around 35% efficient and produce an RF output power of 3 MW, a beam current of around 120 A is required. For limiting the current in each beamlet to 6 A, 20 beamlets are required. Finally, for having a round 12 mm between each cathode, a mean radius of around 38 mm is necessary. After optimisation of the cavity geometry, the final radius was 37.6 mm with operation in the the $TM_{20,0}$ and a beam tunnel aperture of 2 mm, and width = height = 5.9 mm. With a 2 mm aperture, the required magnetic field is 0.55 T (3–4 times the Brillioun field) which can be generated with a normal conducting magnet.

One issue with the HOM cavity was detuning. When exciting the cavity with a single port or beam, the excited mode was found to have a varying field amplitude around the ring as nearby modes were excited. Figure 72 shows the operating mode and one of the nearby modes. However, it was also found that exciting with multiple beams, or with a distributed coupling, the other modes field components were completely canceled out leaving only a pure $TM_{20,0}$ mode. A study was performed to understand the tolerance to beam current variations or failure of beamlets. This showed that the cavity was largely insensitive to very large fluctuations or multiple failed beamlets.

With the basic cavity geometry designed the exact positions and frequencies of each cavity were optimized using the disk-model code KlyC, with final verification in CST Studio Suite. The optimized tube provided 33.3% efficiency (2.4 MW peak power), 50 MHz frequency bandwidth at a level of −3 dB and a power gain of 40.7 dB. The parameters are listed in Table 20. The effect of a single beamlet being turned off was studied to ensure stability.

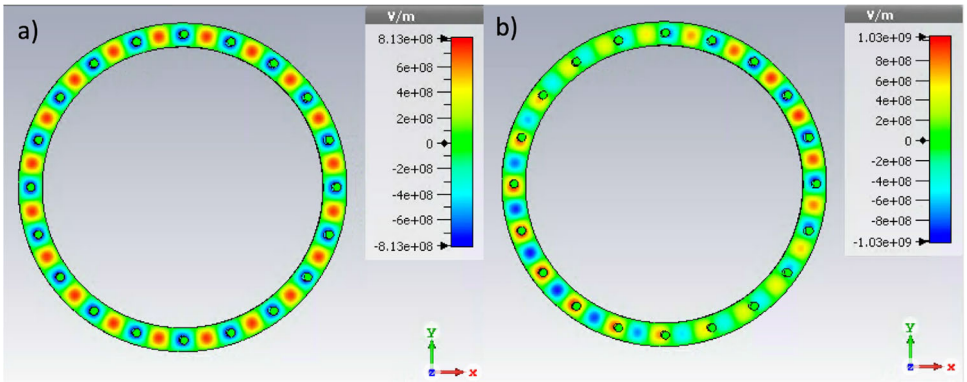

Fig. 72 TE20,1,0 mode (**a**) and TE21,1,0 mode (**b**) in the coaxial cavity with integrated beam tunnels

Table 20 The HOM-MBK parameters

Parameter	Units	Value
Operating frequency	GHz	36
Output power	MW	2.4
Bandwidth	MHz	50
Electron beam voltage	kV	60
Electron beam current	A	120
Beamlet current	A	6
Magnetic field strength	T	0.55
Small-signal linear gain	dB	40.7
Efficiency	%	33.3

The observed RF power reduction in this case was only 7% which is consistent with the reduction in beam current of 5%. The spectrum of the output signal was observed up to 100 GHz and did not show any other major frequency component apart from the input 36 GHz. The electric fields in the HOM MBK are shown in Fig. 73.

As CompactLight has very tight tolerances on phase variations of RF cavities, a study was performed to assess the variation in output RF phase with variation of the modulator voltage. Variation of the cathode voltage by 1 part in 10,000, which is believed to be a conservative estimate of modulator stability, resulted in a phase shift of 0.36 degrees. While this is greater than the specification, it should be noted that most modulators achieve a greater stability than the conservative estimate used here. The required manufacturing tolerance was also assessed and was found to be 5 μm which is similar to that of an X-band RF cavity and so feasible.

An upgrade requirement of CompactLight is operation at 1 kHz. The main limitation to achieving this is the average power density in the collector. A new code was developed to calculate this. This code was then used to optimize the collector geometry to minimize the heat load for two cases: (1) no RF input (DC mode) and

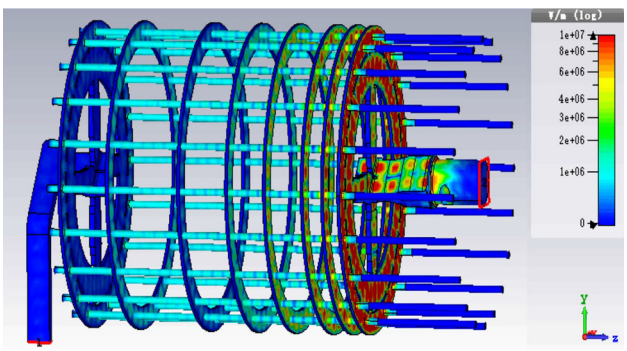

Fig. 73 The electric field plot on the HOM MBK surface

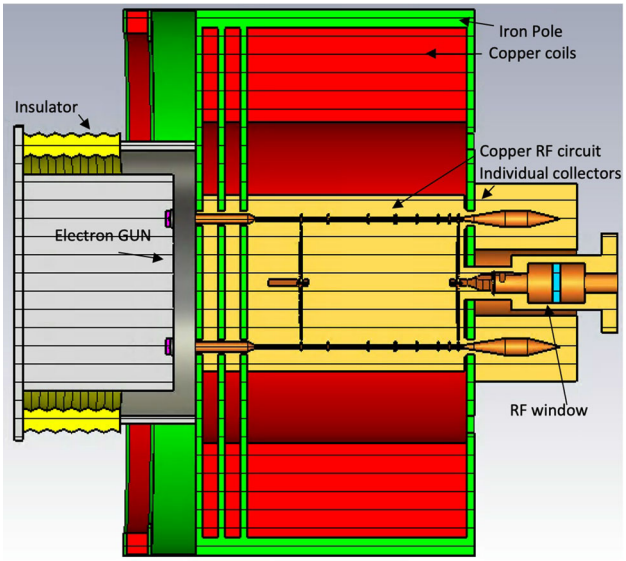

Fig. 74 Artistic view of the Ka-band HOM MBK

(2) saturated RF output. While the beam power is higher for the DC case, in the saturated RF output case, the location of the heat deposition on the collector wall is shifted with respect to the DC case, and hence, the maximum power density in both modes of operation must be assessed. The maximal power density is below 70 W/cm^2 which is below the standard limit of 100 W/cm^2 typically used in collectors with water cooling systems. The final HOM MBK geometry is shown in Fig. 74. A detailed description of on the design of this multi-beam klystron has also been published in [142].

Gyroklystron

The gyrotron klystron is a vacuum electronic-based amplifier that relies on the fast beam–wave electron cyclotron maser interaction for its operation [143]. Compared with a conventional klystron normally used in accelerators, the electron beam interacts with the TE resonant mode in the gyroklystron cavities and the bunching is mainly in the azimuthal direction. The small gap length in a klystron which determines the operating frequency is no longer a constraint in a gyroklyston which allows it to produce high power at the higher operating frequency, for example, to achieve MWs of power at high (Ka-band) frequency. A schematic drawing of a gyroklystron is shown in Fig. 75. Its main components include: (1) the magnetron injection gun (MIG) to generate a rotating electron beam with optimized transverse to axial velocity ratio and small velocity spread; (2) beam–wave interaction circuit to effectively convert the power in the electron beam into the microwave radiation; (3) a cryogen-free superconducting magnet system to properly guide the electron beam and maintain the electron beam cyclotron frequency; (4) the input and output microwave window to couple the input and output radiation; (5) the ultra-high vacuum system; and (6) the depressed collector to reduce the thermal load when operating at high pulse repetition frequencies of 100 Hz or greater.

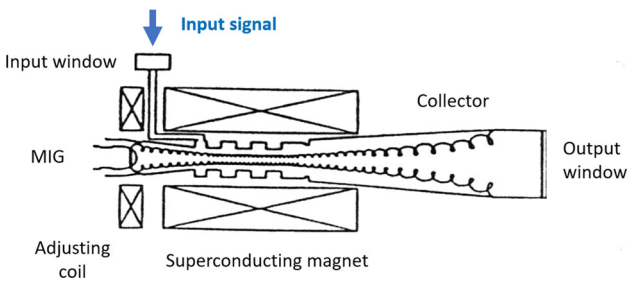

Fig. 75 Schematic drawing of a gyroklystron

Design of the interaction circuit

During the design of the 36 GHz gyroklystron with 3 MW output power, a three-cavity configuration was chosen as a trade-off between gain improvements using more cavities, thermal issues, design complexity, and bunching quality. It included an input cavity to couple in the driving RF signal, a bunching cavity to enhance the electron bunch, and an output cavity to induce a strong resonance with the bunched electron beam for effective beam–wave interaction. The input and bunching cavities are operating with the TE_{01} mode, and the output cavity operates with a TE_{02} mode to improve the power capability.

The design of the gyroklystron interaction circuit follows an iterative process [144, 145]. First, a small-signal linear theory based on the point-gap approximation was used to find the constraints of the initial parameters, such as the beam voltage, current, the transverse-to-axial velocity ratio α, and the magnetic field strength at the interaction region, as shown in Table 21. The dispersion curve of the operating modes of the output cavity based on the interaction principle is shown in Fig 76. The possible competing modes are the TE_{11} and TE_{01}.

After selecting the core beam parameters, the proper eigenfrequencies, and the quality factors for the cavities, the dimensions of the cavities could be decided. The resonant frequencies of the input and intermediate cavities, f_1 and f_2, were chosen using the following equations:

$$f_1 = f_0 + f_0/(3Q_0), \tag{24}$$

$$f_2 = f_0 - f_0/(3Q_0), \tag{25}$$

Table 21 The requirements and initial parameters from the linear theory

Parameter	Units	Value
Operating frequency	GHz	36
Output power	MW	3.2
Bandwidth	MHz	200
Electron beam voltage	kV	150
Electron beam current	A	50
Magnetic field strength	T	1.5
Beam transverse-to-axial velocity ratio		1.4
Small-signal linear gain	dB	48
Efficiency	%	42

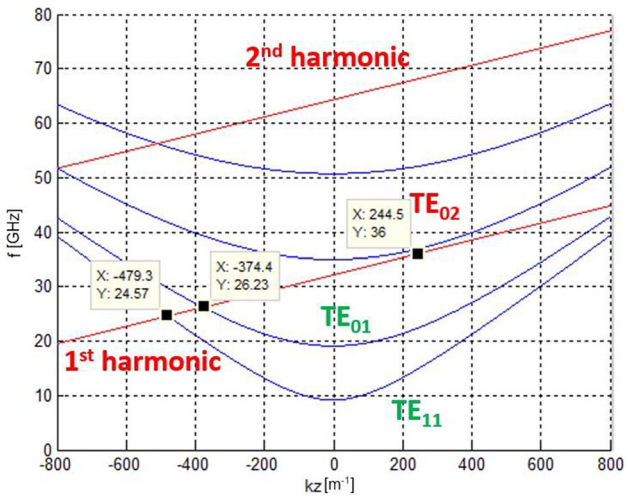

Fig. 76 Dispersion relation of the operating mode of the output cavity

where f_0 and Q_0 are the eigenfrequency and quality factor of the output cavity. The dimensions of the cavities and the radius of the guiding center can be determined from

$$f = c/\lambda_0 = c/2\pi\sqrt{(\nu_{mp}/R)^2 + (n\pi/L)^2}, \tag{26}$$

$$C_{mp}(r) = (J^2_{m\pm1}(k_{\perp r})/((\nu^2_{mp} - m^2)J^2_m(\nu_m p)), \tag{27}$$

where f is the eigenfrequency of the operating mode $\mathrm{TE}_{m,p,n}$, R and L are the radius and length of the cavity, J is the Bessel function of the first kind, and ν_{mp} is the Bessel root corresponding to the mode in question.

The parameters chosen from these equations were then put into the nonlinear theory, which can include the accurate field profiles of the cavities in the calculation enabling the beam–wave coupling equation to be solved. The nonlinear theory provides a balance between accuracy and simulation time. It provides useful information on the bunching process and the trends that occur when changing the parameters. The initial dimensions of cavities, as well as the length of the drift tube sections from the linear theory, were then further optimized using the nonlinear theory calculations to achieve optimal efficiency. The maximum interaction efficiency was about 40%. Figure 77 shows the interaction efficiencies at the intermediate and output cavity as a function of the cavity positions.

The most accurate simulation of the beam-wave interaction is based on finite-difference time-domain particle-in-cell simulations carried out using the optimal geometry suggested by the nonlinear theory calculations. This enables the space-charge effect in the gyro-klystron cavities, the beam energy spread and velocity spread to be included in the simulations. The design goal is to achieve the required output power, frequency, and efficiency from a gyrotron klystron amplifier that can be manufactured with acceptable tolerances. The particle-in-cell simulation requires large computation time. This makes it suited only for final optimization and validation, sweeping across a range of parameters suggested by the nonlinear simulations. Figure 78a shows the structure of the gyroklystron and the phase space of the electrons. The phase space of the electron energy is shown in Fig. 78b, where at the output cavity, most of the electrons lose their energy to the electromagnetic wave which results in the amplification of the input signal.

The simulation showed that more than 3 MW output power can be generated, satisfying the requirements. The Fourier transformation of the amplitude of the electric field at the output port showed that a distinct frequency component of 36 GHz exists in the frequency spectrum. No other frequency components were found except a relatively weak second harmonic. Further PIC simulations were carried out to investigate the effect of the electron beam velocity spread and the variation of the magnetic field strength. The output power remained greater than

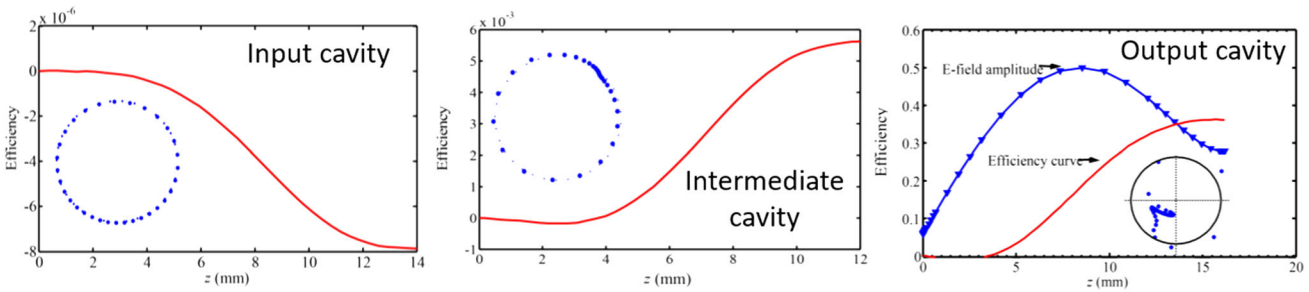

Fig. 77 The efficiency as the function of the cavity position for each cavity from nonlinear theory results

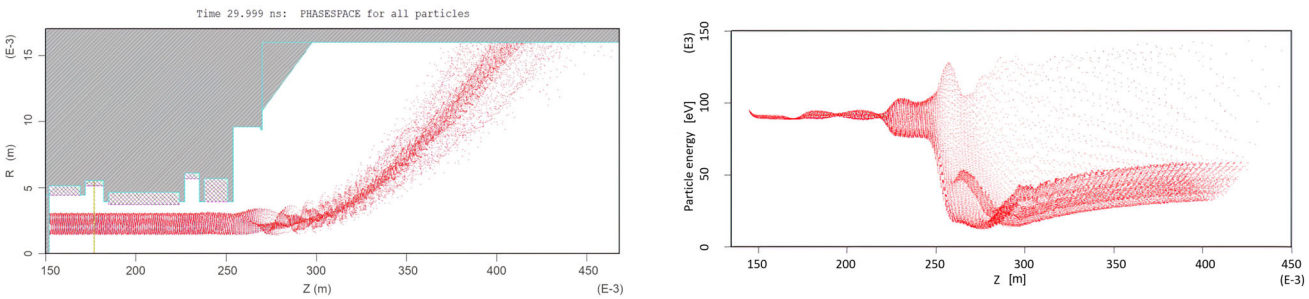

Fig. 78 Simulated gyroklystron structure and the simulated phase space of the electrons

3 MW if the variation of the transverse-to-axial velocity ratio was less than 4%. The output power as the function of input power and bandwidth are shown in Fig. 79.

The MIG gun design for the 36 GHz gyroklystron

The small-orbit gyrating electron beam used for the gyroklystron is generated from a magnetron injection gun (MIG). A triode-type gun that can provide better control of the beam velocity ratio by adjusting the modulating anode voltage was designed. The initial parameters of the MIG were derived from the theoretical model using the final optimized beam parameters of the gyroklystron, as listed in Table 22. The geometry dimensions were further optimized using the particle tracking code EGUN. The optimized beam velocity spreads were about 4% for the desired beam parameters. The simulation results were also validated using other simulation codes, MAGIC, and CST particle studio. The trajectory of the electron beam of the optimized MIG is shown in Fig. 80. The beam transverse-to-axial velocity ratio can be adjusted by varying the modulation anode voltage, as shown in Fig. 81.

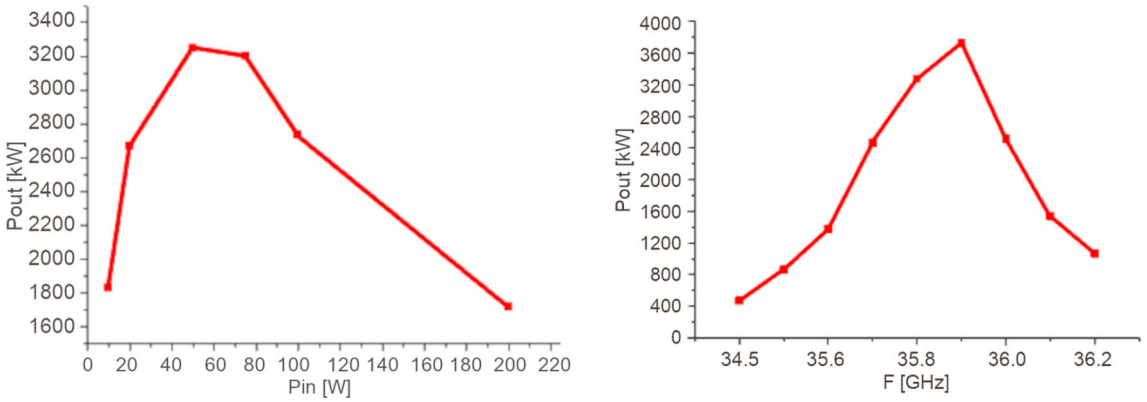

Fig. 79 The output power as input power and bandwidth function

Table 22 The optimized beam parameters of the gyroklystron

Parameter	Units	Value
Electron beam voltage	kV	150
Electron beam current	A	50
Magnetic field strength	T	1.46
Beam transverse-to-axial velocity ratio		1.4
Gain	dB	39 (max. 42)
Efficiency	%	44
Beam guide radius	mm	2.3
Magnetic field compression ratio		10.5
Modulation anode voltage	kV	38.5

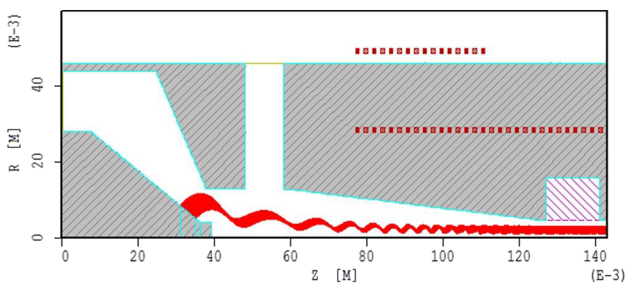

Fig. 80 The trajectories of the electron beam in the MIG

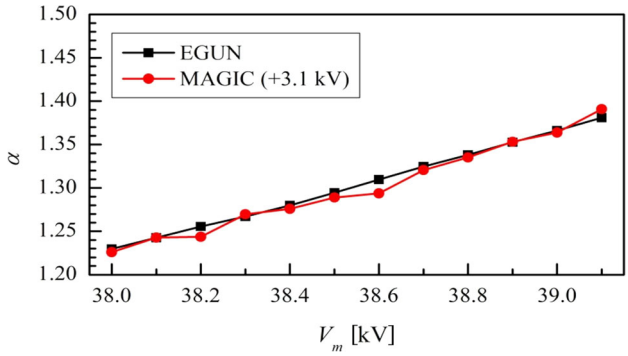

Fig. 81 The beam transverse-to-axial velocity ratio as the function of modulation anode voltage

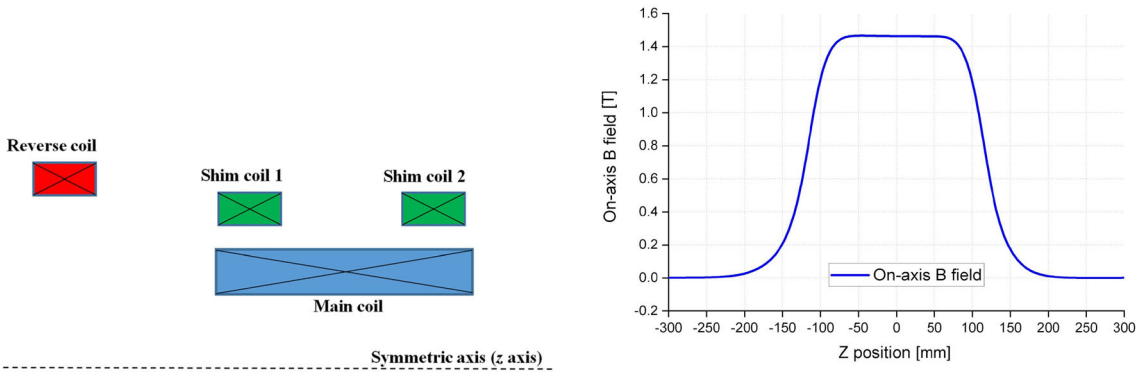

Fig. 82 The superconducting magnet system and the on-axis magnetic field profile

Magnetic field design

The simulation showed that the variation of the magnetic field strength at the interaction region was required to be less than 1% to maintain the desired output power. Although it is possible to generate a magnetic field strength of 1.5 T using a water-cooled copper coil, the cooling requirement and field stability are challenging. A better choice is to use a cryo-cooled closed-loop superconducting magnet. A magnet system composed of four solenoids was used to generate the magnetic field, as shown in Fig. 82. It included one main coil and two shim coils to compensate for the field decrease at both ends of the main coil. The reverse coil was used to adjust the magnetic field strength at the emitter surface accurately. The magnet system was initially designed and optimized by analytical equations. Then, the solenoid configurations were modelled and verified by the magnetic field solver using the finite-element method. The on-axis magnetic field profile is shown in Fig. 82.

Specifications of the 36 GHz gyroklystron

A full summary of specifications of the gyroklystron from the simulations is summarized in Table 23, which also details the footprint and the phase stability. Specifications of the commercial superconducting magnet used for the gyrotron are summarized as in Table 24, which is based on the user manual from the potential vendor [146]. The specifications of the power modulator which satisfies the requirements to drive the gyroklystron are summarized as in Table 25, which is based on the user manual from the potential vendor [147].

5.2.8.2 Pulse compression system

Waveguide system

As waveguide losses increase at higher frequencies, it is necessary to use an overmoded waveguide operating in a lower loss TE_{01} mode to limit the RF losses between the RF source and the RF structure. With such a scaling, the circular waveguide diameter is 12 mm. In such a waveguide, the Ohmic losses are − 0.255 dB/m (5.7%/m). For the long straight WG sections, this diameter can be increased (matched taper) to 20 mm (− 0.035 dB/m; 0.8%/m).

The HOM MBK is very compact and does not require an oil tank and hence could be installed in the tunnel next to the structure further limiting transmission loss. The Gyroklystron is larger and requires both an oil tank and

Table 23 The specifications of the 36 GHz gyroklystron

Parameter	Value
Beam voltage/beam current	150 kV/50 A
Output power/2^{nd} harmonic component	3.2 MW/2.3%
Output power stability	0.4% @0.5% variation of the modulator voltage
Output frequency/3 dB bandwidth	36 GHz/108 MHz (0.3%)
Magnetic field and frequency drift	1.46 T and $<$ 1 MHz drift due to magnetic field drift
Frequency drift due to beam voltage	4.8 MHz @0.1% variation of the modulator voltage
Pulse repetition rate/duration	1000 Hz/1.5 μs
Drive power/gain	400 W/39 dB
Input/output waveguide mode	Input TE10 (Rectangular) mode, output TE02 (Circular) mode
Efficiency	42.7% (without energy recovery), 58.0% (with single stage depressed collector)
Average spent beam power	6.5 kW
Dimensions	60 cm (W) × 60 cm (L) × 1200 cm (H)
Phase stability	3.4 deg@0.1%, 0.34 deg@0.01% variation of the modulator voltage

Table 24 Specifications of the commercial superconducting magnet

Parameter	Value
Guide magnetic field	1.46 T
Type	Cryogen free superconducting magnet
Possible vendor	Cryogenic Ltd.
Magnetic field accuracy	0.08%
Stability over time	0.002%/h
Stability over temperature	0.002%/K

Table 25 Specifications of the commercial power modulator

Parameter	Value
Operating voltage	150 kV
Operating current	50 A
Possible vendor	ScandiNova
Product model	K Series K100
Typical pulsed voltage range	115–190 kV
Typical pulsed current range	90–140 A
RMS voltage stability	0.02%
Dimensions	166 cm × 70 cm × 220 cm

a superconducting magnet making it more difficult to place in the tunnel, and will likely need to be in a separate service tunnel or plant room. In both cases, the modulator will have to be in the plant room. The Gyroklystron requires a TE_{02} to TE_{01} mode converter, while the HOM MBK has a TE_{01} output. The proposal is to use an existing rectangular TE_{20} mode hybrid coupler on the pulse-compressor, which requires a simple circular TE_{01} to rectangular TE_{20} mode converter.

Pulse compression

The Gyroklystron and multi-beam klystron can provide 3.2 MW and 2.5 MW, respectively, as Ka-band RF sources. This power level is smaller than the required input power for the linearizer, which means that more than one RF power source is needed for the system if pulse compression is not implemented. However, the required pulse width for the linearizer is much shorter than the output of the power source. Hense pulse compression can be used to reduce the number of power sources and increase the peak power of the RF source to meet the required input power of the linearizer. The passive pulse-compressor consists of a cavity-based SLEDI and a delay-line-based SLEDII [112, 148–150]. The Q factor of the SLEDI cavity needs to be around 100,000. However, the Q factor of the resonant cavity at 36 GHz could not reach that value. An SLEDII pulse compressor could have a good performance at a higher frequency range. A 30 GHz pulse-compressor with resonant delay lines has been built and installed in the CTF3 (CLIC Test Facility) and obtained the high peak power of 150 MW, as shown in Fig. 83 [151]. A delay-line-based dual-moded SLEDII pulse compressor is proposed for the CompactLight linearizer system.

The length of the delay line of SLEDII pulse compressor is proportional to the output pulse width. Reflective delay lines transmit the RF power in several modes by utilizing the transmission lines several times [152–154]. This can reduce the required delay line by a factor of n, where n is the number of modes used simultaneously. The dual-moded SLEDII pulse-compressor utilizes two modes which are circular TE_{01} and TE_{02} modes in the same delay-line, as shown in Fig. 84. This cuts the delay-line length by a factor of 2.

The baseline of CompactLight aims at a two-bunch operation with a spacing of 6 or 10 X-band RF cycles (0.5 or 0.83 ns). The required input pulse width for the linearizer should ensure the two-bunch operation. As the spacing is much smaller than the filling time of the linearizer, the output pulse width from the pulse compression system is mainly dominated by the filling time. This drives a shorter length of the delay line compared with those designed for colliders with wider pulse widths.

The filling time for a 0.3 m traveling-wave linearizer which operates at $2\pi/3$ mode, is 9 ns. The dual-moded delay line needs to have an approximate length of 1.71 m which includes the filling time and rise/fall edge of the RF power source. The diameter of the waveguide for the delay line is 50 mm. The average power gain of the pulse-compressor as a function of RF source pulse width is shown in Fig. 85.

An average power gain of 7.37 is reached when the RF power source width is 984 ns. The input and output pulse shape is shown in Fig 86.

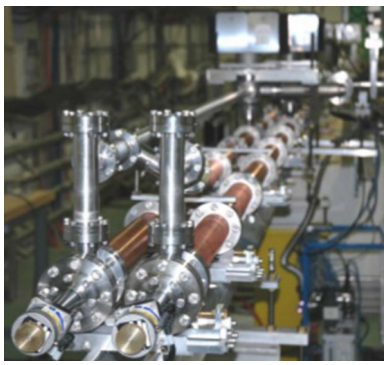

Fig. 83 30 GHz SLED2 pulse-compressor in CTF3

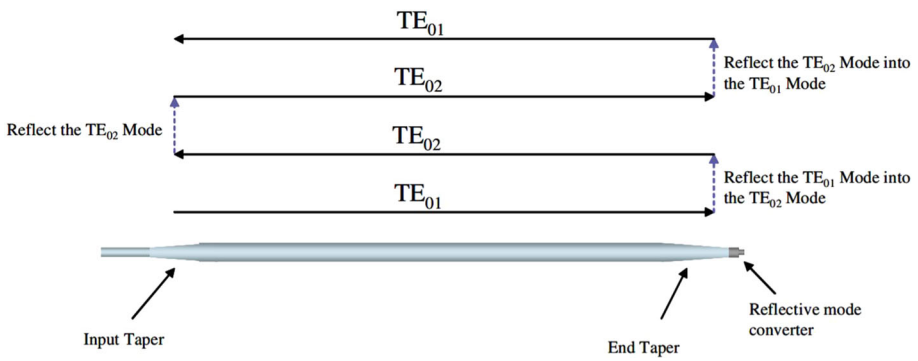

Fig. 84 The delay-line of dual-moded SLEDII pulse-compressor

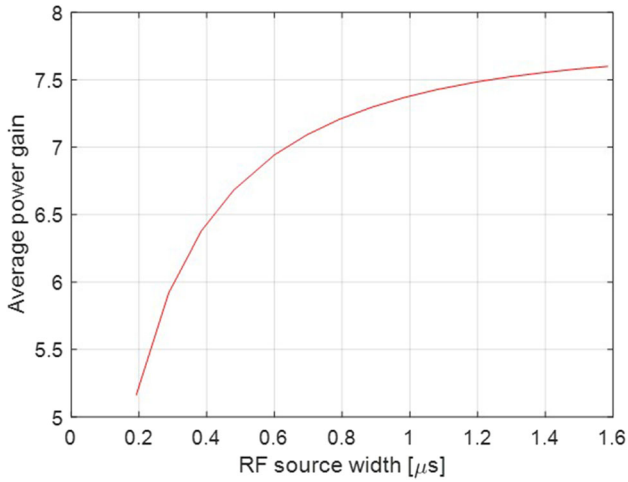

Fig. 85 Average power gain from the pulse-compressor as a function of RF power source pulse width

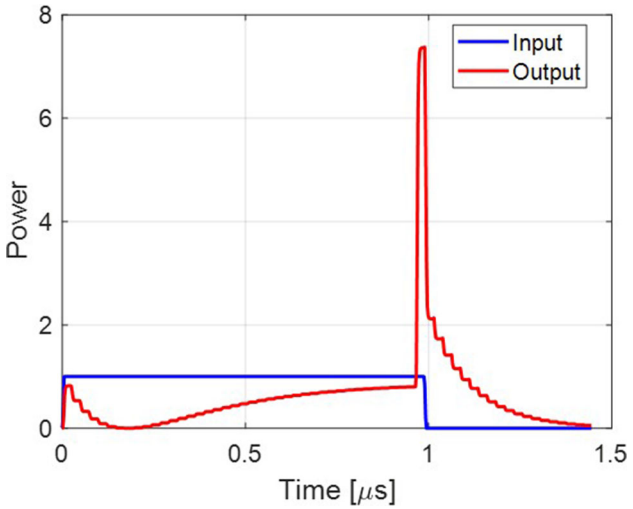

Fig. 86 Input and output pulse shape of the pulse-compressor. The input pulse width is 984 ns and the output pulse width is 24 ns including the rise/fall edge

5.2.8.3 Traveling-wave linearizing structure

At Ka-band, the power available from RF amplifiers is much smaller that that at lower frequencies. While higher powers could potentially be realized in a klystron upconverter the complexity, size, cost, and peak field requirements of such a device would be more risky than other devices. Also, since the lineariser is a single cavity and hence space is not a driving constraint, there was no real requirement for a high gradient and hence high power. This led to an initial limit of 3 MW from the RF source for the purpose of designing the RF structure. A preliminary investigation on SLED-II pulse compressors suggested that this would lead to around 22 MW of RF power being available for the RF structure.

The aperture of the RF structure is limited by short-range wakefields to around 2 mm, although this is weakly dependent on the structure length. The limit thickness of the iris at the Ka-band is not well known; hence, a conservative width of 0.6 mm was chosen based on experience in the CLIC study. One issue with a traveling-wave structure at Ka-band is that the requirement to have a large aperture compared to the wavelength leads to a very high group velocity which can limit the structure's efficiency. Initially, traveling-wave structures with phase advances $2\pi/3$ and $5\pi/6$ were investigated. With smaller apertures, the higher phase advance normally has a lower group velocity for a given aperture size; however, it was found that where the aperture is large compared to the wavelength, the $2\pi/3$ structure had the lower group velocity of 11.9% the speed of light. This resulted in a minimum structure length of 300 mm to achieve a voltage of 12.75 MV with the available RF power.

Using a standing-wave structure would initially appear to be more efficient as there is no power flow out of the structure. However, there are two issues with a standing-wave cavity. The first issue is that there are no Ka-band 3 MW circulators, and hence, the structures would need to be split and fed through hybrid couplers to cancel out the reflections in pairs by choosing the correct phase delay between each structure. Several structures are also required as there is a limit to the number of cells that can be used in a standing-wave structure and the Ka-band cells are very short. The second issue is the longer filling time of the structure leads to significantly longer SLED-II pulse-compressor delay lines. This second issue can be avoided by partly filling the structure, but in doing so, the performance of the standing-wave structure becomes comparable to the traveling-wave structure. Due to the added complication of the standing-wave scheme, the baseline structure design was chosen to be a $2\pi/3$ traveling-wave structure with a length of 300 mm.

Cell design

The single cell geometry (see Fig. 87) was optimized for three different phase advances of the traveling-wave structure (TWS) at 36 GHz, and the general parameters of each one are presented in Table 26, for comparison.

From Table 26, we observe that for a structure with relatively large apertures such as this one (where $R_{iris} \approx \lambda/4$), going from phase advances (ϕ) of $2\pi/3$ to $6\pi/7$, the change of the shunt impedance and group velocity are minimal, $\sim$ 3% and $\sim$ 2%, respectively. Although the attenuation factor changes by $\sim$ 40% and the Q factor by $\sim$ 22%, the shunt impedance remains virtually the same. The peak surface magnetic field increases by close to 19%, while the peak surface electric field increases by less than 9%. Finally, and as expected, the length per cell increases by up to a 28%, between $\phi = 2\pi/3$ and $6\pi/7$. All of these factors make the lower phase advance

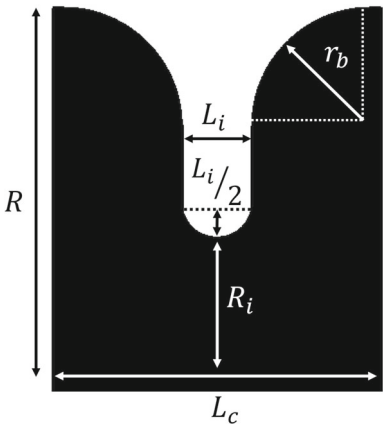

Fig. 87 Single cell geometrical parameters

Table 26 The TWS single cell parameters

Parameter	$\phi = 2\pi/3$	$5\pi/6$	$6\pi/7$	Units
Frequency f	36			GHz
Q factor	4392	5251	5365	–
Shunt impedance r_L	106	109	109	MΩ/m
Group velocity ν_g	0.119	0.138	0.145	c
Attenuation α_0	0.7	0.5	0.5	m^{-1}
Peak surface field E_p^a	2.57	2.99	3.05	MV/m
Peak surface field B_p^a	4.45	4.76	4.83	mT
Cavity radius R	3.96	3.86	3.85	mm
Iris radius R_{iris}	2.00			mm
Cell length L_c	2.78	3.47	3.57	mm
Iris thickness L_i	0.60			mm
Cavity blending radius r_b	1.00			mm

[a]Normalized to $E_z = 1\,\text{MV/m}$

option more attractive to reach the target integrated voltage (i.e., 12.75 MV), with lower power requirements for a given structure length (see Fig. 88), which is not the expected result when dealing with structures with smaller apertures.

Figure 88 shows: in orange, all the possible combinations of input power (after compression) and structure length ($\phi = 6\pi/7$) that deliver at least 12.75 MV of integrated voltage, and in blue, the same for $\phi = 2\pi/3$. This makes the lower border of the colored areas the optimal front, where minimal input power is needed to deliver the required voltage, for a given structure length. Highlighted in red dashed lines is the point where 15 MW of input power after compression provides the 12.75 MV, for a 30 cm long TWS with $\phi = 2\pi/3$. This point is chosen as a trade-off between the available power and a reduced number of cells (108 cells in this case). It is obvious that a structure with phase advance greater than $2\pi/3$ will fail to provide the linearising voltage for the input power available based on both RF source designs and the performed pulse-compressor studies. From this graph, it is clear that to reduce the total structure length by one-third (i.e., from 30 to 20 cm), it would mean doubling the required input power, making it unpractical to go to shorter structure lengths.

Finally, preliminary thermal analysis simulations have been done on the single-cell geometry to understand the thermal losses. An interesting outcome of the simulations is that, since the iris is the highest temperature point, and because this design has a large aperture, the thermal path between the tip of the iris and the cavity body remains relatively short and wide, making the heat transfer to the copper, and eventually the cooling channels, easy and quick. Therefore, using 10 mm diameter for the cooling channels and water at 27 deg C at peak gradient (42.5 MV/m), the increment is only 1 deg on the iris at the CW steady state (see Fig. 89). For all these reasons,

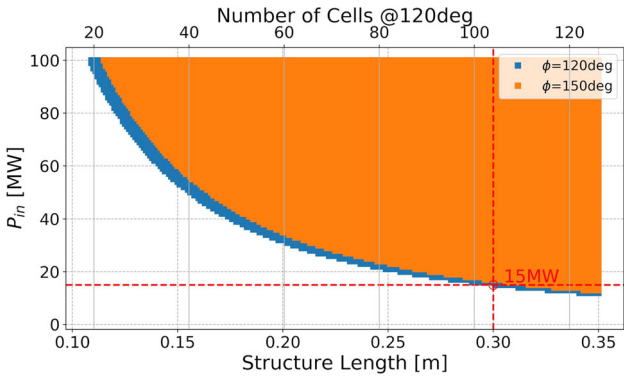

Fig. 88 Power requirement as a function of structure length at 36 GHz to provide 12.75 MV integrated voltage for $2\pi/3$ and $5\pi/6$ phase advance options

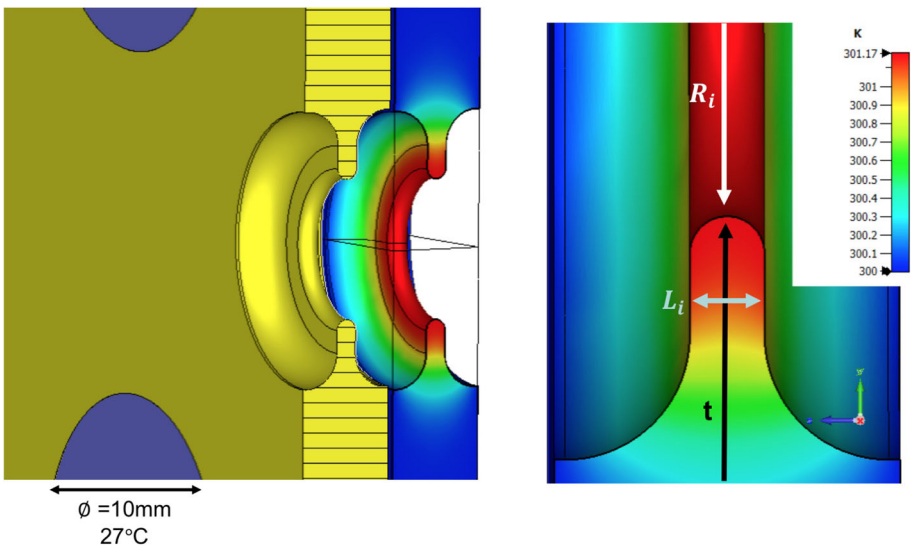

Fig. 89 Setup on CST® (left) and results of the steady-state thermal simulations at peak gradient (right)

the cooling should not present a considerable challenge for the operation of this structure.

Couplers

A double feed mode launcher was designed for the Ka-band TWS. Figure 90 shows both the mode launcher topology (top) and the S-parameters for a 10 cm-long structure (bottom), as an illustration of its performance. Inductive notches are included in the mode launcher's rectangular waveguides. These notches, along with a matching cell after the mode launcher's circular waveguide, are used to tune the coupling and eliminate any residual standing wave due to internal reflections in the structure.

A mode converter option was designed in an effort to simplify a low-loss transport network. Such a converter couples to a TE20 mode coming directly from a low-loss waveguide, and feeds symmetrically a TE01 circular mode to the structure's mode launcher (see Fig. 91). This mode converter requires the feeding paths to the mode launcher to be asymmetrical, which allows for the correct power flow into the structure. Inductive notches are introduced at the side of the splitting bifurcation to control and reduce any standing wave trapped in this section. There is, however, a residual standing wave that stays present in such a TE20-to-TE01 mode launcher. Nevertheless, this

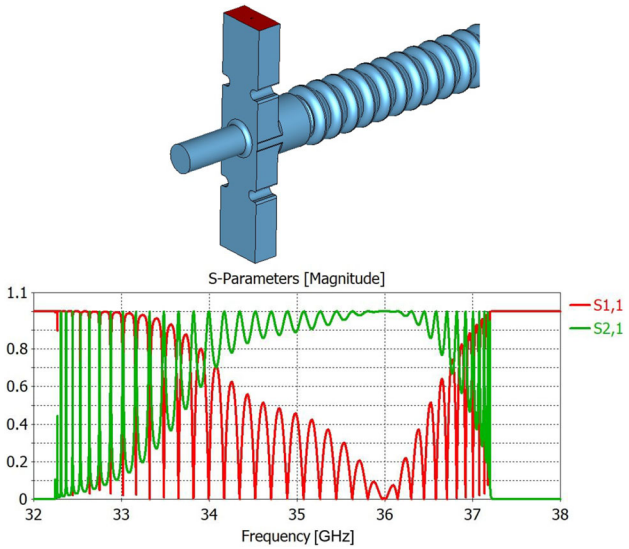

Fig. 90 Mode launcher geometry (top) and S-parameters for a 10 cm-long structure (bottom)

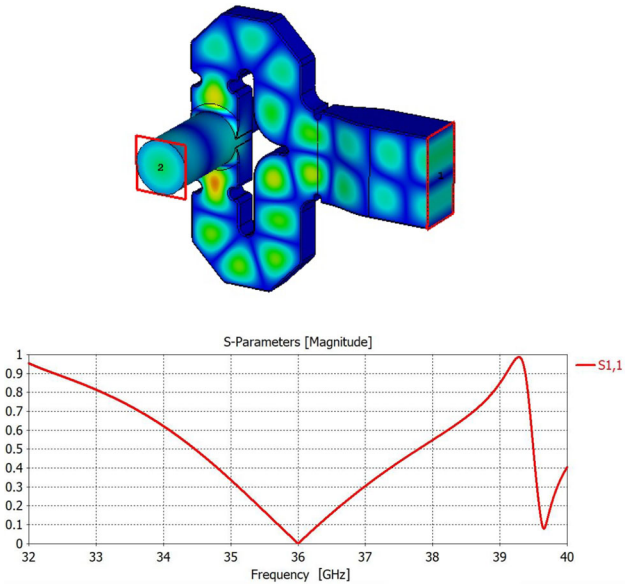

Fig. 91 TE20 to TE01 mode converter (top) and its matched S_{11} parameters (bottom)

Table 27 Ka-band traveling wave structure parameters at nominal voltage

Parameter	Value	Units
Active length l	300	mm
Phase advance ϕ	$2\pi/3$	rad
Number of cells	108	–
Filling time τ	8.4	ns
Frequency f	36	GHz
Compressed power P	15	MW
Design gradient E_{acc}	42.5	MV/m
Peak surface field E_p	109.2	MV/m
Peak surface field B_p	189.1	mT
Modified Poynting vector S_c	4.84	W/μm^2

has been reduced to a practical level and can be further optimized. Figure 91 (bottom) shows the linear magnitude of the mode converter's S_{11} parameter. It is centred at 36 GHz and its broad bandwidth makes it a suitable coupler for the TWS.

Full structure

Following the comparison presented in Table 26, we propose a $2\pi/3$, 30 cm long (108 cells), constant impedance TWS as the lineariser baseline. This structure can reach the required 12.75 MV of integrated voltage, for a feasible input power of 15 MW after compression (see Fig. 88). Table 27 shows the operational parameters of the baseline structure at the required integrated voltage for the bunch linearisation.

The peak fields of $E_p \approx 109$ MV/m, $B_p \approx 189$ mT, and $S_c \approx 5$ W/μm^2 at a nominal gradient, are all within the practical limits of operation. A 108 cell structure is deemed feasible from the manufacturing viewpoint, and a filling time of 8.4 ns allows for good performance of the pulse-compressor, see Figs. 85 and 86.

Table 28 shows a comparison of the power dissipation of the Ka-band linearizer to two X-band examples. The power dissipation at the Ka-band (2.5 kW/m) is comparable to that of the CompactLight main linac (2.4 kW/m), when both are operating at 1 kHz repetition rate. This makes the Ka-band TWS a consistent option, in terms of its power dissipation, for this application.

To benchmark the wakefield effects discussed in Sect. 5.2.8, long-range and short-range wakefield simulations have been done for a 10 cm-long structure with couplers. Figure 92 shows the magnitude of the longitudinal wake fields for a single, 75 nC, 300 μm electron bunch, up to 216 GHz. A more advanced analysis of this work will include the calculated wakefields on the beam dynamics studies for proper benchmarking of the codes used and their results. The long-range transverse wakefield of a 30 cm long structure was simulated by GdfidL [155]. The

Table 28 Comparison of average dissipated power

Structure	Rep. rate [Hz]	Ave. dissipated power [kW/m]
CLIC	50	3.06
CompactLight main linac	1000	2.44
Ka-band 300 mm TWS	1000	2.47

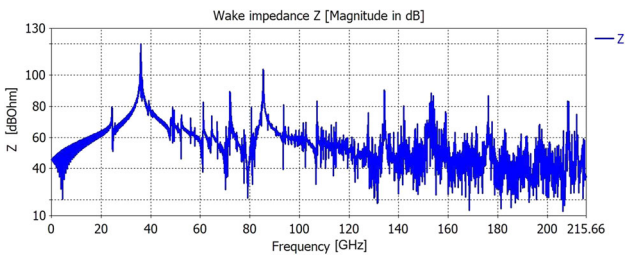

Fig. 92 Magnitude of the longitudinal wakefields on a 10 cm TWS for a single XLS nominal electron bunch

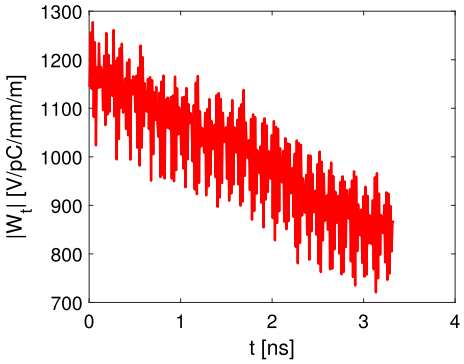

Fig. 93 Magnitude of the long-range transverse wakefield on a 30 cm TWS for a single XLS nominal electron bunch

transverse wake potential for a 300 μm electron bunch is shown in Fig. 93. Further studies are required to include long-range wake fields and gain trust in the codes employed for the beam dynamics calculations.

5.2.8.4 Alternatives

Standing-wave linearizing structure

Using a standing-wave structure would initially appear to be more efficient as there is no power flow out of the structure. However, there are two issues. The first issue is that there are no Ka-band 3 MW circulators; hence, the structures would need to be split and fed through hybrid couplers to cancel out the reflections in pairs by choosing the correct phase delay between each structure. Several structures are also required as there is a limit to the number of cells that can be used in a standing-wave structure and the Ka-band cells are very short. The second issue is the longer filling time of the structure leads to significantly longer SLEDII pulse-compressor delay lines. This second issue can be avoided by partly filling the structure, but in doing so, the performance of the standing-wave structure becomes comparable to the traveling-wave structure.

A standing-wave structure option is retained as an alternative structure due to its lower average power requirement. The traveling-wave structure requires around 16 MW of input power to the structure, which needs a 1-microsecond pulse from the klystron/gyroklystron, resulting in an average power dissipated per unit length along the structure of 2.5 kW/m at a 1 kHz repetition frequency which is similar to the main linac. Initial studies of structure heating suggest that the maximum allowable heat load per unit length is independent of the cavity frequency however further studies are required to confirm this. In the event that the smaller K-band structures cannot handle the same power per unit length as the main linac, then we would require an option with a lower heat load.

The standing-wave structure design is based on four 19-cell standing-wave structures. An aperture of 2 mm is chosen which is the same as that in the traveling-wave option. Cell geometry is shown in Fig. 94 and the general parameters are presented in Table 29.

A length of 2.08 m is chosen for the dual-moded SLEDII pulse-compressor delay line to increase the input power to the standing-wave structures. This length is comparable with that for the traveling-wave option and will give a flat top width of 30 ns. The standing-wave structure could be partially filled to 68% of the steady state voltage with the compressed pulse. Each structure would require a peak input power of 2.70 MW to achieve a total integrated voltage of 12.43 MV, requiring only a 240 ns pulse from the amplifier. This results in a much lower heating per

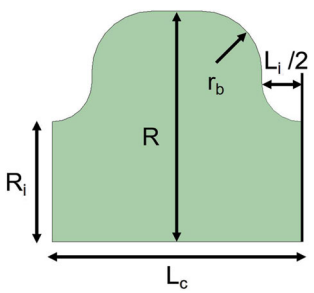

Fig. 94 Geometry of the standing-wave structure cell

Table 29 SWS single cell parameters

Parameter	Value	Units
Frequency f	36	GHz
Q factor	5941	–
Shunt impedance r_L	97	MΩ/m
Peak surface field E_p^{a}	2.67	MV/m
Filling time $T_{\mathrm{fill}}^{\mathrm{b}}$	121	ns
Cavity radius R	3.86	mm
Iris radius R_i	2.00	mm
Cell length L_c	4.16	mm
Iris thickness L_i	0.667	mm
Cavity blending radius r_b	1.00	mm

[a]Normalized to $E_z = 1\,\mathrm{MV/m}$

[b]Time to fill 99% of the the steady state electrical field

unit length of 1.6 kW/m. However, three hybrid couplers are needed to cancel out the reflection which makes the whole setup complicated.

Ka-band cryo-cooled structures

The amplifier development is a complex project and there is a risk that it is not successful and results in a much lower saturated output power in practice. If that occurs a more efficient structure would be required. One option would be to make a longer structure, however, this would use more cells, and using multiple amplifiers would increase the cost significantly. Another option is to use a cryogenic-cooled copper standing-wave cavity. A 10 cm-long structure, operating at 77 K, would have an estimated shunt impedance of 349 $M\Omega/m$, so two 10 cm structures could be utilized with a hybrid to cancel reflections to protect the amplifier. These structures could alternatively be used to reduce the length of the lineariser by increasing the gradient; however, there seems to be little need to reduce the length at present. It would require significant additional development to design a cryostat and prototype, and hence, this is reserved as a future option rather than an alternative. It should be noted, however, that this technology can potentially deliver very high gradients and hence could be a future route to high-gradient accelerators.

The use of cryogenic structures to both diminish the RF dissipation and mitigate breakdown is by now well established, particularly through testing of X-band and S-band devices. In these experiments, the scaling of RF dissipation according to the theory of the anomalous skin effect (ASE) [156] has been verified, and surface fields over 500 MV/m have been achieved before breakdown is observed [157]. The advantage in dissipation effects diminishes somewhat at high frequency but is still notable up to Ka-band. This component is critically important for applications such as the MaRIE XFEL [158], the CompactLight FEL, and the Ultra-Compact XFEL at UCLA [159]. Paired with the CompactLight sponsored initiative to develop a preliminary design of a 15 MW-class klystron at 36 GHz, a compact, high gradient cryogenic linearizer in this frequency range now seems within reach [160].

This section reviews the scaling laws that allow approximate prediction of the performance of such a linearizer, based on a derated 5 MW input. To orient the expected performance, it is noted that the shunt impedance calculated for an optimized 36 GHz structure at room temperature is 158 MΩ/m. The expected behavior of this shunt impedance can be scaled from detailed calculations of ASE enhancement at low temperatures in S-band by a factor of 5. To extend this to Ka-band, it is noted that the ohmic model scaling of surface resistivity is $R_{s,\Omega} \propto \omega^{1/2}$, while for ASE, the scaling in the low-temperature limit is $R_{s,\,\mathrm{ASE}} \propto \omega^{2/3}$. This means that the expected enhancement in the quality factor has a scaling $Q_{\mathrm{enh}} \propto \omega^{-1/6}$, and for low temperature (below 40 K), one may expect in Ka-band $Q_{\mathrm{enh}} \simeq 3.3$. For less ambitious cooling designs, operating with liquid nitrogen at 77 K, an enhancement of 2.2 may be foreseen.

To give an idea of what is possible with this approach, the assumption is made, as stated above, of a 5 MW matched input into a 10 cm long structure, operating at 77 K, with estimated shunt impedance of 349 $M\Omega/m$. In this case, the accelerating field is 130 MV/m, which is well below the breakdown limit of 250 MV/m. The corresponding surface field of 260 MV/m is also below the threshold of dark-current emission of $\sim$ 300 MV/m that is strong enough to beam load the structure [161]. Further, at this frequency, the normalized vector potential is a factor of three below that needed to capture and accelerate dark current, further mitigating potential issues with spurious field emission effects.

Table 30 RF parameters' list of the SW Ka-band structure

Parameter	Unit	Value
Frequency	GHz	35.982
Operating mode		π
Input power	MW	8
E_p/E_a		1.55
H_p/E_a	mT/MV/m	2.68
Effective accelerating electric field	MV/m	125
Shunt impedance	MΩ/m	188
Unloaded quality factor, Q		5628
Build-up (coupling beta = 1)	ns	12.5
RF pulse-length flat top	ns	50
Repetition rate	kHz	1
Average RF power per meter	KW/m	4.2
Structure length	cm	8
Iris radius a/λ ratio		0.12
Coupling coefficient, K	%	0.83
Iris thickness	mm	0.667
Ellipse semi-axes iris ratio shape		5/7
Cavity radius	mm	3.628

For a cryogenic structure with a/λ = 0.12 (or a = 1 mm radius) and $r_1 = r_2 = 5/7$ ellipse semi-axes ratio and assuming an input power of 8 MW, with only one cryogenic structure, it is possible to achieve an integrated voltage of about 15 MV. It should be noted that this structure's iris radius does not meet the CompactLight beam dynamics specification; hence, further work would be required to redesign the cavity to meet the requirements should a cryo-cooled option be utilized.

High gradient Ka-band structures

There is a strong demand for accelerating structures able to achieve higher gradients and more compact dimensions for the next generation of linear accelerators for research, and industrial and medical applications. In the framework of the CompactLight project, an ultra-high gradient higher harmonic RF accelerating structure was also developed. The aperture chosen for this design is smaller than the minimum value dictated by beam dynamics requirements for CompactLight, so it is not considered for the lineariser, but may have applications in other X-band FEL projects with less stringent impedance requirements. To minimize the input power requirements for a given accelerating gradient, the RF accelerating structures have to be designed with the aim of maximizing the shunt impedance.

Presented here is a discussion of the electromagnetic design of an ultra-compact Ka-band standing-wave (SW) linearizer, 8 cm long, working on π mode. It has an ultra-high accelerating gradient (beyond 100 MV/m) and minimum surface electric field for minimizing the probability of RF breakdown without affecting the beam dynamics quality [160, 162, 163]. It is assumed the beam energy is about 300 MeV, a bunch charge of 75 pC, and an emittance of $\epsilon = 0.18$ μm rad. As a result, from a compromise among the beam dimensions and the RF parameters, to minimize the peak surface electric field and to get a satisfactory surface magnetic field for the optimum design [160], the geometry chosen has an iris radius $a/\lambda = 0.12$ (or $a = 1$ mm radius), a cavity radius $b = 3.628$ mm and $r_1/r_2 = 5/7$ ellipse semi-axes ratio for the optimum design [160]. While this iris radius does not meet the CompactLight beam dynamics specification, it may well be suitable for other future projects. The main RF properties of the structure are summarized in Table 30.

A practical tolerable limit on the higher gradient operation came out recently from experimental activity [79, 164, 165] by estimating the modified Poynting vector (MPV) and pulse heating (PH) effects. The breakdown rate (BDR) is a measure of the RF sparks per unit of time and length inside an accelerating structure. Estimations of the MPV by assuming an RF 50 ns flat top length pulse and HV in case of the cavity geometry are reported in Table 31.

In all cases, both the MPV and PH are well below the safety thresholds [164, 166, 167]. To achieve an integrated voltage of at least 15 MV, two separated normal conducting SW structures provide an integrated voltage of 20 MV. The average RF power per meter is 4.2 kW/m which, while double the other designs, is believed to be below the

Table 31 MPV and PH as function of the accelerating gradient

E_{acc} [MV/m]	EF [MV/m]	HF [MA/m]	MPV [MW/mm^2]	PH [°C]
100	155	0.2205	1.88	8
132	204	0.2911	3.27	14
150	232	0.3308	4.23	18

EF surface electric fields, *HF* surface magnetic field

safety threshold, although further simulations are required to confirm this. The RF power source can be provided by an RF amplifier plus a SLED system [168]. Assuming a compression of 4, it is possible to achieve 12 MW. A hybrid device should give no problem for the power reflection to the power source.

5.3 Beam dynamics

The user requirements for CompactLight were established by interacting with the existing and potential FEL users in various channels, and the required parameters are given in Sect. 3.2. Key requests from the user community, which affect the facility layout significantly, are:

- Wide range of photon energy (0.25–16 keV).
- Repetition rate 100 Hz and up to 1 kHz for the soft X-ray option.
- Simultaneous HXR/SXR operation at 100 Hz.
- Pulse duration 1–50 fs.

The facility is proposed in three stages as a baseline layout and two upgrade scenarios to satisfy various user requirements. Figures 8, 9, and 10 show the schematic layout of the machine for different upgrade and operation modes. The target photon parameters of CompactLight are given in Table 1, and the corresponding electron beam repetition rate and energies for various operation modes are given in Table 2. To achieve the requested photon beam parameters, the electron beam must have parameters as given in Table 32.

As can be seen in Table 32, the electron beam energy tuning range is large (i.e. 5.5– 0.95 GeV), the implications of which must be considered for the linacs operating at X-band frequency. Operation at different repetition rates brings another challenge to the facility design: multi-bunch operation and adjustment of the bunch spacing. To avoid over-complex operation, the beam parameters at various locations have been fixed by tuning different sections of the facility at different settings for different operating modes. Figure 95 shows the beam energies at different

Table 32 Main parameters of the CompactLight FEL

Parameter	Unit	Hard X-ray	Soft X-ray
Beam energy	GeV	5.5–2.75	2.35–0.95
Photon energy range	keV	16.0–2.0	2.0–0.25
Peak current (minimum)	kA	5.0–1.5	0.92–0.35
RMS sliced emittance	mm mrad	0.2	
RMS sliced energy spread	keV	550	
Bunch charge	pC	75	

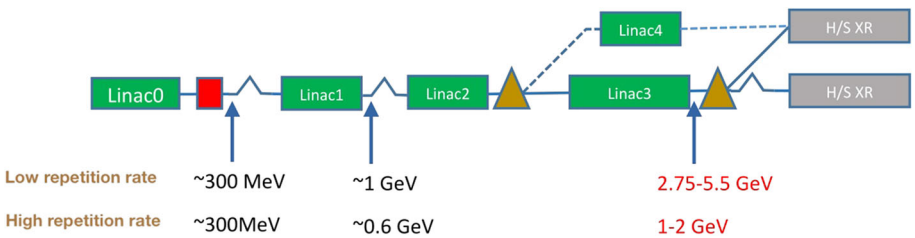

Fig. 95 Electron beam energy for various operation modes of the facility for different operation frequencies

locations along the beamline.

To determine the performance of the machine for all operating modes, it is sufficient to simulate the following operating modes.

1. Soft-X-ray 100–250–1000 Hz 0.97 GeV targeting shortest bunch length for SXR (nominal + bba + jitter coh & inc).
2. Hard-X-ray 100 Hz 5.5 GeV targeting shortest bunch length (nominal + bba + jitter coh & inc).
3. Hard-X-ray 100 Hz 2.75 GeV targeting shortest bunch length (only nominal performance).
4. HXR/SXR Linac 4 (only nominal performance).

This section of the report summarizes the integrated performance studies of the facility using the simulation tools discussed in [169]. Start-to-end (S2E) simulations have been performed from the cathode to the end of the undulator, including space-charge effects, coherent synchrotron radiation in magnetic compressors, wakefield effects in the X-band linac, and FEL performance. The injector optimization is reported in Sect. 5.3.1, while the lattice optimization and beam transport along the main accelerating sections is given in Sect. 5.3.2. The beam dynamics simulations also include the study of key tolerances and mitigation strategies to deal with imperfections. The beam distribution obtained by the linac optimization has been imported into FEL simulations, and the expected FEL performance is reported in Sect. 4.2.

5.3.1 Beam dynamics in injector

The proposed final injector design consists of a C-band RF gun and C-band accelerating structures operating for both the operational modes, high (1 kHz) and low (100 Hz) repetition rate, which implies operating the whole injector at the same accelerating gradient while keeping the beam quality within the requirements. The final layout (see Fig. 31) includes a 2.6 cell C-Band RF Gun (see Sect. 5.1.1) followed by C-Band Booster structures (see Sect. 5.1.2.1) for acceleration up to 120 MeV. This configuration meets the design goals of the CompactLight injector of Table 5

The reference working point for the CompactLight injector is a 75 pC electron bunch that reaches the laser heater entrance with $< 0.15\,\mu$mrad transverse normalized emittance and $\sim$ 100 MeV energy. For this reason, the photoinjector is operated on-crest, nearly according to the invariant envelope criteria [170], imposing at the entrance of the first C-band structure a laminar envelope ($\sigma'_{x,y} = 0$) with the beam spot size $\sigma_{x,y}$ matched to the accelerating structures. The generation of the electron beam has been studied in detail by means of beam dynamics simulations. The layout reported in deliverable D3.4 was used (up to the laser heater) in simulations using the multi-particle codes Astra [171] and GPT [172], which take into account the space-charge effects relevant at very low energies and the beam features defined by the emission from the cathode. It was found that the bunch length at the entrance to the laser heater has to be $\sim$ 300 µm to achieve a final peak current of up to 1 kA at the end of BC1. It was assumed that the copper cathode is excited by a laser pulse with a flat-top longitudinal profile of 4 ps RMS duration with 0.5 ps rise/fall time. The transverse spot size is a uniform distribution of $\sigma_{x,y} = 180$ µm. With these laser parameters and a peak field at the copper cathode of 160 MV/m, the transverse intrinsic emittance is of the order of 0.1 mm.mrad.

To perform precise simulations, particularly to understand CSR effects in dispersive sections, 1 million macro-particles were considered a good compromise between reliability and computational time. The position of the first C-band structure, the strength of the solenoids to match the beam to the first structure, and the phase of the RF structures were optimized to obtain the minimum slice and projected emittances. The simulated projected emittance is ε =0.13 mmmrad and the bunch length is $\sigma_z \approx 1$ ps. Figure 96 shows the energy gain, bunch length variation, normalized horizontal emittance, and transverse beam size along the beamline after optimization.

Figure 97 represents the bunch's horizontal, longitudinal, and beam parameters at the exit of the first C-band section of the injector. The structures are operated on crest to minimize relative energy spread.

5.3.2 Beam dynamics in main Linac

The CompactLight FEL will operate within a range of wavelengths from 0.08 to 5 nm, covered by two distinct undulator beamlines at electron beam energy between 5.5 and 0.95 GeV. Two operation modes have been developed: "short bunch length mode" to achieve 5 kA peak current for HXR production and "long bunch mode" to achieve 1.5 kA for SXR production. The main accelerator has to be designed with sufficient flexibility to accommodate these operational modes. The main linac must be able to operate at three repetition frequencies: 100 Hz, 250 Hz, and 1000 Hz, while providing an electron beam with constant peak current and a small slice energy spread. Since the RF photocathode gun produces 75 pC over a bunch length of 1 ps, the bunch must be compressed by a total factor of more than 100 before it enters the undulator. The acceleration and compression is achieved in the main linac sections, as shown in Fig. 8. The two bunch compressors (BCs) consist of symmetric magnetic chicanes.

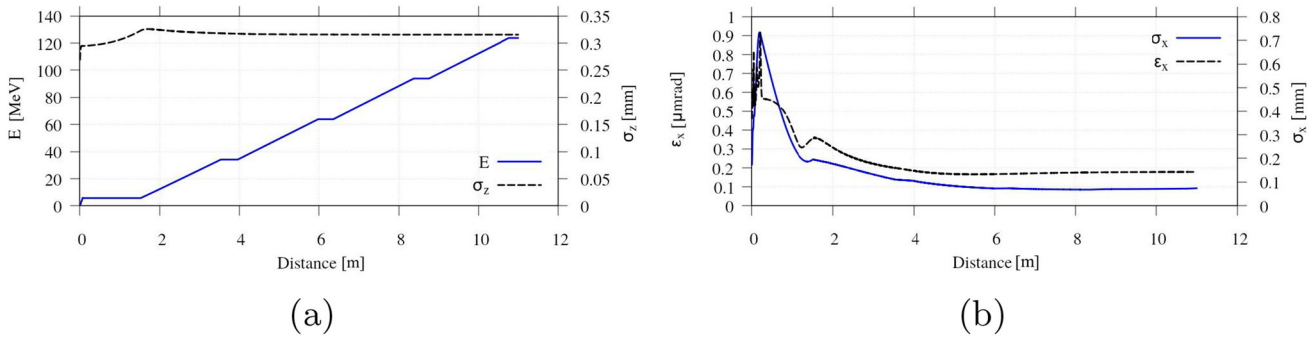

Fig. 96 Evolution of **a** the RMS bunch length and energy gain **b** the transverse normalized emittance and transverse spot size along the photo-cathode RF gun and first C-Band section of the injector

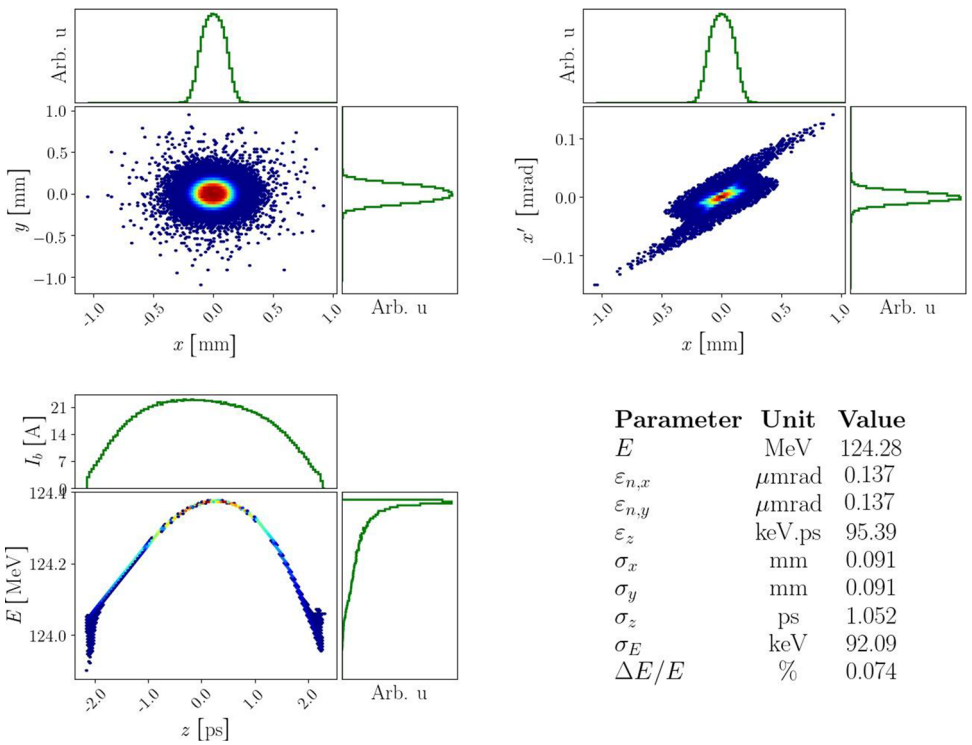

Parameter	Unit	Value
E	MeV	124.28
$\varepsilon_{n,x}$	μmrad	0.137
$\varepsilon_{n,y}$	μmrad	0.137
ε_z	keV.ps	95.39
σ_x	mm	0.091
σ_y	mm	0.091
σ_z	ps	1.052
σ_E	keV	92.09
$\Delta E/E$	%	0.074

Fig. 97 Transverse beam distribution (top left), and horizontal (top right) and longitudinal (bottom left) phase spaces with associated histograms representing the projection along the respective axis and beam parameters of the bunch at the exit of the first C-band section of the injector

The two chicanes' layout and compression factor have been optimized to minimize the 6D emittance dilution due to space-charge forces and wakefields in the linacs. The electron energy at the first chicane (BC1) was fixed to ~ 300 MeV to avoid space-charge effects while compressing the bunch to increase the peak current and reduce the effects of transverse wakefields in the downstream linacs. The energy of the second compressor (BC2) depends on the operation mode: ≈ 1 GeV when the machine operates at a low repetition rate, or ~ 600 MeV at a high repetition rate. Table 32 reports the beam parameters in HXR operation mode. Compressing the bunches at ~ 1 GeV balances the conflicting requirements of minimizing the transverse and the longitudinal emittance dilution due to coherent synchrotron radiation (CSR), the final energy requirement, and cancellation of the final correlated energy spread by means of the downstream longitudinal wakefield after BC2. The CSR effects can be reduced by using a weak chicane with a bending angle smaller than 5 degrees per dipole and a large initial correlated energy spread. Still, the chromatic aberrations make the tolerances on the magnetic field quality tighter.

A short Ka-band RF structure is used prior to the first compressor to linearize the longitudinal phase space, as discussed in Sect. 5.2.8.3. A laser heater is also foreseen at ~ 100 MeV just after the photoinjector to avoid the micro bunching instability, as described in Sect. 5.1.3. Dedicated diagnostic sections after the laser heater,

the BCs and beam delivery sections are also included in the beamline. Start-to-end simulations have been carried out to evaluate the linac's emittance growth due to transverse wakefields, CSR, and unwanted dispersion due to element misalignment. These simulations, which included realistic imperfections and correction techniques, successfully demonstrated that the required level of transverse emittance preservation is achievable. Jitter studies implemented in full start-to-end simulations have been performed and a tolerance budget of the linac stability has been defined according to the FEL specifications.

The beam delivery system ends with a transfer line between the end of the linac and the entrance of the FEL. This section includes the emittance diagnostic section, the electron beam switchyard for the two FELs, called the "spreader", and the matching sections. The design meets the constraints imposed by the existing and planned building boundaries, the desire to utilize existing equipment, and the demands for various diagnostic instruments. To cover all operation options either a single bunch per pulse, or a train of two bunches per pulse, have to be transported through the following sections of the facility:

Option-i HXR/HXR: Two bunches @ 100 Hz

a —1st bunch (E_f =2.75–5.5 GeV): LN0 $\mapsto$ BC1 $\mapsto$ LN1 $\mapsto$ BC2 $\mapsto$ LN2 $\mapsto$ LN3 $\mapsto$ SP1 $\mapsto$ FEL1.
b —2nd bunch (E_f =2.75–5.5 GeV): LN0 $\mapsto$ BC1 $\mapsto$ LN1 $\mapsto$ BC2 $\mapsto$ LN2 $\mapsto$ LN3 $\mapsto$ TC $\mapsto$ FEL2.

Option-ii SXR/SXR: Two bunches @ 250 Hz

a —1st bunch (E_f =0.95–2.4 GeV): LN0 $\mapsto$ BC1 $\mapsto$ LN1 $\mapsto$ BC2 $\mapsto$ LN2 $\mapsto$ LN3 $\mapsto$ SP1 $\mapsto$ FEL1.
b —2nd bunch (E_f =0.95–2.4 GeV): LN0 $\mapsto$ BC1 $\mapsto$ LN1 $\mapsto$ BC2 $\mapsto$ LN2 $\mapsto$ LN3 $\mapsto$ TC $\mapsto$ FEL2.

Option-iii HXR/SXR: Two bunches @ 100 Hz

a —1st bunch (E_f =0.95–2.4 GeV): LN0 $\mapsto$ BC1 $\mapsto$ LN1 $\mapsto$ BC2 $\mapsto$ LN2 $\mapsto$ SP2 $\mapsto$ LN4 $\mapsto$ FEL1.
b —2nd bunch (E_f =2.75–5.5 GeV): LN0 $\mapsto$ BC1 $\mapsto$ LN1 $\mapsto$ BC2 $\mapsto$ LN2 $\mapsto$ LN3 $\mapsto$ TC $\mapsto$ FEL2.

Here, LNi represents Linac-i $\{i = 0, 1..4\}$; BCi represents Bunch Compressor-i $\{i = 1, 2\}$; SPi represents Spreader Beamline-i $\{i = 1, 2\}$ for high and low energy, respectively; FELi represents Free Electron Laser Beamline-i $\{i = 1, 2\}$ and TC represents timing chicane (see Fig. 10). *Option-i* and *Option-ii* beamlines are valid for the Baseline, while *Option-iii* is possible after Upgrade-2. The target beam parameters for all these operation modes are summarized in Table 32.

This chapter describes the accelerator physics aspects and the choice of parameters that led to the design of the CompactLight accelerator. The accelerator covers the region from the exit of the first C-band section of the injector to the entrance of the first FEL undulator. The tracking results of the electron beam dynamics from the photocathode to the end of different beamlines are discussed in the following sections.

5.3.2.1 RF module configuration

When a beam enters the linac with an offset, for example, due to a transverse jitter or an alignment error, the head of the bunch experiences a normal betatron transverse oscillation. In contrast, the tail feels the kicks due to the rf structure wakefields excited by the bunch head. At the end of a linac of length L, the amplitude of such transverse deflections of the bunch tail due to all structures is proportional to

$$\Delta x_{\text{tail}} \propto \int_0^L \frac{\beta(s)}{E(s)} \Delta V_\perp(s) \mathrm{d}s, \tag{28}$$

where $\beta(s)$ is the beta function along the linac, $E(s)$ is the beam energy, and $\Delta V_\perp(s)$ is the transverse deflection due to transverse wakefield kick at location s [173]. For a particle at relative position z, one can write

$$\Delta V_{\perp,\parallel}(s, z) = Ne^2 \int_{-\infty}^{z} W_{\perp,\parallel}(s, z' - z)\lambda(z')\mathrm{d}z', \tag{29}$$

where N is number of particles per bunch and $\lambda(z)$ is the longitudinal charge distribution. $W_\perp(z)$ and $W_\parallel(z)$ are the RF structure single-particle transverse and longitudinal wake potentials, respectively [174]. In the evaluation of Eq. (29), $W_\perp(s)$ has been calculated using the analytic approximation of the wake potential presented in [141],

applied to a two-particle beam model such as

$$W_{\perp}(s) = \frac{4Z_0 c s_{\perp 0}}{\pi a^4}\left[1 - \left(1 + \sqrt{\frac{s}{s_{\perp 0}}}\right)\exp\left(-\sqrt{\frac{s}{s_{\perp 0}}}\right)\right],$$
$$W_{\parallel}(s) = \frac{4Z_0 c}{\pi a^2}\exp\left(-\sqrt{\frac{s}{s_{\parallel 0}}}\right),$$

where $Z_0 = 120\,\pi\Omega$ is the impedance of free space, a is the average aperture radius of the structure, g is the gap length, d is the length of the cell, $s_{\parallel 0} = 0.41 a^{0.18} g^{1.6}/d^{2.5}$ and $s_{\perp 0} = 1.69 a^{1.79} g^{0.38}/d^{1.17}$. Equation (28) implies that the amplification factor is proportional to the beta function along the beam line. Therefore, to enhance the beam stability, the betatron function of the lattice has to be small enough to minimize the effect introduced by wakefields. An FODO-type lattice was chosen, optimized in the number of structures per module, and calculating the transverse deflection, in normalized coordinates, for different type of charge distributions along the X-band structures of the linac.

Space-charge effects in the linacs have been deemed negligible, following the indications in [175], where it is stated that the transition energy, $\gamma_{\rm tr}$, between the space-charge dominated regime and the thermal regime, is approximated by the following equation:

$$\gamma_{\rm tr} = \frac{\hat{I}}{2I_A}\frac{\sigma^2}{\varepsilon_n^2}, \tag{30}$$

where $\hat{I}$ is the peak current, and I_A is the the Alfvén current ($\sim$ 17 kA). With an average β function of 5 m, a bunch length of about 300 μm, a bunch charge of 75 pC, and a normalized emittance of 0.2 μm, one obtains: $E_{\rm tr} = m_e\gamma_{\rm tr} \sim 120$ MeV. As it can be seen on Fig. 96b, the change in emittance due to space-charge is negligible by the end of the second structure. To further minimize the effect of space-charge forces in the injector, the beta functions were minimized ($\sim$ 5 m) up to the first BC, using 2 structures per FODO cell. The lattice is relaxed in the second stage of acceleration where the bunches have a length of $\sim 20\,\mu$m, with 2 structures between each pair of quadrupoles in Linac-1, Linac-2, and Linac-4. The beta functions in the last stage of acceleration can be even larger, since the bunch is quite short. Thus, we have chosen 4 X-band structures between each pair of quadrupoles in Linac-3. The Twiss functions and phase advances per FODO have been optimized by considering the following factors:

- Offsets of the structures (thus offset of the beam inside the structures) cause increasing wakefield effect (minimum deflection requires a strong lattice).
- Quadrupole misalignment causes transverse deflection of the beam and introduces dispersion, thus increasing the emittance growth. Various alignment techniques are used to align the beam (requiring a weak lattice and fewer quadrupoles).

5.3.2.2 Bunch compression scheme (from Booster 2 to BC2)

The overall CompactLight design parameters are motivated by the goal of 75 pC bunch charge, accelerated to 5.5 GeV and compressed to a peak current of about 5 kA. To maximize the FEL brightness, a flat top longitudinal current profile is required, so that the maximum number of electrons contributes to the FEL lasing and all longitudinal slices of the bunch reach FEL saturation at the same distance through the undulator. A two-stage bunch compression system is used to achieve this goal. Apart from the two magnetic chicanes, the whole bunch compression system comprises two linac sections (Linac-0 and Linac-1) to imprint the energy chirp on the beam and an X-band section to linearise the energy–time correlation along the bunch. After compression, the energy chirp is reduced by virtue of the longitudinal wakefields in Linacs 2 and 3.

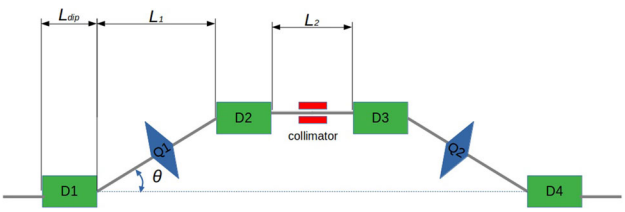

Fig. 98 A schematic of the bunch compressors

A 4-dipole chicane geometry has been selected for BC1 and BC2 to achieve the required bunch length at the entrance of the undulators. A schematic of the bunch compressor is shown in Fig. 98. The chosen geometry has been identified as the most compact and suitable. Because of its symmetry, this bunch compressor is a perfect achromat. Nevertheless, leakage of the dispersion function after the last bend may occur due to errors. For this reason, trim quadrupoles (shown in the figure between the first and second bends and the third and fourth bends) are added for fine-tuning the dispersion function. The electron bunch undergoes compression in the BCs according to the following equation:

$$\sigma_{z,f} = \sqrt{\left(\frac{\sigma_{z,i}}{C}\right)^2 + (R_{56}\sigma_{\delta,i})^2 + \left(3T_{566}{h_i}^2{\sigma_{z,i}}^2\right)^2}, \tag{31}$$

where $\sigma_{z,i}$ and $\sigma_{z,f}$ are initial and final RMS length of the electron bunch, R_{56} and T_{566} the first and second order chicane matrix elements, h the linear energy chirp of the electron bunch, and C the linear compression factor defined as

$$C = \frac{1}{|1 + hR_{56}|}. \tag{32}$$

An initial 2D optimization was performed using fast Track1D. This code was developed within the CompactLight collaboration [176] and described in D6.1. It follows a similar approach to LiTrack [177], without taking into account the CSR effects. However, one needs to consider CSR and indirect emittance excitation via longitudinal-to-transverse coupling as in

$$\varepsilon = \varepsilon_0\sqrt{1 + \frac{H}{\varepsilon_0}\sigma_{\delta,CSR}}, \tag{33}$$

where $\sigma_{\delta,CSR}$ is the energy spread due to CSR wake, $H = \left(\eta^2 + (\beta\eta' + \alpha\eta)^2\right)/\beta$ is the optics function for coupled betatron and dispersive motion, and β, α and η are the Twiss parameters [178].

To reduce the relative effect of CSR on emittance growth, Eq. 33 indicates that the BC lattices need to have small H. One can minimize H by choosing small bending angle (thus used large energy spread) and minimizing β-function considering beam divergence angle, in the latter half of the chicane. On the other hand, while the emittance excitation due to CSR requires small H, the micro-bunching instability might need larger H. To address both problems, an integrated optimization of both bunch compressors has been performed using ELEGANT [179] taking into account both CSR and space-charge.

The simulations in the injector booster have been described previously, in Sect. 5.3.1. The second part of the Linac-0, consisting of 6 C-band structures, generates the necessary longitudinal chirp, through off-crest operation, for the bunch compression. An harmonic linearizer operating at K-band frequency (see Sect. 5.2.8) is employed at the end of Linac-0 to control energy modulation of the bunch. Chirp adjustments between the compressor chicanes are carried out on the X-band structures of Linac-1. Linac-0, Linac-1, and the BCs are optimized simultaneously to have quasi-uniform charge distribution at the end of BC2. The transverse beam optics are controlled by quadrupoles downstream of each bunch compressor to minimize the effect of CSR. Parameters, such as RF gradient, RF phase, or bending angle, are only slightly different for different operating modes.

The electron bunch profiles (horizontal phase space, energy spread, current, and emittance) directly after the second bunch compressor BC2 are shown in Figs. 100 and 101 for low and high repetition modes, respectively. In the low repetition mode, the bunch is compressed from initially $\sigma_t = 1$ ps to $\sigma_t = 65$ fs after the first chicane, and to $\sigma_t = 5$ fs final bunch length, with a peak current of 5 kA at 75 pC. In the case of high repetition mode, since the Linac-0 (injector) has fixed operation parameters for both modes, the compression scheme is identical to up the BC1 and the bunch is compressed to the final bunch length of $\sigma_t = 18$ fs at BC2 with a peak current of 1.2 kA. Figure 99 shows the Twiss parameters through the first and second bunch compressors. Three quadrupole magnets are used to match the optics functions and optimize the H parameters for both compressors. The CSR effect on the slice emittance is mitigated by obtaining a waist in the horizontal beam size in the fourth dipole of the chicane. The optimization results for both BCs are reported in Table 33 for different operating modes. Peak currents of 5 kA and 1.2 kA are obtained for low and high repetition rate modes, respectively.

5.3.2.3 Linac-2 to Linac-4

The main bunch acceleration is driven by three X-band linacs (Fig. 8). The first of these (Linac-1) is located between the bunch compressors and has already been described in Sect. 5.3.2.2. Downstream of the second bunch compressor, Linac-2 defines the energy at the spreader through to Linac-4, with the extraction point to the simultaneous SXR/HXR operation. Final acceleration to the short-wavelength FEL line is achieved in Linac 3. A

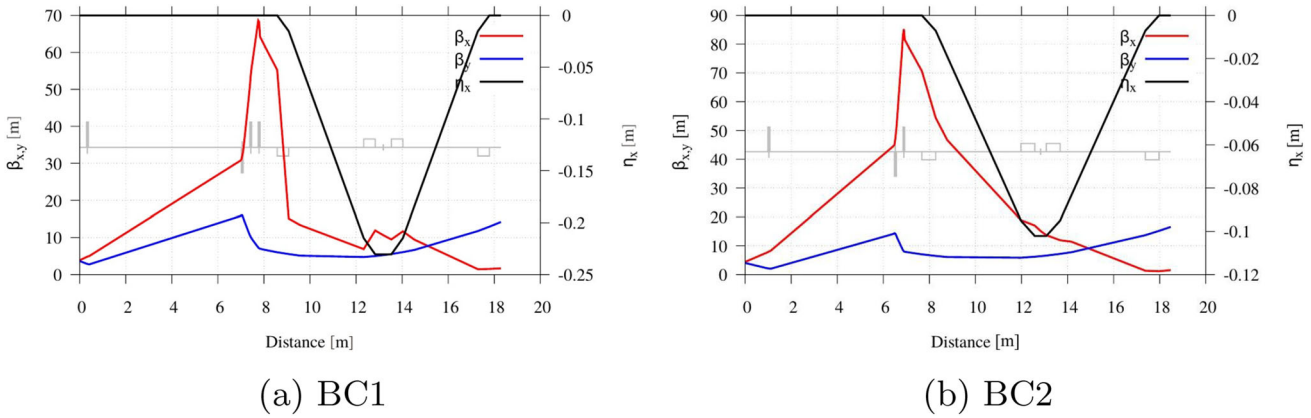

Fig. 99 Twiss functions along BC1 and BC2

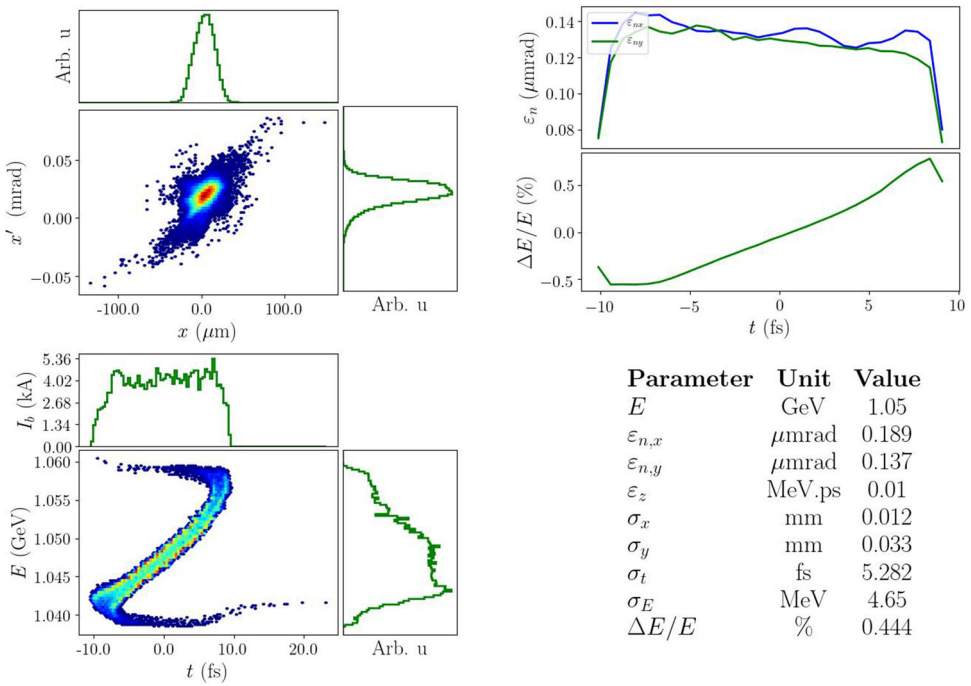

Parameter	Unit	Value
E	GeV	1.05
$\varepsilon_{n,x}$	μmrad	0.189
$\varepsilon_{n,y}$	μmrad	0.137
ε_z	MeV.ps	0.01
σ_x	mm	0.012
σ_y	mm	0.033
σ_t	fs	5.282
σ_E	MeV	4.65
$\Delta E/E$	%	0.444

Fig. 100 Horizontal (top left), and longitudinal (bottom left) phase spaces with associated histograms representing the projection along the respective axis and sliced emittance/energy spread and beam parameters of the bunch at the exit of BC2 for low repetition operation

simple FODO type of lattice is proposed which has the advantage of easy operation. The detailed configurations of the Linac FODO cells are given in Sects. 5.2.5.2 and 5.2.5.3. As discussed in Sect. 5.3.2.1, the Twiss functions are optimized along the linacs to minimize wakefield effects, considering the trade-off between sensitivity to quadrupole errors. The parameters of the main linac sections are summarized in Table 34.

Despite its technical challenges, an X-band linac does present some advantages for the beam dynamics in comparison to a C-band linac. At higher frequencies, a higher effective gradient is possible, allowing a shorter linac length. The lower iris diameter of X-band structures, compared to C-band, results in stronger wakefields. While wakefield effects on the transverse emittance are tolerable, the longitudinal component helps in the reduction of the energy chirp generated for the compressors, resulting in FEL bandwidth reduction.

The phases in Linac-1 are optimized for maximum compression and a flat top current profile with peak current above 5 kA. Linacs 2 and 3 phases are chosen to be on-crest for maximum acceleration. Note that the choice of the phases takes into account longitudinal wakefields. To reach 5.5 GeV, Linac-3 requires a large number of structures. The matching condition for the FODO lattice is 81° and 101° phase advance (which is not a strong condition) per cell for Linacs 1/2/4 and 3, respectively. It can be adjusted if needed, to ease the matching from or to other sections. Diagnostic sections after BC1 and Linac-2 have been foreseen to diagnose the longitudinal profile of the

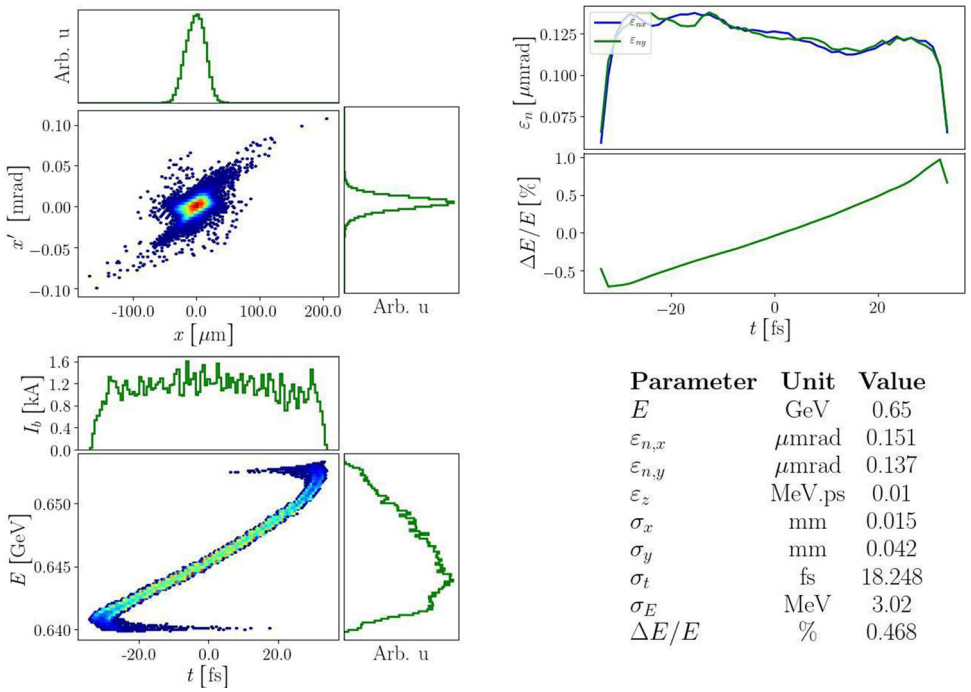

Parameter	Unit	Value
E	GeV	0.65
$\varepsilon_{n,x}$	μmrad	0.151
$\varepsilon_{n,y}$	μmrad	0.137
ε_z	MeV.ps	0.01
σ_x	mm	0.015
σ_y	mm	0.042
σ_t	fs	18.248
σ_E	MeV	3.02
$\Delta E/E$	%	0.468

Fig. 101 Horizontal (top left), and longitudinal (bottom left) phase spaces with associated histograms representing the projection along the respective axis and sliced emittance/energy spread and beam parameters of the bunch at the exit of BC2 for high repetition operation

Table 33 Chicane parameter table for low and high repetition mode operation

Parameter	Units	Low rep-rate		High rep-rate	
		BC1	BC2	BC1	BC2
Beam energy	GeV	0.28	1.1	0.28	0.68
Initial rms bunch length	μm	315	26	315	26
Final rms bunch length	μm	18	1.5	18.6	5.56
RMS relative energy spread	%	1.09	0.41	1.08	0.44
Bending angle	deg	3.83	1.375	3.83	1.25
Dipole length (L_{dip})	m	0.4	0.6	0.4	0.6
Outer drift length (L_1)	m	3.25	3.7	3.25	3.7
R_{56}	mm	−31.58	−4.72	−31.58	−3.9
T_{566}	mm	47.58	7.09	47.58	5.86

Table 34 Parameters of the main linac sections

Parameter	Unit	Linac-1	Linac-2	Linac-3	Linac-4
Cell layout		FODO			
Cell length	m	4.91	4.91	9.23	4.91
Phase advance	deg	81	81	101	81
Cavities per half cell		2	2	4	2
Number of cells		4	2	17	2
Cavity frequency	GHz	X-band (12 GHz)			
Max cavity gradient @high rep.	MV/m	30			
Max cavity gradient @low rep.	MV/m	65			
Quadrupole length	cm	16.5 (8 cm effective)			

bunch before it is transported to Linac-4 and Linac-3 (see Sect. 5.2.4). Profile monitors are foreseen per linac cell to measure the optical functions. The orbit response function completes the measurement using the BPMs inside the quadrupole chamber (see Sect. 5.4).

During the transport from BC2 to the FEL-2 undulator beamline, the Linac-2 and Linac-3 wakefields shape the current profile for optimum FEL lasing. The final longitudinal bunch current profile before the FEL2 beamline, for the shortest wavelength operation, has a quasi-flat top profile together with a small slice emittance.

The beam optics design comprises FODO channels in each linac section through to the undulators, and a diagnostic line downstream of BC1. Four quadrupoles between these sections enable beam matching during the transition to another section and to special elements such as the chicanes or the spreader beamlines. The overall beam optics through to the FEL-2 beamline are shown in Fig. 103.

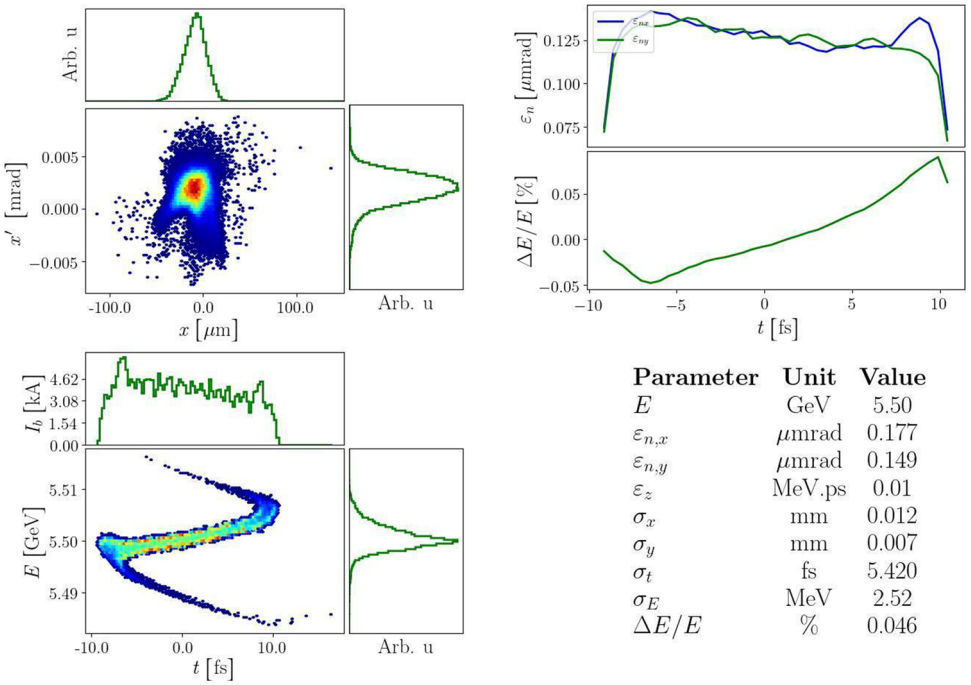

Parameter	Unit	Value
E	GeV	5.50
$\varepsilon_{n,x}$	μmrad	0.177
$\varepsilon_{n,y}$	μmrad	0.149
ε_z	MeV.ps	0.01
σ_x	mm	0.012
σ_y	mm	0.007
σ_t	fs	5.420
σ_E	MeV	2.52
$\Delta E/E$	%	0.046

Fig. 102 Horizontal (top left) and longitudinal (bottom left) phase spaces with associated histograms representing the projection along the respective axis and sliced emittance/energy spread and beam parameters of the bunch at the entrance of FEL2 undulator beamline for low repetition operation

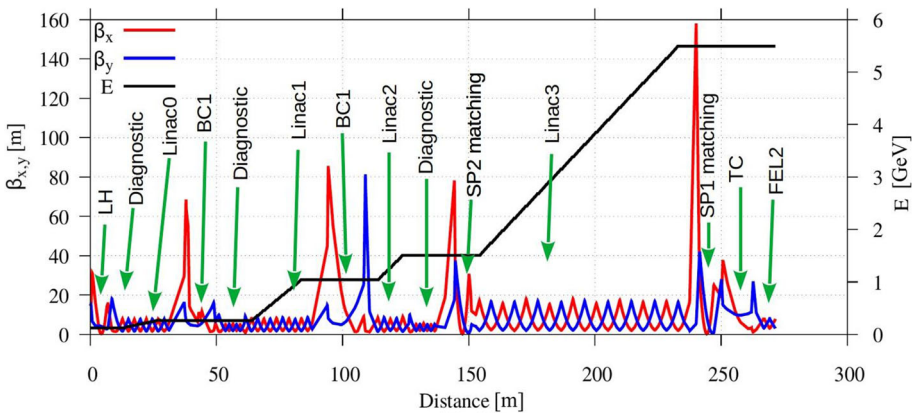

Fig. 103 Start-to-end beta functions and energy gain of the bunch through to the FEL-2 beamline

5.3.2.4 Spreader beamlines

The low energy spreader for CompactLight diverts the the first bunch coming from Linac-2 to Linac-4 for SXR/HXR operation, while the high energy one is used to deliver the first bunch to FEL1 beamline for SXR/SXR or HXR/HXR. At the entrance of both spreaders is a TDC operating at S-band frequency (see Sects. 5.2.7 and 4.1.3.5) followed by a septum magnet. For the former case, the nominal bunch length is desirable; however, for the latter case, the beam goes through a series of dispersive sections and CSR effects spoil the beam quality, so a slightly longer bunch is preferable. In view of these requirements, and to allow some flexibility for this beamline, it is possible to set up the spreaders for a range of values of R_{56}.

The electron bunches are longitudinally compressed below 5 fs (rms) and the peak current reaches about 5 kA. When such high peak current bunches pass through the dogleg, electron beam orbit instability and projected emittance growth in the deflecting plane can occur. The use of two sets of Double-Bend Achromat (DBA) structures is the simplest solution to cancel out the CSR effects of the dogleg [180]. If one adjusts the betatron phase advance between adjacent dipoles to an odd multiple of π in the deflecting plane, the sum of the CSR dispersion becomes zero at the end of the dogleg. Since the betatron phase advance between the two dipoles of the DBA is naturally π, only the phase advance between the two DBA structures is adjusted close to π. To control the bunch length along the spreaders, quadrupoles are tuned for adjusting R_{56}. The design is similar to that in [181]. The total length is approximately 20 m and the separation between the FEL-1 and FEL-2 beamlines is 2.5 m, with a net bending angle equal to zero, making the two beamlines parallel to each other as shown schematically in Fig. 104 for first and second spreaders.

To evaluate emittances and beam size changes throughout the spreaders, simulations have been done with an electron distribution at the entrance of the septum magnet. The initial beam conditions are shown in Table 35.

Another consideration for the spreader design is the synchronization of dual bunch operation, as discussed in Sect. 6.2.1.3. The twin bunches will follow identical dynamics in the accelerator before being separated by the S-band TDC. By virtue of the odd number of C-band cycles in the injector, the twin bunches will be horizontally deflected by kicks with opposite signs at the deflector. About 30 MV peak deflecting voltage at the maximum beam energy of 5.5 GeV will impose angular kicks of the order of half a degree, and will allow the two bunches to be separated by $\sim$ 5 mm after a 0.5 m-long drift section. At this position, a DC out-of-vacuum thin septum magnet will direct the leading bunch to FEL-1, and the trailing bunch to FEL-2. The same scheme is proposed for the low-energy spreader to transport the first and second bunch through Linac-4 and Linac-3, respectively.

The leading bunch directed to FEL-1 (or Linac-4) has to be delayed by 526 ps w.r.t. the trailing bunch. Note that this value is not the same at the timing separation of the twin bunches as they enter the spreader which is

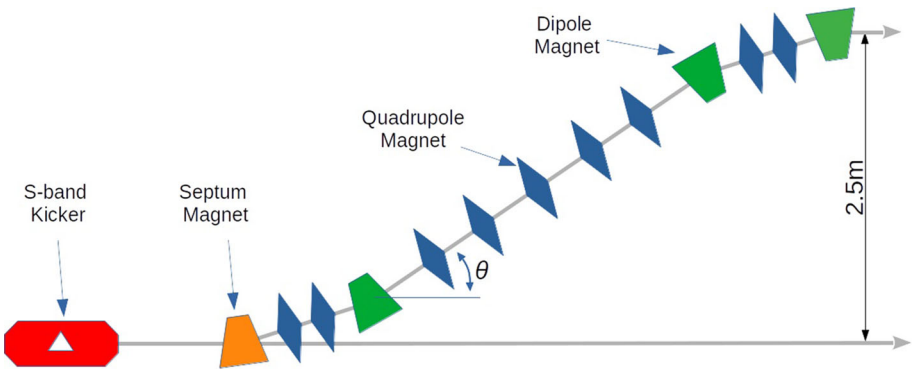

Fig. 104 Schematic layout of the spreader which is composed two DBA with opposite bending angle

Table 35 Beam parameters at the entrance of low- and high-energy spreaders

Parameter	Units	Low energy spreader	High energy spreader
Beam energy	GeV	1.5	5.5
Rms bunch length	μm	1.5	1.5
RMS relative energy spread	%	0.25	0.02
RMS relative energy spread	%	0.25	0.02
Horizontal beta function	m	0.33953	1.1547
Horizontal alpha function		0.8569	1.6341
RMS horizontal emittance	mm mrad	0.178	0.181

either 3 or 5 cycles of X-band (500ps 0r 833ps). However, this 526 ps delay, in combination with the path length delays in the optical beamlines, allows all permutations of HXR and SXR FEL pulses to be combined in one user station for pump-probe experiments. The 526p̃s delay is accomplished by means of a dog-leg-like switchyard from the septum to FEL-1. This has to satisfy a minimum longitudinal occupancy of 20 m, for a lateral separation of the undulator lines by ~ 2.5 m. On the other hand, to minimize the impact of CSR on the beam emittance, parasitic energy dispersion, and energy distribution, the bending angle needs to be smaller than 5 degrees at the minimum beam energy of 0.95 GeV. From the schematic given with Fig. 193, and as described earlier, the optical delay partly compensates for the electron delay in the spreaders. The required time delay on the spreaders can be simply computed by

$$\Delta t_{\mathrm{DL}} - \Delta t_{\mathrm{opt}} = nT, \tag{34}$$

where Δt_{DL} is the time delay in dogleg, Δt_{opt} is the time delay in optical beamlines, and $T = 166$ ps is the period of the C-band frequency.

The bunches meeting the same beam dynamics conditions through the accelerator will have identical bunch lengths when they leave BC-2. Therefore, the most challenging beam transport for both spreaders, due to strong CSR, is the 5 kA case which is required for SXR/HXR with HXR in the range of 8–16 keV (i.e., $E_{LN4} = 0.95$ GeV $E_{LN3} = 5.5$ GeV; see Table 32). For this case, as it can be seen in Table 35, the projected energy spread at the entrance of the low energy spreader is too large due to less wakefield compensation in Linac-2. Defining the derivative of the dispersion function in the middle of the bending magnet as D', the kick to the electron trajectory at the end of the bending magnet is

$$\Delta x' = D' \delta E, \tag{35}$$

where δE is the energy spread of the bunch which can be the initial energy spread or the energy spread introduced by CSR in dispersive sections. For that reason, it is useful to increase the bunch length in the low-energy spreader by tuning the R_{56}. On the other hand, in the case of the HXR/HXR operation, if both FEL lines are operating close together in wavelength, the length of the bunches has to be identical; thus, the lattice needs to be achromatic and isochronous. The quadrupoles located at the center of the DBA allow tuning of the R_{56} of the beamline (see Fig. 104).

Figures 105 and 106 show the lattice functions and first- and second-order momentum compaction factors of the low- and high-energy spreaders, respectively. The beta functions are designed to be symmetric with respect to the center of the dogleg and the horizontal beta function takes its minimum at the dipoles. As it can be seen on the figure, the R_{56} of the beamline is tuned with the central quadrupoles between bending magnets and both spreaders are achromatic, while the high-energy spreader is isochronous and the low one is not.

The tracking results are shown in Figs. 107 and 108 for low- and high-energy spreaders, respectively. Since the beam energy spread is too high in the low-energy spreader, chromatic aberrations coming from the quadrupoles cause high non-linear effects. To correct this, two sets of sextupoles were placed in the bending sections (maximum dispersion, Fig. 105 left). The corrections are localized (closing dispersion and minimizing the beta-beat) at the end of each bending section so as to minimize the sextupole strengths. However, the emittance growth is still larger than in the high-energy beamline. The same approach can be used for the high-energy spreader, as well.

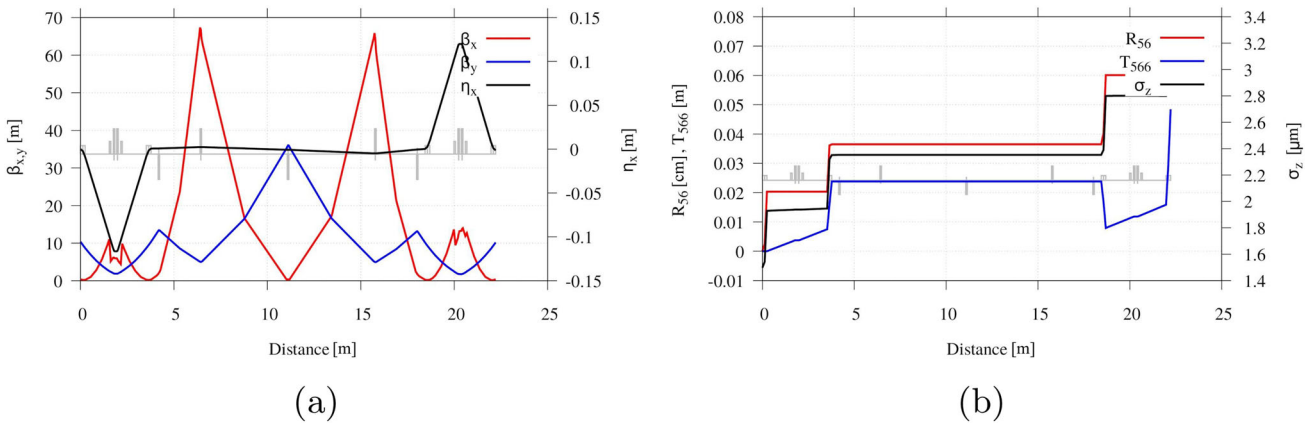

Fig. 105 Lattice function for the low-energy spreader 105a twiss functions along beamline 105b first- and second-order momentum compaction factors

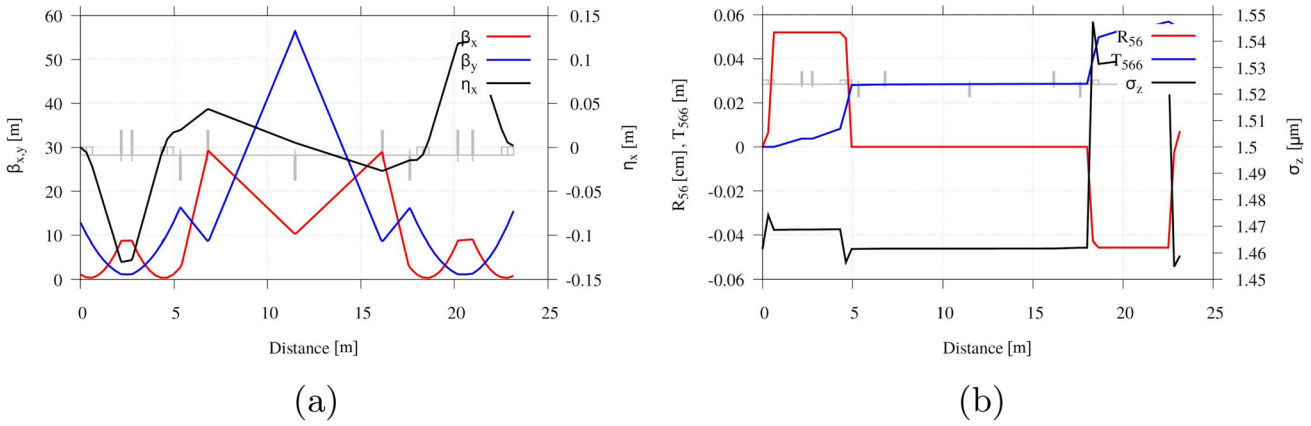

Fig. 106 Lattice function for the low-energy spreader 106a twiss functions along beamline 106b

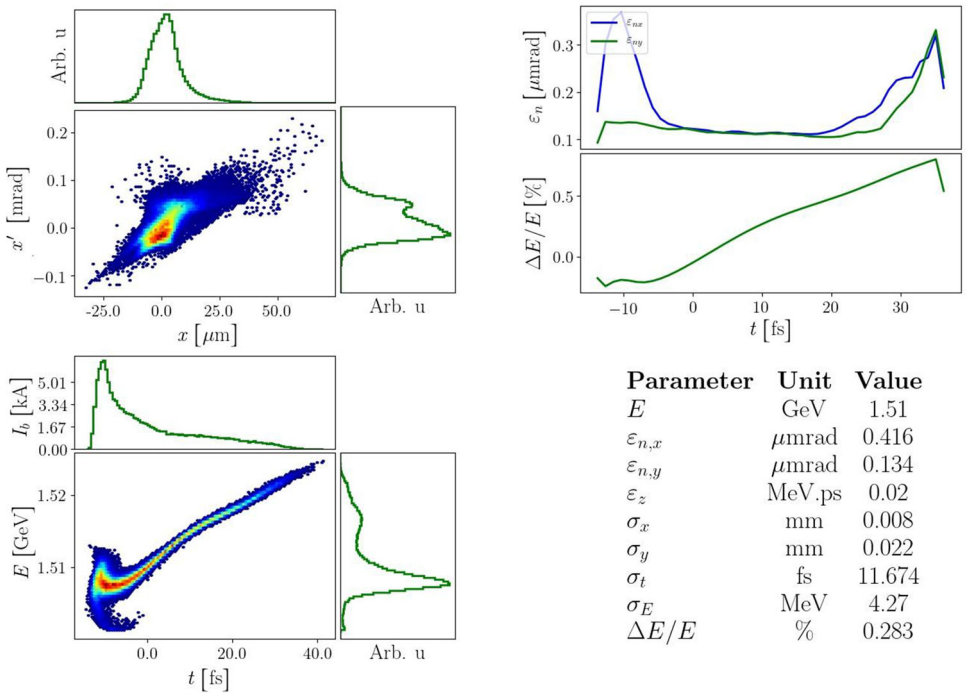

Parameter	Unit	Value
E	GeV	1.51
$\varepsilon_{n,x}$	μmrad	0.416
$\varepsilon_{n,y}$	μmrad	0.134
ε_z	MeV.ps	0.02
σ_x	mm	0.008
σ_y	mm	0.022
σ_t	fs	11.674
σ_E	MeV	4.27
$\Delta E/E$	%	0.283

Fig. 107 Horizontal (top left) and longitudinal (bottom left) phase spaces with associated histograms representing the projection along the respective axis and sliced emittance/energy spread and beam parameters of the bunch at the exit of low-energy spreader

The spreaders provide 526 and 535 ps delay for low and high energy, respectively. The main parameters are given in Table 36 for the shortest bunch length operation of CompactLight.

In Figs. 107 and 108, it is possible to see the distortions in longitudinal phase space caused by CSR. The current profile is fixed for the high-energy spreader while it is distorted by nonzero R_{56} in the high-energy one. The total effect of CSR on the emittance is not negligible; however, the amount of projected emittance growth can be minimized by changing the phase advance between the two bending sets. Although the projected emittance is very sensitive to the phase advances, the slice emittance, which is the important parameter to minimize for best FEL performance, is conserved at the end of the spreaders. For longer bunch lengths, the operation would be much easier because of the low CSR effect in the present dogleg designs in which the R_{56} can be tuned.

5.3.2.5 Start-to-end simulation through different beamlines

Start to end Twiss functions for the FEL-2 beamline (*Option-i* b, *Option-ii* b or *Option-iii* b) are given in Fig. 103 and beam phase space for shortest wavelength at the matching location is shown in Fig. 102.

In the Baseline and Upgrade-1 configuration, the accelerator drives both HXR/HXR and SXR/SXR FELs. FEL-1 will be generated through *Option-i* a or *Option-ii* a beamlines by the first bunch deflected by the S-band TDC

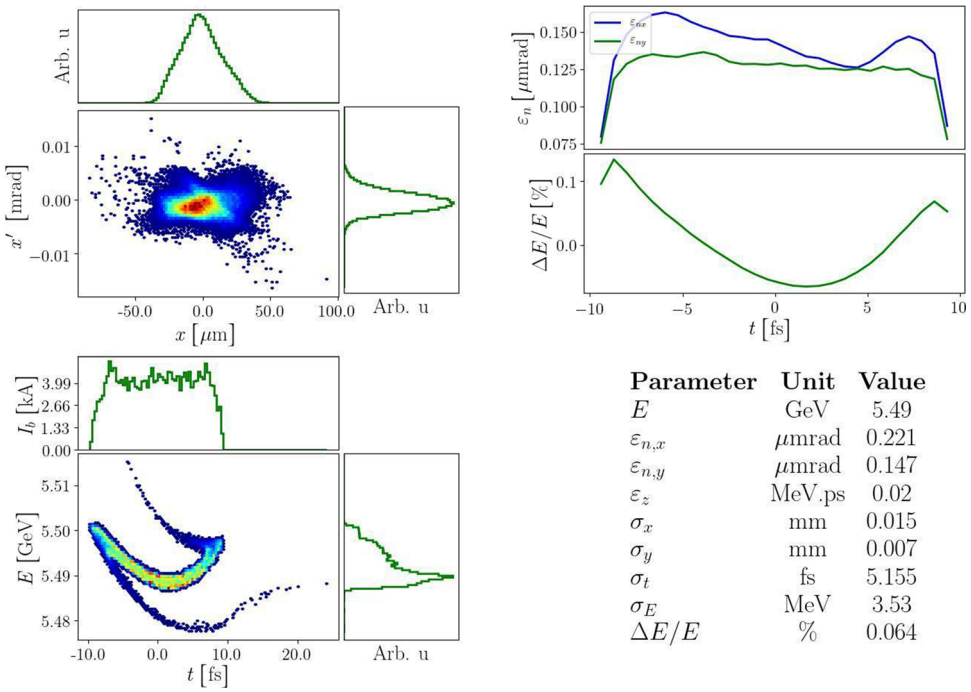

Parameter	Unit	Value
E	GeV	5.49
$\varepsilon_{n,x}$	μmrad	0.221
$\varepsilon_{n,y}$	μmrad	0.147
ε_z	MeV.ps	0.02
σ_x	mm	0.015
σ_y	mm	0.007
σ_t	fs	5.155
σ_E	MeV	3.53
$\Delta E/E$	%	0.064

Fig. 108 Horizontal (top left) and longitudinal (bottom left) phase spaces with associated histograms representing the projection along the respective axis and sliced emittance/energy spread and beam parameters of the bunch at the exit of high energy spreader

Table 36 Lattice parameters for low- and high-energy spreaders

Parameter	Units	Low-energy spreader	High-energy spreader
Maximum beam energy	GeV	1.5	5.5
Bending angle	deg	4	4
Length of septum magnet	m	0.3	0.7
Length of dipole magnet	m	0.3	0.7
R_{56}	mm	0.7	0.0
T_{566}	mm	53	48
Time delay	ps	526	535
Final RMS bunch length	μm	3	1.5
Final RMS horizontal emittance	mm mrad	0.41	0.28

after Linac-3. The twin bunches in the RF pulse will follow identical dynamics in the accelerator up to the end of Linac-3. Figure 109 shows the Beta functions and energy variation through Linac 3 to FEL-1 beamline for shortest wavelength operation, while Fig. 108 shows the phase space at the matching location to the FEL-1 undulator line. According to this plot, the projected emittance growth is about 50% while the sliced emittance growth is smaller. Due to the short bunch, and therefore strong CSR, the energy spread is increased by almost 100%. Since the peak current requirement is smaller for longer FEL wavelengths, transportation through the high-energy spreader would be relaxed.

In the case of the second upgrade (see Fig. 10), a low-energy spreader and Linac-4 are added. Similar to the high-energy spreader, the first bunch will be deflected horizontally by an S-band TDC after Linac-2 at about 1.5 GeV. Linac-4 will be used to accelerate the bunch up to 2 GeV or decelerate down to 1 GeV for driving the FEL-1 beamline (*Option-iii* a). As discussed in Sect. 5.3.2.4, similar to the case of simultaneous HXR/HXR generation, for short-wavelength HXR FEL generation on FEL-2 beam transport through the low-energy spreader becomes challenging because of strong CSR wake due to high peak current. Figure 110 shows the Beta functions and energy variation along *Option-iii* a beamline.

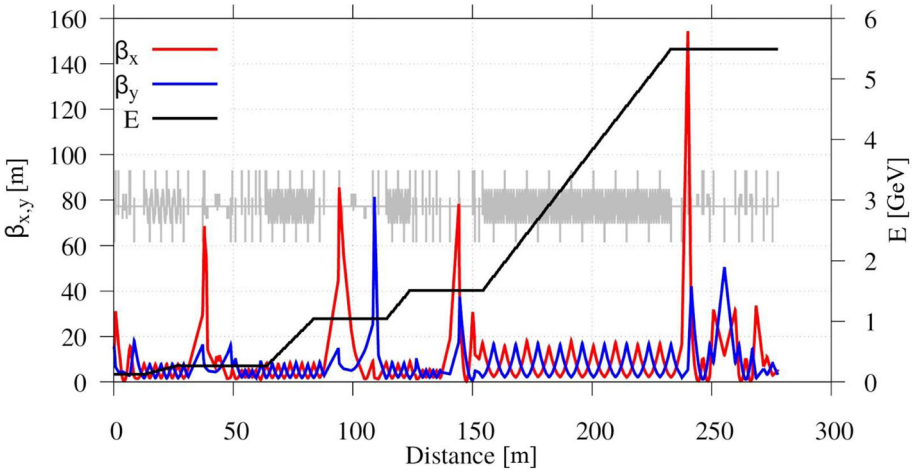

Fig. 109 Twiss functions and beam energy through Linac 3 to FEL-1 beamline (*Option-i* a)

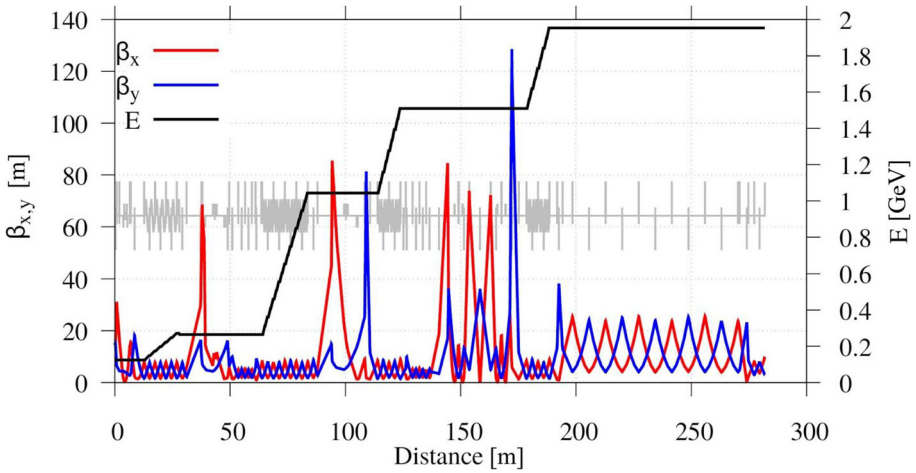

Fig. 110 Twiss functions and beam energy through Linac 4 to FEL-1 (*Option-iii* a)

Linac-4 consists of 8 structures (2 modules) and has the same lattice configuration as Linac-2. It is only about 20 m length; therefore, one needs to have a 75 m long transport line for matching the beam to the FEL-1 undulators. This section can also be used for diagnostic purposes. Figure 111 shows the final phase space of the first bunch at the matching position to the FEL-1 undulators. It is possible to see the distortions in longitudinal phase space and current distribution caused by the strong CSR effect due to the short bunch. The length of the bunch is increased due to a positive value of the R_{56} in the low-energy spreader, which can be tuned to smaller values. For this particular case, since the 2nd bunch of the train is optimized for the shortest wavelength, the energy profile of the 1st bunch is set at the extraction point to the low-energy spreader, and the total wakefield experienced in Linac-4 is not sufficient to remove the chirp. It is also noted that the smallest sliced emittance is at the centre of the electron bunch which has sufficient current for lasing in the SXR regime. The head of the bunch, which has about 0.35 mmmrad sliced emittance, has a current up to 5 kA. The FEL performance of this bunch is discussed in Sect. 4.2. Transportation of longer bunches would simplify the situation and one can also try to accelerate the 1st bunch at a different phase on the beamline which is adjusted for 2nd (nominal) bunch for HXR lasing.

5.3.3 Linac performance

To achieve excellent FEL performance, the beam quality must be preserved along the accelerator. The emittance growth must be kept at a minimum, and the energy spread and peak current of the bunch must be preserved. Several effects harm the beam quality during its passage through the linacs, the bunch compressors, and spreaders. The geometric and chromatic aberrations of the lattice, beam break up (BBU) instability, and CSR-induced energy spread are all effects that contribute to emittance degradation or bunch current fluctuations. In particular, trajectory distortions caused by element misalignment errors at installation, which are typically of the order of

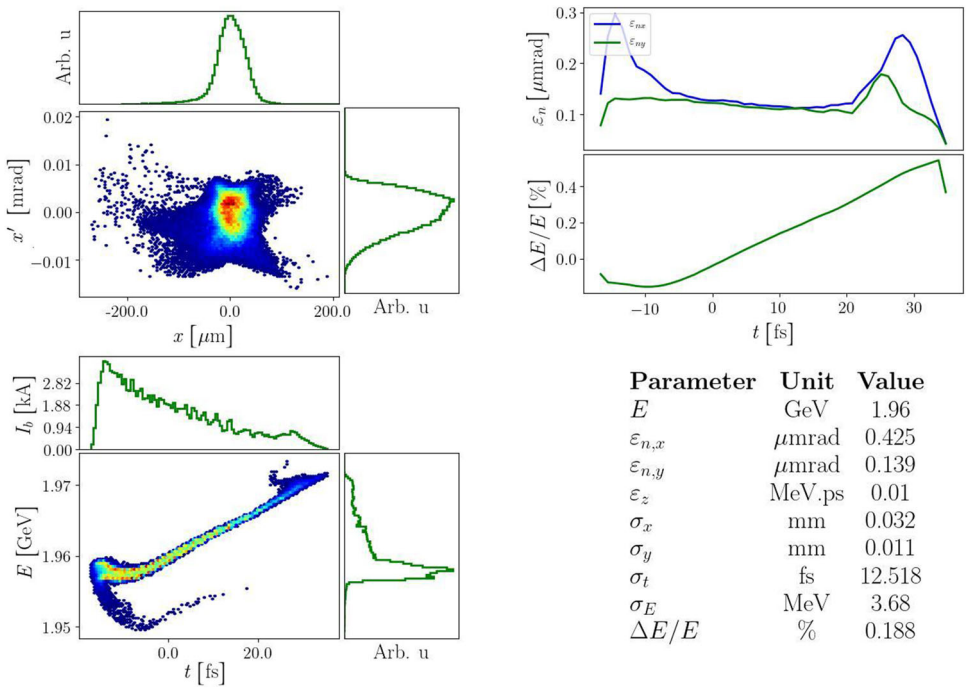

Parameter	Unit	Value
E	GeV	1.96
$\varepsilon_{n,x}$	μmrad	0.425
$\varepsilon_{n,y}$	μmrad	0.139
ε_z	MeV.ps	0.01
σ_x	mm	0.032
σ_y	mm	0.011
σ_t	fs	12.518
σ_E	MeV	3.68
$\Delta E/E$	%	0.188

Fig. 111 Horizontal (top left) and longitudinal (bottom left) phase spaces with associated histograms representing the projection along the respective axis and sliced emittance/energy spread and beam parameters of the bunch at the matching location of FEL undulators after Linac-4

100 µm and 100 µrad RMS, are the source of a number of detrimental effects, as well as variations of the operational conditions with time. These effects can be classified as static and dynamic imperfections. To counteract them, a set of horizontal and vertical magnetic correctors and beam position monitors are attached to each quadrupole magnet to apply beam-based alignment.

Other unavoidable effects, such as the emission of coherent synchrotron radiation in the bending magnets, introduce emittance growth and an increase of the energy spread. These effects are mitigated by optimized design of the magnetic chicanes and of the spreaders. As previously described, a laser heater is inserted before Linac-0 to dampen the micro-bunching in the bunch compressors.

5.3.3.1 Static imperfections

Static imperfections include the effects of element misalignment, which can harm the beam in different ways. We list the effects focusing on their impact on the beam.

Quadrupole misalignment Quadrupole misalignment introduces transverse deflections and unwanted dispersion, which, respectively, cause trajectory deflections and emittance growth. These effects can be cured in two different ways: improving the quadrupole alignment during the installation process, or using beam-based correction techniques. This latter technique is the preferred choice of CompactLight, as it will be needed anyway for routine operation. The details of the beam-based alignment (BBA) techniques will be outlined in the following paragraphs.

Accelerating structure misalignment. The off-axis passage of the beam through the accelerating structures can excite short-range wakefields. The strength of the wakefields depends on the iris aperture inside the structures. The CompactLight accelerator features structures in the C, X, and Ka bands of frequencies. It is well known that wakefield effects depend non-linearly on the inverse of the iris aperture. In the approximations presented in [174], one can find the following relations:

$$W_{\parallel}\ [\mathrm{V/pC/m}] \propto \frac{1}{a^2}, \quad W_{\perp}\ [\mathrm{V/pC/m/mm}] \propto \frac{1}{a^4}. \tag{36}$$

The smaller the aperture is, the stronger the effect. The X-band structures, which constitute nearly 80% of the entire linac, are characterized by small iris apertures. In the longitudinal plane, the short-range wakefields introduce a correlated momentum spread that must be compensated by operating the RF off-crest. In the transverse plane, the head-to-tail deflections that can introduce single-bunch beam-breakup can be mitigated by design using BNS damping, and in operation using BBA techniques. Even though the CompactLight X-band structure has been designed to provide a relatively large aperture (see CompactLight Deliverable 4.3) to mitigate these effects, the

impact on the beam is strong due to the large number of structures in the linacs. The off-axis passage of the beam through the accelerating structures excites also long-range wakefields, that is, high-order modes that can persist in the structure for long enough to affect the trailing bunches. This can induce bunch-to-bunch transverse deflections, potentially leading to beam breakup. The simplest solution to mitigate this effect is to space the bunches sufficiently for the wakefields to be damped below the harmful threshold. Figure 51 shows the evolution of the transverse long-range wakefields in the CompactLight X-band structure.
Element roll Roll installation errors of dipole magnets, quadrupoles, and correctors introduce horizontal-to-vertical coupling. Roll errors in BPMs mislead the beam-based alignment algorithms and hamper their effectiveness. An RMS error of 200 μrad has been assumed in the simulations.

All the imperfections simulations were performed using the code PLACET [182] on the lattice created by ELEGANT for optimization of ideal bunches.

5.3.3.2 Beam-based alignment

To preserve the beam quality under the effects of static element misalignment, three steps of beam-based alignment are applied.

1. Orbit correction: The beam is steered using all correctors to minimize the bpm readings. This is the first step and allows the beam to travel along the accelerator.
2. Dispersion-free correction: The beam dispersion is measured by running the RF structures in Linac-0 and Linac-1 off-crest by 10 deg to obtain a small energy difference. Then, the measured dispersion is minimized using all available correctors.
3. Wakefield-free correction: The impact of short-range wakefields is assessed using a test beam with 90% of the nominal charge and measuring its relative deflection to the nominal beam using the BPMs; then, the deflection is minimized using all available correctors.

Each step uses the beam position information from each quadrupole BPM and corrector magnet. A simulation study of the performance has been performed, using the errors reported in Table 37, for the shortest hard X-ray FEL and longest soft X-ray FEL modes. Figures 112 and 113 show the emittance growth along the CompactLight accelerator after each step of beam-based alignment for HXR and SXR operation, respectively. Each curve is the average of 100 random machines featuring the imperfections reported in Table 37.

Each curve in the plot is the average of 100 randomly misaligned machines. The figure shows that WFS gives the best results in terms of final emittance, while One-to-One (orbit) correction does not meet the CompactLight requirement of achieving a final emittance below 0.2 mm mrad. The emittance increase visible at about $\approx$ 100m is due to CSR effects in the second bunch compressor when operating in HXR mode. In SXR operation, since the bunch length is longer than in HXR mode, the emittance growth at the end of the linac is smaller.

Table 37 Table of RMS static imperfections considered in the simulations

	RMS position offset Δx, Δy [μm]	RMS angle error $\Delta x'$, $\Delta y'$ [μrad]	RMS roll error [μrad]
Quadrupoles	100	100	200
C-band structures	100	100	–
Ka-band structure	100	100	–
X-band structures	100	100	–
BPMs	100	100	200
BPM resolution	5	–	–
Correctors	–	100	200

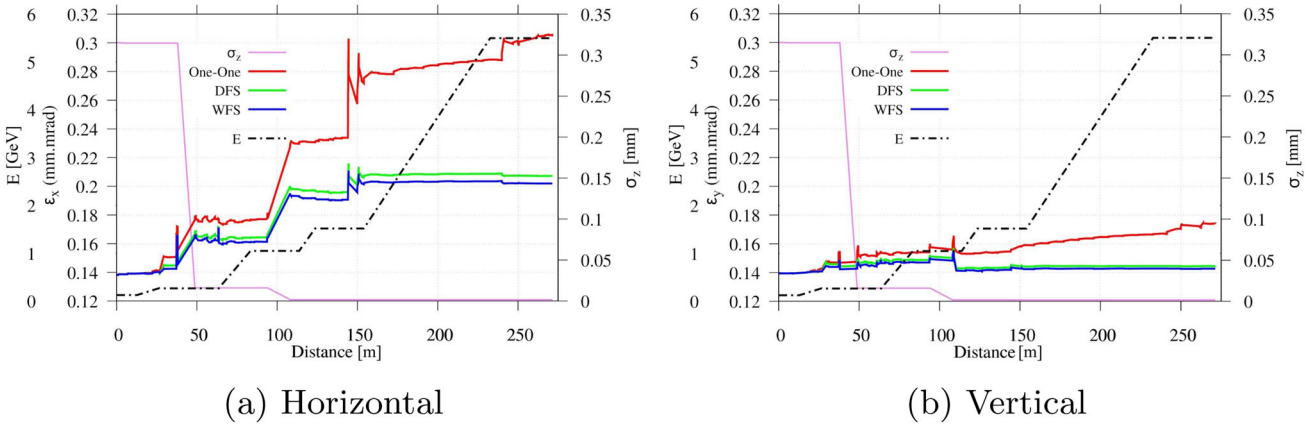

Fig. 112 Horizontal and vertical emittance growth, energy, and bunch length variation along the CompactLight accelerator, for shortest wavelength operation mode, after three consecutive steps of beam-based alignment

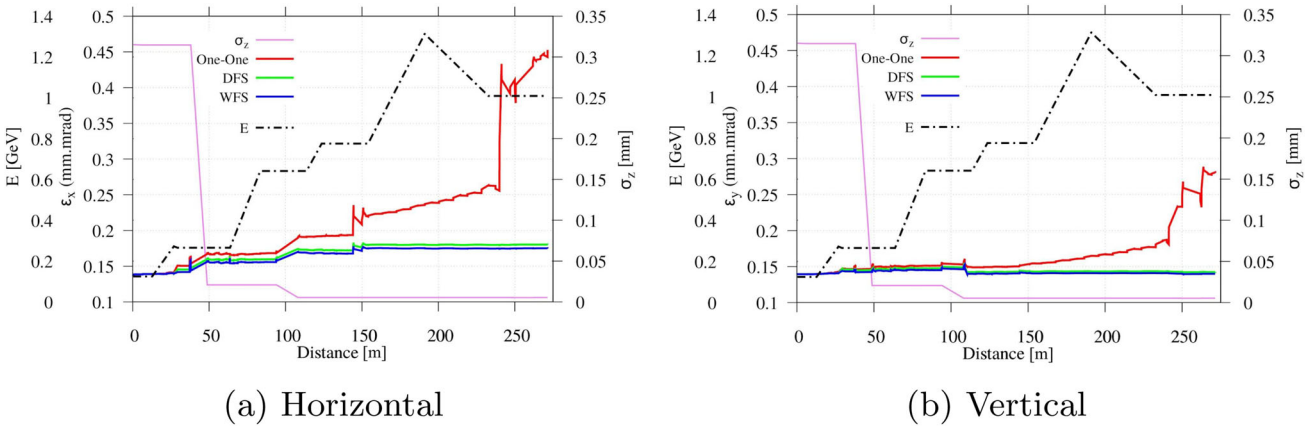

Fig. 113 Horizontal and vertical emittance growth, energy, and bunch length variation along the CompactLight accelerator, for longest wavelength operation mode, after three consecutive steps of beam-based alignment

5.3.3.3 Dynamic imperfections

The FEL operation requires stringent specifications for the stability of the linac output parameters: electron bunch arrival time, relative peak current, and relative mean energy. Dynamic effects which can harm the online operation of the accelerator, may result in the variation of these parameters. Sensitivity studies have been performed to determine the variation of the linac output parameters with respect to the phase and amplitude jitters of the accelerating fields, electron bunch charge, and electron emission time at the cathode. We summarize the impact of these imperfections below.

Beam transverse jitter: If too strong, the long-range wakefield effects in the accelerating structures can lead to jitter amplification, or ultimately beam breakup. The extent of the jitter amplification can be evaluated through the action amplification experienced by the second bunch due to the wakefield excited by the first bunch, as a function of the amplitude of the transverse long-range wakefield kick. Figure 114 shows the action amplification factor. The plot shows that kicks up to about 35 V/pC/m/mm can be tolerated, as they induce an action amplification factor less than the threshold, fixed at 1.15 (i.e., 15% action increase). The maximum kick tolerable, in our case 35 V/pC/m/mm, determines the minimum bunch spacing: this is about 500 ps, as visible in Fig. 51. The threshold has been fixed to 1.15 on the basis that the FEL can tolerate an electron beam jitter up to 20% of the beam size and divergence at the undulator—this is therefore satisfied by the 15% action increase and an assumed beam jitter of 5% at the injector.
Injector laser variations: Injector laser variations include laser timing errors and intensity variations (which result in bunch charge variations) induce variation on acceleration phase and wake potential introduced inside accelerating structures.

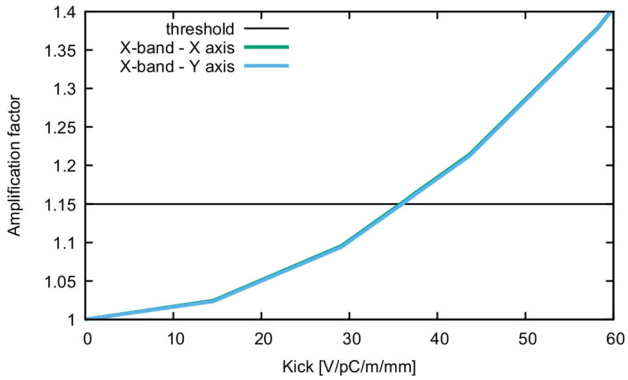

Fig. 114 Action amplification factor as a function of the amplitude of the transverse long-range wakefield kick at the 2nd bunch

RF variations. RF variations such as RF phase offset and gradient errors impact the beam transport and induce timing errors, energy offsets, and energy spread variations.

All these dynamic imperfections, in addition to mismatched bunch transport, can cause large oscillations in peak current and mean energy. To obtain the sensitivities for each segment of the machine, the sources of errors need to provide a collection of tolerances that need to be met.

The stability goals given in the tables below are determined from the SASE dynamics by analyzing intrinsic fluctuations of the FEL process given in Sect. 4.2.3. To define the level of allowed peak current fluctuations, a series of Genesis runs were accomplished. Beam arrival time jitter is assumed to be on the order of the photon pulse-length ($\sim$ 10 fs). A jitter of 0.035 % in the mean energy would keep the resonant condition within the FEL bandwidth.

The stability goals of the machine can be divided by the corresponding sensitivity to obtain the allowed deviation from the design parameter (jitter budget or tolerance). Since some components are driven by uncorrelated jitter sources, such as for the linac RF stations, one can take the square root of the number of independent sources (3 klystrons for the C-band injector, 4 klystrons for the X-band linac 1, 2 klystrons for the X-band linac 2, 17 klystrons for X-band linac 3, and 1 klystron for K-band linearizer). To evaluate if those stability goals can be met, we used expected jitter values (Table 38) for all critical accelerator components and run 500 simulations for the shortest wavelength generation case. The results of the simulation are summarized in Table 39.

Figures 115 and 116 show the variations of some beam parameters

Table 38 Table of RMS dynamic imperfections of CompactLight subsystems considered in the simulations

Parameter	Unit	Value
Incoming bunch energy jitter	%	0.01
Incoming bunch charge jitter	%	1
Incoming bunch timing jitter	fs	25
C-band phase stability	deg	0.04
C-band voltage stability	%	0.02
X-band phase stability	deg	0.08
X-band voltage stability	%	0.02
Ka-band phase stability	deg	0.16
Ka-band voltage stability	%	0.02

For the RF cavities, the same error was applied to all the cavities within an RF module. The errors between modules were uncorrelated

Table 39 Summary of dynamic jitters of some beam parameters

Parameter	Units	Value
RMS mean energy error	%	0.016
RMS arrival time error	fs	8.52
RMS energy spread	(keV)	165
RMS bunch length error	(μm)	0.28
RMS horizontal emittance	mm mrad	0.029
RMS peak current error	kA	1.05

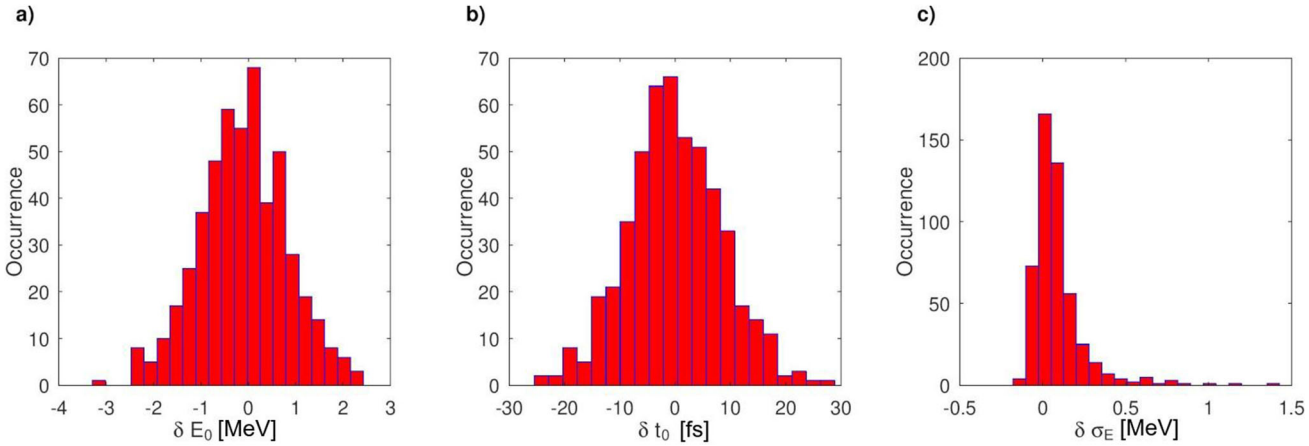

Fig. 115 Simulated distribution of average energy variation, arrival time difference, and energy spread difference at linac end for 500 jittering machines

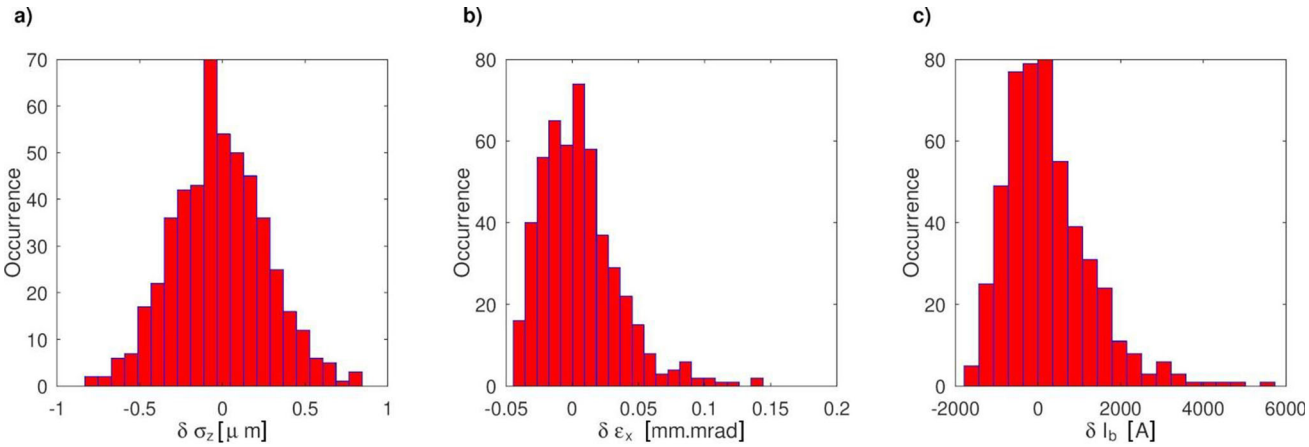

Fig. 116 Simulated distribution of bunch length variation, horizontal normalized emittance difference, and peak current difference at linac end for 500 jittering machines

5.4 Electron beam diagnostics

There is an old statement which says that an accelerator is only as good as its diagnostics. In machines where high brightness is essential to drive a light source, particular care has to be taken at the beam source.

A great advance in high-brightness accelerators was the introduction of photoinjectors, allowing the possibility to shape the beam using a laser transversely and longitudinally. The space-charge-dominated beam leaving the photocathode is immediately focused by a solenoid, providing emittance compensation [103] to reduce the emittance growth due to slice misalignment in the phase space. It was noted that an unexpected emittance oscillation in

the drift downstream of the rf gun showed a double emittance minimum [183]. The experimental validation of this behaviour [184, 185] opened the way for the so-called Ferrario's working point, to drive high-brightness machines that produce beams with high brilliance. However, this solution is a delicate equilibrium between several parameters, for example, beam transverse spot size, bunch length, solenoid field, drift length, injection phase, and total charge. During the acceleration process, precise control of the beam envelope, correct manipulation of the longitudinal phase space, and correct matching (to preserve the transverse emittance) are mandatory to achieve a beam with a high enough peak current and small enough slice energy spread to drive an X-ray FEL.

The diagnostics detailed here allow some flexibility in the machine's working point. Here, the beam rigidity is considered at the highest energy of 5.5 GeV; this is particularly important when considering the drift of the active elements like transverse deflecting structures.

5.4.1 Beam instrumentation

The right choice of device is the basis for accurate measurements of the beam parameters. This section discusses the principal devices that will be used for CompactLight.

5.4.1.1 Charge measurement

Charge measurements are performed using integrated current transformer (ICT) devices. These can measure down to fC (in the Turbo-ICT variation); they are easy to implement and very compact, using only 10 cm of space.

Conventional ICTs measure both the beam charge and the dark current. In a state-of-the-art machine, the main source of dark current is the RF-Gun. Only a small fraction of the dark current is transported—that which occurs at the right phase to be accelerated. Usually, the poor transverse properties of this current produce just a halo in the beam. Switching off the laser in a photo injector allows the dark current to be isolated. In CompactLight, the X-band linac structures can be an additional source of unwanted dark current.

It is too early to understand if dark current can perturb the charge measurements. However, there are solutions that can be implemented for the mitigation of both gun and linac dark current. Conventional ICTs can measure charges from a few pC up to several nC and they will be extensively used in the accelerator. In recent years, Bergoz Instrumentations has introduced a new toroid, called Turbo-ICT, which operates in the frequency domain rather than the time domain. This means that the detector is insensitive to the dark current and the measurement is very precise, down to very small charges of tens of fC. This device is very useful, but in modern accelerators, radiation safety usually requires an online and full-time measurement of the dark current. As this device is not suitable for this task, another ICT is needed. To save space and to integrate both functions in a single device, Bergoz Instrumentations have recently developed an integrated device that is under test at SPARC_LAB at INFN-LNF. It combines the conventional ICT and turbo toroid and is named Combo-Turbo-Toroid. This device will be placed in the CompactLight injector area where the dark current is likely to be an issue.

For the rest of the machine, a decision will be made later, after clear characterization of the dark current emitted by the X-band structures at a high gradient, on whether to install the conventional toroids or combo ones. The cost estimation assumes the use of combo toroids only in the injector area.

Faraday cups (FC) are another charge diagnostic. They use an absorber block (usually made of copper) to stop the beam. The block is connected to the ground through an ammeter to measure the total charge deposited by the beam. Unlike ICTs, FCs intercept the beam and thus can only be installed at the end of the beamline. Because all the charge is absorbed, it is an absolute measurement requiring no calibration. The absorber size must be adjusted depending on the beam energy. An FC will be very useful, especially in the commissioning phase. One will also be placed in the injector.

5.4.1.2 Position measurements

Beam position monitors (BPMs) are essential for non-invasive monitoring of the beam trajectory. Several types of monitors are available—buttons, striplines, and cavity BPMs. The relatively low charge of the CompactLight bunches means that buttons are not considered suitable due to their limited sensitivity and poor single pass. Stripline BPMs are often used. They give reasonable sensitivity to the beam position—about tens of microns at tens of pC—and their cost is acceptable. Cavity BPMs are the only type that can offer micrometer resolution, even at only a few pC. For much of the accelerator, where 1 μm resolution is not required, stripline BPMs are simpler and cheaper. However, striplines are longer than cavity BPMs. So far, one of the shortest striplines working in an accelerator is in PAL-XFEL [186] and is 16 cm long. Several labs are developing shorter straplines—for example, Fig. 117 shows the mechanical drawings of a project running at LNF-INFN. The length of this device is just a couple of cm more than a cavity BPM.

The striplines also offer the possibility of being integrated inside the quadrupoles. The model in Fig. 117 has a diameter of 30 mm, while the quads in CompactLight have an inner diameter of 25 mm. However, the BPM diameter can be reduced by more than 5 mm without changing the technology, so a more compact design is certainly achievable.

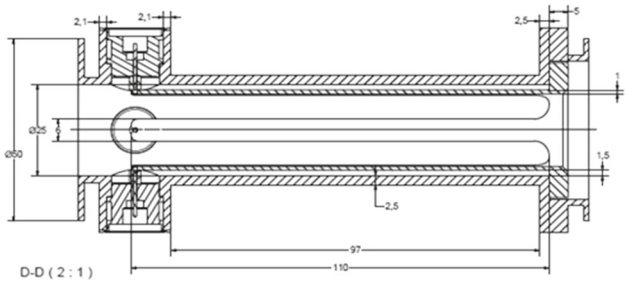

Fig. 117 A compact stripline BPM in development at LNF-INFN (courtesy G. Di Raddo)

A different approach is considered for the beam position monitors between the undulator modules. The main issue is the low temperature. Several examples worldwide of cavity BPMs operating at cryogenic temperatures are discussed in [187, 188]. These are usually embedded in cryostats and are between accelerating modules. Being very close to superconducting modules, even a single dust particle can severely affect the cavity performance and eventually drive it to a quench. For such a reason, the choice of a low-frequency cavity BPM, usually in L-band, has the advantage of larger dimensions, easing the cleaning of these devices. These dimensions impact also the longitudinal occupancy of the devices, which is in the order of 170 mm. However, in CompactLight, these devices are used between undulators and there are no superconducting cavities nearby, so the constraint on the dimensions is different. In this case, the longitudinal dimension is the most important factor. While there is not a single example of a cold BPM working at cryogenic temperature in the X-band, there is also no evidence that it is not possible to rescale the device to smaller dimensions.

Usually, cavity BPM modules are about 100 m long [189]. One of the main concerns about these devices working at such low temperatures is the material choice. In particular, the feedthrough has to be well designed, because the ceramic must work not only under vacuum conditions but also in a low-temperature regime. A R &D program is needed to develop these devices, but there is no evidence that they cannot be developed in a few years.

5.4.1.3 View screens

View screens are particularly important where an intercepting diagnostic is allowed. Their use is widespread: for envelope measurements; for transverse emittance measurements by means of quadrupole scans; and for longitudinal phase space measurements in which the beam is imaged after a transverse deflecting structure and a dipole.

There are only two types of screens that are routinely used—scintillators and optical transition radiation (OTR) monitors. Several materials can be used for the scintillator screens [190]. Their main advantage is the strong photon yield, which makes these devices suitable for imaging beams with charges as low as a few pC. However, the bulk emission can result in resolution degradation if the geometry is not properly chosen and the crystal is not very thin.

A compact accelerator must have also compact diagnostics. A small vacuum chamber of 80 mm length can host several screens on a mobile actuator. A thin scintillator, like for instance YAG:Ce, can be mounted orthogonal to the beam direction with a 45-degree mirror on the back to prevent blurring. The emitted radiation is then collected through an optical window by a camera. A drawing is shown in Fig. 118.

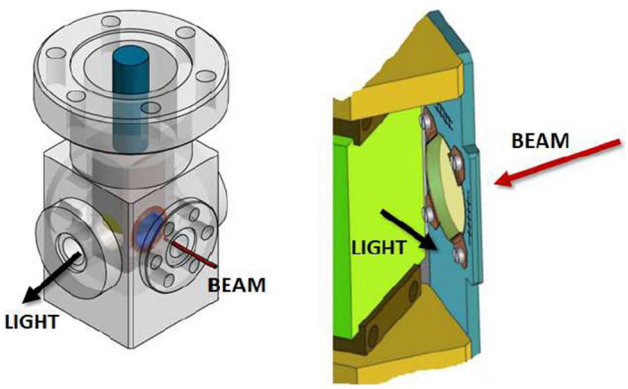

Fig. 118 Drawing of a compact view screen. A thin scintillator (typically 100 μm) is placed orthogonal to the beam direction. A 45-degree mirror on the back reflects the emitted radiation toward a detector outside the vacuum chamber

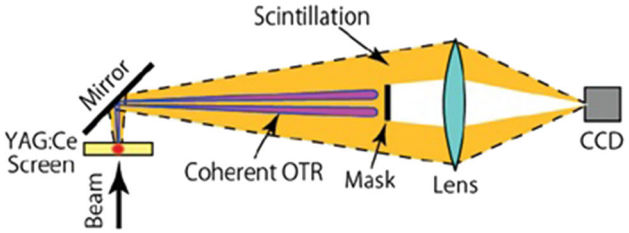

Fig. 119 COTR suppression system in use at SACLA [192]

On the same holder, unplugging the scintillator, an optical transmission radiation (OTR) screen, usually an aluminium-coated silicon plate, can be placed at the mirror position. OTR is emitted when a charge crosses the boundary between two media with different refractive indices. The radiation is emitted backwards and forward in a narrow cone with an angular aperture of about $2/\gamma$, with γ the relativistic factor. The main advantages of OTR screens are their linearity, even with strong signals, their fast response with respect to the beam structure, and their resolution which is close to the diffraction limit. Their main limitation is the number of emitted photons. In visible light, it is possible to estimate somewhere between 10^{-3} and 10^{-4} photons per incident electron.

OTR screens are, therefore, used for high-resolution transverse measurements and for all applications of coherent transition radiation, including longitudinal diagnostics. In CompactLight, the resolution is not an issue, so scintillator screens will be used extensively and OTR screens will only be employed to produce radiation useful for longitudinal diagnostics using coherent emission.

One problem associated with photoinjectors with high current and magnetic compression is the possibility of microbunching. This can affect the FEL performance but the induced CSR emitted in the bunch compressor can also interfere with the optical diagnostics [191].

Several solutions, with different levels of success, have been proposed and implemented. For CompactLight space is the priority, so the choice must be the scheme that prevents the detection of CSR and at the same time is the most compact. Coherent OTR (COTR) is emitted in a narrow cone, even with a scintillator. However, the scintillator light has a very wide distribution. The solution implemented in [192] and reported in Fig. 119 makes use of a mask to suppress the COTR contribution, while the rest of the radiation is collected by a lens. This is the best choice for CompactLight, and it has other important advantages—the whole device is outside of the vacuum chamber, so can be easily installed if there is evidence of microbunching, and there is no impact on the machine layout.

5.4.1.4 Transverse deflecting structure

The longitudinal properties of the electron bunch are very important. Often, the right parameters to drive the FEL effectively are not reached along the whole bunch but only in some longitudinal slices. The bunch peak current (the charge divided by the bunch duration) is also a parameter of paramount importance in an FEL, so the correct evaluation of the beam length is fundamental. There are several techniques that can be used. Some of them are single shots, others are not intercepting. Usually, a certain redundancy is needed in every machine, and hence, it makes sense to use multiple different techniques.

Transverse deflection structures (TDS) [193, 194], often called RF-deflectors, are RF cavities providing a time-dependent transverse force which can be exploited to measure the bunch longitudiunal properties. These are powerful devices, able to attain measurements with few-femtosecond resolution in the X-band [195]. The working principle is shown in Sect. 5.4.1.4. A time-dependent transverse deflecting voltage is present in a standing or traveling-wave structure. Different parts of the beam, in different longitudinal positions, experience a correlated transverse force that imprints a transverse momentum on the bunch. After a drift, imaging the bunch on a screen reveals the longitudinal charge distribution (Fig. 120).

The measured bunch length, using the average between the results obtained at the two zero cross phases separated by 180 degrees, as stated in [196], is

$$\sigma = \sqrt{\sigma_0^2 + \sigma_z^2}. \tag{37}$$

The dimension of the beam on the screen, with no power in the TDS, is indicated with σ_0 and

$$\sigma_z^2 = \beta\beta_0 \sin^2 \Delta \left(\frac{qV_0}{pc} k \right)^2 \langle z^2 \rangle, \tag{38}$$

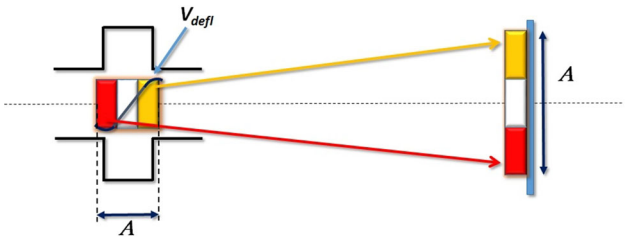

Fig. 120 Principle of operation of RF deflector. The longitudinal structure is mapped on the transverse profile, because different longitudinal positions experience different transverse kicks

where β and β_0 are, respectively, the betatron function at the TDS and on the screen, Δ is the betatron phase advance between the TDS and the screen, V_0 is the integrated voltage along the TDS, p is the particle momentum, q is the charge, c is the speed of light, and z is the longitudinal position inside the bunch. This term contains the required quantity, the second moment of the longitudinal charge distribution $\langle z^2 \rangle$ multiplied by a calibration factor. Equating the two terms under the square root in Eq. 37, it is possible to find the resolution

$$\sigma_z^{\text{res}} = \frac{E}{q} \frac{\sigma_0}{V_0 L} \frac{\lambda}{2\pi}, \tag{39}$$

where λ is the wavelength of the RF.

To increase the resolution of the device, the term σ_0^2 must be much smaller than σ_z^2, so the spot on the screen with the TDS off must be as small as possible. From Eq. 39, other methods to improve the resolution are to increase the deflecting voltage V_0 or the device length L, or to decrease the RF wavelength. Working in the X-band can therefore give the best resolution although for beams of only a few hundred MeV C-band or S-band structures can be considered.

A new transverse deflecting device called PolariX [197, 198] has an innovative feature that allows the polarization of the field to be rotated. The streaking direction can then be rotated allowing the characterization of the slice emittance [199] in both planes. This feature, together with the high resolution and the availability of X-band RF power when the downstream linac structures are not in use, makes Polarix a suitable design choice for CompactLight. It is used in several positions along the machine, at energies of 120 MeV, 1 GeV, 1.5 GeV, and 5.5 GeV. Figures 121 and 122 show the resolution versus voltage for these four different energies.

To obtain the best resolution the drift between the TDS and the screen can be optimized, increasing the length at high energy. The natural decrease of the beam spot helps also at high energy. At low energy, an integrated voltage of 10 MV is enough for 10 fs resolution, well beyond the bunch length. This value can be reached with a shorter structure, for example, 0.5 m long, while at larger energy, the use of a 1 m structure is foreseen, due to the larger beam rigidity.

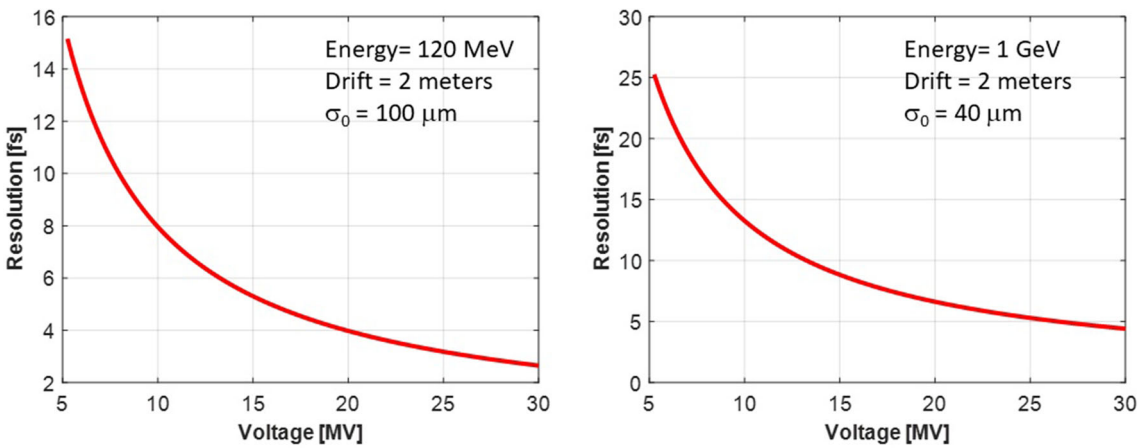

Fig. 121 Resolution vs voltage for 120 MeV (left) and 1.0 GeV (right). Beam size and drift between TDS and the screen are shown on the plots

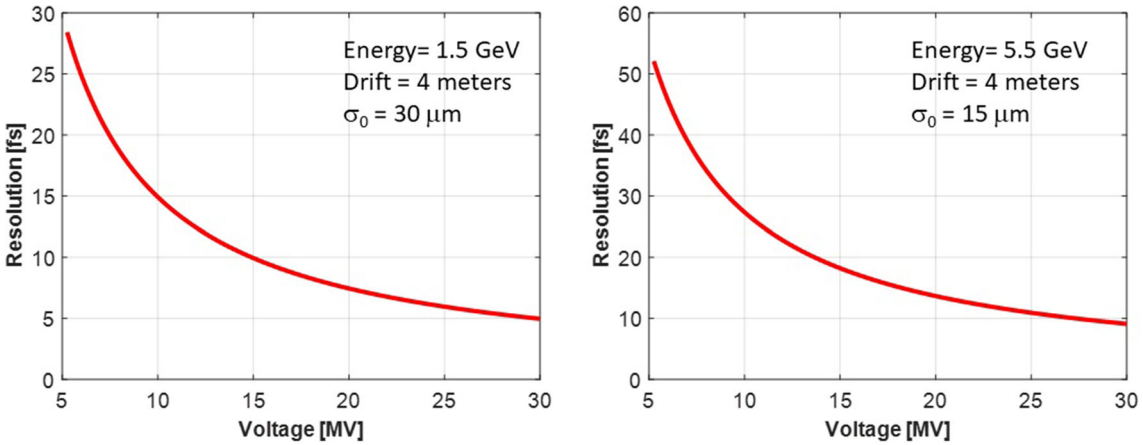

Fig. 122 Resolution vs voltage for 1.5 GeV (left) and 5.5 GeV (right). Beam size and drift between TDS and the screen are shown on the plots

The Polarix can be used not only in the main linac but also after the undulator chain, following the experience at SLAC [200]. The measurement of the longitudinal phase space after the undulators allows a precise reconstruction of the light pulse giving an insight into the radiation emission process.

5.4.1.5 Coherent radiation monitors

Ultra-short electron bunches allow the use of coherent radiation spectroscopy techniques in the infrared, where well-established spectrum characterization methods exist. Such schemes have been demonstrated in single-shot diagnostics, either measuring the CTR spectrum directly with a far-infrared spectrometer based on a dispersive prism [201] or with a cascaded grating setup in [202].

When a bunch of N electrons emits radiation, whether synchrotron radiation, transition radiation, or Smith–Purcell radiation, for example, the spectral-angular distribution of the produced radiation is given by

$$\left.\frac{\mathrm{d}^2W}{\mathrm{d}\Omega\mathrm{d}\omega}\right|^{\text{total}} = \left[N + N(N-1)|F(\lambda)|^2\right]\left.\frac{\mathrm{d}^2W}{\mathrm{d}\Omega\mathrm{d}\omega}\right|^{\text{single}}. \tag{40}$$

Here, $\left.\frac{\mathrm{d}^2W}{\mathrm{d}\Omega\mathrm{d}\omega}\right|^{\text{single}}$ is the spectral-angular distribution of the radiation produced by a single particle, strongly dependent on the particular physical process but well known, λ is the observed radiation wavelength, and $|F(\lambda)|^2$ is the squared amplitude of the bunch form-factor which is represented by the Fourier transform of the normalized longitudinal bunch distribution $\rho(z)$

$$F(\lambda) = \int_{-\infty}^{\infty} \rho(z)\exp\left(\frac{-2\pi i z}{\lambda}\right)\mathrm{d}z. \tag{41}$$

The contribution of the transverse bunch size to the form factor is negligible for high energies ($\gamma \gg 1$) and small observation angles ($\theta \ll 1$). The radiation is considered to be coherent if the second term in Eq. 40 dominates. From Eq. 41, the information about the longitudinal bunch profile is contained in the form factor and can be retrieved from it by measuring the coherent radiation spectrum.

In general, the form-factor defined by Eq. 41 is a complex-valued function and can be represented as $\mathcal{F}(\lambda) = F(\lambda)\exp[i\Phi(\lambda)]$. To achieve a unique reconstruction of the longitudinal charge distribution, both amplitude $F(\lambda)$ and phase $\Phi(\lambda)$ must be known. By measuring the spectrum of coherent radiation, only the absolute value $F(\lambda) = |\mathcal{F}(\lambda)|$ of the longitudinal form-factor can be obtained leaving the phase $\Phi(\lambda)$ undefined. There are two methods for obtaining this: analytical, such as Kramers–Kronig or Blashke phase retrieval, and iterative methods, for example, weighted greedy sparse phase retrieval (WGESPAR) [203]. A very good overview of the different bunch shape reconstruction algorithms can be found in [204] and references therein.

The advantage of using coherent radiation, rather than a deflecting structure, is the compactness of the system. A simple screen for OTR is sufficient. A spectrometer (the specification depends on the type of measurement

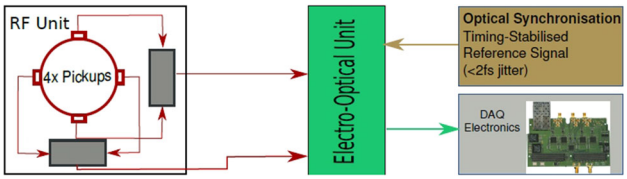

Fig. 123 BAM main components [205]

required) can be placed outside the vacuum chamber and sometimes even outside the linac hall. However, the main drawback of the technique is an unavoidable cut in some frequencies, or simply a frequency-dependent system transfer function up to the detector, that can influence the bunch reconstruction algorithm. However, coherent radiation can be very effective as a *relative* compression monitor. Because the signal intensity depends on the form factor, which increases as the bunch length decreases, it is possible to monitor the compression factor without the need to reconstruct the bunch profile—this can be done online, for every shot, and in a non-intercepting way. Such an online compression monitor can be used for RF feedback, using the output as a probe of RF phase stability. In CompactLight, there is a relative compression monitor after Bunch Compressor 1 (BC-1) and another station for full bunch length reconstruction after BC-2.

5.4.1.6 Time of arrival monitors

Measuring the bunch arrival time supplies crucial information for the beam-based feedback system. The best result in this field, a resolution of a few fs, is achieved with the beam arrival monitor (BAM) developed at DESY for XFEL. We refer mainly to this system [205, 206].

The BAM system comprises three parts, as shown in Fig. 123—the RF unit, the electro-optical unit, and the data acquisition system. The electromagnetic field induced by the electron bunch is captured by four broadband pickups. The electro-optical unit (EOM), see Fig. 124, combines the signals from the RF unit and a reference signal provided by an external source to perform the measurement. The result is then stored in the DAQ system. Modulation occurs via a Mach–Zehnder-type interferometer. If no RF signal is encountered by the probe laser pulse, or if the laser pulse is perfectly synchronized with it, no change in the laser pulse height is observed. If the two signals are not synchronized, the pulse height is modulated. The working principle of the EOM is shown in Fig. 125.

5.4.1.7 Intensified CCD camera

The diagnostics should be able to discriminate the longitudinal and transverse properties of two different bunches at the same energy, produced for the two FEL lines, with a temporal separation of about 883 ps, equal to ten wavelength periods. The TDS in the X band cannot separate these two bunches, because they are separated by exactly an integer number of periods, and so, they see the same phase in the device. Using a device in the other band will allow their separation, but it will also reduce the measurement resolution following the formula (39). Also, their distance is quite large with respect to the usual time window of a TDS, in the order of ps. The only way to select a single bunch is the use of an Intensified CCD camera (ICCD). This device can expose its sensor for a few nanoseconds. The idea is to collect two different images, one in the first window containing only the first

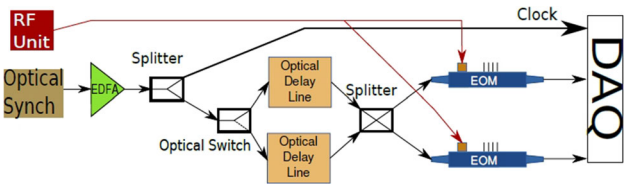

Fig. 124 Layout of the electro-optical unit.[205]

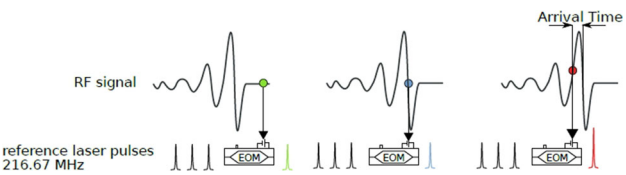

Fig. 125 Working principle of the electro-optical unit (EOM)

bunch and the second having the last one. It will work, because the jitter in the start and stop of the exposure in the multi-channel plate (the intensifier) is smaller than the time separation between bunches.

Two ICCDs can be considered, one at the spreader position and one after BC-1. The radiation will be produced by OTR screens which have a fast response, shorter than the bunch time separation.

5.4.2 Layout integration

In this section, the integration of the diagnostics with the machine layout is introduced. The injector is covered comprehensively in deliverable D3.3. Presented here is a schematic layout, although adequate space for each component is allocated. The principles used for determining the layout positions of the elements within the machine are as follows.

For transverse phase space diagnostics, for example, emittance measurements with the quad-scan method,

- The best choice is using only one quadrupole at a time. Every quad increases the error, given mostly by chromatic effect and depending on the beam size, beam divergence, and beam energy spread at the quadrupole entrance [207]. However, if we use only one quadrupole, the beam could be largely defocused in the other plane. Considering reasonable screen size and camera magnification, a spot larger than 3 mm rms will be quite difficult to image. Therefore, if we run in this situation, we have to use two quadrupoles.
- What is important in the quad scan is the region around the minimum spot size. To have a realistic measurement, it is important to have an increase in the spot size by at least of a factor 2.5, changing the magnet current accordingly.
- The distance between the quad and screen is chosen to fulfil these conditions. The minimum spot size depends mostly on the optics and the camera. However, as a rule of thumb, if we want to have better measurements with more sampling points, going much lower than 20 um, even if it is possible, it is not recommended. We can measure a spot down to a few microns but with much more uncertainty.

For longitudinal phase space measurements, the main rules followed for the design are:

- To improve the resolution of the TDS, the beam focus should be on the screen where the measurement is made.
- The focus should be mainly on the streak plane. However, if the beam is large in the other plane, a poor signal-to-noise ratio could be a problem; therefore, a small round beam is preferable.
- With the use of Polarix, which adds the possibility of rotating the polarization, the optics should have the flexibility to make a small spot in both planes.
- The phase advance between the TDS and the screen must be 90 degrees or a value very close to it. Again, the use of the deflector with rotating polarization means that this condition must be fulfilled in both transverse planes.

To give a clearer definition of every single part of the machine and the related measurements, the layout has been divided into several parts that do not reflect the usual subdivision into Linac-0, Linac-1, and so on. However, for clarity, the nomenclature used in the other CompactLight deliverables is always shown.

5.4.2.1 Injector

In this area, due to the reduced space availability, the layout is considered in more detail, with reasonable estimates given of the length of every device to demonstrate the feasibility of the design (see sketch in Fig. 126).

The lengths of the elements are assumed as follows: for view screens 100 mm including flanges, for stripline BPMs 200 mm including bellows and flanges. Starting from the gun, after a solenoid and a vacuum valve to separate the cathode from the rest of the machine, there is the laser port, to allow the laser light to arrive on the cathode. In this device, a mirror is also included to make an image of the cathode that is visible from the window opposite the laser input. Then, there is the first stripline embedded in a corrector to reduce the space occupancy. The Combo-Turbo-ICT toroid is placed just after the stripline and before a view screen where it is possible to measure the beam envelope. The energy measurement is performed using the first corrector and measuring the change in the beam position vs. current. Another stripline embedded in a corrector is placed before the entrance of the first accelerating module. In this way, the trajectory is determined from the start and the entrance point in the accelerating structure is monitored. Between every accelerating structure, there is a view screen, to monitor the envelope, and a stripline BPM inside a corrector.

5.4.2.2 Laser heater region

A complete 6D phase space reconstruction is considered here. Refer to Fig. 127 for a schematic definition of the diagnostics layout. Inside every quadrupole is a stripline to measure the beam trajectory. The correctors are also embedded in the quadrupoles. The envelope is monitored using the view screens before and after the undulator.

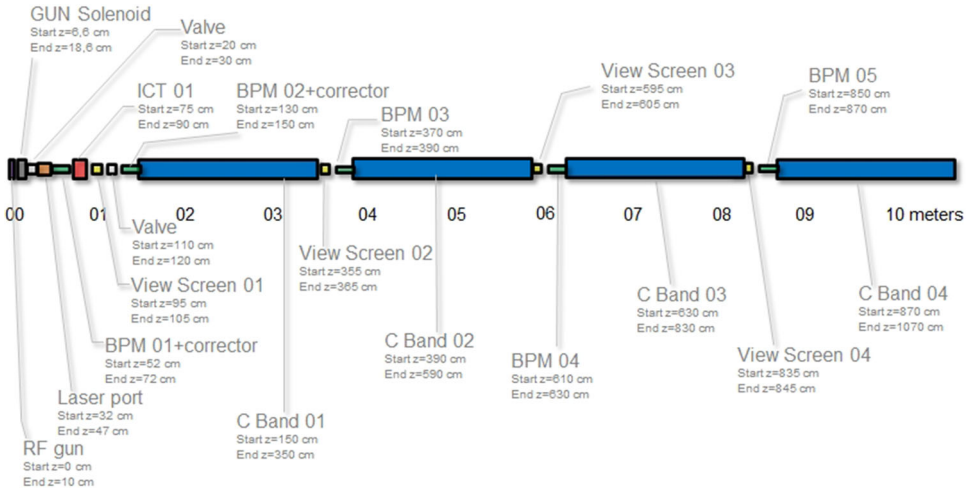

Fig. 126 Sketch of the injector layout including quotes and diagnostics up to the end of the C-band structures

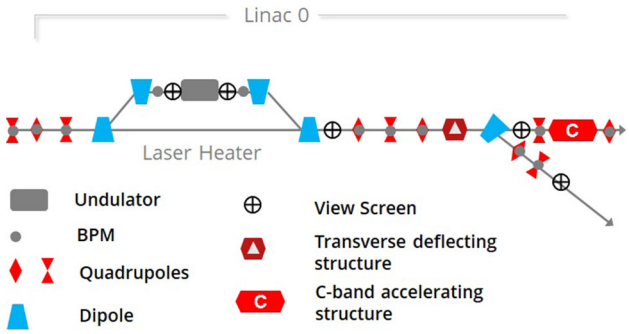

Fig. 127 Schematic definition of the diagnostics layout in the laser heater, including the full 6D phase space characterization region

Two striplines are placed to measure the beam trajectory before and after the undulator. After the chicane, a full 6D phase space characterization is implemented. A triplet of quadrupoles are also used to match the beam in the following accelerating sections, and can be used for a quadrupole scan and to tune the beam for the spectrometer arm. On the view screen in the spectrometer, it will be possible to perform a longitudinal phase space measurement, while the screen before the accelerating structure will be used for emittance measurement.

5.4.2.3 Bunch compressor 01 region

Refer to Fig. 128 for a schematic of the diagnostics layout in this sector. In Linac-0, the striplines are inside the quads, and for every four accelerating modules, there is a view screen for beam envelope measurement. Before the bunch compressor, other view screens are placed to check the envelope during and after the process of longitudinal bunch length linearization with the K-band structure. In the bunch compressor, a stripline is placed between the two upper dipoles. There is also a screen which can be used for emittance measurement in a straight line. The charge is monitored by means of an ICT before and after the compression.

After the bunch compressor, the first part of Linac-1 is dedicated to the full 6D characterization of the beam, by means of a TDS and emittance measurement. The spectrometer is also placed here to measure energy, energy spread, and longitudinal slice properties. The first view screen location in Linac-1 will also be equipped with a diffraction radiation radiator to produce coherent radiation for a non-invasive online compression monitor, useful for feedback purposes.

5.4.2.4 Bunch compressor 02 region

Refer to Fig. 129 for a schematic definition of the diagnostics layout in this sector. In Linac-1, the same scheme is used—a view screen for every four accelerating modules and striplines inside the quadrupoles. At the end of Linac-1 is BC-2, with diagnostics similar to those for BC-1. However, in this sector, there is not a full 6D characterization

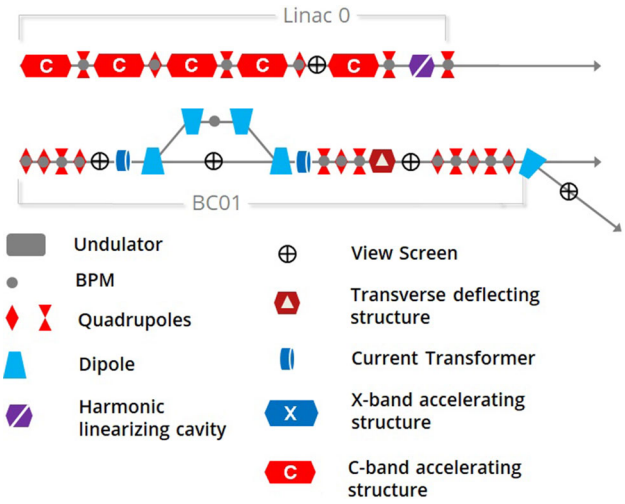

Fig. 128 Schematic definition of the diagnostics in the region surrounding the bunch compressor 01

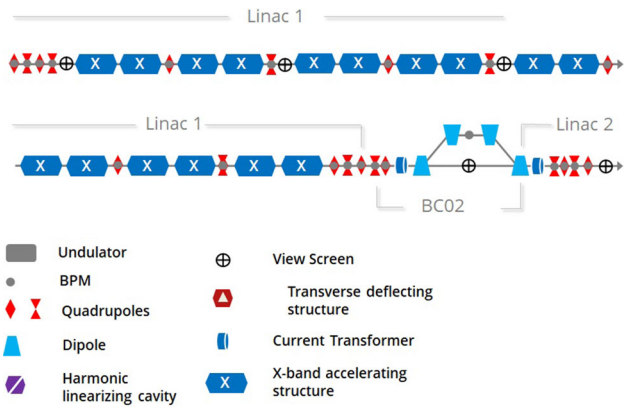

Fig. 129 Schematic definition of the diagnostics in the region surrounding the bunch compressor 02

of the phase space; instead, this is done after Linac-2. The last screen of the scheme shown in Fig. 129 can be also used for coherent radiation measurement to monitor the compression.

5.4.2.5 Spreader zone to Linac 4

Refer to Fig. 130 for a schematic definition of the diagnostics layout in this sector.

In this region, the beam is divided between Linac3 and Linac4. For better matching in the dogleg, the full 6D characterization is placed here rather than after BC-2. A transverse deflecting cavity and spectrometer are used for longitudinal characterization. An ICT is placed after the beamline separation for charge measurement. Transverse emittance, as well as slice emittance, can be monitored with the view screen at the beginning of Linac3.

5.4.2.6 Linac 03

Refer to Fig. 131 for a schematic definition of the diagnostics layout in this sector. This section is fully dominated by the presence of X-band accelerating structures. Stripline bpms are inside the quadrupoles, while view screens are now placed every 8 sections for beam envelope checking.

Spreader and matching area

Refer to Fig. 132 for a schematic of the diagnostics layout in this sector. At the end of Linac-3, there is another 6D phase space characterization area. Quadrupole scans are used for measuring transverse emittance, and a spectrometer with TDS allows the longitudinal phase space measurement. Both of these are fundamental to properly match the beam inside the undulator. The charge is monitored by an ICT just in front of the undulator.

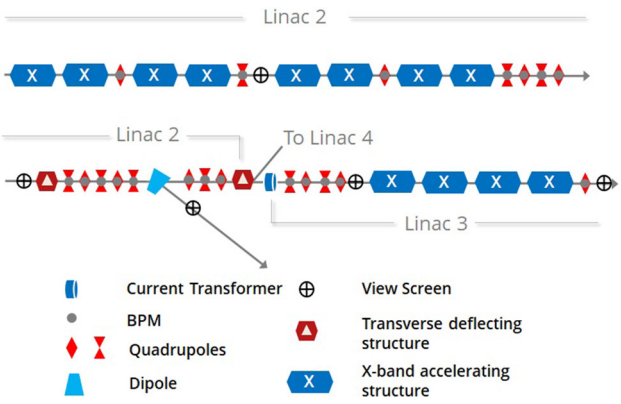

Fig. 130 Schematic definition of the diagnostics in the region surrounding the spreader

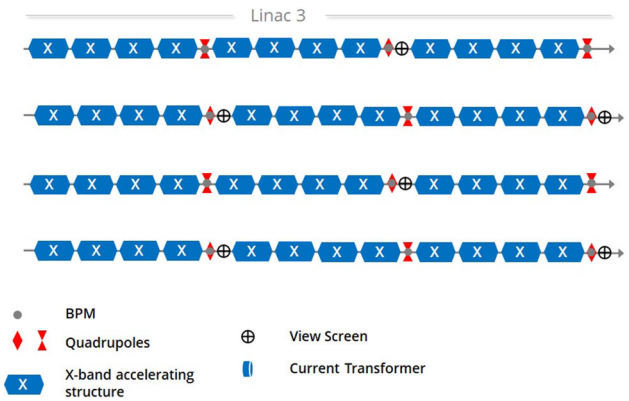

Fig. 131 Schematic definition of the diagnostics layout in Linac03

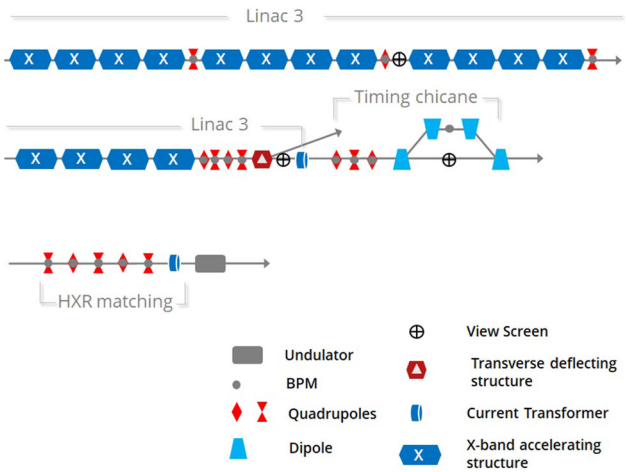

Fig. 132 Schematic definition of the diagnostics in the last part of the machine, before the undulator in the high energy line

5.5 Timing and synchronization

The timing system in a modern light source determines the timing of all time-critical subsystems, with stability of a few femtoseconds. Over the last 15–20 years, several 4th-generation light sources have been brought into regular user operation. Different timing system solutions have been adopted in these facilities, depending on the specifications and the local expertise available at the laboratory. Currently deployed solutions still include mixed

copper/fibre schemes. Optical timing systems have been in operation for 10 years, with FERMI being the first fully optically synchronized light source.

Frequently, timing is used as a synonym for synchronization as these two systems work in close connection. Often the term T &S is used, for timing and synchronization. However, these are well-separated systems as the 'timing' system takes care of the generation and ultra-stable distribution of the 'phase reference' signal, which needs to be femtosecond class in a 4th-generation light source, plus some ancillary triggers. synchronization systems are mainly local optical or electro/optical devices that 'lock' the timing system client to the phase reference. These units are typically laser locking or low-level RF (LLRF) devices.

In a timing system, a single ultra-stable phase clock oscillator generates the phase reference signal for the whole facility. The phase reference information is distributed throughout the facility, and is transmitted using either RF-modulated CW light, best suited for RF system synchronization, or as pulsed light, which may be directly used in laser system synchronization. The overall design may incorporate different synchronization methods, optimized for their particular application. The main 'clients' of a timing system are:

- Injector
- LLRF electronics for stabilisation of the accelerating voltages.
- Harmonic linearizer.
- Various local laser oscillators used throughout the machine, such as in the photoinjector and endstation lasers.
- Femtosecond class longitudinal diagnostics.

The fiber optical components used in optical timing systems are, as much as possible, standard 1550 nm wavelength telecommunication devices, for enhanced reliability. Controls are implemented digitally and communicate via Internet connections, to enable easy optimization as well as facilitate remote control and diagnostics. Also, trigger signals defining the coarse machine repetition rate, used in coarsely timed low repetition rate devices throughout the facility, are usually considered as part of the timing system.

5.5.1 CompactLight specifications relevant to the timing system

The CompactLight design is quite innovative as it deploys different frequencies for electron acceleration while providing FEL radiation over a broad spectrum. The FEL pulses repetition rate varies over a large interval from 100 Hz to 1 kHz, both in single-pulse or twin-pulse configuration.

The FEL radiation production includes different schemes, implemented at the different phases of the project, ranging from SASE FEL to self-seeding schemes. A brief outline of the CompactLight timing system is presented in [208]. Typically, in 4th-generation light sources, three main sections are present: the linac, the undulator line, and the experimental section. The phase reference signal has to be distributed to, and used within all three sections.

A peculiarity of CompactLight is the combination of a C-band gun and Linac0, with the CLIC-based, 12 GHz, accelerating structures, operating at a frequency that is the 4th harmonic of the normal S-band. In Table 40, the operating frequencies are listed; it is assumed that the Reference Master Oscillator (RMO) is set at the X-band frequency. The various n factors needed to divide, or multiply, the RMO X-band frequency to obtain all the operating frequencies are indicated. The Ka-band harmonic linearizer is set to operate at 35.3982 GHz. A possible integer divider (30) of the X-band is also indicated, yielding a possible repetition rate for the laser oscillators equal to 374.750 MHz [209].

An important feature to be addressed is the ability to trigger (generate) two laser pulses within the same shot to create two closely spaced radiation pulses. Given the limited delay between the two pulses (100 fs), it seems convenient to handle this feature using optical delays using stabilised optical delay lines.

Table 40 CompactLight RF operating frequencies

Item	Frequency, MHZ	n factor, X-band/n	τ_{RF}, ps	1 deg, fs	0.5 deg, fs
X-Band	11,994.0	Master	83.38	231.60	11.58
C-Band	5997.0	÷ 2	166.75	463.19	23.16
S-Band	2998.5	÷ 4	333.50	926.39	46.32
Ka-Band	35,982.0	× 3	27.79	77.20	3.86
f_{laser}	399.8	÷ 30	2501.25	6,948	347

The RF degrees are shown in time units

Table 41 CompactLight timing system main specifications

Parameter	Value	Unit	Comment
f_{RUB}	10.00	MHz	
f_X	11.994	GHz	
$Jitter_{XRMS}$	0.05	deg	At delivery point; $t = 11.5$ fs
f_C	5.997	GHz	
$Jitter_{CRMS}$	0.05	deg	At delivery point; $t = 23.1$ fs
f_{LASER}	339.8	MHz	
t_{JIT}	≤ 10	fs	Laser clients f_{off}=100 HZ–10 HZ
t_{DRIFT}	≤ 20	fs	24 h

Table 42 CompactLight timing system topological parameters

Timing clients	n	Comment
S-Band	1	Sub-harmonic deflector
C-Band clients	≤ 20	Gun, linac0
X-Band clients	≤ 30	Linac1-3, deflectors
Ka-band	1	Harmonic linearizer
Laser clients	≤ 5	
Diagnostics	≤ 10	

5.5.2 Specifications for the CompactLight FEL timing system

The main specifications of the CompactLight FEL Timing system are listed in Table 41. From the 'topological' viewpoint, the number of clients and key facility parameters are listed in Table 42.

5.5.3 Proposed layout for the CompactLight FEL timing system

Given the above specifications, both in terms of:

- absolute jitter values.
- adopted RF frequencies.
- physical extension of the facility.

An optical timing system is the most appropriate for ultra-low phase noise distribution of the reference phase signal. As is typically the case for linac driven FEL sources, two main categories of timing system clients may be identified, which are intrinsically either pulsed or CW. At the very end of the timing path, the signal used as the phase reference by the remotely synced device has necessarily to have the features listed in Table 43.

The ultra-low phase noise source in the timing system consists of a tightly locked electronic oscillator and a femtosecond laser. It offers both pulsed and CW-RF reference signals at a central location with the help of short ($\leq$2 m) phase-stabilised and temperature-compensated coaxial cables, all operated inside a temperature and humidity-stabilised timing hutch. The number of Electro/Optical (E/O) conversions should be minimized and performed in a controlled environment. Finally, these central phase reference signals should adopt the physical

Table 43 List of timing system clients

Timing clients	Synced device type	Regime	Comment
Klystron	Electronic	CW	LLRF board
Laser	Optical	Pulsed	X-Correlator
Long diagnostic	Optical	Pulsed	BAM, EOS

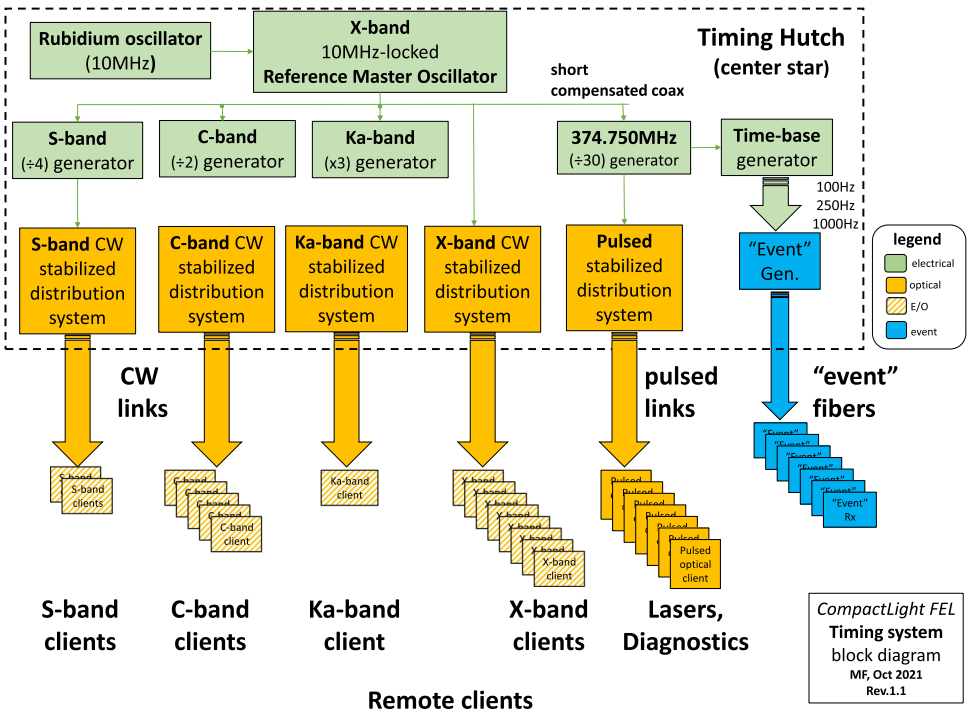

Fig. 133 CompactLight timing system schematic layout; the number of "clients" is merely indicative

layer that best suits the specific remote timing client, adopting the optimum stabilised link technique to transfer them to the endpoint.

A characteristic of CompactLight is the number of different frequencies involved in the bunch creation and acceleration processes. This poses some extra requirements for the source signal implementation. This is particularly true for the most critical generation of ultra-stable phase carriers at C-band and X-band to achieve overall facility stability by design. The adopted frequencies are direct sub/multiple of each other. Both signals can be conveniently generated either from the same optical reference pulse train in a completely phase-stable way or by deducing the C-band signal from the X-band signal by simple frequency division phase preserving. Ka-band carrier may be generated using even multipliers.

The proposed layout for the CompactLight timing system is shown in Fig. 133. This schematic has two main sections: on the left, the femtosecond class ultra-low phase noise part, and on the right, the low jitter picosecond class event system for the trigger distribution.

The devices indicated in the layout are color-coded:

- green for electronic/μ-wave ultra-low phase noise devices.
- orange for optical ultra-low phase noise devices.
- patterned orange for electro/optical devices.
- blue for event class devices.

The same color code applies also to the links, indicated as large arrows.

The centralized devices are within the dashed line. This indicates the so-called timing hutch, which will be located in a central position for minimizing the lengths of the different optical links. In the lower part of the schematic, the remote clients are indicated. These are typically optical devices (for the pulsed reference clients) and electro/optical for the CW clients and for the diagnostics.

As stated above, the overall timing system performance is critically related to the ultra-low phase noise performance of the Reference Master Oscillator (RMO). The RMO is an RF/μ-wave ultra-low phase noise generator at X-band, locked to the 10 MHz reference provided by the Rubidium Reference Oscillator, for improved long-term stability. From this reference frequency, the C-band and S-band can be obtained by even division. The Ka-band is obtained by an odd multiplier (×3). The laser repetition rate has been set equal to 374.750 MHz, directly obtained by division. This frequency is a value compatible with current state-of-the-art laser products [209]. Finally, the actual low-frequency bunch clock signals at 100, 250 and 1000 Hz may be obtained by dividing the laser repetition rate. The triggers are then distributed to the facility using an event-like system based on the low noise transmission over the MM fibre of a given frame.

5.5.4 Timing distribution

Due to the short reference pulses, typical 100 fs, of optical timing distribution systems and high-resolution timing detectors based on integrated balanced optical cross-correlators (BOC), today's optical timing detectors easily have a resolution of 0.1 fs. If ultra-low noise seed oscillators for optical amplifier systems are used, such as low noise Er- and Yb- lasers, few femtosecond synchronization of different oscillators over km distances is possible [210]. A possible implementation scheme of an optical distribution system is shown in Fig. 134. With the new generation of the Menhir ultra-low jitter oscillators [209], with a repetition rate of 400 MHz, one can also co-integrate out-of-loop delay stages that can be used for precise tuning of all-optical pulses without excessively long delay stages, up to 2.5 ns only.

The low-power consumption of integrated BOCs, up to 20 times less than previous BOCs, allows powering up to 20 times more timing links from the same laser source than earlier timing systems, thus greatly simplifying pulsed optical timing systems. RF signals are conveniently transferred via RF over fibre delivery systems, with the required precision of a few tens to few femtoseconds. Also, using a pulsed optical timing distribution system, RF signals may be regenerated at the far end node using a Balanced Optical Microwave Phase Detector (BOMPD), assuring the lowest-noise synchronization between laser and RF sources.

In Fig. 135, a possible scheme of a (commercial, by Cycle GmbH, [211]) pulsed optical timing system feeding both pulsed and CW clients is shown.

Here, the optical master oscillator (OMO) is phase-stably locked to the user-supplied reference master oscillator (RMO) (here the X-band RMO) via a BOMPD-OMO. The OMO output is split via a 1:16 splitter to possibly 16 outputs or more, driving up to 16 fibre links. The fibre links are length stabilised to better than 1 fs (RMS) via fibre stabilisation units (FLS). Two possibilities at the output of each fibre link could be considered: (a) regeneration of an ultra-low noise CW-microwave signal from the optical pulse stream with the help of a BOMPD at frequencies equal to a harmonic of the laser's repetition rate, or (b) another laser at a different wavelength (0.8, 1 or 1.5 μm) can be synchronized to the output pulse stream at 1.5 μm with a BOC or two-color BOC (TC-BOC).

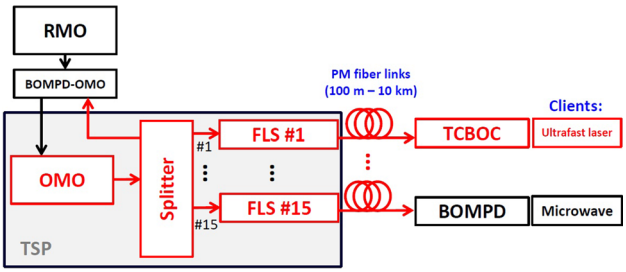

Fig. 134 CompactLight optical timing system schematic layout

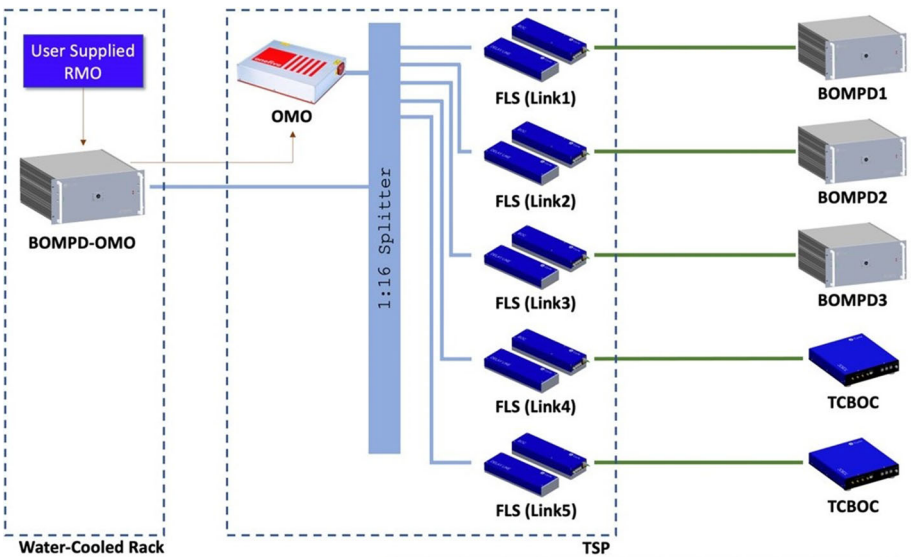

Fig. 135 Layout of an optical pulsed timing system with stabilized distribution fibre links

6 Light production

6.1 Undulators

6.1.1 Choice of undulator technology

In this section, a quantitative comparison is made of a comprehensive range of current and emerging undulator technologies, using the parameterisations of the estimated field as a function of undulator period and gap, reported in Deliverable D5.1. Two approaches are combined. First, the semi-analytical model of Ming Xie [68] is used. The model, briefly described in Sect. 3.3.4.1, extends the one-dimensional FEL theory, which applies in the limit of a 1D monoenergetic beam, to the case where degradation of performance due to finite emittance and energy spread is included. This model reliably predicts the FEL saturation power and saturation length via the FEL ρ-parameter using corrections based on a parameterisation of a set of 3D numerical simulations. The results from the Xie analysis are combined with the analytical theory of Saldin [60], which allows the FEL longitudinal and transverse coherence to be calculated. Hence, the FEL spectral brilliance can be determined. This is a key parameter of interest to users, because it tells them how many photons per second within a given bandwidth, they can focus onto a sample of given transverse dimensions—i.e., it tells them how *useful* the light is.

One figure of merit chosen for the quantitative comparison is the ratio between the FEL peak brilliance and the saturation length, as this is a convenient measure of performance vs. compactness. The second figure of merit chosen is the FEL peak brilliance itself (i.e., not normalized to the saturation length), because there is a specific user requirement for a minimum brilliance of 10^{33} ph/s/mm^2/mrad^2/0.1% bandwidth. The analysis of both figures of merit is conducted as a function of electron beam energy to illustrate the advantage obtained using the undulator technologies with the strongest fields and to determine the required electron beam energy that would be required, so that the peak brilliance exceeds the user requirement. This allows us an upper limit to be set on the electron beam energy for CompactLight that allows the following criteria to be satisfied:

- The electron beam energy of 5.5 GeV is lower than any other X-ray FEL facility.
- The photon energy reach of 16 keV is higher than that of SwissFEL, which has a beam energy higher than CompactLight.
- There are a number of viable options for undulator technology that can be reserved as technology alternatives.

The beam energy was varied in small steps for the figure of merit calculations. Snapshots of the calculations are shown in Fig 136 where the top plot is for beam energy 4.5 GeV, the middle plot is for 5.5 GeV and the bottom plot is for 6.5 GeV. The electron beam parameters used in the calculations are peak current I =5 kA, normalized emittance ε_n =0.2 mm mrad, relative RMS energy spread $\sigma_\gamma/\gamma_0 = 10^{-4}$, and average β-function $\bar{\beta} = 9$ m. In each plot, the horizontal axis is the undulator period λ_u, and the vertical axis is the undulator $K_{\rm rms}$. Each line shows the dependence of $K_{\rm rms}$ vs λ_u for a different undulator technology, as represented in the legend. For some technologies, a full parameterisation over the space is not available—these technologies (for example, the Microwave undulators) are represented by single points on the plot. The colored region represents the $[K_{\rm rms}, \lambda_u]$ parameter space in which the undulator resonant wavelength lies between $\lambda_r = 0.155$ nm (top edge) and $\lambda_r = 0.0775$ nm (bottom edge). The color represents the value of the figure of merit $B/L_{\rm sat}$.

The interpretation of these plots is as follows. The intersection of each undulator curve with the $\lambda_r = 0.155$ nm line defines the period required for that undulator, at that beam energy, to be resonant at $\lambda_r = 0.155$ nm. To tune to $\lambda_r = 0.0775$ nm, the undulator K strength is reduced. For beam energy 4.5 GeV (top plot), it can be seen that for a number of technologies, for example, APPLE-II, the merit function drops to zero at $\lambda_r = 0.0775$ nm, indicating that these technologies are unviable at 4.5 GeV—they provide an insufficient field to cover the required tuning range. In fact, at 4.5 GeV only those technologies for which the $[K_{\rm rms}, \lambda_u]$ curve intersects the $\lambda_r = 0.155$ nm line at $\lambda_u < 12$mm provide any output at $\lambda_r = 0.0775$ nm.

By increasing the beam energy to 5.5 GeV (middle plot), all of the technologies are able to tune across the required range. Still, the merit function is low for those technologies with weaker fields, indicating that a threshold could, in principle, be defined. Finally, the trend continues to improve performance at 6.5 GeV.

In general, then, it is seen that:

- The undulator technologies that provide the strongest K as a function of period, or the 'strongest' undulators, have the highest merit function.
- At low beam energies, only the strongest undulator can give any photon output across the whole tuning range.
- As the beam energy is increased, more technologies become viable, and the merit function increases for all technologies.

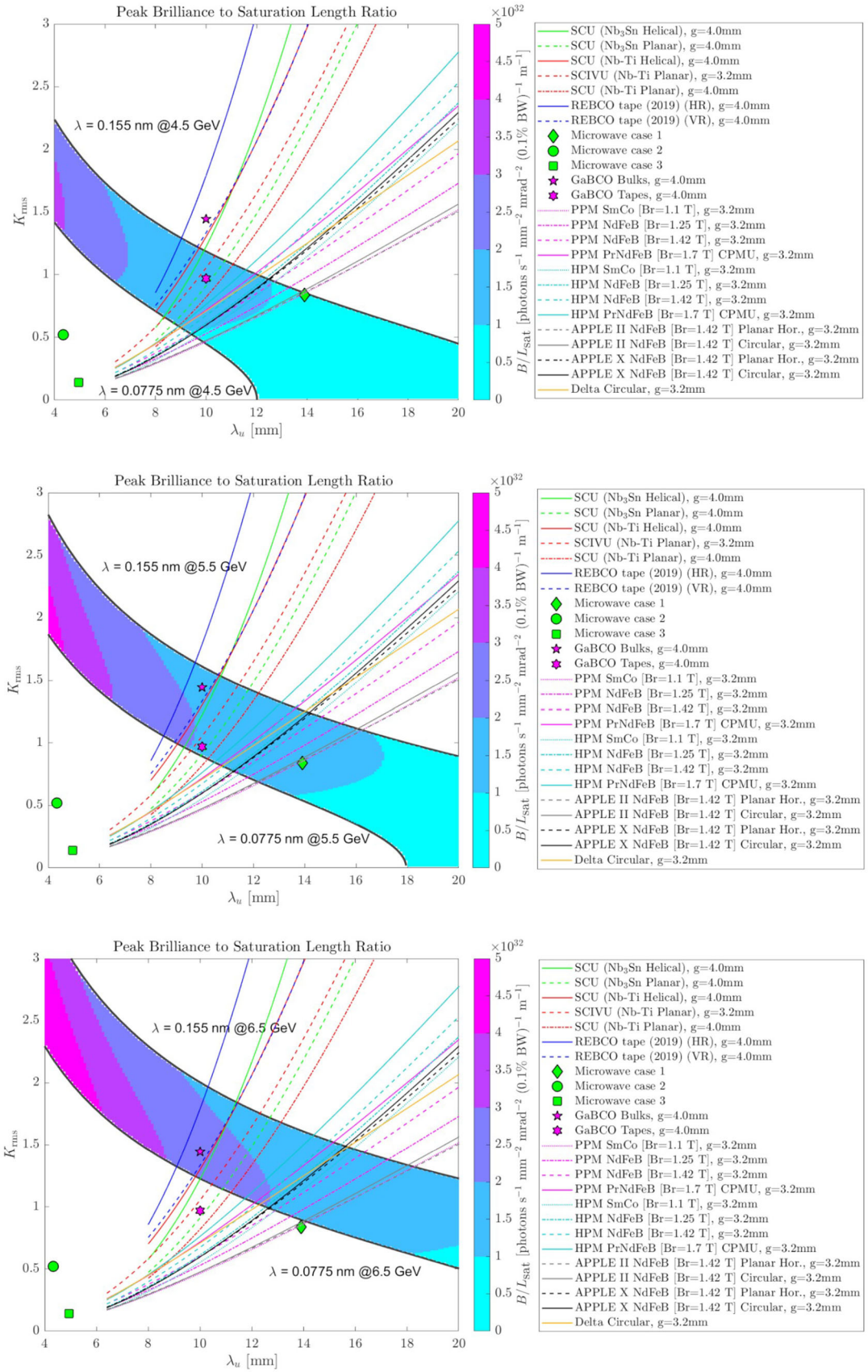

Fig. 136 Figure of merit B/L_{sat} for electron beam energies 4.5 GeV (top), 5.5 GeV (middle) and 6.5 GeV (bottom)

Therefore, the beam energy must be chosen appropriately—it must be as low as possible to enable a compact facility but high enough to provide the required FEL output. Also, the decision was made that the beam energy choice must allow a number of undulator technologies to remain viable alternative technology options.

The peak brilliance is calculated for the different technologies at three different beam energies to further assess the required beam energy. The users' specification is that peak brilliance should satisfy $B > 1 \times 10^{33}$ph/s/mm^2/mrad^2/0.1% bandwidth at higher photon energies. It is noted that the calculations here are for an ideal case and that, in reality, some effects may degrade the performance—for example, the bunch may have an energy chirp, or there may be bandwidth broadening or power reduction due to undulator wakefields. Therefore, a factor of two contingency is added to the required peak brilliance, i.e., the choice of undulator technology and beam energy must provide $B > 2 \times 10^{33}$ph/s/mm^2/mrad^2/0.1% bandwidth. The calculations are shown in Fig 137, where the yellow region corresponds to the peak brilliance exceeding the threshold, including contingency. Clearly, at $E = 4.5$ GeV, none of the technologies provides sufficient brilliance, whereas, at $E \geq 5.5$ GeV, all undulator technologies are satisfactory.

Based on the previous analysis, a nominal CompactLight beam energy of 5.5 GeV was chosen. This is the minimum beam energy at which all undulator technologies will provide sufficient FEL brilliance. Still, this energy is also lower than that of SwissFEL at PSI, which has a lower photon energy reach.

The semi-analytical predictions in the figures were later supported by initial time-dependent FEL simulations using ideal nominal electron bunches and selecting a specific design from four groups of the technology options assessed—a CPMU design, a DELTA design, a Hybrid design and a helical SCU design. The results are summarized in Table 44. The analysis and simulations concluded that CompactLight should adopt helical SCU undulator technology as the baseline technology choice.

The selectable polarization is varied by means of two APPLE-X-type afterburners positioned downstream of the SCU devices. The analysis that informed this design choice is described later in Sect. 6.1.2.5. The electron beam becomes microbunched by the FEL at the required wavelength in the SCU, and then, just prior to saturation, when the level of microbunching is sufficient, yet the energy spread growth is still modest, it enters the afterburner. It radiates strongly, producing coherent output with the required polarization. The afterburner can have a longer period λ_{AB}: the resonant energy range of the afterburner must be matched to that of the SCU. The maximum period length is limited by the maximum photon energy, and the minimum period length is given by enough field strength to meet the minimum photon energy. The λ_{AB} value is selected, so that when the SCU and the afterburner are both at maximum field, they are resonant at the same wavelength. The caveat is that the afterburner cannot produce output at 16 keV, because the resonance condition cannot be satisfied here. However, as will be shown in Sect. 6.1.2.5, the afterburner can provide satisfactory polarized output at photon energies as high as 12 keV, in line with the science case requirements, and crucially, the decision to employ an afterburner for variably polarized output enables the SCU device to be optimized to produce output at photon energies exceeding that available from variably polarizing devices, i.e. up to 16 keV. It should be noted that obtaining variable polarization in the HXR range by means of optical manipulation in the photon beamline is still considered very inefficient and deemed too high risk for a user facility.

Therefore, the FEL concept consists of identical undulator lines for both SXR and HXR operation regimes supplied by different electron beam energies. Figure 138 shows a schematic view of these lines. Given the simultaneous requirement of large wavelength tuning and two-color operation with close photon energies, both undulator lines are constrained to have identical parameters and tunability, with the exception that the two SCU undulators will have opposite helicity, as already discussed.

The next section presents the derivation of the main parameters of the SCU and the afterburner. Unless otherwise stated, the electron beam parameters assumed for all subsequent calculations and simulations are the nominal parameters given in Table 3: charge 75 pC, peak current 5 kA, normalized emittance 0.2 mmmrad, bunch length 5 μm, energy range 2–5.5 GeV, and rms energy spread 1×10^{-4} at 5.5 GeV. The following major sections concern the detailed design of the helical SCU devices (Sect. 6.1.3) and associated beamline elements and finally the afterburner devices (Sect. 6.1.4).

6.1.2 Derivation of undulator specification

This section presents a summary of the analysis which was used to determine the required specification of the SCU and the afterburner. The parameters determined are the SCU aperture, which is dependent on the degrading effect of wakefields on the FEL performance, the SCU period, the SCU module length, the SCU field tolerances, and the required length of afterburner.

6.1.2.1 SCU aperture

The electron beam generates an image current on the finite conducting vacuum chamber, which acts back to the electron bunch due to its small size. This effect is known as the resistive wall wakefield effect and has a magnitude inversely proportional to the aperture and bunch duration. Wakefield effects inside the undulator can

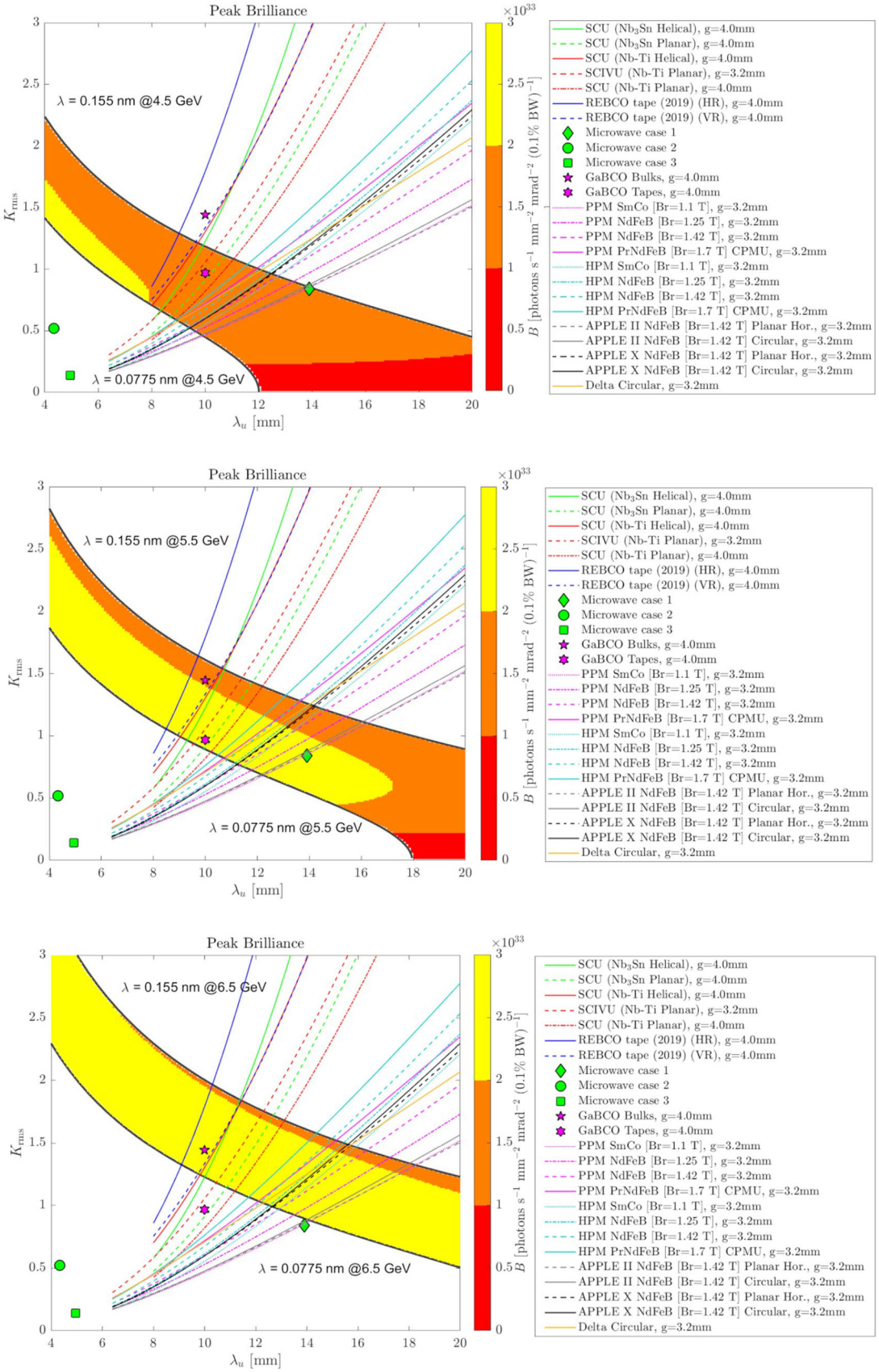

Fig. 137 Peak brilliance for electron beam energies 4.5 GeV (top), 5.5 GeV (middle), and 6.5 GeV (bottom)

Table 44 Results of GENESIS time-dependent simulations

Parameter	Units	CPMU	Delta	Hybrid	SCU
Saturation power	GW	9.1	8.9	7.6	9.8
Saturation length	m	24.5	26.5	29.1	15.6
Sat. pulse energy	μJ	49	48	29	54
FWHM bandwidth	10^{-3}	0.987	0.975	0.996	1.16
Peak brightness	$\times 10^{33}$ ph/s/mm^2/mrad^2/0.1%bw	2.39	2.37	1.98	2.18

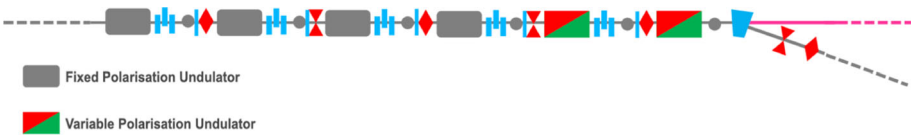

Fig. 138 Schematic of the XLS undulator line for both HXR and SXR FEL layouts

cause significant electron beam energy loss and energy spread growth, which can degrade the performance of the FEL by reducing the saturation power and increasing the bandwidth. The wakefields, therefore, determine the minimum SCU aperture for effective FEL performance. The analyses in this section of the effect of the wakefields on the FEL performance and the effectiveness of the mitigating strategy of applying a longitudinal taper to the undulator field estimate that a full aperture of 4.2 mm is aggressive, yet acceptable.

For an accelerator operating at room temperature, the vacuum chamber material is generally assumed to be in the regime of the normal skin effect (NSE). The effects of resistive wakefields in the NSE regime have been detailed in several studies for round and flat beam-pipes [212–215]. In the case of (ultra-)cold metal surfaces, the resistive wall effects enter the anomalous skin effect (ASE) regime, where metals' AC conductivity differs from in the NSE. The effect of resistive walls in the ASE regime has been studied for long and short beams in [216, 217]. For a bunch of a few μm duration, the resistive wakefield effect is essentially independent of the skin regime (i.e., temperature) and material choice (i.e., aluminium or copper): any difference due to skin effect regime and material choice is negligible.

The wake potential, i.e., the wakefield-induced energy loss per meter along the single bunch, can be calculated by convolving the single particle wake function $\omega(z)$ with the electron longitudinal line charge density $\rho(z')$ [218]

$$E_\omega(z) = \int_{-\infty}^{z} \omega(z - z')\rho(z')\mathrm{d}z', \tag{42}$$

where z is the position along the undulator and z' is the electron longitudinal coordinate with respect to the head of the bunch. The generated current distribution and wake potentials along the bunch for different apertures are shown in Fig. 139.

The effect of the wakefield on the FEL was investigated by importing the calculated wake potential (Eq. 42) into the Genesis 1.3 simulation code [219]. The undulator period was the nominal 13 mm and the wavelength was 0.76 Å (photon energy 16 keV). The simulation was performed for a helical undulator and the vacuum chamber was assumed to be copper and round.

It is seen that the energy loss due to the wakefield can be compensated by gradually tapering the undulator field strength. The left panel of Fig. 140 shows the evolution of the FEL power for different apertures and tapering options, while the right panel shows the evolution of the bandwidth. It is seen that the saturation power decreases for smaller aperture values. For a 4 mm aperture ($r = 2$ mm), linearly tapering the undulator field by 0.9 % along the undulator (from the beginning to the end) compensates the negative effect of the wakefield on the saturation power, with only a small increase in bandwidth. It is, therefore, concluded that an aperture of 4 mm is a realistic design choice—the wakefields are seen to affect the FEL, but a practical mitigating technique is effective.

6.1.2.2 SCU period length

In the XLS design, the same undulator line is used in both the SXR *and* the HXR—this feature allows the facility to be more compact and cost-effective than other FEL facilities which have separate undulator lines for different wavelength regimes, but it does mean that care has to be taken to ensure that the undulator parameters are chosen appropriately to balance the output performance equally between the SXR and the HXR. As will be shown, pushing to shorter undulator periods is better for the HXR, but this is at the cost of reduced performance

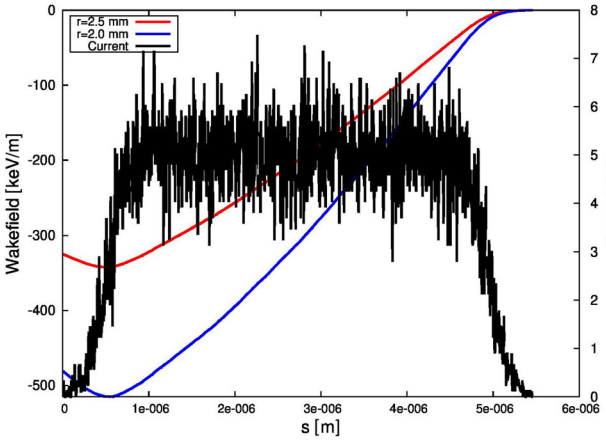

Fig. 139 Generated current distribution of 5.5 GeV electron bunch and the wake potentials along the bunch for different beam-pipe radii (the head of the beam is to the right)

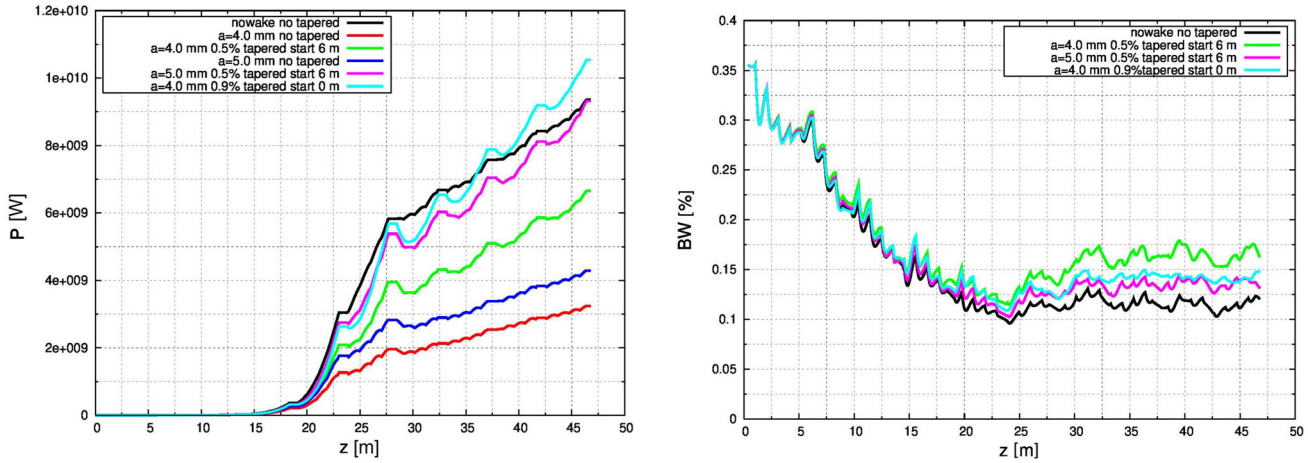

Fig. 140 Left: evolution of power in undulator region for different apertures (averaged over the full FEL pulse). Right: bandwidth along the undulator for different apertures

in the SXR, which favors longer periods. An assessment has, therefore, been made of the required undulator period to properly balance the FEL output performance across the whole SXR and HXR tuning range.

The assessment was done using the widely used semi-analytical model developed by Ming Xie [67], described in Sect. 3.3.4.1, which provides a rapid comparison of relative FEL performance for different undulator periods. The results of the calculations are shown in Fig. 141. The top plot shows the pulse energy as a function of photon energy, and the middle plot shows the estimated saturation length, neglecting the length of any gaps between the undulator sections, i.e., the active undulator length. The bottom plot shows the electron beam energy. The calculations assume the nominal electron bunch parameters. The pulse energy is calculated as $\Delta_t \times P_{sat} \times FF$, where Δ_t is the full pulse duration, P_{sat} is the saturation power, and $FF = 0.6$ is an empirical 'filling factor' accounting for the spikiness of the SASE radiation pulse. To maximize the pulse energy at each wavelength, both electron beam energy and undulator field should be maximized, fulfilling the already defined resonance condition

$$\lambda_r = \frac{\lambda_w}{2\gamma^2}\left(1 + a_w^2\right), \tag{43}$$

so to operate at maximum beam energy for a given wavelength, the undulator parameter a_w must be as large as possible. However, the beam energy for CompactLight is capped at 5.5 GeV for 100 Hz operation and 2.36 GeV for 1 kHz operation, so at some point as the wavelength is reduced (the photon energy is increased), it becomes necessary to start reducing the undulator parameter which gives weaker performance. For example, for 11 mm undulator period, this occurs at a photon energy of approximately 15 keV. Figure 141 therefore shows the *maximum* pulse energies obtainable by freely varying the electron beam energy. In reality, operating at a set of fixed beam

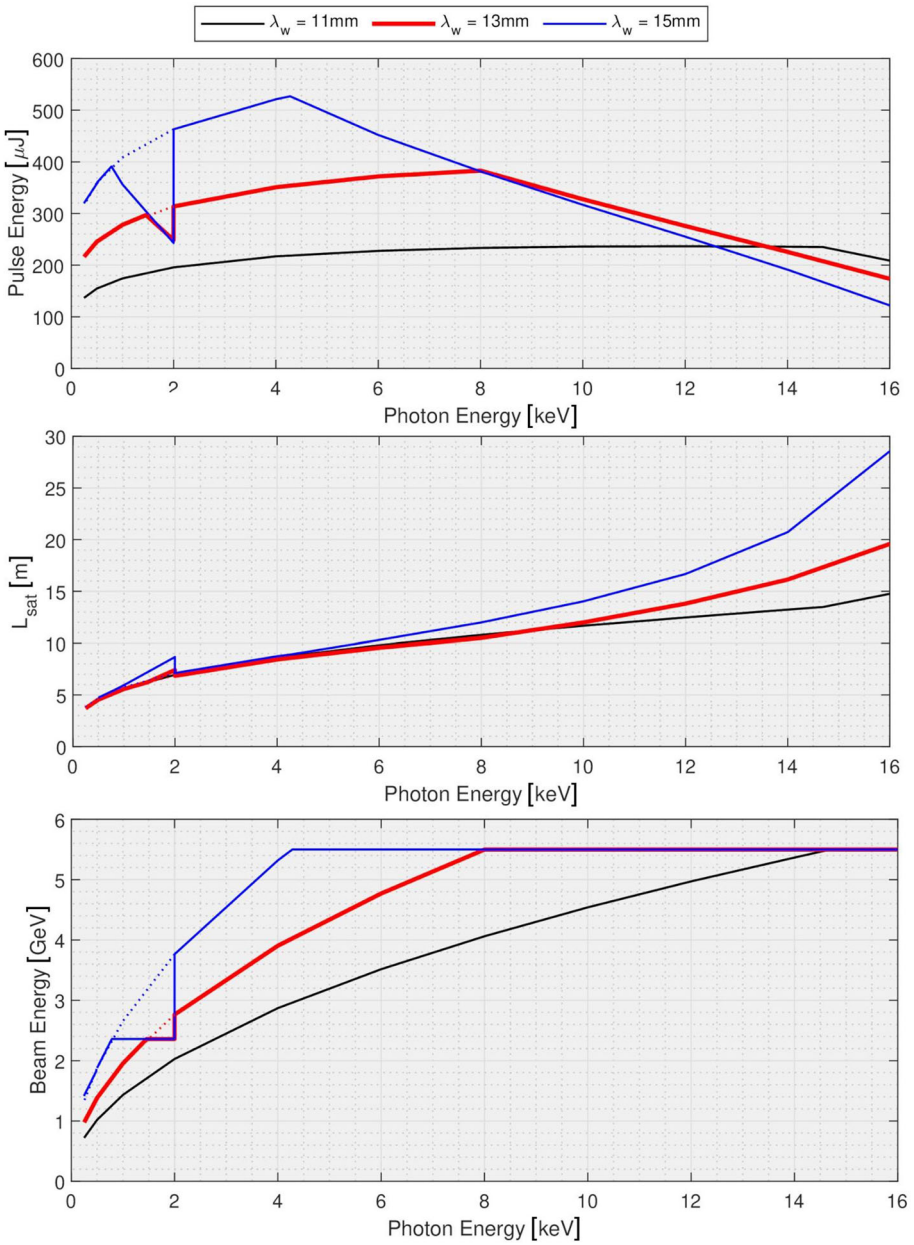

Fig. 141 Semi-analytical performance calculations, showing comparison between 11 mm SCU period, 13 mm SCU period (baseline choice), and 15 mm SCU period, showing pulse energy (top), saturation length (middle), and electron beam energy (bottom). The solid lines are relevant to the case where the electron beam energy in the SXR is limited to 2.36 GeV, which is required for operation at 1 kHz repetition rate. The dashed lines at photon energies less than 2 keV are for the case where SXR operation is at 100 Hz in which case the 2.36 GeV energy limit does not apply

energies is more convenient. The dotted lines relate to the case where CompactLight operates in the SXR at 100 Hz.

The calculations show that compared to the baseline period choice of 13 mm, 11 mm only gives higher pulse energy at photon energies greater than 14 keV and reduced saturation length at photon energies above 10 keV, whereas 15 mm gives progressively lower pulse energy and longer saturation length above 8 keV. However, at lower photon energies, the situation is reversed—below 12 keV, the 11 mm period is significantly worse, and below 8 keV, the 15 mm period offers the best performance. It is anticipated that will be fewer users for photon energies above $\approx$ 14 keV where the 11 mm period is the best choice, and the 15 mm period would require another 10 m

of undulator, compared to the 13 mm period, to reach saturation at 16 keV. Therefore, the optimum choice for balanced performance across the whole operating range is $\lambda_w = 13\,\text{mm}$.

6.1.2.3 SCU module length

The long undulator required for the FEL will comprise a number of individual modules in series. This allows the periodic insertion between modules of focusing quadrupoles, phase shifters, diagnostics, and vacuum components. A study was done to determine the optimum length of the individual undulator modules. The primary consideration was the output performance of the FEL, with secondary consideration given to compactness, cost, and ease of construction and operation.

Simulations were performed using Genesis 1.3. Module lengths from 1 m to 4 m were considered, and for each module length, the quadrupole focusing was scanned over a range to determine the maximum saturation power and minimum saturation length for each length of undulator module. The gap between modules was fixed at 0.5 m. This study was done using nominal electron beam parameters, once in the HXR for 16 keV photon output, and once in the SXR for 2 keV photon output. More weighting was given to the HXR results when choosing the optimum module length. Figure 142 shows the results for the HXR with the left plot showing the saturation

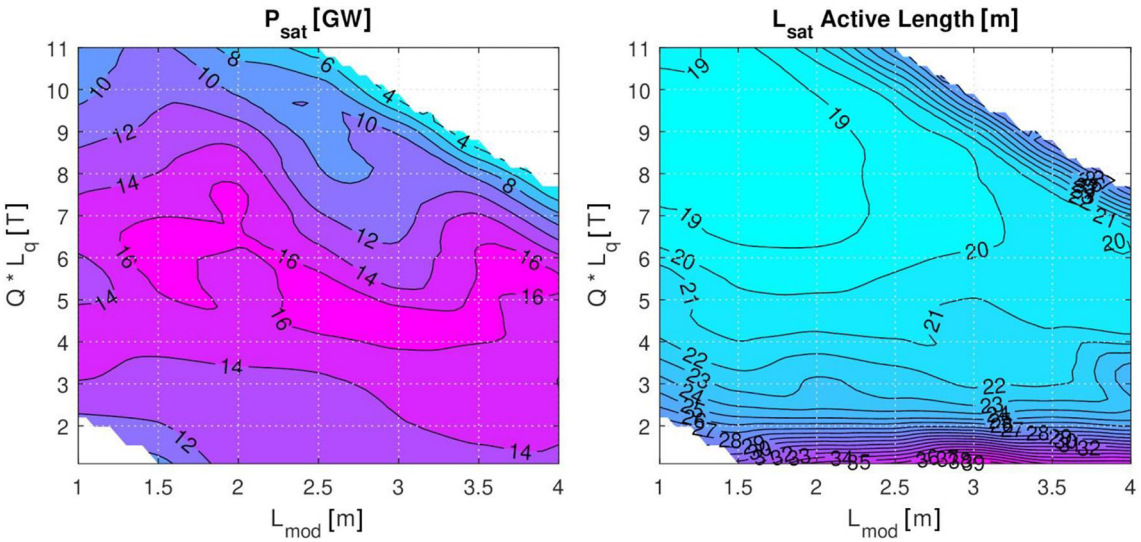

Fig. 142 HXR saturation power and *active* undulator length (i.e., excluding the length of the gaps between the modules) as a function of module length and integrated quad strength

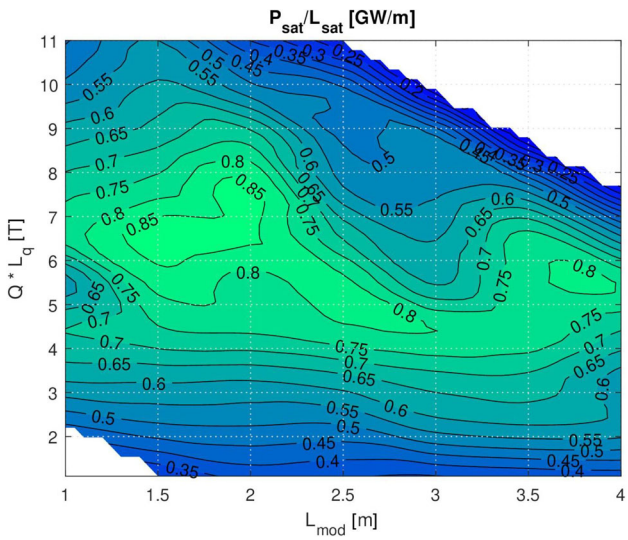

Fig. 143 Saturation power normalized by active saturation length as a function of module length and integrated quad strength

power and the right plot showing the *active* undulator length (i.e., excluding the length of the gaps between the modules), which is a more useful measure for cost optimisation than floor length. Figure 143 shows the same data but expressed in terms of undulator 'efficiency', i.e., saturation power normalized by the active saturation length.

The data show that to obtain maximum saturation power, the module length can be between 1.25 m and 4 m, but to minimize the active undulator length. Hence, the total cost of the undulator, the module length should be less than 2.1 m. To obtain maximum undulator efficiency, $P_{\rm sat}/L_{\rm sat}$, the optimum length is 1.75 m. The equivalent data for the SXR (not shown) indicated that for maximum saturation power, the module length should be 2.25 m, but the optimum is broad, and for a module length of 1.75 m, the reduction is only 5 %. The data for SXR saturation length are not relevant, because the saturation lengths are much shorter in the SXR and so do not determine the total length of undulator required for the facility. The conclusion, therefore, is that the optimum module length is 1.75 m.

6.1.2.4 SCU field tolerances

The mechanism of exponential gain in the FEL is a resonant process that amplifies a narrow bandwidth of radiation. The radiation bandwidth at saturation σ_λ/λ is approximately equal to the FEL ρ-parameter, with typical value $\rho \approx 5 \times 10^{-4}$ at HXR wavelengths. The FEL wavelength is given by the resonance condition, Eq. 43, and any variation during the exponential gain process of parameters in this equation acts to broaden the bandwidth and degrade the FEL gain. It is, therefore, critical that errors of the undulator parameter a_w along the beamline are within a satisfactory tolerance level.

An estimate of the tolerable variation in the undulator parameter can be derived by differentiating the resonance condition to find

$$\frac{\sigma_{a_w}}{a_w} = \frac{1+a_w^2}{2a_w^2}\frac{\sigma_{\lambda_r}}{\lambda_r} \approx \frac{1+a_w^2}{2a_w^2}\rho, \tag{44}$$

and using CompactLight parameters for 16 keV operation, this gives an estimated field variation tolerance of $\sigma_{a_w}/a_w \approx 8 \times 10^{-4}$.

Simulations were also done using Genesis 1.3 with the FEL operating at 16 keV. The code allows random field errors to be added to each period, with the errors correlated to minimize the field integrals. This ensures that any degradation in FEL performance is due to perturbations of the resonance condition rather than trajectory wander. The results are shown in Fig. 144. This shows that errors in the undulator parameter exceeding $\sigma_{a_w}/a_w \approx 1 \times 10^{-3}$ could give a reduction in output power of more than 5 % and increase in the saturation length of more than 0.6 m. This level of error is close to the analytically derived specification.

The baseline tolerance is specified as $\sigma_{a_w}/a_w < 1 \times 10^{-3}$. From SCU modelling, this translates to a tolerance in the placement of the windings of approximately 20 μm which is acceptable. Reducing field errors below 1×10^{-3}

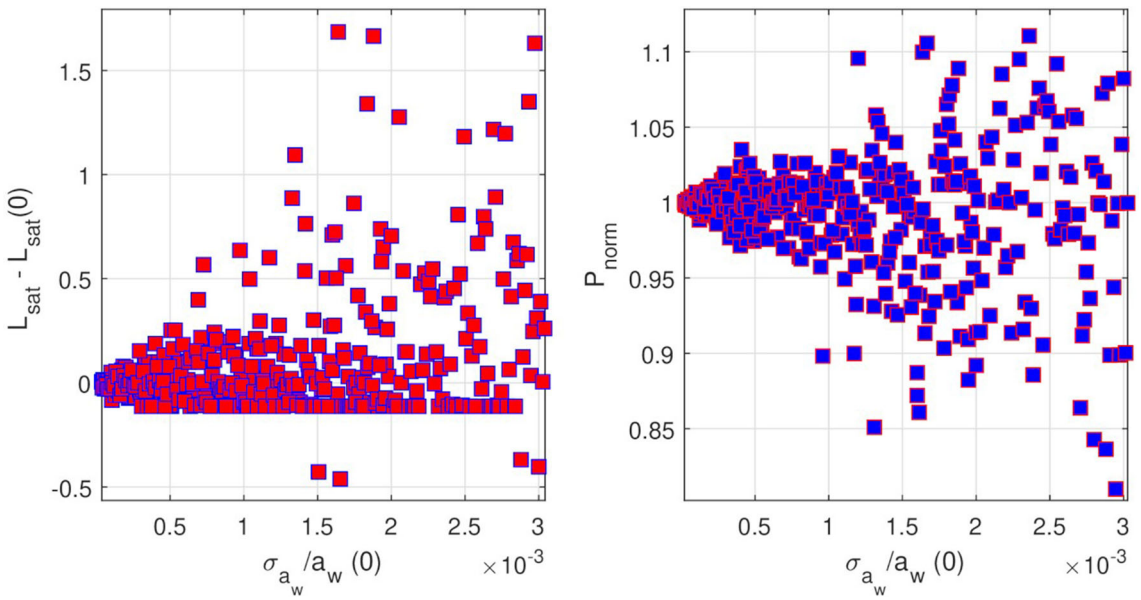

Fig. 144 Increase in saturation length and peak power degradation due to random errors in the undulator parameter a_w

would provide a small advantage for FEL performance, but this would have to be balanced against the feasibility and cost of the tighter tolerance.

6.1.2.5 Afterburner requirements

As described in Sect. 6.1.1, the baseline design comprises a helical SCU followed by a variably polarizing APPLE-X afterburner. This section presents a simulation study (using Genesis 1.3) that optimizes the output performance of the afterburner in the SXR and the HXR and determines the length of afterburner required to produce useful output. A comparison is also made between the baseline configuration and an alternative scenario for providing variably polarized FEL output comprising an undulator line built entirely from APPLE-X devices.

In the simulations, the microbunched electron beam from the SCU section is propagated into the afterburner section, but the radiation is artificially blocked. This means that the degree of polarization of the afterburner output can be assumed to be near perfect (in fact, this cannot be proven from the simulations, because polarized fields are not supported by Genesis 1.3). In practice, the radiation from the SCU can be 'blocked' by setting the afterburner at a small angle and kicking the electron beam onto its axis with a corrector [220] or by applying an inverse taper in the SCU, which allows the electron beam bunching to develop but suppresses the radiation output [221].

To obtain optimum flux from the afterburner, the level of microbunching in the beam as it enters must be sufficient to create an initial intense burst of coherent output, but not so great that the associated energy spread growth prohibits further exponential growth. This optimisation was studied in the SXR at 250 eV and in the HXR at 12 keV. The afterburner period is set to 19 mm. This assumes an in-vacuum device of gap 5 mm, and means that the resonant photon energy at the maximum field is the same as that of the SCU at the maximum field, so that the tuning ranges of the two devices are matched to each other. Note that out-of-vacuum and cryogenic versions of the APPLE-X design are also under consideration, as will be discussed in Sect. 6.1.4.2. These versions might require a slightly different period choice, but the results of this section are still relevant. The peak brilliance, the total length of the undulator line, and the pulse energy at the end of the afterburner are used as the figures of merit to characterize the FEL performance.

The results in the HXR, at 12 keV resonant photon energy, are summarized in the top plot of Fig. 145 which shows the pulse energy and peak brightness as a function of the number of SCU modules and number of afterburner modules. Peak brightness of 9×10^{32} photons/s/mm^2/mrad^2/0.1%bw can be obtained using 6 modules of the SCU and two modules of the afterburner. This configuration generates a pulse energy of 35 μJ. Adding another afterburner module increases the brightness slightly to 10×10^{32} and the pulse energy to 50 μJ. The equivalent results in the SXR, at 250 eV photon energy, are shown in the bottom plot of Fig. 145. At this photon energy, only a single SCU module and a single afterburner module are required to obtain the maximum peak brightness of 6×10^{31} photons/s/mm^2/mrad^2/0.1%bw and a pulse energy of 230 μJ. Using a second afterburner module does not increase the brightness but increases the pulse energy to 260 μJ.

From these results in the HXR and SXR, a single afterburner module is insufficient—two are required to achieve near-maximum brightness. The extra brightness and pulse energy that could be obtained in the HXR by adding a third afterburner is modest. The baseline configuration is, therefore, specified to comprise the helical SCU followed by two APPLE-X afterburner modules. It is also proposed, for contingency, to consider leaving an empty slot in the lattice for later installation of a third afterburner device if required.

The SCU + APPLE-X baseline configuration is now compared to alternative scenarios where the entire undulator line is a helical SCU or an APPLE-X. The HXR results are shown in Fig. 146, and for completeness, the SXR results are shown in Fig. 147. The z-axis is the distance through the undulator line. In the HXR baseline, the SCU extends to 13.6 m and the two modules of APPLE-X afterburner are from 13.6 m to 18.1 m. In the SXR baseline configuration, the changeover from SCU to APPLE-X occurs earlier, because there is only one SCU module in use. It is clear that in the HXR, the baseline configuration has the advantage of being significantly more compact than the alternative scenario of using an APPLE-X undulator for the whole FEL line. The disadvantage is that the peak brightness obtained is only 25 % of that obtainable from the APPLE-X on its own, and the pulse energy is only 27 %. However, the baseline configuration allows the FEL to operate at much higher photon energies—the SCU is effective at up to 16 keV whereas the APPLE-X cannot reach much above 12 keV without operating at very weak a_w values which give very poor performance.

To conclude, the baseline configuration of a helical SCU followed by two modules of APPLE-X afterburner is a significantly more compact solution for the production of variably polarized FEL output in the HXR than the alternative scenario of using a variably polarizing APPLE-X undulator for the whole FEL line. Variably polarized light can be produced at photon energies up to about 12 keV which satisfies the user requirements. A disadvantage

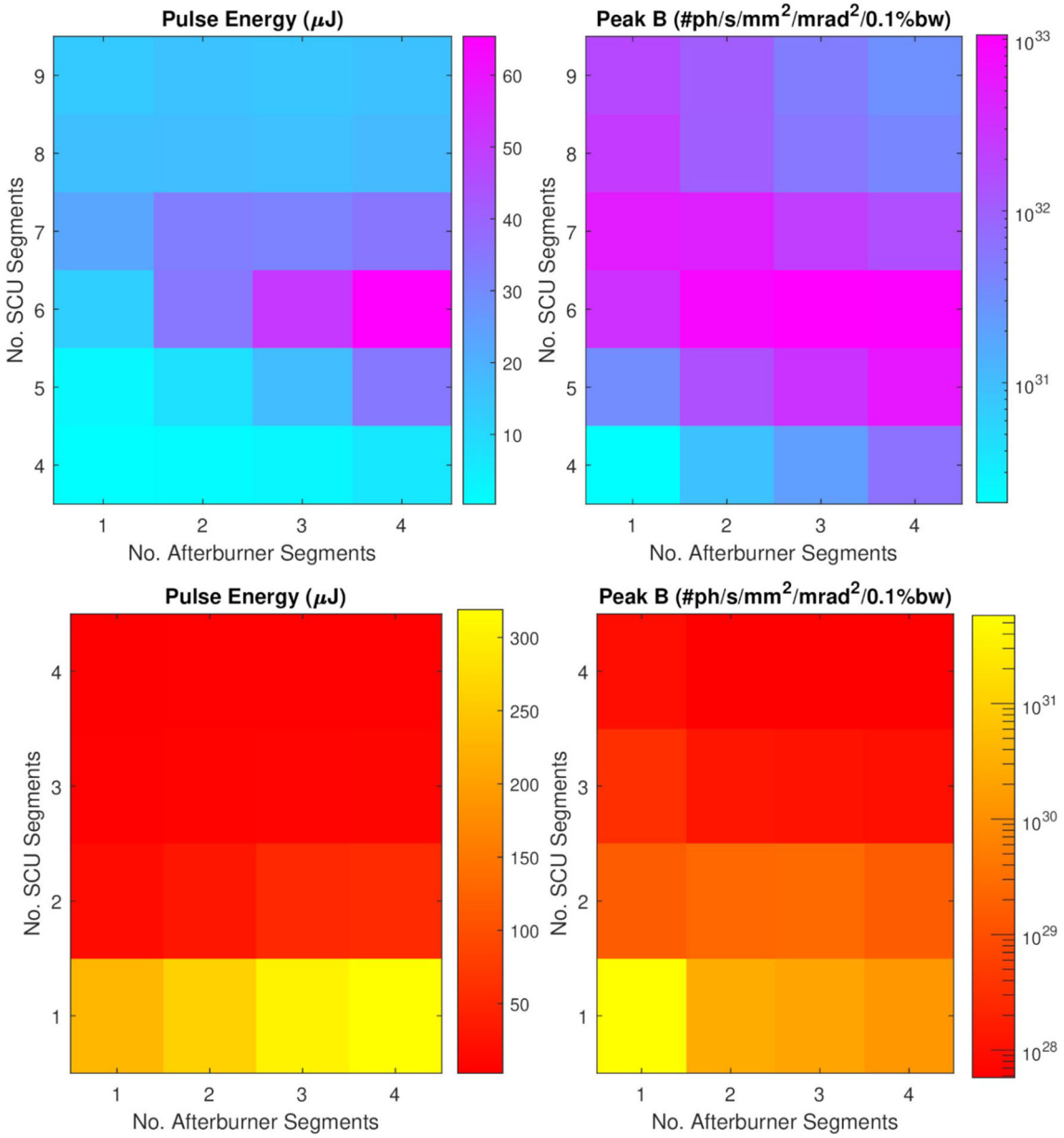

Fig. 145 Top: aterburner pulse energy and peak brightness in the HXR at 12 keV photon energy, as a function of the number of SCU modules and number of afterburner modules. Bottom: equivalent results in the SXR at 250 eV photon energy

is that the pulse energies and brightness are reduced to less than 50 % of that available with a standalone APPLE-X, but this is more than offset by the fact that using the SCU section on its own circularly polarized FEL light can be produced with pulse energies in the 100 s of μJ at photon energies up to 16 keV.

6.1.2.6 Parameter summary

The main parameters of the SCU and APPLE-X afterburners are summarized in Table 45.

6.1.3 The self-amplified spontaneous emission lines

The investigations reported in the deliverable report D5.1 [222], comparing a wide range of undulator technologies in terms of achievable key parameters determining both the performance and compactness of the facility, lead to the choice of helical superconducting undulators as the baseline for the Self-Amplified Spontaneous Emission

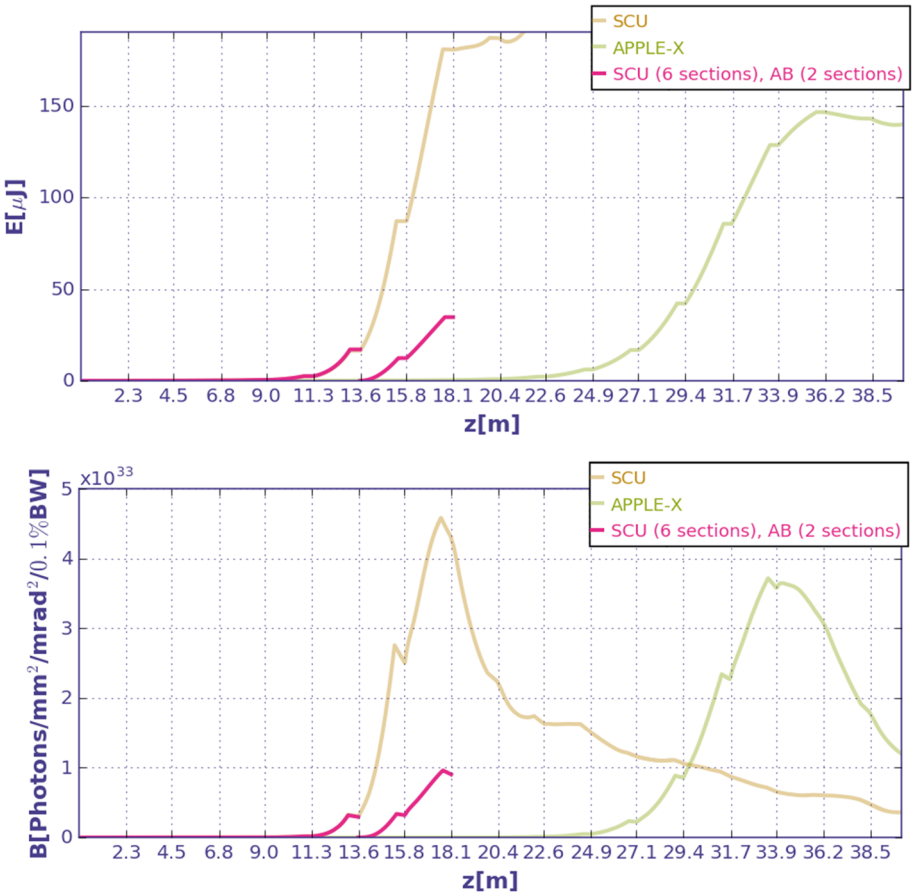

Fig. 146 HXR: comparison of 12 keV pulse energy (left) and peak brightness (right) for three different scenarios: an SCU, an APPLE-X in vertically planar configuration, and the baseline SCU and APPLE-X configuration. The tick marks and labels on the z-axis correspond to the locations of the ends of individual undulator modules

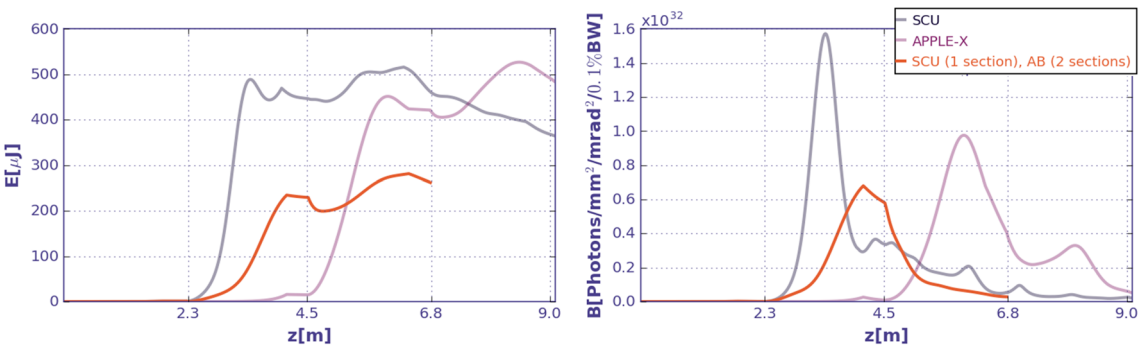

Fig. 147 SXR: comparison of 250 eV pulse energy (left) and peak brightness (right) for three different scenarios: an SCU, an APPLE-X in vertically planar configuration, and the baseline SCU and APPLE-X configuration

(SASE) lines for CompactLight. Table 46 summarizes the main functional parameters of the SASE line according to the specifications derived in Sect. 6.1.2.

In terms of electron beam optics, the SASE lines form an FODO lattice with one undulator magnet inserted into each half cell. In addition, each half FODO cell is equipped with a phase shifter to keep the phases of radiation field and undulating particle motion matched between subsequent undulator modules, and a cavity beam position monitor for minimal beam diagnostics. A balancing of the optimisation objectives for the hard and the soft X-ray cases (see Sect. 6.1.2) led to the Pareto optimal choice of geometric and focusing parameters and subsequent requirements for the focusing and phase-shifting magnets described in the following sections.

Table 45 Summary of the main undulator parameters

	Main undulator	Afterburner
Technology	NbTi superconducting	APPLE-X
polarization	Helical	Variable
Period length λ_w	13 mm	$\approx$ 19 mm
Maximum a_w	1.33	1.80
Beam gap	4.2 mm	5 mm
Module length	1.755 m	1.75 m

Superconducting undulators have been considered for the Linac Coherent Light Source upgrade (LCLS-II) [223], and the conceptual design for the CompactLight SASE line adopts conceptions developed in the conceptual design phase of the LCLS-II superconducting undulators [224, 225].

For the superconducting undulator, the phase shifters and the quadrupoles, for the cooling scheme of each of these components, as well as for the overall layout of the supporting and cooling infrastructure, there are a number of technological choices. The choice was made to use virtually iron-free designs for all magnetic components, i.e., they are laid out as coil-dominated superconducting magnets based on NbTi technology. That implies that the magnets at least of each half FODO cell, including the beam pipe, form a cold mass which needs to be maintained at an operating temperature range below 4.5 K. For the cryomodule design, as well as for the refrigeration scheme and infrastructure, a set of different options was considered. Each of these options comes with advantages and disadvantages in terms of investment, running costs, efficient use of resources, downtimes due to maintenance, and likely also overall reliability of operation.

6.1.3.1 Basic concept layout

Table 46 General functional parameters of the CompactLight SASE lines

	Value	Units
Undulator		
Period length	13	mm
Length (incl. matching periods)	1.755	m
(Periods)	135	
Magnetic gap	5.0	mm
Beam-pipe bore diameter	4.2	mm
a_w (8 keV)	1.33	
a_w (16 keV)	0.617	
$B_{\max}$ on axis (at 80 % on the load line)	1.09	T
Phase shifter		
Phase integral	2000	T^2 mm^3
Geometric length	$\leq$ 170	mm
FODO quadrupole magnet		
Integrated field gradient	10	T
Active length	60	mm
(Geometric length)	$\leq$ 100	mm
Alignment Quadrupole magnet		
Integrated field gradient	2	T
Geometric length	$\leq$ 50	mm
FEL lines		
Cryomodule length	2.255	m
Number of modules	2×16	

From the multi-objective optimisation of the undulator module length and the integrated FODO quadrupole strength described in Sect. 6.1.2.3, it was concluded that the optimum undulator module length is $L_u = 1.75\,m$ with an integrated focusing gradient of about 7 T. The gap between undulator modules was fixed at 500 mm: this value has to accommodate quadrupoles, phase shifters, diagnostics, and transitions between cryomodules. For the conceptual undulator design, an undulator module length of $L_u = 1.755\,m$ is chosen, corresponding to 135 periods of 13 mm length, including the matching periods at both ends of the undulator. According to the simulations of the $E_{ph} = 16\,keV$ photon energy working point described in Sect. 4.2, FEL saturation would be reached after 11 undulator magnet units. Accounting for contingency, the design includes 16 units per SASE line.

Each of the two SASE lines consists of 16 identical, 2.255 m-long cryomodules, each housing one undulator module plus the components for focusing, phase matching, diagnostics, and beam-based alignment, all operated at liquid helium temperature. These modules can either be minimally sectioned, i.e., forming together one long, continuous cryostat, or sectioned, i.e., intercepted by cold-warm transitions. In the former case, two additional short transition modules at the entrance and the exit of the minimally sectioned cryostat are required. The two options for the cryostat layout will be discussed later on in more detail.

A unique property of the CompactLight facility is enabled by applying different winding schemes for the undulators in FEL-1 and FEL-2, respectively, namely a left-handed helical winding scheme for FEL-1 and a right-handed one for FEL-2. This arrangement will allow for ultra-fast helicity switching in that sub-set of photon beamlines which is served by both FEL lines.

Cryomodule structure

The general structure of the cryomodules is sketched in Fig. 148. The cold mass consists, in the order upstream to downstream, of a superconducting short-alignment quadrupole magnet, the superconducting helical undulator magnet, a superconducting phase shifter, which also serves as a vertical and horizontal field integral corrector magnet, a superconducting FODO quadrupole magnet and a cold, i.e., capable of operation at ∼4 K, cavity beam position monitor.

The beam pipe is an integral part of the cold mass. The pipe is made of aluminium and has a round aperture with 4.2 mm bore diameter. It is sectioned in at least four parts: (1) undulator section, (2) straight section, (3) BPM section, and (4) cryostat interconnection section.

In the undulator section, the winding body incorporates the beam-pipe meaning that the pipe is directly cooled to the SCU operation temperature level. The other parts of the beam pipe not in direct mechanical contact with the phase shifter and quadrupole magnet apertures are indirectly cooled by contact with the undulator section and, if required, through additional thermal connections to directly cooled parts. Details have to be elaborated in the course of the technical design for the particular cryogenic concept chosen. The BPM section will accommodate a cold cavity beam position monitor which for the sake of compactness is assumed to operate in the X-band, as will be discussed in more detail in Sect. 6.1.3.4.

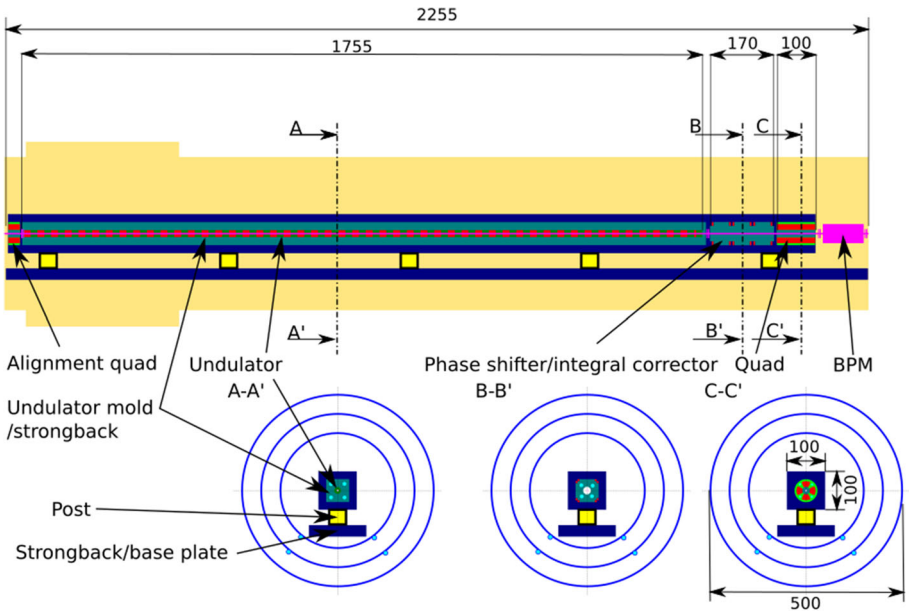

Fig. 148 Basic layout of the SCU cryomodule

The design of the cryostat interconnection section depends on the chosen overall cryostat layout options. In the case of a minimally sectioned cryostat layout, the interconnection section of the beam pipe is designed for compensating the thermal contraction of the cold mass. In the case of a sectioned layout, cold-warm transitions have to be realized in addition.

In the following subsections, the conceptual designs for the elements forming the cold mass are described, along with the underlying design principles and considerations on the design requirements and general considerations for the integration of these components into a complete, modular system.

Superconducting undulator design features

A helical superconducting undulator (HSCU) is chosen for use in the CompactLight undulator lines. For the hard X-rays, the HSCU must be able to produce photons in the energy range 8–16 keV from an electron beam of energy 5.5 GeV. Given this photon energy range, the undulator must be capable of producing a peak transverse on-axis field of 1.09 T, corresponding to an a_w value of 1.33. The undulator will have a beam-pipe bore diameter of 4.2 mm and a magnetic inner winding diameter of 5 mm. The parameters of the HSCU are summarized in Table 46.

The undulator fields can be generated by a bifilar winding of superconducting wire. The winding consists of two helical coils separated by half an undulator period, with current flowing in opposite directions in the two coils. There are several choices for the use of superconducting wire for the HSCU. Given the short period and winding diameter, the niobium–titanium (NbTi) wire, which is more malleable than the niobium–tin (Nb_3Sn) wire, was chosen. For the design work, the choice of superconducting wire was chosen to be SuperCon VSF-678 0.44 mm-diameter NbTi wire.

The choice of material for the HSCU former and poles was investigated. The use of ferromagnetic helical poles between the undulator windings can be used in bifilar undulators to boost and shape the on-axis field. However, due to the short undulator period, the pole thickness would be very short, resulting in saturation of the poles at low currents. Also, it would be difficult to manufacture a ferromagnetic double helix and mount it separately on a non-ferromagnetic tube. It would be easier to machine a single ferromagnetic piece into a helix with a remaining thickness. The on-axis fields for different wire currents and the corresponding load lines for three cases are shown in Fig. 149 left and right, respectively. The cases are for conductors with no iron poles, a model with iron poles but non-ferromagnetic beam tubes, and poles and beam tubes made from iron. The models assume a coil stack consisting of 100 wires, poles which are 2 mm thick and a beam tube of 0.5 mm thickness.

From Fig. 149 left, iron poles can help boost the undulator on-axis field. However, the iron also increases the field on the conductor at a given wire current and hence increases the operating point of the superconductor at a given current. Given the boost to the fields from the poles, an undulator with iron poles could achieve the target field at a lower current than an undulator without iron poles.

However, in the case where both the poles and beam pipe are made from iron, the on-axis field is reduced compared to the case where only the poles are made from iron. The iron beam pipe partially shields the bore from the undulator field. Also, for a given wire current, the peak field on the conductor is higher for the case with the iron beam pipe than for the case with iron poles only. Manufacturing a double helix with an iron beam pipe will reduce the on-axis field and increase the operating point of the superconductor for a given current. Although a non-ferromagnetic former would not increase the field generated by iron poles, the effects of the iron beam-pipe shielding the field and increasing the field on the conductor could be avoided.

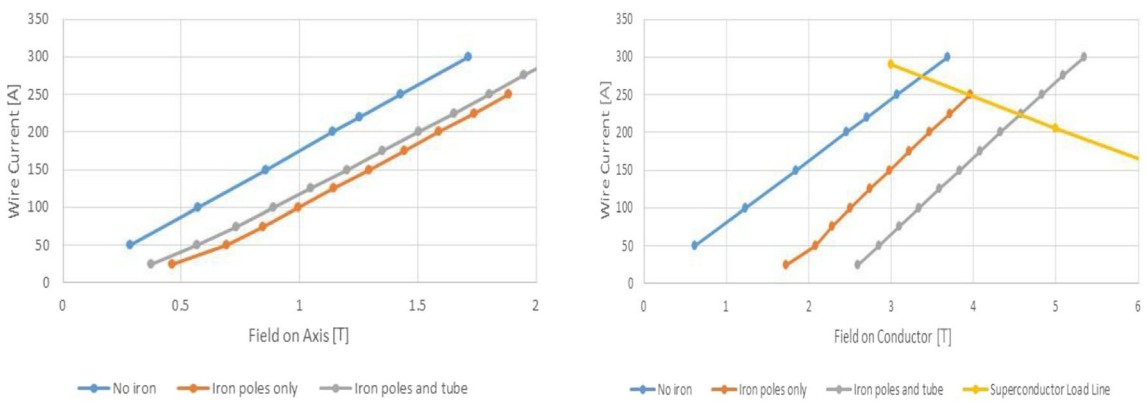

Fig. 149 On-axis fields for different wire currents for models with and without iron (left). Superconductor load lines for models with and without iron (right)

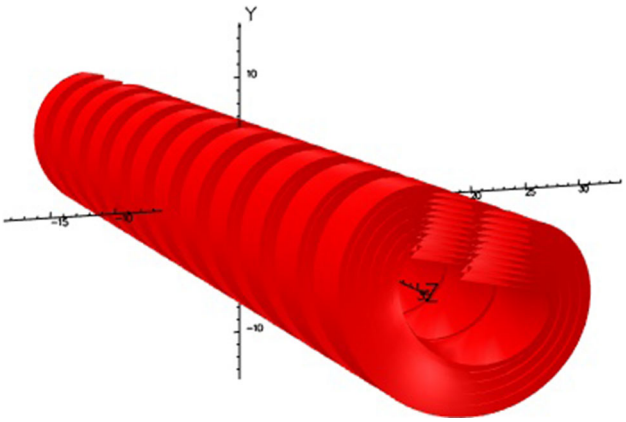

Fig. 150 Image of the Opera-3D conductor model used to investigate the load lines of different winding stack configurations

Therefore, the superconducting undulator windings were assumed to be wound onto an aluminium helical former. As well as reducing the superconducting operating point, an aluminium former would be beneficial due to its high heat conductivity, allowing the former to be cooled to cool the superconducting wires indirectly.

Given the choice of an aluminium winding former, different winding stack configurations were investigated. A model in which the layers of conductors were modelled as conductor bricks of different thicknesses (depending on the number of turns of wire in the layer) was developed to investigate the load lines of different stack configurations. Figure 150 shows an image of the model used. The model does not contain any end effects.

A winding stack consisting of 10 layers of NbTi wire with a 9-8-9-8 turn arrangement was chosen. This arrangement would produce the maximum on-axis field of 1.09 T at 78.9 % of the NbTi wire critical current. The load

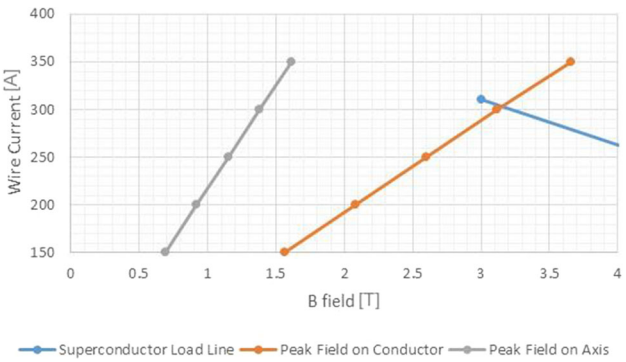

Fig. 151 Load line for chosen wire stack arrangement

Fig. 152 Cut through of undulator winding, showing the winding stack

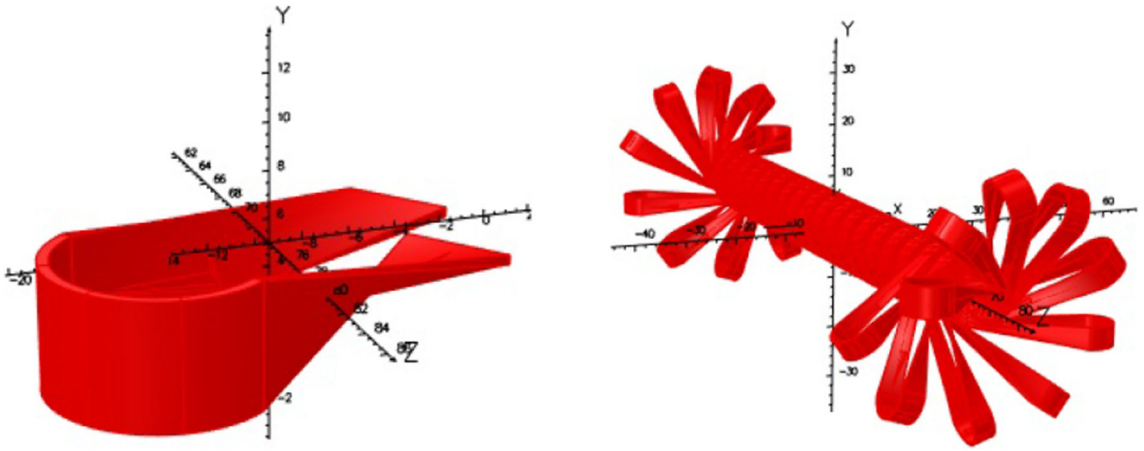

Fig. 153 Left: image of a single turnaround model. Right: image of 10-period long undulator module with turnarounds modeled

line for this stack arrangement is shown in Fig. 151. For this stack configuration, the winding stack would have a width of 4.98 mm at the bottom and a radial height of 3.87 mm. Therefore, the minimum wall thickness between the grooves will be 1.52 mm. Figure 152 shows an image of a cut-through of the undulator, showing the winding stack.

A turnaround design has been developed to allow the undulator to be wound from a single length of superconducting wire without the need for superconducting joints between wire sections. At the ends of the undulator, the wires come away from the helix at a tangent to the helix. The wires are turned around a non-ferromagnetic pin which is perpendicular to the winding direction, and then returned into the adjacent winding groove. There are ten turnaround pins at each end of the undulator former, spaced 36° apart from each other. There is one

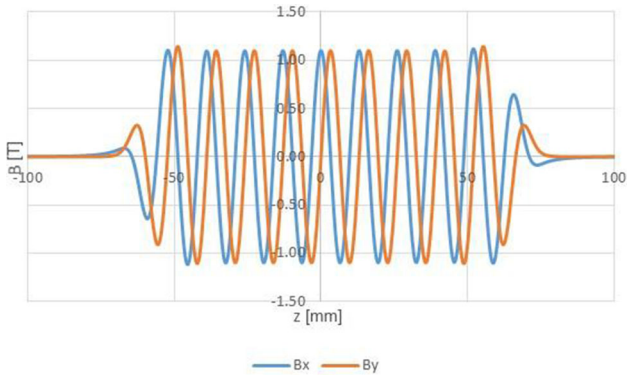

Fig. 154 Example field profile through an Opera 3D model of the superconducting undulator containing ten full periods

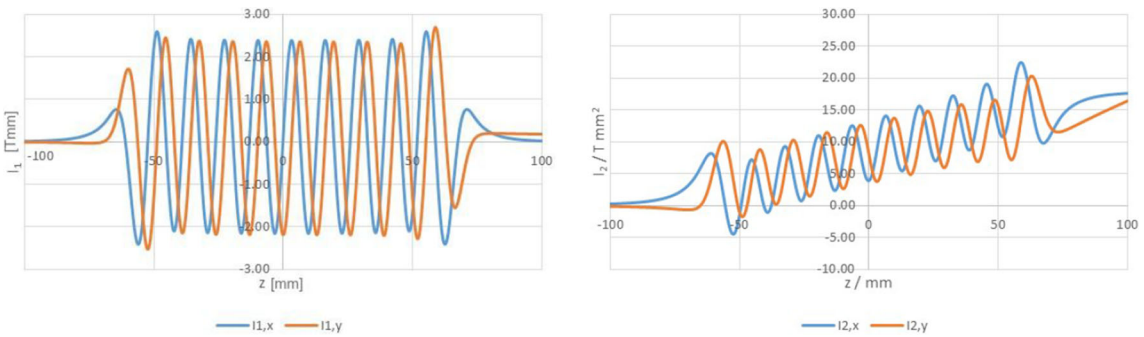

Fig. 155 First (left) and second (right) field integral of the field profiles shown in Fig. 154

turnaround pin per layer of wire in the winding stack. The turnarounds are spaced by one-tenth of the undulator period in the axial direction. The turnarounds occur over a single period at each end of the undulator. In this way, the magnitude of the transverse field is decreased over the end undulator period. In Fig. 153, the left panel shows the Opera-3D conductor model of a single 20 mm long turnaround, while the right panel shows the complete 10-period long model with all turnarounds.

Figure 154 shows an example field profile generated by the HSCU model with the turnarounds modelled. The peak transverse field in the undulator main body is 1.10 T. The perpendicular distance from the undulator axis to the centre of the turnaround pin was 20 mm. Figure 155 shows the first (left) and second (right) field integrals through this model field profile. From the figures, it is apparent that the field integrals through the undulator with the turnarounds would be non-zero. Therefore, correction magnets would be needed outside the HSCU to correct the trajectory of the electron beam. These correction magnets can be integrated into the design of the phase shifters between undulator modules.

The magnitude of correction depends on the distance of the turnaround pins from the undulator axis. The larger the distance, the smaller the effect of the turnarounds on the on-axis field and hence the small correction required. From the average first field integrals measured in the main body of a 10-period undulator model as a function of the turnaround length, it results that a maximum first field integral correction of approximately 0.3 Tmm will be required. Increasing the turnaround length decreases the necessary field integral correction, but it will make it harder to cool the wires at the turnarounds. If the turnarounds are kept close to the undulator body, they can be kept cold to prevent the turnarounds from quenching.

6.1.3.2 Phase shifters

General considerations

The radiation phase, $\Phi(z)$, in an undulator is defined by Eq. 45 [226], where λ_r is the wavelength of radiation produced in the undulator, z is the coordinate on the longitudinal axis where the phase is measured, γ is the relativistic Lorentz factor of the electron beam, e is the electron charge, m_e is the electron rest mass, c is the speed of light in vacuum, and the term PI is referred to as the phase integral and is defined in Eq. 46 [227], where $B_x(z')$ and $B_y(z')$ are the field profiles in the x- and y-directions, respectively

$$\Phi(z) = \frac{\pi}{\lambda_r}\left(\frac{z}{\gamma^2} + \left(\frac{e}{\gamma m_e c}\right)^2 \times \mathrm{PI}\right), \tag{45}$$

$$\mathrm{PI} = \int_{-\infty}^{\infty}\left(\left(\int_{-\infty}^{z} B_x(z')\mathrm{d}z'\right)^2 + \left(\int_{-\infty}^{z} B_y(z')\mathrm{d}z'\right)^2\right)\mathrm{d}z. \tag{46}$$

Equation 45 can also be rewritten in terms of the undulator wavelength, λ_u, and the undulator deflection parameter, K (defined in Eq. 48 [226])

$$\Phi(z) = \frac{2\pi}{\lambda_\mathrm{u}(1 + K_\mathrm{rms}^2)}\left(z + \left(\frac{e}{m_e c}\right)^2 \times \mathrm{PI}\right), \tag{47}$$

$$K_\mathrm{rms} = \frac{eB_\mathrm{rms}\lambda_\mathrm{u}}{2\pi m_e c}. \tag{48}$$

In an ideal undulator, the phase advances by 2π per period [226].

Undulator lines in an FEL or synchrotron require many periods to reach saturation, and hence need to be many meters long. It is not practical to construct undulators which are many meters long due to manufacturing tolerances and strict requirements on the electron beam properties [228]. Instead, undulator lines are designed with undulator modules with break sections between the undulators. These break sections contain elements including quadrupoles, beam position monitors, and phase shifter magnets [229].

Over a break section, the transverse magnetic field profile is different to that inside an undulator; therefore, the phase advance over the break section will be different to the phase advance through the body of the undulator. This will cause a phase difference between the photons produced in one undulator module and those produced in subsequent modules. This change in phase results in an interruption to the amplification process by causing electrons to gain energy from the radiation field. This phase mismatch then results in an increase in saturation length [230] and a decrease in pulse energy for the undulator system [231].

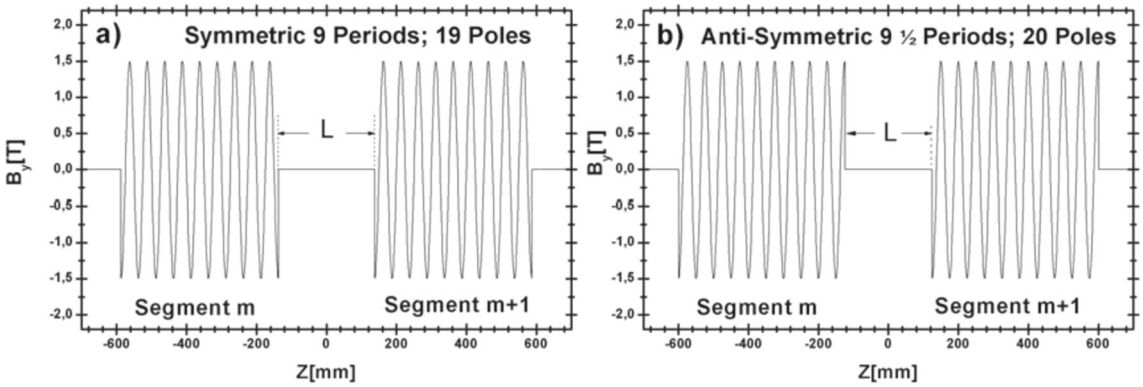

Fig. 156 Examples of simplified symmetric and antisymmetric undulator arrangements. These figures assume no undulator fringe fields [228]

If an electron traverses a break section of length L which has no transverse magnetic fields, the phase advance can be calculated using Eq. 49

$$\Phi(L) = \frac{2\pi L}{\lambda_{\mathrm{u}}(1 + K_{\mathrm{rms}}^2)}. \tag{49}$$

In a simplified picture with no undulator fringe fields, there are two cases of undulator cells that need to be considered. These are the symmetric case when the last pole of one undulator segment and the first pole of the following segment have the same polarity (Fig. 156a) and the antisymmetric case when the first and last poles of subsequent sections have opposite polarity (Fig. 156b) [228].

To maintain the condition for constructive interference of radiation between separate undulator modules, the phase advances over the break section must meet the condition specified in Eq. 50

$$\Phi(L_{\mathrm{b}}) = \nu\pi, \tag{50}$$

where ν is called the Phase Number [228]. For even symmetry, ν must be a positive, even integer; for odd symmetry, ν must be a positive, odd integer.

If the undulator K value is changed, the phase advance over a break of fixed length L_{b} will change. To maintain the constructive interference condition in Eq. 50 for multiple undulator K values, the phase advance over the break section needs to be variable.

A variable phase advance over a break section can be achieved using a magnetic structure known as a phase shifter. This structure creates a magnetic chicane which causes a phase delay across a break section without affecting the overall trajectory of the electron beam. The standard requirement for phase shifters to ensure no overall effect on the electron trajectory is that the first and second field integrals through the undulator go to zero [228]. The first and second field integrals are directly proportional to the angle between the electron beam and the axis and the transverse displacement of the beam from the axis, respectively [226]. If the break section contains a transverse magnetic field profile, the phase advance over the break section can be calculated from Eq. 47.

The phase integral term is a useful metric for quantifying the phase delay imparted by a phase shifter magnetic field in an undulator break section. Equations 47 and 50 can be combined to define the minimum necessary phase integral of a phase shifter as a function of the break length L_{b} and undulator deflection parameter K

$$\mathrm{PI} = \left(\frac{m_e c}{e}\right)^2 \left(\frac{\nu\lambda_{\mathrm{u}}(1 + K_{\mathrm{rms}}^2)}{2} - L_{\mathrm{b}}\right) \geq 0. \tag{51}$$

The inequality in Eq. 51 must be met, because the phase shifter can only impart a positive phase delay on the electron beam [232]. To allow for a constant range of tuning of the undulator K parameter, the phase number ν should be chosen, so that the same value of ν can be used for all undulator parameters and that the phase integral will always be greater than 0 [228]. Therefore, the largest phase integral needed for a device will be determined by the smallest undulator K parameter that will be used in the undulator lines (i.e., the highest energy radiation).

In reality, the actual phase integral required for an undulator line will be more complicated than Eq. 51. The fringe fields at the ends of the undulator modules will need to be accounted for. The actual phase advance between main body poles in the undulator modules would be calculated by integrating the field data, and the necessary

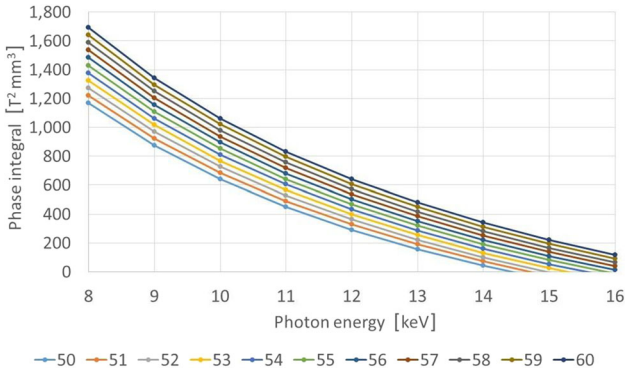

Fig. 157 Required phase integral to reach different phase numbers, as a function of photon energy

Table 47 Summary of the phase shifter requirements

Parameter	Value	Units
Maximum phase integral	2000	T^2 mm^3
Maximum overall length	170	mm

phase integral in the break section to achieve constructive interference would have to be determined. Equation 51 provides a good first estimate for the magnitude of the phase integral required for a given undulator break section.

XLS phase shifter requirements

The preliminary specifications give an intersection length between undulator modules of 500 mm. Assuming that 500 mm is the distance from the end pole of one undulator to the first pole of the next undulator, the phase advance over the intersection can be calculated using Eq. 47. The actual phase advance between modules would have to be measured, to account for the end fields of the undulators.

Equation 51 can be used to determine the phase integral that is required through a phase shifter magnet to satisfy Eq. 51 as a function of the undulator K parameter for different values of the phase number, ν. Assuming a break length, L_b, of 500 mm, the required phase integral as a function of the XLS radiation energy range for different phase numbers is shown in Fig. 157.

Figure 157 shows that for a given photon energy, a larger phase integral is required to achieve a larger phase number, ν. For lower phase numbers, the required phase integral for a given photon energy may be negative. A phase shifter cannot generate a negative phase integral, because the chicane can only delay the electron beam. The minimum even phase number (referring to the symmetric case in Fig. 156) that requires a positive phase integral for the whole tuning range is 56. The minimum odd phase number (referring to the asymmetric case in Fig. 156) that requires a positive phase integral for the whole tuning range is 57.

The maximum required phase integrals for values of ν of 56 and 57 are 1482 T^2 mm^3 and 1535 T^2 mm^3, respectively, which are the phase integrals required for the lowest photon energy of 8 keV. Therefore, if the end fields of the undulator are not considered, the maximum phase integral through a phase shifter for the XLS FEL will be 1535 T^2 mm^3. To allow for some tolerance on this value and to potentially account for an extra delay required due to the undulator end fields, a maximum target phase integral of 2000 T^2 mm^3 was considered for the phase shifter conceptual design. The requirements for the XLS phase shifters are summarized in Table 47.

Phase shifter conceptual design

The basic conceptual magnetic design for the CompactLight phase shifters consists of six pairs of superconducting coils oriented to create three dipole chicane in the horizontal (x) and vertical (y) directions simultaneously. A model of the basic conceptual magnetic design as modelled in Opera 3D is shown in Fig. 158.

In the arrangement shown in Fig. 158, the current in the central coils would be twice that in the corresponding end coils. This would provide a magnetic field profile consisting of three dipole kicks in the x and y directions, where the central kick would be of twice the magnitude and in the opposite direction to the end kicks. The result to the electron trajectory would be to introduce a non-zero phase shift while imparting no overall change to the direction or displacement of the electron beam (the first and second field integrals measured through the phase shifter would go to zero).

Figure 159 shows example field profiles, first field integrals, second field integrals, and phase integrals, respec-

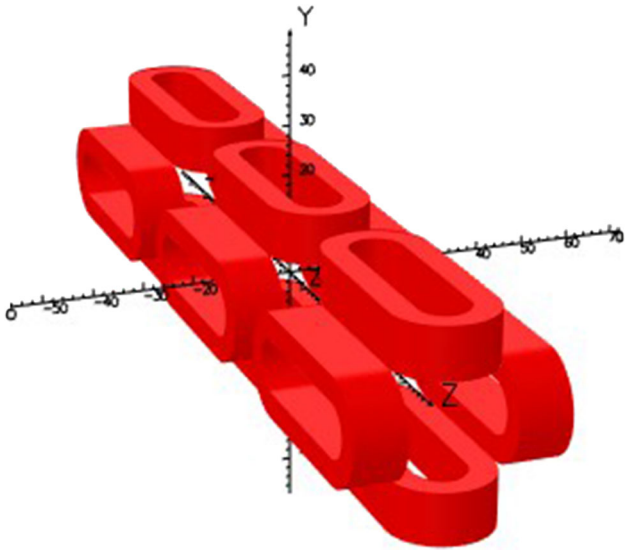

Fig. 158 Image of Opera 3D model of phase shifter conceptual magnetic design. The red rings represent superconducting coils

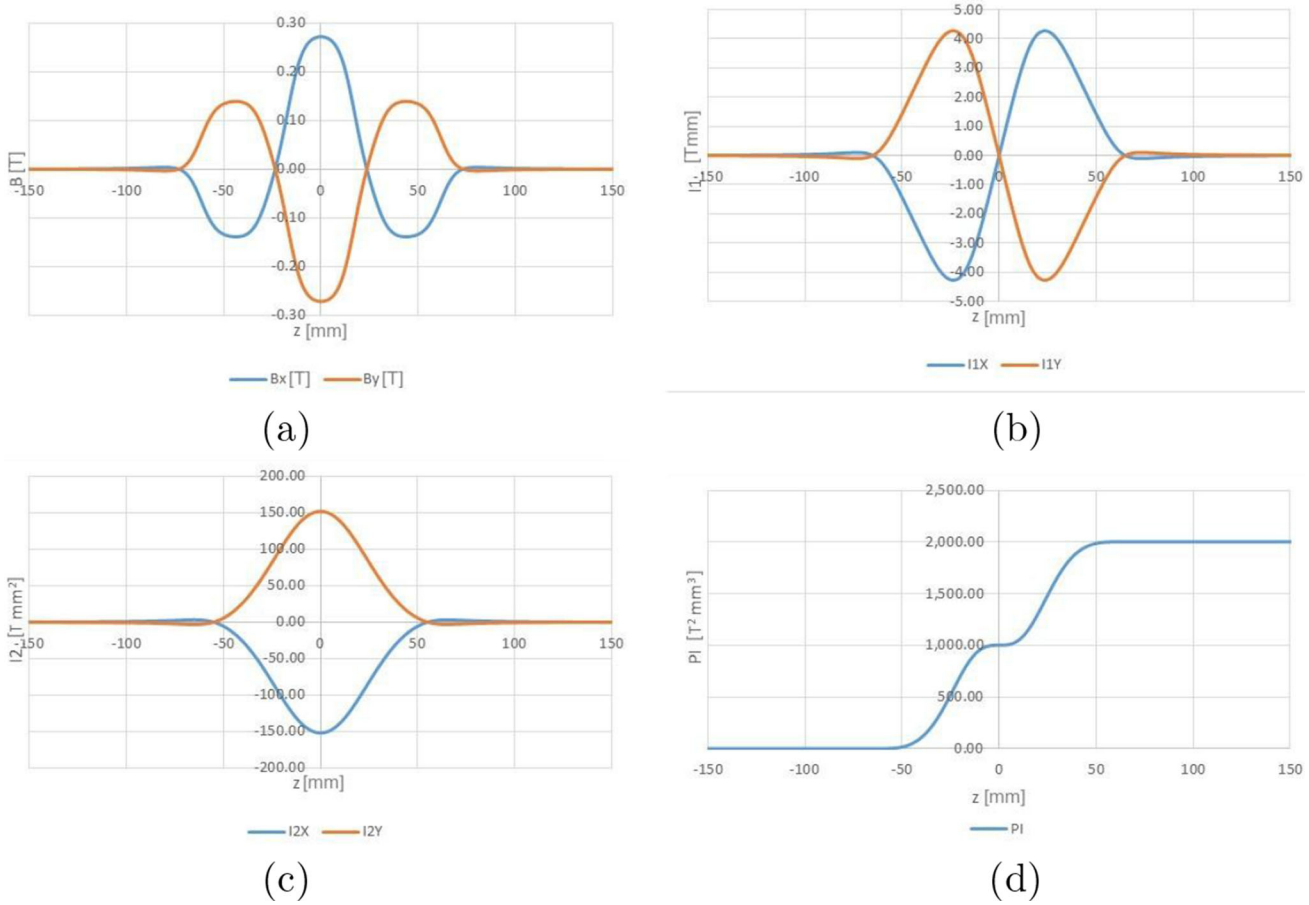

Fig. 159 Field profile (**a**), first field integrals (**b**), second field integrals (**c**), and phase integral (**d**) through an example coil-dominated phase shifter model

tively, for the conceptual magnetic design. This arrangement causes the first and second field integrals to go to zero, while providing a non-zero phase integral. Figure 159b, c shows that the first and second integrals of both the B_x and B_y fields go to zero when measured through the length of the phase shifter. This shows that the change to the angle of the electron beam trajectory from the axis and the corresponding transverse displacement of the beam from the axis would not be affected by the presence of the phase shifter. This is one of the common requirements for a phase shifter magnet. Figure 159d shows that while the first and second field integrals through the magnet can be made to go to zero, the phase integral through the magnet is non-zero. Therefore, this coil arrangement can provide a phase shift and hence provide the necessary correction to maintain the condition for constructive interference of the synchrotron radiation.

The conceptual design could also be used as an integrated phase shifter and trajectory corrector. If the 6 coil pairs are all powered individually, it should be possible to tune the field and phase integrals across the undulator break section to give any desired combination of first and second field integral and phase integral. This would allow correction to angular and positional displacements of the electron beam caused by the non-periodic fields at the ends of the undulators. If the field strengths can be tuned independently, then any combination of trajectory correction (in both planes) and phase correction should be achievable.

This design produces fields using superconducting coils only. The field is not boosted by iron poles. The use of iron poles would boost the fields produced by the phase shifter at low currents. However, at higher coil currents, the pole pieces would become saturated. Saturation of the iron poles would change the field integrals through the phase shifter and make it difficult to achieve zero field integrals because each of the poles would saturate differently. It was decided that a current-dominated design would allow larger phase integrals to be achieved while maintaining the condition for cancellation of the first and second field integrals. Also, with a current-dominated design, the on-axis fields scale linearly with the coil current and the phase integral scales linearly with the square of the coil current. This would make it easier to tune the value of the phase integral through the phase shifter.

Size considerations

Several example coil geometries and current densities—as required in the central coils (assuming the same current density in Bx and By coils)—have been considered to achieve the target phase integral of $2000\,\mathrm{T}^2\ \mathrm{mm}^3$. The different geometrical parameters of the coils will have an influence over the current and size requirements of the phase shifter:

- Decreasing the physical length of the phase shifter will provide more space for other components in the inter-undulator sections, such as quadrupoles and beam position monitors. Minimizing the current in the coils will reduce the heat load from the current leads and reduce the operating point of the superconducting coils, making them less likely to quench.
- Increasing the inner length of the coils allows the fields to cover a longer axial distance. Consequently, the on-axis fields can be lowered to achieve a given phase integral and the current density in the coils can be reduced. However, the total physical length of the phase shifter will increase.
- Increasing the coil width increases the minimum separation between coils and the total length of each coil but increases the number of turns in the coils.
- Increasing the coil thickness also increases the number of turns. Increasing the number of turns in the coils allows larger fields (and hence phase integrals) to be achieved for lower current densities in the coils. The current can be minimized by increasing the coil cross-sectional area, at the cost of using more superconducting wire to wind the coils.
- Increasing the inner width of the coils, the minimum face-to-face separation between a coil pair increases, and therefore decreases the magnitudes of the on-axis fields (and hence phase integrals) for a given current density. However, the inner radius needs to be large enough to allow for a sufficiently large bend radius at the ends of the coils for the wires to be turned around.
- Increasing the axial separation between coils increases the phase integral through a phase shifter at the cost of increased total length.
- The coil dimensions can be optimized for the space and cooling power available in the XLS SCU cryostat. The general trend is that longer phase shifters require smaller current densities to achieve the target phase integral of $2000\,\mathrm{T}^2\ \mathrm{mm}^3$.

Overall, this coil design would be capable of simultaneously correcting the phase shift and trajectory errors between undulator modules by providing tuneable dipole chicanes in the horizontal and vertical directions. The exact coil dimensions would need to be optimized. Total lengths as short as 85 mm could be achieved using NbTi wires, but would require higher currents in the coils. This would require more cooling power and the coils would operate closer to their quench point. This would provide less margin for tuning the fields for combined phase and trajectory correction. Increasing the coil dimensions would reduce the required currents in the coils; this would reduce the heat loads and operating points of the superconductor.

Proposed mounting and cooling structure

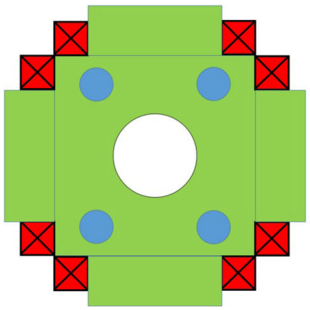

Fig. 160 Proposed method for mounting and cooling phase shifter coils

The coils shown in Fig. 158 would need to be mounted and cooled. The proposed mounting method is shown in Fig. 160. Each coil would be wound onto a former made from non-magnetic material with high thermal conductivity, which would act as a heat sink. Aluminum would be a desirable choice for this heat sink. The coils could then be potted in these aluminium formers. Pipes containing a forced flow of liquid helium through the heat sink would provide cooling to the coils.

The conceptual magnetic design presented here is of six superconducting coil pairs, which could act as a simultaneous phase and trajectory corrector between the undulator modules for the CompactLight FEL. At the nominal physical length of 170 mm, the phase shifter would be able to achieve phase integrals larger than the target maximum of $2000\,\mathrm{T}^2\,\mathrm{mm}^3$ at low coil current densities. The coil dimensions could be reduced, and hence, the total physical length of the phase shifter could be reduced below 170 mm. At physical lengths of 85 mm, the arrangement would still be able to reach the target maximum phase integral. However, if the coil dimensions and total physical length are reduced, the coil currents required to achieve the target phase integrals will increase. Therefore, there will be a larger heat load from the coil current leads that need to be cooled.

6.1.3.3 Quadrupoles

The undulator line FODO cells are composed of a focusing quadrupole (F), a defocusing quadrupole (D) and the virtually non-focusing superconducting undulators which for the beam optics in first order can be treated as drift spaces. Superconducting coil-dominated quadrupole magnets are proposed. These consist of four current-carrying coils which create a magnetic flux density that grows proportionally to the radial distance

$$B_x = gy, \quad B_y = gx, \tag{52}$$

where g is the nominal field gradient.

In the following, the multipole expansion of the transverse magnetic field in the complex plane is used:

$$B = B_y + iB_x = \sum_{n=1}^{\infty} (B_n + iA_n)(x + iy)^{n-1}, \tag{53}$$

with B_n and A_n are the normal and skew multipole components, respectively, $n = 2$ refers to the quatrupole component. The field gradient is related to the multipole component of order $n = 2$ by

$$g = \frac{B_2}{R_{\mathrm{ref}}} \tag{54}$$

with the reference radius R_{ref} which is typically chosen to be 2/3 of the magnet aperture.

The main parameters for the FODO quadrupoles are specified in Table 48. The design should be accurate enough to achieve $\Delta g/g \leq 0.1\,\%$ over the specified good field region. To meet this field quality requirement and to minimize the content of higher order multipole components, a coil configuration of sectors and wedges of 12°–18°–30° has been developed for the SASE FODO quadrupole magnets, following concepts described, e.g., in [233, 234]. The coil configuration is depicted in Fig. 161. Calculations and optimisations were carried out with the magnet design software OPERA [235].

The four superconducting coils forming the quadrupole winding are held together by means of laminated non-magnetic collars which are surrounded by laminated iron yokes. The inner radius of the coils and the coil width are considered to be 7 mm and 3 mm, respectively. Simulations were done for a NbTi coil-based quadrupole with a

Table 48 FODO quadrupole main parameters

Parameter	Value	Units
Integrated field gradient	10	T
Field gradient	167	Tm^{-1}
Effective length	60	mm
Inner aperture radius	7	mm
Horizontal good field region	±5	mm

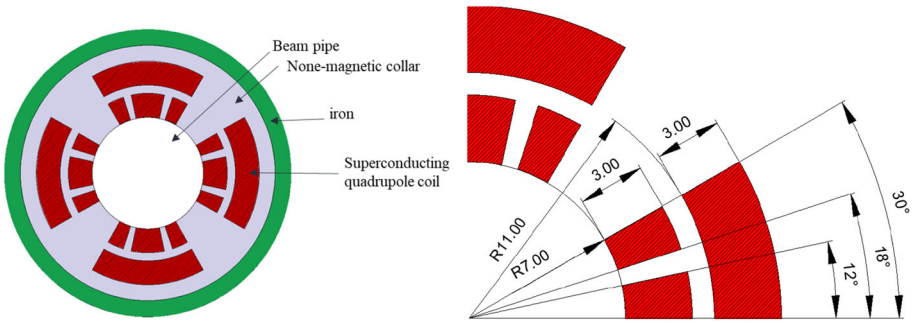

Fig. 161 Geometry layout (left) and coil configuration in one quadrant of the magnet (right)

field gradient of 167 Tm^{-1} and magnetic length of 60 mm. The current density to achieve the desired field strength is taken to be 380 A mm^{-2} which is well below the limitations of NbTi for the applied magnetic field at 4.5 K.

The modulus of the magnetic flux density in the central plane $z = 0$ is shown in Fig. 162.

For calculating the field gradient at $x = 5$ mm versus the longitudinal direction in Opera 3D, the field is calculated on circles with radius 5 mm which are moved in the beam direction in steps of 2 mm. Using a Fast Fourier Transformation, the magnetic field, the field gradient, and higher order harmonics are obtained in each location. Having the field gradient at different longitudinal locations, one can calculate the integrated field gradient

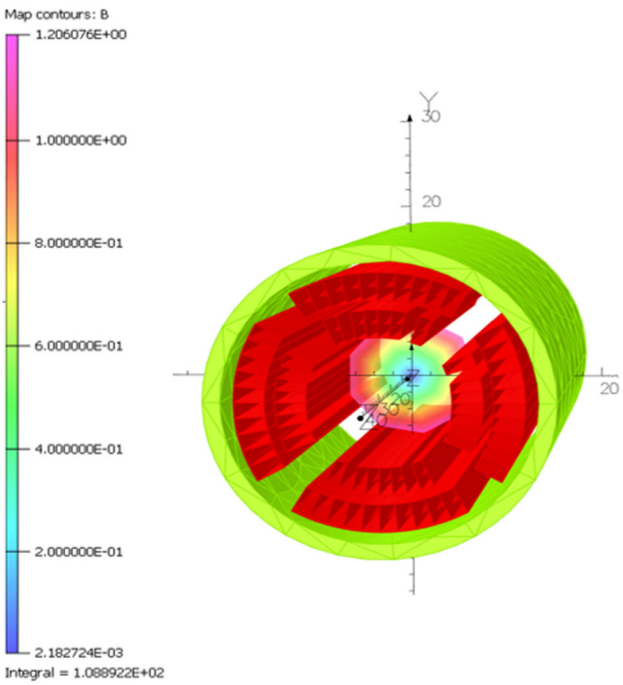

Fig. 162 Magnetic flux density in the central plane $z = 0$

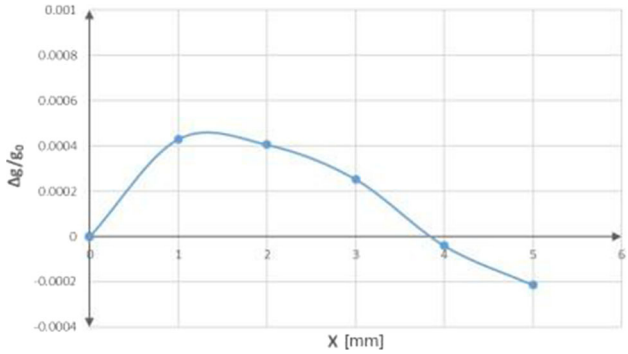

Fig. 163 Field quality in terms of relative gradient deviation as a function of x in the centre plane $z = 0$

Table 49 FODO quadrupole field coefficients

n	Type	$B_n(5\,\text{mm})$ [T]	B_n/B_2 (5 mm)
2	Q	8.23×10^{-1}	1
6	Q	5.48×10^{-3}	6.65×10^{-3}
10	Q	1.67×10^{-3}	2.03×10^{-3}
14	Q	9.55×10^{-5}	1.16×10^{-4}

at $x = 5\,\text{mm}$ to be 9.898 T. The field gradient uniformity in terms of $\Delta g/g_0 = (g - g_0)/g_0$ in the central plane $z = 0$ is displayed in Fig. 163. The relative deviation is within a few units of 10^{-4} in the good field region up to 5 mm. The strength and relative strength of nominal and the first three allowed higher order multipole components for the FODO quadrupole are summarized in Table 49.

6.1.3.4 Integrated diagnostics

The electron beam diagnostics in the SASE line will consist of a set of cavity beam position monitors (BPMs), one in each cryomodule. These BPMs will provide the feedback signal required for the intra-module beam steering as well as for the inter-module beam-based alignment. The BPM will be operated in a cold environment. For example, Cold cavity BPMs are operating in superconducting linacs at the European XFEL [188, 236]. State-of-the-art cold cavity BPMs are L-band structures. Since the size of these structures is directly related to their operation frequency, L-band cavities seem not optimally suited for integration into the CompactLight SASE undulator cryomodules. The limited space in the gap between the undulator units favors more compact structures. For the conceptual design of the CompactLight FEL lines, we foresee cold X-band cavity BPMs. The length of these BPMs could be 100 mm (as compared to 180 mm for the L-band cavities).

Such devices do not exist today. L-band cavities are preferred for the application of superconducting linacs due to the extremely demanding requirements on surface cleanliness for operation in proximity to the superconducting cavities. However, vacuum and cleanliness requirements will be much less demanding for application in the superconducting undulator cryomodules. It is reasonable to assume that X-band cavity BPMs for this application are feasible and could become available on the 5-year development time horizon considered for CompactLight.

6.1.3.5 System integration

The design concept for the cryomodules will likely follow a bottom–up approach similar to that suggested in [225]. A room-temperature strongback at the bottom forms the basis of the supporting structure, directly supported by the girder outside the cryomodule. The cold mass is mounted onto this strongback on thermally intersected fibreglass posts. These thermal interceptions at three temperature levels (∼80 K, ∼20 K and ∼4 K from outer to inner) are connected to concentric radiation shields at the same temperature levels. The cold mass elements, SCU, quadrupole magnets, phase shifter magnet, and BPM are integrated into a common, stiff frame which will also provide magnetic shielding. Within this frame, the components are mutually aligned to the required precision (see Sect. 6.1.3.7). To avoid internal cooling channels with interconnecting tubes, contact cooling of the cold mass elements, e.g., through heat exchanger plates on top and/or at the base of the common frame, is favored.

No active internal alignment of the cold mass elements is foreseen. The inter-module alignment is achieved through motorized stages as part of the outer girders, to which the room-temperature strongback inside the

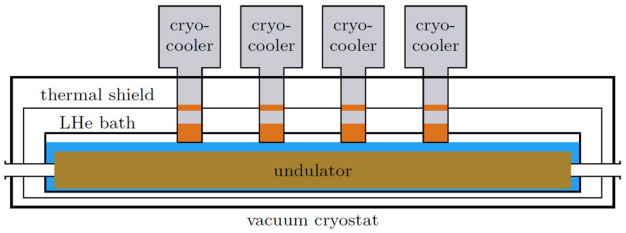

Fig. 164 Proposed Cryostat layout I—segmented design cooled by cryocoolers

cryomodule is rigidly connected. The design of the cryostat interconnection region has to account for the mechanical flexibility required for the alignment of the entire cryomodule with neighbouring cryomodules.

6.1.3.6 Cooling concept

Requirements and conceptional options—overall facility layout

For the cooling of the beamlines, three basic options are considered. These include a *segmented design* approach, where liquid helium (LHe) is re-condensed by cryocoolers located at a number of individual cryostat modules, a *minimal segmentation concept* with LHe provided by a central LHe cryoplant, and a novel *hybrid approach* that provides LHe individually for each cryomodule. In the latter case, cryocoolers and Joule–Thomson cycles shall be combined to enhance the cooling capacity of cryocoolers and enable forced-flow LHe cooling. In the following, these options are presented in greater detail, and their individual benefits are discussed.

Cryostat layout I—segmented design cooled by cryocoolers

The segmented design rests on separating the beamline into 16 individual modules comparable to the suggestion for storage ring application in [224]. Following this design, each module is surrounded by a thermal shield and installed inside a vacuum cryostat. The components inside each module are submersed in an LHe bath, where the boil-off gas is re-condensed at the second stage of pulse tube cryocoolers. Figure 164 depicts a scheme of one module of the segmented cryostat layout.

Based on the assumptions in [224], the heat load onto the LHe by the components alone can be estimated to be in the order of 1 Wm^{-1} module length. For the planned modules with length 2.3 m, this would sum up to a total heat load of $\dot{Q} \approx 2.3\,\mathrm{W}$ @ 4.2 K per cryomodule. This estimation does not include the heat load originating from the cold-warm transitions between the individual modules. As these heat loads depend on the beamline design, the contribution of cold-warm transitions must be optimized during the technical design phase. In any case, the most powerful cryocooler available today provides 2 W @ 4.2 K [237], resulting in the need of about two-to-four cryocoolers per module, or 32–64 cryocoolers per beamline, respectively.

The main benefit of the segmented design approach is its flexibility in maintenance and alignment. During maintenance, only the individual module needs to be warmed up to ambient temperature, while the rest of the beamline remains at 4.2 K, minimizing the overall beam downtime [238]. Moreover, following the design suggestions provided in [238], the components can be aligned precisely within each module, and the position of the modules to each other can be adjusted independently.

The main drawbacks of the segmented design approach are the higher overall heat load due to the transitions from 4.2 K to ambient temperature between the modules and the large amount of helium needed for helium bath cooling. A certain helium infrastructure will also be necessary for initial cool-down, LHe filling and helium recovery. Since cryocoolers have a periodic working principle, many cryocoolers are expected to cause vibrations in the system and acoustic noise. Moreover, the system cost due to the more complex design of the cryostat modules should be considered.

Cryostat layout II—minimal segmented cryostat design cooled by a cryoplant

Following the minimal segmentation design suggested in [238] for the LCLS-II Hard-X-Ray FEL, the beamline with all its components is housed inside one single long stretched vacuum chamber with an integrated LHe distribution system along the undulator string. Unlike the segmented design option, there are no cold-warm transitions for the beamline between the single undulator passages, reducing the overall heat load onto the LHe. Figure 165 depicts a scheme of one undulator module of the suggested minimal segmented cryostat layout.

In the case of the minimal segmented cryostat design, the LHe is provided by a helium refrigeration plant located offside, reducing both acoustic noise and vibrations onto the beamline. Moreover, the LHe plant provides a pressure gradient for fluid circulation inside the cooling channels along the strongback according to the design presented in Fig. 160. Due to the enhanced heat transfer in forced-flow convection, the amount of LHe inside the cryostats can be reduced compared to cryostat layout I, reducing the size of pressure relief devices to ensure cryostat safety.

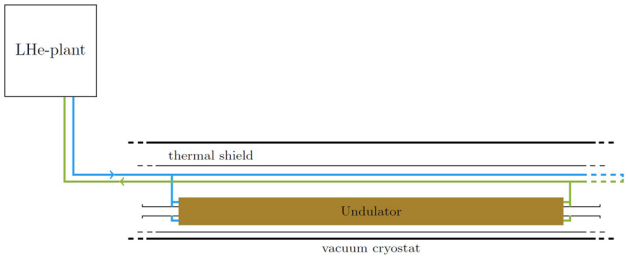

Fig. 165 Proposed Cryostat layout II—minimal segmented cryostat design cooled by a cryoplant

In addition, the cooling system inside the cryostat is maintenance-free, an advantage compared to the cryocoolers according to layout option I. Due to the less complex cryostat design, the system cost is expected to be lower than for the segmented design discussed before [238]. The disadvantage of the minimal segmented design is its limited flexibility concerning the maintenance of individual parts of the beamline. Due to the single-piece cryostat design, accessing one of the magnets along the beamline requires a warm-up of the system to ambient temperature. The cooling power provided by the smallest standard helium refrigeration plants is in the range of 130–210 W [239]. The cooling capacity of one helium plant will hence be compatible with the requirements of one entire beamline, which are to be defined in the technical beamline design phase.

Cryostat layout III—segmented design cooled by a hybrid cryoplant

Besides the established cryostat designs discussed before, current developments in cryogenic mixed-refrigerant cycles (CMRC) provide the basis for a novel hybrid cooling system design. CMRC are refrigeration systems using a wide-boiling mixture instead of a pure fluid as a working fluid. By adjusting the mixture's composition, the efficiency of a refrigeration process can be increased significantly, as the heat exchanger performance is enhanced and the pressure ratio lowered [240]. In previous years, CMRC technology evolved toward the temperature range of high-temperature superconducting (HTS) applications [241], making it an interesting option, especially for the cooling of current leads [241, 242]. A novel heat exchanger technology combining large heat transfer areas with compact dimensions [243] promises a compact modular design.

Cooling current leads with CMRC; a major fraction of the overall heat load can be absorbed by this new technology [242]. In addition, it can be used for efficient pre-cooling of helium in a Joule–Thomson cycle, which is cooled further by a cryocooler operated at an elevated temperature of e.g. 10 K with larger cooling power, before the helium is expanded to the 4.2 K temperature level (cf. Fig. 166). This combination may extend the 4.2 K cooling power limitation of cryocoolers, so significantly fewer cryocoolers are needed in a segmented design. The main advantage of such a hybrid cooling system is the scalability, enabling forced-flow LHe supply for medium-power applications, where typically several cryocoolers are needed, and LHe cryoplants are oversized. However, it is important to note that this novel refrigeration strategy is still in development, and its potential for 4.2 K applications needs to be investigated. Therefore, the achievable performance is not yet clear, and there is no prototypical application today. From a thermodynamic point of view, though, CMRC technology is the only feasible way to close the cooling power gap of about two orders of magnitude between cryocoolers and cryoplants.

Components cooling options

Besides the LHe cooling of the magnets along the beamline, the current leads as well as the thermal shield inside the vacuum cryostat, have to be cooled. Strategies for these components shall be presented in the following.

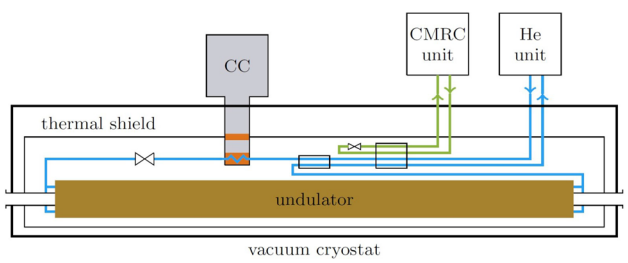

Fig. 166 Proposed Cryostat layout III—segmented design cooled by a hybrid cryoplant

Table 50 Comparison of the overall cooling requirements for the segmented and minimally segmented layouts of the SASE SCU cryostat

	Segmented	Minimally segmented
Per SASE line		
Heat load shields/W	2625	2620
Heat load @ 4 K/W	67	70
Refrigeration infrastructure	48 cryocoolers, 2 W@4 K	Cryoplant, 100 W@4 K
Wall plug power/kW	550	45–75

Cooling of current leads
To reduce the heat load onto the cryogenic system, the usage of high-temperature superconducting (HTS) current leads is recommended. To keep the HTS current leads below their transition temperature, conduction cooling to the first stage of cryocoolers is an option for the cryostat layout I. For cryostat layout II, the current leads might be cooled by either conduction or convective gas cooling with cold helium gas, flowing back to the LHe cryoplant. For cryostat layout III, CMRC cooling is the ideal option for the current leads. The required cooling power in these cases has to be calculated on the basis of the total power consumption and the required current of the magnets along the beamline. This is expected to be done during the technical design phase.

Cooling of the thermal shield

For cryostat layout I, thermal shielding is typically cooled via conduction by the first stage of the cryocoolers [244]. For cryostat layout II, a convective cooling circuit with either He of liquid nitrogen (LN_2) is possible [244]. For cryostat layout III, shield cooling can be realized by the first stage of the cryocooler in combination with the CMRC system. An optimisation of the shielding temperature for the FRIB cryomodule is described in [245]. A similar study should be performed during the technical design phase to minimize the static heat load onto the beamline.

Summary on cooling requirements To evaluate and compare the layout concepts I and II, which are based on currently available technologies, the heat loads on the cold mass and shields due to radiation and heat conduction, particularly through the required current leads, have been preliminarily estimated [246]. Table 50 summarizes the results. The estimates favor the minimally segmented SASE line supplied by a central cryoplant.

6.1.3.7 Tolerance considerations and alignment strategies

The specification of accuracy requirements is a work in progress, as well as the development of design strategies for achieving the required tolerances. Three levels of accuracy requirements need to be addressed: (1) field quality requirements for the individual magnetic components, which are related, but not necessarily limited to mechanical accuracy requirements for these components; (2) mutual alignment tolerances of the components forming the cold mass; (3) mutual alignment of the cryomodules forming the SASE line. At all levels, alignment accuracies are subject to mechanical variations upon cooling due to thermo-mechanical stress and subsequent deformation. Above that, also magnetic forces have to be taken into account.

Mechanical variations upon cooling. A detailed investigation of forces occurring due to thermal contraction upon cooling, subsequent stresses, and deformation have to be performed in the course of elaborating a detailed technical design for the cryomodules. General design strategies to cope with thermo-mechanical effects include, but are certainly not limited to, a careful choice of materials, appropriate pre-stressing of composed components, and avoiding stresses by design, e.g., allowing elements to slide against each other in a well-defined way.

Magnetic field quality requirements. Magnetic field quality requirements are the same for the main FEL undulators as for the afterburner undulators: A straight trajectory and a reasonable phase error are the most important. Trajectory straightness requirements differ with wavelength. Because the XLS undulators and afterburner will serve both soft X-ray and hard X-ray, the requirements need to fulfil the demands for the hard X-ray case. Trajectory straightness of 2 μm is required. Beam wander, in addition, depends on the frequency. Long-range beam wander is more forgiving in the exponential growth regime, because the electron beam can take the light with it. Short-range trajectory errors such as kicks can stop the FEL process and must be avoided [247]. The phase error of the FEL undulators and afterburner as well are not very stringent. Only the fundamental harmonics are used, so that the maximum rms phase error can be specified to 10° .

Specifications on multipoles, which mainly refer to off-axis field quality, are less important. The only possibility which might need to be controlled is the presence of gradients over the undulator axis. Such gradients would appear systematically in a circular mode in a fixed gap undulator.

In an SCU, the described field properties are determined by the accuracy of the winding placement, both locally and long-range. How the requirements stated here and in Sect. 6.1.2.4 translate into specifications for mechanical tolerances is to be investigated, and their practical feasibility to be proven. Additional coil-based field integral correctors along the SCU can be employed to control trajectory straightness actively.

Intra-module component alignment. The components forming the cold mass, which are the relevant components with respect to the FEL performance, will be mutually aligned in warm conditions within a common, stiff frame. Magnet centres have to be aligned through mechanical reference only, since no fiducialisation of individual components with respect to their magnetic axis will be available. The aforementioned design strategies must be applied to maintain the mutual alignment upon cooling as far as achievable. To correct residual deformations and alignment changes, settings for the field integral correctors providing zero beam offset in the quadrupole centres and zero overall beam deflection can be found using stretched- or pulsed-wire-based magnetic field integral measurement methods. That has to be done offline for each individual cryomodule and over the entire tuning range of the undulator.

The accuracy of the internal alignment and the external alignment control achieved by these methods has to be good enough that the K variation requirements described in Sect. 6.1.2.4 can be met across the modules through their mutual alignment. To first order, this requires that the components of the cold mass are aligned to each other within 20 µm.

Cross-module mutual alignments Each individual cryomodule will be fiducialised with reference to, e.g., pulsed-wire measurements for the alignment and FODO quadrupoles only. And the advantage of the iron-free design of all magnets inside the cryomodule is that remanent fields will not disturb such measurements. The external fiducials will allow for an initial mutual alignment of the cryomodules with respect to the quadrupole centres, sufficient for the beam to pass through the FODO lattice along the SASE line. That will enable a refined beam-based alignment employing the FODO and alignment quadrupoles.

6.1.4 The afterburner undulators The afterburners are undulators placed after the main FEL undulator, generating the electron microbunching and the exponential growth in intensity of the emitted light. The afterburners use the microbunched electrons to generate either background-free higher harmonics [248] or allow polarization control [221]. An alternative polarization control approach is building the entire FEL undulator line with variably polarizing undulators like the SwissFEL Athos beamline [249] at PSI. However, in terms of compactness and overall costs, the afterburner allows FEL undulators with the shortest possible period length to be used, while the

afterburner may have relaxed parameters. This is especially true if polarization control is not required over the entire photon energy range. Simulations of the expected afterburner performance, including a study determining the required number of afterburner modules, were presented in Sect. 6.1.2.5.

Variably polarizing undulators have been dominated by APPLE-type permanent magnet undulators [250] for more than 25 years now. Figure 167 shows an example of an in-vacuum APPLE-X undulator. Electromagnetic

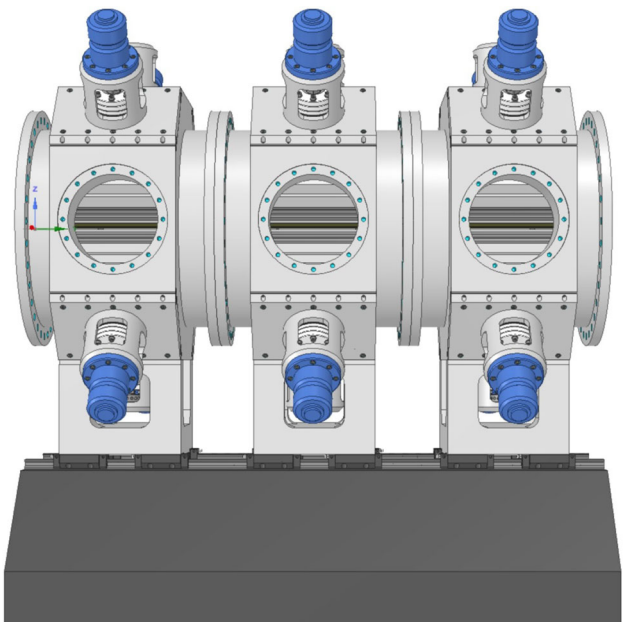

Fig. 167 Permanent magnet-based in-vacuum APPLE-X undulator as an afterburner

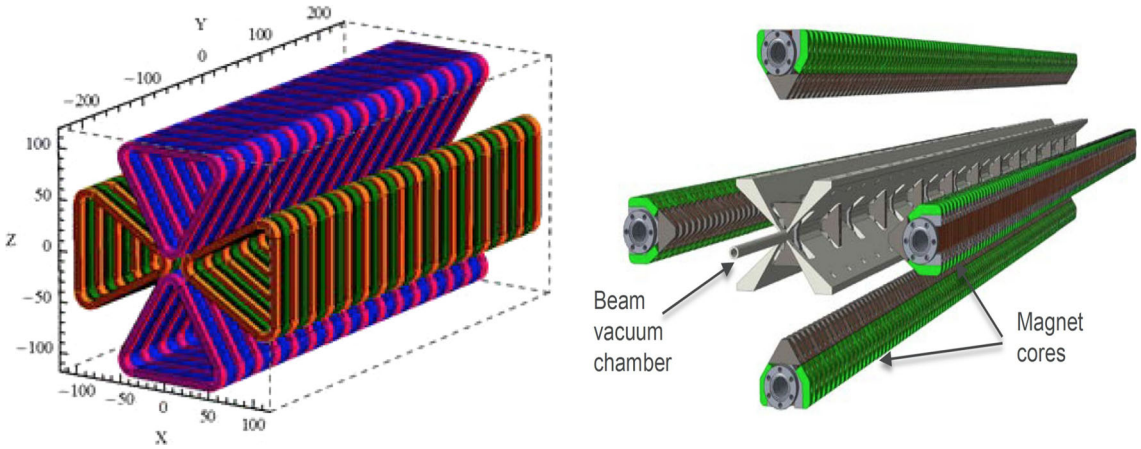

Fig. 168 Superconducting arbitrary polarized emitter SCAPE. Radia model (left) and assembly (right) (courtesy Yuri Ivanyushenkov, ANL)

undulators are used for very long periods only. Recently, a variably polarizing superconducting undulator named SCAPE (superconducting arbitrarily polarizing emitter) has been proposed for a short period. [251]. Figure 168 shows the design principle of the SCAPE undulator; it consists of two planar undulators shifted by a quarter of a period.

A 0.5 m-long SCAPE prototype with a period length of 30 mm has been successfully tested. A study for fast helicity switching with this device is also under study [252]. This is a very interesting device with high potential for shorter period length. However, based on a great deal of experience in Europe with APPLE-type undulators on one hand and in-vacuum and cryogenic planar undulators on the other hand, for CompactLight, it was decided to use in-vacuum or even cryogenic APPLE-X undulator technology as the baseline. However, this decision can be revisited in the future as technology evolves.

APPLE undulators have been used so far only for soft X-ray applications and have, therefore, in general, a longer period length (mostly between 38 and 70 mm). Also, only recently, a first in-vacuum APPLE with a period length of 32 mm has been realized at HZB for the storage ring BESSY II [253, 254]. For FEL applications, the vacuum stays clear apertures can be smaller, which will allow for a shorter period length.

Besides strong vertical forces, APPLE-type undulators, in general, have strong forces in the horizontal and longitudinal directions. To handle these forces, APPLE-type undulators are large. Classical C-shape undulators for storage rings have widths of up to 2 m. The already compact design for the Athos UE38 APPLE-X undulators with a closed support structure still has a width of 1.4 m. Similarly to CompactLight, SwissFEL has two parallel beamlines, and the width of the undulators defines the separation as 4 m to allow the installation and eventual replacement of undulators. CompactLight requires a smaller separation of only 2.5 m. This reduces the building volume and allows a feasible design for the electron beam spreader and photon beamlines, which combine light from the two parallel FELs in the endstations for pump-probe experiments.

6.1.4.1 Basic concept

The FEL undulators will be superconducting helical undulators with 13 mm period length and K-value ranging between 1.85 and 0.85. The period length of the afterburner is not necessarily the same as the main undulators—it can be longer but needs to cover the same photon energy range. The initial study of afterburner performance in Sect. 6.1.2.5 used a provisional period of 19 mm. Hence, the afterburner needs also to be linked to the FEL undulator by

$$\lambda_{AB}\left(1+\frac{K_{AB}^2}{2}\right)=\lambda_U\left(1+\frac{K_U^2}{2}\right), \tag{55}$$

with λ the wavelength and $K = 0.934\ B\,[\mathrm{T}]\ \lambda_{U/AB}\,[\mathrm{cm}]$ the product of field and period length. The lowest energy is defined by the achievable field strength or K value of the afterburner at a given period length, and the highest energy by the chosen period length at the lowest acceptable K value. The main SASE undulators yield circular FEL light, but they provide no polarization control. The helicity is implemented with the winding direction of the superconducting wire. It is worth noting that the emitted light is therefore circularly polarized—in contrast to the horizontally polarized light from conventional vertical undulators. LCLS-II provides vertical polarization in the hard X-ray beamline and horizontal polarization in the soft X-ray.

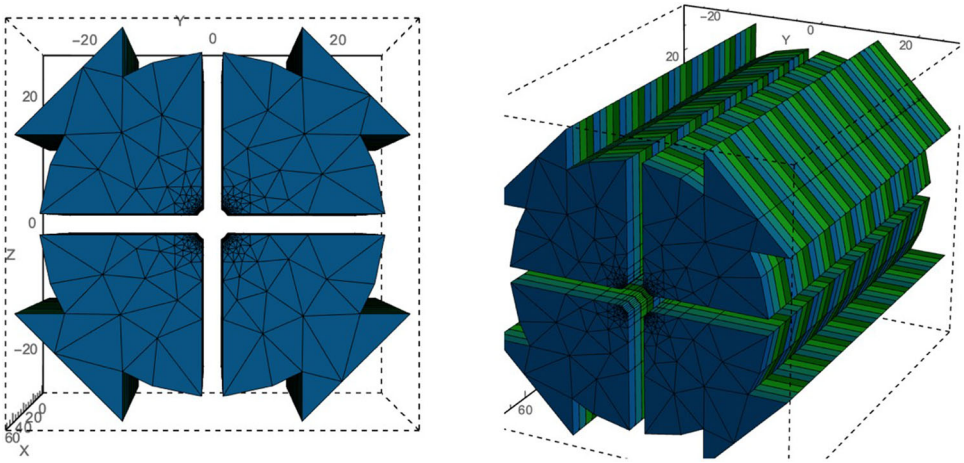

Fig. 169 RADIA [255] model of the APPLE-X magnet configuration. The magnetic gap, here, the free diameter depends on in- or out-of vacuum solutions. For a 5 mm inner diameter vacuum chamber, a magnetic diameter of 6.5 mm is required. For in-vacuum undulators, this can be reduced to about 5.2 mm. The slit can be minimum 2.5 mm to allow magnetic measurements and support of a vacuum chamber

The APPLE-III, DELTA, and APPLE-X designs are optimized for use in single-pass accelerators with round vacuum chambers giving equal space requirements in horizontal and vertical directions. They all enclose the beam-pipe with four magnet arrays, but DELTA and APPLE-X maximize the on-axis field by radial magnetisation. While the polarization is changed by symmetric or antisymmetric shift of diagonal magnet arrays, the field amplitude can be changed by a gap variation or with fixed gap and longitudinal shift of adjacent magnet arrays. This results in a simplified design, but results in operation always at the lowest gap and thus higher risk of radiation-induced demagnetisation of the magnets. Another aspect to be considered is the appearance of field gradients over the beam axis in the circular mode. The APPLE-X provides a radial gap drive which has symmetric conditions in all polarization modes. In addition, this device has the feature of producing controlled gradients [249] and is the most flexible APPLE-type undulator. This type is chosen as baseline for the afterburner. Figure 169 shows a model of the APPLE-X magnet.

The possible remanent magnetic field B_r, especially of NdFeB magnets, has increased over the last years. Techniques such as Dysprosium (Dy) and recently Terbium (Tb) diffusion enable an increase in the coercivity H_{cj} without decreasing B_r which can be up to 1.35 T with sufficiently high stability against radiation damage. The diffuse heavier rare-earth materials replace the Nd at the grain boundaries from where demagnetisation starts. Therefore, with a cost-effective low concentration, the coercivity can be increased sufficiently without reducing the remanence. This works well for thin magnets, for instance those used in short-period undulators. The strength of the magnets can be further increased by operating the undulator under cryogenic conditions at liquid nitrogen temperatures. Stronger grades of the magnetic material can be used, because both coercivity and remanence show a negative temperature gradient. It is only necessary to control demagnetisation effects during assembly. Radiation effects in operation are not harmful any more. The material of choice is PrFeB. NdFeB also works, but shows a spin reorientation below 135 K which reduces the fields when the temperature is further lowered. The cryogenic design needs to be careful to meet this maximum, but it has shown stable operation on the flat top with temperature gradients. With both materials, remanent magnetic fields of 1.65 T are achievable. Room-temperature devices can be built in or out of vacuum. The thinnest vacuum chambers so far have been used for the Athos beamline at SwissFEL with a wall thickness of only 200 μm. The magnet gaps of in-vacuum undulators can be slightly reduced, since, for impedance reasons, they need to be covered by a thin copper-nickel foil with a typical thickness of 100 μm. However, the effective loss in gap is larger for out-of vacuum undulators because of the required alignment tolerances. At PSI, a vacuum chamber of 5 mm is used, but the minimum magnetic gap is 6.5 mm, so the effective loss in gap is 1.5 mm, compared to 0.2 mm for in-vacuum applications. Cryogenic undulators are mandatory in-vacuum, of course.

6.1.4.2 Magnetic optimisation of the afterburner

The optimisation parameters for the magnetic design of the afterburner are the

- B_r, depending on cryogenic or room-temperature.
- Magnet dimensions.
- Gap/slit.

- Number of magnets per period.
- Field shape.

In the APPLE-X design, the shape of the magnets makes effective use of the available volume. Variations are possible, mainly in the clamping and symmetry. For the studies for CompactLight, the SwissFEL Athos UE38 design is used, scaled from a period length of 38 mm to the much shorter period length of 16–20 mm. While the gap is determined by wakefield considerations to 5 mm, the distance of the magnet blocks (slit) is determined by the practical consideration of allowing magnetic measurements from the side. Therefore, a minimum slit is 2.5 mm (UE38: 3 mm). The classical Halbach approach uses 4 magnets per period. However, using more magnets increases the effective field. Using 8 magnets per period, the peak field can be increased by 8 %. Field shaping, an inhomogeneous magnetisation of the magnets, has been used for the UE38 in combination with SmCo magnets, which are however not an option where maximum fields are required.

Table 51 shows possible K-values as function of the period for a round vacuum gap of 5 mm for the three options. The K-values assigned are required to match the tuning range. Full tuning is only possible for period length of less than 17 mm. Longer periods reduce the maximum energy of polarization control for XLS. For all models, a 5 mm diameter vacuum stay clear aperture is assumed. A period length of 18 mm could just be feasible even at out-of vacuum with 4 magnets per period (1st number) and 8 (2nd number), respectively. An afterburner with a period length of 18 mm would just match the nominal tuning range of the FEL undulator. However, for high energies, the K-value would be unusually small which will have an impact on the efficiency (see Sect. 6.1.2.5). Therefore, studies of in-vacuum technology including the cryogenic option are required. However, polarization control is mandatory for the entire soft X-ray range starting from 250 eV. In the hard X-ray regime, circular dichroism is limited to the K_α absorption lines up to about 12.5 keV. Afterburners with periods longer than 20 mm reduce successively the high-energy part, meaning that only circular polarization is available. In principle, this is not a problem, but the standard the users would expect and find anywhere else is linearly polarized light. This limitation would need to be explicitly indicated to the users. However, from magnetic calculations, it seems to be possible to cover the entire wavelength range at the expense of efficiency. From the point of pulse energy, a longer period length might

Table 51 Link between the FEL undulator with 13 mm period and a range of the K-value of 1.85–0.85 and the longer period afterburner (left)

$\lambda_{U/AB}$ [mm]	K_{max}	K_{min}	$E_{ph,\,max}$ [keV]
13	1.85	0.85	16
14	1.74	0.73	16
15	1.64	0.6	16
16	1.55	0.46	16
17	1.47	0.3	16
18	1.38	0.3	15.3
19	1.30	0.3	14.4
20	1.23	0.3	13.7

λ_{AB} [mm]	Out-vac $B_r = 1.37\,\mathrm{T}$	In-vac $B_r = 1.37\,\mathrm{T}$	Cryo $B_r = 1.65\,\mathrm{T}$
13			
14			
15			1.29/1.39
16	1.07/1.16	1.23/1.32	1.48/1.60
17	1.23/1.31	1.38/1.50	1.68/1.82
18	1.39/1.51	1.56/1.69	1.89/2.04
19	1.57/1.68	1.75/1.88	
20	1.74/1.87	1.93/2.07	

Maximum K-values calculated with RADIA [255] for APPLE-X undulators in and out of vacuum and cryogenic in-vacuum technology (right)

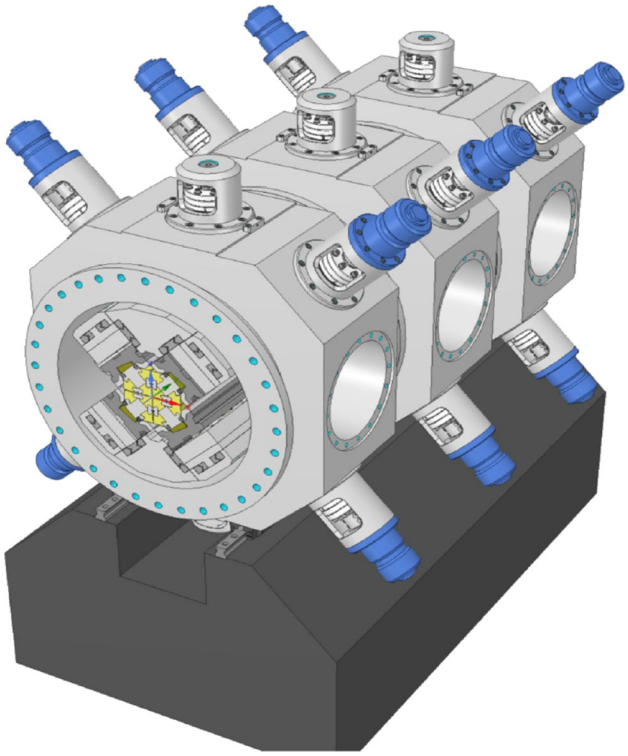

Fig. 170 Design study for a compact and modular, in-vacuum APPLE-X undulator

be favorable (see Sect. 6.1.2.5 for details). For systematic studies, it is helpful to parametrise the gap dependence of the field.

Support mechanics

A design study has been explicitly carried out for this project by Kyma for a compact, modular, in-vacuum APPLE-X undulator, as shown in Fig. 170. This study follows a compact and modular design for the next generation of in-vacuum undulators for SLS2.0 at PSI. A vacuum chamber machined out of a massive aluminium block plays the role of the support structure. In the APPLE-X configuration, every magnet array is adjustable in radial and longitudinal directions. A very compact drive system can be realized with hydraulic cylinders. The intelligent valve (Bosch-Rexroth) can provide sub-μm resolution. The undulator is segmented in modules, and each of the modules has its own drive system, which can allow even for a segmented taper inside the undulator. The compact modules will be placed on a girder similar to the multipole magnets. Various options have been analyzed, which follow various concepts. All drive systems are out-of-vacuum. The design shown here combines elements such as external longitudinal shifts. The magnet arrays are internally connected to increase stiffness to handle the large magnetic forces and to allow fine alignment of the magnetic axis. The magnet keeper is equipped with force-compensating magnets, which could make the internal connection between the magnet arrays obsolete.

Magnetic force compensation solutions

As already mentioned above, the challenge of APPLE-type undulators is coping with three-dimensional forces which can even change sign with the mode of operation. In addition, these forces act differently on the individual magnet arrays, which results in moments through the entire support structure. The forces are responsible for the large dimensions of the support structures for these devices and are a major obstacle to designing in-vacuum solutions. The key idea seems to be magnetic field compensation as proposed for the BESSY-II in-vacuum APPLE and studied for APPLE-type undulators at ALS at LBNL in Berkeley. For planar undulators, magnetic field compensation has been also successfully tested.

Figure 171 shows a possible implementation for the APPLE-X configuration using identical magnets for field compensation. It is obvious that the number of magnets increases significantly, by a factor of 3. However, the field quality is not so stringent as for the centre magnets, so the specification could be relaxed for the field compensation magnets only. Alternatively, the specification could be relaxed for all the magnets, which could then be sorted to find the best magnets for the centre. However, it is interesting to see that the field compensation is very successful. In contrast to planar undulators, the field compensation cannot be 100 %, because there is only compensation to the neighbouring magnet arrays, but no compensation to the diagonal magnet array. However, the forces are

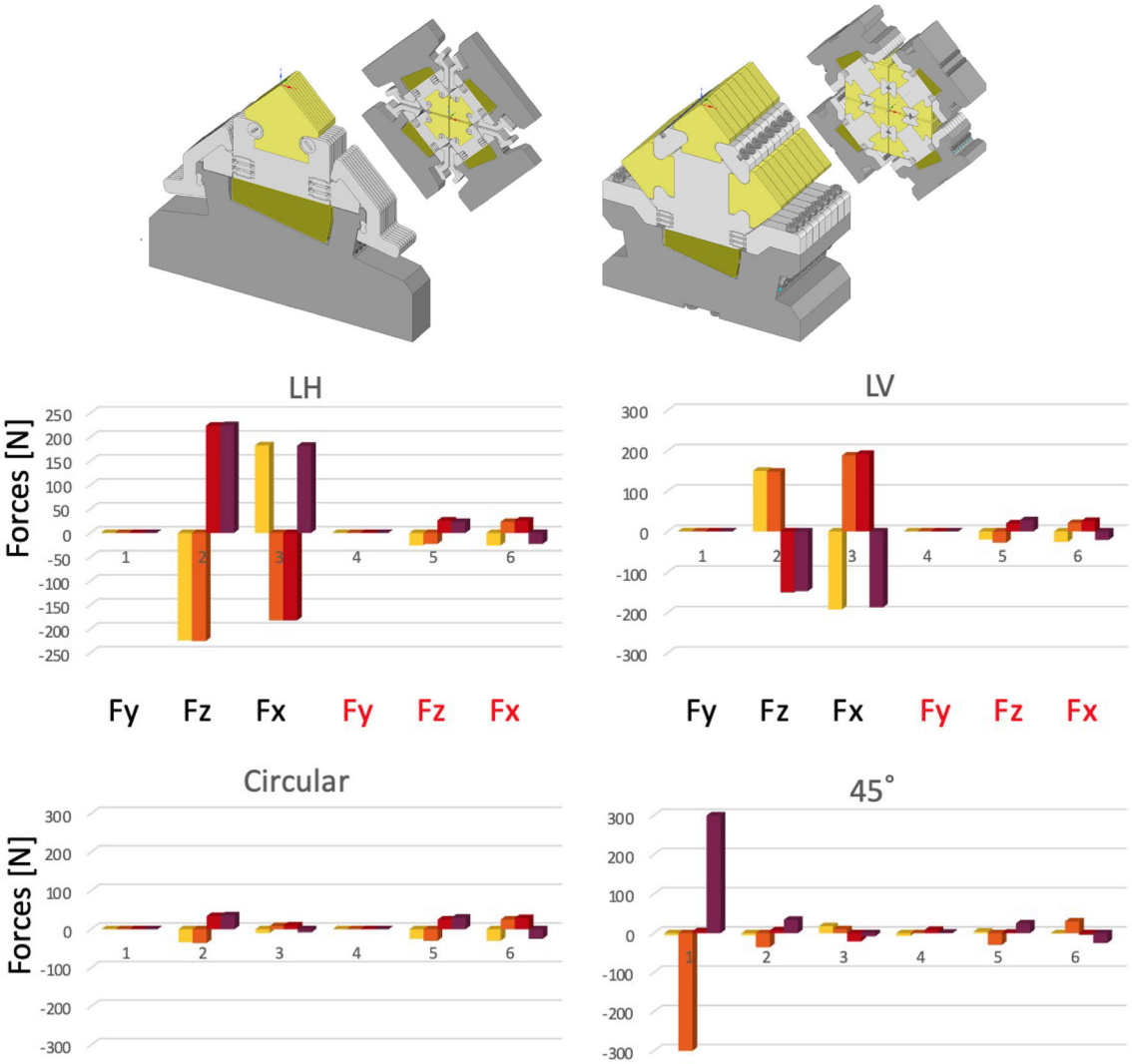

Fig. 171 Force compensation for the APPLE-X design. On top is shown a possible field compensation using identical magnets without increasing the complexity of the keeper by additional clamps. The graphs plotted below show the forces on the individual magnet arrays for the different operation modes linear horizontal and vertical (LH, LV), helical and inclined. On the left are the forces (calculated for a few periods only) for the standard APPLE-X configuration and on the right, marked in red, for the force compensation case. The reduction is remarkable, even though it is not zero. However, it is drastically reduced and is identical for the major operation modes. The forces further reduce with radial opening of the gap

drastically reduced as seen from the graphs in Fig. 171, and are constant for the major polarization modes of linear vertical, linear horizontal, and circular with both helicities. Only in the inclined mode are the remaining forces different, but of the same small level. It is certainly worth studying carefully the field compensation for in-vacuum applications.

6.1.4.3 Analyses of the mechanical support structure

The mechanical structure is exposed to three-dimensional forces as described above. The use of compensating magnets is proposed to minimize the undulator support structure. The load analyses of the proposed support structure were carried out by Kyma, where the magnetic load without compensating magnets was simulated, and the results were compared to the simulations with the reduced magnetic load achieved with the compensating magnets. Simulations were carried out for the four main modes of operation:

- Linear horizontal mode.
- Circular mode.
- Linear vertical mode.
- 45° mode.

Mechanical structure main features A detailed description of the support structure presented by Kyma is shown in Fig. 172. The magnetic forces acting on the array are transferred to the magnet holder support (1) screwed onto the in-vacuum girder (2), and transferred across the girder onto the radial pistons (3) with linear bushings (4). Part of the load would be transferred via linear bushings onto the guiding plate (5), whereas the remaining load would be transferred onto the radial frame plate (9) via locking nuts (10). Part of the loads would be (vertically) compensated, by means of a preloaded linear bearing with needle bearing elements (6), with inner rails screwed onto the radial guiding plate (6.1) and outer rails screwed onto the top frame (6.2). The top and radial connecting rods would be mounted onto the frame and radial frame plates using a bolted connection.

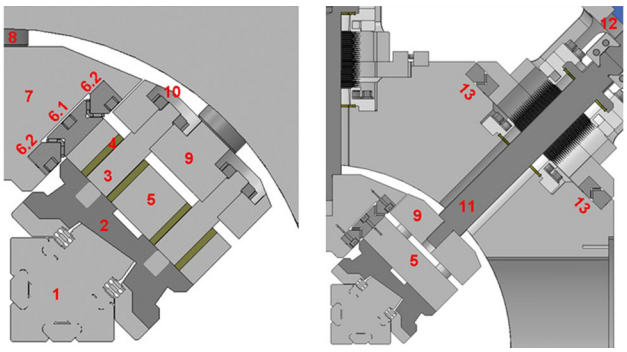

Fig. 172 Cross-section at radial piston (left) and at radial acting rod axis depth (right)

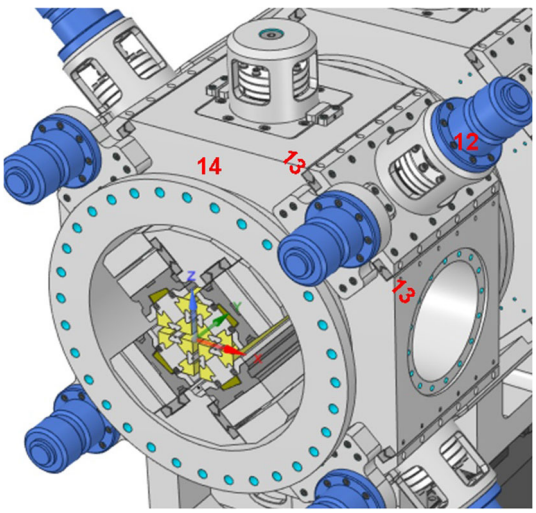

Fig. 173 Vacuum chamber with radial and phase actuation mechanism

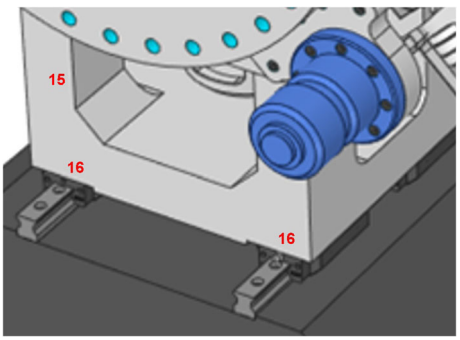

Fig. 174 Vacuum chamber bottom support with bottom linear rail guides

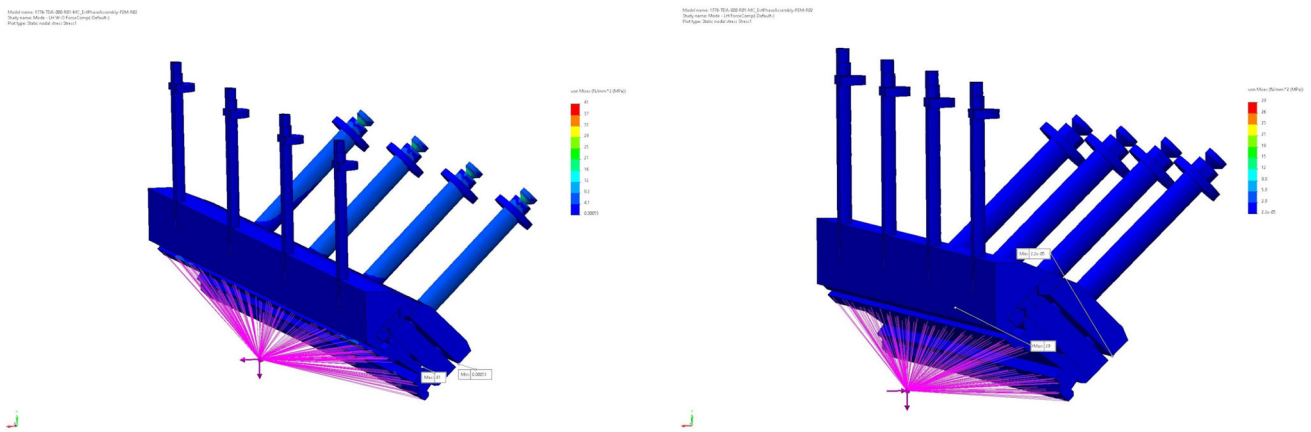

Fig. 175 von Mises stress without (left) and with (right) force compensation in linear horizontal mode

The structural response chain extends further onto the radial actuator assembly (12), external linear rail guides (13) and the vacuum chamber housing (14). Given several vacuum chamber housing segments within this design concept, the longitudinal loading extends along the beam axis across the entire vacuum chamber. Figures 173 and 174 show the vacuum chamber with radial and phase actuation mechanism and the vacuum chamber bottom support with bottom linear rail guides, respectively. The response chain extends further down across the vacuum chamber support (15) and across bottom linear rail guides (16) onto the foundation. Results of simulations for the four main modes of operation are presented in the next section.

Mechanical simulation results The proposed APPLE-X undulator is mechanically symmetrical across the vertical longitudinal plane and horizontal longitudinal plane. The advantage of this symmetry is that only one-quarter of the whole structure can be considered when performing the simulations. Although the simulated model is very complex, the symmetry minimizes the complexity and greatly reduces the simulation time without losing the precision of simulation results.

Linear horizontal mode

Figure 175 shows the von Mises stress without (left) and with (right) compensation in the case of linear horizontal mode. Figure 176 shows the URES displacement in the same configurations. The overall improvement in stress reduction and deformation using compensating magnets is presented in Table 52.

Circular mode Figure 177 shows the von Mises stress without (left) and with (right) compensation in the case of circular mode. Figure 178 shows the URES displacement without (left) and with (right) compensation. The overall improvement in stress reduction and deformation using compensating magnets is presented in Table 53.

Linear vertical and 45° *modes* In both configurations, the proposed mechanical solution can only be used with compensating magnets. In the case where compensating magnets are omitted, the longitudinal force acting on the girder is too large for these proposed solutions. The overall performance in stress reduction and deformation using compensating magnets in both modes is presented in Table 54.

Figures 179 and 180, respectively, show the von Mises stress and the URES displacement with compensation in linear vertical (left) and 45° (right) mode.

The proposed mechanical solution can only be used with compensating magnets for the linear vertical mode of operation. In the case where compensating magnets are omitted, the longitudinal force acting on the girder is too large for the proposed mechanical solution.

Table 52 Linear horizontal mode with and without compensating magnets

	von Mises stress [Nmm $^{-2}$]	Overall deformation [µm]
Without compensating magnets	41	123
With compensating magnets	29	47
Improvement	29 %	62 %

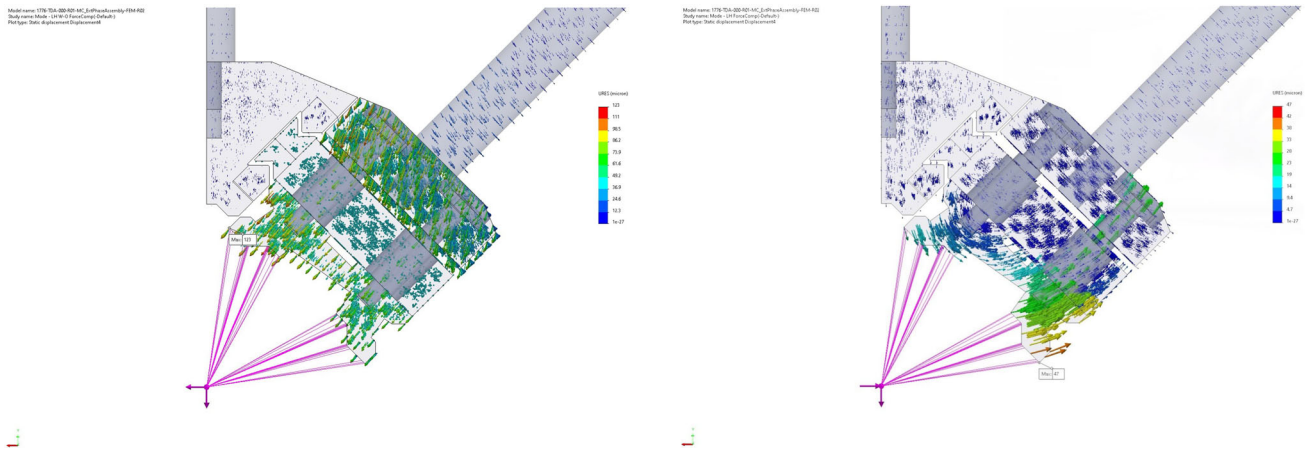

Fig. 176 URES displacement without (left) and with (right) force compensation in linear horizontal mode

Table 53 Circular mode with and without compensating magnets

	von Mises stress [Nmm $^{-2}$]	Overall deformation [μm]
Without compensating magnets	34	54
With compensating magnets	24	50
Improvement	29 %	7.4 %

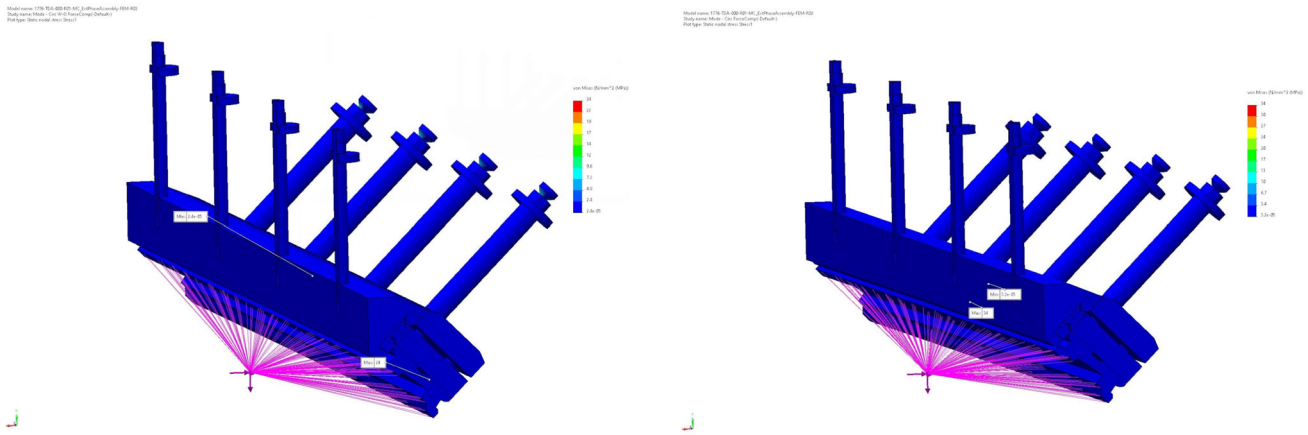

Fig. 177 von Mises stress without (left) and with (right) force compensation in circular mode

Simulation results conclusion

As shown, the load on the support structure is significantly reduced with the use of compensating magnets. In the case of linear vertical and 45° polarization modes, the use of compensating magnets is even mandatory for such a structure to withstand the magnetic load. The deformations of the structure are much lower, and the central magnets maintain their theoretical position better in all modes of operation. In theory, such a device could perform better magnetically, because the magnets will better maintain their positions. Consequently, the magnetic errors should be lower in different modes of operation in respect to a device without magnetic compensation.

The presented mechanical structure is a conceptual idea which should be further developed, evaluated, and optimized, before a prototype of such a device could be built. Nevertheless, the benefit of using compensating magnets has been confirmed using mechanical simulations.

Layout of the afterburner section The afterburner line will consist of two undulator modules with an intersection, which continues the layout in the undulator section. The intersection hosts a phase matcher, quadrupoles, beam position monitors, corrector magnets, and bellows. The vacuum chamber in the intersection should be small and

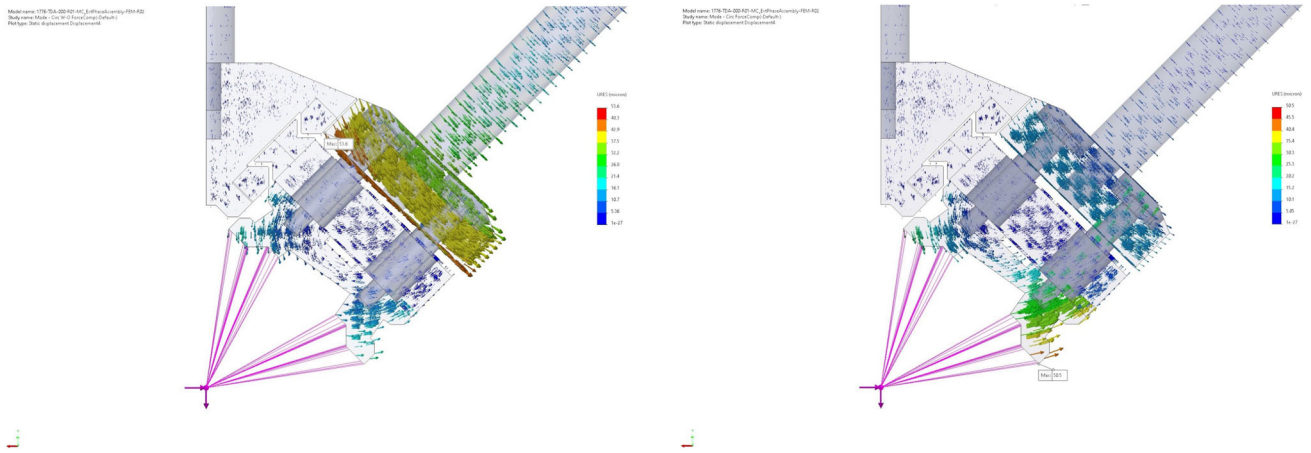

Fig. 178 URES displacement without (left) and with (right) force compensation in circular mode

Table 54 Stress reduction and deformation performance

	von Mises stress [Nmm^{-2}]	Overall deformation [µm]
Linear vertical mode	28	42
45° mode	36	64

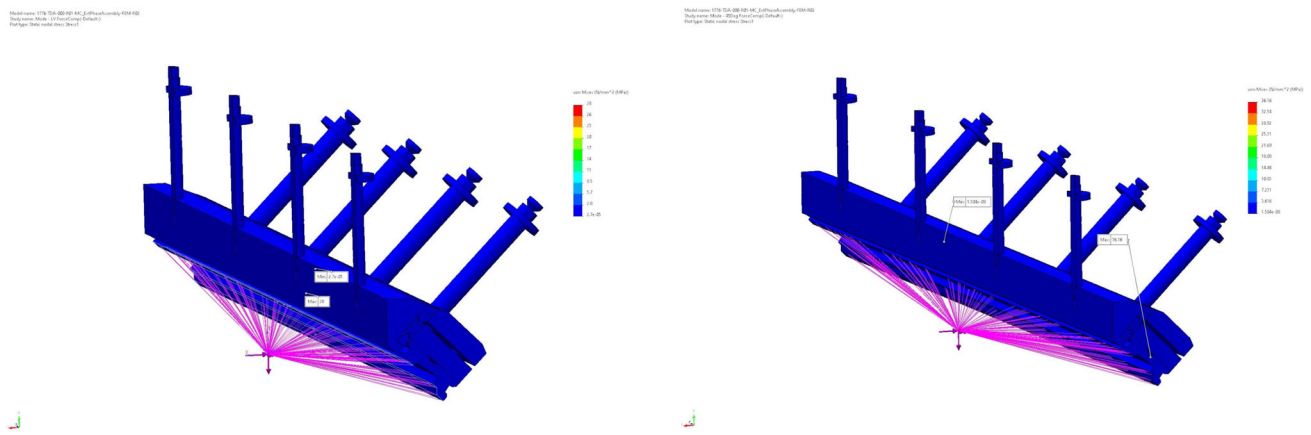

Fig. 179 von Mises stress with force compensation in linear vertical (left) and 45° (right) mode

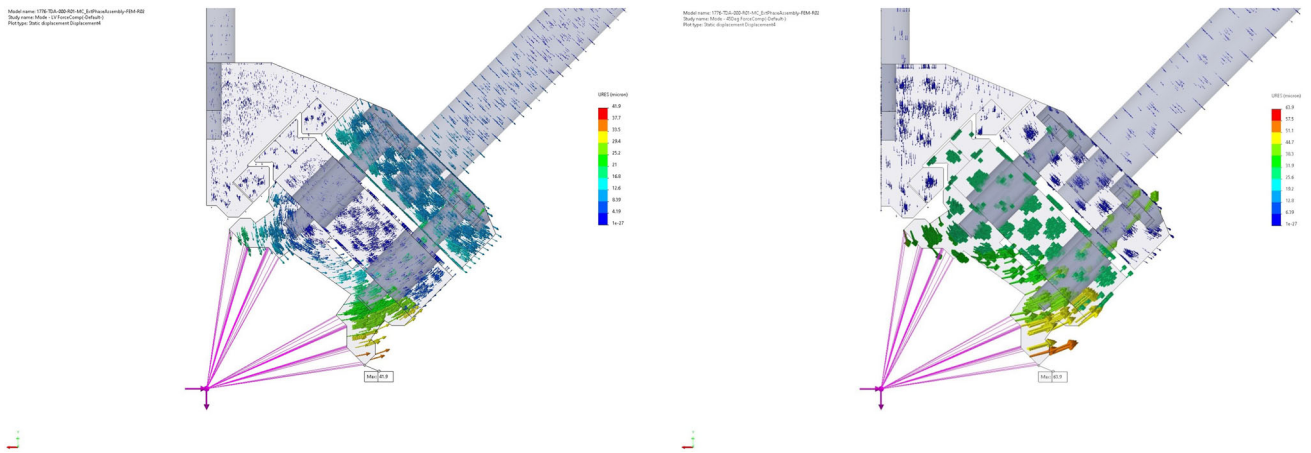

Fig. 180 URES displacement with force compensation in linear vertical (left) and 45° (right) mode

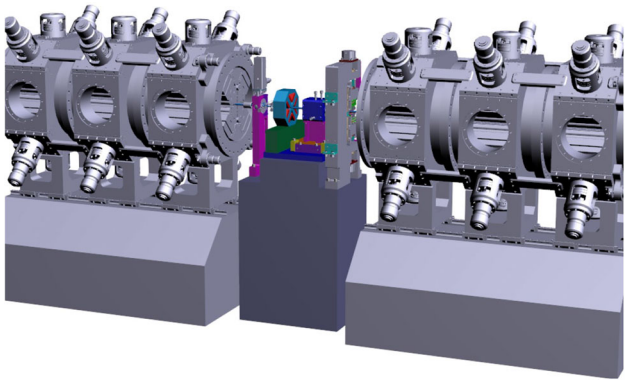

Fig. 181 Intersection between the two afterburners with sector valve, quadrupole, BPM, and bellows

has a diameter of 6 mm, which would allow the quadrupole magnets to have a full gap as small as 8 mm. The periodicity of the quadrupoles should remain the same as shown in Fig. 148 for the SCU cryomodule, hence a length of 2255 mm. The length of the afterburner module will be given then by the space required for the intersection elements. The goal is to use also only 500 mm for the intersection elements, so that the length of the afterburner module will around 1700 mm. For comparison, the intersection in the SwissFEL Aramis beamline is 750 mm. This is already quite compact, and the major components can be used either directly or as an initial design concept. As the in-vacuum undulators allow already a distributed pumping along the entire undulators, no additional space is required in the intersection. However, a sector valve would be helpful in case of a possible failure and repair demand. Figure 181 shows the intersection between the two afterburners.

Drive and control system

For the drive system for the radial and axial adjustments of the magnet arrays, a hydraulic drive system is proposed, because it combines compactness, force, and precision. The heart of the system is an electronic valve from Bosch-Rexroth, which adds high resolution of less than 100 nm. The system has been tested for applications in APPLE undulators in a framework of a Master's thesis in co-operation of PSI and Fachhochschule Nordwestschweiz and is currently under test in a prototype study for SLS2.0 planar compact in-vacuum undulators. The digital valve of the 4WRPH series (see Fig. 182) is compatible with the ENDAT 2.2 interface for direct integration of Heidenhain encoders and fast field bus, i.e., EtherCAT bus for integration into the control system.

The APPLE-X undulators have a good field region of about 50 µm in both directions. A remote alignment system is, therefore, highly recommended for the afterburner, with control of the horizontal and vertical position and pitch and yaw angles. The concept of dedicated alignment quadrupoles allows for a beam-based alignment strategy. It has been used in LCLS where undulator and quadrupole were placed on the same girder table, and by SwissFEL with dedicated, small fixed permanent magnet quadrupoles. After magnetic optimisation the quadrupoles will be aligned to the magnetic axis. Placed on a simple pneumatic stage with two hard stops, a reproducibility of less than 10 µm can be achieved. For beam-based alignment, these quadrupoles are brought successively into the beam. Misalignment results in kicks, which can be detected with downstream beam position monitors. Therefore, the FODO optics scheme needs to be extended beyond the afterburner. After alignment, the quadrupoles are pushed back to minimize distortion of the electron beam. A compact mover system allowing for five degrees of freedom is based on cam-shaft movers, which allows for sub- µm resolution.

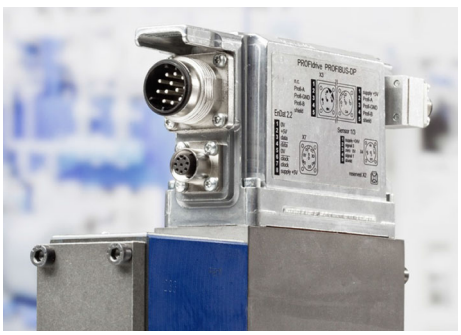

Fig. 182 Digital regulation valve for the hydraulic drive system

6.1.4.4 Tolerance studies

The main requirements on field quality and tolerances for the main FEL undulators as well as for the afterburners are described in Sect. 6.1.3.7. The trajectory in the afterburner undulators can be optimized only in one setting (K parameter and polarization state). The mechanics of the undulator structures then determines the dynamic errors coming with load change. In addition, permanent magnet-based undulators show systematic errors because of the permeability of the magnet material. Although this value is low, especially compared to iron, it is a source of kicks especially caused by the end magnets due to the change of the magnetic environment coming along with changes in gap and shift. There are shimming techniques which can reduce these kicks, but in general, active correction by coils in the x- and y-directions is required at both extremities of an undulator. In practice, therefore, there are no specifications for the end-kicks as long as the strength of the correction coils is sufficient.

To avoid field gradients over the undulator axis, the afterburner concept is based on a variable-gap APPLE undulator. The APPLE-X concept, on the other hand, would be able to produce gradients, but in an intentional and controlled way. The algorithms to control field and gradients in APPLE-X undulators can be found in [256].

6.1.4.5 Afterburner quadrupoles

In the following sections, the design of the small normal conducting FODO quadrupole magnets with solid conductor air-cooled coils is explained.

Pole and yoke design

Using the three-dimensional code OPERA and the two-dimensional codes Poisson and FEMM, a pole and yoke geometry was developed for the FODO quadrupoles which met the magnets' operational requirements. Simulations were done for a quadrupole with a field gradient of 165 Tm^{-1} and effective length of 60 mm using the following equation for the pole profile:

$$xy = R^2/2. \tag{56}$$

The main parameters for the FODO quadrupoles are specified in Table 55 and simulated 2D and 3D geometries are shown in Fig. 183. Applying the low-carbon steel AISI-1010, the magnetic field intensity inside the quadrupole is shown in Fig. 184. Figure 185 shows the magnet dimensions (left) as well as the coil specifications and geometry (right). Figure 186 shows the obtained magnetic field gradient with respect to the longitudinal axis.

Table 55 FODO quadrupole main parameters

Parameter	Value	Units
Integrated field gradient	10	T
Field gradient	165	Tm^{-1}
Effective length	60	mm
Aperture radius	4	mm

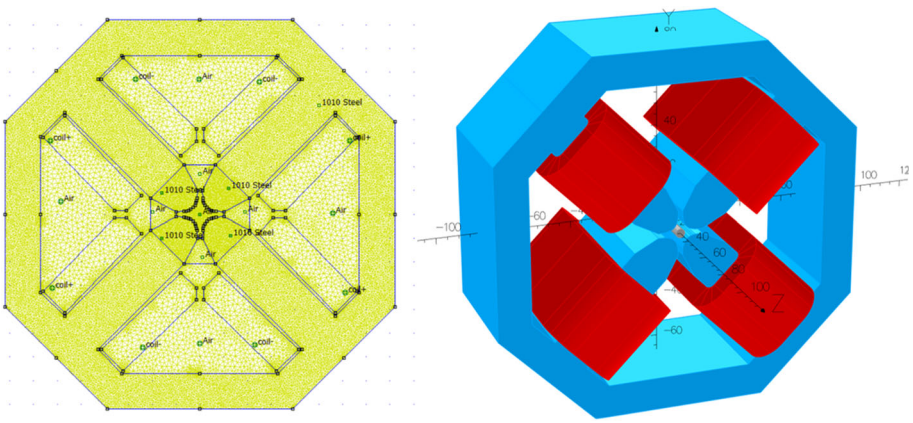

Fig. 183 2D (left) and 3D (right) models of the FODO quadrupole magnet

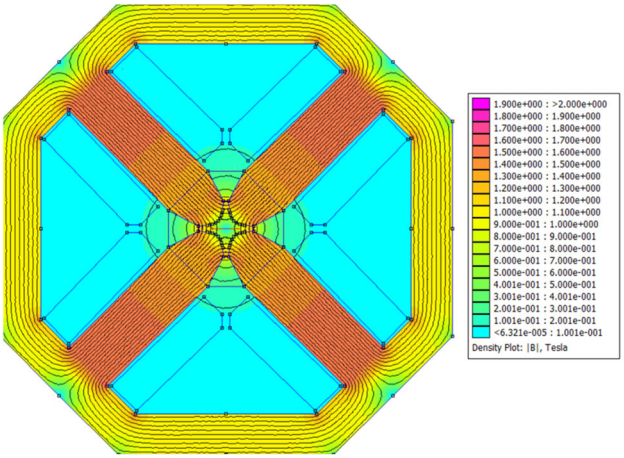

Fig. 184 Magnetic field intensity inside the FODO quadrupole magnet

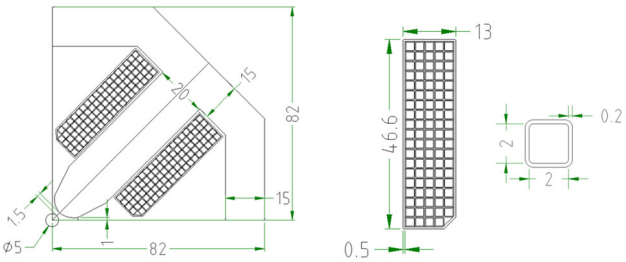

Fig. 185 Left: FODO quadrupole magnet. Right: coil cross-section for the FODO quadrupoles. Dimensions in mm

To calculate the field gradient at $x = 2\,\text{mm}$ versus the longitudinal direction in Opera 3D, the field is calculated on circles with radius 2 mm moving along the beam direction in steps of 4 mm. Using a Fast Fourier Transformation, the magnetic field, the field gradient, and higher order harmonics are obtained in each location. Having the field gradient at different longitudinal locations, the integrated field gradient at $x = 2\,\text{mm}$ is calculated to be 10 T.

Harmonic analysis

The strength and relative strength of nominal and the first three allowed higher order multipole components for the FODO quadrupole are summarized in Table 56 and Fig. 187.

6.1.4.6 Electrical and cooling parameters

FODO quadrupole magnets in the afterburner line have a small gap radius of 4 mm, which increase the quadrupole strength significantly. Therefore, having a small amount of current in each coil and a dissipated power of 100 W per magnet, the coils can be wound from solid copper conductors, rather than hollow conductors. Table 57 shows the FODO magnets electrical and cooling parameters.

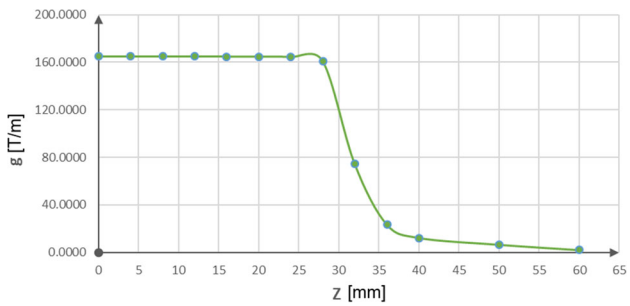

Fig. 186 FODO quadrupole field gradient versus longitudinal distance z

Table 56 FODO quadrupole field coefficients at 2 mm

n	Type	B_n(2 mm) [T]	B_n/B_2 (2 mm)
2	Q	3.300×10^{-1}	1
6	Q	-1.271×10^{-5}	3.85×10^{-5}
10	Q	1.937×10^{-6}	5.87×10^{-6}
14	Q	7.029×10^{-9}	2.13×10^{-8}

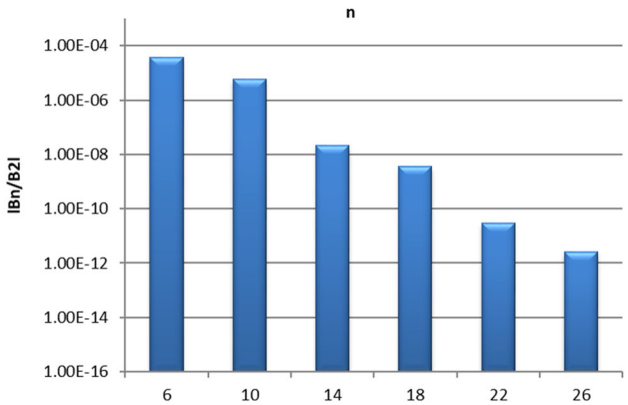

Fig. 187 Absolute normalized multipole errors in the 2 mm radius. The quadrupolar component, $n = 2$, is not shown

Table 57 Afterburner FODO quadrupole magnets electrical and cooling parameters

Parameter	Value	Units
Effective length	0.06	m
Field strength	165	Tm^{-1}
Full gap	8	mm
Total ampere-turns per coil	1230	At
Operating current	13	A
Number of turns per coil	94	–
Conductor dimensions	2×2	mm
Copper area	4	mm^2
Current density	3.27	$\mathrm{A\,mm}^{-2}$
Voltage drop per magnet	7.41	V
Resistance per magnet	0.56	Ω
Power per magnet	97	W

6.2 Photon beamlines

Experiments performed at FEL facilities can be broadly divided into two distinct categories: time-resolved microscopy and photon energy-resolved spectroscopy. In the first category of experiments, fs FEL pulses are used to follow the temporal dynamics of the system in question. Meanwhile, in the second category, the sub-eV energy resolution is employed to study, for instance, element-specific X-ray absorption peaks with respect to position and spectral line shape. To enable the second category, the photon beam is monochromatised to a sub-eV spectral width using a dispersive optical element and a system that allows for the transmission of X-rays only in the desired photon energy range. The corresponding beamline is referred to as a mono beamline. For time-resolved experiments, the full bandwidth of photon pulses is used to maximize the photon flux on the sample. The corresponding beamline must provide high transmission and is commonly referred to as a pink beamline. The CompactLight design provides mono and pink beamline capabilities in the whole operation range from 0.25 to 16 keV.

The CompactLight design has a unique feature of two independently tunable undulator lines driven by twin bunches from the same accelerator. The twin-bunch approach creates an opportunity for X-ray pump/X-ray probe experiments in a wide range of photon energies not accessible with any other existing or planned FEL. The time and energy separation between the photon pulses from twin bunches can be varied to a large extent. To utilize these unique X-ray pump/X-ray probe capabilities, three *dual* endstations are foreseen: (i) a Soft X-ray (SXR) endstation, 0.25–2 keV, for SXR pump/SXR probe experiments; (ii) an SXR/Tender X-ray (TXR) endstation with an SXR pump and a probe in the TXR, 2–8 keV, range; and (iii) a Hard X-ray (HXR) station with the pump and probe being both either in the TXR or HXR, 8–16 keV, range. In addition, two standalone endstations (one SXR, one HXR endstation) are also foreseen to efficiently utilize the available beam time.

6.2.0.1 Optical layout

Figure 188 shows the optical layout (not to scale) of a photon transport system for the FEL-1 and FEL-2. The photon transport system starts with a so-called front end containing a bremsstrahlung collimator, a photon shutter and a set of photon diagnostics. The bremsstrahlung collimator removes non-coherent, strongly divergent bremsstrahlung radiation and broadband spontaneous undulator radiation. The photon shutter is the first element of a safety system and must withstand full FEL fluence in case of a sudden beamline shutdown.

The front end is followed by photon beamlines and an experimental area hosting user end stations. To facilitate the discussion of individual photon beamlines, Fig. 189 introduces a *naming convention for beamlines*. The SXR endstations are primarily concentrated on the FEL-1 side, whereas the HXR ones are mostly located on the FEL-2 side. This choice is dictated by the fact that after the complete upgrade, FEL-1 can be independently operated in an SXR range of 0.25–3.1 keV at 1 kHz repetition rate (the corresponding electron energy range is 0.95–2.4 GeV). Hence, it is convenient to place SXR endstations close to FEL-1. Three SXR beamlines serving FEL-1, $B_{1s,\,S,\,m}$, $B_{1d,\,S,\,m}$ and $B_{1d,\,S/T,\,m}$, share the same monochromator based on variable-line-spacing gratings. Two interchangeable gratings are available in the monochromator to cover the 0.25–2.2 keV photon energy range.[3] These beamlines can also operate in pink mode by retracting the gratings. In addition, an HXR beamline up to 16 keV, $B_{1d,\,H,\,m}$, from FEL-1 is used for X-ray pump/probe experiments at the central dual end station. FEL-2 is served by 4 beamlines: (i) one SXR beamline, $B_{2d,\,S,\,p}$, providing the beam to the dual SXR endstation, (ii) one HXR pink/mono beamline, $B_{2s,\,H,\,p/m}$, providing the beam to a standalone station, (iii) two HXR and TXR beamlines, $B_{2d,\,H,\,m}$ and $B_{2d,\,S/T,\,p}$ providing the beam to the other two dual stations. The hard beamlines contain mirrors with two types of coatings to cover the whole range from 2 to 16 keV.

The beamlines include steering mirrors that direct the X-ray beam into corresponding end stations, refocusing Kirkpatrick–Baez (KB) optics to refocus the beam at the sample position and monochromators in monochromatic mode. The mirrors are operated in the regime of total external reflection with incidence angles of a few tens of milliradians for SXR and a few milliradians for HXR. Incoupling of attosecond UV pulses from a high-harmonic generation (HHG) source is foreseen for some pink beamlines for ultrafast pump-probe experiments.

6.2.0.2 Overview of the performance of beamlines

Table 58 summarizes the performance of photon beamlines based on simulations performed with RAY [257]. To realize efficient total external reflection by the beamline mirrors, different mirror materials depending on the photon energy range are used. Based on the simulation results for different materials, it is convenient to define three-photon energy ranges: (i) SXR from 0.25 to 2.2 keV with Au mirrors, (ii) TXR from 2 to 8 keV with B_4C mirrors, and (iii) HXR from 8 to 16 keV with mirror coating composed of 5 nm B_4C on 25 nm of Rh. The successful deposition of B_4C on Rh is demonstrated for the European XFEL [258]. The mono-beamlines can also be operated in pink mode by retracting dispersive elements (a grating or a crystal).

6.2.0.3 Overview of the photon transport area and experimental hall

The CompactLight experimental area of 24.5 by 85 m (2060 m^2) is located 65 m away from the undulator end. The area comprises 5 X-ray hutches, 2 laser laboratories, 2 control rooms, and a technical gallery to access the hutches. For comparison, the total area of the SwissFEL experimental facility is also around 2000 m^2 with 1200 m^2 allocated for X-ray hutches. The hutches host refocusing optics, photon diagnostics, endstations, local control electronics, and data acquisition systems. The optical laser beam can be transported from the laser room, located upstream of the hutches, to incoupling mirrors positioned close to the endstations. The hutches and laser laboratories are surrounded by a technical gallery for easy access. Note that the walls of the two hutches are positioned in such a way that they are exactly on straight lines from the accelerators. Partly, this naturally prevents personnel from being illuminated by neutron radiation from the accelerators.

[3] The acceptance range of photon beamlines in terms of photon energies is designed with some margin.

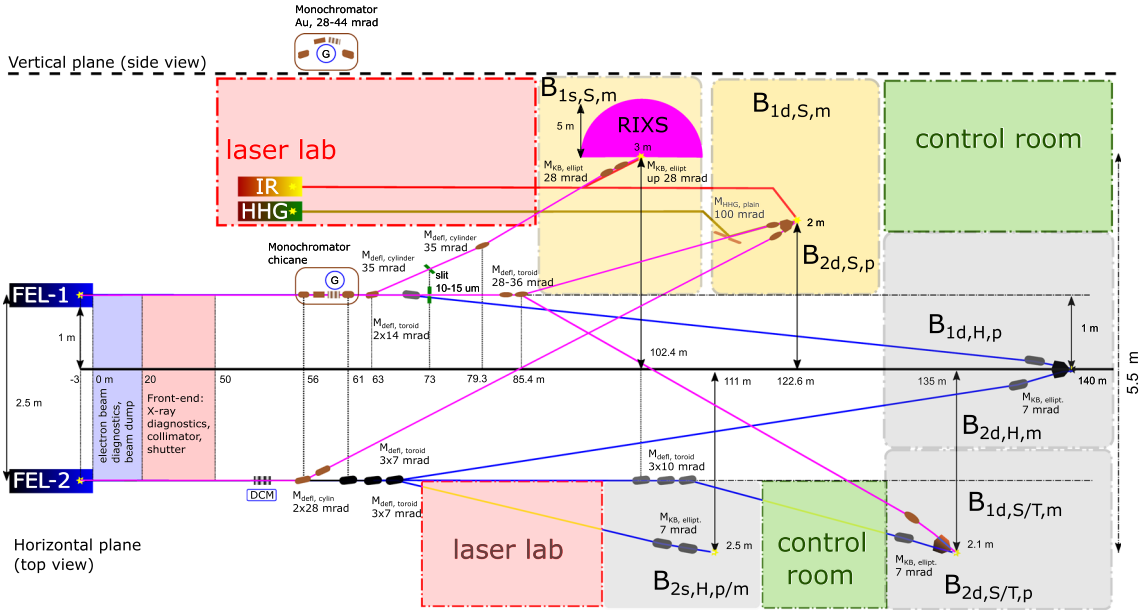

Fig. 188 Schematic of the optical layout of the photon beamlines. The two virtual sources of FEL-1 and FEL-2, correspondingly, are depicted by the yellow stars (on the left). The photon beam path is shown by the blue (hard X-rays) and pink (soft X-rays) lines. The beam is focused into five endstations: three dual stations and two standalone ones. The main optical elements are mirrors denoted by "M" (the deflection angle and the type of curvature are indicated in the subscript) and monochromators (grating-based, "G", or double-crystal-based, "DCM"). The hutches (shaded areas) hosting the endstations are also schematically indicated. External lasers for pumping the sample in the IR and VUV ranges will be available

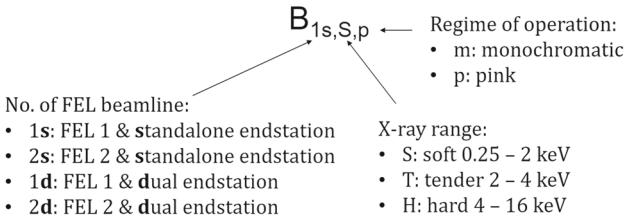

Fig. 189 Naming convention for photon beamlines: the numeral in the subscript indicates the FEL from which the photon beam comes. The letter, next to the numeral, indicates whether the beamline serves a standalone endstation or a dual one. The capital letter after the first comma specifies the operation photon energy range of the beamline. The last letter indicates whether the beamline is operated in monochromatic mode or pink mode (unaltered photon energy range of the FEL beam)

6.2.1 General aspects of photon transport

6.2.1.1 Virtual FEL source

FEL lasing occurs over an extended interaction length in the undulator, but in the far-field zone, the emitted radiation can be approximated as the one emitted by a localized source [259]. This source is called a virtual FEL source, and its use simplifies the design of beamlines. The calculation of the FEL source parameters requires massive simulations, which were carried out at 12 keV. A simple analytical model is used to calculate the FEL source parameters over the whole photon range. Most of the FEL pulse energy is emitted in the last undulator modules. The electron beam is usually well bunched and emits strong, coherent undulator radiation. Then, the FEL intensity is approximately constant, and the virtual source position can be estimated as

$$z_{\mathrm{vir}} = \frac{\int_0^L z\mathrm{d}z \int_0^\infty I_{\mathrm{und}} r\mathrm{d}r}{\int_0^L \mathrm{d}z \int_0^\infty I_{\mathrm{und}} r\mathrm{d}r} \approx \frac{L}{2}\left(1 + \frac{L^2}{6z_R^2}\right). \tag{57}$$

Table 58 Overview of the performance of photon beamlines

X-ray range	Mode of operation	Beamline	Mirror material	Transmission (%)	Photon energy resolution (meV)	Pulse stretch (fs)	Beam size FWHM (μm)
Soft: 0.25-2 keV	Pink	$B_{2d,\,S,\,p}$	25 nm Au	75–85	–	–	6.5–2; 4–3
		$B_{2d,\,S/T,\,p}$		53–82	–	–	2.8–1.1; 2–1.1
	Mono	$B_{1s,\,S,\,m}$		1–4	40–500	200–10	8–5; 4–2
		$B_{1d,\,S,\,m}$		1–6	40–500	200–10	9–4; 7–3
		$B_{1d,\,S/T,\,m}$		0.6–3	40–500	200–10	4–2.4; 3.2–1.6
Tender: 2–8 keV	Pink	$B_{2s,\,H,\,p}$	25 nm B_4C	83–97	–	–	0.99; 0.83
		$B_{2d,\,H,\,p}$		68–98	–	–	0.77; 0.65
		$B_{2d,\,S/T,\,p}$		73–97	–	–	0.83; 0.7
	Mono	$B_{2d,\,H,\,m}$		1.2–11.2	120–1000	–	0.77; 0.65
Hard: 8–16 keV	Pink	$B_{2s,\,H,\,p}$	5 nm B_4C on 25 nm Rh	85–69	–	–	0.71
		$B_{1d,\,H,\,p}$		86–75	–	–	0.55
	Mono	$B_{2d,\,H,\,m}$		2.1	230–470	–	0.55
		$B_{2s,\,H,\,m}$		2	230–470	–	0.71

The results are obtained with software RAY [257]. A relative FEL bandwidth of 0.1% is assumed in the simulations

Here, $I_{\rm und}$ is the intensity of undulator radiation with a transverse Gaussian distribution and $z_R = 4\pi\sigma_u^2/\lambda$ is the Rayleigh length, and σ_u is the rms size of the radiation mode. For coherent undulator radiation [260], $I_{\rm und} = I_{0,\rm und}\exp(-r^2/\sigma_u^2)$ and $\sigma_u^2 = \sigma_b^2(1 + z^2/z_R^2)$, where σ_b is the electron beam size.

The rms size of the virtual undulator source is defined as

$$\sigma_{\rm vir}^2 = \frac{\int_0^L {\rm d}z \int_0^\infty r^2 I_{\rm und} r {\rm d}r}{\int_0^L {\rm d}z \int_0^\infty I_{\rm und} r {\rm d}r} = \sigma_b^2\left(1 + \frac{1}{3}\frac{L^2}{z_R^2}\right). \tag{58}$$

The virtual source size $\sigma_{\rm vir}^2$ scales with the wavelength as $(1+\alpha\lambda^2)$, where α is a scaling parameter. The divergence of the virtual source is calculated as $M^2\lambda/(4\pi\sigma_{\rm vir})$, where M^2 is the optical beam parameter.

Figure 190 shows the estimated virtual source parameters over the entire CompactLight operation range. There are jumps in the photon beam size because of different electron beam energies and different focusing conditions.

6.2.1.2 Material X-ray absorption and damage

An important consideration in the beamline design is the choice of the material of the optical components and the operational angle of incidence on them. Figure 191 shows the absorption coefficient for different materials in a range from 0.25 to 16 keV. Because of absorption edges several materials have to be used: (i) gold (Au) for SXR

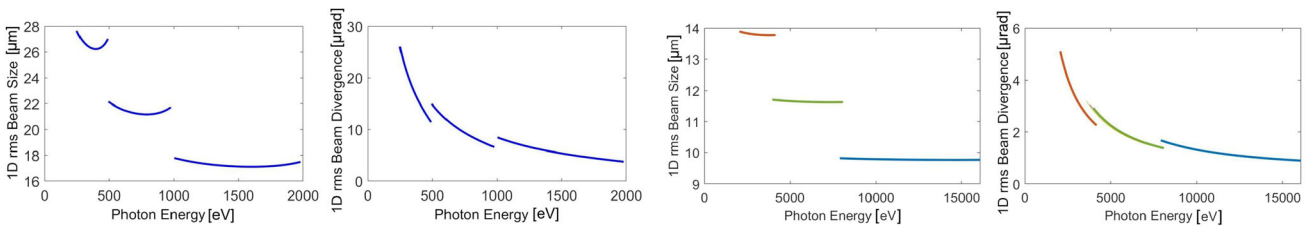

Fig. 190 Analytically estimated parameters of the virtual FEL source

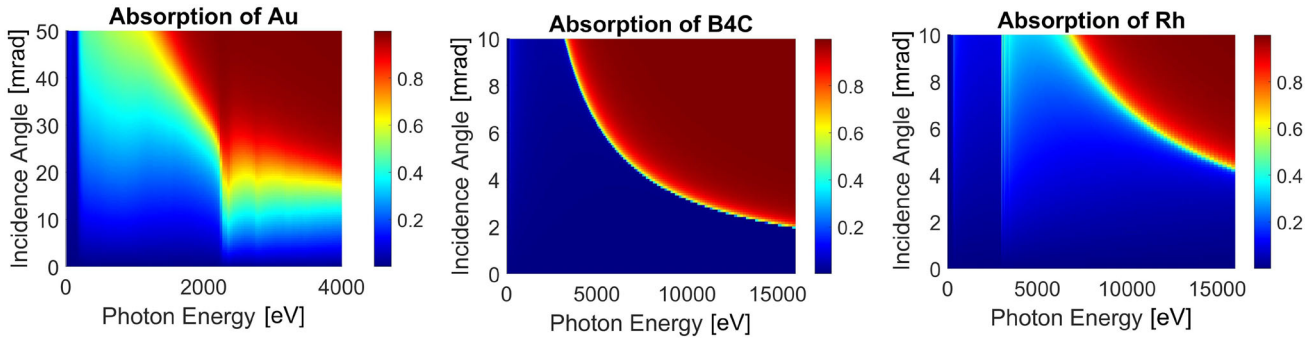

Fig. 191 Absorption of materials vs photon energy and incidence angle

(0.25–2.2 keV) with a critical incidence angle of around 25 mrad; (ii) boron carbide (B_4C) for TXR (2–8 keV) with a critical angle of 4 mrad; and (iii) rhodium (Rh) for HXR (8–16 keV) with a critical angle of 4 mrad. Boron carbide has the lowest absorption coefficient in the entire operation region compared to many other materials. It has also the highest X-ray damage threshold but simultaneously exhibits a sharp absorption peak at 285 eV due to the carbon edge. In addition, B_4C has a small critical angle at 16 keV. Hence, B_4C is used only for TXR. For transportation and incoupling of VUV pulses for pump-probe experiments, Au is a suitable material.

Some nonlinear experiments require a very clean spectrum without harmonics. For that, the incidence angle on KB mirrors can be increased beyond the critical angle of the harmonic. The sample position and detectors must, however, be adjustable to accommodate for a change in the focus position that might reach a few millimeters.

The left plot in Fig. 192 shows the maximum incident fluence of X-ray radiation that Au, B_4C, and Rh can handle depending on the incidence angle and photon energy. Note that the damage threshold considerably increases with photon energy because of the increased attenuation length, i.e., the material becomes transparent and the energy deposition is distributed over a larger volume. The right plot in Fig. 192 presents the calculation results for the fluence of FEL pulses 50 m away from the undulator. The FEL fluence is on average one order of magnitude below the damage level.

It is noted that the SASE FEL process is stochastic and pulse energies much higher than the mean pulse energy are statistically possible [60]. The statistical analysis of SASE pulses shows that within a 10-year operation period at 100 Hz repetition rate, the statistically possible maximum energy of the FEL pulse may exceed the mean pulse energy by around 50%. However, the resulting fluence would still be one order of magnitude lower than the damage limit. Hence, there is room for increasing the FEL pulse energy in the future.

6.2.1.3 Dual endstations and synchronization

Figure 193 shows a simplified layout of the electron and optical paths in the CompactLight facility. Consider the synchronization of HXR pulses. From the schematic, it follows that the optical delay, Δt_{opt}, partly compensates for the electron delay in the dogleg DL-1. This allows one to write a condition $\Delta t_{\mathrm{DL1}} - \Delta t_{\mathrm{opt}} = nT$, which determines the required electron delay Δt_{DL1} depending on the number of RF cycles n and an RF period, T, of 166 ps. For 5 RF cycles, $\Delta t_{\mathrm{DL1}} = 860$ ps. For the synchronization of SXR either of dog-legs can be used, $\Delta t_{\mathrm{DL2}} - \Delta t_{\mathrm{opt}} = nT$ and for 3 RF cycles, $\Delta t_{\mathrm{DL2}} = 526.5$ ps. For S/TXR, the optical delay increases the electron delay so that $\Delta t_{\mathrm{DL1}} + \Delta t_{\mathrm{opt}} = nT$. Hence, DL-1 can be used to synchronize photon pulses at all three dual

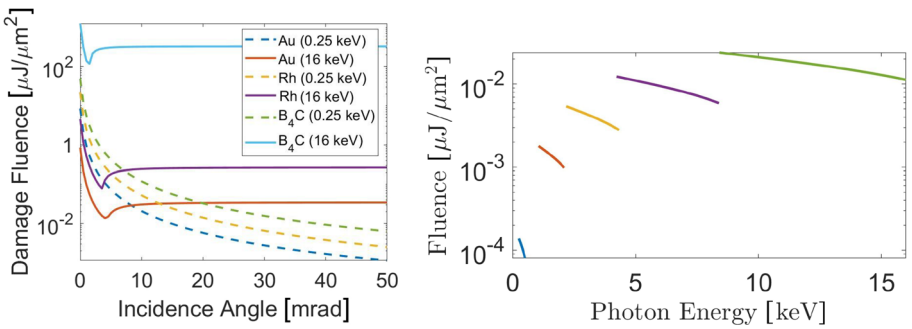

Fig. 192 Maximum tolerable fluence vs incidence angle for Au, B_4C, and Rh (left plot). The FEL fluence vs photon energy at 50 m away from the virtual source (right plot)

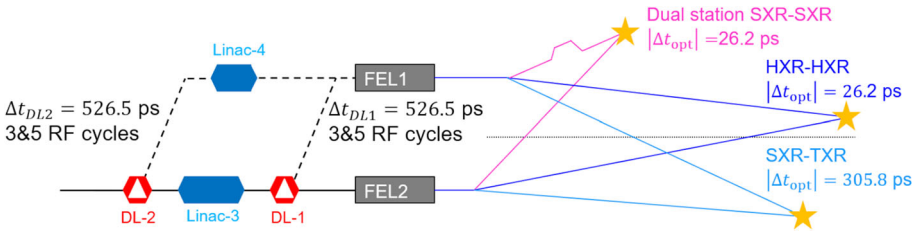

Fig. 193 Schematic layout of the accelerator with full upgrade, two doglegs (DL-1) and (DL-2), two undulators, and three dual endstations. The relative optical delays are indicated

endstations. Meanwhile, DL-2 adds additional flexibility in tuning the photon energy range by means of the Linac-4. Any residual differences between the photon pulses will be compensated for with a small timing chicane for electron bunches.

6.2.1.4 External laser incoupling

For pump-probe experiments with external lasers, pumping capabilities in the IR and VUV regions are foreseen and a high-harmonic generation source in the laser laboratory is planned. While IR pulses can easily be focused on the sample from the side, VUV pulses usually require refocusing and a more complex incoupling scheme. In this design, VUV pulses are incoupled via a holed mirror placed in the X-ray beam path, see Fig. 188. A sufficiently large hole in the centre allows the X-ray beam to pass through and simultaneously sends the oversized VUV beam onto the KB mirrors. To balance the losses of the incoupled VUV beam and the transmission of the X-ray beam through the incoupling mirror, the mirror aperture will have a diameter corresponding to 5σ of the maximum X-ray beam size. The VUV-incoupling setup will be located approximately 2 m before the corresponding first KB mirror. In the beamline, $B_{2d,S,p}$ the holed mirror will collimate the VUV beam, so that its focus matches that of the X-ray beam, which is also collimated.

6.2.2 Soft X-ray beamlines

6.2.2.1 Grating monochromator

The central element of the SXR monobeamlines is a monochromator composed of a grating, a monochromator mirror, and an exit slit. The CompactLight design makes use of a regular grating combined with a cylindrical mirror focusing in the dispersive plane, Fig. 194A. The grating is used in the regime of a constant-deviation mount, i.e., the deflection angle of the grating is independent of the wavelength. This allows the focusing mirror to be kept in a fixed position. The photon energy scan (selection) is done by changing the yaw angle of the grating. In this type of mount, the illuminated grating area changes during an energy scan, so that the resolving power also slightly varies. The focal length of the system is independent of the wavelength. Compared to other configurations of the grating type and mount, Fig. 194B, C, the mount presented in Fig. 194A provides the simplest operation. Note that the configuration (C), based on a varied-line-spacing (VLS) toroidal grating, provides almost wavelength-independent focusing via a linear chirp of the local grating period. The configuration (C) is widely used in synchrotron beamlines. However, in a wide photon energy range, the effect of wavelength-dependent focusing is noticeable and the position of the slit must be adjusted to compensate for a shift in focus. This makes the configuration (C) more difficult to operate compared with the configuration (A).

Downstream in the mono beamline, the monochromator is followed by a spectral diagnostic unit. A set of KB mirrors is used to refocus the monochromatised beam onto the sample in the mono endstation.

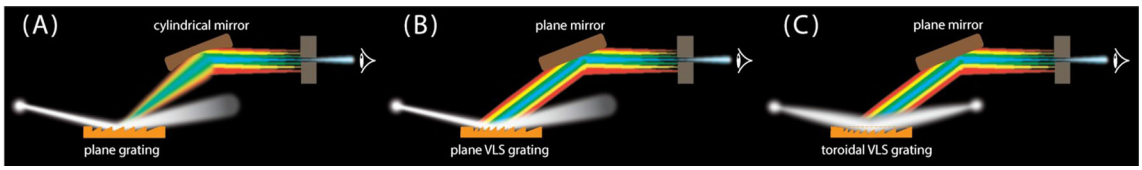

Fig. 194 Types and mount of a grating-based monochromator

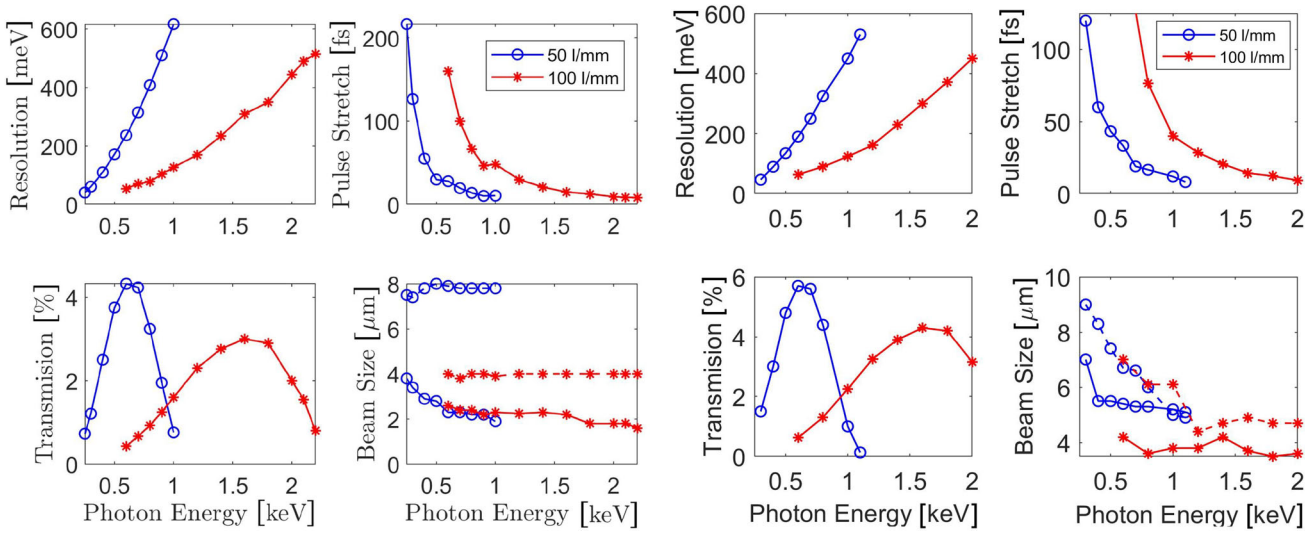

Fig. 195 Photon beam parameters on the sample for the $B_{1s,S,m}$ (left) and $B_{1d,S,m}$ (right) beamlines

6.2.2.2 Photon beam parameters on the sample

The main parameters of the SXR beamlines are summarized in Table 58 and Fig. 195 presents further details of the photon beam parameters for the $B_{1s,S,m}$ and $B_{1d,S,m}$ mono beamlines. Two gratings with line spacings of 50 and 100 lines/mm are used to maximize the transmission over the whole photon energy range while allowing high resolution and limited pulse stretching. By switching from the 50 l/mm grating to the 100 l/mm grating at photon energies above 1 keV, pulse stretching below approximately 100 fs is provided in the 0.25–2 keV photon energy range, while the transmission and resolution are high. To further increase the resolution, a grating with a higher line spacing can be used. The gratings have blaze angles of 0.15° (50 l/mm) and 0.2° (100 l/mm) and are roughly 0.5 m long. Note that nowadays blazed SXR gratings as long as 0.5 m can be produced [261].

6.2.3 Hard X-ray beamlines

6.2.3.1 Photon beam parameters at the sample

Similarly to the SXR beamlines, the main parameters of the HXR beamlines are summarized in Table 58, and Fig. 196 presents two illustrative cases of the performance of the $B_{2d,H,m}$ and $B_{2s,H,p}$ beamlines. A double-crystal monochromator based on a Si crystal cut either in the (111) or (311) orientation is used to cover the operational range from 2 to 16 keV.

6.2.3.2 X-ray mirrors

FEL radiation possesses a high degree of transverse coherence (typically 90%) and an optical transport system must preserve this coherence. To this end, the optical system must satisfy the Marechal criterion that an overall rms wavefront distortion is smaller than 1/14 of the wavelength of interest. For a transport system composed of N mirrors, the condition for preserving the wavefront is $\lambda/14 = \sqrt{N}2h\sin\alpha$, where α is the grazing incidence angle and h is the rms surface roughness [262]. In the CompactLight design, α is around 15 mrad, so that the maximum acceptable peak-to-valley surface roughness is 2.5 nm at 2 keV. For comparison, for the LCLS SXR beamline, the surface roughness requirement is 1.5 nm. For HXR, the maximum acceptable roughness is 1.24 nm. The simulation results for the intensity reduction due to the surface roughness of a single mirror are depicted in Fig. 197. The result is somewhat dependent on the mirror coating material. It is noted that, for example at LCLS, thickness uniformity better than 0.14 nm rms has been demonstrated for B_4C coatings on top of a Si substrate [263].

6.3 Photon beam diagnostics and instruments

6.3.1 Overview of diagnostic methods

The CompactLight source (XLS) will deliver an X-ray photon beam with wavelength 5–0.08 Å (photon energy: 0.25–16 keV) and pulse-length 0.1–50 fs at repetition rate 0.1–1 kHz.

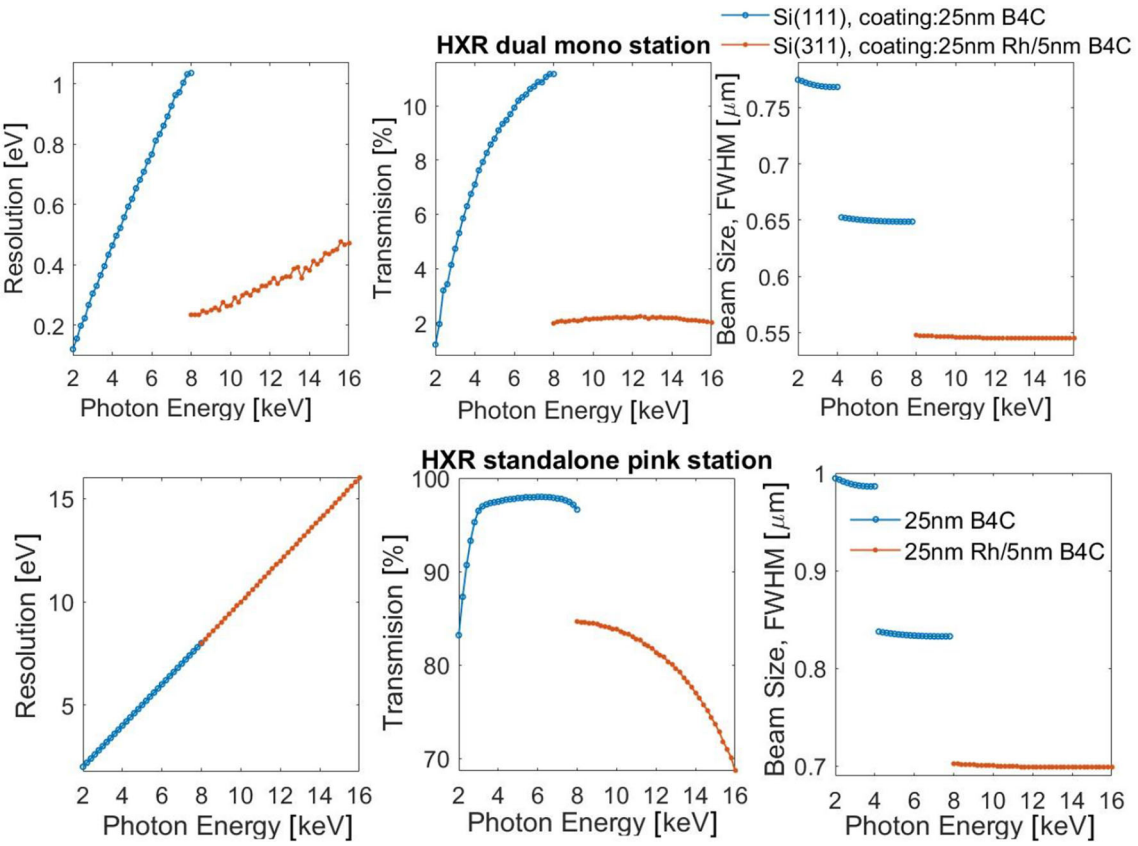

Fig. 196 Photon beam parameters on the sample for the $B_{2d,H,m}$ (top) and $B_{2s,H,p}$ (bottom) beamlines. The drop in transmission toward the lower photon-energy range, particularly visible in the bottom figure, is due to clipping of the X-ray mirrors at large beam divergence

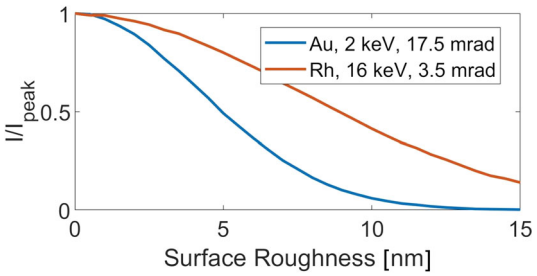

Fig. 197 Simulation of the normalized intensity transmitted by a mirror for different heights of surface roughness. The simulations are performed with RAY

The machine physicists and the experimental user groups will need to know as completely as possible the characteristics of the photon beam. For the machine physicists, the information about the FEL radiation will be used for setup, operation and optimization of the accelerator, undulators, and X-ray optics during every phase from commissioning to user operation. Similarly, the knowledge of the photon beam properties will be necessary for users for experimental data normalization and interpretation. Consequently, to provide the most useful information about the FEL photon beam, dedicated diagnostics should be implemented to assess properties such as intensity, position, shape, lateral dimensions, and spectrum. A further mandatory request is that the beam properties should be determined on a pulse-to-pulse basis and, whenever possible, in a non-invasive or quasi-non-invasive fashion. Of course, especially at the beginning of the commissioning process and for specific checks and verifications, invasive diagnostics will also be implemented.

Besides the already-mentioned properties that will be characterized and monitored by diagnostics installed all along the photon beam transport (starting from the undulators), other diagnostics will be integrated in the experimental hall, close to the endstations. In particular, temporal diagnostics, devoted to monitoring the pulse arrival time, the pulse duration and possibly the temporal shape, will be employed together with wavefront- and coherence-dedicated instruments in the experimental hall. Figure 198 shows an overview of the instruments and

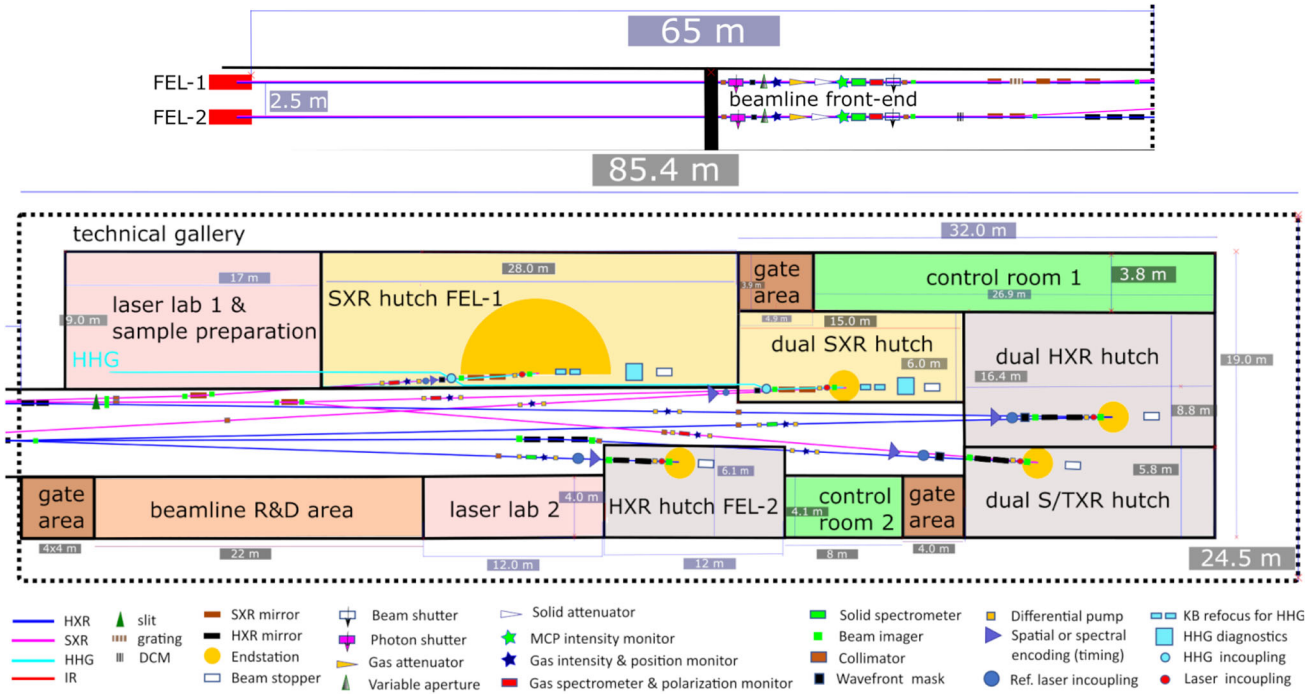

Fig. 198 Beamline front-end, experimental area, and diagnostics

diagnostics along the beamlines. Most of these can operate parasitically to enable online characterization and monitoring of the FEL beam.

After the front-end hall, the beamlines split into several branchlines, as shown in Fig. 198 (bottom). The branchlines are equipped with diagnostics suitable for the photon-energy range of the specific branch. An online spectrometer, intensity monitor and position monitor are included in every mono-branch to characterize the FEL beam after passing through the monochromator. An arrival-time monitor is placed relatively close to the endstation of each branch to accurately characterize the femtosecond-scale FEL pulses. The arrival-time monitor will use spatial or spectral encoding with a temporal resolution of ~ 10 fs. Higher Harmonic Generation (HHG) diagnostics are placed after endstations that can couple the FEL and the HHG beam. The HHG beam is coupled out and directed toward the diagnostics station after the endstation using a holed mirror, exploiting the larger spot size of the HHG beam compared to the FEL beam that passes through the hole. Refocusing of the HHG beam after the endstation is obtained by KB mirrors. A Resonant Inelastic X-ray Scattering (RIXS) spectrometer, equipped with a 5 m rotatable spectrometer arm that allows angular resolved RIXS experiments with a resolving power of approximately 10,000, is foreseen at one SXR beamline.

6.3.2 Intensity and position

The determination of the intensity of the FEL photon beam (i.e., pulse energy in μJ or number of photons per pulse) is mandatory and, at least during user operation, should be exploited non-invasively and shot-to-shot. To accomplish this task the most important instrument is the X-ray gas monitor (XGM), which is used during normal operation. Besides the XGM, other intensity diagnostics can be employed during the early stages of machine preparation and optimization, such as MCP-based detectors.

For monitoring of the photon beam position, the same XGM can be used, together with invasive diagnostics such as imagers (of several kinds) useful for initial commissioning with spontaneous radiation (synchrotron radiation), for FEL commissioning, or for the setup of measurements.

6.3.2.1 X-ray gas monitor

The X-ray gas monitor is a gas-based system that operates employing a photoionization process induced by the FEL beam in a gas-filled vacuum chamber [264–267]. The X-ray pulse, traveling through the XGM, ionizes the gas, which is dosed into the vacuum chamber at a base pressure of about 10^{-5} mbar, and photo-electrons and photo-ions are generated and collected. The system, using rare gases (Xe, Kr, Ne) or nitrogen, to cover the X-ray beam wavelength range, is thus practically transparent and indestructible, and is well suited for high average flux

Fig. 199 CAD rendering of the XGM used at the European XFEL. Figure from [267]

and peak energies, since there is no damage or heating. Moreover, this diagnostic has no influence on the wavefront and coherence of the transmitted pulses and can be operated at very high pulse repetition rates (up to MHz).

An XGM consists of at least two vacuum chambers containing one X-ray gas monitor detector (XGMD) each, one dedicated to measuring the single-shot-resolved photo-electron signal and the other dedicated to measuring the averaged calibrated photo-ion signal. Each chamber also includes electrodes for measuring the X-ray beam position in one transverse direction: combining two of them (as in one XGM) then gives the beam position in the transverse plane. As a consequence, individual X-ray pulses with fs-durations containing from 10^7 to 10^{15} photons can be measured with <10%-absolute accuracy and $\leq$ 1%-relative (pulse-to-pulse) accuracy. For the same pulses, moreover, it is possible to determine the position in both transverse directions with an accuracy about $\pm 10\,\mu m$ over a range of $\pm 1\,mm$.

The XGM developed by a joint effort of DESY and European XFEL operates seamlessly up to 12 keV. For higher energies, it could be necessary to implement two additional modules to the XGM girder hosting two Huge Aperture open Multipliers (HAMP), which measure the single-shot-resolved photo-ion signal at higher sensitivity for harder X-rays than the XGMDs [267]. Figure 199 shows the sketch of the actual XGM used at the European XFEL (including the HAMPs). The implementation of the HAMPs into the CompactLight source will have to be discussed in more detail—the DESY group that developed the XGM are confident that it might not be necessary and that the XGMDs would be enough.

6.3.2.2 Imagers

To determine the position, trajectory, and/or transverse intensity profile of the FEL beam, some invasive diagnostics can be used [267]. This is especially true in the early stages of machine and transport commissioning as well as during beam finding/alignment procedures. Because they are dedicated to different purposes, imagers offer different resolutions, fields of view (FOV), and geometries, and can be located in different parts of the facility. Typically, every imager contains at least one Ce:YAG crystal that is viewed through a lens+camera system. Then, there are:

- Transmissive imagers: These are put close to the FEL sources and employ thin scintillators to allow the beam transmission to another downstream-placed scintillator so to provide beam pointing and beam offset data.
- Spontaneous radiation imagers: These present high photon sensitivity as they are supposed to detect spontaneous synchrotron radiation generated by single undulators during the commissioning phase. In particular, they should be operated together with a monochromator system (K-mono) used to analyze the radiation and measure the angular pointing and the a_w-parameter of single undulator segments.
- FEL imagers: These are used to determine precisely the transverse spatial intensity distribution of the FEL beam, thus providing parameters, such as position, size, and shape. There will be one for each FEL line.

- Insertable imagers: They are used all along the photon beam transport system to find and align the beam. They should be typically placed after each major optical element (mirrors, monochromators, etc.).
- Exit slit imagers: they are installed on the exit slit of the monochromator for beam alignment and single-shot spectra acquisition.

6.3.2.3 MCP-based detectors

During the initial commissioning of the undulators, when all the undulator sections are inserted, this kind of detector can measure the intensity signal from the initial stage up to the saturation regime [267]. It can employ either MCP-discs + photodiode or an MCP-intensified phosphor screen to detect the integrated intensity and help operators in setting up the FEL emission process. Moreover, during normal operation, they can provide pulse-resolved intensity monitoring in a parasitic way: they can be placed just outside of the direct FEL beam and detect a signal coming from the scattered radiation from the mirrors.

6.3.3 Spectrum

The determination of the spectral content of the FEL photon beam is mandatory, and it should be obtained non-invasively, online (during machine operation) and on a shot-to-shot basis. The instruments dedicated to this task are energy spectrometers that should cover the whole wavelength range delivered by the source. To efficiently cover it three different spectrometers are envisioned, ranging over the following intervals: 0.25–3 keV, 2–4 keV, and 3–16 keV.

6.3.3.1 Photoelectron spectrometer (0.25–3 keV)

To cover the lower energy part of the FEL emission, a photo-electron spectrometer (PES) can be used [268, 269]. This instrument can measure the spectrum (and polarization) of the photon pulse based on an angularly resolved time-of-flight measurement of photo-electrons. In particular, to be non-invasive, it uses a low-density gas target that is ionized by the passing photon pulse, generating ions and electrons that are collected and linked to the pulse intensity. The collection is realized by means of 16 electron time-of-flight (TOF) spectrometers oriented perpendicularly to the X-ray beam (see Fig. 200).

Each TOF spectrometer has a drift tube with tunable voltage that decelerates the electrons. The (fast) electronics measures the time difference between ionization and detection which is dependent on the photoelectron kinetic energy. The ionization takes place in a gas medium, which can be either a rare gas (Ne, Kr, Xe) or N_2, which is injected into the interaction volume via a capillary. By using these gases, it is possible to cover the 250–3000 eV X-ray region with enough cross-section for single-shot measurements, low photoelectron kinetic energies assuring good energy resolutions, and the ability to efficiently measure the polarization. The injection pressure of the gas is typically in the 10^{-5} - 10^{-7} mbar range, while the base pressure is about 10^{-8} mbar. These values guarantee

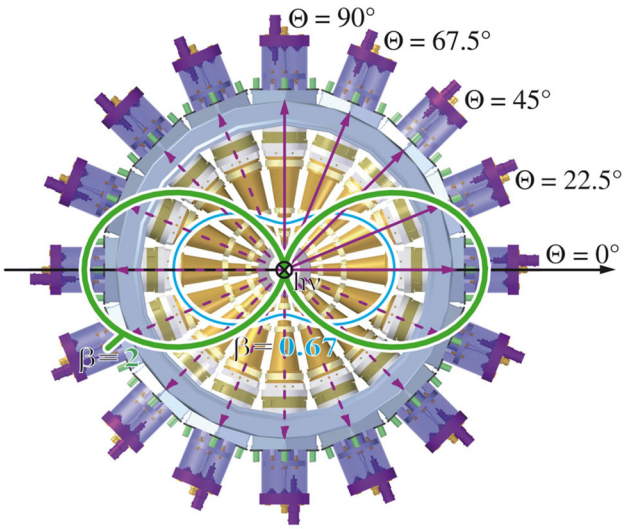

Fig. 200 Geometry of the 16 TOF spectrometers employed in the PES. The FEL beam enters perpendicularly with respect to the plane of the figure. As an example, the angular distributions of Ne 2p (blue) and He 12 (green) are reported. Figure from [269]

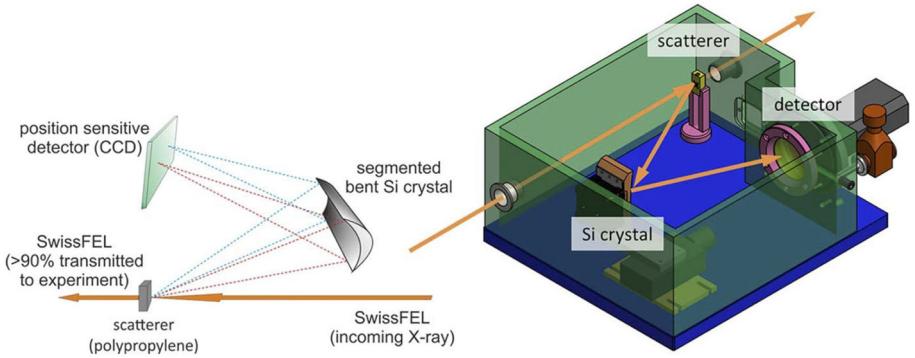

Fig. 201 Scheme of the von Hamos spectrometer used for the diagnostics of tender X-rays at the SwissFEL. Figure from [270]

the near transparency of the instrument with respect to the passing FEL beam. Finally, the PES is capable of determining the spectral content with a relative photon energy resolution of 10^{-3}–10^{-4}.

Besides the spectrum characterization, since the 16 TOF spectrometers of the PES can determine the photoelectron angular distribution, the PES can also non-invasively measure the (linear) polarization in a pulse-resolved way.

6.3.3.2 Tender X-ray spectrometer (2–4 keV)

The so-called tender X-ray range (from 2 to 4 keV) can be characterized with a spectrometer currently used at SwissFEL (PSI) [270]. The instrument is based on a dispersive von Hamos geometry-spectrometer combined with the use of a scattering sample to be inserted into the FEL beam. The sample, being a low atomic number and density material, once hit by the photon beam gives rise to an elastic Rayleigh scattering spectrum that replicates the incoming FEL pulse spectrum. The sample should be thin enough to guarantee the maximum possible transparency to the FEL beam and absorption edges should be avoided in the scatterer. Figure 201 shows the working principle and mechanical scheme of the spectrometer. The setup presents a single interaction point with the FEL beam and the generated photons are scattered over a large angle hitting an optical element made by a cylindrically bent substrate that has Si crystals glued on it. Working in a back-scattering geometry, the spectrometer can collect enough signal and determine the FEL spectrum with 10^{-4} energy resolution and a 2% bandwidth.

6.3.3.3 High-resolution hard X-ray spectrometer (3–16 keV)

In the hard X-ray range of the FEL emission, above 3 keV, a different energy spectrometer should be employed, based on a system of elements that utilize just a small fraction of the photon beam to determine the spectral content. Such an instrument, called a HIgh REsolution hard X-ray single-pulse diagnostic (HiREX) spectrometer at the European XFEL [271], is made of a diamond diffraction grating used in transmission to split off a small fraction (0.1%) of the photon beam, a bent crystal as a dispersive element, and a 1D MHz-repetition rate detector. The working principle is sketched in Fig. 202. Typically, over the whole range of operation of this spectrometer, about 95% transmission is achieved, while 5% is spread into all diffraction orders.

The initial diffraction of the FEL beam is realized by a diamond transmission grating that is inserted directly into the beam, splitting a portion of it while leaving the transmitted beam almost unchanged for the experiments in the endstations. To cover efficiently the entire photon energy range a set of gratings has to be used with different pitches. Diamond is chosen as the material for grating fabrication as it presents high thermal conductivity (2052 W/mK at 300 K), low absorption for hard X-rays, and a higher single-shot damage threshold as compared to silicon.

Once the first diffraction order has been generated, it hits a bent silicon crystal where it is Bragg-reflected and thus dispersed spectrally. To cover the whole photon energy range different crystals with different bending radii are employed, which are then optimized to match the detecting camera parameters (pixel size, detector chip dimension, and detector distance).

The overall performance of such a spectrometer includes a transmission of about 95%, energy resolution in the 10^{-5} range and a bandwidth of 0.5%, working on a shot-to-shot basis during normal operation.

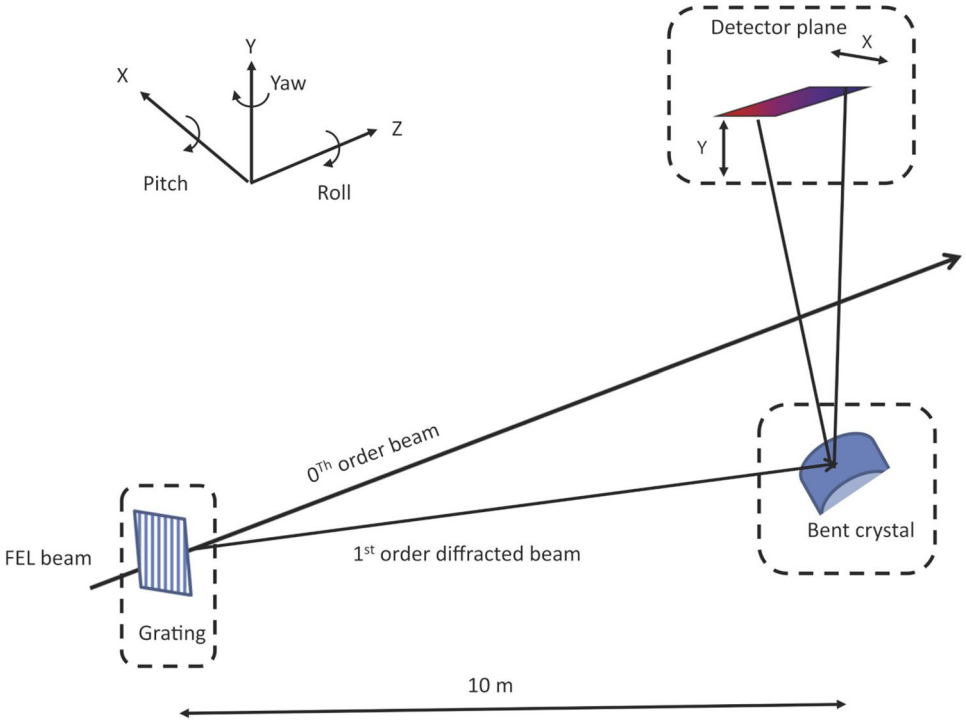

Fig. 202 Schematic of the HIREX spectrometer at the European XFEL. The grating lines are oriented in the vertical direction perpendicular to the FEL, so that the diffraction takes place in the horizontal plane. The bent crystal, then, deviates the radiation vertically onto the detector. Figure from [271]

6.3.4 Temporal monitors

Precise determination of the X-ray pulse arrival time is necessary for accurate analysis of pump-probe experiments as it allows one to compensate for the temporal jitter of the SASE pulses. In addition, characterization of the pulse duration can be useful for obtaining the X-ray pulse peak intensity, which is of importance, e.g., for nonlinear experiments. Table 59 provides a comparison of different methods for temporal characterization of FEL pulses. All these methods have already been demonstrated at other FEL facilities. The streaking techniques are relatively complicated methods that require overlapping an IR or THz pulse with the X-ray pulse in a gas. The X-ray-generated photoelectrons experience different E-fields depending on the relative delay between the IR/THz fields and X-ray pulses, which results in a varying kinetic energy with the delay. Thus, the delay, as well as the pulse duration, of the X-ray pulse can be obtained by measuring the photoelectron kinetic energies. Angular streaking uses circularly polarized streaking fields, which permits higher temporal resolution, because the pulse delay is imprinted in the angle of the ejected photoelectron. In contrast, spatial and spectral encoding are less complicated methods in which the X-ray-induced reflectivity change of an optical pulse, overlapping with the X-ray pulse on a solid sheet, is measured. In spectral encoding, the delay between the pulses is encoded in the spectrum of a chirped optical pulse, while spatial encoding relies on the varying delay along the beam cross-sections of two beams at an angle.

In the baseline design, the X-ray pulse arrival time will be measured using spatial and spectral encoding. Both of the methods have advantages and disadvantages and it is common to implement them both for better accuracy and reliability as done, for example, at the SACLA FEL. Since the arrival time will be measured for all beams individually, nearly overlapping pulses from two beams entering a dual station can be resolved, and therefore, the possibility of resolving double pulses, offered by streaking experiments, is not critical. Streaking experiments may, however, be included as a future upgrade as a tool to monitor the pulse profile. In the baseline design, the XLS pulse duration will be obtained indirectly. The measured parameters of the electron beam such as the emittance, current and duration will be fed into a computer program simulating the XLS performance and calculating the XLS pulse duration. Such an approach was taken at the SACLA FEL before their implementation of THz streaking. The subsequent comparison of the FEL pulse duration from the THz streaking measurement results, and from the simulation results based on experimental measurements of the electron beam, showed a very good agreement. Hence, one can expect the indirect approach to work also for CompactLight.

Table 59 Overview of methods for temporal characterization of X-ray pulses

Method	Arrival time, accuracy (fs)	Pulse duration, resolution (fs)	Measurement interval (ps)	Double pulses, accuracy (fs)	References
Spatial encoding	1.5	–	2	–	[272]
Spectral encoding	4.5	–	3	–	[273]
Spectrogram	< 1	–	4	–	[274]
THz streaking	10	10	0.5	25	[275]
IR angular streaking	1	0.25 (0.1 for double pulses)	0.34	1	[276]
VMI streaking	< 50	0.1	0.3	–	[277]

The left column lists the names of the methods described in the references specified in the last column. The second column lists the measured rms accuracy of the arrival time of X-ray pulses with respect to the reference laser pulse. The third column gives the rms resolution of the pulse duration measurement when this is applicable. The fourth column specifies the time window, in which the arrival time and pulse duration of X-ray pulses can be measured. This time window is defined by the reference laser pulse duration and is the full length of the measurement interval, in which the specified accuracy can be achieved. The fifth column specifies capabilities for measurements of double FEL pulses with the same photon energy and for measurements of FEL pulses with different photon energies called two-color pulses. The dash in the cell implies that the measurement capability is not available. The principle of these methods is generally applicable to both soft and hard X-rays; however, VMI streaking has only been demonstrated for soft X-rays

6.3.5 Other elements

6.3.5.1 Wavefront monitors

The wavefront of the X-ray beam is subject to shot-to-shot fluctuations associated with the statistical FEL process and with changes in beam alignment on the optics that occur every shot, or as drifts. The wavefront quality affects the shape and the minimum size of the focused beam at the sample. Therefore, it is useful to be able to characterize the wavefront as part of the FEL optimization and optical alignment procedure. These monitors will be placed in the front-end before all other optical components to measure the direct output from the FEL, and just before the KB mirrors to observe the influence of the optics.

A simple and highly accurate wavefront-sensor setup operating on a single-shot basis has recently been developed, (see Fig. 203) [278]. It is based on Talbot interferometry, which exploits the phase sensitivity of the Talbot effect, i.e., self-images of a coherently irradiated periodic structure occurring in the near-field. Using a single grating and detecting the Talbot image on a scintillating screen, high-quality measurements can be obtained. The demonstrated sensitivity and accuracy are both at the level of $\lambda/100$.

6.3.5.2 Beam shutters and stoppers

Beam shutters are part of the personnel safety system that prevents radiation from the FEL from entering a downstream hutch where access is permitted. The beam shutters will be composed of a B_4C layer in front of a thicker tungsten block. The B_4C layer blocks the soft X-rays and the tungsten blocks the hard X-rays. Upstream of all optical components, there will also be a photon shutter of B_4C that can quickly be inserted when moving optics in and out in order to protect them from harmful soft X-rays. Beam stoppers are similar to beam shutters but are

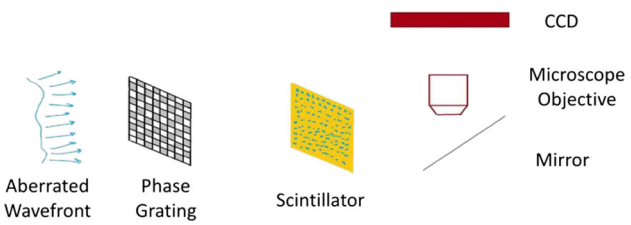

Fig. 203 Sketch of a setup for a sensitive wavefront measurement based on single-grating Talbot interferometry [278]

Table 60 Summary of the beamline diagnostics including their approximate accuracies

Diagnostic	Type	Accuracy
Intensity and position monitor (parasitic)	X-ray gas monitor detector [264–267]	1% rel. intensity, 10 μm
Spectrometers (parasitic)		
0.25–3 keV	eTOFS (cookie box) [268, 269]	10^{-3}–10^{-4}
2–4 keV	Bent crystal [270]	10^{-4}
3–16 keV	Bent crystal [271]	10^{-5}
Polarization monitor (parasitic)	Cookie box [268]	10^{o}
Arrival-time monitor (parasitic)	Spatial and spectral encoding [272, 273]	10 fs
Beam profile and position monitor (destructive)	YAG screens [267]	10 μm
Wavefront sensor (destructive)	Talbot interferometer [278] or Hartmann sensor [279]	$\lambda/100$
		$\lambda/10$

permanently placed typically at the end of a beamline to stop the beam. Burn-through monitors are connected with the beam shutters and stoppers to be able to shut off the FEL in case of failure to block the beam.

6.3.5.3 Slits and collimators Slits and collimators limit the transmittance of the spontaneous radiation, which has a large angular spread, and thus predominantly filter out the FEL beam. Like the beam shutters, they have to tolerate the full FEL power and will have a similar layer structure.

6.3.5.4 Attenuators

Attenuators that permit adjustable reduction of the X-ray flux will be installed in the front end. Different designs are required for the SXR and HXR beamlines. The SXR beamlines will use a gas attenuator. It comprises a gas volume set to specific pressures to reduce the X-ray flux, and differential pumping on each side. The apertures of the gas volume and the differential pumping need to be sufficiently large to transmit 5σ of the beam size. For hard X-rays, the gas attenuator becomes ineffective. Instead, the HXR beam will be attenuated by solid samples of, e.g., B_4C or Silicon with a thickness adjusted to the desired attenuation level. The attenuating crystals need to be of sufficient quality with respect to density uniformity and thickness variations across the beam in order not to degrade the wavefront (Table 60).

6.4 Experimental hall

6.4.1 Layout of the experimental area

The beamline branches end up in separate hutches in the experimental area, shown in Fig. 198. The experimental area also hosts the laser labs that produce the IR and VUV pulses used for pump-probe experiments, gate areas for bringing in large equipment, and control rooms. The control room areas are sufficiently large, so that they can accommodate one control room for each endstation. The three gate areas are located as to enable easy transport of equipment to the hutches and to the beamlines. Transverse cranes in the ceiling can also move components along the beamlines.

6.4.2 X-ray hutches and endstations

The endstations are marked with yellow circles or half-circles in Fig. 198. The radius of the circles is 1 m to indicate the required space around the endstations. The half-circle represents the available space for the spectrometer arm of the RIXS instrument, which is $\sim$ 5 m long and can be moved almost 180 degrees. There is space in the X-ray hutches to fit equipment such as electronics racks and computers, and some beamline components before and after the endstations. The endstations comprise both the standard single stations dedicated to one FEL beam, as well as, a dual station that can couple in two FEL beams. The new scientific applications offered by the dual stations are described in Sect. 3.1.3.

6.4.3 Laser laboratories

Two laser labs are foreseen committed to the beamlines of each FEL. The laser labs house the IR lasers that can be used for IR pump/X-ray probe experiments. VUV laser pulses can also be produced by HHG in laser lab 1. This hutch will have additional space for sample preparation.

6.4.4 Timing and synchronization

Synchronization between the external, IR or VUV, lasers and the X-ray FEL pulses is crucial for pump-probe experiments. In such measurements, a synchronization level below the FEL-pulse duration is typically desired to avoid a significant influence of the timing jitter between the external and FEL pulses, on the temporal resolution. The total timing jitter results from both electron bunch arrival time jitter and external laser to optical master oscillator jitter. An overall synchronization level on the order of 10 fs has been demonstrated at present FELs [280].

7 Examples of CompactLight facilities

7.1 Soft X-ray facility

The core electron-binding energy of many important elements, such as carbon (290 eV), nitrogen (400 eV), oxygen (530 eV), and all the 3d transition metals, lies in the soft X-ray range. Soft X-ray spectroscopy techniques are element-specific and allow revealing details of an atom's chemical bonding state. Specifically, absorption spectroscopy, photoemission spectroscopy, resonant inelastic X-ray scattering, and Auger electron spectroscopy in the soft X-ray range are powerful core-level spectroscopy techniques for studying the nature of chemical bonding, local geometric structure, and dynamics of electron transfer processes at the atomic site. The core-level spectroscopy techniques are well established at synchrotrons, but soft X-ray FELs have opened a new research dimension in ultrafast soft X-ray science by providing access to the 1–100 fs time range with an unprecedented brightness of the X-ray beam. The access to ultrafast time scales allows studying, for example, how activation barriers are lowered by unusual bonding situations in reaction intermediates, which represent crucial bottlenecks for understanding and controlling the efficient conversion of solar energy into other forms of energy. To address the challenges of harnessing and storing, for example, solar energy, direct time-resolved studies of charge-carrier dynamics at interfaces of new solar cells and energy storage devices are needed.

The strong need for an ultrafast soft X-ray source justified the construction of a new generation of soft X-ray FELs, such as the LCLS-II project—a high-repetition-rate SXR FEL based on a superconducting accelerator. Note that the LCLS-II FEL provides a continuous train of FEL pulses with *uniform spacing* between the pulses. User end stations at LCLS-II are planned to provide the FEL beam at a 100 kHz repetition rate. Also, note that a high-repetition FEL with uniform pulse spacing will also be available in China as part of the hard X-ray FEL facility SHINE. In Europe, only the Athos beamline at SwissFEL at 100 Hz repetition rate (currently under commissioning) provides the SXR FEL beam with uniform pulse spacing. The soft X-ray beamline of the European XFEL based on the SASE3 undulator operates in burst mode and is sub-optimal for many pump-probe experiments in condensed matter physics, where the sample must be thermalised between pump pulses.

As evidenced from the FEL requirements Sect. 3.2, there is a clear need for SXR FELs with increased pulse stability and uniform spacing between the pulses. The operation mode of the FEL must be compatible with the

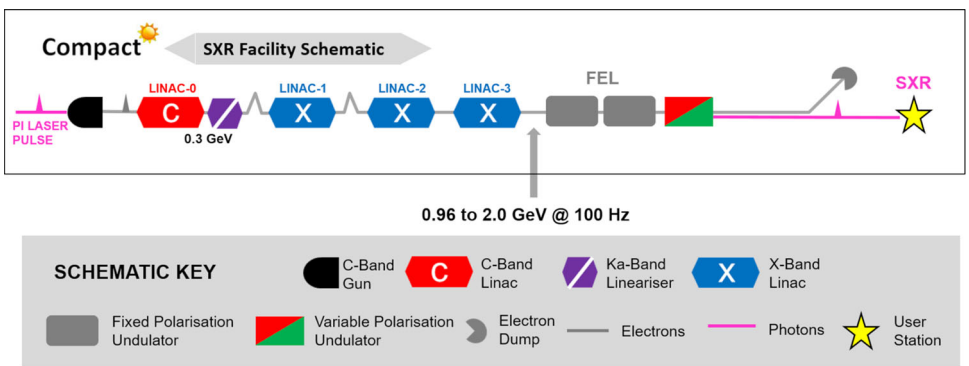

Fig. 204 Schematic layout of the SXR facility

type of pump-probe experiments, in which the non-equilibrium state of a sample must decay before the next pair of pump-probe pulses come. Furthermore, a repetition rate of 100 Hz or 1 kHz is perfectly compatible with high-power optical lasers used in some pump-probe experiments.

The CompactLight technology offers a unique capability of building a 100 Hz or even a 1 kHz FEL at a cost lower than that of a 100 Hz machine based on the previous generation C-band accelerator technology. The compactness and cost efficiency of a 100 Hz standalone SXR FEL lowers the barrier for entering the world of femtosecond X-ray science for small national user communities. In addition, an upgrade to the 1 kHz option would fill an important gap between the first and second generations of low and very high repetition rate FELs. On the one hand, the 1-kHz FEL will provide a tenfold increase in repetition rate, but on the other hand, it will still provide enough time between X-ray shots for sample replacement and preparation, such as for liquid droplet dispensers for exceptionally precious samples, or for measurements on solid surfaces where time is needed to deposit molecules.

7.1.1 Facility layout

The facility design is a simplified version of the Baseline configuration, reduced to the essential components for 100 Hz SXR output over the photon energy range 0.25–2.0 keV from a single FEL. A schematic layout is shown in Fig. 204. Note that, compared to the Baseline configuration, the facility is substantially more compact for the following reasons:

- There is no need to reserve space between Linac-2 and Linac-3 for the deflecting cavity and spreader beamline required for Upgrade-2.
- Similarly, there is no need for space after Linac-3 for the deflecting cavity and spreader beamline to split the twin bunches into the twin FEL lines.
- There is no need for the timing chicane to tune the temporal separation of twin FEL pulses.
- The FEL undulator can be shorter, because the saturation length in the SXR is less than that in the HXR.
- The photon beamline is shorter, because the divergence of SXR output is larger, meaning that the first optical element can be placed closer to the undulator source without being damaged.

The accelerator and FEL lattices were reoptimized for standalone SXR operation. Starting from the injector, all structures are used at their highest gradient—C-band structures in the injector are at 30 MV/m and the X-band structures are at 65 MV/m. A maximum beam energy of 2 GeV is attained at about 150 m with a peak current of 1 kA.

The lattice β-functions and beam energy are shown in Fig. 205. The transverse and longitudinal phase spaces of the 2 GeV bunch are shown in Fig. 206, together with the slice emittance and energy spread. The helical superconducting undulator period remains unchanged from the full CompactLight facility, at $\lambda_u = 13$ mm, so the undulator design is directly transferrable into the standalone SXR machine. At 2 GeV beam energy and with the FEL set to 2 keV photon output, the undulator parameter is $a_w = 0.706$. By tuning to maximum field, the photon energy reduces to 1 keV. By operating at 1.35 GeV, the tuning range covers 500 eV to 1 keV, and to reach the lowest photon energies of 250–500 eV, the beam energy is reduced to 0.96 GeV. The total undulator length is 19.75 m with the lattice comprising nine 2.75 m long SCU modules with 0.5 m gaps between them. After the SCU modules, two variably polarizing afterburner modules provide selectable polarization for users.

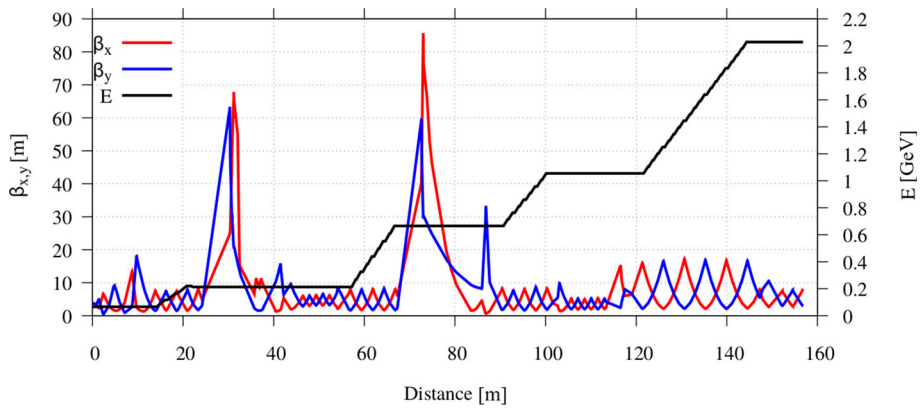

Fig. 205 Lattice β-functions and beam energy

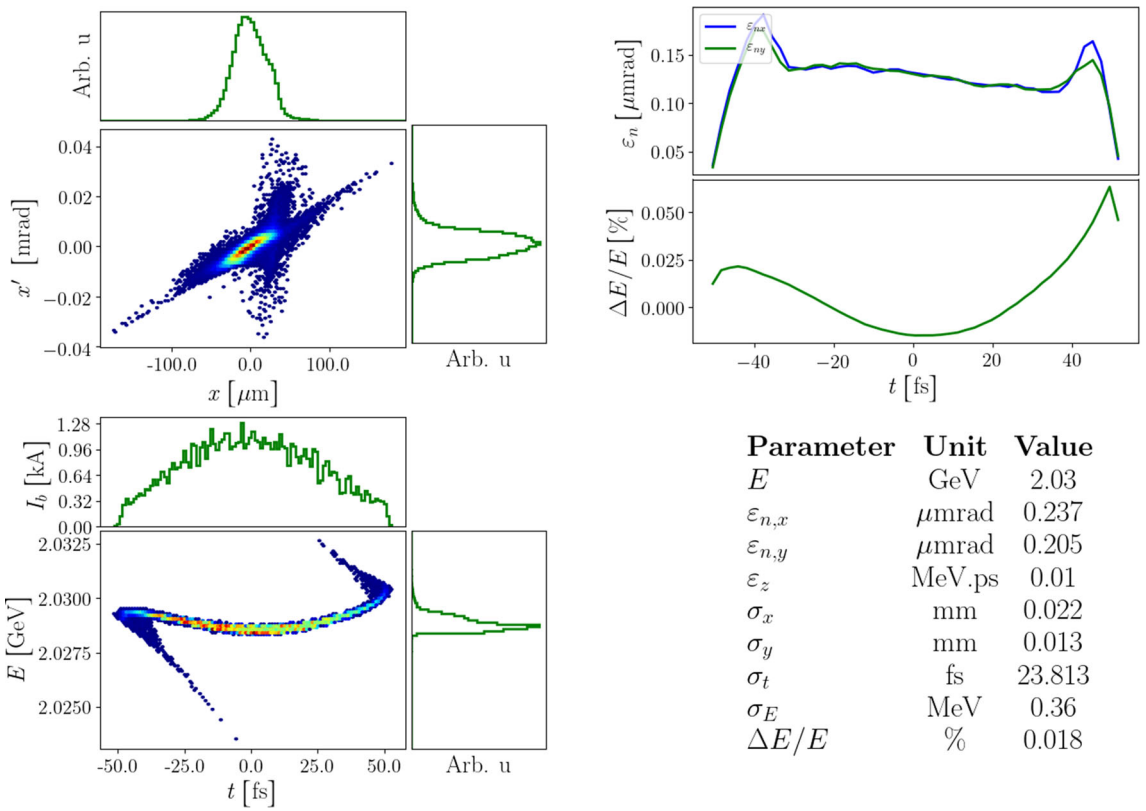

Parameter	Unit	Value
E	GeV	2.03
$\varepsilon_{n,x}$	μmrad	0.237
$\varepsilon_{n,y}$	μmrad	0.205
ε_z	MeV.ps	0.01
σ_x	mm	0.022
σ_y	mm	0.013
σ_t	fs	23.813
σ_E	MeV	0.36
$\Delta E/E$	%	0.018

Fig. 206 Properties of the simulated electron bunch used to drive the SXR FEL

7.1.2 FEL performance estimates

The FEL simulation results are shown in Fig. 207. Here, the FEL is tuned to 2 keV photon output. The pulse energy saturates at a distance of 15.5 m through the undulator at a value of 90 μJ and the peak power is around 4 GW. The total undulator length of 19.75 m thus allows a reasonable contingency to ensure saturation is reached at 2 keV, and also allows the possibility of post-saturation tapering at lower photon energies for which the saturation length is shorter.

7.1.3 Photon beamline

Compared to the Baseline configuration, the photon beamline design is greatly simplified as only one FEL line is serving user endstations. The optical layout of the photon transport is shown in Fig. 208. The beamline starts with the front-end containing a bremsstrahlung collimator, a photon shutter, and a set of photon diagnostics. The first optical element, a steering mirror, can direct the photon beam to one of the two beamlines: a pink beamline for time-resolved experiments or a mono beamline for photon energy-resolved experiments. The former provides broadband transmission and the temporal structure of FEL pulses is preserved. The pink beamline also includes a split-and-delay system for X-ray pump-probe experiments. Incoupling of external optical and UV lasers is foreseen for optical/UV pump–X-ray probe experiments with fs resolution. The mono beamline provides meV-energy resolution by employing a grating-based monochromator.

An important consideration in the photon beamline design is the choice of material for optical components as the beamline has to support transmission over a wide photon energy range from 0.25 to 2 keV. Figure 209 presents a comparison of the absorption coefficient vs photon energy for several materials commonly used in photon beamlines. Given the CompactLight parameters, Au is the preferred option, even though the absorption level is as high as 20%. As a result, the transmission on the pink beamline composed of three mirrors is around 50%.

An example of the main output parameters of the beamlines at 250 eV (5 nm) and 2000 eV (0.62 nm) is presented in Table 61. Two grazing-incidence gratings are used to cover the entire photon energy range providing a good balance between photon energy resolution and pulse stretching due to the waveform tilt by the grating. The pink beamline contains no dispersive elements and preserves the FEL pulse bandwidth.

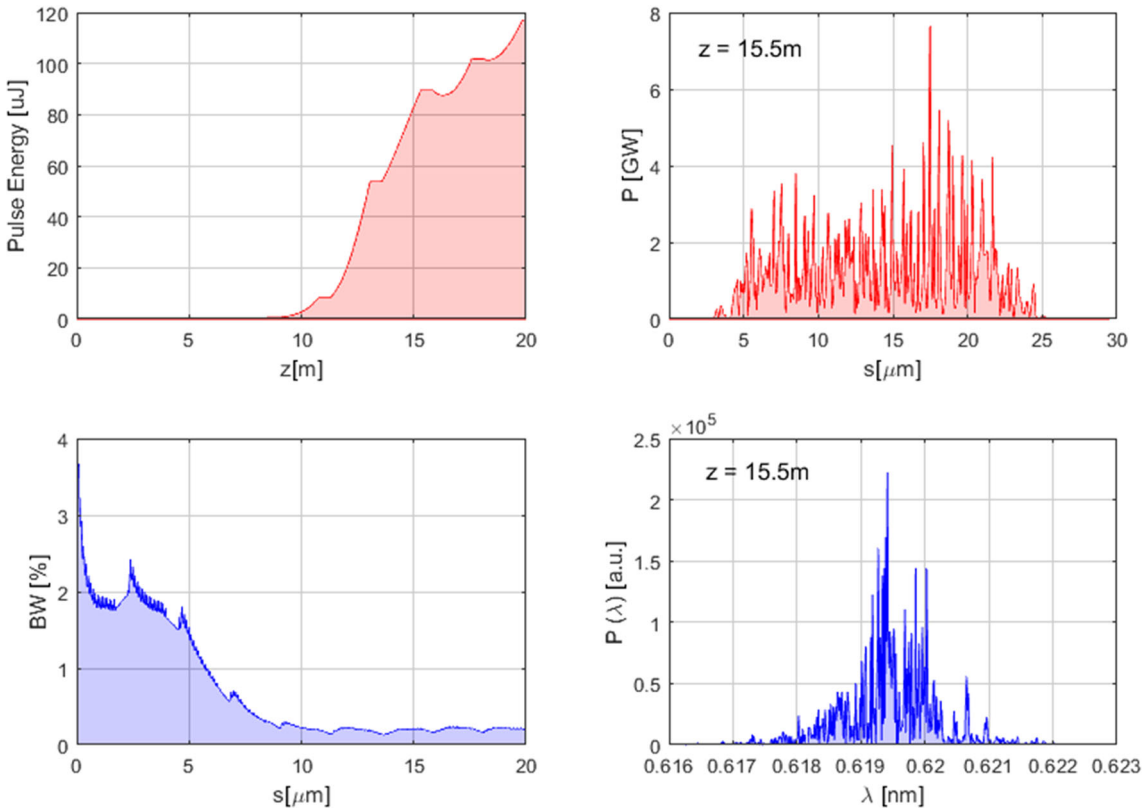

Fig. 207 FEL simulation results of the SXR FEL performance, showing (top left) pulse energy *vs* distance through the undulator z, (top right) power profile of output pulse at saturation, occurring at $z = 15.5$ m, (bottom left) rms bandwidth *vs* z, and (bottom right) pulse spectrum at saturation

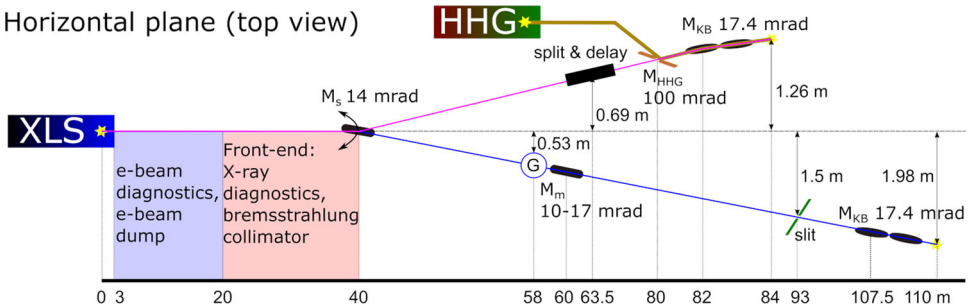

Fig. 208 Optical layout of the SXL beamlines. The position of the virtual FEL source (yellow star on the left) is taken as the origin. At 40 m downstream from the virtual source, the FEL beam is steered by means of a steering mirror M_s into one of the two main beamlines: a pink beamline (solid pink line) and a mono beamline (solid blue line). Other notations in the figure are: G stands for the monochromator grating, M_m for the monochromator mirror, M_{KB} for the set of KB mirrors, M_{HHG} for the holey mirror for incoupling of UV pulses from a high-harmonic generation (HHG) source. Typical operation angles of incidence are indicated next to the mirror symbol. The incoupling of HHG pulses and the split & delay-line are shown. The positions of the final FEL beam focus are depicted by the yellow stars

7.1.4 Cost estimate

Tables 62 and 63 show the breakdown of cost estimates for a 100 Hz and a 1 kHz option. The 1 kHz SXR FEL makes use of the full accelerator including the upgrade of RF power sources to provide the high repetition rate mode. The full-scale linac makes the 1 kHz SXR machine easily up-gradable to the 100 Hz HXR regime. Furthermore, comparing the cost per photon the proposed SXR FEL facility is clearly more cost efficient than the corresponding SXR FEL at SwissFEL.

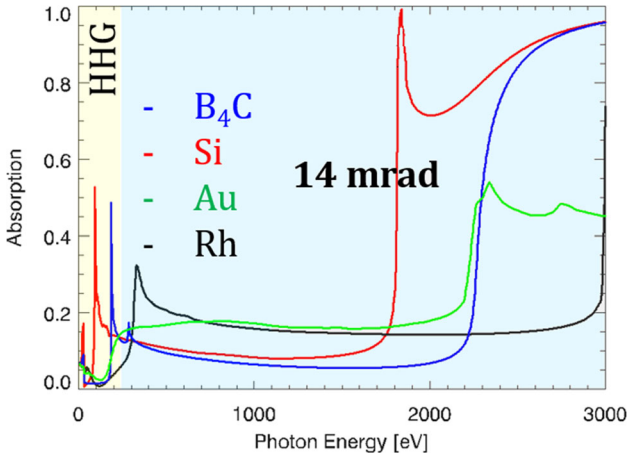

Fig. 209 Optical absorption for several materials vs photon energy at an incidence angle of 14 mrad

Table 61 Parameters of the FEL beam at the sample position in the experimental station

Parameter	Pink		Mono, high energy	Mono, low energy
Grating	–	–	100 l/mm, 0.25° blaze	50 l/mm, 0.15° blaze
Wavelength (nm)	0.62	5	0.62	5
Photon energy (eV)	2000	250	2000	250
Transmission (%)	60	55	3.15	1.33
Pulse energy (μJ)	54	83	2	2.84
Beam size (μm×μm)	2×1	2.8×1.1	3.2×1.6	4×2.4
Pulse stretching (fs)	–	–	10	200
Resolution (meV)	–	–	450	47

Table 62 Cost breakdown for the standalone 100 Hz SXR FEL

Section of the facility	Cost (MEURO)
Injector	15.4
Linac 1	12
Linac 2–3	12.7
Bunch compressors 1 and 2	1.6
Machine timing, controls and protection	4
FEL 1	16
Photon beamline	18
Civil engineering	18
Electrical system	2.9
Cooling and ventilation	4.4
Total	105

The uncertainty of the total cost amounts to around 20–30% and depends on specific scientific requirements on the FEL pulse length, stability, photon energy resolution, polarization control, and other parameters

Table 63 Cost breakdown for the standalone 1-kHz SXR FEL

Section of the facility	Cost (MEURO)
Injector	15.4
Linac 1	12
Linac 2–3	54.2
Bunch compressors 1 and 2	1.6
Machine timing, controls and protection	4
FEL 1	16
Photon beamline	18
Civil engineering	40
Electrical system	6
Cooling and ventilation	10
Total	138

The uncertainty of the total cost amounts to around 20–30%

7.2 Inverse compton sources

Inverse-compton scattering (ICS) sources offer the potential to achieve quasi-monochromatic X-ray beams of tunable energy at room-size laboratories. Typical applications of ICS sources include medical imaging (using K-edge subtraction or phase-contrast techniques), analyses of cultural heritage, irradiation therapy, protein crystallography, and nuclear waste management, depending on the flux and on the energy of the generated X-rays. The attractiveness of ICS sources rests on their small footprint and reduced cost, which make them ideal tools for institutions, such as universities, hospitals, and museums.

The number of ICS sources worldwide has steadily increased over the last few years. Most ICS designs are based on storage rings since the circular layout of a storage ring maximizes the repetition rate and the flux. This comes at the cost of needing significantly large facilities. Moreover, collective effects in storage rings lead to larger normalized emittances, which limit the maximum brilliance. In the years 2000s, Energy Recovery Linacs (ERLs) have also garnered interest and several ICS designs based on ERLs. However, these sources are normally based on superconducting technology, which is not feasible for use in hospitals or small laboratories due to the handling of cryogenics. Normal-conductive, low-emittance linacs like that of CompactLight can also be adapted for compact ICS designs. Linac-based ICS sources tend to exhibit lower fluxes, since the electron bunches are used only once but offer higher brilliance due to the lower emittance obtained from the photoinjector. One example of such a design is Smart*Light in Eindhoven, part of the CompactLight consortium. A summary of designed, commissioned, and already existing ICS sources is visible in Fig. 211.

Recent developments in high-power compact lasers, combined with the high-intensity electron beams provided by the CompactLight technology, enable the conception of a new generation of very compact ICS sources. CompactLight's technology, based on X-band high-gradient normal-conductive RF combined with high-rep-rate, low-emittance injectors, has the potential to provide both high fluxes and high brilliance. This chapter examines the preliminary parameters of an ICS source based on CompactLight technology. Figure 210 shorts a schematic layout of an ICS source.

7.2.1 ICS parameters' optimisation

The parameters that characterize an ICS source in terms of X-rays are its photon flux, i.e., the number of emitted photons per second, the brilliance, which indicates the coherency of the source, and the energy bandwidth. The photon flux is the number of scattered photons, N_γ, produced in a collision between a bunch of N_e electrons and

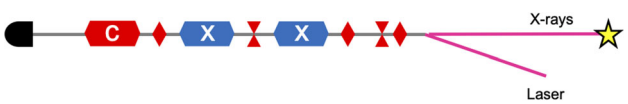

Fig. 210 Schematic layout of an ICS source based on the CompactLight C-band gun and a short X-band linac

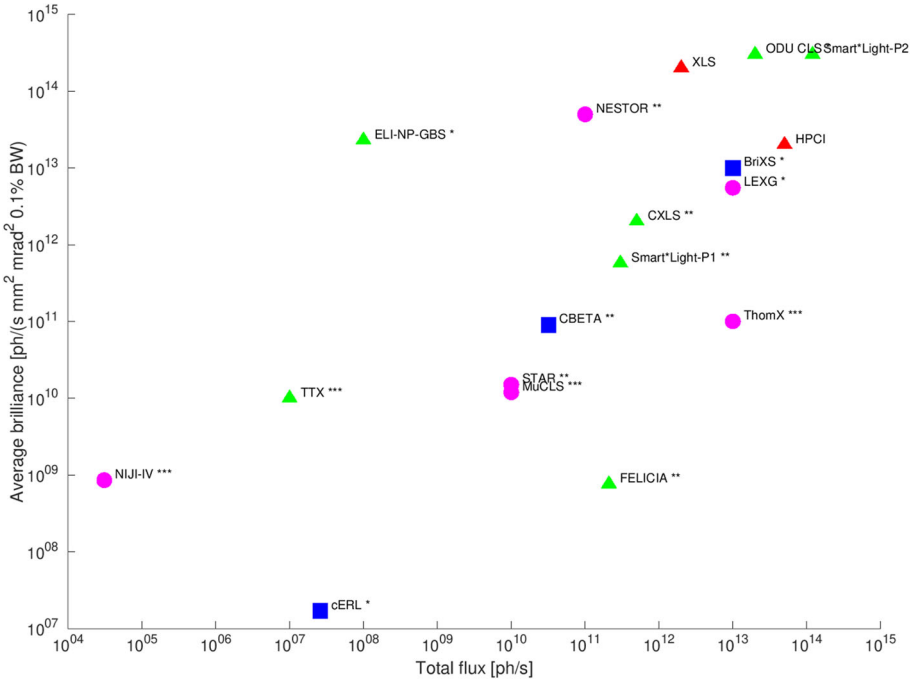

Fig. 211 Landscape of ICS sources. Circles indicate storage-ring-based sources; triangles indicate linac-based sources and squares indicate energy-recovery-linac-based sources. Stars indicate: ⋆, design study; ⋆⋆, under commissioning; ⋆⋆⋆, existing

a laser pulse of N_l photons

$$N_\gamma = \sigma_C \frac{N_e N_l \cos(\phi/2)}{2\pi\sigma_y \sqrt{\sigma_x^2 \cos^2(\phi/2) + \sigma_z^2 \sin^2(\phi/2)}}, \tag{59}$$

where σ_C is the Compton scattering cross-section, $\sigma_i^2 = \sigma_{e,\,i}^2 + \sigma_{l,\,i}^2$ is the convoluted spot size of the electron and laser beam in each direction $i = x$, y, z, and ϕ is the crossing angle (typically 2 deg). The total flux is defined as

$$\mathcal{F}_{\text{total}} = \dot{N}_\gamma \text{ [ph/s]}, \tag{60}$$

and depends on the number collisions per second occurring. The flux within a 0.1% bandwidth at the Compton edge is defined as:

$$\mathcal{F}_{0.1\%} \simeq 1.5 \times 10^{-3} \dot{N}_\gamma \text{ [ph/s]}. \tag{61}$$

The brilliance, in the non-diffraction limit where the electron and the laser beams have similar spot size and comparable divergence, is defined as

$$\mathcal{B} \simeq \frac{\gamma^2 \mathcal{F}_{0.1\%}}{4\pi^2 \epsilon_x^N \epsilon_y^N}, \tag{62}$$

where ϵ_i^N is the normalized emittance in the direction $i = x$, y, and γ is the Lorentz factor of the electrons.

The energy bandwidth is given by

$$\frac{\sigma_{E_\gamma}}{E_\gamma} = \sqrt{\left(\frac{\sigma_{E_\theta}}{E_\theta}\right)^2 + \left(2\frac{\sigma_{E_e}}{E_e}\right)^2 + \left(\frac{\sigma_{E_l}}{E_l}\right)^2 + \left(\frac{\sigma_{E_\epsilon}}{E_\epsilon}\right)^2}, \tag{63}$$

where appear:

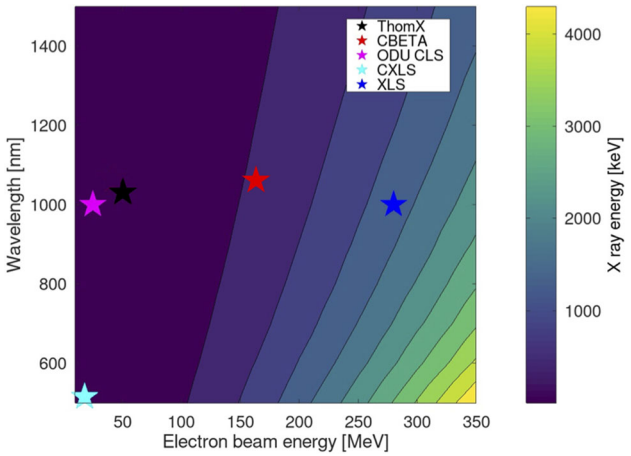

Fig. 212 Parametric scan of wavelength against electron beam energy with color coded X-ray energy. The scan confirmed the square dependence on the electron beam energy, and the linear dependence on E_{laser}

- The contribution from the small collection angle, θ

$$\frac{\sigma_{E_\theta}}{E_\theta} = \frac{1}{\sqrt{12}} \frac{\gamma^2\theta^2}{1+\gamma^2\theta^2/2}. \tag{64}$$

- The contribution from the beam emittance

$$\frac{\sigma_{E_\epsilon}}{E_\epsilon} = \frac{2\gamma^2\epsilon}{\beta}. \tag{65}$$

- The relative energy spread of the electron and of the laser beam

$$\frac{\sigma_{E_e}}{E_e}, \text{ and } \frac{\sigma_{E_l}}{E_l}. \tag{66}$$

Equation 59 shows the direct proportionality between the flux and the rate of electron–laser collisions. The flux can be maximized by increasing both the electron beam current and the laser pulse energy. Equation 62 shows that the brilliance is maximized by reducing the normalized electron beam emittance in both the horizontal and vertical axes.

The output X-ray energy depends on the electron beam's relativistic factor γ, the laser's photon energy E_L, the crossing angle ϕ between the electron beam and laser, and the scattering angle θ between the generated X-rays and the electron beam

$$E_X = 2\gamma^2 E_L \frac{1+\cos\phi}{1+\gamma^2\theta^2}. \tag{67}$$

In head-on collisions, ϕ can be approximated to 0, which leads to a maximum X-ray energy of $E_{X,\,\max} = 4\gamma^2 E_L$.

The CompactLight linac module enables electron beam energies that can easily reach hundreds of MeV. A parametric scan of the laser wavelength against the electron beam energy up to 300 MeV, shown in Fig. 212, confirms the larger X-ray energy achievable using XLS technology with respect to other sources. X-ray energies of the order of several MeV can be obtained.

7.2.2 Facility layout

7.2.2.1 The electron gun

The 2-bunch train at 1 kHz of the CompactLight injector provides insufficient average current to make a CompactLight-based ICS competitive with respect to existing designs. The effective bunch repetition rate f_{eff} was maximized by increasing the number of bunches per train, while the single-bunch charge was increased from 75 to 200 pC. Due to the larger charge extracted from the cathode, it was assumed that the electron beam normalized emittance would increase from 0.15 to 0.3 mm mrad. Table 64 summarizes the beam parameters for the

Table 64 Baseline parameters of CompactLight ICS electron beam

Parameter	Symbol	Value	Unit
Bunch repetition rate	f	1	kHz
Nb of bunches per train	n_b	50	
Effective nb of bunches per second	f_{eff}	50×10^3	
Bunch length	σ_z	1	ps
Bunch charge	Q	200	pC
Bunch spacing		5	ns
normalized emittance	$\epsilon^N_{x,\,y}$	0.3	mm mrad
Final energy	E	100 − 300	MeV

ICS.

7.2.2.2 The Linac

The electron beam is then be accelerated in a short linac. The CompactLight baseline injector reaches 300 MeV, whereas typical applications of ICS X-rays require beam energies below 100 MeV. The performance estimates thus considered two electron beam energies: 100 MeV, for a very compact facility; and 300 MeV, to explore to potential of more energetic X-rays. The energy of 100 MeV could be easily achieved directly using the baseline XLS injector upstream of the laser heater. To reach 300 MeV, while maintaining compactness, one could consider the alternative injector designs proposed for CompactLight, for instance, the full X-band solution where both gun and linac are in X-band.

7.2.2.3 The laser system

The performance estimates used the TRUMPF's 1 kW Dira 1000 [281]. The Dira 1000 is a state-of-the-art high power compact laser with a pulse-length of 0.6 ps and wavelength of 1 μm.

Considering the XLS injector running with a repetition rate of 1 kHz as in Table 64, a 1 kW laser power would lead to a pulse energy per train of 1 J. Given that each pulse consists of a train of 50 bunches, a modest 20 mJ pulse energy would be available for the laser–electron beam scattering. To increase the pulse energy, an optical enhancement cavity should be used.

An optical enhancement cavity suitable to sustain the 1 kHz repetition rate of the XLS injector and a bunch spacing of 5 ns, would need to operate in CW mode. In CW mode, considering the Dira 1000's 1 kW laser and a 200 MHz cavity, the laser pulse energy per bunch would be of 5 μJ, requiring an enhancement factor of at least 4×10^3 is required to match the "no cavity" intensity. Recent developments in enhancement cavities allow for factors up to 10^5–10^6; however, assumed here is a conservative factor of 10^4 for safety considerations, which results in a final pulse energy of 50 mJ.

A different electron beam time structure could also be considered, with lower rep-rates and longer trains (e.g., 10 Hz repetition rate, and 1000 bunches per train). This configuration would enable the use of the enhancement cavity in burst mode. Preliminary simulations revealed that, for a total laser burst duration of 0.5 μs, the individual laser pulse energy would amount to 66 mJ. With an enhancement factor 100, 6.6 J of laser pulse energy would be available to the single-bunch interaction, attaining very high X-ray fluxes.

7.2.3 Performance estimates

Considering a crossing angle of 2 degrees between electron beam and laser, preliminary parametric scans to determine the dependence of the flux in a 1.5 mrad cone, and of the bandwitdh, on electron and laser spot sizes have been performed. Figure 213 shows that peak fluxes of excess of 10^{11} ph/s are achievable, and the corresponding X-ray energy bandwidth. Table 65 reports first estimates obtained in simulation.

7.2.4 Preliminary cost estimate

A preliminary cost estimate for the ICS source was obtained scaling the cost of the CompactLight injector, which can provide electron beams up to 300 MeV. It must be noted that the injector for the ICS source should be a modified version of the CompactLight injector presented in this document, since for ICS operation, 50 bunches per train are needed, and not just 2 like the CompactLight baseline. A multi-bunch operation would certainly require a partial redesign of the RF system, to include for example high-order-mode damping. Table 66 summarized this

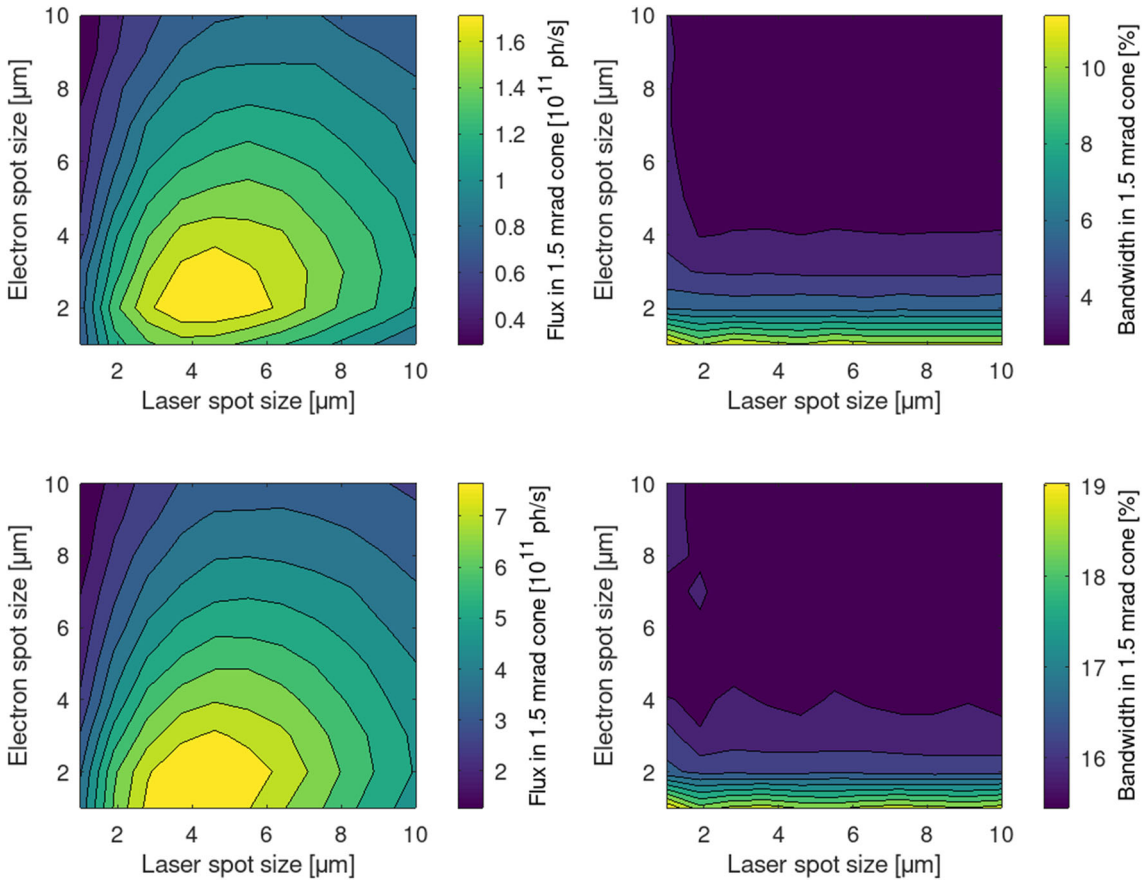

Fig. 213 Parametric scan of electron spot size versus laser spot size. The flux and the bandwidth are calculated in a cone with 1.5 mrad aperture. The two top plots refer to an electron beam energy of 100 MeV; the two bottom plots refer to an electron beam energy of 300 MeV

preliminary cost estimate. The cost of the laser system for ICS includes the control system and locking electronics of the laser to the cavity and an external reference. The final cost will depend on the final repetition rate and average power requirements. The cost of the laser beam delivery includes vacuum chamber, optomechanics, optics, windows, motors eventually, beam pointing stabilisation, and Basler cameras for beam visualizations. The Fabry–Pérot cost estimate includes granite table, vacuum chamber, optics, and motorisations. Vacuum pumping, gauges, and related safety are not included in this estimate.

Table 65 Summary of parameters required to maximize the flux in a 1.5 mrad cone of the XLS-based ICS source

Parameter	Symbol	Electron beam energy		Unit
Electron beam energy	E_e	100	300	MeV
Electron spot size	σ_e	1 to 4	0.5 to 3.0	μm
Laser pulse energy	E_p	50	50	mJ
Laser spot size	σ_{laser}	3 to 6	3 to 6	μm
Total flux	$\mathcal{F}$	1.8×10^{12}	1.8×10^{12}	ph/s
Flux in 1.5 mrad	$\mathcal{F}_{1.5\text{ mrad}}$	1.6×10^{11}	7.0×10^{11}	ph/s
Average brilliance	$\mathcal{B}$	2.0×10^{14}	5.0×10^{14}	[a]
Bandwidth in 1.5 mrad	$\text{BW}_{1.5\text{ mrad}}$	4–8	16–19	%

[a] ph/(s mm^2 mrad^2 0.1%BW)

Table 66 Preliminary cost estimate for a CompactLight-based Inverse-Compton Scattering source

Sub-system	Estimated Cost (kEURO)
1-kHz Gun laser and photo cathode system	1800
C-band RF	3500
Magnets	509.5
Beam instrumentation	317
Vacuum	300
Laser system for ICS	600
Laser beam delivery system	200
Fabry–Pérot enhancement cavity	210
Total	7436.5

8 Alternative technology solutions

8.1 X-band RF injector option

8.1.1 An X-band traveling-wave RF photogun

A fully X-band injector is a natural progression in the development of an even more compact light source. Using an X-band standing-wave (SW) RF photogun is one possibility and, as such, is under investigation as part of the CompactLight project. However, the strict mechanical tolerances of SW photoguns, and the necessity of using a high-power RF circulator, make it a challenging task. An alternative to a conventional standing-wave RF photogun is the traveling-wave (TW) RF photogun. A TW photogun was first proposed in 1991 but never gained popularity in the injector community. The development of high-gradient linear accelerators has made the TW RF photogun a more feasible option. Here, we present a brief overview of the electromagnetic design of an X-band, high-gradient TW RF photogun based on one of the CLIC structures. This work is still in its preliminary stages and merely aims to demonstrate possible alternatives in future compact light sources.

8.1.1.1 Electromagnetic design

The RF design for the TW photogun was based on the CLIC-G Open structure, which was a CLIC prototype fabricated from milled halves. The choice of this style of accelerating structure was due to the unique gap in the geometry which is used to couple in the photo-cathode laser. The RF design of the TW RF photogun is illustrated in Fig. 214.

A coaxial input coupler is used to correct the quadrupole field component induced by the dual-feed RF input couplers. All cells in the structure use a racetrack geometry, primarily for fabrication reasons, although it is possible to further reduce the quadrupole fields through an adjustment of the cells' relative horizontal and vertical dimensions. At the end of the input coupling cell, the electron velocity is 0.8 c. Consequently, the first three cells are adjusted in length to match the beta of the electrons, given the accelerating gradient expected in each respective cell for an input power of 28 MW. The remainder of the RF photogun downstream of these cells keeps

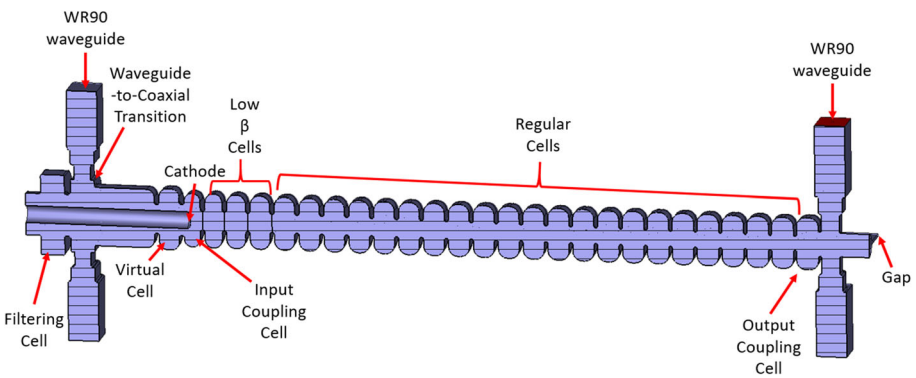

Fig. 214 The vacuum design of the RF photo gun based on the CLIC-G Open

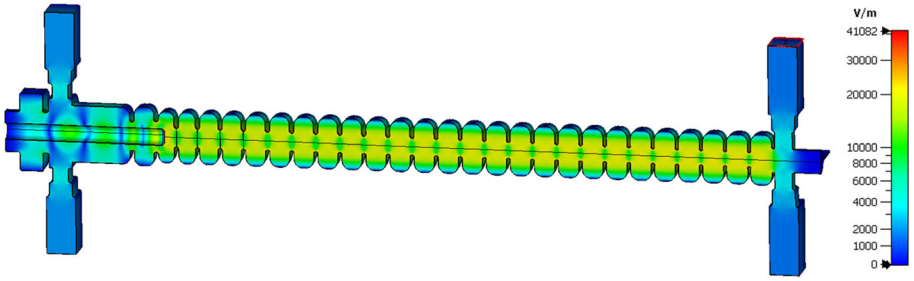

Fig. 215 Magnitude of the electric field distribution in the TW RF photogun

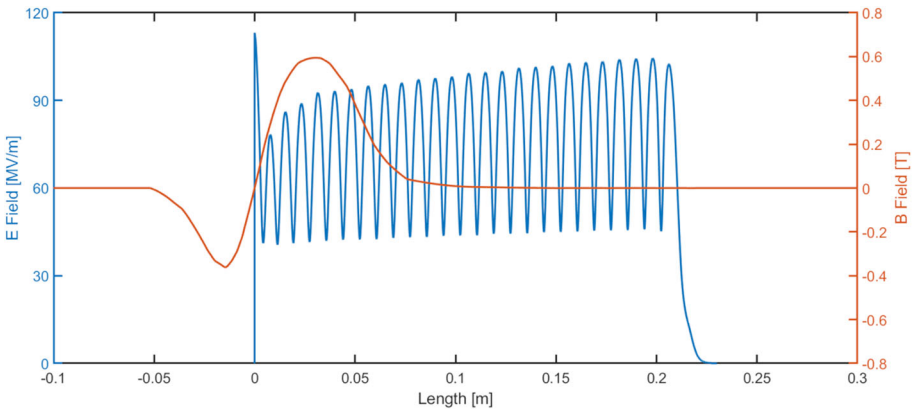

Fig. 216 The magnitude of the axial electric field in the z-direction

the geometry of the CLIC-G open accelerating structure. Whether the structure should be shortened to allow for further emittance compensation techniques downstream is to be investigated further.

The vacuum model was simulated in CST using the frequency domain solver. Figure 215 displays the magnitude of the electric field distribution. The new coaxial input coupler is observed to have surface electric fields lower than in the remainder of the structure, which is important for the gun's high-power RF performance. The magnitude of the field distribution along the beam axis is plotted in Fig. 216. The field on the cathode is observed to peak at 113 MV/m. The low-beta cells have a reduced peak axial field which is to be expected from their shortened length. The remainder of the RF photogun is observed to have similar behavior to the CLIC-G Open structure, as would be expected. A summary of the properties of the TW RF photogun is presented in Table 67.

8.1.1.2 Beam dynamics

Using the one-dimensional axial field distributions, preliminary beam dynamics calculations of the RF photogun were modelled using GPT to understand what beam quality was possible. These calculations give an idea of the possibility of a TW photo gun but do not demonstrate the specific effects of the unique design choices, such as the two halves design. The cathode was modelled as a Gaussian distribution cut off at 2σ with a beam waist of 250 μm and an intrinsic emittance of 0.5 mm mrad/mm. The main solenoid, bucking coil, and an additional solenoid downstream were modelled utilizing the 1D axial magnetic field. A CLIC-style X-band accelerating structure was placed 10 cm downstream of the end of the RF photogun. Figure 217 illustrates the beam parameters over the length of the fully TW photoinjector.

The injector simulation demonstrates the ability to achieve a 32 MeV electron bunch in less than 0.6 m with an energy spread of 0.1%. The emittance for an 80 pC bunch is 0.5 mm mrad which is greater than the requirement for CompactLight although further developments are expected to yield similar results to a SW photogun.

8.1.1.3 Discussion

The preliminary RF model demonstrates the feasibility of a fully X-band TW RF photoinjector. Such a concept is desirable as this would reduce the complexity of the RF system, given that the gun could be driven using the same RF infrastructure as the X-band linac. For such a structure to achieve the emittance requirement of CompactLight, some steps would need to be taken. Particularly the concept of emittance compensation, which is vital to low emittance injectors, still needs to be investigated in detail. It is expected that a shorter accelerator would lead to better emittance compensation. A lower emittance is deemed feasible as this has already been achieved in a TW

Table 67 Main parameters of the traveling-wave gun

Parameter	Value	Unit
Length	216	mm
Regular Cells	24	
Phase Advance	120	°
Frequency	11.994	GHz
Attenuation	−2.26	dB
Power	28	MW
Fill time	50.2	ns
Gradient	79	MV/m
Peak cathode field	113.2	MV/m
Peak surface E field	216	MV/m
Pulsed surface heating ($\tau = 50$ ns)	7.7	K
Repetition rate	1	kHz
Flow rate	15	L/min

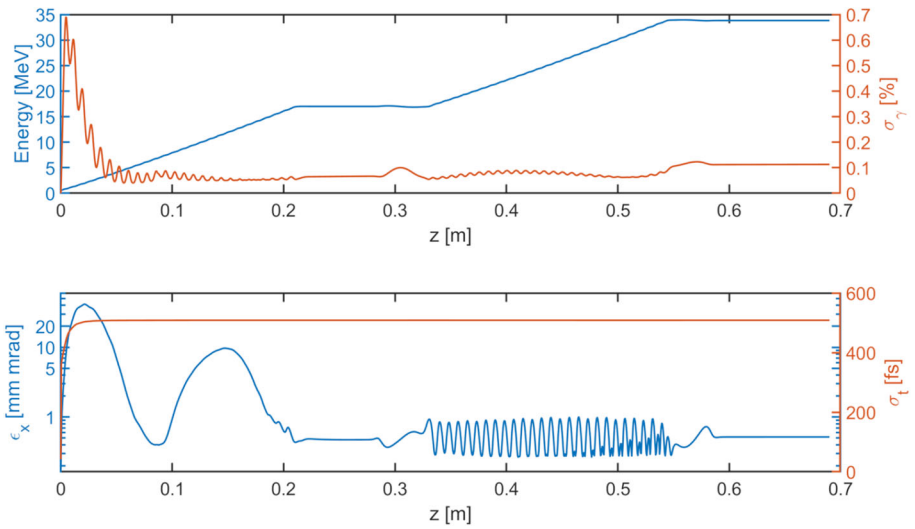

Fig. 217 Beam dynamics of the electron bunch produced by the TW RF photogun

RF photogun model developed at C-band [282]. Further simulations using the full three-dimensional field-maps are recommended.

8.1.2 X-band standing-wave RF photoinjector

Another option for the RF photoinjector is based on a 5.6-cell standing-wave RF gun intended to operate at an RF frequency of 11.994 GHz with a high-gradient RF electric field at the cathode of 200 MV/m. The injector is intended to generate an electron beam with low emittance and a final kinetic energy of nearly 300 MeV. To reach this aim, it will be necessary to add a solenoid to compensate the beam emittance growth due to the space-charge forces during the early stages of the beam acceleration. Since the beam's kinetic energy at the output of the 5.6-cell RF gun is typically a few MeV, seven RF accelerating sections will be required after the gun to achieve the goal of reaching an energy of 300 MeV. The traveling-wave (TW) structures downstream of the gun would also operate at 12 GHz. Thus, the total length of the photoinjector layout is 8.2 m and is schematized in Fig. 218. The main parameters of the photoinjector prototype are summarized in Table 68 and will be discussed in detail in the next

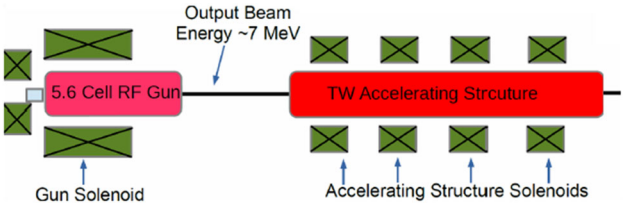

Fig. 218 Partial view of the RF photoinjector layout. After the 5.6-cell RF gun seven identical TW accelerating structures are added to accelerate the beam (in the current scheme, only the first of the seven TW structures is shown). Only the first TW section includes solenoids

Table 68 Main parameters of the X-band SW photoinjector

Parameter	Value	Unit
Frequency f_π	GHz	11.994
RF electric cathode field	MV/m	200
Maximum superficial RF electric field (for 1 MV/m at cathode)	MV/m	0.998
Coupling factor, β		1.008
Mode separation, Δf	MHz	27.1
Filling time, τ	ns	112.5
Required magnetic field to suppress multipactor	mT	360
Breakdown Rate, BDR (for pulse of 400 ns)	bpp/m	5.6×10^{-6}
Pulse heating (for pulse of 400 ns), ΔT	°C	31

section.

8.1.2.1 Electromagnetic design of the RF gun

The cross-section of the RF gun geometry is shown in Fig. 219. It consists of six accelerating cavities, each with length $\lambda/2$ (λ being the wavelength of the RF electromagnetic wave in vacuum), except for the first cell, which has a length of 0.6 times the others—this has been optimized over several beam dynamic iterations similar to the approach in [283]. The cells are coupled by means of elliptical irises, instead of circular ones, to reduce the RF electric field at the surface of the gun [284, 285], thus reducing the rate of RF breakdown. The material chosen for the bulk of the photoinjector is copper. The photoinjector is connected to the RF generator's external circuit by means of a coaxial coupler with a door-knob geometry [286]. Due to the choice of this coupling scheme, the entire RF gun structure is axisymmetric, allowing the use of the free distribution software SUPERFISH [287] for the electromagnetic design of the gun. SUPERFISH is a 2D eigenmode solver applicable for geometries with cylindrical axisymmetry, and it has the advantage of being much faster than 3D codes.

In the design, the shape of the main cell is tuned to minimize the RF electric field on the surface relative to the corresponding value on the cathode surface. Also, the gun geometry is intended to maximize the separation between the operating π-mode and the nearest neighbor mode to avoid the residual excitation of such a mode during RF transients. The effect of this undesirable neighbor mode on the gun RF electric field pattern has also been taken into account in the design process using an equivalent circuit model to characterize the system consisting of the gun cavity plus the coaxial coupler, following a procedure similar to that described in [84].

After the gun optimization, for the final prototype, it was found that the maximum value of the surface electric field is 0.998 MV/m, assuming a cathode RF electric field amplitude of 1 MV/m. Other relevant gun parameters are

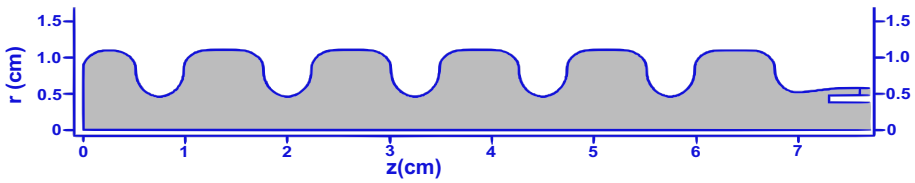

Fig. 219 Scheme of the longitudinal section of the 5.6 cell RF photoinjector with the coaxial coupler. The structure has a revolution symmetry around the z axis

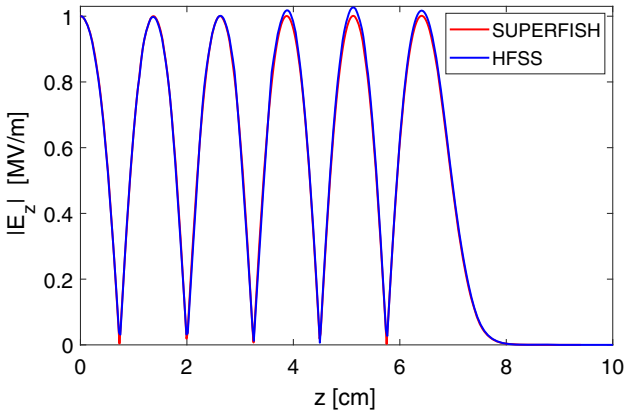

Fig. 220 RF electric field along the axis of the RF gun, normalized for 1 MV/m at the cathode, computed with SUPERFISH plus a circuit model for the neighbouring modes (red curve), and with HFSS (blue curve)

the coupling factor, $\beta = 1.008$, the separation between the π-mode and the nearest neighbouring mode, $\Delta f = 27.1$ MHz, and the gun cavity filling time, $\tau = 112.5$ ns. These results, obtained with SUPERFISH in combination with the circuit model, were benchmarked at the design frequency with the 3D numerical electromagnetic field solver HFSS [288]. The steady-state HFSS result is also plotted in Fig. 220 and agrees well with the model. The comparison thus validates the theoretical approach employed for the RF gun design.

8.1.2.2 Multipactor analysis in the coaxial coupler

During RF gun operation, the coupler coaxial line will be exposed to high-power RF electromagnetic fields that may cause the appearance of multipactor discharges. The multipactor phenomenon is an electron avalanche-like discharge occurring in components operating under vacuum conditions and high-power RF electromagnetic fields [289]. This process can lead to an exponential increase of the electron population, which degrades the component's performance and can physically damage the structure.

To assess the multipactor risk in the coaxial coupler, a set of multipactor numerical simulations was performed to determine the susceptibility zones in which the discharge is expected to occur. The multipactor numerical simulations for the coaxial line were carried out with an in-house developed code based on the Monte Carlo method, which relies on the single effective electron model [290]. This technique is based on 3-D tracking a set of effective electrons governed by the electromagnetic field. Each effective electron describes a particular electron population that evolves in time by colliding with the coaxial metallic walls of the waveguide (inner and outer coaxial conductors).

According to the results of the numerical simulations for the coaxial coupler of the photoinjector, which is intended to operate with a cathode RF electric field of 200 MV/m, there are two multipactor bands within the operating range. In terms of RF peak voltage in the coaxial waveguide, these bands correspond to the intervals of 0.891–3.565 kV and 5.219–8.388 kV. At the RF power level required to operate the gun, the RF voltage in the coaxial line is 13.2 kV, which is above the second multipactor window, and hence, no multipactor discharge is expected at this operating point. However, when the RF power is turned on, there will be a transient increase in the RF electromagnetic field, both in the coaxial line and in the RF gun cavity, until the field reaches a steady state. In fact, during the filling of the cavity, there will be two-time intervals of 15 ns and 23 ns (corresponding to the first and second window, respectively) in which multipactor discharges are expected to occur. Similarly, multipactoring will appear during the emptying of the cavity in two-time spans of 53 ns and 156 ns.

Despite the multipactor risk, it does not represent an insurmountable problem, since it can be suppressed by means of an external magnetic field. This method was theoretically and experimentally demonstrated for coaxial lines in [291]. In our case, the numerical simulations reveal that a static magnetic field equal to or higher than 360 mT suppresses the discharge. Accordingly, a solenoid will be included in the RF photoinjector layout for multipactor mitigation in the coupler coaxial line, as well as for beam emittance compensation purposes.

8.1.2.3 RF breakdown risk

RF breakdown is a phenomenon that appears in RF accelerating structures at high electric surface field gradients [292]. During breakdown, an electric current is emitted from the walls of the device, forming a plasma that causes a sudden increase in the vacuum pressure level. The risk of RF breakdown is characterized by a normalized breakdown rate (BDR), defined as the expected number of breakdowns per pulse per meter length of the structure. According to [79], the BDR can be roughly estimated based on the maximum of a modified Poynting vector, S_c, that is computed along the device's surface. The relationship between the modified Poynting vector, BDR, and

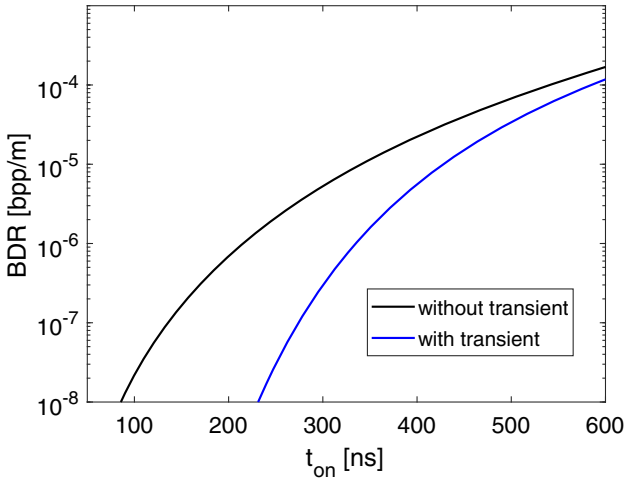

Fig. 221 BDR in the gun as a function of the RF pulse-length for a constant cathode electric field of 200 MV/m

the RF pulse-length t_{on} is given by the empirical expression

$$\text{BDR} = \frac{S_c^{15} t_{\text{on}}^5}{C}, \tag{68}$$

where $C = 9.765625 \times 10^{27}$ $\text{W}^{15}\text{ns}^5\mu$ $\text{m}^{-30}\text{bpp}^{-1}\text{m}$ is a constant found from measured breakdown rate data provided in [79]. The above expression allows one to estimate the BDR during a period when the gradient is constant. However, this is not the case for the RF gun, where the gradient varies during the filling and emptying of the cavities. For the RF gun case, the modified Poynting vector will vary with time, and this effect must be taken into account to calculate properly the BDR for the RF pulse in the gun. To do this, the pulse is split into the sum of many short pulses, assuming that for each of them, the corresponding BDR is given by the uniform S_c amplitude case

$$\text{BDR}_{\text{pulse}} = \frac{1}{C} \lim_{n\to\infty} \sum_{k=1}^{n} S_c^{15}(t_k) \left(\frac{T_p}{n}\right)^5 = \frac{5}{C} \int_0^{T_p} S_c^{15}(t)\, t^4 \, \text{d}\, t, \tag{69}$$

where $T_p = nt_p$ is the total pulse length, n is the number of short pulses into which the total pulse is divided, and t_p is the length of each short pulses. Figure 221 shows the resulting BDR in the RF gun as a function of the pulse length. The BDR predictions corresponding to the constant gradient case are also included for comparison. There is a significant difference between the two curves, which shows the importance of taking into consideration the transient effect. For $t_{\text{on}} \gg \tau$, the transient result approaches that of the constant gradient case as expected.

8.1.2.4 RF pulse heating

The surface currents associated with the RF fields in a structure induce Ohmic losses on the walls that increase the metal's temperature. Pulsed temperature increases over 50°C–60°C significantly increase the BDR in copper structures [293]. Thus, one wants to avoid operating at gradients and pulse lengths that produce such peak temperature rises during the RF pulse.

The temperature increase during an RF pulse in the photoinjector can be estimated by means of a 1D model that solves analytically the heat transfer differential equation for a metallic wall where the wall boundaries are assumed to be thermally isolated. Given these assumptions, the 1D heat transfer equation can be solved analytically following a similar procedure to that described in [165, 294]. For our calculations, the equations given in [294] are employed, since they take into account the effect of the RF pulse transient. In Fig. 222 (left), the maximum temperature increase during the RF pulse in the photoinjector walls is shown as a function of the pulse length, and Fig. 222 (right) shows a color map of the peak temperature rise in the gun for $t_{on} = 400$ ns. For a pulse length of $t_{\text{on}} = 400$ ns, the maximum temperature rise is $\Delta T = 31°\text{C}$, which is below the limit of 50°C–60°C.

8.1.2.5 RF power system

The proposed RF gun is intended to operate with a high-gradient cathode field of 200 MV/m when the laser beam hits the cathode to generate the electron beam. To achieve this field at the cathode, an input RF power of

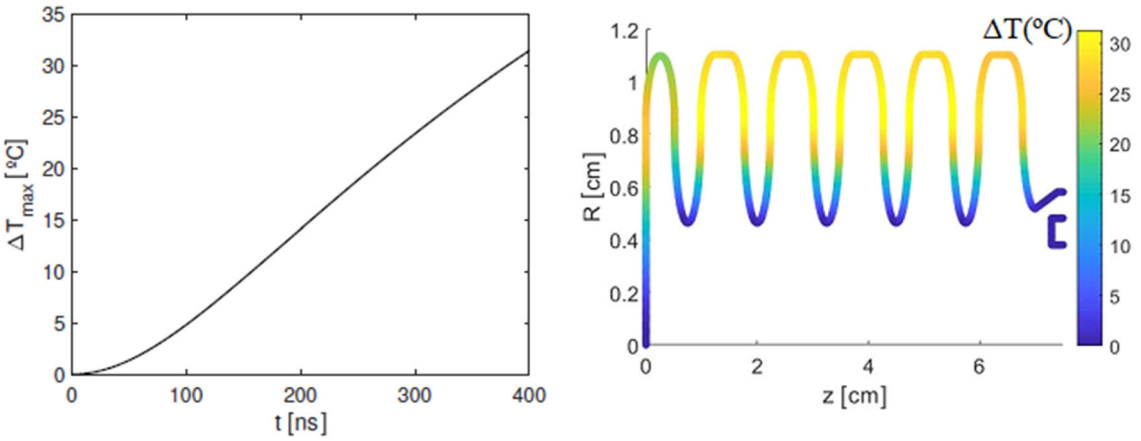

Fig. 222 Left: maximum temperature increase in the RF gun copper walls as a function of the pulse duration for a steady-state cathode electric field of 200 MV/m. Right: maximum temperature increase in the RF gun copper surfaces when operating with a steady-state cathode field of 200 MV/m and $t_{\text{on}} = 400$ ns

11.58 MW must be delivered at the coaxial coupler port. During the RF transient phase, a significant amount of RF power is reflected back to the klystron. To protect the klystron, a delay line between the klystron and the RF gun has been added, thus ensuring that when the reflected power starts to arrive, the RF pulse has finished and the klystron is switched off. For our design, the intended pulse duration ($t_{\text{on}} = 400$ ns) would require a length of $L = 50.24$ m to protect the klystron. However, taking into account the attenuation of the standard copper WR-90 rectangular waveguide ($\alpha_{at} = 0.11$ dB/m) operating with the fundamental TE_{10} mode, this will result in a total attenuation of 5.52 dB, which implies that nearly 72% of the input power is lost before reaching the RF gun, and hence results in a very inefficient design. A solution to that problem is to shorten the RF pulse and excite the gun with a square-step RF pulse [84]. The initial part of the RF pulse has a power ΛP_{in}, P_{in} being the RF input power required to obtain the desired RF electric field amplitude at the cathode (after the filling transient) for the RF gun operation and $\Lambda > 1$ is the power magnification factor at the first part of the RF pulse. At the time t_h, there is a sharp change in the RF power to the value P_{in}, which is maintained for the rest of the pulse. It is chosen that $\Lambda = 4$ ($\Lambda P_{\text{in}} = 46.32$ MW) and $t_h = 77.2$ ns. Using such an RF pulse, it is found that for a time of $t_{\text{inj}} = 85$ ns, the axial pattern of the RF electric field matches well with the steady-state case and with the desired amplitude of 200 MV/m at the cathode. Hence, the electron beam must be injected at this time. For this case, the length of the delay-line is $L = 10.67$ m and a total RF power of 60.7 MW must be finally delivered by the klystron to feed the photoinjector circuit (taking into account the power losses of the delay-line).

To achieve this RF power, a layout similar to that existing in Xbox 3 at CERN is proposed [295]. The layout is composed of four combined Toshiba E37113 klystrons and SLED pulse compressors. Each of the klystrons can provide an RF pulse with a peak power of 6 MW and a pulse length of up to 4–5μs. Thus, combining the four klystrons a pulse with a peak power of 24 MW and pulse length up to 4–5μs can be obtained. Now, if this combined pulse is compressed by means of an SLED pulse-compressor with a compression factor between 3 and 4, a final output pulse with peak power in the range between 70 and 80 MW, pulse-length of up to 300 ns, and a maximum repetition rate of 400 Hz can be achieved [295]. A pulse with such characteristics would be suitable for feeding the proposed RF gun.

8.1.2.6 Photoinjector beam dynamics

The beam simulations of the photoinjector have been carried out with the simulation codes GPT [172], ASTRA [296], and RF-Track [297]. 20k macro-particles were used to simulate a 75 pC bunch charge that is excited by a uniform laser which has a 0.3 ps long flat pulse with a 0.25 mm rms transverse width. It was also assumed that the particles emerging from the cathode at room temperature have a kinetic energy of $E_k = 0.05$ eV with an intrinsic emittance of $\varepsilon = 0.06$ μm rad.

To examine the performance of the RF photoinjector, an optimization procedure was carried to achieve a bunch with good properties (low emittance, small uncorrelated energy spread, etc.) at the injector output. Beam dynamics modelling was carried out by optimizing the overall photoinjector design, in particular, by adjusting the bunch phase, solenoid strength, the accelerating TW phase, and the spacing between the gun and the first TW structure in order to achieve the best emittance compensation. An exploration of different combinations of the above parameters was required to find the optimum working point. The spacing between the gun to accelerating structure is chosen according to Ferrario's working point [183], which states that the entrance to the accelerating structure after the gun must be at the position where the beam size has a minimum, and the emittance is optimized

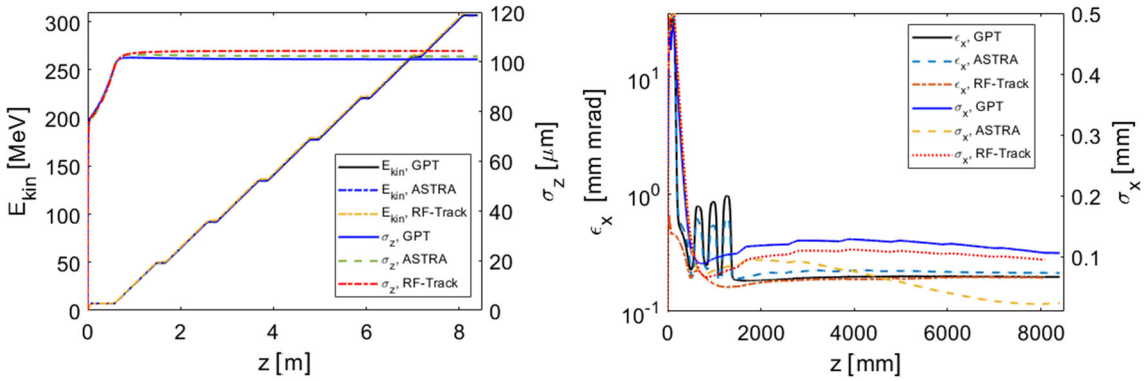

Fig. 223 Left: energy gain and the bunch length evolution along the injector. Right: projected normalized horizontal emittance and transverse RMS beam size along the injector

Table 69 Electron beam properties at the output of the photoinjector

Parameter	Units	GPT	ASTRA	RF-Track
Kinetic energy	MeV	307	306	308
Bunch length	fs	337	341	348
Energy spread	%	0.50	0.56	0.43
Peak current	A	64	64	62
Rms norm. emittance	mm.mrad	0.20	0.21	0.19
Transverse size	mm	0.10	0.02	0.09

for minimum at the end of the first TW structure. The optimum set of parameters was obtained using the code GPT that produced a minimum projected emittance at the end of the first TW structure.

The results from the GPT simulations have been benchmarked with the codes ASTRA [296] and RF-Track [297], finding a good agreement between them, and thus giving confidence in the simulations. The energy gain and length of the bunch in the X-band gun and TW structures are shown in Fig. 223 (right). The evaluation of rms emittance as well as the transverse beam size along the injector are shown in Fig. 223 (left).

The final beam properties obtained with each code are listed in the Table 69.

8.2 Undulator option

8.2.1 Cryogenic permanent magnet undulators

The helical SCU solution adopted as the baseline undulator, discussed in Sect. 6.1.1, has open issues that cannot be addressed in detail at this conceptual design stage. The engineering challenges are the main factors that have, to date, prevented SCUs from being widely adopted, especially at FEL user facilities. The following issues are mentioned on a qualitative level:

- The mechanical tolerances are tight and have to be maintained as the coils are cooled down from room temperature to about 4 K.
- Any heat transfer due to wakefields or synchrotron radiation from the electron beam has be minimized to prevent magnet quenching.
- Concerning the phase error, conventional field correction schemes used for permanent magnet devices cannot be directly applied to SCUs.

These considerations suggest that an alternative option for the main radiator should be considered as a precaution.

Such an option is the cryogenic permanent magnet undulator (CPMU) in which permanent magnets are cooled by means of either refrigerant channels or cryocoolers, down to the temperature of liquid nitrogen.

The operation of the magnet blocks at cryogenic temperatures provides a threefold benefit:

(a) It removes the need to bake the magnets at high temperature.

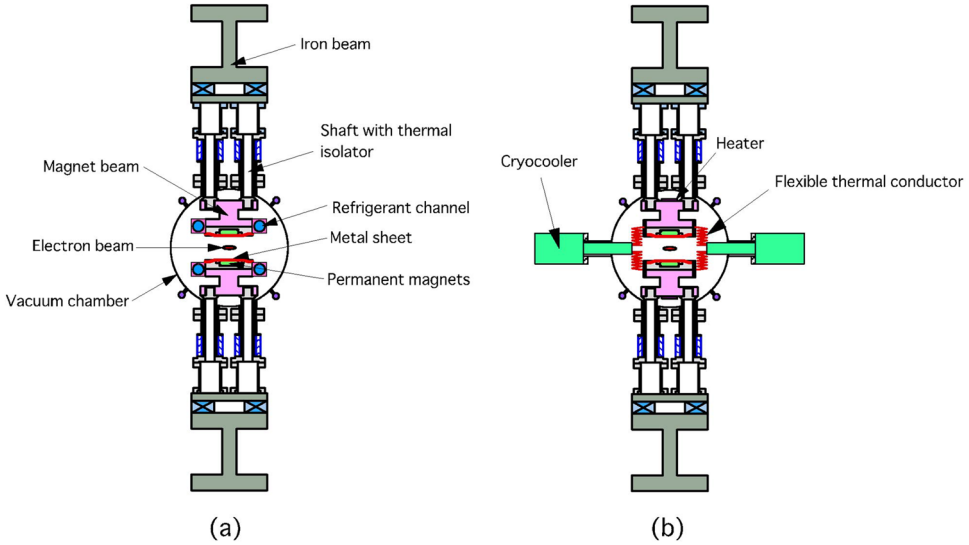

Fig. 224 Diagram of a typical CPMU structure with two different cooling schemes. Left: refrigerant channels with liquid nitrogen. Right: cryocooler coldheads. Reproduced from [298]

(b) It enhances the coercive force of the magnets, making them more resistant to demagnetising effects.
(c) It increases the remanence of the magnets, with the subsequent increase of the undulator magnetic peak field.

This scheme can be easily adapted to currently existing in-vacuum undulators and the magnetic field strength is improved over room temperature devices by $\sim 30\%$ for pure permanent magnet types and $\sim 50\%$ for hybrid types. Compared to a room temperature in-vacuum undulator of equivalent spectral range, the flux performance is enhanced thanks to the field increase and to the additional number of periods for a given module length. In summary, CPMUs fit well the demand of short period undulators.

Unlike SCUs operating around the liquid helium temperature where the heat load budget is a few watts, with CPMUs, there is no big technological issue such as the thermal shield, so a heat load as high as several hundred watts is allowed. In addition, existing field correction techniques are applicable to the CPMUs, and since there is no quench possibility CPMUs have a similar reliability to conventional permanent magnet undulators.

Figure 224 shows two available schemes for magnet cooling. The most straightforward one is using refrigerant channels with liquid nitrogen. This solution provides a cooling capacity of more than a kW, and it is the solution used at the first directly cooled CPMU to be operated at 77 K, built at SOLEIL [299]. The other cooling concept is based on coldheads, each providing a cooling capacity at 77 K of $\sim$ 180–200 W [253]. Nevertheless, several CPMU key components need to be adapted, in particular the cooling system, the magnet girder, and the gap measurement systems. Moreover, the magnetic field characterization of cryogenic undulators is challenging, given that magnetic measurements have to be performed inside the vacuum chamber at cryogenic temperature to optimize the undulator in the final operation conditions. More technical considerations as well as details on risk, benefit, and cost challenges are reported on the deliverable document D5.1 [300].

8.2.2 Comparison of SCU and CPMU

Following the method of the study presented in Sect. 6.1.2.2 which determined the optimal undulator period of the helical SCU to balance the FEL output across the whole Soft and Hard X-ray tuning range, the semi-analytical Xie model [67] is used to evaluate the performance. This model is widely adopted as it yields quick calculations of the FEL parameters,

accounting for the main effects deteriorating the gain performance due to energy spread, emittance, and finite transverse bunch size, and as it provides reliable comparisons among different undulator period and strength configurations. Calculations assume the average electron beam parameter values listed in Table 70. The analyzed quantities are the gain length $L_{g\,3D}$, whose evaluation is improved in the Xie model by the aforementioned effects over the 1-dimension estimate of Eq. (6) (see Sect. 3.3.2.1), and the pulse energy as defined in Sect. 6.1.2.2. The FEL saturation length is estimated approximately as $20\,L_{g\,3D}$.

Figure 225 shows the comparison, as a function of the FEL resonant photon energy E_{ph}, of pulse energy and $L_{g\,3D}$, between the baseline helical SCU with period $\lambda_u = 13$ mm and three planar CPMUs with the specified

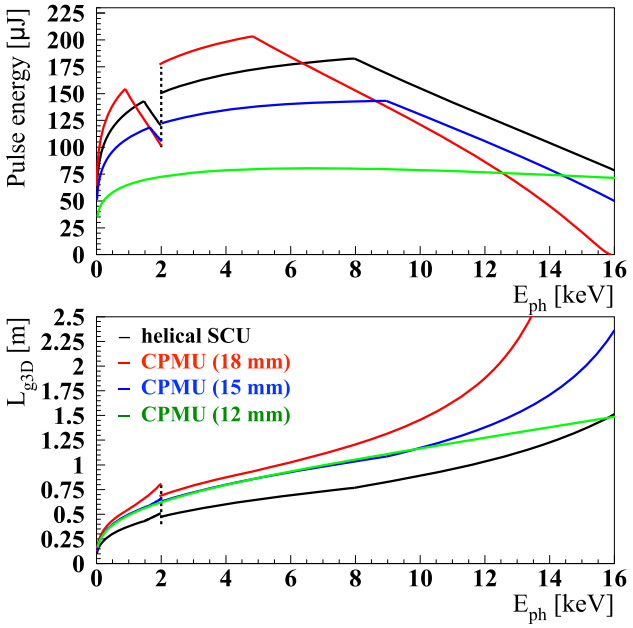

Fig. 225 Semi-analytical performance calculations, showing comparison between the helical 13 mm SCU period (baseline choice) and the CPMU with 18 mm, 15 mm and 12 mm periods, showing pulse energy (top) and gain length (bottom) as a function of the FEL photon energy

Table 70 Reference electron beam parameters

Parameter	Value	Units
Beam energy	5.5	GeV
Peak current	5	kA
normalized emittance	0.2	mm mrad
RMS slice energy spread	0.01	%
Average β function	9	m

undulator periods and the related color code. In particular, the CPMUs under consideration are those designed at Soleil [301, 302].

Following the same definitions discussed in Sect. 6.1.2.2, the pulse energy increases with $E_{\rm ph}$, as the photon energy is sustained by increasing the beam energy at fixed tuning, for each undulator line.

Once the beam energy of 2.36 GeV is reached, namely the maximum value allowed to operate in the Soft X-ray regime at 1 kHz repetition rate, the pulse energy decreases as the $E_{\rm ph}$ increase is provided by the magnetic strength decrease with the subsequent FEL gain decrease. This is the explanation of the turning points located at $E_{\rm ph} < 2\,$keV values. The 12 mm CPMU period is the only exception as this configuration provides a regular resonant photon energy increase for the whole beam energy range under consideration within this project. For photon energies larger than 2 keV, a similar behavior occurs for beam energies up to 5.5 GeV, resulting in a turning point located around 5 keV for the 12 mm CPMU period after which the pulse energy drops. In this range, the pulse energy behavior of the 15 mm CPMU period is very similar to the baseline SCU choice, with the turning point located between 8 and 9 keV. The gain length of the 12 mm and 15 mm CPMU periods is basically the same up to $E_{\rm ph} \simeq 10\,$keV values, with about 50% better length performance at larger photon energies, for the shorter period.

In conclusion, while the gain length does not make any substantial difference between 12 mm and 15 mm CPMU periods, the pulse energy comparison tends to favor the latter one, as it is better balanced along the full $E_{\rm ph}$ range to be covered, very similar to that of the baseline helical SCU, at the price of an overall 25% loss in the output FEL pulse energy.

Acknowledgements The CompactLight collaboration gratefully acknowledges the EU Commission for supporting the project under Grant Agreement No. 777431, Horizon2020, Work Programme 2016–2017, Research and Innovation Action

(RIA), INFRADEV-1-2017 Design Studies. We also would like to thank the Scientific Advisory Board for their valuable support and advice: Marie-Emmanuelle Couprie, Soleil Synchrotron, France; Wolfgang Eberhardt, DESY, DE; and Sverker Werin, Lund University, Lund, SE. All the CompactLight Members, Supporters, and Collaborators for their excellent work.

Data Availability Statement To facilitate a wide use of the project results, most of the CompactLight publications and data are generally "open data". The CompactLight Data Management Plan (DMP) [303] provides a detailed description of how the data have been organised and managed. The CompactLight Data Management Plan (DMP) aimed to show how to collect and preserve all the information generated by the XLS collaboration and document the work done and its results. The data collected were classified as 'open' or 'restricted' depending on their nature and intended internal use and reuse by the partners. Data critical to the partners' follow-up activities, such as projects already underway or planned, are defined as 'restricted', while all other data are 'open'. External researchers can use the currently 'restricted' project data through collaborative projects with the project partners, and any interested parties are strongly encouraged to contact the project team to discuss their ideas.

References

1. CompactLight Partnership, CompactLight Project Website (2018). http://www.compactlight.eu/Main/HomePage%5Ccite%7BXLS%7D
2. Smart*Light Website. https://research.tue.nl/en/impacts/smartlight
3. CXFEL–Compact X-ray Free Electron Laser. https://physics.asu.edu/innitiativecenter/CFXELUni
4. W. Ackermann, G. Asova, V. Ayvazyan, A. Azima, N. Baboi, J. Bähr, V. Balandin, B. Beutner, A. Brandt, A. Bolzmann, R. Brinkmann, O.I. Brovko, M. Castellano, P. Castro, L. Catani, E. Chiadroni, S. Choroba, A. Cianchi, J.T. Costello, D. Cubaynes, J. Dardis, W. Decking, H. Delsim-Hashemi, A. Delserieys, G. Di Pirro, M. Dohlus, S. Düsterer, A. Eckhardt, H.T. Edwards, B. Faatz, J. Feldhaus, K. Flöttmann, J. Frisch, L. Fröhlich, T. Garvey, U. Gensch, C. Gerth, M. Görler, N. Golubeva, H.J. Grabosch, M. Grecki, O. Grimm, K. Hacker, U. Hahn, J.H. Han, K. Honkavaara, T. Hott, M. Hüning, Y. Ivanisenko, E. Jaeschke, W. Jalmuzna, T. Jezynski, R. Kammering, V. Katalev, K. Kavanagh, E.T. Kennedy, S. Khodyachykh, K. Klose, V. Kocharyan, M. Körfer, M. Kollewe, W. Koprek, S. Korepanov, D. Kostin, M. Krassilnikov, G. Kube, M. Kuhlmann, C.L.S. Lewis, L. Lilje, T. Limberg, D. Lipka, F. Löhl, H. Luna, M. Luong, M. Martins, M. Meyer, P. Michelato, V. Miltchev, W.D. Möller, L. Monaco, W.F.O. Müller, O. Napieralski, O. Napoly, P. Nicolosi, D. Nölle, T. Nũez, A. Oppelt, C. Pagani, R. Paparella, N. Pchalek, J. Pedregosa-Gutierrez, B. Petersen, B. Petrosyan, G. Petrosyan, L. Petrosyan, J. Pflüger, E. Plönjes, L. Poletto, K. Pozniak, E. Prat, D. Proch, P. Pucyk, P. Radcliffe, H. Redlin, K. Rehlich, M. Richter, M. Roehrs, J. Roensch, R. Romaniuk, M. Ross, J. Rossbach, V. Rybnikov, M. Sachwitz, E.L. Saldin, W. Sandner, H. Schlarb, B. Schmidt, M. Schmitz, P. Schmüser, J.R. Schneider, E.A. Schneidmiller, S. Schnepp, S. Schreiber, M. Seidel, D. Sertore, A.V. Shabunov, C. Simon, S. Simrock, E. Sombrowski, A.A. Sorokin, P. Spanknebel, R. Spesyvtsev, L. Staykov, B. Steffen, F. Stephan, F. Stulle, H. Thom, K. Tiedtke, M. Tischer, S. Toleikis, R. Treusch, D. Trines, I. Tsakov, E. Vogel, T. Weiland, H. Weise, M. Wellhöfer, M. Wendt, I. Will, A. Winter, K. Wittenburg, W. Wurth, P. Yeates, M.V. Yurkov, I. Zagorodnov, K. Zapfe, Operation of a free-electron laser from the extreme ultraviolet to the water window. Nat. Photonics **1**(6), 336–342 (2007). https://doi.org/10.1038/nphoton.2007.76
5. DESY, FLASH Free Electron Laser. https://flash.desy.de/accelerator/
6. SACLA X-ray Free Electron Laser. http://xfel.riken.jp/eng/
7. Elettra Sincrotrone Trieste, FERMI Conceptual Design Report. Technical report (2007). https://www.elettra.eu/files/Documents/FERMI%20Machine/Machine/CDR/FERMI_CDR.pdf
8. Elettra Sincrotrone Trieste, FERMI Website. https://www.elettra.eu/lightsources/fermi.html
9. Stanford Linear Accelerator Center, Linac Coherent Light Source (LCLS) Conceptual Design Report. Slac-R-593 (2002). https://doi.org/10.2172/1029479
10. Linac Coherent Light Source—SLAC National Accelerator Laboratory. https://lcls.slac.stanford.edu/
11. European XFEL, European XFEL: Overview (2021). https://www.xfel.eu/facility/overview/index_eng.html
12. M. Altarelli, R. Brinkmann, M. Chergui, W. Decking et al., The European X-Ray Free-Electron Laser—Technical design report. Technical report, DESY, Hamburg (2007)
13. M. Pedrozzi, SwissFEL Injector Conceptual Design Report. Technical report, PSI (2010)
14. SwissFEL, SwissFEL—Paul Scherrer Institut (PSI) (2021). https://www.psi.ch/en/swissfel
15. Pohang Accelerator Laboratory, https://pal.postech.ac.kr/paleng/Menu.pal?method=menuView&pageMode=paleng&top=7&sub=6&sub2=1&sub3=0

16. Z.Y. Zhu, Z.T. Zhao, D. Wang, Z. Liu, R.X. Li, L.X. Yin, Z.H. Yang, SCLF: an 8-GeV CW SCRF Linac-based X-Ray FEL Facility in Shanghai, in *Proceedings of the 38th International Free-Electron Laser Conference*, FEL 2017, pp. 182–184 (2018). https://doi.org/10.18429/JACOW-FEL2017-MOP055
17. J.N. Galayda, The LCLS-II: a high power upgrade to the LCLS (2018). https://doi.org/10.18429/JACoW-IPAC2018-MOYGB2
18. LCLS-II, Linac Coherent Light Source. https://lcls.slac.stanford.edu/lcls-ii
19. W. Hopkins, V. Verzilov, G. Sciaini, I. Burgess, M. Boland, Establishing a Canadian free-electron laser research program. Can. J. Phys. (2019). https://doi.org/10.1139/cjp-2019-0238
20. M. Aicheler, P. Burrows, M. Draper, T. Garvey, P. Lebrun, K. Peach, N. Phinney, H. Schmickler, D. Schulte, N. Toge, A Multi-TeV Linear Collider Based on CLIC Technology: CLIC Conceptual Design Report. CERN Yellow Reports: Monographs. CERN, Geneva (2012). https://doi.org/10.5170/CERN-2012-007. http://cds.cern.ch/record/1500095
21. J.M. Rodenburg, A.C. Hurst, A.G. Cullis, B.R. Dobson, F. Pfeiffer, O. Bunk, C. David, K. Jefimovs, I. Johnson, Hard-X-ray lensless imaging of extended objects. Phys. Rev. Lett. **98**(3), 034801 (2007). https://doi.org/10.1103/PHYSREVLETT.98.034801/FIGURES/3/MEDIUM
22. S. Boutet, L. Lomb, G.J. Williams, T.R.M. Barends, A. Aquila, R.B. Doak, U. Weierstall, D.P. DePonte, J. Steinbrener, R.L. Shoeman, M. Messerschmidt, A. Barty, T.A. White, S. Kassemeyer, R.A. Kirian, M.M. Seibert, P.A. Montanez, C. Kenney, R. Herbst, P. Hart, J. Pines, G. Haller, S.M. Gruner, H.T. Philipp, M.W. Tate, M. Hromalik, L.J. Koerner, N. Van Bakel, J. Morse, W. Ghonsalves, D. Arnlund, M.J. Bogan, C. Caleman, R. Fromme, C.Y. Hampton, M.S. Hunter, L.C. Johansson, G. Katona, C. Kupitz, M. Liang, A.V. Martin, K. Nass, L. Redecke, F. Stellato, N. Timneanu, D. Wang, N.A. Zatsepin, D. Schafer, J. Defever, R. Neutze, P. Fromme, J.C.H. Spence, H.N. Chapman, I. Schlichting, High-resolution protein structure determination by serial femtosecond crystallography. Science **337**(6092), 362–364 (2012). https://doi.org/10.1126/SCIENCE.1217737/FORMAT/PDF
23. T. Masuda, M. Suzuki, S. Inoue, C. Song, T. Nakane, E. Nango, R. Tanaka, K. Tono, Y. Joti, T. Kameshima, T. Hatsui, M. Yabashi, B. Mikami, O. Nureki, K. Numata, S. Iwata, M. Sugahara, Atomic resolution structure of serine protease proteinase K at ambient temperature. Sci. Rep. (2017). https://doi.org/10.1038/SREP45604
24. M.O. Wiedorn, D. Oberthür, R. Bean, R. Schubert, N. Werner, B. Abbey, M. Aepfelbacher, L. Adriano, A. Allahgholi, N. Al-Qudami, J. Andreasson, S. Aplin, S. Awel, K. Ayyer, S. Bajt, I. Barák, S. Bari, J. Bielecki, S. Botha, D. Boukhelef, W. Brehm, S. Brockhauser, I. Cheviakov, M.A. Coleman, F. Cruz-Mazo, C. Danilevski, C. Darmanin, R.B. Doak, M. Domaracky, K. Dörner, Y. Du, H. Fangohr, H. Fleckenstein, M. Frank, P. Fromme, A.M. Gañán-Calvo, Y. Gevorkov, K. Giewekemeyer, H.M. Ginn, H. Graafsma, R. Graceffa, D. Greiffenberg, L. Gumprecht, P. Göttlicher, J. Hajdu, S. Hauf, M. Heymann, S. Holmes, D.A. Horke, M.S. Hunter, S. Imlau, A. Kaukher, Y. Kim, A. Klyuev, J. Knoška, B. Kobe, M. Kuhn, C. Kupitz, J. Küpper, J.M. Lahey-Rudolph, T. Laurus, K. Le Cong, R. Letrun, P.L. Xavier, L. Maia, F.R.N.C. Maia, V. Mariani, M. Messerschmidt, M. Metz, D. Mezza, T. Michelat, G. Mills, D.C.F. Monteiro, A. Morgan, K. Mühlig, A. Munke, A. Münnich, J. Nette, K.A. Nugent, T. Nuguid, A.M. Orville, S. Pandey, G. Pena, P. Villanueva-Perez, J. Poehlsen, G. Previtali, L. Redecke, W.M. Riekehr, H. Rohde, A. Round, T. Safenreiter, I. Sarrou, T. Sato, M. Schmidt, B. Schmitt, R. Schönherr, J. Schulz, J.A. Sellberg, M.M. Seibert, C. Seuring, M.L. Shelby, R.L. Shoeman, M. Sikorski, A. Silenzi, C.A. Stan, X. Shi, S. Stern, J. Sztuk-Dambietz, J. Szuba, A. Tolstikova, M. Trebbin, U. Trunk, P. Vagovic, T. Ve, B. Weinhausen, T.A. White, K. Wrona, C. Xu, O. Yefanov, N. Zatsepin, J. Zhang, M. Perbandt, A.P. Mancuso, C. Betzel, H. Chapman, A. Barty, Megahertz serial crystallography. Nat. Commun. **9**(1), 1–11 (2018). https://doi.org/10.1038/s41467-018-06156-7
25. M.L. Grünbein, J. Bielecki, A. Gorel, M. Stricker, R. Bean, M. Cammarata, K. Dörner, L. Fröhlich, E. Hartmann, S. Hauf, M. Hilpert, Y. Kim, M. Kloos, R. Letrun, M. Messerschmidt, G. Mills, G. Nass Kovacs, M. Ramilli, C.M. Roome, T. Sato, M. Scholz, M. Sliwa, J. Sztuk-Dambietz, M. Weik, B. Weinhausen, N. Al-Qudami, D. Boukhelef, S. Brockhauser, W. Ehsan, M. Emons, S. Esenov, H. Fangohr, A. Kaukher, T. Kluyver, M. Lederer, L. Maia, M. Manetti, T. Michelat, A. Münnich, F. Pallas, G. Palmer, G. Previtali, N. Raab, A. Silenzi, J. Szuba, S. Venkatesan, K. Wrona, J. Zhu, R.B. Doak, R.L. Shoeman, L. Foucar, J.P. Colletier, A.P. Mancuso, T.R.M. Barends, C.A. Stan, I. Schlichting, Megahertz data collection from protein microcrystals at an X-ray free-electron laser. Nat. Commun. **9**(1), 1–9 (2018). https://doi.org/10.1038/s41467-018-05953-4
26. B. Henrich, J. Becker, R. Dinapoli, P. Goettlicher, H. Graafsma, H. Hirsemann, R. Klanner, H. Krueger, R. Mazzocco, A. Mozzanica, H. Perrey, G. Potdevin, B. Schmitt, X. Shi, A.K. Srivastava, U. Trunk, C. Youngman, The adaptive gain integrating pixel detector AGIPD a detector for the European XFEL. Nucl. Instrum. Methods Phys. Res. Sect. A **633**(SUPPL. 1), 11–14 (2011). https://doi.org/10.1016/J.NIMA.2010.06.107
27. R. Neutzo, R. Wouts, D. Van Der Spoel, E. Weckert, J. Hajdu, Potential for biomolecular imaging with femtosecond X-ray pulses. Nature **406**(6797), 752–757 (2000). https://doi.org/10.1038/35021099
28. Z. Sun, J. Fan, H. Li, H. Jiang, Current status of single particle imaging with X-ray lasers. Appl. Sci. (Switzerland) (2018). https://doi.org/10.3390/APP8010132
29. D. Milathianaki, S. Boutet, G.J. Williams, A. Higginbotham, D. Ratner, A.E. Gleason, M. Messerschmidt, M.M. Seibert, D.C. Swift, P. Hering, J. Robinson, W.E. White, J.S. Wark, Femtosecond visualization of lattice dynamics in shock-compressed matter. Science **342**(6155), 220–223 (2013). https://doi.org/10.1126/SCIENCE.1239566/SUPPL_FILE/MILATHIANAKI.SM
30. M.G. Gorman, R. Briggs, E.E. McBride, A. Higginbotham, B. Arnold, J.H. Eggert, D.E. Fratanduono, E. Galtier, A.E. Lazicki, H.J. Lee, H.P. Liermann, B. Nagler, A. Rothkirch, R.F. Smith, D.C. Swift, G.W. Collins, J.S. Wark, M.I.

McMahon, Direct observation of melting in shock-compressed bismuth with femtosecond X-ray diffraction. Phys. Rev. Lett. **115**(9), 095701 (2015). https://doi.org/10.1103/PHYSREVLETT.115.095701/FIGURES/4/MEDIUM
31. D. Kraus, A. Ravasio, M. Gauthier, D.O. Gericke, J. Vorberger, S. Frydrych, J. Helfrich, L.B. Fletcher, G. Schaumann, B. Nagler, B. Barbrel, B. Bachmann, E.J. Gamboa, S. Göde, E. Granados, G. Gregori, H.J. Lee, P. Neumayer, W. Schumaker, T. Döppner, R.W. Falcone, S.H. Glenzer, M. Roth, Nanosecond formation of diamond and lonsdaleite by shock compression of graphite. Nat. Commun. **7**(1), 1–6 (2016). https://doi.org/10.1038/ncomms10970
32. J. Kern, R. Alonso-Mori, R. Tran, J. Hattne, R.J. Gildea, N. Echols, C. Gloöckner, J. Hellmich, H. Laksmono, R.G. Sierra, B. Lassalle-Kaiser, S. Koroidov, A. Lampe, G. Han, S. Gul, D. DiFiore, D. Milathianaki, A.R. Fry, A. Miahnahri, D.W. Schafer, M. Messerschmidt, M.M. Seibert, J.E. Koglin, D. Sokaras, T.C. Weng, J. Sellberg, M.J. Latimer, R.W. Grosse-Kunstleve, P.H. Zwart, W.E. White, P. Glatzel, P.D. Adams, M.J. Bogan, G.J. Williams, S. Boutet, J. Messinger, A. Zouni, N.K. Sauter, V.K. Yachandra, U. Bergmann, J. Yano, Simultaneous femtosecond X-ray spectroscopy and diffraction of photosystem II at room temperature. Science (New York, N.Y.) **340**(6131), 491–495 (2013). https://doi.org/10.1126/SCIENCE.1234273
33. P. Salén, P. Van Der Meulen, H.T. Schmidt, R.D. Thomas, M. Larsson, R. Feifel, M.N. Piancastelli, L. Fang, B. Murphy, T. Osipov, N. Berrah, E. Kukk, K. Ueda, J.D. Bozek, C. Bostedt, S. Wada, R. Richter, V. Feyer, K.C. Prince, Experimental verification of the chemical sensitivity of two-site double core-hole states formed by an x-ray free-electron laser. Phys. Rev. Lett. **108**(15), 153003 (2012). https://doi.org/10.1103/PHYSREVLETT.108.153003/FIGURES/2/MEDIUM
34. N. Berrah, L. Fang, B. Murphy, T. Osipov, K. Ueda, E. Kukk, R. Feifel, P. Van Der Meulen, P. Salen, H.T. Schmidt, R.D. Thomas, M. Larsson, R. Richter, K.C. Prince, J.D. Bozek, C. Bostedt, S.I. Wada, M.N. Piancastelli, M. Tashiro, M. Ehara, Double-core-hole spectroscopy for chemical analysis with an intense X-ray femtosecond laser. Proc. Natl. Acad. Sci. **108**(41), 16912–16915 (2011). https://doi.org/10.1073/PNAS.1111380108
35. S.E. Canton, K.S. Kjær, G. Vankó, T.B. Van Driel, S.I. Adachi, A. Bordage, C. Bressler, P. Chabera, M. Christensen, A.O. Dohn, A. Galler, W. Gawelda, D. Gosztola, K. Haldrup, T. Harlang, Y. Liu, K.B. Møller, Z. Németh, S. Nozawa, M. Pápai, T. Sato, T. Sato, K. Suarez-Alcantara, T. Togashi, K. Tono, J. Uhlig, D.A. Vithanage, K. Wärnmark, M. Yabashi, J. Zhang, V. Sundström, M.M. Nielsen, Visualizing the non-equilibrium dynamics of photoinduced intramolecular electron transfer with femtosecond X-ray pulses. Nat. Commun. **6**(1), 1–10 (2015). https://doi.org/10.1038/ncomms7359
36. P. Wernet, K. Kunnus, I. Josefsson, I. Rajkovic, W. Quevedo, M. Beye, S. Schreck, S. Grübel, M. Scholz, D. Nordlund, W. Zhang, R.W. Hartsock, W.F. Schlotter, J.J. Turner, B. Kennedy, F. Hennies, F.M.F. De Groot, K.J. Gaffney, S. Techert, M. Odelius, A. Föhlisch, Orbital-specific mapping of the ligand exchange dynamics of Fe(CO)5 in solution. Nature **520**(7545), 78–81 (2015). https://doi.org/10.1038/nature14296
37. H. Öström, H. Öberg, H. Xin, J. LaRue, M. Beye, M. Dell'Angela, J. Gladh, M.L. Ng, J.A. Sellberg, S. Kaya, G. Mercurio, D. Nordlund, M. Hantschmann, F. Hieke, D. Kühn, W.F. Schlotter, G.L. Dakovski, J.J. Turner, M.P. Minitti, A. Mitra, S.P. Moeller, A. Föhlisch, M. Wolf, W. Wurth, M. Persson, J.K. Nørskov, F. Abild-Pedersen, H. Ogasawara, L.G.M. Pettersson, A. Nilsson, Probing the transition state region in catalytic CO oxidation on Ru. Science **347**(6225), 978–982 (2015). https://doi.org/10.1126/SCIENCE.1261747/SUPPL_FILE/PAP
38. M. Dell'Angela, T. Anniyev, M. Beye, R. Coffee, A. Föhlisch, J. Gladh, T. Katayama, S. Kaya, O. Krupin, J. LaRue, A. Møgelhøj, D. Nordlund, J.K. Nørskov, H. Öberg, H. Ogasawara, H. Öström, L.G.M. Pettersson, W.F. Schlotter, J.A. Sellberg, F. Sorgenfrei, J.J. Turner, M. Wolf, W. Wurth, A. Nilsson, Real-time observation of surface bond breaking with an X-ray laser. Science **339**(6125), 1302–1305 (2013). https://doi.org/10.1126/SCIENCE.1231711/SUPPL_FILE/DELLANGELA-SOM
39. D.J. Higley, K. Hirsch, G.L. Dakovski, E. Jal, E. Yuan, T. Liu, A.A. Lutman, J.P. Macarthur, E. Arenholz, Z. Chen, G. Coslovich, P. Denes, P.W. Granitzka, P. Hart, M.C. Hoffmann, J. Joseph, L. Le Guyader, A. Mitra, S. Moeller, H. Ohldag, M. Seaberg, P. Shafer, J. Stöhr, A. Tsukamoto, H.D. Nuhn, A.H. Reid, H.A. Dürr, W.F. Schlotter, Femtosecond X-ray magnetic circular dichroism absorption spectroscopy at an X-ray free electron laser. Rev. Sci. Instrum. **87**(3), 033110 (2016). https://doi.org/10.1063/1.4944410
40. K. Yamamoto, Y. Kubota, M. Suzuki, Y. Hirata, K. Carva, M. Berritta, K. Takubo, Y. Uemura, R. Fukaya, K. Tanaka, W. Nishimura, T. Ohkochi, T. Katayama, T. Togashi, K. Tamasaku, M. Yabashi, Y. Tanaka, T. Seki, K. Takanashi, P.M. Oppeneer, H. Wadati, Ultrafast demagnetization of Pt magnetic moment in L10-FePt probed by magnetic circular dichroism at a hard x-ray free electron laser. New J. Phys. **21**(12), 123010 (2019). https://doi.org/10.1088/1367-2630/AB5AC2
41. T. Wang, D. Zhu, B. Wu, C. Graves, S. Schaffert, T. Rander, L. Müller, B. Vodungbo, C. Baumier, D.P. Bernstein, B. Bräuer, V. Cros, S. De Jong, R. Delaunay, A. Fognini, R. Kukreja, S. Lee, V. López-Flores, J. Mohanty, B. Pfau, H. Popescu, M. Sacchi, A.B. Sardinha, F. Sirotti, P. Zeitoun, M. Messerschmidt, J.J. Turner, W.F. Schlotter, O. Hellwig, R. Mattana, N. Jaouen, F. Fortuna, Y. Acremann, C. Gutt, H.A. Dürr, E. Beaurepaire, C. Boeglin, S. Eisebitt, G. Grübel, J. Lüning, J. Stöhr, A.O. Scherz, Femtosecond single-shot imaging of nanoscale ferromagnetic order in co/pd multilayers using resonant x-ray holography. Phys. Rev. Lett. **108**(26), 267403 (2012). https://doi.org/10.1103/PHYSREVLETT.108.267403/FIGURES/4/MEDIUM
42. C.E. Graves, A.H. Reid, T. Wang, B. Wu, S. De Jong, K. Vahaplar, I. Radu, D.P. Bernstein, M. Messerschmidt, L. Müller, R. Coffee, M. Bionta, S.W. Epp, R. Hartmann, N. Kimmel, G. Hauser, A. Hartmann, P. Holl, H. Gorke, J.H. Mentink, A. Tsukamoto, A. Fognini, J.J. Turner, W.F. Schlotter, D. Rolles, H. Soltau, L. Strüder, Y. Acremann, A.V. Kimel, A. Kirilyuk, T. Rasing, J. Stöhr, A.O. Scherz, H.A. Dürr, Nanoscale spin reversal by non-local angular

momentum transfer following ultrafast laser excitation in ferrimagnetic GdFeCo. Nat. Mater. **12**(4), 293–298 (2013). https://doi.org/10.1038/nmat3597
43. A.X. Gray, M.C. Hoffmann, J. Jeong, N.P. Aetukuri, D. Zhu, H.Y. Hwang, N.C. Brandt, H. Wen, A.J. Sternbach, S. Bonetti, A.H. Reid, R. Kukreja, C. Graves, T. Wang, P. Granitzka, Z. Chen, D.J. Higley, T. Chase, E. Jal, E. Abreu, M.K. Liu, T.C. Weng, D. Sokaras, D. Nordlund, M. Chollet, R. Alonso-Mori, H. Lemke, J.M. Glownia, M. Trigo, Y. Zhu, H. Ohldag, J.W. Freeland, M.G. Samant, J. Berakdar, R.D. Averitt, K.A. Nelson, S.S.P. Parkin, H.A. Dürr, Ultrafast terahertz field control of electronic and structural interactions in vanadium dioxide. Phys. Rev. B **98**(4), 045104 (2018). https://doi.org/10.1103/PHYSREVB.98.045104/FIGURES/7/MEDIUM
44. R. Mankowsky, A. Subedi, M. Först, S.O. Mariager, M. Chollet, H.T. Lemke, J.S. Robinson, J.M. Glownia, M.P. Minitti, A. Frano, M. Fechner, N.A. Spaldin, T. Loew, B. Keimer, A. Georges, A. Cavalleri, Nonlinear lattice dynamics as a basis for enhanced superconductivity in YBa2Cu3O6.5. Nature **516**(7529), 71–73 (2014). https://doi.org/10.1038/nature13875
45. F. Perakis, G. Camisasca, T.J. Lane, A. Späh, K.T. Wikfeldt, J.A. Sellberg, F. Lehmkühler, H. Pathak, K.H. Kim, K. Amann-Winkel, S. Schreck, S. Song, T. Sato, M. Sikorski, A. Eilert, T. McQueen, H. Ogasawara, D. Nordlund, W. Roseker, J. Koralek, S. Nelson, P. Hart, R. Alonso-Mori, Y. Feng, D. Zhu, A. Robert, G. Grübel, L.G.M. Pettersson, A. Nilsson, Coherent X-rays reveal the influence of cage effects on ultrafast water dynamics. Nat. Commun. **9**(1), 1–10 (2018). https://doi.org/10.1038/s41467-018-04330-5
46. A. Gorel, K. Motomura, H. Fukuzawa, R.B. Doak, M.L. Grünbein, M. Hilpert, I. Inoue, M. Kloos, G. Nass Kovács, E. Nango, K. Nass, C.M. Roome, R.L. Shoeman, R. Tanaka, K. Tono, L. Foucar, Y. Joti, M. Yabashi, S. Iwata, K. Ueda, T.R.M. Barends, I. Schlichting, Two-colour serial femtosecond crystallography dataset from gadoteridol-derivatized lysozyme for MAD phasing. Sci. Data **4**(1), 1–7 (2017). https://doi.org/10.1038/sdata.2017.188
47. S. Serkez, W. Decking, L. Froehlich, N. Gerasimova, J. Grünert, M. Guetg, M. Huttula, S. Karabekyan, A. Koch, V. Kocharyan, Y. Kot, E. Kukk, J. Laksman, P. Lytaev, T. Maltezopoulos, T. Mazza, M. Meyer, E. Saldin, E. Schneidmiller, M. Scholz, S. Tomin, M. Vannoni, T. Wohlenberg, M. Yurkov, I. Zagorodnov, G. Geloni, Opportunities for two-color experiments in the soft X-ray regime at the European XFEL. Appl. Sci. (Switzerland) **10**(8), 2728 (2020). https://doi.org/10.3390/APP10082728
48. P. Abbamonte, F. Abild-Pedersen, P. Adams, M. Ahmed, F. Albert, R.A. Mori, P. Anfinrud, A. Aquila, M. Armstrong, J. Arthur, J. Bargar, A. Barty, U. Bergmann, N. Berrah, G. Blaj, H. Bluhm, C. Bolme, C. Bostedt, S. Boutet, G. Brown, P. Bucksbaum, M. Cargnello, G. Carini, A. Cavalleri, V. Cherezov, W. Chiu, Y. Chuang, D. Cocco, R. Coffee, G. Collins, A. Cordones-Hahn, J. Cryan, G. Dakovski, M. Dantus, H. Demirci, P. Denes, T. Devereaux, Y. Ding, S. Doniach, R. Dorner, M. Dunne, H. Durr, T. Egami, D. Eisenberg, P. Emma, C. Fadley, R. Falcone, Y. Feng, P. Fischer, F. Fiuza, L. Fletcher, L. Foucar, M. Frank, J. Fraser, H. Frei, D. Fritz, P. Fromme, A. Fry, M. Fuchs, P. Fuoss, K. Gaffney, E. Gamboa, O. Gessner, S. Ghimire, A. Gleason, S. Glenzer, T. Gorkhover, A. Gray, M. Guehr, J. Guo, J. Hajdu, S. Hansen, P. Hart, M. Hashimoto, J. Hastings, D. Haxton, P. Heimann, T. Heinz, A. Hexemer, J. Hill, F. Himpsel, P. Ho, B. Hogue, Z. Huang, M. Hunter, G. Hura, N. Huse, Z. Hussain, M. Ilchen, C. Jacobsen, C. Kenney, J. Kern, S. Kevan, J. Kim, H. Kim, P. Kirchmann, R. Kirian, S. Kivelson, C. Kliewer, J. Koralek, G. Kovacsova, A. Lanzara, J. LaRue, H. Lee, J. Lee, W. Lee, Y. Lee, I. Lindau, A. Lindenberg, Z. Liu, D. Lu, U. Lundstrom, A. MacDowell, W. Mao, J. Marangos, G. Marcus, T. Martinez, W. McCurdy, G. McDermott, C. McGuffey, M. Minitti, S. Miyabe, S. Moeller, R. Moore, S. Mukamel, K. Nass, A. Natan, K. Nelson, S. Nemsak, D. Neumark, R. Neutze, A. Nilsson, D. Nordlund, J. Norskov, S. Nozawa, H. Ogasawara, H. Ohldag, A. Orville, D. Osborn, T. Osipov, A. Ourmazd, D. Parkinson, C. Pellegrini, G. Phillips, T. Rasing, T. Raubenheimer, T. Recigno, A. Reid, D. Reis, A. Robert, J. Robinson, D. Rolles, J. Rost, S. Roy, A. Rudenko, T. Russell, R. Sandberg, A. Sandhu, N. Sauter, I. Schlichting, R. Schlogl, W. Schlotter, M. Schmidt, J. Schneider, R. Schoenlein, M. Schoeffler, A. Scholl, Z. Shen, O. Shpyrko, T. Silva, S. Sinha, D. Slaughter, J. Sobota, D. Sokaras, K. Sokolowski-Tinten, S. Southworth, J. Spence, C. Stan, J. Stohr, R. Stroud, V. Sundstrom, C. Taatjes, A. Thomas, M. Trigo, Y. Tsui, J. Turner, A. van Buuren, S. Vinko, S. Wakatsuki, J. Wark, P. Weber, T. Weber, M. Wei, T. Weiss, P. Wernet, W. White, P. Willmott, K. Wilson, W. Wurth, V. Yachandra, J. Yano, D. Yarotski, L. Young, Y. Zhu, D. Zhu, P. Zwart, New Science Opportunities Enabled by LCLS-II X-Ray Lasers (2015). https://doi.org/10.2172/1630267
49. E. Weckert, The potential of future light sources to explore the structure and function of matter. IUCrJ **2**(Pt 2), 230–245 (2015). https://doi.org/10.1107/S2052252514024269
50. J.M.J. Madey, Stimulated emission of bremsstrahlung in a periodic magnetic field. J. Appl. Phys. **42**(5), 1906–1913 (1971). https://doi.org/10.1063/1.1660466
51. L.R. Elias, W.M. Fairbank, J.M.J. Madey, H.A. Schwettman, T.I. Smith, Observation of stimulated emission of radiation by relativistic electrons in a spatially periodic transverse magnetic field. Phys. Rev. Lett. **36**(13), 717–720 (1976). https://doi.org/10.1103/PhysRevLett.36.717
52. D.A.G. Deacon, L.R. Elias, J.M.J. Madey, G.J. Ramian, H.A. Schwettman, T.I. Smith, First operation of a free-electron laser. Phys. Rev. Lett. **38**(16), 892–894 (1977). https://doi.org/10.1103/PhysRevLett.38.892
53. B.W.J. Mcneil, N.R. Thompson, X-ray free-electron lasers (2010). https://doi.org/10.1038/nphoton.2010.239
54. W.A. Barletta, J. Bisognano, J.N. Corlett, P. Emma, Z. Huang, K.J. Kim, R. Lindberg, J.B. Murphy, G.R. Neil, D.C. Nguyen, C. Pellegrini, R.A. Rimmer, F. Sannibale, G. Stupakov, R.P. Walker, A.A. Zholents, Free electron lasers: present status and future challenges. Nucl. Instrum. Methods Phys. Res. Sect. A **618**(1–3), 69–96 (2010). https://doi.org/10.1016/J.NIMA.2010.02.274

55. E.A. Seddon, J.A. Clarke, D.J. Dunning, C. Masciovecchio, C.J. Milne, F. Parmigiani, D. Rugg, J.C.H.H. Spence, N.R. Thompson, K. Ueda, S.M. Vinko, J.S. Wark, W. Wurth, Short-wavelength free-electron laser sources and science: a review (2017). https://doi.org/10.1088/1361-6633/aa7cca
56. Z. Huang, K.J. Kim, Review of x-ray free-electron laser theory. Phys. Rev. Spec. Top. Accel Beams **10**(3), 34801 (2007). https://doi.org/10.1103/PhysRevSTAB.10.034801
57. Institute of Free Electron Laser Osaka University, Free Electron Laser figure
58. R. Bonifacio, C. Pellegrini, L.M. Narducci, Collective instabilities and high-gain regime in a free electron laser. Opt. Commun. **50**(6), 373–378 (1984). https://doi.org/10.1016/0030-4018(84)90105-6
59. R. Bonifacio, L. De Salvo, P. Pierini, N. Piovella, C. Pellegrini, Spectrum, temporal structure, and fluctuations in a high-gain free-electron laser starting from noise. Phys. Rev. Lett. **73**(1), 70–73 (1994). https://doi.org/10.1103/PhysRevLett.73.70
60. E.L. Saldin, E.A. Schneidmiller, M.V. Yurkov, Statistical and coherence properties of radiation from x-ray free-electron lasers. New J. Phys. **12**(3), 035010 (2010). https://doi.org/10.1088/1367-2630/12/3/035010
61. D. Ratner, A. Brachmann, F.J. Decker, Y. Ding, D. Dowell, P. Emma, A. Fisher, J. Frisch, S. Gilevich, Z. Huang, P. Hering, R. Iverson, J. Krzywinski, H. Loos, M. Messerschmidt, H.D. Nuhn, T. Smith, J. Turner, J. Welch, W. White, J. Wu, Second and third harmonic measurements at the linac coherent light source. Phys. Rev. Spec. Top. Accel Beams **14**(6), 60701 (2011). https://doi.org/10.1103/PhysRevSTAB.14.060701
62. P. Schmüser , M. Dohlus, J. Rossbach, C. Behrens, Free-Electron Lasers in the Ultraviolet and X-ray Regime: Physical Principles, Experimental Results, Technical Realization vol. 258 (Springer International Publishing, Switzerland, 2014), pp. 3–5. https://doi.org/10.1007/978-3-319-04081-3
63. R. Ischebeck, J. Feldhaus, C. Gerth, E. Saldin, P. Schmüser, E. Schneidmiller, B. Steeg, K. Tiedtke, M. Tonutti, R. Treusch, M. Yurkov, Study of the transverse coherence at the TTF free electron laser. Nucl. Instrum. Methods Phys. Res. Sect. A **507**(1–2), 175–180 (2003). https://doi.org/10.1016/S0168-9002(03)00866-0
64. I.A. Vartanyants, A. Singer, A.P. Mancuso, O.M. Yefanov, A. Sakdinawat, Y. Liu, E. Bang, G.J. Williams, G. Cadenazzi, B. Abbey, H. Sinn, D. Attwood, K.A. Nugent, E. Weckert, T. Wang, D. Zhu, B. Wu, C. Graves, A. Scherz, J.J. Turner, W.F. Schlotter, M. Messerschmidt, J. Lüning, Y. Acremann, P. Heimann, D.C. Mancini, V. Joshi, J. Krzywinski, R. Soufli, M. Fernandez-Perea, S. Hau-Riege, A.G. Peele, Y. Feng, O. Krupin, S. Moeller, W. Wurth, Coherence properties of individual femtosecond pulses of an x-ray free-electron laser. Phys. Rev. Lett. **107**(14), 144801 (2011). https://doi.org/10.1103/PhysRevLett.107.144801
65. F. Lehmkühler, C. Gutt, B. Fischer, M.A. Schroer, M. Sikorski, S. Song, W. Roseker, J. Glownia, M. Chollet, S. Nelson, K. Tono, T. Katayama, M. Yabashi, T. Ishikawa, A. Robert, G. Grübel, Single shot coherence properties of the free-electron laser SACLA in the hard x-ray regime. Sci. Rep. **4**, 5234 (2014). https://doi.org/10.1038/srep05234
66. S. Di Mitri, On the importance of electron beam brightness in high gain free electron lasers. Photonics **2**(2), 317–341 (2015). https://doi.org/10.3390/photonics2020317
67. M. Xie, Exact and variational solutions of 3D eigenmodes in high gain FELs. Nucl. Instrum. Methods Phys. Res. Sect. A **445**(1–3), 59–66 (2000). https://doi.org/10.1016/S0168-9002(00)00114-5
68. M. Xie, Design optimization for an X-ray free electron laser driven by SLAC linac, in *Procedures of IEEE Particle Acceleration Conference*, Dallas, TX, USA, pp. 183–185 (2002). https://doi.org/10.1109/pac.1995.504603
69. S. Reiche, GENESIS 1.3: a fully 3D time-dependent FEL simulation code. Nucl. Instrum. Methods Phys. Res. Sect. A Accel. Spectrom. Detect. Assoc. Equip. **429**(1–3), 243–248 (1999). https://doi.org/10.1016/S0168-9002(99)00114-X
70. S. Reiche, Update on the FEL code Genesis1.3, in *Proceedings of FEL Conference*, p. 019 (2014). http://accelconf.web.cern.ch/AccelConf/FEL2014/papers/tup019.pdf
71. CompactLight Website. http://www.compactlight.eu
72. J. Feldhaus, E.L. Saldin, J.R. Schneider, E.A. Schneidmiller, M.V. Yurkov, Possible application of X-ray optical elements for reducing the spectral bandwidth of an X-ray SASE FEL. Opt. Commun. **140**(4–6), 341–352 (1997). https://doi.org/10.1016/S0030-4018(97)00163-6
73. D. Ratner, R. Abela, J. Amann, C. Behrens, D. Bohler, G. Bouchard, C. Bostedt, M. Boyes, K. Chow, D. Cocco, F.J. Decker, Y. Ding, C. Eckman, P. Emma, D. Fairley, Y. Feng, C. Field, U. Flechsig, G. Gassner, J. Hastings, P. Heimann, Z. Huang, N. Kelez, J. Krzywinski, H. Loos, A. Lutman, A. Marinelli, G. Marcus, T. Maxwell, P. Montanez, S. Moeller, D. Morton, H.D. Nuhn, N. Rodes, W. Schlotter, S. Serkez, T. Stevens, J. Turner, D. Walz, J. Welch, J. Wu, Experimental demonstration of a soft x-ray self-seeded free-electron laser. Phys. Rev. Lett. **114**(5), 054801 (2015). https://doi.org/10.1103/PHYSREVLETT.114.054801/FIGURES/5/MEDIUM
74. J. Amann, W. Berg, V. Blank, F.J. Decker, Y. Ding, P. Emma, Y. Feng, J. Frisch, D. Fritz, J. Hastings, Z. Huang, J. Krzywinski, R. Lindberg, H. Loos, A. Lutman, H.D. Nuhn, D. Ratner, J. Rzepiela, D. Shu, Y. Shvyd'Ko, S. Spampinati, S. Stoupin, S. Terentyev, E. Trakhtenberg, D. Walz, J. Welch, J. Wu, A. Zholents, D. Zhu, Demonstration of self-seeding in a hard-X-ray free-electron laser. Nat. Photonics **6**(10), 693–698 (2012). https://doi.org/10.1038/nphoton.2012.180
75. S. Serkez, V. Kocharyan, E. Saldin, G. Geloni, Grating monochromator for soft X-ray self-seeding the European XFEL, in *FEL 2013: Proceedings of the 35th International Free-Electron Laser Conference*, pp. 667–674 (2013)
76. G. Geloni, V. Kocharyan, E. Saldin, A novel self-seeding scheme for hard X-ray FELs. J. Mod. Opt. **58**(16), 1391–1403 (2011). https://doi.org/10.1080/09500340.2011.586473
77. E. Prat, S. Reiche, S.D.J. Dunning, Self-Seeding Design for SwissFEL
78. E Prat, S. Reiche, Self-seeding design for SwissFEL

79. A. Grudiev, S. Calatroni, W. Wuensch, New local field quantity describing the high gradient limit of accelerating structures. Phys. Rev. Spec. Top. Accel Beams (2009). https://doi.org/10.1103/physrevstab.12.102001
80. V.A. Dolgashev, High magnetic fields in couplers of X-band accelerating structures, in *Proceedings of the IEEE Particle Accelerator Conference*, vol. 2, pp. 1267–1269. IEEE, USA (2003). https://doi.org/10.1109/pac.2003.1289674. http://ieeexplore.ieee.org/document/1289674/
81. C. Nantista, S. Tantawi, V. Dolgashev, Low-field accelerator structure couplers and design techniques. Phys. Rev. Spec. Top. Accel Beams (2004). https://doi.org/10.1103/PhysRevSTAB.7.072001
82. C. Limborg, Z. Li, L. Xiao, J.F. Schmerge, D. Dowell, S. Gierman, E. Bong, S. Gilevich, RF Design of the LCLS Gun. Technical report (2005). https://www-ssrl.slac.stanford.edu/lcls/technotes/lcls-tn-05-3.pdf
83. D. Alesini, A. Battisti, M. Ferrario, L. Foggetta, V. Lollo, L. Ficcadenti, V. Pettinacci, S. Custodio, E. Pirez, P. Musumeci, L. Palumbo, New technology based on clamping for high gradient radio frequency photogun. Phys. Rev. Spec. Top. Accel Beams (2015). https://doi.org/10.1103/PhysRevSTAB.18.092001
84. D. Alesini, A. Battisti, M. Bellaveglia, F. Cardelli, A. Falone, A. Gallo, V. Lollo, D.T. Palmer, L. Pellegrino, L. Piersanti, S. Pioli, A. Variola, V. Pettinacci, L. Palumbo, Design, realization, and high power test of high gradient, high repetition rate brazing-free S -band photogun. Phys. Rev. Accel. Beams (2018). https://doi.org/10.1103/PhysRevAccelBeams.21.112001
85. ANSYS Electronics Desktop website. http://www.ansys.com/products/electronics/ansys-electronics-desktop
86. G. Castorina, L. Ficcadenti, M. Migliorati, A. Mostacci, L. Palumbo, F. Cardelli, G. Franzini, A. Marcelli, B. Spataro, G. Sorbello, L. Celona, S. Gammino, G. Torrisi, A. Cahill, J. Rosenzweig, V.A. Dolgashev, A TM01 mode launcher with quadrupole field components cancellation for high brightness applications, in *9th International Particle Accelerator Conference, IPAC18*, vol. 1067. Institute of Physics Publishing, Vancouver (2018). https://doi.org/10.1088/1742-6596/1067/8/082025
87. M. Croia, D. Alesini, F. Cardelli, M. Diomede, M. Ferrario, A. Giribono, S. Romeo, C. Vaccarezza, A. Vannozzi, High gradient ultra-high brightness C-band photoinjector optimization. J. Phys Conf. Ser. (2020). https://doi.org/10.1088/1742-6596/1596/1/012031
88. D. Alesini, G. Castorina, M. Croia, M. Ferrario, A. Gallo, B. Spataro, C. Vaccarezza, A. Vannozzi, Design of a full C-band injector for ultra-high brightness electron beam, in *10th International Particle Accelerator Conference (IPAC2019)* (2019). https://doi.org/10.18429/JACoW-IPAC2019-TUPTS024
89. D. Palmer, The next generation photoinjectors. PhD thesis, Stanford Linear Accelerator Center, Stanford University, Stanford (1998). https://slac.stanford.edu/pubs/slacreports/reports16/slac-r-500.pdf
90. CML link. https://www.cmlengineering.com/
91. J.L. Warren, Reference manual for the POISSON/SUPERFISH Group of Codes. Technical Report LA-UR-87-126 (1987). https://doi.org/10.2172/10140827
92. H. Busch, Berechnung der Bahn von Kathodenstrahlen im axialsymmetrischen elektromagnetischen Felde. Ann. Phys. **386**(25), 974–993 (1926). https://doi.org/10.1002/andp.19263862507
93. J. Scifo, The characterization of metal photo-cathode for high brightness electron beam photoinjectors. PhD thesis (2018)
94. K. Flöttmann, ASTRA particle tracking code (2016)
95. A. Bacci, V. Petrillo, M. Rossetti Conti, GIOTTO: a genetic code for demanding beam-dynamics optimizations, in *Proceedings of the 7th International Particle Accelerator Conference (IPAC 2016)*, Busan, Korea, pp. 8–13 (2016). https://accelconf.web.cern.ch/ipac2016/papers/wepoy039.pdf
96. E. Telali, Photoinjector study of a novel XFEL in the CompactLight Collaboration. PhD thesis, National Technical University of Athens (2019). https://inspirehep.net/literature/1819658
97. K.S. Tzanetou, FEL photocathode/laser studies. Master's thesis, National Technical University of Athens (2020)
98. M.B. Danailov, A. Demidovich, R. Ivanov, I. Nikolov, P. Sigalotti, Performance of the FERMI FEL photoinjector laser, in *Proceedings of FEL*, pp. 358–361 (2007). https://accelconf.web.cern.ch/f07/PAPERS/WEPPH014.PDF
99. R.W. Assmann, M.K. Weikum, T. Akhter, D. Alesini, A.S. Alexandrova, M.P. Anania, N.E. Andreev, I. Andriyash, M. Artioli, A. Aschikhin et al., EuPRAXIA Conceptual Design Report. Eur. Phys. J. Spec. Top. **229**(24), 3675–4284 (2020)
100. E. Prat, S. Bettoni, H.-H. Braun, R. Ganter, T. Schietinger, Measurements of copper and cesium telluride cathodes in a radio-frequency photoinjector. Phys. Rev. Spec. Top. Accel. Beams **18**(4), 43401 (2015)
101. Amplitude laser link. https://amplitude-laser.com/products/lasers-for-science/arco/
102. F. Zhou, Recent photocathode R &D for the LCLS injector. Technical report, SLAC National Accelerator Lab., Menlo Park (2018). https://accelconf.web.cern.ch/FEL2014/papers/thp030.pdf
103. B.E. Carlsten, New photoelectric injector design for the Los Alamos National Laboratory XUV FEL accelerator. Nuclear Inst. Methods Phys. Res. A (1989). https://doi.org/10.1016/0168-9002(89)90472-5
104. R. Ganter, M. Bopp, R. Gaiffi, T. Le Quang, SwissFEL cathode load-lock system, in *Proc. 35th Int. Free-Electron Laser Conf.*, New York, p. 259 (2013). https://accelconf.web.cern.ch/FEL2013/papers/tupso21.pdf
105. M. Diomede, D. Alesini, M. Bellaveglia, B. Buonomo, F. Cardelli, N. Catalan Lasheras, E. Chiadroni, G. Di Pirro, M. Ferrario, A. Gallo, A. Ghigo, A. Giribono, A. Grudiev, L. Piersanti, B. Spataro, C. Vaccarezza, W. Wuensch, Preliminary RF design of an X-band linac for the EuPRAXIA at SPARC_LAB project. Nucl. Instrum. Methods Phys. Res. Sect. A Accel. Spectrom. Detect. Assoc. Equip. (2018). https://doi.org/10.1016/j.nima.2018.01.032

106. R. Zennaro, C-band RF Pulse Compressor for SwissFEL, in *Proc. of IPAC 2013*, Shanghai, China (2013). https://s3.cern.ch/inspire-prod-files-f/f5ceba03e3c25c245a77a8de4032b2e6
107. E.L. Saldin, E.A. Schneidmiller, M.V. Yurkov, Klystron instability of a relativistic electron beam in a bunch compressor. Nucl. Instrum. Methods Phys. Res. Sect. A Accel. Spectrom. Detect. Assoc. Equip. (2002). https://doi.org/10.1016/S0168-9002(02)00905-1
108. E.L. Saldin, E.A. Schneidmiller, M.V. Yurkov, Longitudinal space charge-driven microbunching instability in the TESLA Test Facility linac. Nucl. Instrum. Methods Phys. Res. Sect. A Accel. Spectrom. Detect. Assoc. Equip. (2004). https://doi.org/10.1016/j.nima.2004.04.067
109. Z. Huang, A. Brachmann, F.-J. Decker, Y. Ding, D. Dowell, P. Emma, J. Frisch, S. Gilevich, G. Hays, P. Hering, R. Iverson, H. Loos, A. Miahnahri, H.-D. Nuhn, D. Ratner, G. Stupakov, J. Turner, J. Welch, W. White, J. Wu, D. Xiang, Measurements of the linac coherent light source laser heater and its impact on the x-ray free-electron laser performance. Phys. Rev. Spec. Top. Accel. Beams (2010). https://doi.org/10.1103/PhysRevSTAB.13.020703
110. G. Stupakov, Centripetal Transverse Wakefield in Relativistic Beam. Technical report (2019). http://arxiv.org/abs/1901.10745
111. M. Diomede, High-gradient structures and RF systems for high-brightness electron linacs. PhD thesis, Sapienza University of Rome (2020). https://iris.uniroma1.it/retrieve/handle/11573/1357033/1347035/Tesi_dottorato_Diomede.pdf
112. Z.D. Farkas, H.A. Hogg, G.A. Loew, P.B. Wilson, SLED: a method of doubling slac's energy, in *Proceedings of the 9th International Conference on High-Energy Accelerators*, pp. 576–583 (1976). https://inspirehep.net/literature/94052
113. E.D. PM Lapostolle, E.D. AL Septier, Linear accelerators. North-Holland Publ Co, Amsterdam, Wiley Interscience Div, Wiley (1970). https://doi.org/10.1007/978-3-642-16483-5_3
114. R.B. Neal, Design of linear electron accelerators with beam loading. J. Appl. Phys. **29**(7), 1019–1024 (1958). https://doi.org/10.1063/1.1723355
115. M. Diomede et al., RF Design of the X-band Linac for the EuPRAXIA at SPARC_LAB Project, in *Proc. 9th International Particle Accelerator Conference (IPAC'18)*, Vancouver, BC, Canada, 29 April–04 May 2018. International Particle Accelerator Conference, pp. 4422–4425. JACoW Publishing, Geneva (2018). https://doi.org/10.18429/JACoW-IPAC2018-THPMK058. http://jacow.org/ipac2018/papers/thpmk058.pdf
116. R.M. Jones, C.E. Adolphsen, J.W. Wang, Z. Li, Wakefield damping in a pair of X-band accelerators for linear colliders. Phys. Rev. Spec. Top. Accel. Beams (2006). https://doi.org/10.1103/PhysRevSTAB.9.102001
117. R.M. Jones, Wakefield suppression in high gradient linacs for lepton linear colliders. Phys. Rev. Spec. Top. Accel. Beams (2009). https://doi.org/10.1103/physrevstab.12.104801
118. M. Dehler, I.H. Wilson, W. Wuensch, A tapered damped accelerating structure for CLIC, in *Proc. of 19th International Linear Accelerator Conference*, Chicago, 1998 (1987). https://cds.cern.ch/record/364530
119. C. Achard, M. Dehler, E. Jensen, M. Luong, I. Wilson, W. Wuensch, S.C. Adolphsen, M. Ross, T. Slaton, D. McCormick, An asset test of the CLIC accelerating structure, in *Proc. of the 7th European Particle Accelerator Conference*, Vienna (2000). https://cds.cern.ch/record/452944
120. R. Jones, N. Kroll, T. Higo, Z. Li, R. Miller, T. Raubenheimer, J. Wang Slac, Dipole wakefield suppression in high phase advance detuned linear accelerators for the JLC/NLC designed to minimise electrical breakdown and cumulative BBU, in *Proc. of the 2001 Particle Accelerator Conference*, Chicago, pp. 3810–3812 (2001). https://doi.org/10.1109/PAC.2001.988261
121. CPI website. http://www.cpii.com/
122. W. Wuensch et al., Experience Operating an X-band High-Power Test Stand at CERN, in *Proc. 5th International Particle Accelerator Conference (IPAC'14)*, Dresden, Germany, June 15–20, 2014. International Particle Accelerator Conference, pp. 2288–2290. JACoW, Geneva (2014). https://doi.org/10.18429/JACoW-IPAC2014-WEPME016. http://jacow.org/ipac2014/papers/wepme016.pdf
123. W. Wuensch, High-Gradient RF Development and Applications, in *Proc. of Linear Accelerator Conference (LINAC'16)*, East Lansing, MI, USA, 25–30 September 2016. Linear Accelerator Conference, pp. 368–373. JACoW, Geneva (2017). https://doi.org/10.18429/JACoW-LINAC2016-TU2A04. http://jacow.org/linac2016/papers/tu2a04.pdf
124. Canon website. https://etd.canon/en/product/category/microwave/klystron.html
125. N.C. Lasheras, et al., Commissioning of XBox-3: a very high capacity X-band test stand, in *Proc. of Linear Accelerator Conference (LINAC'16)*, East Lansing, MI, USA, 25–30 September 2016. Linear Accelerator Conference, pp. 568–571. JACoW, Geneva (2017). https://doi.org/10.18429/JACoW-LINAC2016-TUPLR047. http://jacow.org/linac2016/papers/tuplr047.pdf
126. Scandinova website. https://scandinovasystems.com/
127. N.C. Lasheras et al., High power conditioning of X-band RF components, in *Proc. 9th International Particle Accelerator Conference (IPAC'18)*, Vancouver, BC, Canada, April 29–May 4, 2018. International Particle Accelerator Conference, pp. 2545–2548. JACoW Publishing, Geneva (2018). https://doi.org/10.18429/JACoW-IPAC2018-WEPMF074. http://jacow.org/ipac2018/papers/wepmf074.pdf
128. G. Riddone, I. Syratchev, S. Atieh, A. Solodko, M. Filippova, A. Olyunin, V. Soldatov, Engineering design and fabrication of X-band RF components. Conf. Proc. C **110904**, 196–198 (2011)
129. G.L. D'Alessandro, Development of X-band high-power RF load for CLIC applications using additive manufacturing techniques. PhD thesis, Salento U. (2015). http://cds.cern.ch/record/2139981
130. H. Zha, I. Syratchev, D. Gudkov, A. Grudiev, Design of a variable X-band RF power splitter. Nucl. Instrum. Methods Phys. Res. Sect. A **859**, 47–51 (2017). https://doi.org/10.1016/j.nima.2017.04.006

131. H. Zha, I. Syratchev, D. Gudkov, A. Grudiev: Design of a variable X-band RF power splitter. Nucl. Instrum. Methods Phys. Res. Sect. A Accel. Spectrom. Detect. Assoc. Equip. **859**, 47–51 (2017). https://doi.org/10.1016/j.nima.2017.04.006. https://inspirehep.net/literature/1418054
132. Wang, P., Chen, H.B., Shi, J., Syratchev, I., Wuensch, W., Zha, H.: The RF Design of a Compact, High Power Pulse Compressor with a Flat Output Pulse. In: Proc. of International Particle Accelerator Conference (IPAC'16), Busan, Korea, May 8-13, 2016. International Particle Accelerator Conference, pp. 3591–3593. JACoW, Geneva, Switzerland (2016). https://doi.org/10.18429/JACoW-IPAC2016-THPMW022. http://jacow.org/ipac2016/papers/thpmw022.pdf
133. B. Woolley, I. Syratchev, A. Dexter, Control and performance improvements of a pulse compressor in use for testing accelerating structures at high power. Phys. Rev. Accel. Beams (2017). https://doi.org/10.1103/PhysRevAccelBeams.20.101001
134. Aicheler, M., Akesson, T., Antoniou, F., Arnalich, A., Sota, P.A.A., Cabral, P.B.M., Bozzini, D., Brugger, M., Brunner, O., Burrows, P.N., Calaga, R., Capstick, M.J., Corsini, R., Doebert, S., Dougherty, L.A., Dutheil, Y., Dyks, L.A., Etisken, O., Evans, L., Farricker, A., Ortega, R.F., Fraser, M.A., Gall, J., Gessner, S.J., Goddard, B., Grenard, J.-L., Grudiev, A., Gschwendtner, E., Gulley, J., Jensen, L., Jones, R., Lamont, M., Latina, A., Lefevre, T., Lopes, R., Durand, H.M., Marsh, S., Mcmonagle, G., Montesinos, E., Morton, R., Muggli, P., Cornago, A.N., Nonis, M., Osborne, J.A., Papaphilippou, Y., Rossi, A.M., Rossi, C., Ruehl, I., Schadegg, S., Shaposhnikova, E., Schulte, D., Stapnes, S., Widorski, M., Williams, O.E., Wuensch, W.: A primary electron beam facility at CERN – eSPS Conceptual design report (2020). https://doi.org/10.23731/CYRM-2020-008
135. M. Aicheler, P.N. Burrows, N. Catalan, R. Corsini, M. Draper, J. Osborne, D. Schulte, S. Stapnes, M.J. Stuart, The Compact Linear Collider (CLIC) - Project Implementation Plan. Technical report (March 2019). https://doi.org/10.23731/CYRM-2018-004
136. G.A. Loew, O.H. Altenmueller, Design and applications of R.F. deflecting structures at slac. Technical report, SLAC (1965). https://s3.cern.ch/inspire-prod-files-c/c1be43e925db8226d80778005361b3a7
137. D. Alesini, G. Di Pirro, L. Ficcadenti, A. Mostacci, L. Palumbo, J. Rosenzweig, C. Vaccarezza, RF deflector design and measurements for the longitudinal and transverse phase space characterization at SPARC. Nucl. Instrum. Methods Phys. Res. Sect. A **568**(2), 488–502 (2006). https://doi.org/10.1016/j.nima.2006.07.050
138. S. Jiaru, C. Huaibi, Z. Shuxin, J.M. Byrd, D. Li, A three-cell superconducting deflecting cavity design for the ALS at LBNL, in *Proceedings of the IEEE Particle Accelerator Conference*, vol. 2005, pp. 4287–4289 (2005). https://doi.org/10.1109/PAC.2005.1591795
139. D. Esperante, C. Blanch, M. Boronat, J. Fuster, D. Gonzalez Iglesias, A. Vnuchenko, B. Gimeno, N. Catalan Lasheras, G. McMonagle, I. Syratchev, W. Wuensch, B. Woolley, A. Faus Golfe, Construction and commissioning of the S-Band high gradient RF laboratory at IFIC, in *9th International Particle Accelerator Conference*, vol. 1067. Institute of Physics Publishing, Vancouver (2018). https://doi.org/10.1088/1742-6596/1067/8/082024
140. R.W. Assmann, F. Becker, R. Bossart, H. Braun, A 3 TeV E+e- Linear Collider Based on CLIC Technology, p. 83. CERN, Switzerland (2000). http://cds.cern.ch/record/461450
141. K. Bane, Short range dipole wakefields in accelerating structures for the NLC. SLAC-PUB-9663 (2003)
142. J.C. Cai, I. Syratchev, G. Burt, Design study of a high-power Ka-band high-order-mode multibeam klystron. IEEE Trans. Electron Devices **67**(12), 5736–5742 (2020). https://doi.org/10.1109/TED.2020.3028348
143. K.R. Chu, The electron cyclotron maser (2004). https://doi.org/10.1103/RevModPhys.76.489
144. L. Wang, K. Dong, J. Wang, Y. Luo, W. He, A.W. Cross, K. Ronald, A.D.R. Phelps, Design of a Ka-band MW-level high efficiency gyroklystron for accelerators, in *2017 10th UK-Europe-China Workshop on Millimetre Waves and Terahertz Technologies, UCMMT 2017*. Institute of Electrical and Electronics Engineers Inc., UK (2017). https://doi.org/10.1109/UCMMT.2017.8068506
145. L.J.R. Nix, L. Zhang, W. He, C.R. Donaldson, K. Ronald, A.W. Cross, C.G. Whyte, Demonstration of efficient beam-wave interaction for a MW-level 48 GHz gyroklystron amplifier. Phys. Plasmas (2020). https://doi.org/10.1063/1.5144590
146. Magnet Gyrotron link. http://www.cryogenic.co.uk/sites/default/files/product_files/sms_series_sample_users_manual.pdf
147. Power Modulator link. https://scandinovasystems.com/content/uploads/2020/04/scandinova-productsheet-k100-200421.pdf
148. P.B. Wilson, Z.D. Farkas, R.D Ruth, SLED II: a new method of RF pulse compression, in: *Proceedings of the Linear Accelerator Conference 1990*, Albuquerque, (1990). https://inspirehep.net/literature/298685
149. J.W. Wang, S.G. Tantawi, C. Xu, M. Franzi, P. Krejcik, G. Bowden, S. Condamoor, Y. Ding, V. Dolgashev, J. Eichner, A. Haase, J.R. Lewandowski, L. Xiao, Development for a supercompact X -band pulse compression system and its application at SLAC. Phys. Rev. Accel. Beams (2017). https://doi.org/10.1103/PhysRevAccelBeams.20.110401
150. R. Ruth, C. Nantista, N.M. Kroll, Z.D. Farkas, T.L. Lavine, A. Menegat, C. Nantista, R.D. Ruth, P.B. Wilson, A high-power SLED II pulse compression system, in *Proceedings of the 3rd European Particle Accelerator Conference* (1992). https://www.researchgate.net/publication/236524267
151. I. Syratchev, Status of 30 GHz High Power RF Pulse Compressor for CTF3, in *Proceedings of EPAC 2006*, Edinburgh, Scotland (2006). https://accelconf.web.cern.ch/e06/PAPERS/TUPCH163.PDF
152. S.G. Tantawi, Multimoded reflective delay lines and their application to resonant delay line rf pulse compression systems. Phys. Rev. Spec. Top. Accel Beams **7**(3), 13–18 (2004). https://doi.org/10.1103/PhysRevSTAB.7.032001

153. S. Tantawi, C. Nantista, V.A. Dolgashev, S.G. Tantawi, C.D. Nantista, V.A. Dolgashev, Status of high-power tests of dual mode SLED-II system for an X-band linear collider. Technical report (2004). https://www.researchgate.net/publication/238792134
154. S.G. Tantawi, C.D. Nantista, V.A. Dolgashev, C. Pearson, J. Nelson, K. Jobe, J. Chan, K. Fant, J. Frisch, D. Atkinson, High-power multimode X-band rf pulse compression system for future linear colliders. Phys. Rev. Spec. Top. Accel Beams **8**(4), 88–106 (2005). https://doi.org/10.1103/PhysRevSTAB.8.042002
155. GdfidL. www.gdfidl.de
156. G.E.H. Reuter, E.H. Sondheimer, Theory of the anomalous skin effect in metals [6] (1948). https://doi.org/10.1038/161394a0
157. A.D. Cahill, J.B. Rosenzweig, V.A. Dolgashev, S.G. Tantawi, S. Weathersby, High gradient experiments with X -band cryogenic copper accelerating cavities. Phys. Rev. Accel. Beams (2018). https://doi.org/10.1103/PhysRevAccelBeams.21.102002
158. B.E. Carlsten, P.M. Anisimov, C.W. Barnes, Q.R. Marksteiner, R.R. Robles, N. Yampolsky, High-brightness beam technology development for a future dynamic mesoscale materials science capability. Instruments (2019). https://doi.org/10.3390/instruments3040052
159. J.B. Rosenzweig, N. Majernik, R.R. Robles, G. Andonian, O. Camacho, A. Fukasawa, A. Kogar, G. Lawler, J. Miao, P. Musumeci, B. Naranjo, Y. Sakai, R. Candler, B. Pound, C. Pellegrini, C. Emma, A. Halavanau, J. Hastings, Z. Li, M. Nasr, S. Tantawi, P. Anisimov, B. Carlsten, F. Krawczyk, E. Simakov, L. Faillace, M. Ferrario, B. Spataro, S. Karkare, J. Maxson, Y. Ma, J. Wurtele, A. Murokh, A. Zholents, A. Cianchi, D. Cocco, S.B. van der Geer, An ultra-compact x-ray free-electron laser. New J. Phys. (2020). https://doi.org/10.1088/1367-2630/abb16c
160. M. Behtouei, L. Faillace, M. Ferrario, B. Spataro, A. Variola, Initial Design of a High-Power Ka-Band Klystron. J. Phys. Conf. Ser. (2020). https://doi.org/10.1088/1742-6596/1596/1/012023
161. A.D. Cahill, J.B. Rosenzweig, V.A. Dolgashev, Z. Li, S.G. Tantawi, S. Weathersby, Rf losses in a high gradient cryogenic copper cavity. Phys. Rev. Accel. Beams (2018). https://doi.org/10.1103/PhysRevAccelBeams.21.061301
162. B. Spataro, RF parameters and Wakefielkds estimations on the structure at F = 35.982 GHz for the Compact light XLS project. Technical report, INFN-LNF, Barcelona (2018)
163. M. Behtouei, L. Faillace, M. Ferrario, B. Spataro, A. Variola, A Ka-band linearizer TW accelerating structure for the Compact Light XLS project. J. Phys. Conf. Ser. (2020). https://doi.org/10.1088/1742-6596/1596/1/012021
164. K.N. Sjobak, A. Grudiev, E. Adli, New criterion for shape optimization of normal-conducting accelerator cells for high-gradient applications, in *Proceedings, 27th Linear Accelerator Conference, LINAC2014*, p. 028 (2014). https://inspirehep.net/literature/1363323
165. D.P. Pritzkau, RF Pulsed Heating. PhD thesis, Stanford University (2001). http://inspirehep.net/record/569074/files/
166. A. Grudiev, W. Wuensch, A new local field quantity describing the high gradient limit of accelerating structures, in *Proceedings of the 24th Linear Accelerator Conference, LINAC 2008* (2009). https://doi.org/10.1103/physrevstab.12.102001
167. D.P. Pritzkau, R.H. Siemann, Experimental study of rf pulsed heating on oxygen free electronic copper. Phys. Rev. Spec. Top. Accel. Beams (2002). https://doi.org/10.1103/PhysRevSTAB.5.112002
168. O.A. Ivanov, M.A. Lobaev, A.L. Vikharev, A.M. Gorbachev, V.A. Isaev, J.L. Hirshfield, S.H. Gold, A.K. Kinkead, Active microwave pulse compressor using an electron-beam triggered switch. Phys. Rev. Lett. (2013). https://doi.org/10.1103/PhysRevLett.110.115002
169. A. Aksoy, et al., XLS Deliverable D6.1: Computer codes for the facility design. Technical report, CompactLight Collaboration (2019). https://www.compactlight.eu/uploads/Main/D6.1_XLS_Computer Codes for Facility Design.pdf
170. L. Serafini, J.B. Rosenzweig, Envelope analysis of intense relativistic quasilaminar beams in rf photoinjectors: a theory of emittance compensation. Phys. Rev. E **55**(6), 7565–7590 (1997). https://doi.org/10.1103/physreve.55.7565
171. K. Flöttmann, Astra: a space charge tracking algorithm (2011)
172. General Particle Tracer. http://www.pulsar.nl/gpt/
173. M. Ferrario, Instabilities in Linacs, in *CERN Accelerator School: 5th Advanced Accelerator Physics Course* ed. by S. Turner, p. 459. CERN, Geneva (2011). https://cas.web.cern.ch/sites/cas.web.cern.ch/files/lectures/chios-2011/ferrariowf.pdf
174. P.B. Wilson, Introduction to wakefields and wake potentials **184**(1), 525–564 (2008). https://doi.org/10.1063/1.38045
175. A.W. Chao, K.H. Mess, M. Tigner, F. Zimmermann, Handbook of Accelerator Physics and Engineering, Chap. 2.4.4, pp. 133–137. World Scientific, Singapore (2013). https://doi.org/10.1142/8543. https://www.worldscientific.com/worldscibooks/10.1142/8543
176. A. Latina, The 1D tracking code, Track1D, Geneva (2020). https://gitlab.cern.ch/XLS-Git/WP6/-/tree/master/simulation_codes/beam_dynamics/Track1D
177. K.L.F. Bane, P. Emma, LiTrack: a fast longitudinal phase space tracking code with graphical user interface, in *Proceedings of the IEEE Particle Accelerator Conference* (2005). https://doi.org/10.1109/PAC.2005.1591786
178. C. Mitchell, J. Qiang, P. Emma, Longitudinal pulse shaping for the suppression of coherent synchrotron radiation-induced emittance growth. Phys. Rev. Spec. Top. Accel Beams (2013). https://doi.org/10.1103/PhysRevSTAB.16.060703
179. M. Borland, ELEGANT: a flexible SDDS-compliant code for accelerator simulation. Tech. Rep. (2000). https://doi.org/10.2172/761286

180. S. Di Mitri, M. Cornacchia, S. Spampinati, Cancellation of coherent synchrotron radiation kicks with optics balance. Phys. Rev. Lett. (2013). https://doi.org/10.1103/PhysRevLett.110.014801
181. T. Hara, C. Kondo, T. Inagaki, K. Togawa, K. Fukami, S. Nakazawa, T. Hasegawa, O. Morimoto, M. Yoshioka, H. Maesaka, Y. Otake, H. Tanaka, High peak current operation of x-ray free-electron laser multiple beam lines by suppressing coherent synchrotron radiation effects. Phys. Rev. Accel. Beams **21**(4), 040701 (2018). https://doi.org/10.1103/PhysRevAccelBeams.21.040701
182. A. Latina, E. Adli, H. Burkhardt, G. Rumolo, D. Schulte, R. Tomas, Y. Renier, Recent improvements in the tracking code placet. EPAC 2008—contributions to the proceedings, pp. 1750–1752 (2008)
183. M. Ferrario, J.E. Clendenin, D.T. Palmer, J.B. Rosenzweig, L. Serafini, HOMDYN study for the LCLS RF photoinjector, in *2nd ICFA Advanced Accelerator Workshop on the Physics of High Brightness Beams*, pp. 534–563. World Scientific, Los Angeles (2000). https://inspirehep.net/literature/524888
184. M. Ferrario, D. Alesini, A. Bacci, M. Bellaveglia, R. Boni, M. Boscolo, M. Castellano, L. Catani, E. Chiadroni, S. Cialdi et al., Direct measurement of the double emittance minimum in the beam dynamics of the sparc high-brightness photoinjector. Phys. Rev. Lett. **99**(23), 234801 (2007)
185. A. Cianchi, D. Alesini, A. Bacci, M. Bellaveglia, R. Boni, M. Boscolo, M. Castellano, L. Catani, E. Chiadroni, S. Cialdi et al., High brightness electron beam emittance evolution measurements in an rf photoinjector. Phys. Rev. Spec. Top. Accel. Beams **11**(3), 32801 (2008)
186. C. Kim, S. Lee, J. Hong, D. Shin, H.-S. Kang, I.S. Ko, Stripline beam position monitor for X-ray free electron laser of Pohang Accelerator Laboratory. Rev. Sci. Instrum. **90**(9), 93306 (2019)
187. A Heo, E.S. Kim, H. Hitoshi, Status of cold cavity beam position monitor for STF, in *IPAC 2011—2nd International Particle Accelerator Conference*, pp. 1236–1238 (2011)
188. C. Simon, C. Boulch, P. Carbonnier, P. Contrepois, P. Daniel-Thomas, F. Eozenou, Y. Gasser, F. Gouit, O. Napoly, J. Novo, C. Servouin, J. Kruse, D. Noelle, M. Schalwat, S. Vilcins-Czvitkovits, N. Rouvière, J.P. Prestel, Production process for the european XFEL re-entrant cavity BPM, in *International Beam Instrumentation Conference, IBIC 2014* (2014). https://accelconf.web.cern.ch/IBIC2014/papers/tupf05.pdf
189. B. Keil, R. Baldinger, R. Ditter, D. Engeler, W. Koprek, R. Kramert, A. Malatesta, F. Marcellini, G. Marinkovic, M. Roggli, M. Rohrer, M. Stadler, Status of the Swissfel BPM system, in *Proceedings of the 4th International Beam Instrumentation Conference, IBIC 2015*, vol. 13, pp. 497–501 (2015). https://doi.org/10.18429/JACoW-IBIC2015-TUPB065
190. G. Kube, C. Behrens, W. Lauth, Resolution studies of inorganic scintillation screens for high energy and high Brilliance electron beams. in *IPAC 2010—1st International Particle Accelerator Conference*, pp. 906–908 (2010)
191. H. Loos, R. Akre, A. Brachmann, F.J. Decker, Y. Ding, D. Dowell, P. Emma, J. Frisch, S. Gilevich, G. Hays, P. Hering, Z. Huang, R. Iverson, C. Limborg-Deprey, A. Miahnahri, S. Molloy, H.D. Nuhn, J. Turner, J. Welch, W. White, J. Wu, D. Ratner, Observation of coherent optical transition radiation in the LCLS LINAC, in *30th International Free Electron Laser Conference, FEL 2008*, pp. 485–489 (2008). https://www.google.com/url?sa=t&rct=j&q=&esrc=s&source=web&cd=&cad=rja&uact=8&ved=2ahUKEwjkg7y7kb_xAhVH1hoKHakFAaMQFnoECBMQAA&url=https%3A%2F%2Faccelconf.web.cern.ch%2Ffel2008%2Fpapers%2Fthbau01.pdf&usg=AOvVaw0yJzpLhtwzxZLi-nBWVrqn
192. S. Matsubara, H. Maesaka, S. Inoue, Y. Otake, Improvement of screen monitor with suppression of coherent-OTR effect for SACLA, in *IBIC 2012—Proceedings of the 1st International Beam Instrumentation Conference*, pp. 34–37 (2013). https://www.google.com/url?sa=t&rct=j&q=&esrc=s&source=web&cd=&cad=rja&uact=8&ved=2ahUKEwiz-eHakb_xAhVSxhoKHdpTBTwQFnoECAQQAA&url=https%3A%2F%2Faccelconf.web.cern.ch%2FIBIC2012%2Fpapers%2Fmocc04.pdf&usg=AOvVaw1Evt8V0sbpXAECIHoUSfsA
193. P. Emma, J. Frisch, P. Krejcik, A transverse RF deflecting structure for bunch length and phase space diagnostics. LCLS Technical Note, vol. 12 (2000)
194. C. Behrens et al., Measurement and Control of the Longitudinal Phase Space at High–Gain Free–Electron Lasers, in *Proc. of 33rd International Free Electron Laser Conference*, Shanghai (2011). https://accelconf.web.cern.ch/FEL2011/talks/thoci1_talk.pdf
195. C. Behrens, F.-J. Decker, Y. Ding, V.A. Dolgashev, J. Frisch, Z. Huang, P. Krejcik, H. Loos, A. Lutman, T.J. Maxwell, J. Turner, J. Wang, M.-H. Wang, J. Welch, J. Wu, Few-femtosecond time-resolved measurements of X-ray free-electron lasers. Nat. Commun. **5**(1), 3762 (2014). https://doi.org/10.1038/ncomms4762
196. A. Cianchi, Diagnostics Examples from lepton-linacs and FELs (2020). arXiv:2005.07469
197. P. Craievich, M. Bopp, H.-H. Braun, A. Citterio, R. Fortunati, R. Ganter, T. Kleeb, F. Marcellini, M. Pedrozzi, E. Prat et al., Novel X-band transverse deflection structure with variable polarization. Phys. Rev. Accel. Beams **23**(11), 112001 (2020)
198. B. Marchetti, A. Grudiev, P. Craievich, R. Assmann, H.-H. Braun, N.C. Lasheras, F. Christie, R. D'Arcy, R. Fortunati, R. Ganter et al., Experimental demonstration of novel beam characterization using a polarizable X-band transverse deflection structure. Sci. Rep. **11**(1), 1–14 (2021)
199. D.H. Dowell, P.R. Bolton, J.E. Clendenin, S.M. Giennan, C.G. Limborg, B.F. Murphy, J.F. Schmerge, Analysis of slice emittance measurements for the slac gun test facility, in *Proceedings of the 2003 Bipolar/BiCMOS Circuits and Technology Meeting (IEEE Cat. No.03CH37440)*, vol. 3, pp. 2104–2106. IEEE, France (2003). https://doi.org/10.1109/PAC.2003.1288795. http://ieeexplore.ieee.org/document/1288795/

200. Y. Ding, F.-J. Decker, V.A. Dolgashev, J. Frisch, Z. Huang, P. Krejcik, H. Loos, A. Lutman, A. Marinelli, T.J. Maxwell, D. Ratner, J. Turner, J. Wang, M. Wang, J. Welch, J. Wu, S. National, M. Park, C. Behrens, Results from the Lcls X-band transverse deflector with femtosecond temporal resolution. SLAC Publication 1, 2–6 (2014)
201. T.J. Maxwell, C. Behrens, Y. Ding, A.S. Fisher, J. Frisch, Z. Huang, H. Loos, Coherent-radiation spectroscopy of few-femtosecond electron bunches using a middle-infrared prism spectrometer. Phys. Rev. Lett. **111**(18), 184801 (2013). https://doi.org/10.1103/PhysRevLett.111.184801
202. S. Wesch, B. Schmidt, C. Behrens, H. Delsim-Hashemi, P. Schmüser, A multi-channel THz and infrared spectrometer for femtosecond electron bunch diagnostics by single-shot spectroscopy of coherent radiation. Nucl. Instrum. Methods Phys. Res. Sect. A **665**, 40–47 (2011). https://doi.org/10.1016/j.nima.2011.11.037
203. Q.Q. Su, J.F. Hua, Z. Nie, Y. Ma, S. Liu, Y.F. Zheng, C.H. Pai, W. Lu, Temporal diagnostics of femtosecond electron bunches with complex structures using sparsity-based algorithm. Phys. Rev. Accel. Beams **21**(11), 112801 (2018). https://doi.org/10.1103/PhysRevAccelBeams.21.112801
204. D. Mihalcea, C.L. Bohn, U. Happek, P. Piot, Longitudinal electron bunch diagnostics using coherent transition radiation, in *Proceedings of the IEEE Particle Accelerator Conference*, vol. 2005, pp. 4254–4256 (2005). https://doi.org/10.1109/PAC.2005.1591782
205. M.K. Bock, Measuring the electron bunch timing with femtosecond resolution at FLASH (2013). https://bib-pubdb1.desy.de/record/139310/files/
206. M. Viti, M.K. Czwalinna, H. Dinter, C. Gerth, K. Przygoda, R. Rybaniec, H. Schlarb, et al., The bunch arrival time monitor at FLASH and European XFEL, in *Proceedings of the 16th International Conference on Accelerator and Large Experimental Physics Control Systems (ICALEPCS 2017)*, Barcelona, October 8–13 (2017). https://inspirehep.net/literature/1656225
207. A. Mostacci, M. Bellaveglia, E. Chiadroni, A. Cianchi, M. Ferrario, D. Filippetto, G. Gatti, C. Ronsivalle, Chromatic effects in quadrupole scan emittance measurements. Phys. Rev. Spec. Top. Accel Beams **15**(8), 82802 (2012). https://doi.org/10.1103/PhysRevSTAB.15.082802
208. Design report of the optimized RF units XLS Deliverable D4.2. Technical report
209. Menhir timing system. https://menhir-photonics.com/applications/timing-distribution/
210. K. Şafak, M. Xin, M.Y. Peng, F.X. Kärtner, Synchronous multi-color laser network with daily sub-femtosecond timing drift. Sci. Rep. (2018). https://doi.org/10.1038/s41598-018-30348-2
211. Cyclelasers (2021). https://www.cyclelasers.com/
212. K.L.F. Bane, M. Sands, The Short-Range Resistive Wall Wakefields (2008). https://doi.org/10.1063/1.50300
213. K.L.F. Bane, G. Stupakov, Resistive wall wakefield in the LCLS undulator, in *Proceedings of the IEEE Particle Accelerator Conference* (2005). https://doi.org/10.1109/PAC.2005.1591481
214. K. Bane, G. Stupakov, Using surface impedance for calculating wakefields in flat geometry. Phys. Rev. Spec. Top. Accel Beams (2015). https://doi.org/10.1103/PhysRevSTAB.18.034401
215. H. Henke, O. Napoly, Wake fields between two parallel resistive plates, in *2nd European Particle Accelerator Conference*, p. 12 (1990). https://cds.cern.ch/record/202863
216. B. Podobedov, Resistive wall wakefields in the extreme anomalous skin effect regime. Phys. Rev. Spec. Top. Accel Beams (2009). https://doi.org/10.1103/PhysRevSTAB.12.044401
217. G. Stupakov, K.L.F. Bane, P. Emma, B. Podobedov, Resistive wall wakefields of short bunches at cryogenic temperatures. Phys. Rev. Spec. Top. Accel Beams (2015). https://doi.org/10.1103/PhysRevSTAB.18.034402
218. J. Qiang, Suppression of wakefield induced energy spread inside an undulator through current shaping, in *FEL 2013: Proceedings of the 35th International Free-Electron Laser Conference* (2013). https://accelconf.web.cern.ch/fel2013/papers/mopso65.pdf
219. S. Reiche, GENESIS 1.3 User Manual. Technical report. http://genesis.web.psi.ch/download/documentation/genesis_manual.pdf
220. A.A. Lutman, J.P. MacArthur, M. Ilchen, Polarization control in an X-ray free-electron laser. Nat. Photonics **10**(7), 468–472 (2016). https://doi.org/10.1038/nphoton.2016.79
221. E.A. Schneidmiller, M.V. Yurkov, Obtaining high degree of circular polarization at x-ray free electron lasers via a reverse undulator taper. Phys. Rev. Spec. Top. Accel Beams **16**(11), 110702 (2013). https://doi.org/10.1103/PhysRevSTAB.16.110702
222. F. Nguyen, A. Bernhard, T. Schmidt, N. Thompson, J. Arnsberg, M. Breitenbach, M. Calvi, M. Carpanese, A. Cianchi, J.A. Clarke, H.M.C. Cortés, S. Danner, D. Dunning, S. Fatehi, R. Geometrante, J. Gethmann, S. Grohmann, A. Hinton, M. Kokole, B. Krasch, J. Marcos, T. Milharcic, Z. Nergiz, A. Petralia, J. Pockar, S.C. Richter, B. Shepherd, Design Studies for the Undulator, XLS-CompactLight Deliverable D5.2. Technical report (2021). https://espace.cern.ch/compactlight/Shared Documents/D5.2_XLS_Final.pdf
223. P. Emma, N. Holtkamp, H.-D. Nuhn, D. Arbelaez, J. Corlett, S. Myers, S. Prestemon, R. Schlueter, C. Doose, J. Fuerst, Q. Hasse, Y. Ivanyushenkov, M. Kasa, G. Pile, E. Trakhtenberg, E. Gluskin, A plan for the development of superconducting Undulator prototypes for LCLS-II and future FELs, in *Proceedings of the 36th International Free Electron Laser Conference, FEL 2014*, pp. 649–653 (2014)
224. J.D. Fuerst, E. Gluskin, Q.B. Hasse, Y. Ivanyushenkov, M. Kasa, I. Kesgin, Y. Shiroyanagi, Review of new developments in superconducting undulator technology at the APS, in *Proc. 60th ICFA Advanced Beam Dynamics Workshop (FLS'18)*, Shanghai. JACoW Publishing, Geneva (2018). https://doi.org/10.18429/JACoW-FLS2018-MOA2PL03. http://jacow.org/fls2018/papers/moa2pl03.pdf

225. M. Leitner, S. Prestemon, D. Arbelaez, S. Myers, SCU Segmented Cryostat Concept (2014). https://portal.slac.stanford.edu/sites/ad_public/FEL_RandD/scu_rd/_layouts/mobile/dispform.aspx?List=10182c32-8d3b-4c87-b668-e805a44ecab4&View=d6924684-e4ca-4239-b6ef-9a323f73942e&RootFolder=%2Fsites%2Fad_public%2FFEL_RandD%2Fscu_rd%2Fshared_docs%2FLCLS-I
226. J.A. Clarke, The Science and Technology of Undulators and Wigglers. Oxford University Press, UK (2004). https://doi.org/10.1093/acprof:oso/9780198508557.001.0001
227. S.D. Chen, K. Fang, L. Zhu, H.D. Nuhn, C. Pellegrini, J. Wu, S.D. Chen, C.S. Hwang, C.S. Hwang, Phase shifter design for iSASE, in *Proceedings of the 36th International Free Electron Laser Conference, FEL 2014* (2014). https://accelconf.web.cern.ch/FEL2014/papers/mop045.pdf
228. H.H. Lu, Y. Li, J. Pflueger, M. Wang, J. Zhuang, D. Wang, B. Faatz, Y. Li, J. Pflueger, A permanent magnet phase shifter for the European X-ray free electron laser. Nucl. Instrum. Methods Phys. Res. Sect. A Acceler. Spectrom. Detect. Assoc. Equip. (2009). https://doi.org/10.1016/j.nima.2009.03.217
229. M. Tischer, P. Neumann, A. Schöps, P. Vagin, Phase shifters for the FLASH2 FEL, in *IPAC 2014: Proceedings of the 5th International Particle Accelerator Conference* (2014). https://accelconf.web.cern.ch/ipac2014/papers/wepro032.pdf
230. H.P. Freund, Phase-matching segmented wigglers in free-electron lasers. Physical Review E—Statistical Physics, Plasmas, Fluids, and Related Interdisciplinary Topics (2004). https://doi.org/10.1103/PhysRevE.70.015501
231. G. Parisi, F. Ciocci, G. Dattoli, L. Giannessi, G.K. Voykov, PHase shifters for the sparc undulator system, in *Proceedings of the 27th International Free Electron Laser Conference, FEL 2005* (2005). http://accelconf.web.cern.ch/f05/PAPERS/MOPP056.PDF
232. J. Pflüger, M. Tischer, A Prototype Phase Shifter for the Undulator Systems at the TESLA X-Ray FEL. Technical report (2000). https://flash.desy.de/sites2009/site_vuvfel/content/e403/e1642/e810/e704/infoboxContent791/fel2000-08.pdf
233. L. Rossi, L. Bottura, Superconducting magnets for particle accelerators, in *Reviews of Accelerator Science and Technology: Volume 5 2012 Applications of Superconducting Technology to Accelerators* (2013). https://doi.org/10.1142/9789814449953_0
234. E. Todesco, Magnetic design of superconducting magnets, in *CAS-CERN Accelerator School: Superconductivity for Accelerators—Proceedings* (2014). https://doi.org/10.5170/CERN-2014-005.269
235. Cobham Technical Services: Opera (2d/3d) Vector Fields Software, Oxford, UK (2018)
236. D. Nölle, The diagnostic system at the European XFEL: commissioning and first user operation, in *Proceedings of the 7th International Beam Instrumentation Conference, IBIC 2018* (2018). https://doi.org/10.18429/JACoW-IBIC2018-tuoa01
237. Cryomech Inc., PT420 Cryooolers (2021). https://www.cryomech.com/products/pt420/
238. P. Emma, W. Craddock, C. Emma, J. Frisch, H.-D. Nuhn, C. Pellegrini, D. Arbelaez, J. Corlett, M. Leitner, S. Myers, S. Prestemon, R. Schlueter, C. Doose, J. Fuerst, Q. Hasse, Y. Ivanyushenkov, M. Kasa, G. Pile, E. Trakhtenberg, M. White, E. Gluskin, Conceptual Design of a Superconducting Undulator System for the LCLS-II Hard-X-Ray FEL (2014). https://portal.slac.stanford.edu/sites/ad_public/FEL_RandD/scu_rd/shared_docs/LCLS-II Conceptual Design/SCU-CDR.docx
239. Linde Kryotechnik AG: L-Series, The new standard for helium liquefiers and refrigerators (2021). https://www.linde-kryotechnik.ch/wp-content/uploads/2016/10/Linde_Kryotechnik_Produktbrosch_L-Series.pdf
240. G. Venkatarathnam, Fundamental principles and processes, in *Cryogenic Mixed Refrigerant Processes*, pp. 1–50 (2008). https://doi.org/10.1007/978-0-387-78514-1_
241. T. Kochenburger, Kryogene Gemischkältekreisläufe für Hochtemperatursupraleiter-Anwendungen. PhD thesis, Karlsruhe Institute of Technology (2018). https://publikationen.bibliothek.kit.edu/1000093562
242. E. Shabagin, S. Grohmann, Development of 10 kA current leads cooled by a cryogenic mixed-refrigerant cycle, in *IOP Conference Series: Materials Science and Engineering* (2019). https://doi.org/10.1088/1757-899X/502/1/012138
243. D. Gomse, Development of heat exchanger technology for cryogenic mixed-refrigerant cycles. PhD thesis, Karlsruhe Institute of Technology (2019). https://publikationen.bibliothek.kit.edu/1000119417
244. E. Gluskin, P. Emma, Y. Ivanyushenkov, A Superconducting Helical Undulator-Based FEL Prototype Cryomodule (2016). https://portal.slac.stanford.edu/sites/ad_public/FEL_RandD/scu_rd/shared_docs/SCU-Phase-II/FEL SCU Prototype proposal.pdf
245. Y. Xu, M. Barrios, F. Casagrande, M. Johnson, M. Leitner, D. Arenius, V. Ganni, W.J. Schneider, M.A. Wiseman, Integrated thermal analysis of the FRIB cryomodule design, in *IPAC 2012—International Particle Accelerator Conference 2012* (2012). https://www.osti.gov/servlets/purl/1047739
246. J. Arnsberg, Wärmelastberechnung CompactLight SCU, Internal Technical Report. Technical report, Karlsruhe Institute of Technology (2021)
247. S. Reiche, Tolerance studies for the hard X-ray beamline of SwissFEL, in *FEL 2009—31st International Free Electron Laser Conference* (2009). https://accelconf.web.cern.ch/FEL2009/papers/wepc58.pdf
248. EA Schneidmiller, M.V. Yurkov, Reverse undulator tapering for polarization control and background-free harmonic production in XFELs: results from FLASH, in *Proceedings of the 38th International Free-Electron Laser Conference, FEL 2017* (2017). https://doi.org/10.18429/JACoW-FEL2017-MOP032
249. T. Schmidt, M. Calvi, APPLE X undulator for the SwissFEL Soft X-ray beamline athos. Synchrotron Radiat. News **31**(3), 35–40 (2018). https://doi.org/10.1080/08940886.2018.1460174

250. S. Sasaki, K. Kakuno, T. Takada, T. Shimada, K.I. Yanagida, Y. Miyahara, Design of a new type of planar undulator for generating variably polarized radiation. Nuclear Inst. Methods Phys. Res. A (1993). https://doi.org/10.1016/0168-9002(93)90153-9
251. Y. Ivanyushenkov et al., Status of the development of superconducting undulators for storage rings and free electron lasers at the advanced photon source, in *Proceedings, 2nd North American Particle Accelerator Conference (NAPAC2016): Chicago, Illinois*, USA, October 9–14, 2016, pp. 1–06 (2017). https://doi.org/10.18429/JACoW-NAPAC2016-THA1CO06
252. I. Kesgin, M. Kasa, Q. Hasse, Y. Ivanyushenkov, Y. Shiroyanagi, J. Fuerst, E. Barzi, D. Turrioni, A.V. Zlobin, E. Gluskin, Development of short-period Nb3Sn superconducting planar undulators. IEEE Trans. Appl. Supercond. **29**(5), 1–4 (2019). https://doi.org/10.1109/TASC.2019.2897645
253. J. Bahrdt, E. Gluskin, Cryogenic permanent magnet and superconducting undulators. Nucl. Instrum. Methods Phys. Res. Sect. A **907**, 149–168 (2018). https://doi.org/10.1016/j.nima.2018.03.069
254. J. Bahrdt, S. Grimmer, In-vacuum APPLE II undulator with force compensation. AIP Conf. Proc. **2054**(January), 030031 (2019). https://doi.org/10.1063/1.5084594
255. O. Chubar, P. Elleaume, J. Chavanne, A three-dimensional magnetostatics computer code for insertion devices. J. Synchrotron Radiat. **5**(3), 481–484 (1998). https://doi.org/10.1107/s0909049597013502
256. M. Calvi, C. Camenzuli, E. Prat, T. Schmidt, Transverse gradient in Apple-type undulators. J. Synchrotron Radiat. **24**(3), 600–608 (2017). https://doi.org/10.1107/s1600577517004726
257. P. Baumgärtel, P. Grundmann, T. Zeschke, A. Erko, J. Viefhaus, F. Schäfers, H. Schirmacher, RAY-UI: new features and extensions, in *AIP Conference Proceedings*, vol. 2054. Taiwan, p. 060034 (2019). https://doi.org/10.1063/1.5084665
258. M. Störmer, F. Siewert, H. Sinn, Preparation and characterization of B4C coatings for advanced research light sources, in *Journal of Synchrotron Radiation*, vol. 23, pp. 50–58. International Union of Crystallography, Italy (2016). https://doi.org/10.1107/S1600577515020901
259. H.M. Castañeda Cortés, D.J. Dunning, M.D. Roper, N.L. Thompson, Optical beam quality analysis of the CLARA test facility using second moment analysis, in *Proceedings of the 38th International Free-Electron Laser Conference, FEL 2017*, pp. 543–546. JACoW Publishing, USA (2017). https://doi.org/10.18429/JACoW-FEL2017-WEP062
260. E.L. Saldin, E.A. Schneidmiller, M.V. Yurkov, A simple method for the determination of the structure of ultrashort relativistic electron bunches. Nucl. Instrum. Methods Phys. Res. Sect. A **539**(3), 499–526 (2005). https://doi.org/10.1016/j.nima.2004.11.002
261. FEL gratings—Inprentus. https://www.inprentus.com/fel-gratings
262. P. Heimann, O. Krupin, W.F. Schlotter, J. Turner, J. Krzywinski, F. Sorgenfrei, M. Messerschmidt, D. Bernstein, J. Chalupský, V. Hájková, S. Hau-Riege, M. Holmes, L. Juha, N. Kelez, J. Lüning, D. Nordlund, M. Fernandez Perea, A. Scherz, R. Soufli, W. Wurth, M. Rowen, Linac Coherent Light Source soft x-ray materials science instrument optical design and monochromator commissioning. Rev. Sci. Instrum. **82**(9), 093104 (2011). https://doi.org/10.1063/1.3633947
263. R. Soufli, M. Fernández-Perea, S.L. Baker, J.C. Robinson, E.M. Gullikson, P. Heimann, V.V. Yashchuk, W.R. McKinney, W.F. Schlotter, M. Rowen, Development and calibration of mirrors and gratings for the Soft X-ray Materials Science beamline at the Linac Coherent Light Source free-electron laser. Appl. Opt. **51**(12), 2118–2128 (2012). https://doi.org/10.1364/AO.51.002118
264. K. Tiedtke, J. Feldhaus, U. Hahn, U. Jastrow, T. Nunez, T. Tschentscher, S.V. Bobashev, A.A. Sorokin, J.B. Hastings, S. Möller, L. Cibik, A. Gottwald, A. Hoehl, U. Kroth, M. Krumrey, H. Schöppe, G. Ulm, M. Richter, Gas detectors for x-ray lasers. J. Appl. Phys. **103**(9), 94511 (2008). https://doi.org/10.1063/1.2913328
265. T. Tschentscher, C. Bressler, J. Grünert, A. Madsen, A.P. Mancuso, M. Meyer, A. Scherz, H. Sinn, U. Zastrau, Photon beam transport and scientific instruments at the European XFEL. Appl. Sci. (2017). https://doi.org/10.3390/app7060592
266. C.J. Milne, T. Schietinger, M. Aiba, A. Alarcon, SwissFEL: The Swiss X-ray free electron laser. Appl. Sci. (2017). https://doi.org/10.3390/app7070720
267. J. Grünert, M.P. Carbonell, F. Dietrich, T. Falk, W. Freund, A. Koch, N. Kujala, J. Laksman, J. Liu, T. Maltezopoulos, K. Tiedtke, U.F. Jastrow, A. Sorokin, E. Syresin, A. Grebentsov, O. Brovko, X-ray photon diagnostics at the European XFEL. J. Synchrotron Radiat. **26**(5), 1422–1431 (2019). https://doi.org/10.1107/S1600577519006611
268. J. Laksman, J. Buck, L. Glaser, M. Planas, F. Dietrich, J. Liu, T. Maltezopoulos, F. Scholz, J. Seltmann, G. Hartmann, M. Ilchen, W. Freund, N. Kujala, J. Viefhaus, J. Grünert, Commissioning of a photoelectron spectrometer for soft X-ray photon diagnostics at the European XFEL. J. Synchrotron Radiat. **26**(4), 1010–1016 (2019). https://doi.org/10.1107/S1600577519003552
269. E. Allaria, B. Diviacco, C. Callegari, P. Finetti, B. Mahieu, J. Viefhaus, M. Zangrando, G. De Ninno, G. Lambert, E. Ferrari, J. Buck, M. Ilchen, B. Vodungbo, N. Mahne, C. Svetina, C. Spezzani, S. Di Mitri, G. Penco, M. Trovó, W.M. Fawley, P.R. Rebernik, D. Gauthier, C. Grazioli, M. Coreno, B. Ressel, A. Kivimäki, T. Mazza, L. Glaser, F. Scholz, J. Seltmann, P. Gessler, J. Grünert, A. De Fanis, M. Meyer, A. Knie, S.P. Moeller, L. Raimondi, F. Capotondi, E. Pedersoli, O. Plekan, M.B. Danailov, A. Demidovich, I. Nikolov, A. Abrami, J. Gautier, J. Lüning, P. Zeitoun, L. Giannessi, Control of the polarization of a vacuum-ultraviolet, high-gain, free-electron laser. Phys. Rev. X **4**(4), 41040 (2014). https://doi.org/10.1103/PhysRevX.4.041040

270. J. Rehanek, C.J. Milne, J. Szlachetko, J. Czapla-Masztafiak, J. Schneider, T. Huthwelker, C.N. Borca, R. Wetter, L. Patthey, P. Juranic, A compact and versatile tender X-ray single-shot spectrometer for online XFEL diagnostics. J. Synchrotron Radiat. **25**(1), 16–19 (2018). https://doi.org/10.1107/S1600577517012796
271. N. Kujala, W. Freund, J. Liu, A. Koch, T. Falk, M. Planas, F. Dietrich, J. Laksman, T. Maltezopoulos, J. Risch, F. Dall'antonia, J. Grünert, Hard x-ray single-shot spectrometer at the European X-ray Free-Electron Laser. Rev. Sci. Instrum. **91**(10), 103101 (2020). https://doi.org/10.1063/5.0019935
272. M. Harmand, R. Coffee, M.R. Bionta, M. Chollet, D. French, D. Zhu, D.M. Fritz, H.T. Lemke, N. Medvedev, B. Ziaja, S. Toleikis, M. Cammarata, Achieving few-femtosecond time-sorting at hard X-ray free-electron lasers. Nat. Photonics **7**(3), 215–218 (2013). https://doi.org/10.1038/nphoton.2013.11
273. M.R. Bionta, N. Hartmann, M. Weaver, D. French, D.J. Nicholson, J.P. Cryan, J.M. Glownia, K. Baker, C. Bostedt, M. Chollet, Y. Ding, D.M. Fritz, A.R. Fry, D.J. Kane, J. Krzywinski, H.T. Lemke, M. Messerschmidt, S. Schorb, D. Zhu, W.E. White, R.N. Coffee, Spectral encoding method for measuring the relative arrival time between x-ray/optical pulses. Rev. Sci. Instrum. **85**(8), 083116 (2014). https://doi.org/10.1063/1.4893657
274. N. Hartmann, W. Helml, A. Galler, M.R. Bionta, J. Grünert, S.L. Molodtsov, K.R. Ferguson, S. Schorb, M.L. Swiggers, S. Carron, C. Bostedt, J.C. Castagna, J. Bozek, J.M. Glownia, D.J. Kane, A.R. Fry, W.E. White, C.P. Hauri, T. Feurer, R.N. Coffee, Sub-femtosecond precision measurement of relative X-ray arrival time for free-electron lasers. Nat. Photonics **8**(9), 706–709 (2014). https://doi.org/10.1038/nphoton.2014.164
275. R. Ivanov, J. Liu, G. Brenner, M. Brachmanski, S. Düsterer, FLASH free-electron laser single-shot temporal diagnostic: Terahertz-field-driven streaking, in *Journal of Synchrotron Radiation*, vol. 25, pp. 26–31. International Union of Crystallography, USA (2018). https://doi.org/10.1107/S160057751701253X. https://pubmed.ncbi.nlm.nih.gov/29271747/
276. N. Hartmann, G. Hartmann, R. Heider, M.S. Wagner, M. Ilchen, J. Buck, A.O. Lindahl, C. Benko, J. Grünert, J. Krzywinski, J. Liu, A.A. Lutman, A. Marinelli, T. Maxwell, A.A. Miahnahri, S.P. Moeller, M. Planas, J. Robinson, A.K. Kazansky, N.M. Kabachnik, J. Viefhaus, T. Feurer, R. Kienberger, R.N. Coffee, W. Helml, Attosecond time-energy structure of X-ray free-electron laser pulses. Nat. Photonics **12**(4), 215–220 (2018). https://doi.org/10.1038/s41566-018-0107-6
277. J. Duris, S. Li, T. Driver, E.G. Champenois, J.P. MacArthur, A.A. Lutman, Z. Zhang, P. Rosenberger, J.W. Aldrich, R. Coffee, G. Coslovich, F.J. Decker, J.M. Glownia, G. Hartmann, W. Helml, A. Kamalov, J. Knurr, J. Krzywinski, M.F. Lin, J.P. Marangos, M. Nantel, A. Natan, J.T. O'Neal, N. Shivaram, P. Walter, A.L. Wang, J.J. Welch, T.J.A. Wolf, J.Z. Xu, M.F. Kling, P.H. Bucksbaum, A. Zholents, Z. Huang, J.P. Cryan, A. Marinelli, Tunable isolated attosecond X-ray pulses with gigawatt peak power from a free-electron laser. Nat. Photonics **14**(1), 30–36 (2020). https://doi.org/10.1038/s41566-019-0549-5
278. Y. Liu, M. Seaberg, D. Zhu, J. Krzywinski, F. Seiboth, C. Hardin, D. Cocco, A. Aquila, B. Nagler, H.J. Lee, S. Boutet, Y. Feng, Y. Ding, G. Marcus, A. Sakdinawat, High-accuracy wavefront sensing for x-ray free electron lasers. Optica **5**(8), 967 (2018). https://doi.org/10.1364/optica.5.000967
279. Home Imagine Optic. https://www.imagine-optic.com/
280. S. Schulz, I. Grguraš, C. Behrens, H. Bromberger, J.T. Costello, M.K. Czwalinna, M. Felber, M.C. Hoffmann, M. Ilchen, H.Y. Liu, T. Mazza, M. Meyer, S. Pfeiffer, P. Predki, S. Schefer, C. Schmidt, U. Wegner, H. Schlarb, A.L. Cavalieri, Femtosecond all-optical synchronization of an X-ray free-electron laser. Nat. Commun. **6**(1), 1–11 (2015). https://doi.org/10.1038/ncomms6938
281. T. Metzger T, Ultrafast Thin-Disk Amplifiers, in *Source Workshop*, Amsterdam, Netherlands, p. 55 (2019). https://www.euvlitho.com/2019/S55.pdf
282. M. Schaer et al., rf traveling-wave electron gun for photoinjectors. Phys. Rev. AB, 72001 (2016)
283. A.E. Vlieks, G. Caryotakis, W.R. Fowkes, E.N. Jongewaard, E.C. Landahl, R. Loewen, N.C. Luhmann, Development of an X-band RF Gun at SLAC. AIP Conf. Proc. **625**(1), 107–116 (2002)
284. A.E. Vlieks, V. Dolgashev, S. Tantawi, S. Anderson, F. Hartemann, R. Marsh, X-band RF gun development, in *Proceedings of IPAC'10*, Kyoto, Japan, pp. 3816–3818 (2010)
285. R.A. Marsh, F. Albert, S.G. Anderson, G. Beer, T.S. Chu, R.R. Cross, G.A. Deis, C.A. Ebbers, D.J. Gibson, T.L. Houck, F.V. Hartemann, C.P.J. Barty, A. Candel, E.N. Jongewaard, Z. Li, C. Limborg-Deprey, A.E. Vlieks, F. Wang, J.W. Wang, F. Zhou, C. Adolphsen, T.O. Raubenheimer, Modeling and design of an X-band rf photoinjector. Phys. Rev. ST Accel. Beams **15**(10), 102001 (2012). https://doi.org/10.1103/PhysRevSTAB.15.102001
286. F.B. Kiewiet, Generation of ultra-short, high brightness relativistic electron bunches. PhD thesis, Technische Universiteit Eindhoven (2003). https://doi.org/10.6100/IR571240
287. K. Halbach, R.F. Holsiger, SUPERFISH—a computer program for evaluation of RF cavities with cylindrical symmetry. Part. Accel. **7**, 213–222 (1976)
288. Ansys High Frequency Simulation Studio. https://www.ansys.com/products/electronics/ansys-hfss
289. J.R.M. Vaughan, Multipactor. IEEE Trans. Electron Devices **35**(7), 1172–1180 (1988)
290. A.M. Perez, C. Tienda, C. Vicente, S. Anza, J. Gil, B. Gimeno, V.E. Boria, D. Raboso, Prediction of multipactor breakdown thresholds in coaxial transmission lines for traveling, standing, and mixed waves. IEEE Trans. Plasma Sci. **37**(10), 2031–2040 (2009)
291. D. Gonzalez-Iglesias, A.M. Perez, S. Anza, J.V. Cardona, B. Gimeno, V.E. Boria, D. Raboso, C. Vicente, J. Gil, F. Caspers, L. Conde, Multipactor mitigation in coaxial lines by means of permanent magnets. IEEE Trans. Electron Devices **61**(12), 4224–4231 (2014)

292. J. Shao, Investigations on rf breakdown phenomenon in high gradient accelerating structures. PhD thesis, Tsinghua U., Beijing, Dept. Eng. Phys. (2016). https://doi.org/10.1007/978-981-10-7926-9
293. M. Behtouei, Design and Measurements of the High Gradient Accelerating Structures. PhD thesis, Universita di Roma 'La Sapienza' (2019). https://doi.org/10.13140/RG.2.2.16781.90086
294. D. Gonzalez-Iglesias, D. Esperante, B. Gimeno, M. Boronat, C. Blanch, N. Fuster-Martinez, P. Martinez-Reviriego, P. Martin-Luna, J. Fuster, Analytical RF pulse heating analysis for high gradient accelerating structures. IEEE Trans. Nucl. Sci. **68**(2), 78–91 (2021). https://doi.org/10.1109/TNS.2021.3049319
295. B.J. Woolley, High Power X-band RF Test Stand Development and High Power Testing of the CLIC Crab Cavity. PhD thesis, Lancaster U. (2015). https://inspirehep.net/literature/1679128
296. K. Flöttmann, Astra: a space charge tracking algorithm (2011). https://www.desy.de/texttildelow mpyflo/
297. A. Latina, RF-Track Reference Manual. Zenodo. https://doi.org/10.5281/zenodo.3887085
298. T. Hara, T. Tanaka, H. Kitamura, T. Bizen, X. Marechal, T. Seike, T. Kohda, Y. Matsuura, Cryogenic permanent magnet undulators. Phys. Rev. Spec. Top. Accel. Beams **27**, 050702 (2004). https://doi.org/10.1103/PhysRevSTAB.7.050702
299. C. Benabderrahmane, N. Bechu, P. Berteaud, L. Chapuis, M.E. Couprie, J.P. Daguerre, J.M. Filhol, C. Herbeaux, A. Lestrade, M. Louvet, J.L. Marlats, K. Tavakoli, M. Valleau, D. Zerbib, Development of Pr2Fe14B cryogenic undulator CPMU at SOLEIL, in *Proceedings of IPAC2011*, p. 149. JACoW, San Sebastián, Spain (2011)
300. ...F. Nguyen, A. Aksoy, A. Bernhard, M. Calvi, J.A. Clarke, H.M. Castañeda Cortés, A.K. Cross, G. Dattoli, D. Dunning, R. Geometrante, J. Gethmann, S. Hellmann, M. Kokole, J. Marcos, Z. Nergiz, F. Perez, A. Petralia, S.C. Richter, T. Schmidt, D. Schoerling, N. Thompson, K. Zhang, L. Zhang, D. Zhu, Technologies for the CompactLight undulator, XLS-CompactLight Deliverable D5.1. Technical report (2019). https://www.compactlight.eu/uploads/Main/D5.1_XLS_Final.pdf
301. A. Ghaith, O. Marcouille, I. Andriyash, J.A. Clarke, G. Sharma, M. Valleau, F. Briquez, F. Nguyen, G. Dattoli, A.R. Maier, M.E. Couprie, EuPRAXIA deliverable 6.1: report on state-of-the-art short period undulators. Technical report (2016). https://theuniversityofliverpool.sharepoint.com/:b:/r/sites/eupraxia/Shared Documents/Deliverables/Reports/EuPRAXIA Deliverable 6 Report SOLEIL 20161031_D6.1.pdf?csf=1&web=1&e=eMZvC6
302. M. Valleau, F. Briquez, A. Ghaith, F. Marteau, O. Marcouille, C. Kitegi, F. Blache, M.E. Couprie, Development of cryogenic permanent magnet undulators at SOLEIL. Synchrotron Radiat. News **31**(3), 42–47 (2018). https://doi.org/10.1080/08940886.2018.1460175
303. G. D'Auria, M. Aicheler, E. Gazis, A. Latina, R. Rochow, XLS – D1.2: Data Management Plan – v1.3. Zenodo. On behalf of the CompactLight Collaboration (2021). https://doi.org/10.5281/zenodo.6103164